

UC Riverside

UC Riverside Electronic Theses and Dissertations

Title

Designing Functional Cages: From Luminescent Sensors to Artificial Enzymes

Permalink

<https://escholarship.org/uc/item/2v88v9j1>

Author

Bogie, Paul Michael

Publication Date

2019

Copyright Information

This work is made available under the terms of a Creative Commons Attribution-NoDerivatives License, available at <https://creativecommons.org/licenses/by-nd/4.0/>

Peer reviewed|Thesis/dissertation

UNIVERSITY OF CALIFORNIA
RIVERSIDE

Designing Functional Cages: From Luminescent Sensors to Artificial Enzymes

A Dissertation submitted in partial satisfaction
of the requirements for the degree of

Doctor of Philosophy

in

Chemistry

by

Paul M Bogie

September 2019

Dissertation Committee:

Dr. Richard J. Hooley, Chairperson

Dr. Boniface Fokwa Tsinde

Dr. Dave Martin

Copyright by
Paul M Bogie
2019

The Dissertation of Paul M Bogie is approved:

Committee Chairperson

University of California, Riverside

ACKNOWLEDGMENTS

First and foremost, I would like to thank my parents Patrick and Mary Bogie, and my brother Sean Bogie and Garrett “Teddy” Dykmann for their loving support. The drive to never give up is strong in all of us, and I really appreciate the endless advice, patience, and confidence that has helped me push through.

To my undergraduate advisor Dr. Jaime Mueller, thank you for teaching me many new techniques and building my passion for organic chemistry, I wouldn't be here without you. Thank you for your continued support along with Dr.'s Brett Bodsgaard and Nathan Lien.

A very special thank you is due to Dr. Richard Hooley, for the massive impact he has had on my professional development as a chemist. I sincerely appreciate all the wisdom and advice you have given me over the past 5 years. As well as your understanding through the many challenges I faced throughout. Your approach to research, and ability to turn unique results into full-fledged publications is one that others should strive for.

I would also like to thank friends and Coworkers here at UC Riverside. The “Hooligans” especially Courtney Ngai, Tabitha Miller and Phil Dietz for the help tackling the endless list of new cage ideas. Finally, I a special thank you to Lauren Holloway. I will forever be in awe of your unwavering patience and work effort. Thank you for showing me how to succeed in the Hooley lab.

To both Phil Dietz and Max Mayther, for our combined creation of “Stout Day”, without which writing would have been unbearable. To Dana Chambers, for all the conversations, coffee breaks, lunches, brunches, winery trips and endless sass that helped

make this past 5 years special. And a big thank you to my amazing group of friends I have had since my first day here, Zack and Emily Palchak, Dejan Stekovic, and Lilly Quint. Thanks for the memories and cheers to the new ones we will make moving forward!

The text of this dissertation, in part or in full, is a reprint of the material as they appear in the following publications:

Chapter 1: Bogie, P. M.; Miller, T. F.; Hooley, R. J. "Synthesis and Applications of Endohedrally Functionalized Metal-Ligand Cage Complexes." *Isr. J. Chem.* **2019**, *59*, 130–139.

Chapter 2: Bogie, P. M.; Holloway, L. R.; Lyon, Y.; Julian, R. R.; Hooley, R. J. "Metal-selective coordination and enhanced fluorescence of a self-assembling ligand scaffold" *Supramol. Chem.* **2017**, *29*, 936–945.

Chapter 3: Holloway, L. R.; Bogie, P. M.; Lyon, Y.; Julian, R. R.; Hooley, R. J. "Stereoselective Postassembly CH Oxidation of Self-Assembled Metal-Ligand Cage Complexes" *Inorg. Chem.*, **2017**, *56*, 11435-11442.

And

Bogie, P. M.; Holloway, L. R.; Lyon, Y.; Onishi, N. C.; Beran, G. J. O.; Julian, R. R.; Hooley, R. J. "A Springloaded Metal-Ligand Mesocate Allows Access to Trapped Intermediates of Self-Assembly" *Inorg. Chem.* **2018**, *57*, 4155–4163.

Chapter 4: Holloway, L. R.; Bogie, P. M.; Lyon, Y.; Ngai, C.; Miller, T. F.; Julian, R. R.; Hooley, R. J. "Tandem Reactivity of a Self-Assembled Cage Catalyst with Endohedral Acid Groups." *J. Am. Chem. Soc.* **2018**, *140*, 8078–8081.

And

Bogie, P. M.; Holloway, L. R.; Ngai, C.; Miller, T. F.; Grewal, D. K.; Hooley, R. J. “A Self-Assembled Cage with Endohedral Acid Groups both Catalyzes Substitution Reactions and Controls their Molecularity.” *Chem. Eur. J.* **2019**, ASAP, DOI: 10.1002/chem.201902049

The co-author Richard J. Hooley listed in these publications directed and supervised the research which forms the basis for this dissertation. All other co-authors listed in these publications contributed technical expertise.

DEDICATION

This dissertation is dedicated to my loving grandparents,

Patrick and Joann Bogie, and Jim and Dorothy Payne

You will always be with me.

ABSTRACT OF THE DISSERTATION

Designing Functional Cages: From Luminescent Sensors to Artificial Enzymes

by

Paul M Bogie

Doctor of Philosophy, Graduate Program in Chemistry
University of California, Riverside, September 2019
Dr. Richard J. Hooley, Chairperson

Self-assembled metal organic cages are supramolecular compounds with a unique internal cavity capable of creating an alternate nanophase inside of a reaction vessel (e.g. creating a hydrophilic environment inside of an organic solvent like acetonitrile). By exploiting this internal cavity, the complexes may be used for a wide array of applications in molecular recognition, small molecule transport, catalysis and even as molecular machines. Often the function of these cages becomes limited due to the flat aromatic ligands used in the assembly process. To improve the function of these cages, new methods for installing reactive groups on the interior of the cage must be explored.

This work focuses on new methods of introducing function to self-assembled cages through modifications of the ligand and cage with the goal of creating new biomimetic catalysts. These modifications can be used introduce new reactivity. By introducing native fluorescence to the chelating motif, a new class of metal selective fluorophores was discovered. While adding reactivity can be more challenging, it can be simplified to three classes: reactions that modify a preformed cage, reactions activated by the cage, and

reactions hosted within the cage. Cages can be modified after their assembly through the introduction of reactive components. Internalized doubly benzylic methylene subunits can be altered post-assembly via radical promoted oxidation, with the resulting products exhibiting an impressive level of stereocontrol. The use of a strained complex enables transamination reactions to be performed at ambient temperatures giving rise to rare intermediates along the assembly pathway. A large Fe^{2+} -iminopyridine cage bearing twelve internal carboxylic acid groups was synthesized which can affect 1000-fold rate enhancements for several reactive processes at high turnover. Further, internalization of the acid functional groups allows a tandem cage-to-cage reaction and can vary the mechanism reactions, which is unattainable by similar “free” acid catalysts. This combined process of molecular recognition and substrate activation is reminiscent of that found in the active site of enzymes. Finally, a unfunctionalized tetrahedral cage exhibiting high binding affinity, up to $200,000 \text{ M}^{-1}$, was synthesized. This high binding can be used to encapsulate a catalyst to accelerate substitution reactions. This reactivity is akin to the symbiotic relationship of an apoenzyme and cofactor and is unprecedented in synthetic hosts. This is because the selective simultaneous encapsulation of multiple different guests is extremely difficult and exhibits high entropic penalties. The results of this process not only affect the reaction rate but also biased selectivity of substrates in forming quaternary complexes enabling a controlled change in the reaction mechanism.

TABLE OF CONTENTS

Acknowledgments	iv
Abstract	viii
Table of Contents	x
List of Figures	xiv
List of Tables	xli
Chapter 1: Design, Assembly and Function of Supramolecular Cages	
1.1. Rational Design of Supramolecular Cages	1
1.2. Ligand Effects in the Stability and Control of Self-Assembly	6
1.3. Molecular Recognition in Unfunctionalized Supramolecular Cages	9
1.4. Endohedral Cages with “Inert” Functions	13
1.5. Molecular Recognition Controlled by Small Endohedral Groups	14
1.6. Reactions with Self-Assembled Cages	19
1.7. Introduction of Endohedral Functionality Through Post-Assembly Modification	20
1.8. Catalysis with Endohedrally Functionalized Cages	22
1.9. Summary and Outlook	25
1.10. References	27
Chapter 2: Metal-Selective Coordination and Enhanced Fluorescence of a Self-Assembling Ligand Scaffold	
2.1. Introduction	34

2.2. Rational Design and Synthesis of Ligands	35
2.3. Investigation of Metal Coordination	36
2.4. Metal Specific Changes in Emission	42
2.5. Structural Characterization and Stability	49
2.6. Conclusion	52
2.7. References	53
Chapter 3: Thermodynamic Control and Post-Assembly Modifications of Iminopyridine Coordination Cages	
3.1. Introduction	55
3.2. Post Assembly Modifications Through Ligand Centered CH Oxidation	55
3.3. Synthesis and Ligand Centered Oxidation of Diaminoxanthene Mesocate	56
3.4. Synthesis and Ligand Centered Oxidation of Diaminofluorene Tetrahedron	59
3.5. Summary of Methylene Oxidations	61
3.6. Transimination of a Strained <i>Meso</i> -Helicate	62
3.7. Displacement of X Using Fluorenyl Ligands	65
3.8. Displacement of X Using the Tripodal APA Ligand	76
3.9. Displacement of X Using Ligands of Similar Electronics	80
3.10. Conclusion	89
3.11. References	90
Chapter 4: Design and Applications of an Acid-Containing Biomimetic Nano Reactor	

4.1. Introduction	93
4.2. Synthesis of Extended Fluorenyl Ligands and Multicomponent Self-Assembly	93
4.3. Acid Catalyzed Solvolysis of Aromatic Acetals	103
4.4. Tandem Reactivity Effecting Cage-to-Cage Transformation	107
4.5. Cage Catalyzed Thioetherification via Acid Promoted Dissociation	110
4.6. Molecular Recognition and Mechanistic Analysis	119
4.7. Catalytic Self-Destruction: Design of a Negative Feedback Loop	130
4.8. Conclusion	131
4.9. References	133
Chapter 5: Biomimetic Catalysis <i>via</i> a Co-Factor Type Mechanism	
5.1. Introduction	136
5.2. Acid Catalyzed Thioetherification Mediated by a Non-Reactive Host	137
5.3. Kinetic Analysis of Nucleophile Variations	139
5.4. Kinetic Analysis of Co-Factor Variations	141
5.5. Determination of Binding Affinities	146
5.6. Summary of Cofactor Mediated Substitution of Trityl Compounds	150
5.7. Investigation of Additional Cofactors for New Forms of Reactivity	151
5.8. References	154
Chapter 6: Additional Projects	
6.1. Introduction	156
6.2. Phenanthroline	156

6.3. Extending the Iminopyridine Scaffold	162
6.4. Reverse Iminopyridine	165
6.6. References	168
Chapter 7: Experimental	
7.1. General Information	170
7.2. Experimental for Chapter 2	171
7.3. Experimental for Chapter 3	180
7.4. Experimental for Chapter 4	189
7.5. Experimental for Chapter 5	207
7.6. Experimental for Chapter 6	208
7.7. Selected Spectra for Chapter 2	221
7.8. Selected Spectra for Chapter 3	233
7.9. Selected Spectra for Chapter 4	236
7.10. Selected Spectra for Chapter 5	289
7.11. Selected Spectra for Chapter 6	295
7.12. References	300

LIST OF FIGURES

- Figure 1.1.** Synthesis of a metal-organic species: a) an M_2L_3 *meso*-helicite made using Fe^{2+} and an iminopyridine chelator; b) an M_4L_6 tetrahedron with Ga^{3+} and a catecholate chelator; c) $M_{12}L_{24}$ and d) $M_{24}L_{28}$ nanospheres made from pyridyl- Pd^{2+} contacts. 2
- Figure 1.2.** Small changes in ligand shape effecting large differences in stoichiometry. 4
- Figure 1.3.** The two isomeric connective possibilities of Fe^{2+} -iminopyridine centers, and the two possible enantiomers of each with Λ (left) and Δ (right) rotation of the *fac* centers. 5
- Figure 1.4.** Ligand exchange in the social self-sorting of Pd_2L_4 complexes. 8
- Figure 1.5.** Self-sorting and subcomponent exchange in Fe-iminopyridine M_2L_3 *meso*-helicites. 9
- Figure 1.6.** Molecular recognition in “featureless” cages: a) stabilization of reactive white phosphorus; b) selective encapsulation of sucrose; c) trigger and stabilization of reactive photoswitches. 10
- Figure 1.7.** Fluorescent self-assemblies. a) Ligand centered emission; b) Metal centered emissive complexes. 12
- Figure 1.8.** Nanostructures possible by decorating the interior of $Pd_{12}L_{24}$ cage complexes. 13
- Figure 1.9.** Selective cation and anion recognition with Pd_2L_4 paddlewheels with internal lone pairs and acidic groups. 15
- Figure 1.10.** Selective anion recognition and structural control in supramolecular cages.

	17
Figure 1.11. Structural switching of M ₄ L ₄ cages via anion templation.	19
Figure 1.12. Reactions with covalently attached groups. a) Polymer growth on the interior of a functionalized cage. b) Cage-promoted nucleophilic addition.	21
Figure 1.13. Organometallic catalysis in endohedrally functionalized nanospheres.	23
Figure 1.14. Concurrent tandem catalysis with two differently functionalized nanospheres.	25
Figure 2.1. Structures of strongly metal coordinating motifs.	35
Figure 2.2. Synthetic route to <i>bis</i> -coordinating HINT ligands 2.1 , and 2.2 .	36
Figure 2.3. UV-Vis absorption spectra of the titration of various metal salts into DMSO solutions of anionic ligand Na• 2.1 : a) MX ₂ = Zn(OTf) ₂ , b) MX ₂ = Fe(ClO ₄) ₂ , c) MX ₂ = Co(ClO ₄) ₂ . [Na• 2.1] = 30 μM. Job plot of the assembly process measured based at specified wavelength: d) Zn(OTf) ₂ – 430 nm, e) Fe(ClO ₄) ₂ – 460 nm, f) Co(ClO ₄) ₂ – 400 nm.	
*Adjusted Absorbance = $Abs - \left(\frac{[ligand]}{[ligand] + [M]} \right) Abs_0$	37
Figure 2.4. a) Stern-Volmer plot for the absorbance titration of Zn(OTf ₂) into a solution of Na• 2.1 in DMSO. b) Titration of Zn(OTf ₂) into a solution of Na• 2.1 in a 2:1 mixture of DMSO and H ₂ O monitored via UV/Vis spectroscopy.	39
Figure 2.5. UV-Vis absorption spectra of the titration of various metal salts into DMSO solutions of anionic ligand Na• 2.2 : a) MX ₂ = Zn(OTf) ₂ , b) MX ₂ = Fe(ClO ₄) ₂ , c) MX ₂ = Co(ClO ₄) ₂ . [Na• 2.2] = 30 μM.	40

Figure 2.6. UV-Vis absorption spectra of the titration of various metal salts into DMSO solutions of anionic ligand Na•2.1: a) $\text{MX}_2 = \text{Hg}(\text{OTf})_2$, b) $\text{MX}_2 = \text{NiSO}_4$, c) $\text{MX}_2 = \text{La}(\text{OTf})_3$. $[\text{Na}\bullet\mathbf{2.1}] = 30 \mu\text{M}$. 41

Figure 2.7. a) Synthesis of ligand 2.3 see Scheme 2.1 for details. UV-Vis absorption spectra of the titration of various metal salts into DMSO solutions of anionic ligand Na•2.3: b) $\text{MX}_2 = \text{Zn}(\text{OTf})_2$, c) $\text{MX}_2 = \text{Fe}(\text{ClO}_4)_2$, d) $\text{MX}_2 = \text{Co}(\text{ClO}_4)_2$. $[\text{Na}\bullet\mathbf{2.3}] = 240 \mu\text{M}$. 42

Figure 2.8. Colorimetric changes upon of the addition of 0.66 mol-eq. MX_n to DMSO solutions of anionic ligands Na•2.1. Upper image: ambient light, lower image: upon long wave UV irradiation (365 nm). $[\text{Na}\bullet\mathbf{2.1}] = 3 \text{ mM}$. 43

Figure 2.9. Fluorescence emission spectra of the titration of metal salts into DMSO solutions of anionic ligand Na•2.1: a) $\text{MX}_n = \text{Zn}(\text{OTf})_2$, b) $\text{MX}_n = \text{Fe}(\text{ClO}_4)_2$, c) $\text{MX}_n = \text{NiSO}_4$. $[\text{Na}\bullet\mathbf{2.1}] = 30 \mu\text{M}$, excitation wavelength = 397 nm. 45

Figure 2.10. a) Colorimetric changes upon of the addition of 0.33 mol-eq. MX_n to DMSO solutions of anionic ligands Na•2.3. Upper image: ambient light, lower image: upon long wave UV irradiation (365 nm). $[\text{Na}\bullet\mathbf{2.3}] = 3 \text{ mM}$. b) Fluorescence emission spectra of the titration of $\text{Zn}(\text{OTf})_2$ into a 6mM solution of Na•2.3 in DMSO. 46

Figure 2.11. Fluorescence spectra illustrating the selective self-assembly of Na•2.1 for $\text{Zn}(\text{OTf})_2$, and tolerance of H_2O in the assembly process. 48

Figure 2.12. a) $\text{Zn}_2\mathbf{2.1}_3$ cage assembly and in-situ protonation; b) ^1H NMR spectra of the assembly process and subsequent protonation/precipitation (500 MHz, $\text{DMSO}-d_6$, 298K); c) minimized structure of $[\text{Zn}_2\mathbf{2.1}_3]^{8-}$ (SPARTAN, AM1 forcefield). 50

Figure 2.13. Predicted vs experimentally obtained mass peaks for (a) $[\text{Zn}_2\mathbf{3}_2\cdot\text{NaOTf}\cdot\text{H}]^+$ ($m/z = 657.00$) and (b) $[\text{Zn}_2\mathbf{3}_3\cdot\text{Na}_4(\text{IPA})\cdot 5\text{H}]^+$ ($m/z = 844.83$). 52

Figure 3.1. a) Synthesis of 2,7-diaminoxanthene (**XE**) and multicomponent self-assembly into Fe_2L_3 *meso*-helicite 1 b) SPARTAN model of xanthyl mesocates **3.1** and **3.2**. 57

Figure 3.2. Ligand-centered Oxidation of xanthene *meso*-helicite **3.1**. a) ^1H NMR spectrum (600 MHz, CD_3CN , 298 K) of xanthene M_2L_3 *meso*-helicite **3.1**; b) ^1H NMR spectrum of the isolated product of reacting **3.1** with $^t\text{BuOOH}$ for 5 h at 23°C ; c) ^1H NMR spectrum of independently prepared xanthone M_2L_3 *meso*-helicite **3**; d) ESI mass spectra of the isolated product (**3.3**) after reacting **3.1** with $^t\text{BuOOH}$ for 5 h at 23°C . e) Side on view of SPARTAN energy minimized models of the xanthene mesocate (**3.1**) and the all-out isomer of oxidation product **3.3**. 58

Figure 3.3. Ligand-centered Oxidation of Fluorene cage **3.4**. a) ^1H NMR spectrum (600 MHz, CD_3CN , 298 K) of the multiple isomers of M_4L_6 fluorene cage; b) ^1H NMR spectrum of the product of reacting **3.4** with $^t\text{BuOOH}$ and NaClO_4 ; c) ^1H NMR spectrum of independently prepared fluorenol cage **1.3**. 60

Figure 3.4. Oxidation of acylated control ligands using catalytic Fe^{2+} or **3.2** *meso*-helicite. 61

Figure 3.5. Simplified mechanism for transimination of an M_2L_3 *meso*-helicite. 63

Figure 3.6. a) Multicomponent self-assembly of 2,7-diaminoxanthone **X** into the **3.2** mesocate. b) Structures of the competitive displacer ligands used. 64

Figure 3.7. Displacement of “springloaded” *meso*-helicate **3.2** by: a) diaminofluorenonol **FOH** and b) diaminofluorene **F** performed at 70 °C in CD₃CN. 66

Figure 3.8. Deconstruction of the “springloaded” **3.2** *meso*-helicate. a) Downfield regions of the ¹H NMR spectra of the addition of diaminofluorene **F** (22.9 mM) to **3.2** (5.8 mM) over time (23 °C, CD₃CN, 400 MHz). b) Full ESI-MS spectrum of reaction progress at 45 min reaction time in pure CH₃CN. 68

Figure 3.9. Transimination of xanthone cage **3.2** using varying concentrations of diaminofluorene ligand **F** a) 17.4 mM, b) 11.6 mM, c) 5.8 mM. 69

Figure 3.10. Multicomponent self-assembly of *p*-phenetidene ML₃ complex and complete assignment of the ¹H NMR spectrum (298 K, CD₃CN, 400 MHz). 70

Figure 3.11. COSY NMR of Fe**F**₃•Py₃ complex and complete assignment of the downfield regions in the ¹H NMR for Fe**F**₃•Py₃ complex. 71

Figure 3.12. Thermodynamic stability of ML₃ complex monitored via heating a displacement experiment post formation of the Fe**F**₃•Py₃ intermediate at 70 °C for 16 h (CD₃CN, 298 K, 600 MHz). 72

Figure 3.13. Relative single point energies (B3LYP-D3(BJ)/def2-TZVP in implicit acetonitrile) of mixed **X/F** Fe₂L₃ heterocomplexes, reactant **3.2** and product *fac*-Fe**F**₃•Py₃ in kcal/mol. 74

Figure 3.14. Destruction of **3.2** *meso*-helicate using the oxidized fluorenyl ligands a) **FOH**, b) **FO** (298 K, CD₃CN, 400 MHz). 76

Figure 3.15. Deconstruction of the “springloaded” **3.2** *meso*-helicate using 3.5 eq **APA**. Downfield region of the ¹H NMR spectra of: a) **3.2** *meso*-helicate, b) displacement of ligand

X after ~2 min, c) isolated Fe**APA**₃•Py₃ mixed complex, d) COSY NMR spectra of isolated complex (298 K, CD₃CN, 400 MHz). 77

Figure 3.16. ESI-MS spectra of the destruction of mesocate **3.2** upon addition of **APA**: a) 1.5 mol.-eq. displacer ligand, b) 3.5 mol.-eq. displacer ligand. 78

Figure 3.17. Deconstruction of the “springloaded” **3.2** mesocate. Downfield regions of the ¹H NMR spectra of the addition of **APA** (5.8 mM) to **3.2** (5.8 mM) over time (298 K, CD₃CN, 400 MHz). 80

Figure 3.18. ¹H NMR spectrum tracking the destruction of **3.2** (5.8 mM in CD₃CN) upon addition of diaminoxanthene **XE** (17.7 mM) over time. (298 K CD₃CN, 400 MHz). 82

Figure 3.19. Synthesis of di(aminodiphenyl)xanthene ligand (**DPX**) and multicomponent self-assembly into Fe₂L₃ mesocate and helicate structures (SPARTAN, semi-empirical). 83

Figure 3.20. Deconstruction of the “springloaded” mesocate **3.2**. Downfield regions of the ¹H NMR spectra of the addition of **DPX** (5.8 mM) to **3.2** (5.8 mM) over time (298 K, CD₃CN, 400 MHz). 84

Figure 3.21. Transient Heterocomplex Formation. a) Downfield regions of the ¹H NMR spectra of the addition of diaminodiphenylmethane **DPM** (36.7 mM) to **3.2** (5.8 mM) over time. (298 K, CD₃CN, 400 MHz). Minimized structures of heterocomplexes b) Fe₂**DPM**₂**X**•Py₆, c) Fe₂**X**₂**DPM**•Py₆ (B3LYP-D3(BJ)/6-31G(d) basis set). 85

Figure 3.22. Summary of reaction outcomes upon addition of competitive amine ligands to **3.2**. a) Xanthyenyl ligands **XE**, **DPX**; b) Fluorene **F**; c) tripodal ligand **APA**; d) flexible ligand **DPM** 87

Figure 4.1. a) Synthesis of extended fluorene ligand **4.A** and multicomponent self-assembly in to M_4L_6 tetrahedron **4.1**; b) 1H NMR spectrum of cage **4.1** (CD_3CN , 273K, 600 MHz). 94

Figure 4.2. a) Molecular modeling of the three isomers of cage **4.2** (SPARTAN, semi-empirical); b) full positive mode ESI-mass spectrum of cage **4.1** obtained in pure CH_3CN ; c) comparison of predicted ion $[4.1]^{8+}$ versus experimentally observed peaks ($m/z = 422.88$). 96

Figure 4.3. Synthesis of ligand **4.D** using 4-nitrophenylboronic acid. 97

Figure 4.4. a) Multi-component self-assembly of **4.D** (Figure 4.3) with $Fe(NTf_2)_2$ and PyCHO. b) 1H -NMR spectrum of the assembly process. 98

Figure 4.5. Synthesis of ligand **4.D** using 4-Bocaminophenylboronic acid, and multicomponent self-assembly into M_4L_6 tetrahedron **4.2** 100

Figure 4.6. a) Molecular modeling of C_3 -**4.2** and S_4 -**4.2**; b) 1H NMR spectrum of **4.2** tetrahedron (CD_3CN , 273K, 600 MHz). 101

Figure 4.7. 1H NMR spectra of the multicomponent self-assembly for acid-cage: a) cage **4.2**; b) neutral ligand **4.D**; c) anionic ligand $4.D^{n-}$; d) self-assembly product using $4.D^{n-}$; product of an overly concentrated reaction (CD_3CN , 273K, 600 MHz). 102

Figure 4.8. UV-Vis absorption spectra and Stern-Volmer analysis of the titration of pyridyl acetal **4.3c** into solutions of: a) acid cage **4.2** (3 μM in CH_3CN); b) unfunctionalized cage

4.1 (3 μM in CH_3CN).	107
Figure 4.9. Tandem acetal solvolysis and cage-to-cage transformation catalyzed with a) cage 4.2 ; b) “free” acid.	108
Figure 4.10. Summary of the acid catalyzed substitution processes tested.	111
Figure 4.11. Accelerated Substitution Catalyzed by Cage 4.2. a) Reaction progress over time for the transformation of electrophiles 4.5a and 4.5b with either 5% cage 4.2 or 30% control acid 4.4 catalyst (CD_3CN , 353 K). b) ^1H NMR spectra of the reaction of 4.5a with PrSH catalyzed by 4.2 at various intervals (CD_3CN , 400 MHz, 298 K). Blue = PrSH ; Red = thioether product; downfield region shows the imine CH region of the C_3/S_4 isomers of 4.2 , and that cage 4.2 remains intact throughout the reaction.	112
Figure 4.12. Thioetherification of PrSH with 4.5a mediated by control processes: a) 30 mol % control acid 4.4 b) 30 mol % control acid 4.4 and 10 mol % suberone <i>meso</i> -helicite 4.7 (400 MHz, 298 K, CD_3CN). 10 mol % of the M_2L_3 4.7 was used to maintain the number of Fe^{II} -iminopyridine units in solution while the smaller structure is unable to bind substrates within a cavity. Both reactions were performed at 80 $^\circ\text{C}$ and monitored over time (400 MHz, 298 K, CD_3CN).	114
Figure 4.13. Thioetherification and oxidative dimerization of <i>p</i> -tolylthiol promoted by acid cage 4.2 . a) methyl region of the ^1H NMR spectrum monitored over time (CD_3CN , 298 K, 400 MHz). b) change in % sulfur containing compounds present over time. c) Initial rate calculations for thioetherification using 5 % cage 4.2 (red) and 30 % control acid 4.4 (orange).	117

Figure 4.14. ^1H NMR spectra of the acid promoted substitution reaction between **4.6a** and a) dimedone or b) diethylmalonate in the presence of 5 mol % cage **4.2**. The reaction was performed at 80 °C and monitored over time (400 MHz, 298K, CD_3CN). 118

Figure 4.15. UV-Vis absorption spectrum of the titration of PrSH into a 3 μM solution of cage **4.2** in CH_3CN . PrSH was added in 1-5 μL aliquots from a 9 mM stock solution in CD_3CN . b) 1:1 binding fit model for guest PrSH ($K_a = 113.9 \pm 15.0 \times 10^3 \text{ M}^{-1}$). c) 1:2 binding fit model ($K_{11} = 182.4 \pm 19.9 \times 10^3 \text{ M}^{-1}$, $K_{12} = 0.75 \pm 0.08 \times 10^3 \text{ M}^{-1}$). Fits were calculated via linear regression analysis using the Nelder-Mead method from the change in absorbance at two points (300 nm and 370 nm) using supramolecular.org. 121

Figure 4.16. Acid promoted substitution reaction between **4.5a** and *n*-propyl thiol in the presence of 5 mol % cage **4.2**, at varying concentrations of PrSH a) 19.75 mM b) 39.5 mM performed at 80 °C and monitored over time (400 MHz, 298K, CD_3CN). 122

Figure 4.17. Initial rates of thioetherification with varying [PrSH] of a) **4.5a** with 5 % **1**, 333 K; b) **4.5b** with 5 % **4.2**, 333 K; c) **4.5a** with 5 % $\text{CF}_3\text{CO}_2\text{H}$, 273 K. $[\mathbf{4.5}] = 15.8 \text{ mM}$, $[\mathbf{4.2}]$, $[\text{TFA}] = 0.8 \text{ mM}$ in CD_3CN ; concentrations confirmed using dioxane as standard (7.9 mM), rates monitored by ^1H NMR. 123

Figure 4.18. Substrate inhibition of the acid-catalyzed substitution of **4.5a** with PrSH in the presence of 5 % cage **4.2** in CD_3CN . a) Averaged percent conversion over time (min); b) initial rates, using 19.75 mM PrSH (red) and 237 mM PrSH (orange). 125

Figure 4.19. a) Minimized structure of the S_4 isomer of cage **4.2** co-encapsulating PrSH and triphenylmethanol **4.5a**, with spacefilling model (Hartree-Fock, SPARTAN). b) UV-Vis absorption spectrum of the titration of a 1:1 solution of **4.5a** and PrSH into a 3 μM

solution of cage 1 in CH₃CN, the guests were added until saturation was achieved. **4.5a** and **PrSH** were added in 10 μL aliquots from a 4.5 mM stock solution in CH₃CN.

126

Figure 4.20. Substrate-dependent thioetherification mechanisms in cage **4.2**. 129

Figure 4.21. Self-destruct sequence. Detritylation of aniline **4.5e** causes a negative feedback loop, whereby the product turns off the catalyst via transimination. [**4.5e**] = 15.8 mM, [**PrSH**] = 19.75 mM, [**4.2**] = 0.8 mM in CD₃CN; concentrations confirmed using dioxane as standard (7.9 mM), rates monitored by ¹H NMR. 131

Figure 5.1. Structural and cartoon representations of unfunctionalized cage **4.1** and acid-decorated cage **4.2**. 137

Figure 5.2. a) summary of the acid catalyzed substitution processes tested (**4.1**•**4.4** = 1:6 ratio of cage); b) reaction progress over time for the thioetherification of triphenyl methanol **4.5a** with **PrSH** and either 5 % cage **4.2** or 5 % cage **4.1**/30 % **4.4** as catalyst. [**4.5a**] = 15.8 mM, reactions were performed at 80 °C in CD₃CN. 138

Figure 5.3. Reaction progress over time for the thioetherification of a) triphenyl methanol **4.5a**, or b) O-trityl ethyl ether **4.5b**, with **OctSH** and 5 % cage **4.1**/30% **4.4** as catalyst. [**4.5a**] = 15.8 mM, reactions were performed at 80 °C in CD₃CN. 140

Figure 5.4. Reaction progress over time for the thioetherification of electrophile **4.6a** with **PrSH** a) 5 % cage **4.1**/30 % cofactor **5.2a-d** catalyst, and b) 30 % **5.2a-d** alone. [**4.5a**] = 15.8 mM, reactions were performed at 80 °C in CD₃CN. 143

Figure 5.5. Acid promoted substitution reaction between **4.5a** and **PrSH** in the presence of 5 mol % cage **4.1** and 30 mol % **5.2a**, at varying concentrations of **PrSH** a) 9.5 mM b)

22.1 mM and c) 33.2 mM, performed at 80 °C and monitored over time (600 MHz, 298K, CD₃CN). 144

Figure 5.6. a) substitution reaction of **4.5a** with varying concentrations of **PrSH** catalyzed by 5 % cage **4.1** and 30 % cofactor **5.2a**; b) substitution reaction of **4.5a** with 1.25 eq. **PrSH** catalyzed by 5 % cage **4.1** and varying concentration of cofactor **5.2a**. [**4.5a**] = 15.8 mM, reactions were performed at 80 °C in CD₃CN. 145

Figure 5.7. UV/Vis absorption titration of **PrSH** into a solution of **4.1** in CH₃CN. **PrSH** was added in 1 – 5 μL increments from a 9mM solution in CH₃CN, [**4.2**] = 3 μM. 146

Figure 5.8. Minimized structures (Hartree-Fock) of two views (stick and space-filling) a) *S*₄-**4.1**•**4.6b**₂ and b) *S*₄-**4.1**•**5.1a**•**4.6a**•**PrSH**. 149

Figure 5.9. Proposed mechanism and pre-equilibrium for the “holoenzyme” mediated substitution process. 150

Figure 5.10. a) Synthesis of amphiphilic cofactor **5.3**; b) titration of cofactor **5.3** into a 1.5 μM solution of cage **4.1** in CH₃CN; c) 1:1 binding model of the **4.1**•**5.3** complex calculated from the change in absorbance at 370 nm (Nelder Mead). 151

Figure 5.11. UV/Vis titration of Co-salen complex **5.5** into a 3 μM solution of **4.1** in CH₃CN. 153

Figure 6.1. Synthesis of mono-chelating phenanthroline imidazole ligand **6.1**. 157

Figure 6.2. Synthesis of bis-chelating phenanthroline imidazole ligand **6.2**. 158

Figure 6.3. a) ¹ H NMR spectra of ligand 6.2 and self-assembly with various metals: a) ligand 6.2 , b) Fe(ClO ₄) ₂ ; c) Zn(OTf) ₂ ; d) Co(ClO ₄) ₂ (DMSO- <i>d</i> ₆ , 298 K, 500 MHz).	160
Figure 6.4. Synthesis of nitrile-containing phenanthroline ligand 6.3 .	161
Figure 6.5. Synthesis of dibromo ligand cores.	163
Figure 6.6. Synthesis of amphiphilic ligand 6.4 .	164
Figure 6.7. ¹ H NMR spectrum of the multicomponent self-assembly of amphiphilic ligand 6.4 with Fe(NTf ₂) ₂ and PyCHO (CD ₃ CN, 298 K, 600 MHz).	165
Figure 6.8. Synthesis of diester reverse iminopyridine ligand 6.5 .	166
Figure 6.9. ¹ H NMR spectrum of the multicomponent self-assembly of ligand 6.5 with Fe(ClO ₄) ₂ and <i>p</i> -toluidine (CD ₃ CN, 298 K, 500 MHz).	167
Figure 7.1. DOSY NMR spectrum of ligand 2.1 . Diffusion Coefficient = 2.72 x10 ⁻⁹ m ² /s vs. 9.86 x10 ⁻⁹ m ² /s for solvent (DMSO- <i>d</i> ₆ , 600 MHz, 298 K, Δ = 100 ms, δ= 1.8 μs).	221
Figure 7.2. DOSY NMR spectrum of Zn ₂ 2.1 ₃ cage. Diffusion Coefficient = 1.29 x10 ⁻⁹ m ² /s vs. 9.55 x10 ⁻⁹ m ² /s for solvent (DMSO- <i>d</i> ₆ , 600 MHz, 298 K, Δ = 100 ms, δ= 1.8 μs).	222
Figure 7.3. DOSY NMR spectrum of ligand 2.2 . Diffusion Coefficient = 2.85 x10 ⁻⁹ m ² /s vs. 9.62 x10 ⁻⁹ m ² /s for solvent (DMSO- <i>d</i> ₆ , 600 MHz, 298 K, Δ = 100 ms, δ= 1.8 μs).	222

Figure 7.4. DOSY NMR spectrum of Na•**2.2**-Zn(OTf)₂ complex. Diffusion Coefficient = $1.54 \times 10^{-9} \text{ m}^2/\text{sec}$ vs. $9.79 \times 10^{-9} \text{ m}^2/\text{s}$ for solvent (DMSO-*d*₆, 600 MHz, 298 K, $\Delta = 100 \text{ ms}$, $\delta = 1.8 \text{ }\mu\text{s}$). 223

Figure 7.5. DOSY NMR spectrum of ligand **2.3**. Diffusion Coefficient = $3.38 \times 10^{-9} \text{ m}^2/\text{sec}$ vs. $9.23 \times 10^{-9} \text{ m}^2/\text{s}$ for solvent (DMSO-*d*₆, 600 MHz, 298 K, $\Delta = 100 \text{ ms}$, $\delta = 1.8 \text{ }\mu\text{s}$). 223

Figure 7.6. DOSY NMR spectrum of Zn**2.3**₃ complex. Diffusion Coefficient = $2.25 \times 10^{-9} \text{ m}^2/\text{sec}$ vs. $9.33 \times 10^{-9} \text{ m}^2/\text{s}$ for solvent (DMSO-*d*₆, 600 MHz, 298 K, $\Delta = 100 \text{ ms}$, $\delta = 1.8 \text{ }\mu\text{s}$). 224

Figure 7.7. Emission spectra of a solution of Na•**2.1** in spectral grade DMSO (30 μM) upon addition of aliquots of 10 mM Zn(OTf)₂ solution in DMSO. Carried out to 4.51 mol eq. Zn²⁺ (397 nm excitation wavelength). 224

Figure 7.8. Emission spectra of a solution of Na•**2.1** in spectral grade DMSO (30 μM) upon addition of aliquots of 10 mM Co(ClO₄)₂ solution in DMSO. (397 nm excitation wavelength). 225

Figure 7.9. Emission spectra of a solution of Na•**2.2** in spectral grade DMSO (30 μM) upon addition of aliquots of 10 mM Zn(OTf)₂ solution in DMSO. (404 nm excitation wavelength). 225

Figure 7.10. Emission spectra of a solution of Na•**2.2** in spectral grade DMSO (30 μM) upon addition of aliquots of 10 mM Zn(OTf)₂ solution in DMSO. (404 nm excitation wavelength). 226

- Figure 7.11.** Emission spectra of a solution of Na•**2.2** in spectral grade DMSO (30 μ M) upon addition of aliquots of 10 mM Zn(OTf)₂ solution in DMSO. (404 nm excitation wavelength). 226
- Figure 7.12.** Emission spectra of a solution of Na•**2.3** in spectral grade DMSO (60 μ M) upon addition of aliquots of 10 mM Fe(ClO₄)₂ solution in DMSO. (420 nm excitation wavelength). 227
- Figure 7.13.** Emission spectra of a solution of Na•**2.3** in spectral grade DMSO (60 μ M) upon addition of aliquots of 10 mM Co(ClO₄)₂ solution in DMSO. (420 nm excitation wavelength). 227
- Figure 7.14.** Emission spectra of Quinine hemisulfate standard in 1 M H₂SO₄ at varying concentrations (366 nm excitation wavelength). 228
- Figure 7.15.** UV/Vis absorption and normalized emission spectra of **2.1** ligand in DMSO at varying concentrations (excitation wavelength 366 nm). 229
- Figure 7.16.** UV/Vis absorption and normalized emission spectra of Na•**2.1** ligand in DMSO at varying concentrations (excitation wavelength 366 nm). 229
- Figure 7.17.** UV/Vis absorption and normalized emission spectra of Zn₂**2.1**₃ in DMSO at varying concentrations (excitation wavelength 366 nm). 230
- Figure 7.18.** UV/Vis absorption and normalized emission spectra of Fe₂**2.1**₃ in DMSO at varying concentrations (excitation wavelength 366 nm). 230
- Figure 7.19.** UV/Vis absorption and normalized emission spectra of Na•**2.2** ligand in DMSO at varying concentrations (excitation wavelength 366 nm). 231

- Figure 7.20.** UV/Vis absorption and normalized emission spectra of $Zn_x2.2_y$ in DMSO at varying concentrations (excitation wavelength 366 nm). 231
- Figure 7.21.** UV/Vis absorption and normalized emission spectra of $Na\bullet2.3$ ligand in DMSO at varying concentrations (excitation wavelength 366 nm). 232
- Figure 7.22.** UV/Vis absorption and normalized emission spectra of $Zn2.3_3$ in DMSO at varying concentrations (excitation wavelength 366 nm). 232
- Figure 7.23.** 2D-DOSY NMR spectrum of the displacement reaction of **3.2** (5.8 mM) using **F** (17.5 mM). (CD_3CN , 600 MHz, 298 K). **X** = displaced diaminoxanthone **X**. 233
- Figure 7.24.** Full MS of the ligand displacement reaction of **3.2** and dianiline **XE** (3 mol.-eq) in CH_3CN at $t = 6$ h. With stacked comparison of the predicted $[Fe(XE)_3\bullet Py_3]^{2+}$ ion versus the experimentally observed peak. 234
- Figure 7.25.** gCOSY NMR spectrum of fluorene cage **4.1** (CD_3CN , 600 MHz, 298 K). 235
- Figure 7.26.** gCOSY NMR spectrum of fluorene cage **4.1**. Expansion of the 7.2-8.6 ppm region (CD_3CN , 600 MHz, 298 K). 236
- Figure 7.27.** DEPT-HSQC NMR spectrum of fluorene cage **4.1** (CD_3CN , 400 MHz, 298 K). 237
- Figure 7.28.** Expanded DEPT-HSQC NMR spectrum of fluorene cage **4.1** (CD_3CN , 400 MHz, 298 K). 238
- Figure 7.29.** HMBC NMR spectrum of fluorene cage **4.1** (CD_3CN , 400 MHz, 298 K). 239

- Figure 7.30.** Expanded HMBC NMR spectrum of fluorene cage **4.1** (CD₃CN, 400 MHz, 298 K). 240
- Figure 7.31.** ¹H-DOSY NMR spectrum of fluorene cage **4.1** (CD₃CN, 600 MHz, 298 K, Δ = 100 ms, δ = 1.8 μs, Diffusion constant = 3.020 x 10⁻¹⁰ m²/s for cage **1** vs. 3.890 x 10⁻⁹ m²/s for the solvent). 241
- Figure 7.32.** gNOESY NMR spectrum of fluorene cage **4.1** (CD₃CN, 600 MHz, 298 K, mixing time = 300 ms). 242
- Figure 7.33.** Expanded gNOESY NMR spectrum of fluorene cage **4.1** (CD₃CN, 600 MHz, 298 K, mixing time = 300 ms). 243
- Figure 7.34.** Expanded aromatic region of the gNOESY NMR spectrum of fluorene cage **4.1** (CD₃CN, 600 MHz, 298 K, mixing time = 300 ms). 244
- Figure 7.35.** Expanded aromatic regions of the gNOESY NMR spectrum of fluorene cage **4.1** illustrating the presence of three different isomers through correlations of protons a) e and f, b) f and g, c) h and k, and d) e and d. (CD₃CN, 600 MHz, 298 K, mixing time = 300 ms). 245
- Figure 7.36.** TOCSY NMR spectrum of fluorene cage **4.1** (CD₃CN, 600 MHz, 298 K, mixing time = 80 ms). 246
- Figure 7.37.** Expanded TOCSY NMR spectrum of fluorene cage **4.1**. (CD₃CN, 600 MHz, 298 K, mixing time = 80 ms). 247
- Figure 7.38.** ¹H-DOSY NMR spectrum of acid cage **4.2** (CD₃CN, 600 MHz, 298 K, Δ = 100 ms, δ = 1.8 μs, Diffusion constant = 3.090 x 10⁻¹⁰ m²/s for cage **4.2** vs. 3.467 x 10⁻⁹ m²/s for the solvent). 248

- Figure 7.39.** gCOSY NMR spectrum of acid cage **4.2** (CD₃CN, 600 MHz, 298 K).
249
- Figure 7.40.** gCOSY NMR spectrum of acid cage **4.2**. Expansion of the 5.6-8.6 ppm region (CD₃CN, 600 MHz, 298 K).
250
- Figure 7.41.** NOESY NMR spectrum of acid cage **4.2** (CD₃CN, 600 MHz, 298 K, mixing time = 300 ms).
252
- Figure 7.42.** Expanded NOESY NMR spectrum of acid cage **4.2** (CD₃CN, 600 MHz, 298 K, mixing time = 300 ms).
253
- Figure 7.43.** Expanded downfield region of the NOESY NMR spectrum of acid cage **4.2** (CD₃CN, 600 MHz, 298 K, mixing time = 300 ms).
254
- Figure 7.44.** Expanded aromatic regions of the gNOESY NMR spectrum of acid cage **4.2** illustrating the presence of three different isomers through correlations of protons a) e and f, b) h and k, c) f and g, and d) e and d. (CD₃CN, 600 MHz, 298 K, mixing time = 300 ms).
255
- Figure 7.45.** TOCSY NMR spectrum of acid cage **4.2** (CD₃CN, 600 MHz, 298 K, mixing time = 60 ms).
256
- Figure 7.46.** Expanded TOCSY NMR spectrum of acid cage **4.2** (CD₃CN, 600 MHz, 298 K, mixing time = 60 ms).
257
- Figure 7.47.** DEPT-HSQC NMR spectrum of acid cage **4.2** (CD₃CN, 400 MHz, 298 K).
258
- Figure 7.48.** Expanded DEPT-HSQC NMR spectrum of acid cage **4.2** (CD₃CN, 400 MHz, 298 K).
259

- Figure 7.49.** HMBC NMR spectrum of acid cage **4.2** (CD₃CN, 400 MHz, 298 K). 260
- Figure 7.50.** Expanded HMBC NMR spectrum of acid cage **4.2** (CD₃CN, 400 MHz, 298 K). 261
- Figure 7.51.** Full positive mode ESI-mass spectrum of acid cage **4.2** in 100 % CH₃CN. 262
- Figure 7.52.** UV-Vis absorption spectrum of the titration of a 9 mM solution of acetal **4.3a** CH₃CN into a 3 μM solution of cage **4.2** in CH₃CN. **4.3a** was added in 1-5 μL aliquots. 263
- Figure 7.53.** Stern-Volmer plot analysis of cage **4.2** binding to acetal **4.3a** measured by the absorbance change at 335 nm. ($K_d = 76.4 \mu\text{M}$). 263
- Figure 7.54.** UV-Vis absorption spectrum of the titration of a 9 mM solution of acetal **4.3b** CH₃CN into a 3 μM solution of cage **4.2** in CH₃CN. **4.3b** was added in 1-5 μL aliquots. 264
- Figure 7.55.** Stern-Volmer plot analysis of cage **4.2** binding to acetal **4.3b** measured by the absorbance change at 335 nm. ($K_d = 44.7 \mu\text{M}$). 264
- Figure 7.56.** UV-Vis absorption spectrum of titration of acetal **4.3a** into an 18 μM solution of control acid **4.4** in CH₃CN, and absorption spectrum of acetal **4.3a** (15 μM in CH₃CN). 265
- Figure 7.57.** UV-Vis absorption spectrum of titration of acetal **4.3c** into an 18 μM solution of control acid **4.4** in CH₃CN, and absorption spectrum of acetal **4.3c** (15 μM in CH₃CN). 265

Figure 7.58. ^1H NMR spectra (2.60-0.75 ppm) of the acid promoted $\text{S}_{\text{N}}1$ reaction between **4.5b** and *n*-propyl thiol in the presence of: a) 30 mol % control acid **4.4** or b) 5 mol % cage **4.2** in 400 μL CD_3CN . The reaction was performed at 80 $^\circ\text{C}$ and monitored over time (400 MHz, 298K, CD_3CN). 266

Figure 7.59. ^1H NMR spectra (7.80-7.20 ppm, 4.40-4.20 ppm) of the acid promoted substitution reaction between **4.5a** and cyclohexyl thiol in 400 μL CD_3CN in the presence of: a) 30 mol % control acid **4.4** b) 5 mol % cage **4.2**. Both reactions were performed at 80 $^\circ\text{C}$ and monitored over time (400 MHz, 298 K, CD_3CN). 267

Figure 7.60. ^1H NMR spectra (7.90-6.90 ppm) of the acid promoted $\text{S}_{\text{N}}1$ reaction between **4.5b** and cyclohexyl thiol in the presence of: a) 30 mol % control acid **4.4** or b) 5 mol % cage **4.2**. The reaction was performed at 80 $^\circ\text{C}$ and monitored over time (400 MHz, 298K, CD_3CN). 268

Figure 7.61. ^1H NMR spectra (7.80-7.10 ppm, 4.40-3.80 ppm, 2.40-2.20 ppm) of the acid promoted substitution reaction between **4.5a** and 4-methylbenzene thiol in the presence of 30 mol % control acid **4.4**. The reaction was performed at 80 $^\circ\text{C}$ and monitored over time by ^1H NMR (400 MHz, 298 K, CD_3CN). 269

Figure 7.62. ^1H NMR spectra (7.50-6.80 ppm, 2.40-2.20 ppm) of the acid promoted $\text{S}_{\text{N}}1$ reaction between **4.5b** and 4-methylbenzene thiol in the presence of: a) 30 mol % control acid **4.4** or b) 5 mol % cage **4.2**. The reaction was performed at 80 $^\circ\text{C}$ and monitored over time (400 MHz, 298K, CD_3CN). 270

Figure 7.63. ^1H NMR spectra (7.80-7.20 ppm, 4.40-4.20 ppm, 2.20-1.50 ppm) of the acid promoted substitution reaction between **4.5a** and adamantane thiol in the presence of 5 mol

% cage **4.2**. The reaction was performed at 80 °C and monitored over time (400 MHz, 298K, CD₃CN). 271

Figure 7.64. ¹H NMR spectra (7.50-7.20 ppm, 1.30-1.00 ppm) of the acid promoted substitution reaction between **4.5a** and ethanol in the presence of 5 mol % cage **4.2**. The reaction was performed at 80 °C and monitored over time (400 MHz, 298K, CD₃CN).

272

Figure 7.65. ¹H NMR spectra (7.60-7.20 ppm, 1.10-0.70 ppm) of the acid promoted S_N1 reaction between **4.5c** and *n*-propyl thiol in the presence of 5 mol % cage **4.2**. The reaction was performed at 80 °C and monitored over time (400 MHz, 298K, CD₃CN). 273

Figure 7.66. ¹H NMR spectra (7.90-7.45 ppm, 5.6-5.4 ppm, 2.55-0.80 ppm) of the acid promoted S_N1 reaction between **4.5d** and *n*-propyl thiol in 400 μL CD₃CN in the presence of: a) 30 mol % control acid **4.4** or b) 5 mol % cage **4.2**. The reaction was performed at 80 °C and monitored over time (400 MHz, 298K, CD₃CN). 274

Figure 7.67. ¹H NMR spectra (9.60-8.80 ppm, 7.50-5.80 ppm, 1.10-0.80 ppm) of the acid promoted substitution reaction between 4-bromo-*N*-trityl aniline **4.5e** and *n*-propyl thiol in the presence of 5 mol % cage **4.2**. The reaction was performed at 23 °C and monitored over time (400 MHz, 298K, CD₃CN). 275

Figure 7.68. Graphed results of the acid promoted substitution reaction between **4.5a** and cyclohexyl thiol in the presence of: 5 mol % cage **4.2** (red), 30 mol % control acid **4.4** (orange). a) Averaged percent conversion values are plotted against time in minutes. b) Calculation of initial rate based on change in concentration of product [**4.6b**] over time in minutes. 276

Figure 7.69. Graphed results of the acid promoted substitution reaction between **4.5b** and cyclohexyl thiol in the presence of: 5 mol % cage **4.2** (red), 30 mol % control acid **4.4** (orange). a) Averaged percent conversion values are plotted against time in minutes. b) Calculation of initial rate based on change in concentration of product [**4.6b**] over time in minutes. 276

Figure 7.70. Graphed results of the acid promoted S_N1 reaction between **4.5b** and 4-methylbenzene thiol in the presence of: 5 mol % cage **4.2** (red), 30 mol % control acid **4.4** (orange). a) Averaged percent conversion values are plotted against time in minutes. b) Calculation of initial rate based on change in concentration of product [**4.6c**] over time in minutes. 277

Figure 7.71. Graphed results of the acid promoted substitution reaction between **4.5a** and ethanol in the presence of: 5 mol % cage **4.2** (red), 30 mol % control acid **4.4** (orange). a) Averaged percent conversion values are plotted against time in minutes. b) Calculation of initial rate based on change in concentration of product [**4.6b**] over time in minutes. 277

Figure 7.72. ¹H NMR spectra of the acid promoted substitution reaction between **4a** and *n*-propyl thiol in the presence of 5 mol % cage **4.1**, at varying concentrations of **PrSH** a) 8 mM b) 39.5 mM and c) 59.25 mM, performed at 60 °C and monitored over time (400 MHz, 298K, CD₃CN). 278

Figure 7.73. ¹H NMR spectra of the acid promoted substitution reaction between **4.5b** and *n*-propyl thiol in the presence of 5 mol % cage **4.2**, at varying concentrations of **PrSH** a) 20 mM and b) 60 mM, performed at 80 °C and monitored over time (400 MHz, 298K,

CD₃CN). c) Averaged percent conversion over time (min) using 20 mM **PrSH** (orange) and 60 mM **PrSH** (red). 279

Figure 7.74. ¹H NMR spectra of the acid promoted substitution reaction between **4.5b** and **PrSH** in the presence of 5 mol % cage **4.2**, at varying concentrations of **PrSH** a) 9.88 mM, b) 19.75, c) 39.5 mM, and d) 59.25 mM, performed at 60 °C and monitored over time (400 MHz, 298K, CD₃CN). 280

Figure 7.75. UV-Vis absorption spectrum of the titration of **4.5a** into a 3 μM solution of cage **4.2** in CH₃CN. **4.5a** was added in 5 μL aliquots from a 9 mM stock solution in CD₃CN. 281

Figure 7.76. 1:1 binding fit model for guest **4.5a** calculated via linear regression analysis using the Nelder-Mead method from the change in absorbance at two points (300 nm and 370 nm) using supramolecular.org^{1,2} ($K_a = 15.8 \pm 0.3 \times 10^3 \text{ M}^{-1}$). 281

Figure 7.77. UV-Vis absorption spectrum of the titration of **4.5b** into a 3 μM solution of cage **4.2** in CH₃CN. **4.5b** was added in 5 μL aliquots from a 9 mM stock solution in CD₃CN. 282

Figure 7.78. 1:1 binding fit model for guest **4.5b** calculated via linear regression analysis using the Nelder-Mead method from the change in absorbance at two points (330 nm and 370 nm) using supramolecular.org^{1,2} ($K_a = 20.1 \pm 1.2 \times 10^3 \text{ M}^{-1}$). 282

Figure 7.79. UV-Vis absorption spectrum of the titration of **4.5c** into a 3 μM solution of cage **4.2** in CH₃CN. **4.5c** was added in 5 μL aliquots from a 9 mM stock solution in CD₃CN. 283

Figure 7.80. 1:1 binding fit model for guest **4.5c** calculated via linear regression analysis using the Nelder-Mead method from the change in absorbance at two points (300 nm and 370 nm) using supramolecular.org^{1,2} ($K_a = 3.2 \pm 1.3 \times 10^3 \text{ M}^{-1}$). 283

Figure 7.81. UV-Vis absorption spectrum of the titration of **4.5d** into a 3 μM solution of cage **4.2** in CH_3CN . **4.5d** was added in 5 μL aliquots from a 9 mM stock solution in CD_3CN . 284

Figure 7.82. 1:1 binding fit model for guest **4.5d** calculated via linear regression analysis using the Nelder-Mead method from the change in absorbance at two points (330 nm and 370 nm) using supramolecular.org^{1,2} ($K_a = 6.9 \pm 0.4 \times 10^3 \text{ M}^{-1}$). 284

Figure 7.83. UV-Vis absorption spectrum of the titration of **4.6a** into a 3 μM solution of cage **4.2** in CH_3CN . **4.6a** was added in 1-5 μL aliquots from a 9 mM stock solution in CH_3CN . 285

Figure 7.84. 1:1 binding fit model for guest **4.6a** calculated via linear regression analysis using the Nelder-Mead method from the change in absorbance at two points (330 nm and 370 nm) using supramolecular.org^{1,2} ($K_a = 6.5 \pm 1.3 \times 10^3 \text{ M}^{-1}$). 285

Figure 7.85. UV-Vis absorption spectrum of the titration of **CySH** into a 3 μM solution of cage **4.2** in CH_3CN . **CySH** was added in 1-5 μL aliquots from a 9 mM stock solution in CD_3CN . 286

Figure 7.86. a) 1:1 binding fit model for guest **CySH** calculated via linear regression analysis using the Nelder-Mead method from the change in absorbance at two points (300 nm and 370 nm) using supramolecular.org^{1,2} ($K_a = 113.9 \pm 15.0 \times 10^3 \text{ M}^{-1}$). b) 1:2 binding fit model calculated via linear regression analysis using the Nelder-Mead method from the

change in absorbance at two points (300 nm and 370 nm) using supramolecular.org^{1,2} ($K_{11} = 156.1 \pm 11.2 \times 10^3 \text{ M}^{-1}$, $K_{12} = 4.0 \pm 0.4 \times 10^3 \text{ M}^{-1}$). 286

Figure 7.87. UV-Vis absorption spectrum of the titration of **ToISH** into a 3 μM solution of cage **4.2** in CH_3CN . **ToISH** was added in 1-5 μL aliquots from a 9 mM stock solution in CD_3CN . 287

Figure 7.88. 1:1 binding fit model for guest **ToISH** calculated via linear regression analysis using the Nelder-Mead method from the change in absorbance at two points (330 nm and 370 nm) using supramolecular.org^{1,2} ($K_a = 80.6 \pm 9.7 \times 10^3 \text{ M}^{-1}$). 287

Figure 7.89. UV-Vis absorption spectrum of the titration of **AdSH** into a 3 μM solution of cage **4.2** in CH_3CN . **AdSH** was added in 1-5 μL aliquots from a 9 mM stock solution in CD_3CN . 288

Figure 7.90. a) 1:1 binding fit model for guest **AdSH** calculated via linear regression analysis using the Nelder-Mead method from the change in absorbance at two points (300 nm and 370 nm) using supramolecular.org^{1,2} ($K_a = 199.4 \pm 17.0 \times 10^3 \text{ M}^{-1}$). b) 1:2 binding fit model calculated for guest **AdSH** via linear regression analysis using the Nelder-Mead method from the change in absorbance at two points (300 nm and 370 nm) using supramolecular.org^{1,2} ($K_{11} = 362.7 \pm 100.1 \times 10^3 \text{ M}^{-1}$, $K_{12} = 220.8 \pm 45.3 \times 10^3 \text{ M}^{-1}$). 288

Figure 7.91. UV-Vis absorption spectrum of the titration of **4.4** into a 1.5 μM solution of cage **4.1** in CH_3CN . **4.4** was added in 1 μL aliquots from a 4.5 mM stock solution in CD_3CN . 289

Figure 7.92. UV-Vis absorption spectrum of the titration of **5.2a** into a 1.5 μM solution of cage **4.1** in CH_3CN . **5.2a** was added in 1 μL aliquots from a 4.5 mM stock solution in CD_3CN . 289

Figure 7.93. UV-Vis absorption spectrum of the titration of **5.2b** into a 1.5 μM solution of cage **4.1** in CH_3CN . **5.2b** was added in 1 μL aliquots from a 4.5 mM stock solution in CD_3CN . 290

Figure 7.94. UV-Vis absorption spectrum of the titration of **5.2c** into a 1.5 μM solution of cage **4.1** in CH_3CN . **5.2c** was added in 1 μL aliquots from a 4.5 mM stock solution in CD_3CN . 290

Figure 7.95. UV-Vis absorption spectrum of the titration of **5.2d** into a 3 μM solution of cage **4.1** in CH_3CN . **5.2d** was added in 5 μL aliquots from a 9 mM stock solution in CD_3CN . 291

Figure 7.96. UV-Vis absorption spectrum of the titration of **4.5a** into a 3 μM solution of cage **4.1** in CH_3CN . **4.5a** was added in 5 μL aliquots from a 9 mM stock solution in CD_3CN . 291

Figure 7.97. UV-Vis absorption spectrum of the titration of **4.5b** into a 3 μM solution of cage **4.1** in CH_3CN . **4.5b** was added in 5 μL aliquots from a 9 mM stock solution in CD_3CN . 292

Figure 7.98. UV-Vis absorption spectrum of the titration of **4.6a** into a 1.5 μM solution of cage **4.1** in CH_3CN . **4.6a** was added in 1 μL aliquots from a 4.5 mM stock solution in CD_3CN . 292

Figure 7.99. UV-Vis absorption spectrum of the titration of 5.1 into a 1.5 μM solution of cage 4.1 in CH_3CN . 5.1 was added in 1 μL aliquots from a 4.5 mM stock solution in CD_3CN .	293
Figure 7.100. UV-Vis absorption spectrum of the titration of OctSH into a 3 μM solution of cage 4.1 in CH_3CN . OctSH was added in 1-5 μL aliquots from a 9 mM stock solution in CD_3CN .	293
Figure 7.101. UV-Vis absorption spectrum of the titration of (OctS)₂ into a 1.5 μM solution of cage 4.1 in CH_3CN . (OctS)₂ was added in 1-5 μL aliquots from a 4.5 mM stock solution in CD_3CN .	294
Figure 7.102. ^1H NMR spectrum of 5.4 (500 MHz, 298 K, CDCl_3).	294
Figure 7.103. ^1H NMR spectrum of 5.3 (400 MHz, 298 K, $\text{DMSO-}d_6$).	294
Figure 7.104. ^1H NMR spectrum of dialdehyde 6.A (400 MHz, 298 K, CDCl_3).	295
Figure 7.105. ^1H NMR spectrum of phenanthroline ligand 6.2 (400 MHz, 298 K, $\text{DMSO-}d_6$).	295
Figure 7.106. ^1H NMR spectrum of 6.B (400 MHz, 298 K, CDCl_3).	295
Figure 7.107. ^1H NMR spectrum of phenanthroline ligand 6.3 (400 MHz, 298 K, $\text{DMSO-}d_6$).	295
Figure 7.108. ^1H NMR spectrum of 3,7-dibromosuberone (500 MHz, 298 K, CDCl_3).	296
Figure 7.109. ^1H NMR spectrum of 7.5 (500 MHz, 298 K, CDCl_3).	296
Figure 7.110. ^1H NMR spectrum of 6.D (500 MHz, 298 K, CDCl_3).	296
Figure 7.111. ^1H NMR spectrum of 7.6 (500 MHz, 298 K, CDCl_3).	297

Figure 7.112. ^1H NMR spectrum of 6.E (500 MHz, 298 K, CDCl_3).	297
Figure 7.113. ^1H NMR spectrum of 7.7 (500 MHz, 298 K, CD_3CN).	297
Figure 7.114. ^1H NMR spectrum of 6.F (600 MHz, 298 K, CDCl_3).	298
Figure 7.115. ^1H NMR spectrum of 7.8 (500 MHz, 298 K, $\text{DMSO-}d_6$).	298
Figure 7.116. ^1H NMR spectrum of 6.4 (400 MHz, 298 K, CD_3CN).	298
Figure 7.117. ^1H NMR spectrum of 7.G (500 MHz, 298 K, CDCl_3).	299
Figure 7.118. ^1H NMR spectrum of 6.5 (500 MHz, 298 K, CDCl_3).	299

LIST OF TABLES

Table 4.1. Supramolecular catalysis of acetal solvolysis	104
Table 4.2. Acetal solvolysis catalyzed using “free” acid 4.4 .	105
Table 4.3. Supramolecular Substitution Catalysis.	115
Table 4.4. Binding Affinities of Substrates and Products in Cage 4.2 .	120
Table 5.1. Supramolecular Cofactor-Mediated Catalysis.	142
Table 5.2. Binding Affinities of Reaction Components in Cage 4.1 .	147
Table 7.1 Summary of fluorescence data for Na• 2.1 , Na• 2.2 and Na• 2.3 and their respective complexes.	233
Table 7.2 Assigned ions for experimentally observed peaks (7.5 = full iminopyridine ligand of 4.A).	248
Table 7.3. Assigned ions for experimentally observed peaks. (7.6 = full iminopyridine ligand of 4.A).	262

Chapter 1 – Design, Assembly and Function of Supramolecular Cages

1.1 Rational Design of Supramolecular Cages

Since their original discovery in the early 1990s, a variety of supramolecular self-assembled polyhedra have been reported. The inspiration for these structures is the function of enzymes, and a strong focus is in creating molecules with defined cavities capable of controlling reactions. As such, several reviews investigating the rational design of such structures have been published.^{1,2} The development of these complexes has expanded the field into new areas of materials science including use as molecular machines,³ sensors⁴ and drug delivery.⁵

Self-assembled metal-organic cages are created through interactions between organic ligands exhibiting two or more coordinating groups bound to metal atoms. The metals typically used in these complexes are Fe^{2+} , Pd^{2+} , and Pt^{2+} , although self-assembly can be extended to other first row metals such as Co^{2+} and Ni^{2+} ,⁶ as well as lanthanides and actinides.⁷ The possibilities for the metal coordinating group can vary significantly, although the use of monodentate pyridyl coordination,⁸ or bidentate coordination with bipyridyl,⁹ iminopyridine,¹⁰ pyridyl pyrazole,¹¹ or catechol groups¹² is most common (Figure 1.1). The polyhedra accessible via this strategy are equally diverse ranging from small M_2L_3 *meso*-helicates up to very large $\text{M}_{12}\text{L}_{24}$ or $\text{M}_{24}\text{L}_{48}$ nanospheres.

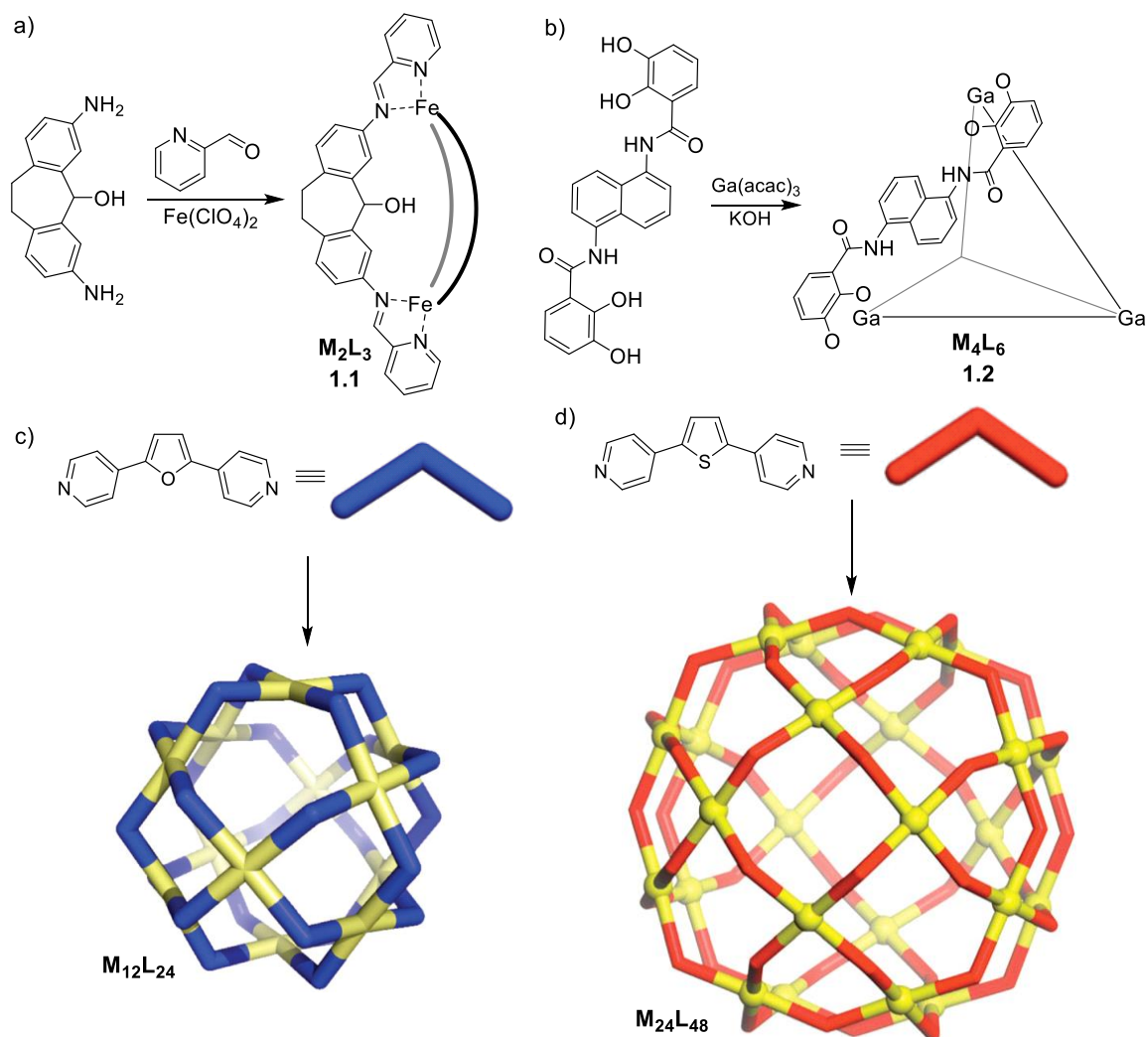


Figure 1.1. Synthesis of a metal-organic species: a) an M_2L_3 meso-helicate made using Fe^{2+} and an iminopyridine chelator;¹³ b) an M_4L_6 tetrahedron with Ga^{3+} and a catecholate chelator;¹⁴ c) $M_{12}L_{24}$ ¹⁵ and d) $M_{24}L_{48}$ nanospheres made from pyridyl-Pd $^{2+}$ contacts.¹⁶

The self-assembly process of these cages is rather complicated, involving multiple simultaneous interactions between the metal and ligand subcomponents (in some cases up to 72 individual molecules), resulting in the formation of discrete products. As diverse as these assemblies may be, almost all of them exhibit similar characteristics in their assembly process: the final product is governed by thermodynamic equilibration. This occurs through reversible metal-ligand coordination. Initial coordination is rapid, forming disordered

aggregates and cage fragments,¹⁷ followed by ligand dissociation and equilibration to form the more ordered assemblies. As a result, despite the multitude of chemical interactions occurring, the anticipated superstructures can often be predicted through energy minimization in molecular modeling.

The stoichiometry of the assembled product is heavily influenced by the nature of the structural ligand. Several factors such as number of coordinating groups, rigidity of the ligand, and the angle and distance between coordinating groups can have significant impacts on the resultant cage. The flexibility of the ligand illustrates one of the largest concerns: too much flexibility can compromise the structural integrity of the target cage, while too rigid of a structure can prevent the formation of the assembly altogether.¹⁸ Despite this, the more rigid ligands remain the favorite among supramolecular chemists as stereochemical communication between the ligand and metal centers can be better controlled resulting in products with a higher degree of symmetry. The coordination angle of the ligand can also play a significant role in the assembly process. More bent ligands such as the one in Figure 1.1a result in the smaller M_2L_3 *meso*-helicite structures,¹⁹ while more linear ligands favor larger M_4L_6 tetrahedra (Figure 1.2a).²⁰ Finally, even small changes such as shifting from 4-pyridyl to 3-pyridyl substitution has significant impacts on the resulting structure (Figure 1.2b,c).

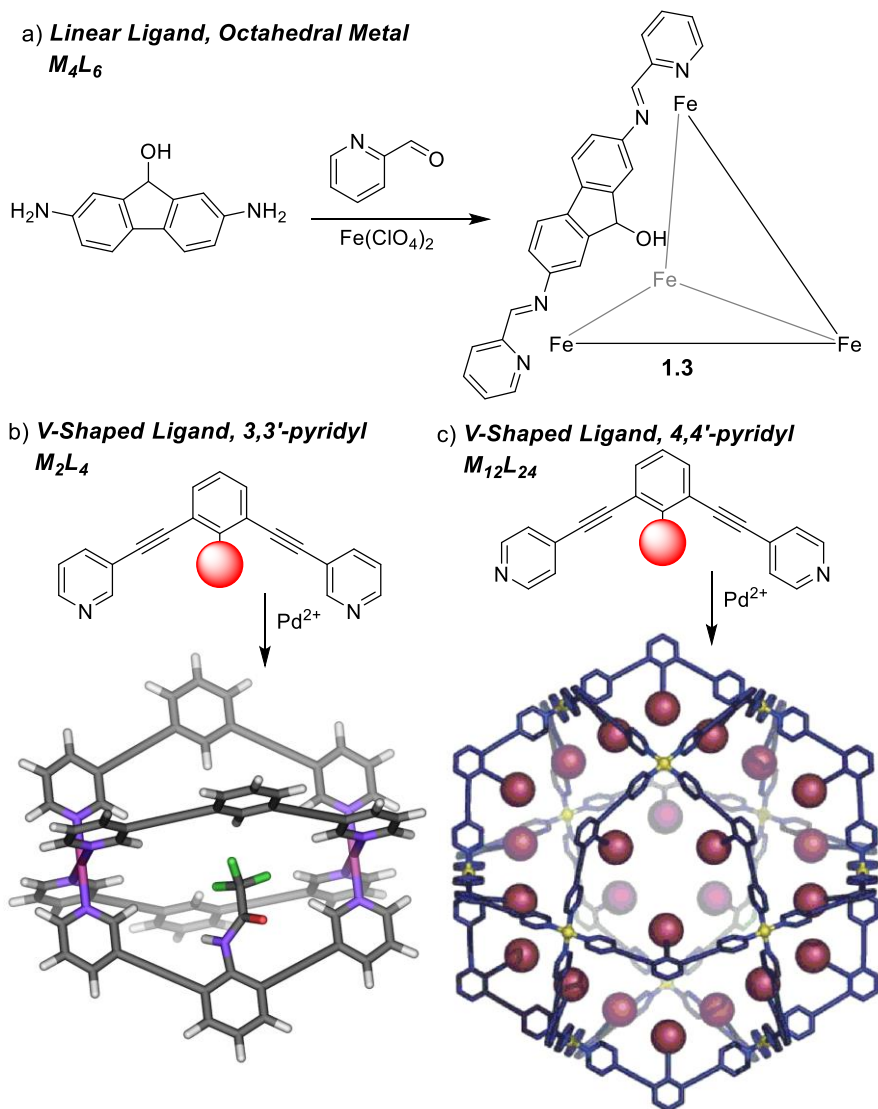


Figure 1.2. Small changes in ligand shape effecting large differences in stoichiometry.

Proper matching of the ligand and metal salt used is also a very important consideration in forming supramolecular cages. If incompatibilities exist in the assembly, non-discrete aggregates are likely to form. Further, while the geometric nature of the metal can be used to direct the stoichiometry of the products, the metals can also lead to synthetic challenges. In octahedral metal salts for example, multiple isomeric possibilities exist when treated with bidentate chelators.²¹ The chelating groups can exist in either the facial or

meridional configurations, with each configuration exhibiting two possible rotational isomers as well (Figure 1.3). As the stoichiometry of the complexes increases (i.e. more metal integrated into the system), so too does the number of possible isomers.

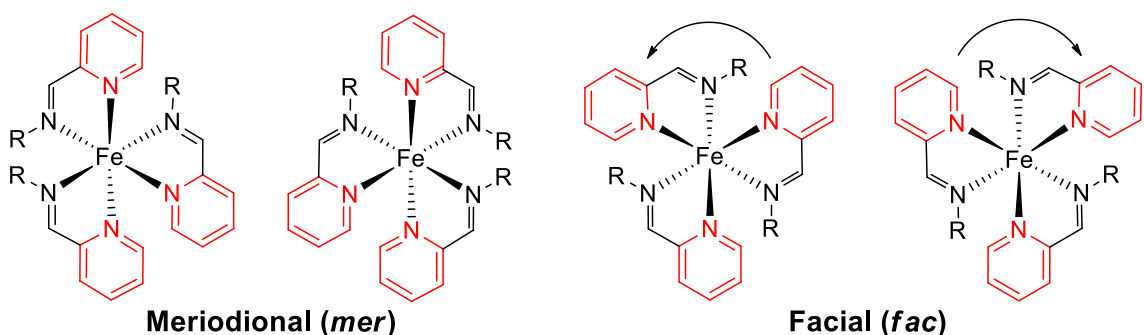


Figure 1.3: The two isomeric connective possibilities of Fe^{II}-iminopyridine centers, and the two possible enantiomers of each with Λ (left) and Δ (right) rotation of the *fac* centers.

Many isomeric possibilities for the self-assembly of *bis*-coordinating ligands such as bipyridine or iminopyridine with octahedral metal centers exist. The smallest, and simplest possibility is the M_2L_3 complex which exists in either a mesocate or helicate structure. The mesocate exists when one metal center is in the *fac*- Δ configuration and the other is in the *fac*- Λ , while the in the helicate the metal centers have matched rotation (i.e. $\Lambda\Lambda$ or $\Delta\Delta$). In these smaller assemblies the *mer* geometry is prohibited as significant strain would be present in all but the most flexible ligands. In contrast the larger M_4L_6 complexes give more rotational freedom to the ligands, enabling the possible incorporation of *mer*-metal centers,²² leading to a greater number of isomeric possibilities. The *mer*-center is generally higher in energy however, so most “linear” ligands favor the all-*fac* isomers.²³ Within these all-*fac* tetrahedra three isomeric possibilities exist: the T-symmetric isomers exists in the completely matched *fac*- $\Lambda\Lambda\Lambda\Lambda$ or *fac*- $\Delta\Delta\Delta\Delta$ geometry giving it the highest

symmetry. Sequentially changing the rotation of one metal center gives rise to the C_3 ($\Delta\Delta\Delta\Delta$ or $\Lambda\Lambda\Lambda\Lambda$) and S_4 ($\Lambda\Lambda\Delta\Delta$) isomers, which exhibit more dissymmetric structures.

1.2. Ligand Effects in the Stability and Control of Self-Assembly

Controlling the assembly process of cages can be quite challenging. While the resulting stoichiometry can be readily predicted, the stereoisomerism and overall stability of the complex is far more ambiguous. An effective method of teasing out information on the stability of a supramolecular cage is to treat a pre-formed complex with a competing ligand. The final product of this experiment will be the most stable complex. Several examples of this are observed in the social self-sorting of Pd-pyridyl complexes. For example, when homocomplex $\text{Pd}_2\mathbf{1.4}_4$ is treated with the more electron rich amine decorated ligand $\mathbf{1.5}$, selective formation of the *cis*-heteroleptic complex $\text{Pd}_2\mathbf{1.4}_2\mathbf{1.5}_2$ (Figure 1.4a).²⁴ DFT calculations confirmed this is the most stable possible product, and no further displacement is observed. By exploiting small differences in coordination angle of the ligand, more effective social sorting (and ligand exchange) can be performed. Varying the size and shape of the internal ligand core in addition to the coordination angle can create heteroleptic complexes that are more favored than their homocomplexes (Figure 1.4b).²⁵ For this strategy to be effective, the ligands must form strained homocomplexes. A bent Pd_2L_4 helical structure is formed using acridone based ligand $\mathbf{1.6}$ (120° coordination angle) while $\mathbf{1.7}$ (60° angle) forms a Pd_4L_8 cube, both demonstrating limited stability. As consequence, mixing of the two ligands with Pd^{2+} salts results in the formation of the mixed $\text{Pd}_2\mathbf{1.6}_2\mathbf{1.7}_2$ heterocomplex. A follow-up study utilized a third ligand $\mathbf{1.8}$ with an intermediate coordination angle (75°).²⁶ Two additional heterocomplexes were formed

(Pd₂1.6₂1.8₂ and Pd₂1.7₂1.8₂) each of which could be converted to Pd₂1.6₂1.7₂ with the proper displacing ligand.

The Fe-iminopyridine scaffold is also well suited to this type of analysis, as the iminopyridine linkages can easily be substituted via subcomponent exchange using a displacing ligand. In this case rather than full displacement of the ligand from the metal, the exchange occurs through transimination at the metal center. Lauren previously demonstrated this in investigating the order of stability in M₂L₃ *meso*-helicates (Figure 1.5a).²⁷ Through this study, a hierarchy of cage stability could be established, both through competitive self-assembly, as well as ligand displacement through treatment of a less favorable cage with a ligand of greater stability. The experiments revealed an impressive preference towards only the formation of the homo-complexes with each ligand, despite essentially the same size and electronics being present in each ligand. The study is impressively capped by a competition experiment between three ligands involving a total 33-separate components in which strict sequential formation of each homocomplex is observed, with no deviation from the order of stability or incorporation of heterocomplexes.

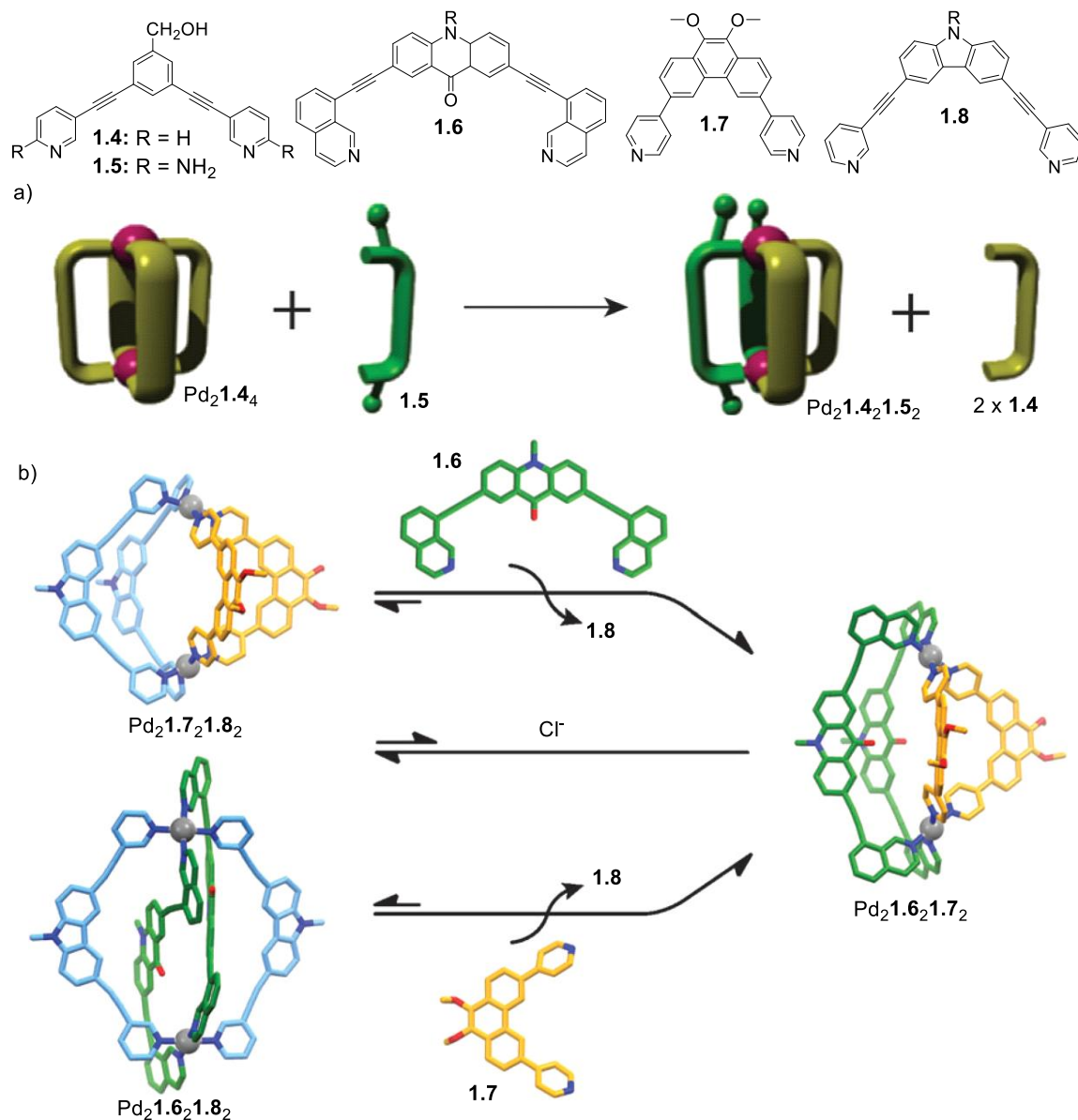


Figure 1.4. Ligand exchange in the social self-sorting of Pd₂L₄ complexes.²⁵⁻²⁷

Following up on this study, the nature of the pyridyl carboxaldehyde group's impact on the stability of the assembly was investigated.²⁸ In this study three different aldehydes were analyzed with varying electronics, the typical 2-pyridine carboxaldehyde (PyCHO), as well as the more electron rich 4-methylpyridine carboxaldehyde (MePyCHO) and electron poor 4-bromopyridine carboxaldehyde (BrPyCHO). In the process of analyzing the stability of

these complexes, a surprising discovery was made: subcomponent exchange is not limited to the amine, and the aldehyde component can also be exchanged in the presence of water (Figure 1.5b). Self-assembly with BrPyCHO is the fastest as the aldehyde is the most amenable to imine condensation, however the coordination is also the weakest of the three possibilities and can be easily exchanged with either PyCHO or MePyCHO.

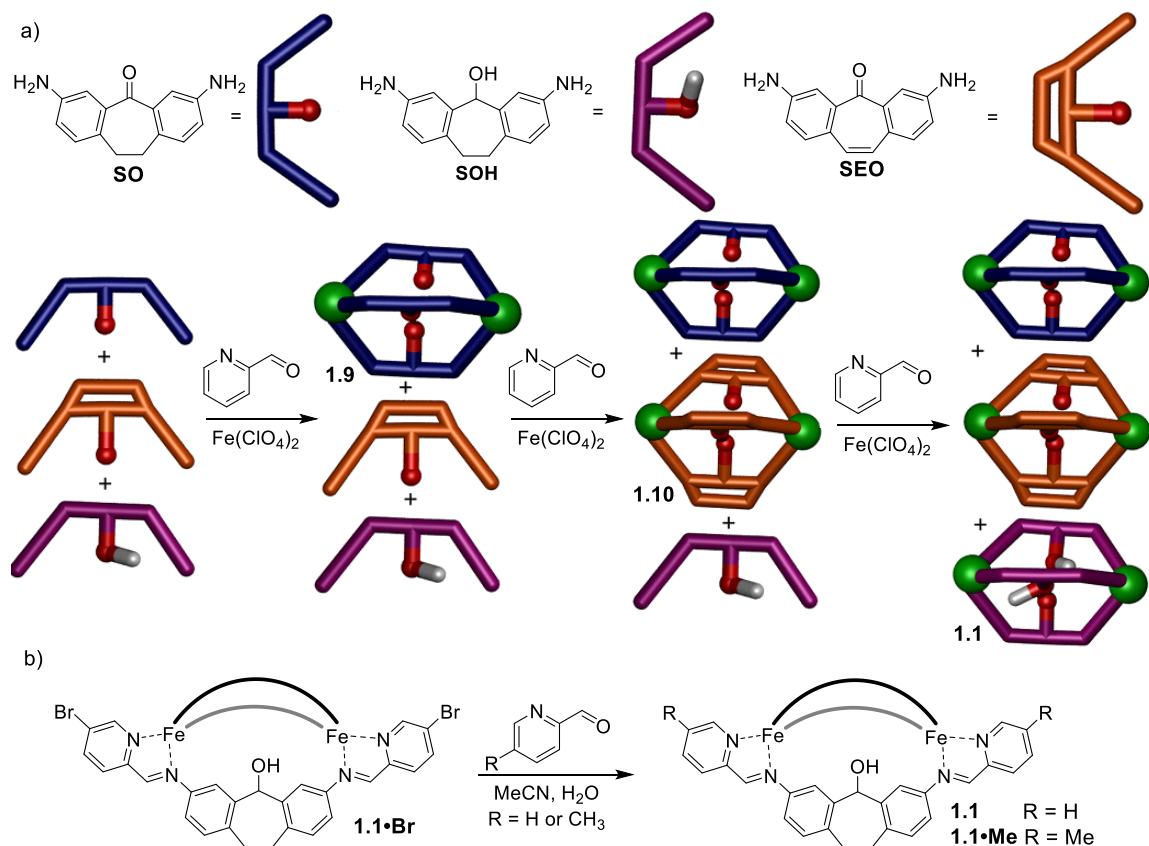


Figure 1.5. Self-sorting and subcomponent exchange in Fe-iminopyridine M_2L_3 *meso*-helicates.^{28,29}

1.3. Molecular Recognition in Unfunctionalized Supramolecular Cages

Cages constructed from ligands containing flat aromatic panels are commonly used in the design of supramolecular hosts.²⁹ The aromatic panels can block the large gaps that exist in between separate ligands, resulting in a more enclosed cavity. By exploiting the hydrophobic effect a general strategy for molecular recognition can be achieved. Nitschke

showed encapsulation of a variety of hydrocarbons specific to the size of the pore and cavity of an M_4L_4 cage (**1.1**).³⁰ Although good binding was observed, there was little selectivity between guests of different size. With proper size and shape matching for the guest to the cavity, a stronger, more selective, molecular recognition can be achieved.

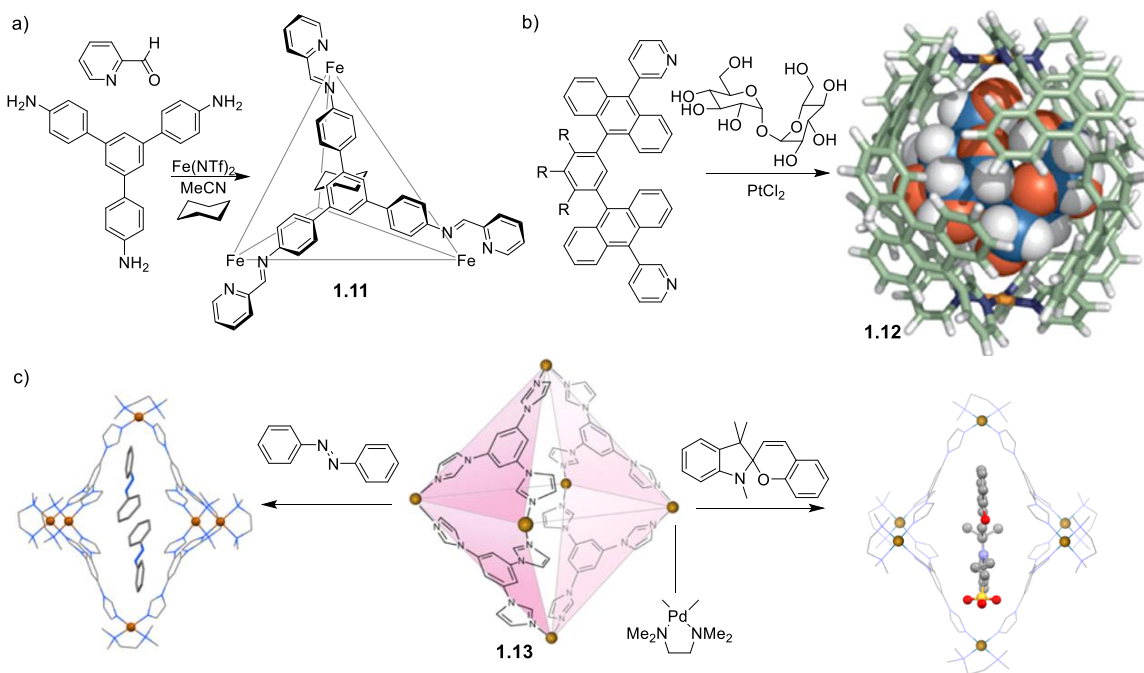


Figure 1.6. Molecular recognition in “featureless” cages: a) stabilization of reactive white phosphorus; b) selective encapsulation of sucrose; c) trigger and stabilization of reactive photoswitches.³⁰⁻³³

Yoshizawa and co-workers demonstrated strong recognition for sucrose in water using an anthracene paneled paddlewheel **1.12**.³¹ Further, the cage exhibited rare selectivity for sucrose over other, putatively similar carbohydrates (Figure 1.4b). Finally, Klajn showed two examples of unique interactions with photo switchable compounds (Figure 1.4c). Upon encapsulation of a spiropyran in icosahedron **1.13** the compound converts to its opened form, after which the reversion process is prevented by stabilization within the

cage.³² Following this investigation, it was discovered that the same cage could also bind azo-benzene enabling control of the switching process.³³

In addition to controlling guest encapsulation, the aromatic panels can be utilized to activate reactive species. Tetrahedron **1.2**, synthesized by Raymond has been extensively used in supramolecular catalysis.³⁴ The naphthalene motif is able to activate encapsulated guests through CH- π interactions enabling high rate accelerations for several organic transformations including the Nazarov cyclization,³⁵ and aza-Cope rearrangement.³⁶ While, these examples of molecular recognition are impressive, most of the interesting phenomena occurring is a result of the encapsulated guest. The cages in these cases are essentially featureless, with the only function being as a host molecule. To create more versatile host molecules, additional properties would need to be added to the self-assembly.

Further, native luminescence in organic molecules is observed most often in aromatic compounds, meaning the molecular paneling approach can be still be a viable method for self-assembly. By using a tetrakis-pyridyl functionalized tetraphenyl ethylene (TPPE) ligand along with 1,3-benzoate and Pt²⁺ salts, a highly emissive cage **1.14** can be synthesized.³⁷ The cage exhibits variable efficiency in emission in different solvents resulting from aggregation induced emission, with a quantum yield up to 50 % in pure THF. Formation of complexes utilizing similarly ligand-centered emission has been demonstrated by Ward, using pyridyl-pyrazole ligands with a naphthalene core.³⁸ Further, more diverse mixed metal M₈L₁₂ complexes can be synthesized using a similar ligand, which exhibited redox activity in addition to the native luminescence.³⁹

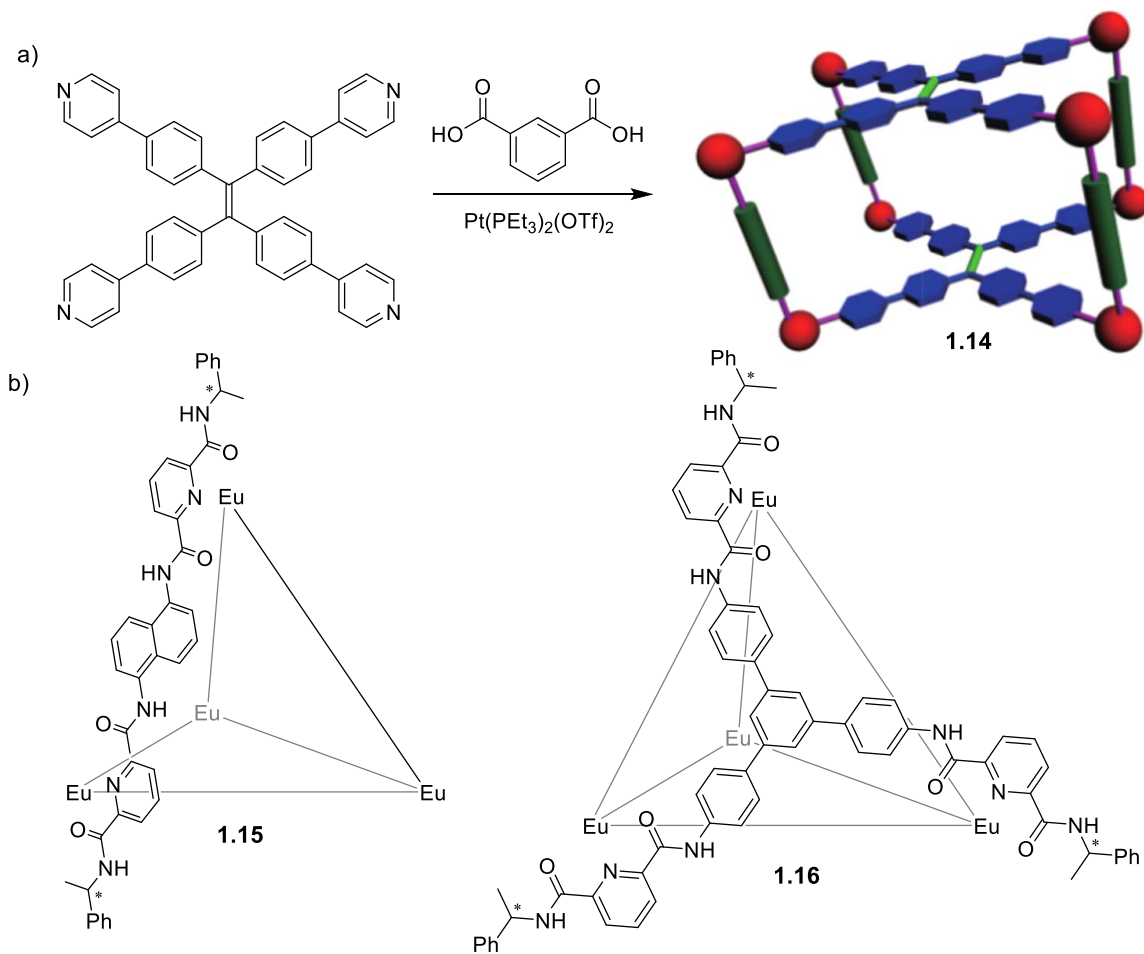


Figure 1.7. Fluorescent self-assemblies. a) Ligand centered emission;³⁷ b) Metal centered emissive complexes.⁴⁰

In addition to the use of fluorophores as ligands, coordination to metals exhibiting native luminescence is also a viable strategy in designing fluorescent cages. As most known emissive metal salts belong to either the lanthanide or actinide family, far fewer examples of this type self-assembled cage exist. There are however a handful of exquisite examples utilizing ligands with tridentate chelators. Sun was able to form a fluorescent cage using a pyridine-2,6-dicarboxamide chelating motif, to chelate Eu^{3+} ions.⁴⁰ The resulting cages **1.15** and **1.16** exhibited a modest efficiency ($\Phi < 1\%$), however exceptional stereocontrol and narcissistic self-sorting were demonstrated. By using a salicylhydrazone coordinating

motif with Ce^{4+} ions, Duan was able to create a luminescent M_4L_4 tetrahedron capable of biological imaging and luminescent tracking of chemical reactions.^{41,42}

1.4. Endohedral Cages with “Inert” Functions

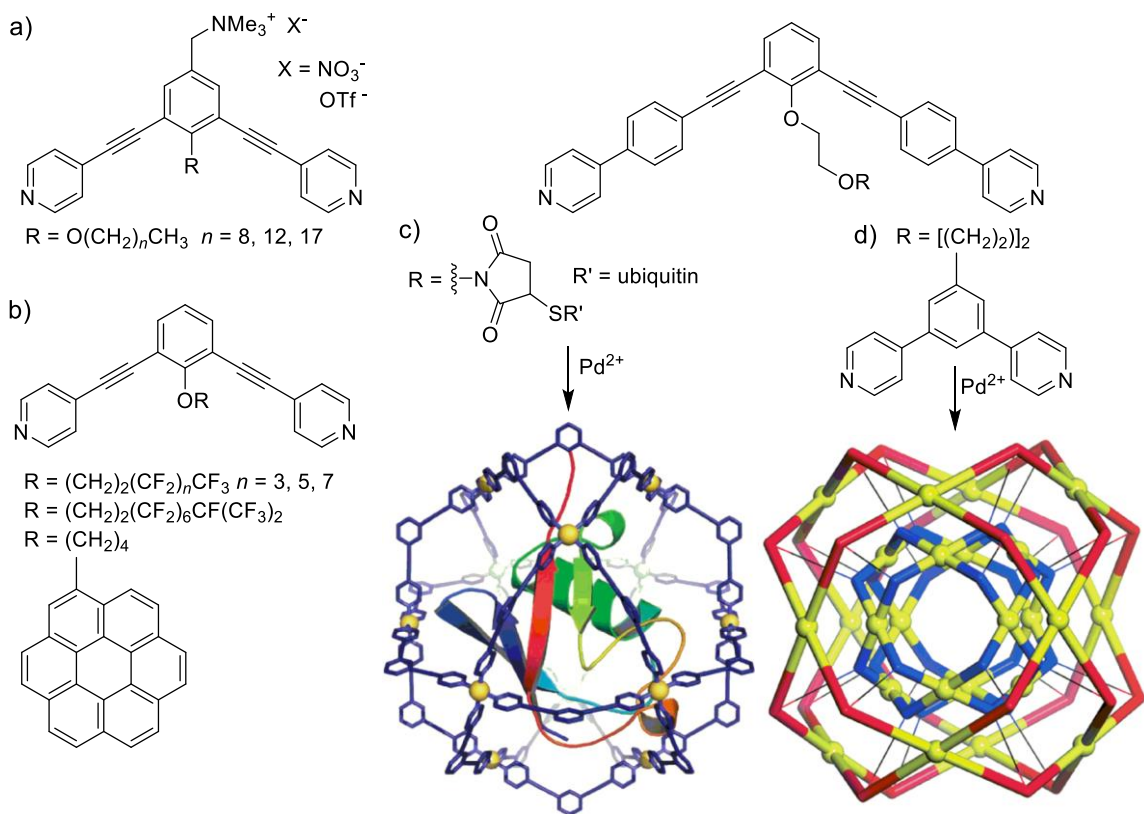


Figure 1.8. Nanostructures possible by decorating the interior of $\text{Pd}_{12}\text{L}_{24}$ cage complexes.⁴⁴⁻⁴⁹

The most versatile scaffolds for use in endohedral functionalization of cages were pioneered by Fujita. Derivatization of the 2 and 6 positions of arene rings with either 4-pyridyl or 4-ethynylpyridyl groups creates rigid, V-shaped ligands capable of self-assembly mediated by Pd.⁴³ Utilizing this strategy, large $\text{M}_{12}\text{L}_{24}$ nanospheres can be formed, and the central arene ring can be easily functionalized both endohedrally (at the 1-position) or exohedrally (at the 4-position). The resulting structures exhibit very large cavities and are extremely stable, as well as highly cationic enabling solubility in water. Initially the

derivatization of nanospheres focused on relatively simple, inert functional groups. By installing long alkyl chains inside the cavity, a distinct hydrophobic phase could be created in aqueous solution, enabling encapsulation of lipophilic compounds such as Nile Red (Figure 2a).⁴⁴ Similarly, the internalization of perfluoroalkyl chains was used to create fluorinated nanodroplets.⁴⁵ Alternatively, a highly aromatic phase capable of binding C₆₀ and naphthalenediimide in water can be obtained through functionalization with coronene.⁴⁶ The robust nature of the nanospheres enables a diverse array of functionalization to be performed, including impressive nanoscale complexes such as inverse dendrimers⁴⁷ and even complexes containing proteins (Figure 1.6c).⁴⁸ More impressively, by attaching a short *bis*-pyridine ligand to the interior of a large *bis*-pyridyl ligand, the formation of a “Matryoshka Doll” or cage within a cage could be synthesized and characterized crystallographically (Figure 1.6d).⁴⁹

1.5. Molecular Recognition Controlled by Small Endohedral Groups

Endohedral functionality does not need to be large to be effective. In fact, functionality as small as a lone pair or H-bonding group can confer novel properties to self-assembled cages if oriented properly. Raymond’s catecholate cage excluded, most self-assembled cages are highly cationic. As a result, encapsulation of positively charged guests is rarely observed in featureless cages shown above.

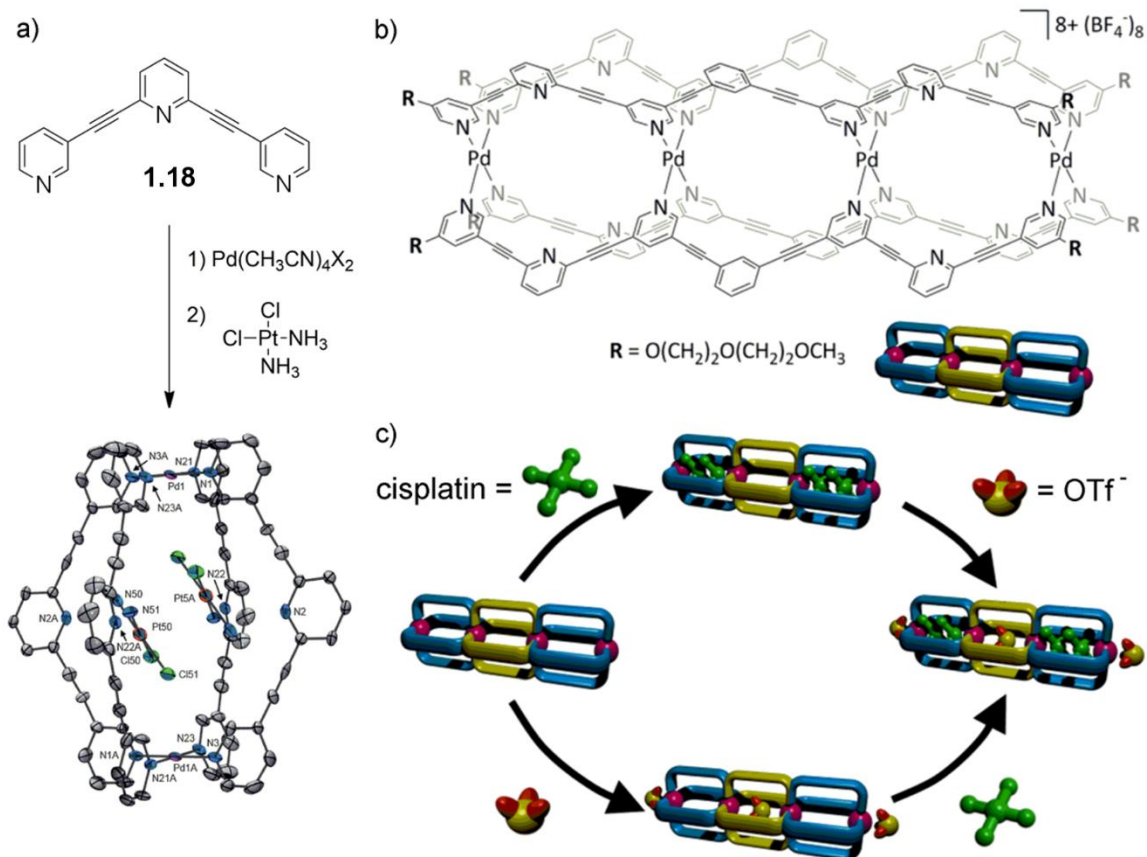


Figure 1.9. Selective cation and anion recognition with Pd_2L_4 paddlewheels with internal lone pairs and acidic groups.^{53, 54}

The use of small functions like lone pairs of course necessitates the use of a smaller cavity. The formation of a large $\text{M}_{12}\text{L}_{24}$ nanosphere with endohedral pyridyl nitrogens has been shown to complex Ag^+ cations on the interior of the cage.⁵⁰ While this is impressive given the 24^+ charge of the complex, the pyridyl rings can largely be considered independent, given the large spacing in the structure. Smaller paddlewheel structures, made by changing the pyridyl orientation from 4,4' to 3,3', can much more effectively direct groups towards the interior with functions including C-H bonds,⁵¹ lone pairs,⁵² and amines.⁵³ The pyridyl variant **1.17** is an effective host for cationic guests, and can encapsulate two molecules of *cis*-platin via hydrogen bonding between the guest and

internalized lone pairs (Figure 1.9). Further, the addition of either DMAP or chloride anion could trigger the release of the encapsulated *cis*-platin, hinting at some potential in drug release. However, no affinity for the guests were observed in water as the encapsulation is reliant on hydrogen bonding. A more impressive demonstration of the impacts of H-bonding on guest encapsulation was shown through the synthesis of a long oligopyridyl ligand exhibiting both pyridyl and aryl central cores.⁵⁴ Treatment of this ligand with Pd²⁺ generates a multicavity cage displaying two separate nano-environments: in cavities containing the pyridyl motif encapsulation of *cis*-platin was observed, whereas the aryl motif, lacking H-bonding interactions, bound only triflate anions.

Binding anionic compounds is significantly easier than cations, but the use of anions as a template can offer unique control of the assembly process when paired with hydrogen bonding interactions. An elegant example of this was presented by Custelcean, who utilized molecular modeling to design a tetrahedral Ni₄L₆ complex that selectively binds the sulfate anion (Figure 1.10a).⁵⁵ Unlike most examples of flexible ligands utilized in self-assembly with octahedral metals, ligand **1.18** favors the formation of the tetrahedral stoichiometry over the generally more favorable M₂L₃ helicate. The tetrahedral shape of the complex Ni₄**1.18**₆ complements the shape of the bound sulfate, and precisely positions the H-bonding urea groups towards the anion. Exquisite affinity is observed in this case ($K_a(\text{Ni}_4\mathbf{1.18}_6 \cdot \text{SO}_4) > 6 \times 10^6 \text{ M}^{-1}$) comparable to that of a sulfate binding protein. This cage was later extended to other tetrahedral oxoanions and an order of affinity was generated ($\text{PO}_4^{3-} \gg \text{CrO}_4^{2-} > \text{SO}_4^{2-} > \text{SeO}_4^{2-} > \text{MoO}_4^{2-} > \text{WO}_4^{2-}$).⁵⁶

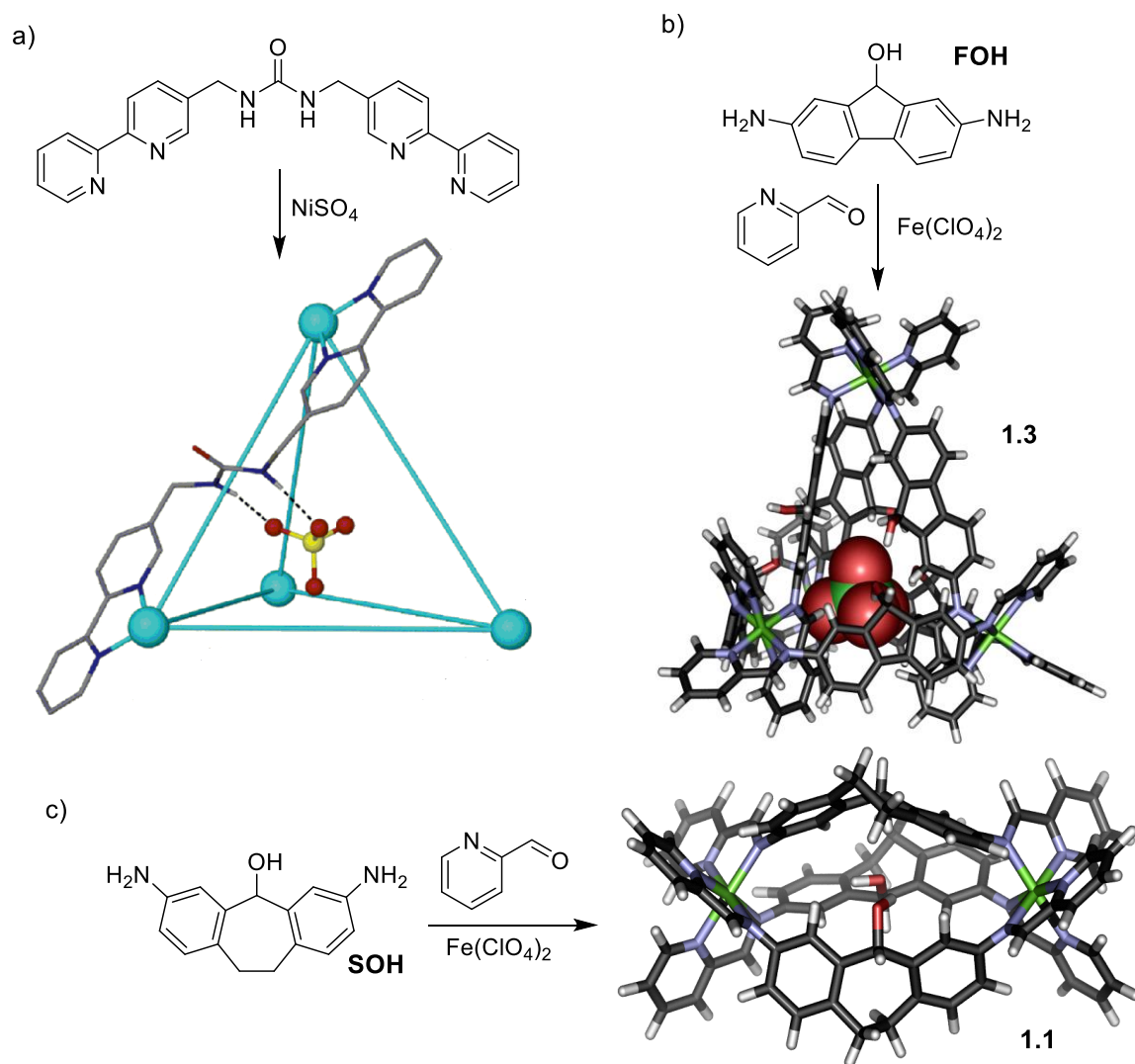


Figure 1.10. Selective anion recognition and structural control in supramolecular cages.⁵⁵⁻⁵⁸

Within the Hooley group it was discovered that the inclusion of other H-bond donors, such as alcohols, can have great impacts on both anion recognition and structural control of the assembly process. By using 2,7-diaminofluorenol **FOH** in an Fe-iminopyridine multicomponent self-assembly, effective stereocontrol of the assembly process can be conferred from specific anions (Figure 1.10b).⁵⁷ When the self-assembly is performed using $\text{Fe}(\text{ClO}_4)_2$, exclusive formation of an unusual *mer_3:fac* M_4L_6 prism **1.3** is observed, as opposed to the typical all-*fac* tetrahedra expected for this class of ligand.²⁵

The control in this assembly is exceptional: taking into account the 4 metal centers, each with 3 possible isomers, as well as the internal OH group which becomes chiral upon assembly, over 100 isomeric possibilities exist, however only the single diastereomer is observed. The control shown with **1.3** is specific to templation with the ClO_4^- ion (and similarly sized BF_4^-), use of other Fe^{2+} salts resulted in the formation of non-discrete coordination polymers. As the assembly is reversible, however, the non-discrete complexes could be converted to cage **1.3** upon heating with exogenous ClO_4^- . The usefulness of alcoholic H-bonding was also shown to a lesser extent in the self-assembly of M_2L_3 meso-helicates. The multicomponent iminopyridine self-assembly of 3,7-diaminosuberol **SOH** results in a stereocontrolled M_2L_3 mesocate **1.1** through inter-ligand hydrogen-bonding (Figure 1.10c).⁵⁸

To direct functional groups towards the interior cavity, most strategies use either V-shaped or linear ditopic ligands as tri- and tetrapodal ligands tend to be planar and therefore unsuitable for endohedral functionalization.^{59,60} In fact, tripodal ligands that use an sp^3 carbon at the center almost exclusively favor exohedral orientation.⁶¹ An outlier in this trend was presented by Nitschke through the formation of an azaphosphatrane decorated Fe_4L_4 tetrahedron (Figure 1.11).⁶² When protonated, the azaphosphatrane unit is cationic and a strong H-bond donor, enabling anion binding in aqueous solution. The cage can exist in two isomeric forms, either a *T*-symmetric isomer with all four phosphatrane groups pointed internally, or a C_3 symmetric isomer with three internally and one externally oriented group. The binding affinity of the cage was analyzed with several anions of varying size 35 \AA^3 (I^-) – 219 \AA^3 ($\text{CB}_{11}\text{H}_{12}^-$). It was discovered that differently sized anions

preferred one isomer over the other: most anions preferred the *T* isomer (with 100:1 bias for guests $> 55 \text{ \AA}^3$), but the small NO_3^- anion resulted in a 95:5 preference for the C_3 isomer. Most importantly, the structure of the cage could be easily interchanged through anion exchange with a suitable guest.

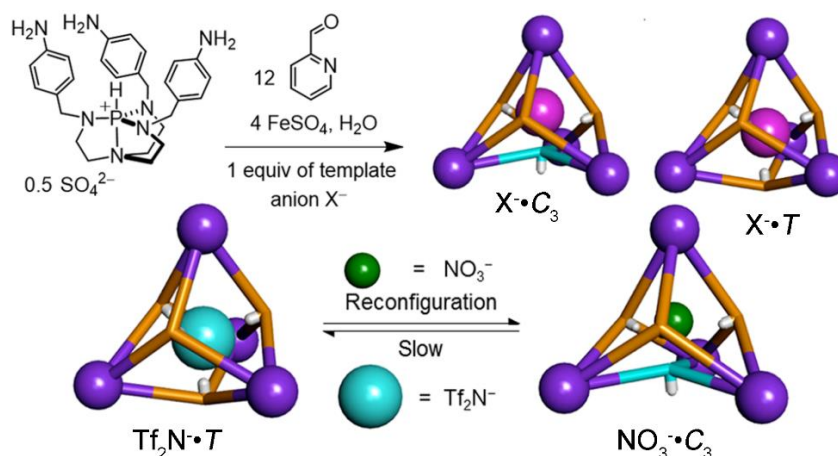


Figure 1.11. Structural switching of M_4L_4 cages via anion templation.⁶²

1.6. Reactions with Self-Assembled Cages

The most enticing function in self-assembled cages is their use in biomimetic catalysis. The internal cavity of cages is ideal for recognition of a wide range of guests, as shown above. However, transitioning from simple host-guest interactions to the more specific recognition necessary for catalysis presents several distinct challenges. In general, the ability of cages to properly differentiate between multiple guests is still underdeveloped, which can cause problems in turn-over through both product and substrate inhibition. Further the coordinating motifs that hold the cages together tend to be sensitive and could be damaged through the reaction process. This is especially true with reactions that require particularly harsh conditions or outside reagents to proceed. As such performing reactions that utilize self-assembled cages require careful selection of reaction

conditions. Given the inherent challenges with introducing reactive functionality to cages, several new methods must be explored, including post-assembly modification of preformed complexes.

1.7 Introduction of Endohedral Functionality Through Post-Assembly Modification

The alteration of metallosuperstructures via post assembly modification (PAM) has been thoroughly investigated in metal-organic frameworks,⁶³ but is far less common in self-assembled cage complexes.^{64,65} Further, the majority of these studies have focused on mild external modifications,⁶⁶ presumably because derivatization of the interior in the reversible complexes is more challenging.⁶⁷ In the cases where PAM has been used on self-assembled cages, the interactions rely on mild transformations such as ring closing metathesis,⁶⁸ or “click” reactions such as CuAAC.⁶⁹ While many examples of reactivity in cages exist, the reactions depend on pre-organization of the substrates and an increases effective concentration of the substrates rather than the cages containing reactive functionality of their own.

The ease of functionalization, and robustness of the large $M_{12}L_{24}$ nanospheres make them ideal candidates for PAM. By linking methyl methacrylate (MMA) groups to the ligand scaffold, atom transfer radical polymerization (ATRP) was made possible within the interior of the cage **1.19** (Figure 1.12a).⁷⁰ The polymerization process could be further optimized by varying the oligoethyleneglycol spacer, with the most optimal length being $n=3$. By encapsulating the reactive components, a discrete polymer could be formed upon

treatment with AIBN. Hydrolysis of the glycol linkages enable isolation and analysis of the resultant polymer which exhibited a polydispersity index (M_w/M_n) of 1.60.

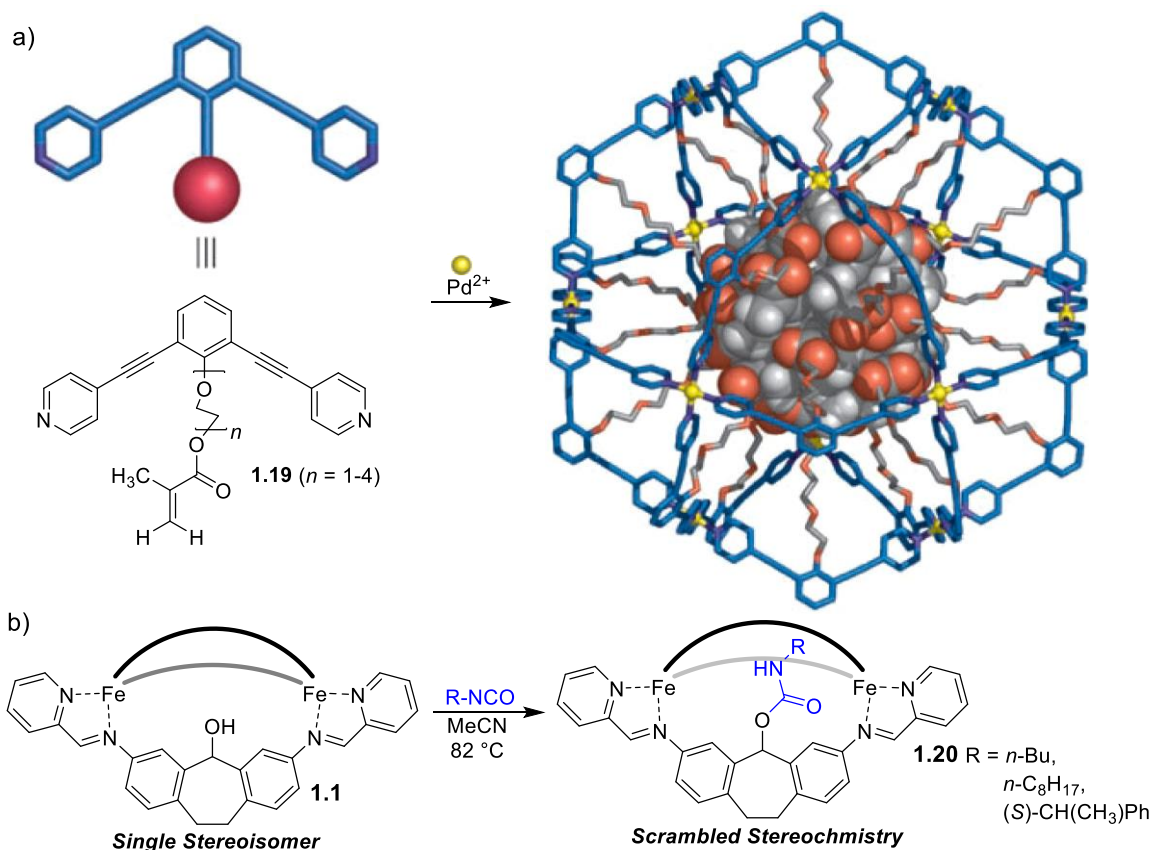


Figure 1.12. Reactions with covalently attached groups. a) Polymer growth on the interior of a functionalized cage.⁷⁰ b) Cage-promoted nucleophilic addition.⁵⁸

By internalizing the reactive functionality, it is possible to control post-assembly modifications. Mesocate **1.1** can react with neutral electrophiles like alkyl isocyanates under mild conditions.⁵¹ Orientation of the alcohol groups towards the internal cavity not only confers stereocontrol on the self-assembly but can also accelerate the reaction. The hydrogen bonding interactions activate the isocyanate enabling the PAM to occur without the need of a catalyst. If similar conditions are utilized on non-assembled ligand surrogates, no reaction is observed. It is also worth noting that as the self-complementary hydrogen-

bonding of the alcohol groups is removed, the stereochemistry of the mesocate structure is scrambled. A similar study was performed by Klosterman through the N-acylation of an aniline decorated di-Cu^{II} paddlewheel cage.⁷¹ By refluxing the cage in DMF in the presence of acetic anhydride, the amide product could be formed. Only a single acylation was possible however, as the small cavity of the paddlewheel complex became crowded following the first reaction.

1.8. Catalysis with Endohedrally Functionalized Cages

To transition from simple reactions on the cage to biomimetic catalysis, the cavity of the complex must of course be large enough to accommodate both the reactive endohedral functionality, as well as the reagent. As consequence, most known examples of endohedrally functionalized catalysis are performed using the large M₁₂L₂₄ nanospheres. The robust nature of the pyridyl-Pd coordination allows the internalization of other, more weakly coordinating functional groups such as phosphines. Efficient catalysis of the hydroalkoxylation of a γ -allenol **1.21** was shown by Reek using an internalized Au(I) phosphine catalyst (Figure 1.13a).⁷² By appending the catalyst to the ligands, the cavity exhibited an increased local concentration of Au(I)Cl resulting in higher activity. In addition to the good yield (88 %), the cage also gave selective formation of the only the 5-membered cyclization product **1.22**. 1,6-eneyne **1.24** was less amenable to cyclo-isomerization, however selective formation of the 5-membered product **1.25** was still observed. The harsher conditions necessary to perform this reaction as well as an intramolecular [4+2] cycloaddition was made possible by replacing the Pd²⁺ vertices with Pt²⁺.⁷³

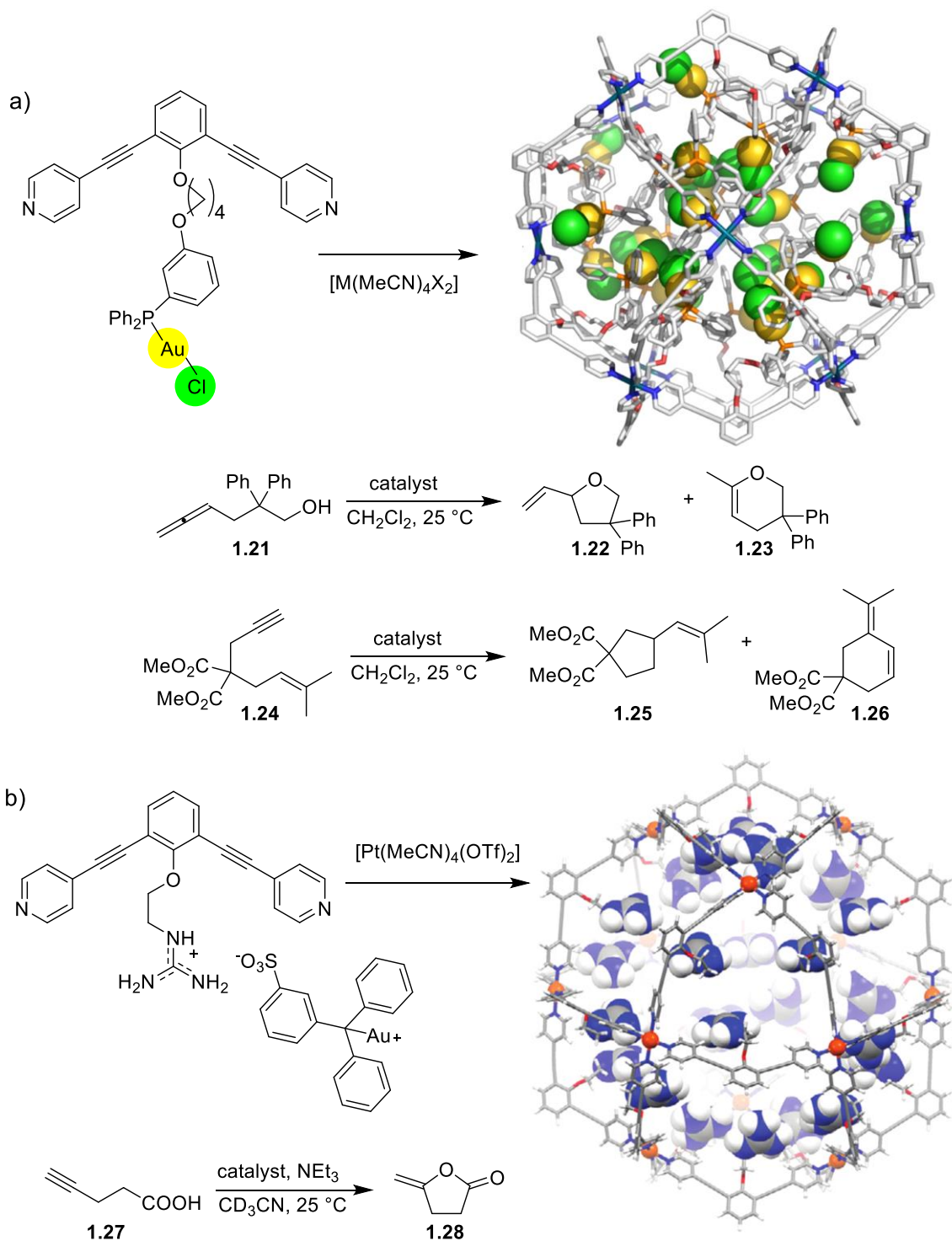


Figure 1.13. Organometallic catalysis in endohedrally functionalized nanospheres.⁷²⁻⁷⁴

In addition to the covalent attachment shown above, incorporation of the Au(I)-phosphine catalyst is possible through non-covalent interactions. Guanidinium groups have high binding affinity for sulfonate and carboxylate anions. By decorating the interior of a Pt₁₂L₂₄ nanosphere with guanidinium groups, strong incorporation of triphenylphosphinomonosulfonate (TPPMS) Au(I)Cl catalysts is made possible (Figure 1.13b).⁷⁴ This strategy provides unique opportunities in supramolecular catalysis. First, it enables additional control in the concentration of Au(I)Cl present within the cavity of the cage. Second, the difference in binding affinity between sulfonate and carboxylate provides the opportunity for preorganization of the sulfonated catalyst and a carboxylate-containing substrate. The addition of four equivalents of TPPMS-AuCl in the presence of base allowed good catalytic activity for the cyclization of acetylenic acid **1.G**. (>95 % conversion, TOF = 5.75). During the cyclization process the carboxylate group is cleaved from the product, facilitating turnover of the catalyst. Using a single hydrogen-bonding species confined to the interior of the cage, increases interactions between the catalyst and reactant, with no observed product inhibition.

The most obvious advantage of endohedrally functionalized nanospheres over small molecule catalysts is the removal of the catalyst from bulk solution. By sequestering the reactive compound, catalytic motifs that would typically be incompatible can be used in a single flask, enabling concurrent tandem catalysis. This concept was expertly demonstrated by Fujita using two cages exhibiting organocatalytic groups on the interior to perform multiple sequential reactions in one pot.⁷⁵ The two new nanospheres contained either 24 TEMPO groups or 24 MacMillan type amine catalysts (Figure 1.14). Oxidation

of an alcohol to an aldehyde is made possible in the TEMPO sphere, while iminium-mediated Diels-Alder reactions can be performed in the MacMillan sphere. Alcohol **1.29** is primed for this sort of reactivity, however when this reaction is attempted using free catalyst no product is observed. By sequestering both catalysts in their respective nanoenvironments, efficient oxidation to aldehyde **1.30**, followed by cyclization to product **1.31** is observed. This reactivity is specific to the use of both cages in a tandem process, in control reactions in which only one cage is used and alternate one free catalyst, minimal yield is observed.

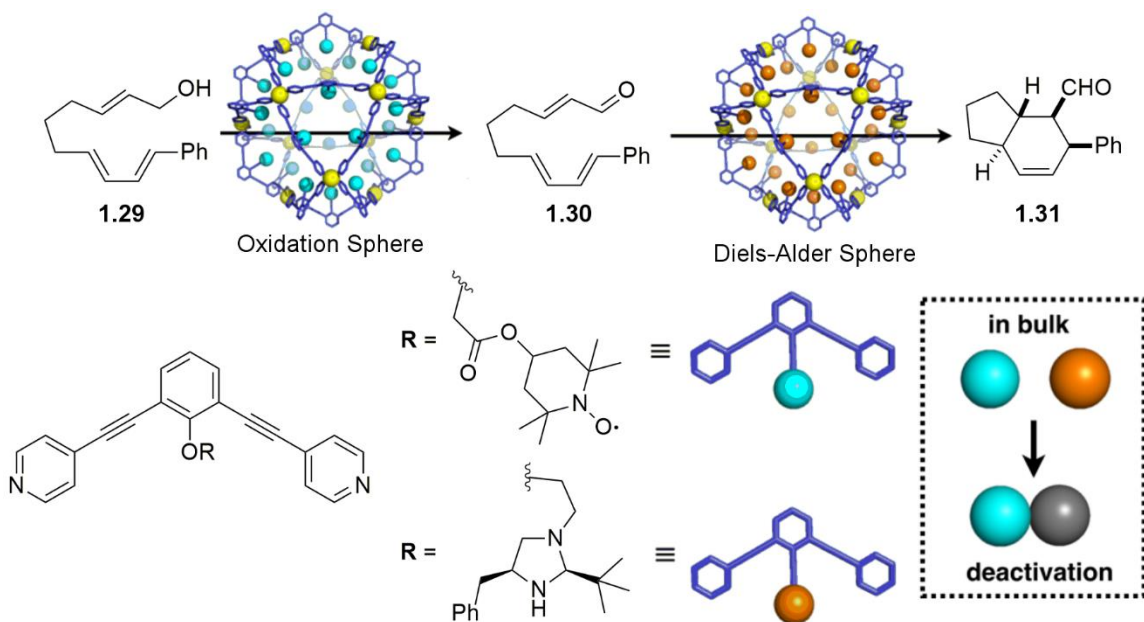


Figure 1.14. Concurrent tandem catalysis with two differently functionalized nanospheres.⁷⁵

1.9. Summary and Outlook

A number of challenges exist in the creation of endohedrally functionalizing supramolecular cages. From ensuring the proper orientation of functional groups, to accounting for the sensitive structural components while introducing active functional groups, as well as stereocontrol of more complicated assemblies. Many of these concerns

have been accounted for: Pt and Pd $M_{12}L_{24}$ nanospheres can tolerate a wide range of internal functions, and the introduction of hydrogen binding in smaller Fe-iminopyridine assemblies is capable of controlling the stereochemical outcome. Further, many exceptional examples of organic and organometallic catalysis using highly complicated nanostructures have been shown. However, the utility of endohedral functionality is far from finished. Much of the molecular recognition presented is limited to small molecules, or in very large nanospheres which exhibit rapid in-out rates for their guest. While several great examples of PAM have been observed, after the reaction is performed the resulting product is inert ending the process. A more ideal PAM would be one that is either reversible, or produces a new reactive product which is as of yet under explored. Finally, true enzyme mimicking catalysis is yet to be achieved: enzymes display a small cavity, containing multiple different functional groups that can selectively bind and activate a chiral substrate. Combining all these requirements into a single species is an ambitious goal, and one that has remained elusive for some time.

1.10 References

1. Bogie, P. M.; Miller, T. F.; Hooley, R. J. "Synthesis and Applications of Endohedrally Functionalized Metal-Ligand Cage Complexes." *Isr. J. Chem.* **2019**, *59*, 130–139.
2. Smulders, M. M. J.; Riddell, I. A.; Browne, C.; Nitschke, J. R. "Building on architectural principles for three-dimensional metallocsupramolecular construction." *Chem. Soc. Rev.* **2013**, *42*, 1728–1754.
3. Erbas-Cakmak, S.; Leigh, D. A.; McTernan, C. T.; Nussbaumer, A. L. "Artificial Molecular Machines." *Chem. Rev.* **2015**, *115*, 10081–10206.
4. Kay, E. R.; Leigh, D. A. "Rise of the Molecular Machines." *Angew. Chem. Int. Ed.* **2015**, *54*, 10080–10088.
5. Zhang, D.; Ronson, T. K.; Mosquera, J.; Martinez, A.; Nitschke, J. R. "Selective Anion Extraction and Recovery Using a Fe^{II}₄L₄ Cage." *Angew. Chem. Int. Ed.*, **2018**, *57*, 3717–3721.
6. Ronson, T. K.; Giri, C.; Beyeh, N. K.; Minkkinen, A.; Topić, F.; Holstein, J. J.; Rissanen, K.; Nitschke, J. R. "Size-Selective Encapsulation of Hydrophobic Guests by Self-Assembled M₄L₆ Cobalt and Nickel Cages." *Chem. Eur. J.* **2013**, *19*, 3374–3382.
7. Johnson, A. M.; Young, M. C.; Zhang, X.; Julian, R. R.; Hooley, R. J. "Cooperative Thermodynamic Control of Selectivity in the Self-Assembly of Rare Earth Metal-Ligand Helices" *J. Am. Chem. Soc.* **2013**, *135*, 17723–17726.
8. Fujita, M.; Tominaga, M.; Hori, A.; Therrien, B. "Coordination Assemblies from a Pd(II)-Cornered Square Complex." *Acc. Chem. Res.* **2005**, *38*, 369–378.
9. Hall, B. R.; Manck, L. E.; Tidmarsh, I. S.; Stephenson, A.; Taylor, B. F.; Blaikie, E. J.; Vander Griend, D. A.; Ward, M. D. "Structures, host-guest chemistry and mechanism of stepwise self-assembly of M₄L₆ tetrahedral cage complexes." *Dalton Trans.* **2011**, *40*, 12132–12145.
10. Mal, P.; Schultz, D.; Beyeh, K.; Rissanen, K.; Nitschke, J. R. "An Unlockable-Relockable Iron Cage by Subcomponent Self-Assembly." *Angew. Chem. Int. Ed.* **2008**, *47*, 8297–8301.
11. Tidmarsh I. S; Faust, T. B.; Adams, H.; Harding, L. P.; Russo, L.; Clegg, W.; Ward, M. D. "Octanuclear Cubic Coordination Cages." *J. Am. Chem. Soc.* **2008**, *130*, 15167–15175.

12. Kersting, B.; Meyer, M.; Powers, R. E.; Raymond, K. N. "Dinuclear Catecholate Helicates: Their Inversion Mechanism." *J. Am. Chem. Soc.* **1996**, *118*, 7221–7222.
13. Young, M. C.; Johnson, A. M.; Hooley, R. J. "Self-Promoted Post-Synthetic Modification of Metal-Ligand M_2L_3 Mesocates." *Chem. Commun.* **2014**, *50*, 5043–5045.
14. Hastings, C. J.; Pluth, M. D.; Bergman, R. G.; Raymond, K. N. "Enzymelike Catalysis of the Nazarov Cyclization by Supramolecular Encapsulation." *J. Am. Chem. Soc.* **2010**, *132*, 6938–6940.
15. Tominaga, M.; Suzuki, K.; Kawano, M.; Kusakawa, T.; Ozeki, T.; Sakamoto, S.; Yamaguchi, K.; Fujita, M. "Finite, Spherical Coordination Networks the Self-Organize from 36 Small Components." *Angew. Chem. Int. Ed.* **2004**, *43*, 5621–5625.
16. Sun, Q.-F.; Iwasa, J.; Ogawa, D.; Ishido, Y.; Sato, S.; Ozeki, T.; Sei, Y.; Yamaguchi, K.; Fujita, M. "Self-Assembled $M_{24}L_{48}$ Polyhedra and Their Sharp Structural Switch upon Subtle Ligand Variation." *Science* **2010**, *328*, 1144–1147.
17. Riddel, I. A.; Smulders, M. M. J.; Clegg, J. K.; Hristova, Y. R.; Breiner, B.; Thoburn, J. D.; Nitschke, J. R. "Anion-induced reconstitution of a self-assembling system to express a chloride-binding $Co_{10}L_{15}$ pentagonal prism." *Nature Chem.* **2012**, *4*, 751–756.
18. T. R. Cook, Y.-R. Zheng, P. J. Stang, "Metal-Organic Frameworks and Self-Assembled Supramolecular Coordination Complexes: Comparing and Contrasting the Design, Synthesis, and Functionality of Metal-Organic Materials." *Chem. Rev.* **2013**, *113*, 734–777.
19. Young, M. C.; Johnson, A. M.; Gamboa, A. S. "Achiral endohedral functionality provides stereochemical control in Fe(II)-based self-assemblies." *Chem. Commun.* **2013**, *49*, 1627–1629.
20. Castilla, A. M.; Ramsay, W. J.; Nitschke, J. R. "Stereochemical Communication within Tetrahedral Capsules." *Chem. Lett.* **2014**, *43*, 256–263.
21. Meng, W.; Clegg, J. K.; Thoburn, J. D.; Nitschke, J. R. "Controlling the Transmission of Stereochemical Information through Space in Terphenyl-Edged Fe_4L_6 Cages." *J. Am. Chem. Soc.* **2011**, *133*, 13652–13660.
22. Kieffer, M.; Pilgrim, B. S.; Ronson, T. K.; Roberts, D. A.; Aleksanyan, M.; Nitschke, J. R. "Perfluorinated Ligands Induce Meridional Metal Stereochemistry to Generate M_8L_{12} , $M_{10}L_{15}$, and $M_{12}L_{18}$ Prisms." *J. Am. Chem. Soc.* **2016**, *138*, 6813–6821.

23. Meng, W.; Ronson, T. K.; Nitschke, J. R. "Symmetry Breaking in Self-Assembled M_4L_6 Cage Complexes." *Proc. Natl. Acad. Sci.* **2013**, *110*, 10531-10535.
24. Preston, D.; Barnsley, J. E.; Grodon, K. C.; Crowley, J. D. "Controlled Formation of Heteroleptic $[Pd_2(L_a)_2(L_b)_2]^{4+}$ Cages." *J. Am. Chem. Soc.* **2016**, *138*, 10578-10585.
25. Bloch, W. M.; Abe, Y.; Holstein, J. J.; Wandtke, C. M.; Dittrich, B.; Clever, G. H. *J. Am. Chem. Soc.* **2016**, *138*, 13750-13755.
26. Bloch, W. M.; Holstein, J. J.; Hiller, W.; Clever, G. H. "Morphological Control of Heteroleptic *cis*- and *trans*- $Pd_2L_2L'_2$ Cages" *Angew. Chem. Int. Ed.* **2017**, *56*, 8285-8289.
27. Holloway, L. R.; Young, M. C.; Beran, G. J. O.; Hooley, R. J. "High Fidelity Sorting of Remarkably Similar Components via Metal-Mediated Assembly." *Chem. Sci.* **2015**, *6*, 4801-4806.
28. Wiley, C. A.; Holloway, L. R.; Miller, T. F.; Lyon, Y.; Julian, R. R.; Hooley, R. J. "Electronic Effects on Narcissistic Self-Sorting in Multicomponent Self-Assembly of Fe-Iminopyridine meso-Helicates." *Inorg. Chem.* **2016**, *55*, 9805-9815.
29. Fujita, M.; Umemoto, K.; Yoshizawa, M.; Fujita, N.; Kusakawa, T.; Biradha, K. "Molecular paneling *via* coordination." *Chem. Commun.* **2001**, 509-518.
30. Bilbeisi, R. A.; Clegg, J. K.; Elgrishi, N.; de Hatten, X.; Devillard, M.; Breiner, B.; Mal, P.; Nitschke, J. R. "Subcomponent Self-Assembly and Guest-Binding Properties of Face-Capped $Fe_4L_4^{8+}$ Capsules." *J. Am. Chem. Soc.* **2012**, *134*, 5110-5119.
31. Yamashina, M.; Akita, M.; Hasegawa, T.; Hayashi, S.; Yoshizawa, M. "A polyaromatic nanocapsule as a sucrose receptor in water." *Sci. Adv.* **2017** Aug 25;3(8):e1701126.
32. Samanta, D.; Galaktionova, D.; Gemen, J.; Shimon, L. J. W.; Diskin-Posner, Y.; Avram, L.; Král, P.; Klajn, R. "Reversible chromism of spiropyran in the cavity of a flexible coordination cage." *Nature Comm.*, **2018**, *9*, 641-650.
33. Samanta, D.; Gemen, J.; Chu, Z.; Diskin-Posner, Y.; Shimon, L. J. W.; Klajn, R. "Reversible photoswitching of encapsulated azobenzenes in water." *Proc. Natl. Acad. Sci. USA* **2018**, *115*, 9379-9384.
34. Hong, C. M.; Bergman, R. G.; Raymond, K. N.; Toste, F. D. "Self-Assembled Tetrahedral Hosts as Supramolecular Catalysts." *Acc. Chem. Res.* **2018**, *51*, 2447-2455.

35. Hastings, C. J.; Pluth, M. D.; Bergman, R. G.; Raymond, K. N. "Enzymelike Catalysis of the Nazarov Cyclization by Supramolecular Encapsulation." *J. Am. Chem. Soc.* **2010**, *132*, 6938–6940.
36. Brown, C. J.; Bergman, R. G.; Raymond, K. N. "Enantioselective Catalysis of the Aza-Cope Rearrangement by a Chiral Supramolecular Assembly." *J. Am. Chem. Soc.* **2009**, *131*, 17350–17351.
37. Yan, X.; Cook, T R.; Wang, P.; Huang, F.; Stang, P. J. "Highly emissive platinum(II) metallacages." *Nature Chem.*, **2015**, *7*, 342–348.
38. Al-Rasbi, N. K.; Sabatini, C.; Barigelletti, F.; Ward, M. D. "Red-shifted luminescence from naphthalene-containing ligands due to π -stacking in self-assembled coordination cages." *Dalton Trans.* **2006**, 4769–4772.
39. Wragg, A. B.; Metherell, A. J.; Cullen, W.; Ward, M. D. "Stepwise assembly of mixed-metal coordination cages containing both kinetically inert and kinetically labile metal ions: introduction of metal-centered redox and photophysical activity at specific sites." *Dalton Trans.* **2015**, *44*, 17939–17949.
40. Yan, L.-L.; Tan, C.H.; Zhang, G.-L.; Zhou, L.-P.; Bünzli, J.-C.; Sun, Q.-F. "Stereocontrolled Self-Assembly and Self-Sorting of Luminescent Europium Tetrahedral Cages." *J. Am. Chem. Soc.* **2015**, *137*, 8550–8555.
41. Jiao, Y.; Wang, J.; Wu, P.; Zhao, L.; He, C.; Zhang, J.; Duan, C. "Cerium-Based M₄L₄ Tetrahedra as Molecular Flasks for Selective Reaction Prompting and Luminescent Reaction Tracing." *Chem. Eur. J.* **2014**, *20*, 2224–2231.
42. Wang, J.; Wu, P.; Wang, J.; Duan, C. "An Amide-Containing Metal–Organic Tetrahedron Responding to a Spin-Trapping Reaction in a Fluorescent Enhancement Manner for Biological Imaging of NO in Living Cells." *J. Am. Chem. Soc.* **2011**, *133*, 12402–12405.
43. Fujita, D.; Takahashi, A.; Sato, S.; Fujita, M. "Self-Assembly of Pt(II) Spherical Complexes via Temporary Labilization of the Metal–Ligand Association in 2,2,2-Trifluoroethanol." *J. Am. Chem. Soc.* **2011**, *133*, 13317–13319.
44. Suzuki, K.; Iida, J.; Sato, S. Kawano, M.; Fujita, M. "Discrete and Well-Defined Hydrophobic Phases Confined in Self-Assembled Spherical Complexes." *Angew. Chem. Int. Ed.* **2008**, *47*, 5780–5782.
45. Sato, S.; Iida, J.; Suzuki, K.; Kawano, M.; Ozeki, T.; Fujita, M. "Fluorous Nanodroplets Structurally Confined in an Organopalladium Sphere." *Science* **2006**, *313*, 1273–1275.

46. Suzuki, K.; Takao, K.; Sato, S.; Fujita, M. "Coronene Nanophase within Coordination Spheres: Increased Solubility of C₆₀." *J. Am. Chem. Soc.* **2010**, *132*, 2544–2545.
47. Sun, Q.-F.; Sato, S.; Fujita, M. "Self-assembled Inverse Dendrimer." *Chem. Lett.* **2011**, *40*, 726–727.
48. Fujita, D.; Suzuki, K.; Sato, S.; Yagi-Utsumi, M.; Yamaguchi, Y.; Mizuno, N.; Kumasaka, T.; Takata, M.; Noda, M.; Uchiyama, S.; Kato, K.; Fujita, M. "Protein encapsulation within synthetic molecular hosts." *Nature Comm.* **2012**, *3*, 1093–1099.
49. Sun, Q.-F.; Murase, T.; Sato, S.; Fujita, M. "A Sphere-in-Sphere Complex by Orthogonal Self-Assembly." *Angew. Chem. Int. Ed.* **2011**, *50*, 10318–10321.
50. Harris, K.; Sun, Q.-F.; Sato, S.; Fujita, M. "M₁₂L₂₄ Spheres with Endo and Exo Coordination Sites: Scaffolds for Non-Covalent Functionalization." *J. Am. Chem. Soc.* **2013**, *135*, 12497–12499.
51. Liao, P.; Langloss, B. W.; Johnson, A. M.; Knudsen, E. R.; Tham, F. S.; Julian, R. R.; Hooley, R. J. "Two-Component Control of Guest Binding in a Self-Assembled Cage Molecule." *Chem. Commun.* **2010**, *46*, 4932–4934.
52. Lewis, J. E. M.; Gavey, E. L.; Cameron, S. A.; Crowley, J. D. "Stimuli-responsive Pd₂L₄ metallosupramolecular cages: towards targeted cisplatin drug delivery." *Chem. Sci.* **2012**, *3*, 778–784.
53. Johnson, A. M.; Moshe, O.; Gamboa, A. S.; Langloss, B. W.; Limtiaco, J. F. K.; Larive, C. K.; Hooley, R. J. "Synthesis and Properties of Metal–Ligand Complexes with Endohedral Amine Functionality." *Inorg. Chem.* **2011**, *50*, 9430–3442.
54. Preston, D.; Lewis, J. E. M.; Crowley, J. D. "Multicavity [Pd_nL₄]²ⁿ⁺ Cages with Controlled Segregated Binding of Different Cages." *J. Am. Chem. Soc.* **2017**, *139*, 2379–2386.
55. Custelcean, R.; Bosano, J.; Bonnesen, P. V.; Kertesz, V.; Hay, B. P. "Computer-Aided Design of a Sulfate-Encapsulating Receptor." *Angew. Chem. Int. Ed.* **2009**, *48*, 4025–4029.
56. Custelcean, R.; Bonnesen, P. V.; Duncan, N. C.; Zhang, X.; Watson, L. A.; Van Berkel, G.; Parson, W. B.; Hay, B. P. "Urea-Functionalized M₄L₆ Cage Receptors: Anion-Templated Self-Assembly and Selective Guest Exchange in Aqueous Solutions." *J. Am. Chem. Soc.* **2012**, *134*, 8525–8534.
57. Young, M. C.; Holloway, L. R.; Johnson, A. M.; Hooley, R. J. "A Supramolecular Sorting Hat: Stereocontrol in Metal-Ligand Self-Assembly by Complementary Hydrogen Bonding." *Angew. Chem. Int. Ed.* **2014**, *53*, 9832–9836.

58. Young, M. C.; Johnson, A. M.; Hooley, R. J. "Self-Promoted Post-Synthetic Modification of Metal-Ligand M_2L_3 Mesocates." *Chem. Commun.* **2014**, *50*, 1378–1380.
59. Percástegui, E. G.; Mosquera, J.; Nitschke, J. R. "Anion Exchange Renders Hydrophobic Capsules and Cargoes Water-Soluble." *Angew. Chem. Int. Ed.* **2017**, *56*, 9136–9140.
60. Samanta, D.; Mukherjee, S.; Patil, Y. P.; Mukherjee, P. S. "Self-Assembled Pd_6 Open Cage with Triimidazole Walls and the Use of Its Confined Nanospace for Catalytic Knoevenagel and Diels–Alder Reactions in Aqueous Medium." *Chem. Eur. J.* **2012**, *18*, 12322–12329.
61. Bilbeisi, R. A.; Clegg, J. K.; Elgrishi N.; de Hatten, X.; Devillard, M.; Breiner, B.; Mal, P.; Nitschke, J. R. "Subcomponent Self-Assembly and Guest-Binding Properties of Face Capped $Fe_4L_4^{8+}$ Capsules." *J. Am. Chem. Soc.* **2012**, *134*, 5110–5119.
62. Zhang, D.; Ronson, T. K.; Mosquera, J.; Martinez, A.; Guy, L.; Nitschke, J. R. "Anion Binding in Water Drives Structural Adaptation in an Azaphosphatrane-Functionalized $Fe^{II}_4L_4$ Tetrahedron." *J. Am. Chem. Soc.* **2017**, *139*, 6574–6577.
63. Tanabe, K. K.; Cohen, S. M. "Postsynthetic Modification of Metal-Organic Frameworks-A Progress Report." *Chem. Soc. Rev.* **2011**, *40*, 498–519.
64. Zheng, Y.-R.; Lan, W.-J.; Wang, M.; Cook, T. R.; Stang, P. J. "Designed Post-Self-Assembly Structural and Functional Modifications of a Truncated Tetrahedron." *J. Am. Chem. Soc.* **2011**, *133*, 17045–17055.
65. Roberts, D. A.; Pilgrim, B. S.; Nitschke, J. R. "Covalent post-assembly modification in metallosupramolecular chemistry." *Chem. Soc. Rev.* **2018**, *47*, 626–644.
66. Acharyya, K.; Mukherjee, P. S. "Post-Synthetic Exterior Decoration of An Organic Cage by Copper(I) Catalysed A3-Coupling and Detection of Nitroaromatics." *Chem. - Eur. J.* **2015**, *21*, 6823–6831.
67. Wang, M.; Lan, W.-J.; Zheng, Y.-R.; Cook, T. R.; White, H. S.; Stang, P. J. "Post-Self-Assembly Covalent Chemistry of Discrete Multicomponent Metallosupramolecular Hexagonal Prisms." *J. Am. Chem. Soc.* **2011**, *133*, 10752–10755.
68. Hiraoka, S.; Yamauchi, Y.; Arakane, R.; Shionoya, M. "Template-Directed Synthesis of a Covalent Organic Capsule Based on A 3 Nm-Sized Metallocapsule." *J. Am. Chem. Soc.* **2009**, *131*, 11646–11647.

69. Chakrabarty, R.; Stang, P. J. "Post-Assembly Functionalization of Organoplatinum(II) Metallacycles Via Copper-Free Click Chemistry." *J. Am. Chem. Soc.* **2014**, *134*, 14738–14741.
70. Murase, T.; Sato, S.; Fujita, M. "Nanometer-Sized Shell Molecules That Confine Endohedral Polymerizing Units." *Angew. Chem. Int. Ed.* **2007**, *46*, 1083–1085.
71. Brega, V.; Zeller, M.; He, Y.; Lu, H. P.; Klosterman, J. K. "Multi-responsive metal–organic lantern cages in solution." *Chem. Commun.* **2015**, *51*, 5077–5080.
72. Gramage-Doria, R.; Hessels, J.; Leenders, S. H. A. M.; Tröppner, O.; Dürr, M.; Ivanović-Burmazović, I.; Reek, J. N. H. "Gold(I) Catalysis at Extreme Concentrations Inside Self-Assembled Nanospheres." *Angew. Chem. Int. Ed.* **2014**, *53*, 13380–13384.
73. Leenders, S. H. A. M.; Dürr, M.; Ivanović-Burmazović, I.; Reek, J. N. H. "Gold Functionalized Platinum M₁₂L₂₄-Nanospheres and Their Application in Cyclization Reactions." *Adv. Synth. Catal.* **2016**, *358*, 1509–1518.
74. Wang, Q.-Q.; Gonell, S.; Leenders, S. H. A. M.; Dürr, M.; Ivanović-Burmazović, I.; Reek, J. N. H. "Self-assembled nanospheres with multiple endohedral binding sites pre-organize catalysts and substrates for highly efficient reactions." *Nature Chem.* **2016**, *8*, 225–230.
75. Ueda, Y.; Ito, H.; Fujita, D.; Fujita, M. "Permeable Self-Assembled Molecular Containers for Catalyst Isolation Enabling Two-Step Cascade Reactions." *J. Am. Chem. Soc.* **2017**, *139*, 6090–6093.

Chapter 2: Metal-Selective Coordination and Enhanced Fluorescence of a Self-Assembling Ligand Scaffold¹

2.1 Introduction

The definition of function is not limited to simply functional groups, but rather anything that provides additional use to the cage. One of the most basic functions one can imagine implementing is the introduction of luminescence for use in fluorescent sensing. In most cases this is done using either a fluorescent ligand^{2,3} or by using a fluorescent metal.^{4,5} While these methods are effective, they are limited to a single reporter. If instead the fluorophore was the metal chelator, the complex could double as a sensor for both guest molecules as well as metal ions. Herein the use of a fluorescent chelator capable of metal specific emission response is reported. The metal coordinating motif is a 1-hydroxy-2-iminonicotinonitrile (HINT) group, which exhibits a similar structure and metal coordination sites to the well-known hydroxypyridinone (HOPO) coordinating ligands (Figure 2.1).⁶ The HOPO ligands have been reported to strongly coordinate group (IV) metals⁷ and lanthanides,⁸ and can enhance the native luminescence of rare earth metals.^{9,10} This emission is localized on the metal, however, as the HOPO ligands are non-emissive by themselves. In contrast, the nicotinonitrile-containing analogs developed by McQuade and coworkers¹¹ exhibit native luminescence and can easily be obtained by rapid cyclization of primary amines with an alkylidene malononitrile enamine. By inducing the cyclization using hydroxylamine in place of an alkyl chain, the second hydroxy-pyridyl coordination site is produced.

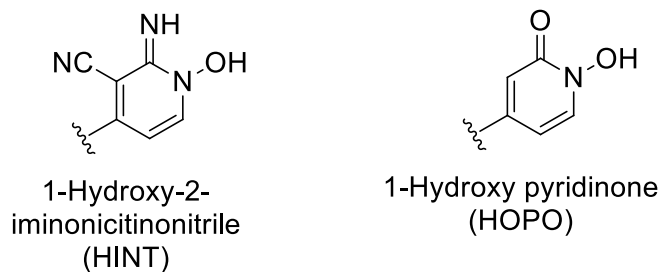


Figure 2.1. Structures of strongly metal coordinating motifs.

2.2 Rational Design and Synthesis of Ligands

Initially two ligand scaffolds were tested for their ability to coordinate metals and self-assemble into cages. Terphenyl ligand **2.1** and fluorenyl ligand **2.2** both contain two HINT groups and should be capable of multicomponent self-assembly into M_xL_y complexes (Figure 2.2). The self-assembly of these two ligands should be predictable as bent terphenyl ligands invariably form M_2L_3 *meso*-helicities,¹² while the more linear fluorenyl scaffold generally forms M_4L_6 tetrahedra.¹³ Ligand **2.1** was synthesized in four steps from 1,3-dibromobenzene. Diketone **2.A** was formed via a Suzuki-Miyaura coupling with 4-acetylphenylboronic acid in 95 % yield. Nitrile **2.B** was formed in 80 % yield via Knoevenagel condensation of **2.A** with malononitrile using $Ti(OiPr)_4$ as Lewis acid. This was converted to enamine **2.C** by treatment with *N,N*-dimethylformamide dimethyl acetal and acetic anhydride. The resulting enamine underwent rapid Pinner cyclization upon addition of hydroxylamine, giving ligand **2.1** in 96 % yield. Fluorenyl diketone **2.D** was formed in 71 % yield via an S_N2 reaction with methyl iodide, followed by Friedel-Crafts acylation. Ligand **2.2** was then formed following the same general procedures used for **2.1** in 54 % overall yield.

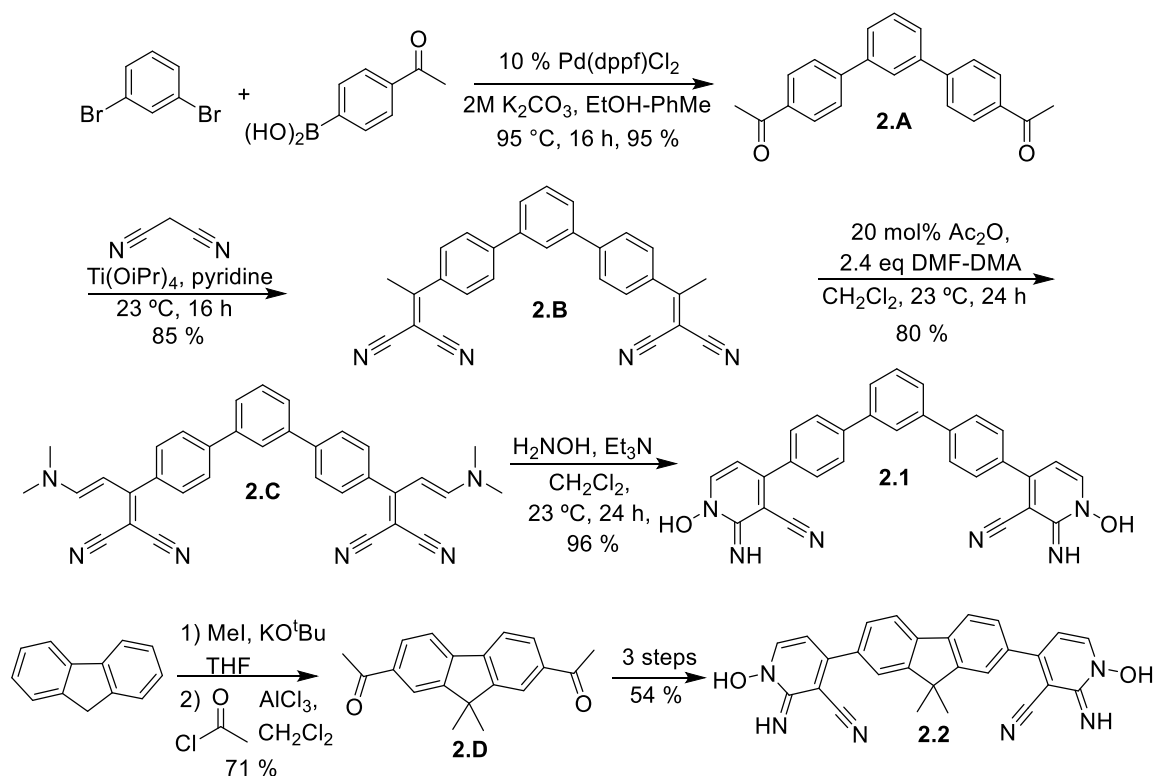


Figure 2.2. Synthetic route to *bis*-coordinating HINT ligands **2.1**, and **2.2**.

2.3 Investigation of Metal Coordination

The metal-coordinating abilities of **2.1** and **2.2** were tested by titrating metal ions into DMSO solutions of the ligands and monitoring the process by UV/Vis absorption spectroscopy. The neutral HINT ligands **2.1** and **2.2** showed poor affinity for metals by themselves, presumably due to the weakly coordinating nature of the terminal imine group. To allow for effective metal coordination, the ligands were pre-treated with NaH suspended in CH₂Cl₂. After ~1 h of stirring a precipitate formed which was isolated via vacuum filtration to yield the anionic sodiated counterparts Na•**2.1** and Na•**2.2**. As expected, the increased donating ability of the anionic ligands enabled strong coordination, and high affinity for a range of oxophilic transition metal ions (Figure 2.3). 30 μM solutions of Na•**1** and Na•**2** in DMSO were prepared in 3 mL quartz cuvettes. Metal salts were then

added from a 10 mM solution in 9 μL increments (0.11 molar equivalent with respect to ligand), with absorption spectra taken at each increment.

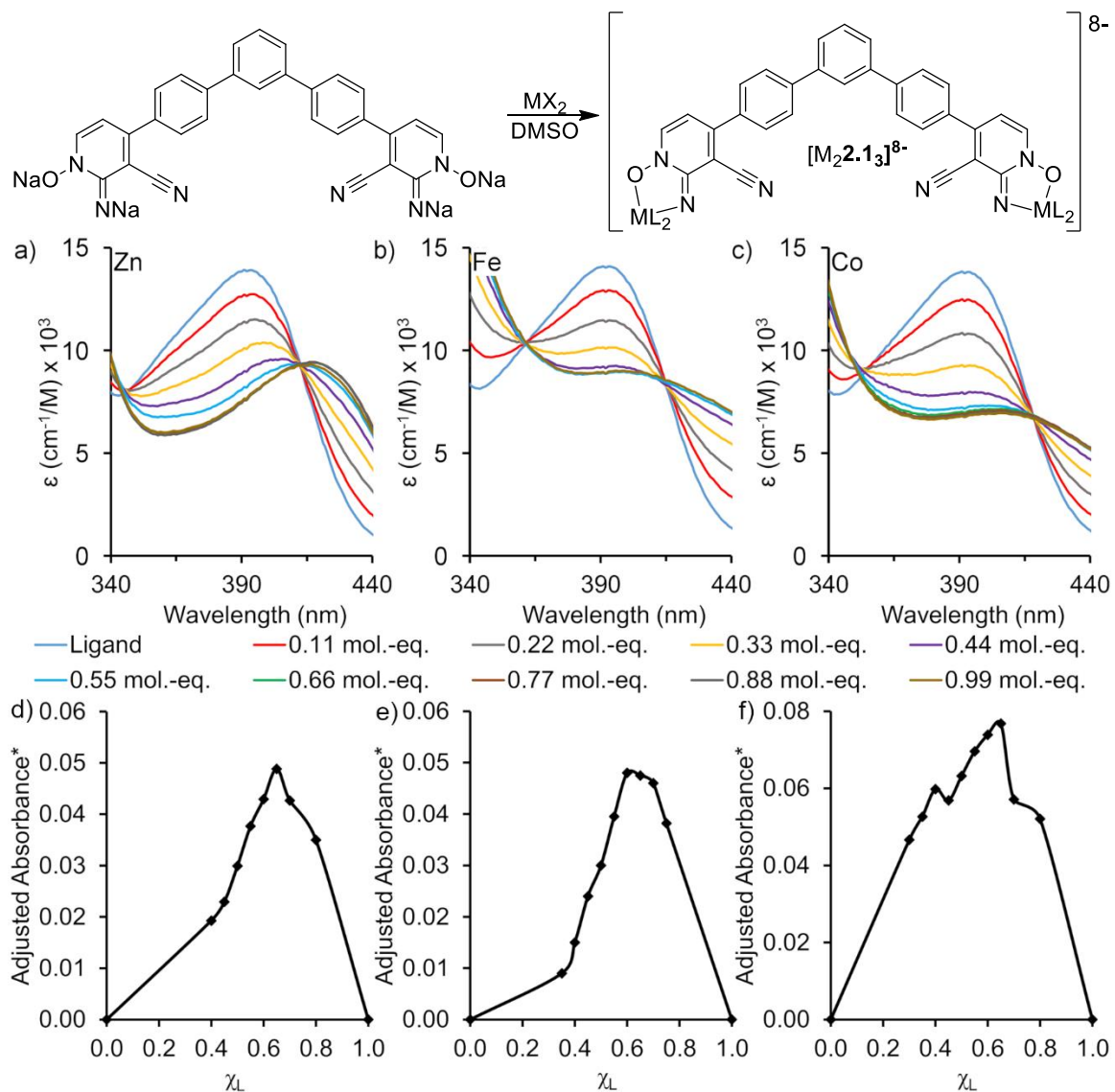


Figure 2.3. UV-Vis absorption spectra of the titration of various metal salts into DMSO solutions of anionic ligand Na•2.1: a) $\text{MX}_2 = \text{Zn}(\text{OTf})_2$, b) $\text{MX}_2 = \text{Fe}(\text{ClO}_4)_2$, c) $\text{MX}_2 = \text{Co}(\text{ClO}_4)_2$. $[\text{Na}\bullet\text{2.1}] = 30 \mu\text{M}$. Job plot of the assembly process measured based at specified wavelength: d) $\text{Zn}(\text{OTf})_2 - 430 \text{ nm}$, e) $\text{Fe}(\text{ClO}_4)_2 - 460 \text{ nm}$, f) $\text{Co}(\text{ClO}_4)_2 - 400 \text{ nm}$. *Adjusted Absorbance = $\text{Abs} - \left(\frac{[\text{ligand}]}{[\text{ligand}] + [\text{M}]} \right) \text{Abs}_0$

A clear red-shift in the λ_{max} of Na•2.1 is observed in the absorption spectrum upon titrating either Zn^{2+} , Fe^{2+} or Co^{2+} into a solution of Na•2.1 in DMSO. The shift is accompanied by easily detectable isosbestic points, indicating the formation of a single discrete metal-ligand complex. In each case the absorbance changes ceased after addition of 0.66 mol.-eq. of metal salt added, consistent with the expected formation of an M_2L_3 complex. To corroborate this assignment, analysis of the stoichiometry of the assembly was carried out using Job's method for the assembly of Na•2.1 with Zn^{2+} , Fe^{2+} and Co^{2+} , each of the plots exhibited a maximum at 0.66 mol.-eq. confirming the 2:3 metal to ligand ratio (Figure 2.3d-f).

The binding affinities of Na•2.1 for each of the metals (Zn^{2+} , Fe^{2+} , and Co^{2+}) were calculated via Stern-Volmer analysis (Figure 2.4a). Anionic ligand Na•2.1 exhibited high affinity for each of the chosen metals, with dissociation constants on the order of 25-50 μM ($K_d(\text{Zn}) = 49.8 \mu\text{M}$, $K_d(\text{Fe}) = 28.5 \mu\text{M}$, $K_d(\text{Co}) = 42.5 \mu\text{M}$). The titration experiments, and formation of complex, were insensitive to counter anion: weakly coordinating ions such as NO_3^{2-} , ClO_4^- or TfO^- all showed similar absorption spectra upon titration with Na•2.1. The affinity for the ligand is lowered, however, when salts with strongly coordinating counterions such as Cl^- are used. Finally, despite the ligand and resulting complex being highly anionic, the assembly process is mildly tolerant to water at μM concentrations. Effective assembly into the $\text{Zn}_2\text{2.1}_3$ complex was observed in the presence of up to 33 % water in the DMSO (Figure 2.3).

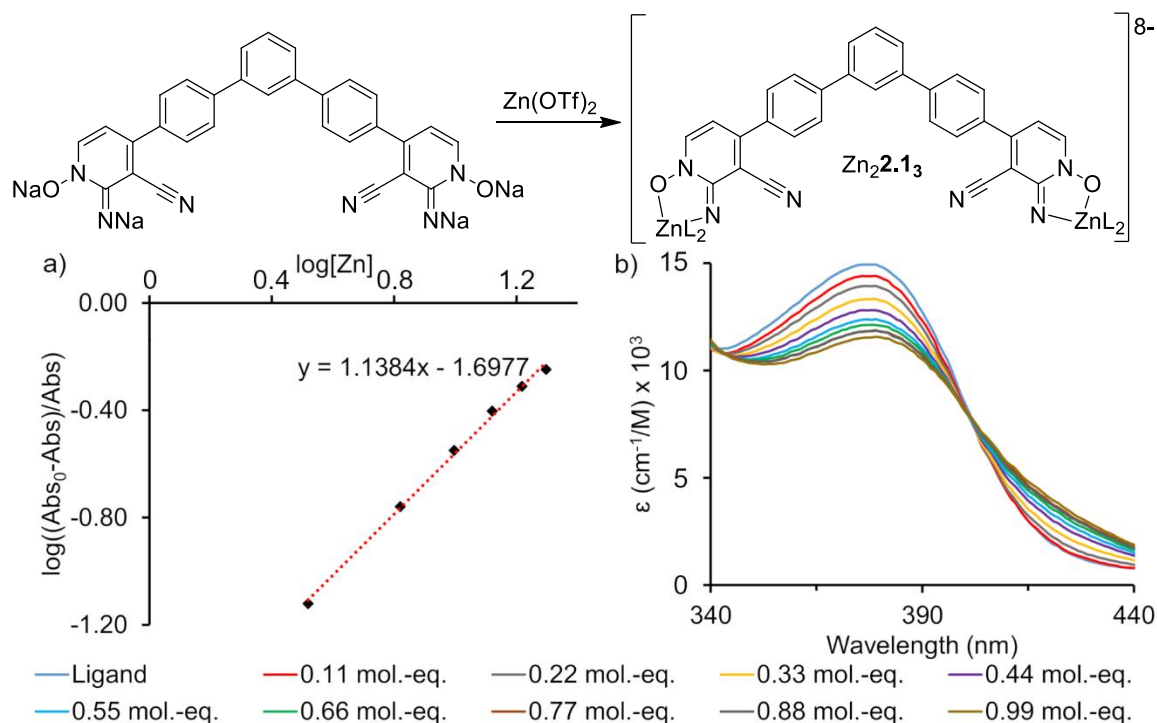


Figure 2.4. a) Stern-Volmer plot for the absorbance titration of $\text{Zn}(\text{OTf})_2$ into a solution of $\text{Na}\cdot\mathbf{2.1}$ in DMSO. b) Titration of $\text{Zn}(\text{OTf})_2$ into a solution of $\text{Na}\cdot\mathbf{2.1}$ in a 2:1 mixture of DMSO and H_2O monitored via UV/Vis spectroscopy.

While the V-shaped bis-HINT ligand **2.1** shows a clear transition from anionic ligand to M_2L_3 self-assembly, the titration of octahedral metals into the fluorenyl bis-HINT ligand **2.2** was far less predictable (Figure 2.5). A clean transition to product is still observed in the titration of $\text{Na}\cdot\mathbf{2.2}$ with Zn^{2+} as evidenced by the presence of isobestic points at 370 nm and 425 nm; however, the endpoint in this case is not the expected 0.66 mol.-eq. of a typical $\text{M}_x\text{L}_{y-x/2}$ complex. Further, treatment of $\text{Na}\cdot\mathbf{2.2}$ with either $\text{Fe}(\text{ClO}_4)_2$ or $\text{Co}(\text{ClO}_4)_2$ resulted in no observable isobestic points over the duration of the titration indicative of a random assembly process. When Co^{2+} is added, the absorbance spectrum ceases to change after the addition of 0.55 mol.-eq. Co^{2+} , in the case of Fe^{2+} , however, no discrete endpoint is attained. The easy explanation in this case is that with $\text{Na}\cdot\mathbf{2.2}$, various coordination modes are present other than discrete M_2L_3 complexes or M_4L_6 tetrahedra.

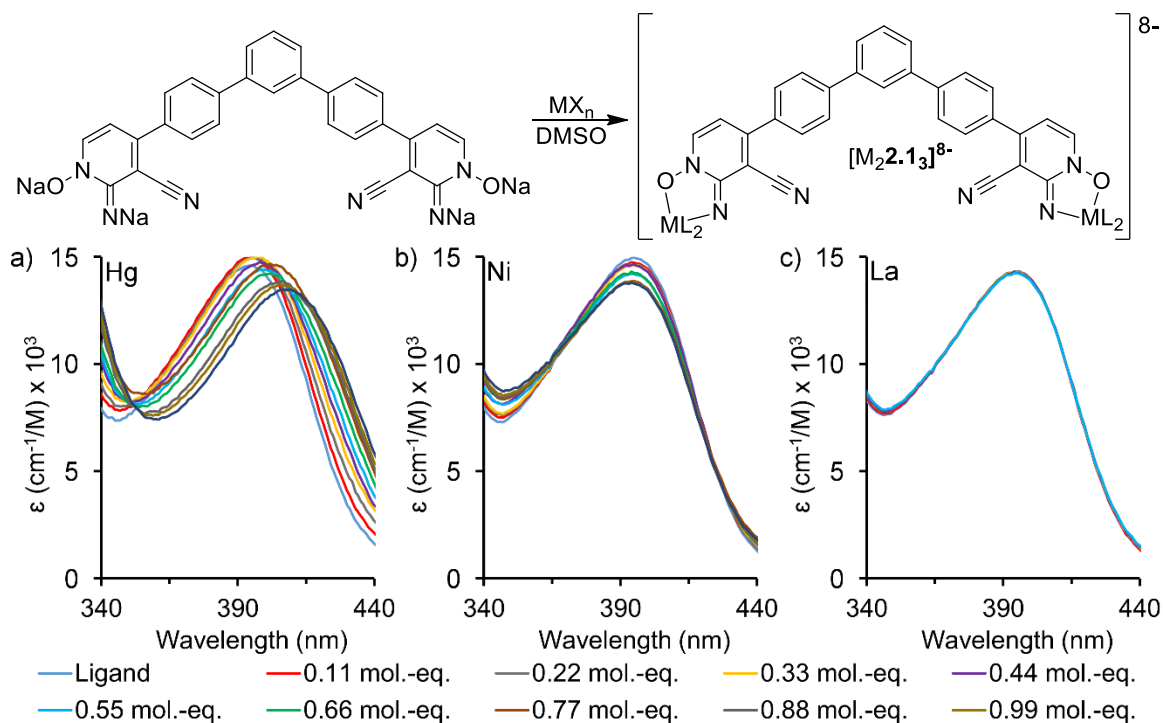


Figure 2.6. UV-Vis absorption spectra of the titration of various metal salts into DMSO solutions of anionic ligand Na•2.1: a) $MX_2 = \text{Hg}(\text{OTf})_2$, b) $MX_2 = \text{NiSO}_4$, c) $MX_2 = \text{La}(\text{OTf})_3$. $[\text{Na}\bullet\mathbf{2.1}] = 30 \mu\text{M}$.

To gain additional information on the coordinative abilities of the HINT motif, a third ligand with a single coordination site was developed. Using an analogous procedure to the previous ligands, Na•2.3 was synthesized in 3 steps and a 30 % overall yield starting from acetophenone (Figure 2.7a). The absence of the second chelating unit required the titrations to be performed at a significantly higher concentration ($[\text{Na}\bullet\mathbf{2.3}] = 240 \mu\text{M}$) to maximize complex formation. The absence of cooperative supramolecular coordinating effects leads to weaker metal coordination for Na•2.3 in comparison to Na•2.1 and Na•2.2. While $\text{Zn}(\text{OTf})_2$, $\text{Fe}(\text{ClO}_4)_2$ and $\text{Co}(\text{ClO}_4)_2$ all showed affinity for ligand Na•2.3, no isosbestic points were observed, indicating an equilibrium between ML , ML_2 and ML_3 stoichiometries is present in solution (Figure 2.7b-d).

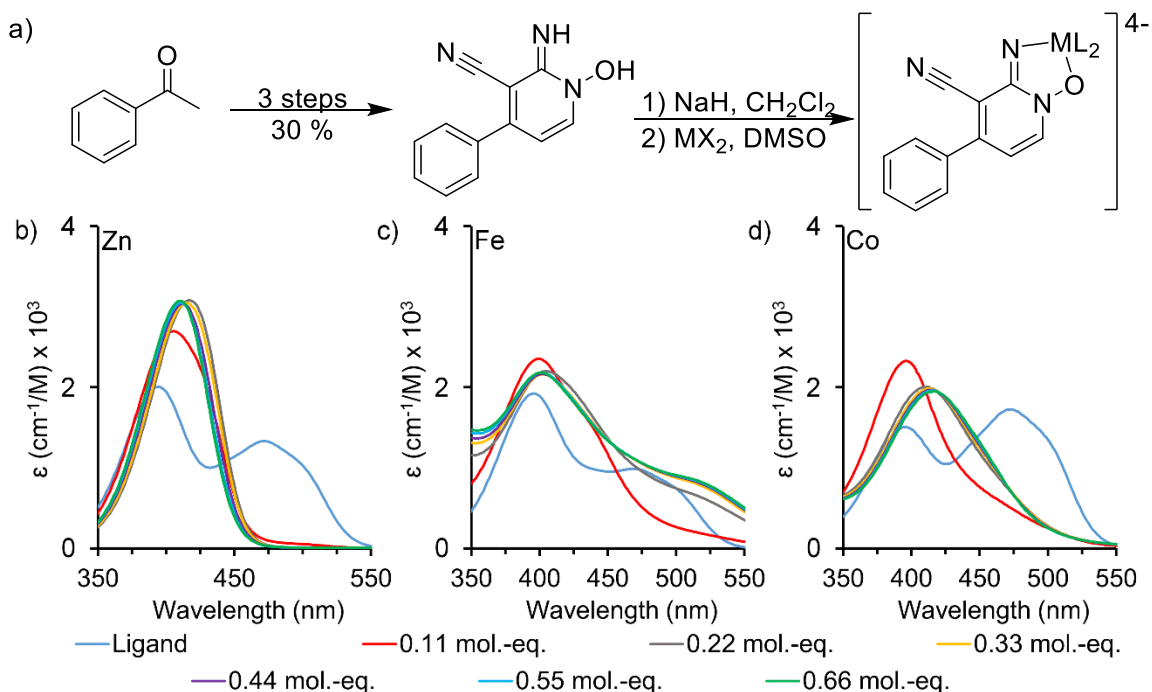


Figure 2.7. a) Synthesis of ligand **2.3** see Scheme 2.1 for details. UV-Vis absorption spectra of the titration of various metal salts into DMSO solutions of anionic ligand Na•**2.3**: b) $\text{MX}_2 = \text{Zn}(\text{OTf})_2$, c) $\text{MX}_2 = \text{Fe}(\text{ClO}_4)_2$, d) $\text{MX}_2 = \text{Co}(\text{ClO}_4)_2$. $[\text{Na}\bullet\mathbf{2.3}] = 240 \mu\text{M}$.

2.4 Metal-Specific Changes in Emission

The coordinating HINT motif in ligands **2.1-2.3** is weakly fluorescent (Figures 2.8 and 2.9). A pale blue emission is present upon exposing solutions of neutral ligands in DMSO to long wave UV light. The quantum yield ϕ of each complex was calculated by comparing the changes in emission at differing concentrations and comparing against the efficiency of a known standard, quinine hemisulfate in 1M H_2SO_4 (See Experimental section for further details). Each of the neutral ligands exhibited a similar emission profile and a modest efficiency (e.g $\phi(\mathbf{2.1}) = 1.0 \%$). Upon deprotonation, the anionic counterparts display a much brighter orange colored emission. All three ligands Na•**2.1**, Na•**2.2** and Na•**2.3** exhibited an emission maximum appearing at 477 nm (upon excitation at 397, 404 and 410 nm respectively) indicating the HINT coordinator itself is responsible for the

emission. The efficiency of the emission has a large variation, depending on the internal core. While both the terphenyl Na•2.1 and singly coordinating Na•2.3 show a roughly 5-fold increase in quantum yield upon deprotonation ($\phi(\text{Na}\bullet\mathbf{2.1}) = 5.2\%$, $\phi(\text{Na}\bullet\mathbf{2.3}) = 4.19\%$), the fluorenyl ligand Na•2.2 is significantly less efficient ($\phi = 1.3\%$).

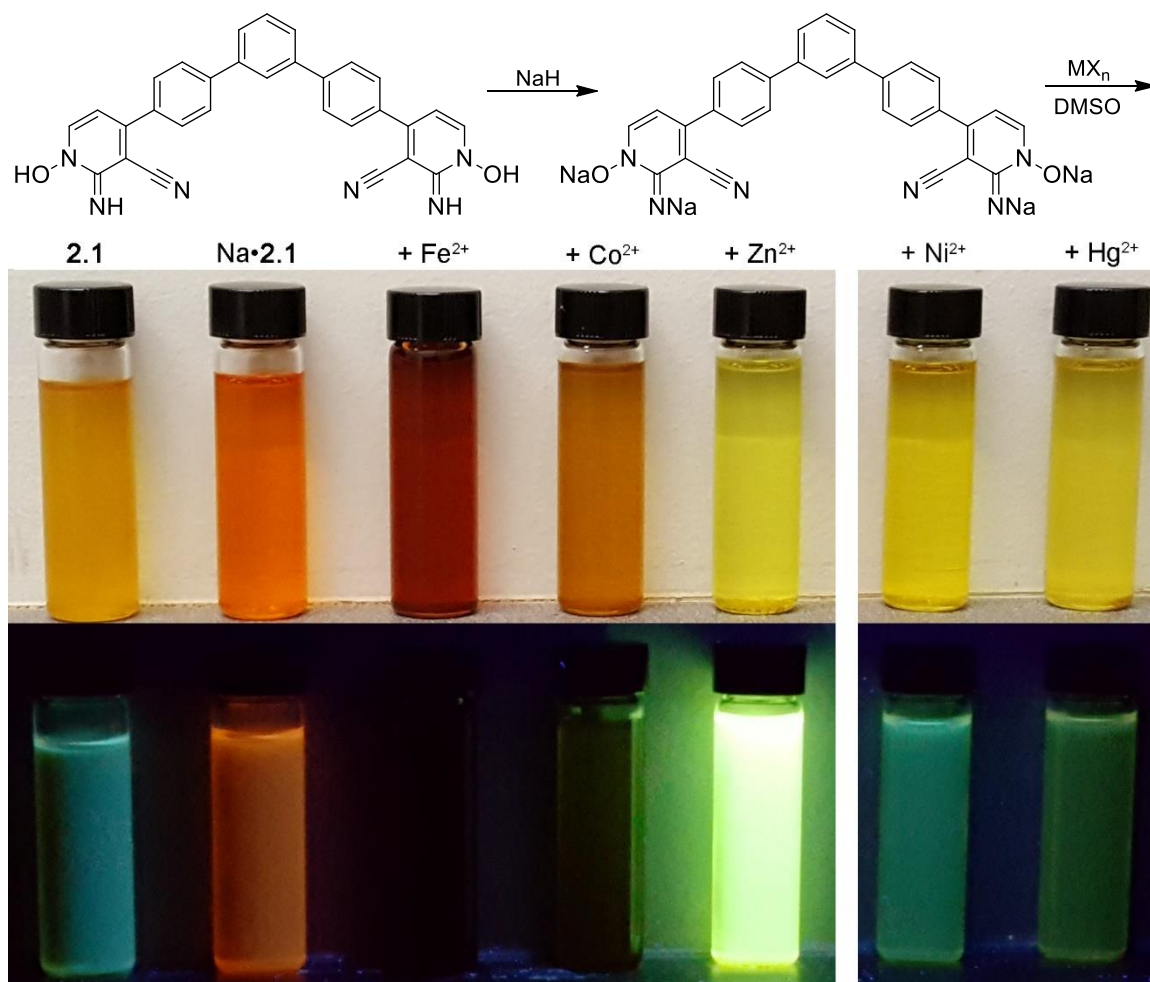


Figure 2.8. Colorimetric changes upon the addition of 0.66 mol-eq. MX_n to DMSO solutions of anionic ligands Na•2.1. Upper image: ambient light, lower image: upon long wave UV irradiation (365 nm). [Na•2.1] = 3 mM.

Upon coordination of various metals, significant deviations in emissive behavior of the metal complexes were observed. When Zn²⁺ is added to solutions of anionic ligands Na•2.1 or Na•2.3, a strong enhancement in fluorescence occurs upon formation of the

complex along with a chromatic shift to a bright green emission. The increased intensity in the emission is highly selective for Zn^{2+} ions: When the other d^{10} metals (Cd^{2+} and Hg^{2+}) were used, the chromatic shift to green was still present, but the change in intensity was far less noticeable. Unlike the smooth transition in absorbance observed upon addition of Zn^{2+} , the titration of Hg^{2+} is shifted at random which indicates a much less favorable assembly or aggregate, which is likely able to transfer some amount of energy through non-emissive pathways such as vibration resulting in moderate quenching.¹⁴ Further, treatment of anionic ligands with the other strongly coordinating metals Fe^{2+} and Co^{2+} resulted in near-complete quenching of the fluorescence upon complex formation. Both the emissive enhancement and quenching are highly specific to metal coordination: when more the weakly-complexing metals such as Ni^{2+} and Ga^{3+} , or the non-coordinating ions such as La^{3+} or Tb^{3+} are added, no changes in the color or intensity of the emission were observed (Figure 2.9c).

To quantify the results observed in Figure 2.8, titrations of the respective metal salts into solutions of the anionic ligands in spectral grade DMSO were performed and monitored by fluorescence spectroscopy. Treatment of a solution of $Na\cdot\mathbf{2.1}$ in DMSO with either Fe^{2+} or Co^{2+} (Figure 2.9b) results in an immediate decrease in emissive intensity, maximal quenching of the emission is observed at 1.0 mol.-eq. of metal added. Despite obvious changes in the color of the solution and the absorbance spectrum, no red-shift is observed in the spectrum indicating that ligand is solely responsible for the emission. The quantum yield of the $Fe_2\mathbf{2.1}_3$ complex was determined, further confirming the quenching phenomenon with $\phi(Fe_2\mathbf{2.1}_3) = 0.12\%$. The quenching of fluorescence via metal salts is well known and is most likely due to unpaired electrons in the Fe (and Co) centers. Zn^{2+}

exhibits filled electron shells which do not cause quenching, but instead fluorescence enhancement.

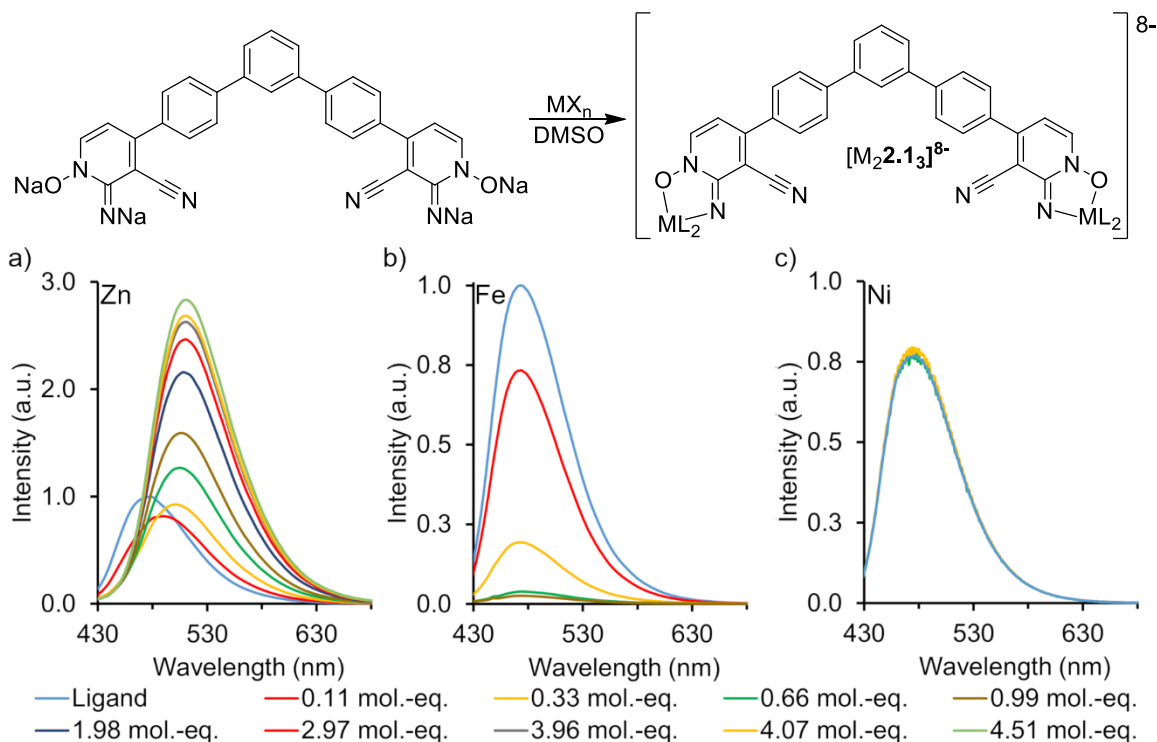


Figure 2.9. Fluorescence emission spectra of the titration of metal salts into DMSO solutions of anionic ligand Na•2.1: a) $MX_n = Zn(OTf)_2$, b) $MX_n = Fe(ClO_4)_2$, c) $MX_n = NiSO_4$. $[Na\bullet\mathbf{2.1}] = 30 \mu M$, excitation wavelength = 397 nm.

As expected from the qualitative results in Figure 2.8, formation of the discrete self-assembled complex $Zn_2\mathbf{2.1}_3$ was accompanied by a large red shift in emission when compared to Na•2.1 from 477 nm to 508 nm upon Zn coordination (Figure 2.9a). Further, the emissive intensity of the complex exhibits a 25 % increase in emissive intensity, and a seven-fold enhancement of efficiency over the protonated ligand 2.1 ($\phi(Zn_2\mathbf{2.1}_3) = 6.4 \%$). The titration of Zn^{2+} exhibits an unusual phenomenon: while the absorbance changes ceased at 2/3 mol.-eq. Zn^{2+} , consistent with formation of the $Zn_2\mathbf{2.1}_3$ complex, the fluorescence enhancement upon titration of Zn^{2+} to Na•2.1 did not. In fact, the intensity

continued increasing until roughly 5 mol.-eq. Zn^{2+} was added, with a final intensity 3 times that of the anionic ligand. Evidently, the fluorescence enhancement of the $\text{Zn}_2\mathbf{2.1}_3$ complex is a dual mode process: initially enhanced fluorescence is observed with respect to formation of the self-assembled cage, then a secondary interaction occurs, further enhancing the emission intensity. We attribute this phenomenon to weak coordination between Zn^{2+} and the nitrile groups on the HINT ligand: the pendant nitriles cause some quenching (likely via photoinduced electron transfer), but weak complexation of Zn^{2+} abrogates this quenching. Upon saturation of the complex at 5 mol.-eq. of metal added, a maximum is reached and the enhancement ceases.

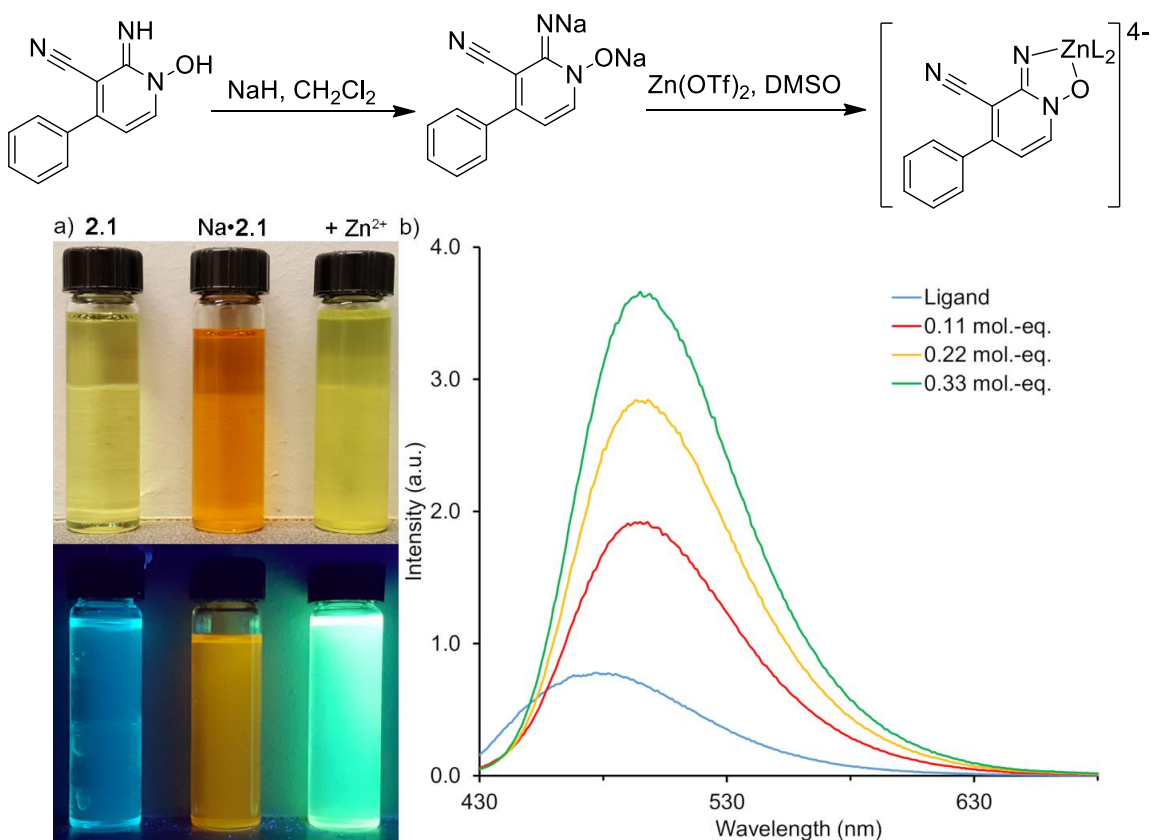


Figure 2.10. a) Colorimetric changes upon the addition of 0.33 mol.-eq. MX_n to DMSO solutions of anionic ligands $\text{Na}\cdot\mathbf{2.3}$. Upper image: ambient light, lower image: upon long wave UV irradiation (365 nm). $[\text{Na}\cdot\mathbf{2.3}] = 3 \text{ mM}$. b) Fluorescence emission spectra of the titration of $\text{Zn}(\text{OTf})_2$ into a 6mM solution of $\text{Na}\cdot\mathbf{2.3}$ in DMSO.

The effects of metal coordination on the HINT assembly were mirrored in the monomeric system (Figure 2.10). Addition of either Co^{2+} or Fe^{2+} to a solution of **Na•2.3** resulted in immediate quenching of the ligand emission. In this case quantum yields were not calculated as values would likely mimic the $\text{Fe}_2\mathbf{2.1}_3$ assembly and be clouded by background noise in the experiment. When Zn^{2+} is titrated into the solution, the same red shift of roughly 31 nm was observed, along with an even more strongly enhanced quantum yield ($\phi(\text{Zn}_2\mathbf{2.3}_3) = 10.5 \%$). The titration of metal salts into the fluorene ligand **Na•2.2** behaved as expected upon addition of quenching metals Co^{2+} and Fe^{2+} . In contrast, upon treatment with Zn^{2+} the expected coordination induced emission enhancement phenomenon is not observed. **Na•2.2** displays obvious coordination to Zn^{2+} and formation of a non-discrete aggregated assembly, as evidenced by the UV-Vis titration and the expected red-shifted emission was observed upon formation of the $\text{Zn}_x\mathbf{2.2}_y$ complex. Despite this, a decrease in emission intensity is observed upon increasing concentration of Zn^{2+} . It is most likely the fluorene core is capable quenching some of the HINT emission through energy transfer. The quantum yields of **Na•2.2** and the $\text{Zn}_x\mathbf{2.2}_y$ are significantly lower than their respective **2.1** and **2.3** analogs ($\phi(\text{Na}\cdot\mathbf{2.2}) = 1.5 \%$, $\phi(\text{Zn}_x\mathbf{2.2}_y) = 2.0 \%$), further supporting this analysis. Evidently in addition to the chelating group, the rigid spacer utilized for the ligand structure plays an important role in the coordination induced emission enhancement seen upon treatment of the HINT ligands with Zn^{2+} .

The HINT coordination to Zn^{2+} was rather robust and was further tested against competing ions and aqueous conditions. In the presence of up to 15 % water in solution the red-shifted emission and fluorescence enhancement of $\text{Zn}_2\mathbf{2.1}_3$ could be observed, albeit at

a lower intensity when compared to pure DMSO (Figure 2.11). Additionally, the enhanced Zn^{2+} fluorescence was persistent in the presence of other metals. Initially metals were added in a 50/50 mixture with a total of 1.33 mol.-eq. added, enough to fully form one homocomplex (e.g. $\text{Zn}_2\mathbf{2.1}_3$ or $\text{Co}_2\mathbf{2.1}_3$) with the remainder being free in solution. When $\text{Na}\cdot\mathbf{2.1}$ was treated with a 50/50 mixture of Zn^{2+} and Co^{2+} the emission at 508 nm characteristic of the $\text{Zn}_2\mathbf{2.1}_3$ complex was observed with an intensity of 80 % of that shown by pure $\text{Zn}_2\mathbf{2.1}_3$. The enhanced emission is still present, albeit at a lower emissive intensity (52 % of pure $\text{Zn}_2\mathbf{2.1}_3$) with 50 % Fe^{2+} present in solution, even in an excess of both competing Co^{2+} and Fe^{2+} salts (32 % emission intensity, 2.0 mol.-eq total metal). These experiments indicate that not only is Zn^{2+} complexation more favorable than that of Co^{2+} or Fe^{2+} , but that free metal ions do not cause quenching of the $\text{Zn}_2\mathbf{2.1}_3$ complex.

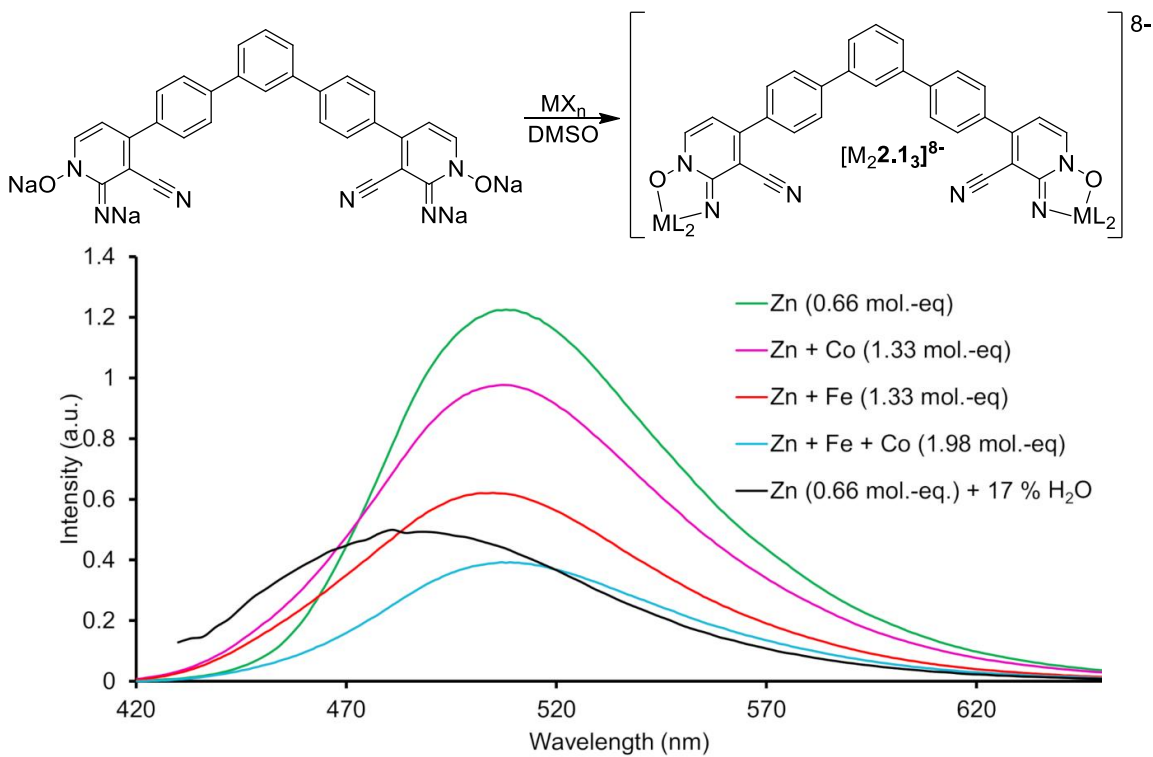


Figure 2.11. Fluorescence spectra illustrating the selective self-assembly of $\text{Na}\cdot\mathbf{2.1}$ for $\text{Zn}(\text{OTf})_2$, and tolerance to H_2O in the assembly process.

2.5 Structural Characterization and Stability

Complex formation observed by NMR analysis was consistent with the UV-Vis titration data. Addition of $\text{Zn}(\text{OTf})_2$ to solutions of **Na•2.1**, **Na•2.2** and **Na•2.3** in anhydrous DMSO- d_6 , resulted in sharp, shifted peaks, indicative of strong coordination. Upon addition of 0.66 mol.-eq. Zn^{2+} to **Na•2.1** complete association was observed, with no further changes following subsequent additions. The formation of a larger more slowly diffusing assembly was confirmed from a reduction in diffusion constant (calculated from 2D DOSY NMR) from $2.72 \times 10^{-9} \text{ m}^2/\text{s}$ for terphenyl ligand **2.1**, to $1.29 \times 10^{-9} \text{ m}^2/\text{s}$ for $\text{Zn}_2\mathbf{2.1}_3$. When metal salts are added to solutions of the neutral ligands, no complexation was observed. These NMR experiments offer important information in understanding of the coordination sphere of HINT:Zn complexes: rapid reaction with Zn^{2+} ions with anhydrous samples of **Na•2.1**, **Na•2.2** and **Na•2.3** occurs, however at the millimolar concentration required for NMR the complexes were highly susceptible to precipitation over time. The $\text{Zn}_2\mathbf{2.1}_3$ complex formed using anhydrous **Na•2.1** is octa-anionic, basic, and highly susceptible to protonation by exogenous water. Neutral cages formed using hydroxamic acid ligands are well-known to show limited solubility in many solvents and can be challenging to characterize.¹⁵ To corroborate this theory, the addition of $\text{Zn}(\text{OTf})_2$ to **Na•2.1** was repeated in DMSO- d_6 in the presence of 20 μL water. Under these conditions no cage complex was observed, merely the gradual loss of ligand peaks, with complete disappearance at 0.66 mol.-eq. $\text{Zn}(\text{OTf})_2$ added, accompanied by the formation of a precipitate (Figure 2.12). The varied protonation states of the $\text{Zn}_2\mathbf{2.1}_3$ complex complicated

further characterization, and low solubility prohibited the formation of crystals suitable for diffraction analysis, as precipitation was far too rapid, resulting in amorphous solids.

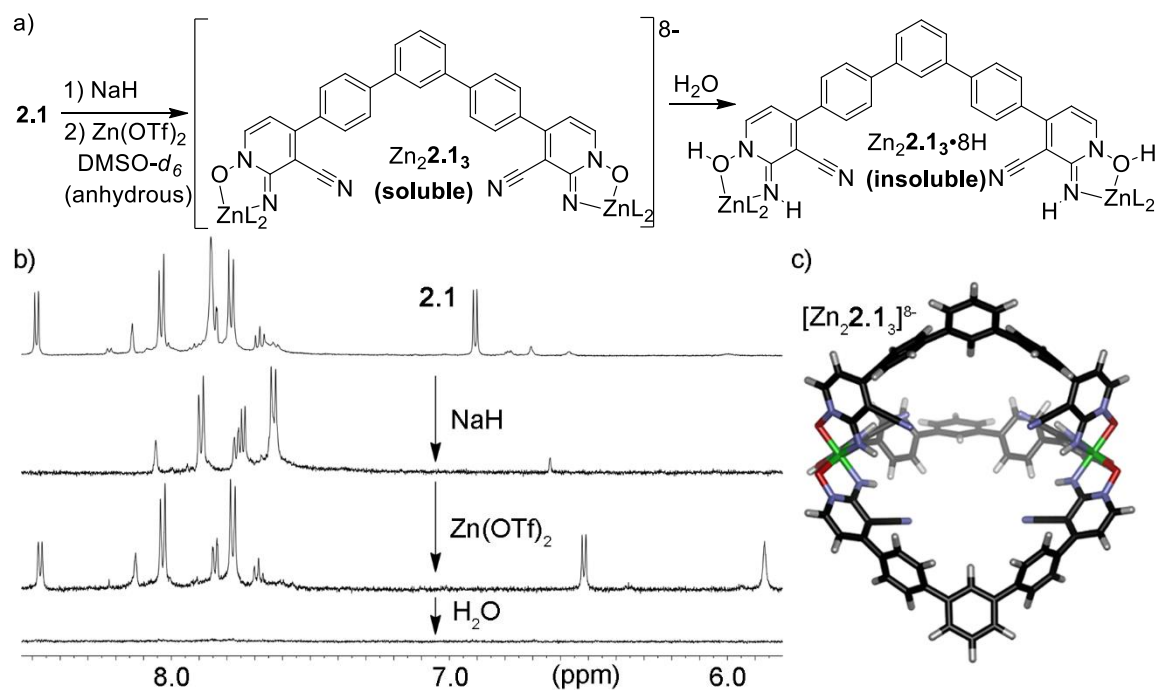


Figure 2.12. a) $Zn_2\cdot 2.1_3$ cage assembly and in-situ protonation; b) 1H NMR spectra of the assembly process and subsequent protonation/precipitation (500 MHz, $DMSO-d_6$, 298K); c) minimized structure of $[Zn_2\cdot 2.1_3]^{8-}$ (SPARTAN, AM1 forcefield).

The challenges with characterization of the M_2L_3 assembly were mirrored in attempted mass spectral analysis, as the complex was highly insoluble in solvents other than DMSO and the protonated species is prone to immediate precipitation. Analysis via MALDI was unsuccessful, but the assembly exhibited moderate solubility in anhydrous CH_3CN , enough to allow for analysis via ESI-MS. To reduce the amount of precipitate, the complex was formed *in situ* from $Na\cdot 2.1$ and $Zn(OTf)_2$ in CH_3CN , and following centrifugation the sample was immediately analyzed. The full M_2L_3 complex could not be observed due to precipitation caused by protonation under the positive ionization method. However, the protonated $Zn_2\cdot 2.1_2$ fragment was observed at a low intensity (e.g. $[Zn_2\cdot 2.1_2-$

$\text{H}\cdot\text{2H}_2\text{O}]^+$ ion ($m/z = 1155.18$)), as well as multiple $\text{Zn}_2\mathbf{2.1}$ fragments. The singly coordinating ligand $\text{Na}\cdot\mathbf{2.3}$ is less prone to precipitation and allowed a more detailed ESI-MS analysis of the coordination process. A 4:1 ratio of $\text{Zn}(\text{OTf})_2:\text{Na}\cdot\mathbf{2.3}$ was combined in $\text{CH}_3\text{CN}/\text{PrOH}$, then centrifuged to remove any complex that had precipitated, and immediately analyzed by ESI-MS using a LTQ mass spectrometer nanosource electrospray ionizer. Ions from both ML_2 and ML_3 coordination were present in the spectra, supporting the expectations from the titration data (Figure 2.13). The fully sodiated ML_3 ion $[\text{Zn}\cdot\mathbf{2.3}_3\text{Na}_4(\text{iPrOH})\cdot 5\text{H}]^+$ and an ML_2 fragment $[\text{Zn}\cdot\mathbf{2.3}_2\text{NaOTf}\cdot 1\text{H}]^+$ were observed when the mixture was analyzed in positive ion mode. Negative ion detection was less effective, and only fragments $[\text{Zn}\cdot\mathbf{2.3}_2(\text{H}_2\text{O})(\text{CN}^-)\cdot 2\text{H}]^-$, $[\text{Zn}\cdot\mathbf{2.3}_2(\text{CN}^-)\cdot 2\text{H}]^-$ were observed, each containing cyanide ions, presumably from ligand fragmentation. Precipitation occurred rapidly in this case also, resulting in arcing occurring between the injection source and the MS instrument barring a more detailed analysis of the observed ions.

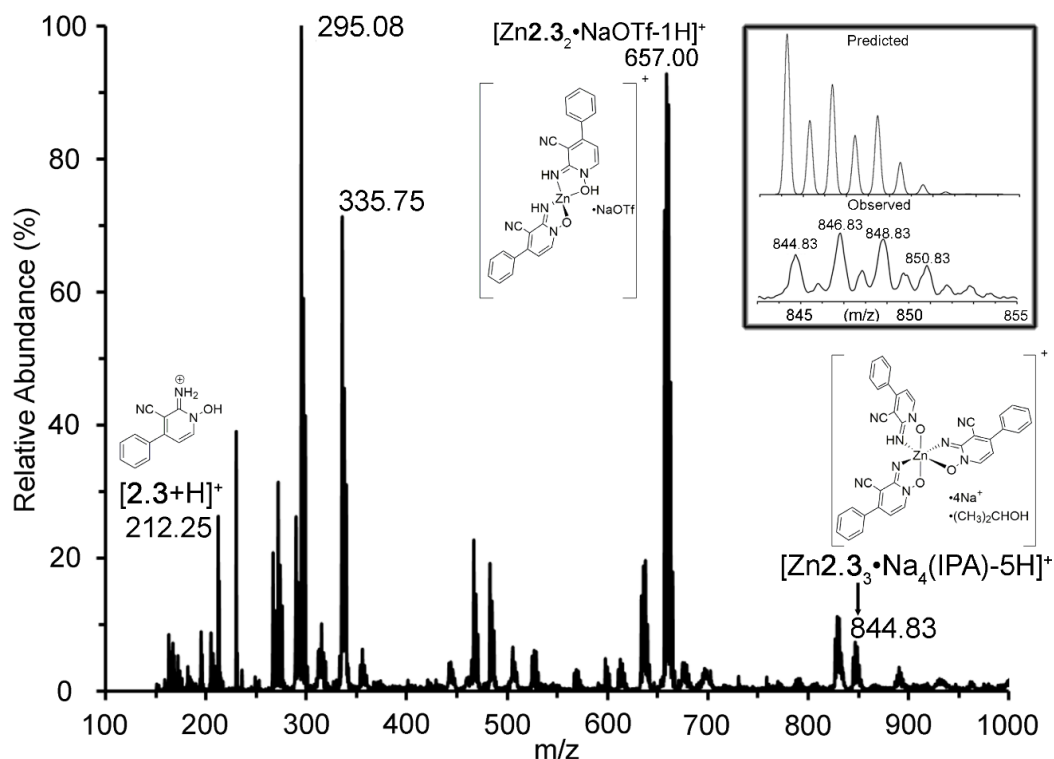


Figure 2.13. Predicted vs experimentally obtained mass peaks for (a) $[\text{Zn}_2\mathbf{2.3}_2\cdot\text{NaOTf-H}]^+$ ($m/z = 657.00$) and (b) $[\text{Zn}_2\mathbf{2.3}_3\cdot\text{Na}_4(\text{IPA})-5\text{H}]^+$ ($m/z = 844.83$).

2.6 Conclusions

We have shown that a novel, fluorescent coordinator can display early transition metal-selective supramolecular self-assembly, and enhanced fluorescence upon selective binding of Zn^{2+} ions. The V-shaped ligand $\text{Na}\cdot\mathbf{2.1}$ forms a discrete, highly anionic assembly with M_2L_3 stoichiometry upon addition of Zn^{2+} , Fe^{2+} , Co^{2+} , etc. Further, the fluorescence enhancement phenomenon is selective both towards Zn^{2+} cations and the specific linker attached. While, the V-shaped $\text{Na}\cdot\mathbf{2.1}$ and the singly coordinating $\text{Na}\cdot\mathbf{2.3}$ exhibit large increases in emissive intensity, the fluorenyl $\text{Na}\cdot\mathbf{2.2}$ forms an indiscrete aggregate resulting in quenched emission. Finally, the HINT chelating motif and resultant complex are highly anionic, and basic, making them highly susceptible to protonation with exogenous water and subsequent precipitation.

2.7 References

1. Bogie, P. M.; Holloway, L. R.; Lyon, Y.; Julian, R. R.; Hooley, R. J. "Metal-selective coordination and enhanced fluorescence of a self-assembling ligand scaffold." *Supramol. Chem.* **2017**, *29*, 936–945.
2. Yan, X.; Cook, T. R.; Wang, P.; Huang F.; Stang, P. J. "Highly emissive platinum(II) metallacages." *Nat. Chem.* **2015**, *7*, 342–348.
3. Wragg, A. B.; Metherell, A. J.; Cullen, W.; Ward, M. D. "Stepwise assembly of mixed-metal coordination cages containing both kinetically inert and kinetically labile metal ions: introduction of metal-centred redox and photophysical activity at specific sites." *Dalton Trans.* **2015**, *44*, 17939–17949.
4. Yan, L. L.; Tan, C. H.; Zhang, G. L.; Zhou, L. P.; Bünzli, J. C.; Sun, Q. F. "Stereocontrolled Self-Assembly and Self-Sorting of Luminescent Europium Tetrahedral Cages." *J. Am. Chem. Soc.* **2015**, *137*, 8550–8555.
5. Chepelin, O.; Ujma, J.; Wu, X.; Slawin, A. M. Z.; Pitak, M. B.; Coles, S. J.; Michel, J.; Jones, A. C.; Barran, P. E.; Lusby P. J. "Luminescent, Enantiopure, Phenylatopyridine Iridium-Based Coordination Capsules." *J. Am. Chem. Soc.* **2012**, *134*, 19334–19337.
6. Moore, E. G.; Samuel, A.P.S.; Raymond, K. N. "From Antenna to Assay: Lessons Learned in Lanthanide Luminescence." *Acc. Chem. Res.* **2008**, *42*, 542–552.
7. Strurzbecher-Hoehne, M.; Choi, T. A.; Abergel, R. J. "Hydroxypyridinonate Complex Stability of Group (IV) Metals and Tetravalent f-Block Elements: The Key to the Next Generation of Chelating Agents for Radiopharmaceuticals." *Inorg. Chem.*, **2015**, *54*, 3462–3468.
8. Werner, E. J.; Kozhukh, J.; Botta, M.; Moore, E. G.; Avedano, S.; Aime, S.; Raymond, K. N. "1,2-Hydroxypyridonate/Terephthalamide Complexes of Gadolinium(III): Synthesis, Stability, Relaxivity, and Water Exchange Properties." *Inorg. Chem.* **2009**, *48*, 277–286.
9. Moore, E. G.; Jocher, C. J.; Castro-Rodriguez, I.; Raymond, K. N. "Highly Luminescent Lanthanide Complexes of 1-Hydroxy-2-pyridinones." *Inorg. Chem.*, **2008**, *47*, 3105–3118.
10. Sturzbecher-Hoehne, M.; Kullgren, B.; Jarvis, E. E.; An, D. D.; Abergel, R. J. "Highly Luminescent and Stable Hydroxypyridinonate Complexes: A Step Towards New Curium Decontamination Strategies." *Chem. Eur. J.* **2014**, *20*, 9962–9968.

11. Longstreet, A. R.; Jo, M.; Chandler, R. R.; Hanson, K.; Zhan, N.; Hrudka, J. J.; Mattoussi, H.; Shatruk, M.; McQuade, D. T. "Ylidenemalononitrile Enamines as Fluorescent "Turn-On" Indicators for Primary Amines." *J. Am. Chem. Soc.* **2014**, *136*, 15493.
12. Caulder, D. L.; Raymond, K. N. "Supermolecules by Design." *Acc. Chem. Res.*, **1999**, *32*, 975-982.
13. Young, M. C.; Holloway, L. R.; Johnson, A. M.; Hooley, R. J. "A Supramolecular Sorting Hat: Stereocontrol in Metal-Ligand Self-Assembly by Complementary Hydrogen Bonding." *Angew. Chem. Int. Ed.* **2014**, *53*, 9832-9836.
14. Hong, Y.; Lam, J. W. Y.; Tang, B. Z. "Aggregation-Induced Emission: Phenomenon, Mechanism and Applications." *Chem. Commun.* **2009**, *29*, 4332-4353.
15. Beissel, T.; Powers, R. E.; Raymond, K. N. "Coordination number incommensurate cluster formation. Part 1. Symmetry-based metal complex cluster formation." *Angew. Chem., Int. Ed. Engl.* **1996**, *35*, 1084-1086.

Chapter 3 – Thermodynamic Control and Post-Assembly Modifications of Iminopyridine Coordination Cages

3.1 Introduction

Adding reactive functional groups to self-assembled cages can be challenging, as the metal-ligand contacts can often be quite sensitive. Additionally, the mechanism of the assembly process is rather complicated, requiring several components to interact and rearrange into the most stable configuration. Introducing functional groups to the ligand prior to assembly can further complicate this mechanism as the added steric bulk may inhibit beneficial interactions thus slowing the assembly process. One method to circumvent these challenges is to modify the cage after the assembly has been completed. The use of simple ligands with a primed handle would enable facile self-assembly while still allowing for the introduction of reactive functional groups to the cage. Herein, two examples of mild post-assembly modifications (PAM) are presented that can cause a structural switch. The reactions are mild enough to enable the observation of rarely observed, reactive intermediates, and are completely controlled by the self-assembled nature of the respective cages.

3.2 Post-Assembly Modification Through Ligand Centered CH Oxidation¹

An ideal PAM would be CH oxidation^{2,3} of methylene or methine groups in an unfunctionalized ligand backbone, as the initial cage synthesis is uncomplicated by the presence of reactive groups on the ligand. However, the post-synthetic reaction must be mild enough to maintain the discrete self-assembled structure, and must occur without oxidation of the metal centers.^{4,5} Doubly benzylic methylene units are relatively reactive towards radical oxidation, which would enable the reaction to occur under mild conditions.

In addition, if the CH₂-subunit were located near the center of the ligand, the reactive handle should be sufficiently far enough away to avoid side reactions with the metal centers. 2,7-Diaminoxanthene (**XE**) and 2,7-diaminofluorene (**F**) are ideal candidates for this study as both ligands can be easily synthesized, and the further oxidized versions, 2,7-diaminoxanthone (**X**) and 2,7-diaminofluorenol (**FOH**) have been shown to self-assemble into discrete cages. Multicomponent self-assembly of **X** with PyCHO and Fe(ClO₄)₂ results in a simple M₂L₃ *meso*-helicite,⁶ while **FOH** results in the formation of a single diastereomer of an unusual *mer*₃•*fac* M₄L₆ prism templated to a single ClO₄⁻ anion.⁷ The synthesis and oxidation reactions present herein (Sections 3.3-3.5) were initially performed by a colleague in the Hooley lab, Dr. Lauren Holloway. To ensure accuracy in the experiments I repeated each of the synthetic steps and oxidations and recorded my personal results. Interpretation of characterization data such as ESI-mass spectra and 2D NMR analysis were performed together, however acquisition (in most cases) was performed by Dr. Holloway.

3.3 Synthesis and Ligand Centered Oxidation of Diaminoxanthene (**XE**) Mesocate

The 2,7-diaminoxanthene ligand (**XE**) was synthesized in 3 steps from commercially available xanthone, via selective nitration followed by two separate reduction steps, to reduce the central carbonyl unit to an alcohol, then exhaustive reduction of the nitro groups and the alcohol to give **XE** (Figure 3.1). As expected, multicomponent self-assembly of **XE** with Fe(ClO₄)₂ and 2-formylpyridine (PyCHO) favors the formation of the simple Fe₂L₃ *meso*-helicite structure, like that previously observed with 2,7-diaminoxanthone (**X**).

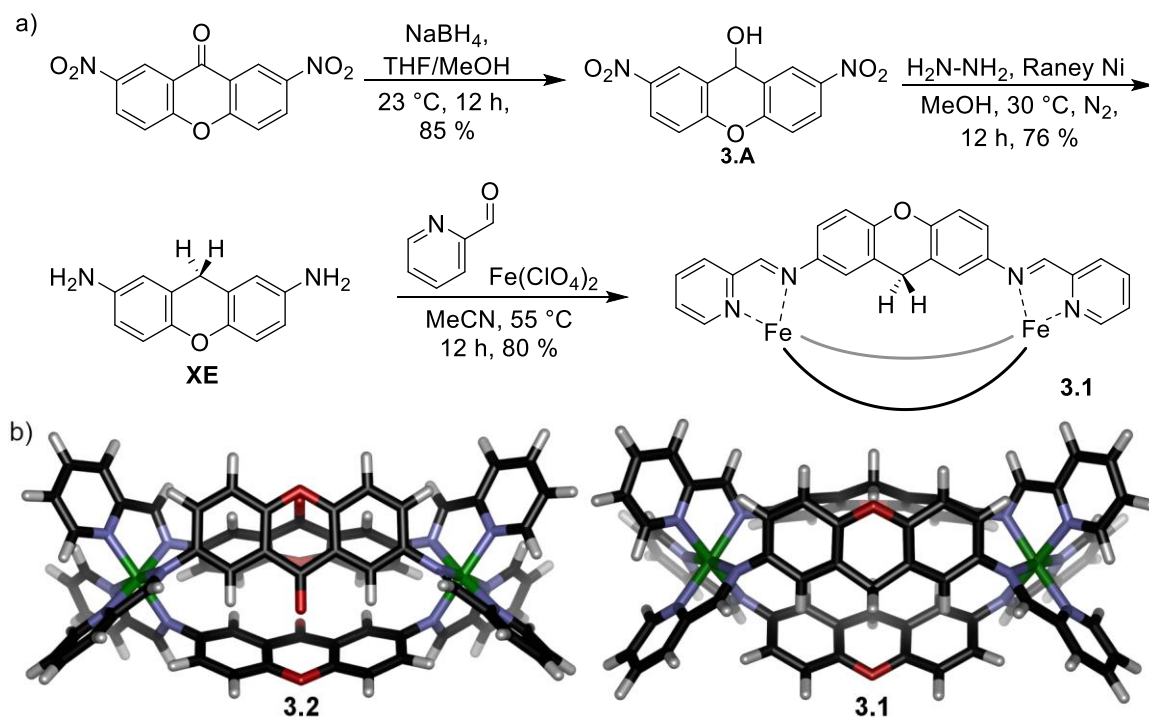


Figure 3.1. a) Synthesis of 2,7-diaminoxanthene (XE) and multicomponent self-assembly into Fe₂L₃ *meso*-helicite 1 b) SPARTAN model of xanthyl mesocates 3.1 and 3.2.

With the 3.1 cage in hand, a screen of known oxidants for radical oxidations was conducted. In most cases these strong oxidants resulted in complete decomposition of the cage. However, when the 3.1 was treated with ^tBuOOH (70 % aqueous solution), clean conversion to a new discrete complex was observed, with complete conversion to the new product after 5 h at 23 °C (Figure 3.2). Throughout the reaction, the deep purple color representative of diamagnetic Fe²⁺-iminopyridine coordination was maintained, indicating minimal metal centered oxidation had taken place. Despite literature precedent for the CH oxidation of doubly benzylic methylene groups invariably forming ketones as the major product,⁸ the sharp ¹H NMR spectrum of the oxidation product (Figure 3.2c) did not correspond to the expected 3.2 mesocate (Figure 3.2d).

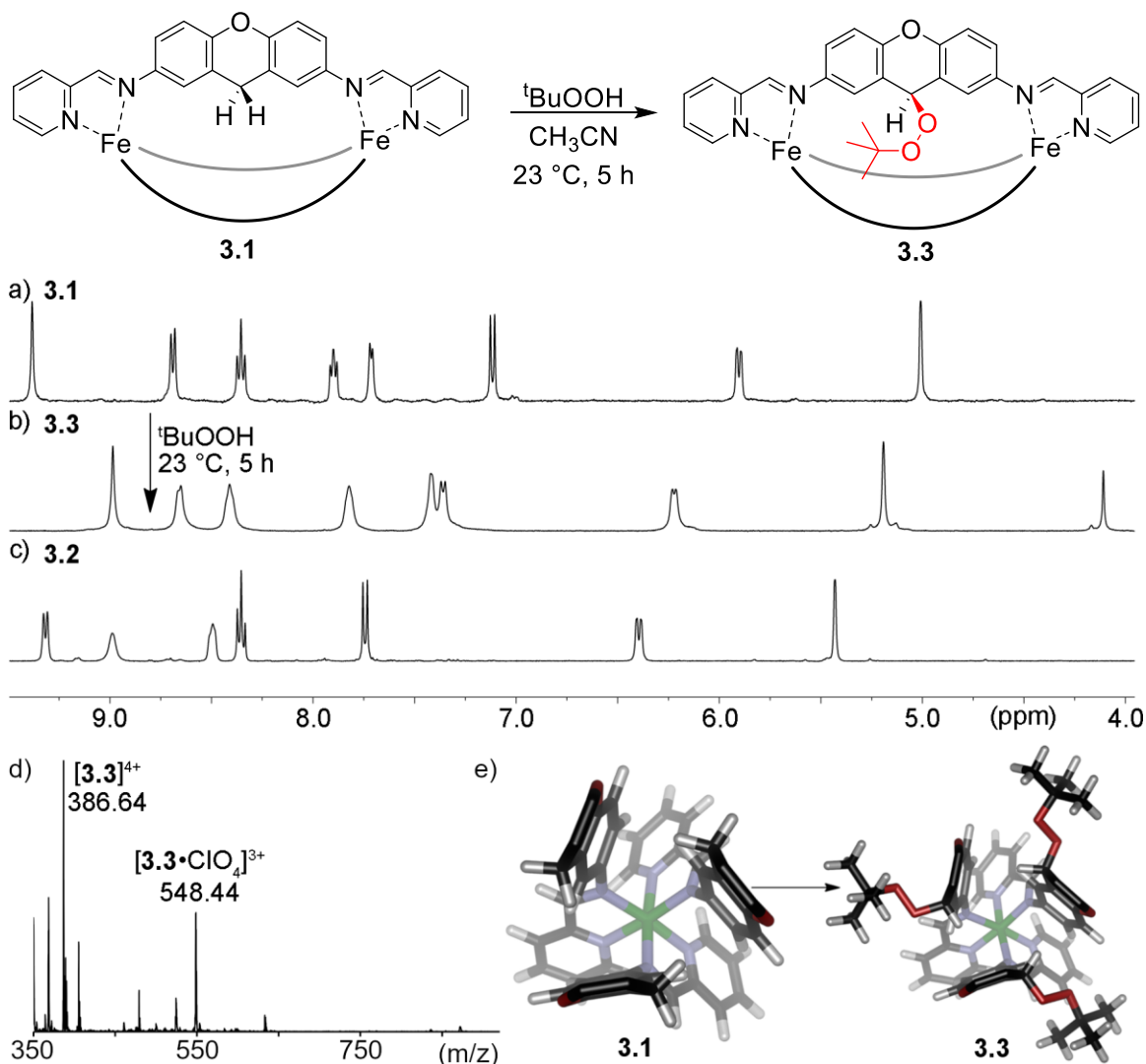


Figure 3.2. Ligand-centered Oxidation of xanthene *meso*-helicate **3.1**. a) ^1H NMR spectrum (600 MHz, CD_3CN , 298 K) of xanthene M_2L_3 *meso*-helicate **3.1**; b) ^1H NMR spectrum of the isolated product of reacting **3.1** with $t\text{BuOOH}$ for 5 h at $23\text{ }^\circ\text{C}$; c) ^1H NMR spectrum of independently prepared xanthone M_2L_3 *meso*-helicate **3**; d) ESI mass spectra of the isolated product (**3.3**) after reacting **3.1** with $t\text{BuOOH}$ for 5 h at $23\text{ }^\circ\text{C}$. e) Side on view of SPARTAN energy minimized models of the xanthene mesocate (**3.1**) and the all-out isomer of oxidation product **3.3**.

The oxidative product **3.3** was sufficiently stable to allow for isolation and analysis via ESI-MS. Surprisingly, the mass spectrum was dominated by the $\text{Fe}_2\text{L}_3^{4+}$ ion of the *tristert*-butyl peroxide intermediate of the oxidation process. Further analysis of the ^1H NMR spectrum of **3.3** reveals the product is highly symmetric, leaving only two possible

conformations: the three -OO^tBu groups directed either *all-in* or *all-out*. Molecular modeling of **3.3** (see Figure 3.2 for a cross-section of the minimized structure) shows that the *all-out* isomer is the only realistic possibility, as significant steric clashes between inwardly facing -OO^tBu groups occur in the *all-in* conformation.

3.4 Synthesis and Ligand Centered Oxidation of Diaminofluorene (F) Tetrahedron

The unusual *mer*₃•*fac* prism created by the self-assembly of diaminofluorene (FOH) is one of the most powerful demonstrations of stereocontrol in supramolecular cages. As diaminofluorene ligand **F** displays a similar backbone to **FOH** it should also be amenable to self-assembled cage formation. In addition, **F** has a similarly reactive methylene to **XE**, making it a suitable compound for post-assembly oxidation. **F** is easily accessed from reduction of commercially available dinitrofluorene. Upon treatment with Fe(ClO₄)₂ and PyCHO, a discrete diamagnetic Fe²⁺ iminopyridine assembly is formed. Despite **F** lacking the prochiral center present in **FOH**, the ¹H NMR spectrum of the **3.4** assembly was significantly more complex than the highly dissymmetric spectrum seen for **1.3** (Figure 3.3a). The controlled assembly of **FOH** is facilitated by hydrogen bonding between the attached alcohols and an encapsulated perchlorate molecule⁹; by removing the directing group the in the case of **F**, control is lost, and multiple metal-centered isomers are formed. The complexity of the ¹H NMR spectrum of **3.4** precludes a complete assignment, however, many peaks resemble those seen for **1.3**, indicating that **3.4** partially exists as the *mer*₃•*fac* M₄L₆ prism structure. It is reasonable to assume that the remaining

signals originate from the all-*fac* tetrahedra (T, S₄ and C₃), that are commonplace for cages formed from linear diamine precursors.¹⁰

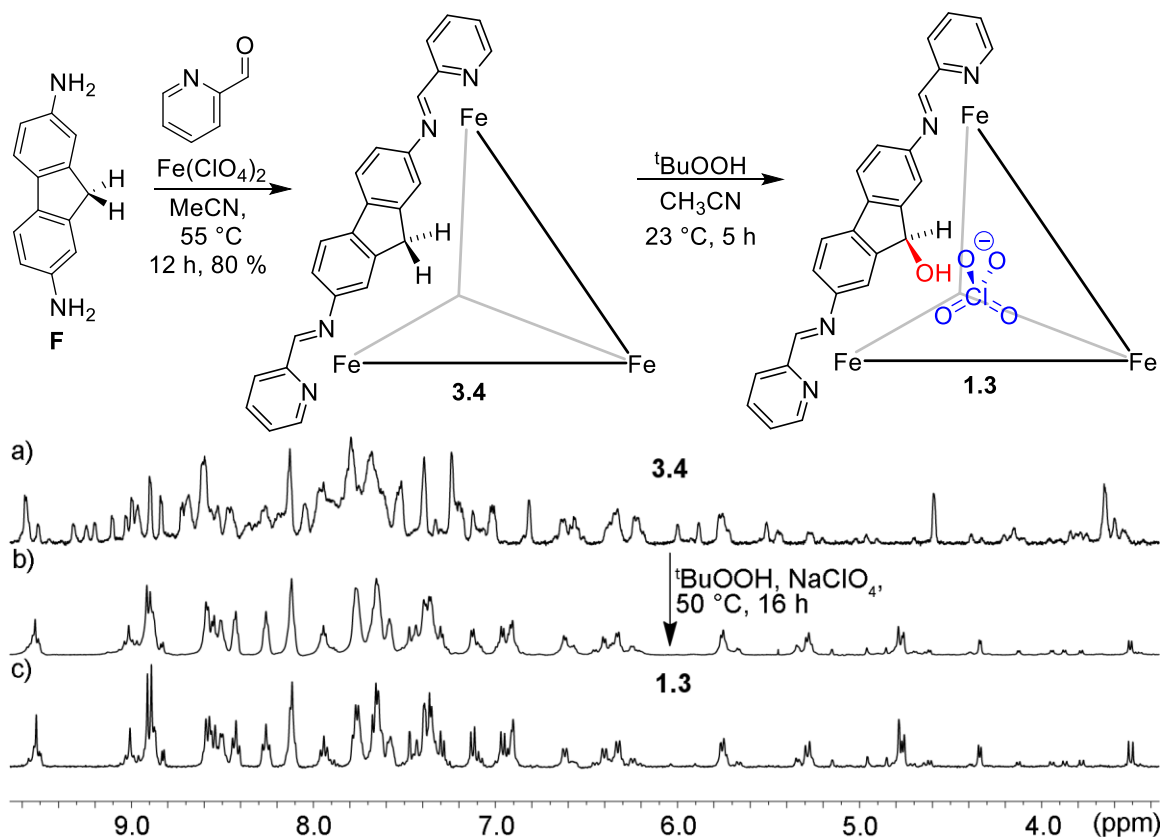


Figure 3.3. Ligand-centered Oxidation of Fluorene cage **3.4**. a) ¹H NMR spectrum (600 MHz, CD₃CN, 298 K) of the multiple isomers of M₄L₆ fluorene cage; b) ¹H NMR spectrum of the product of reacting **3.4** with ^tBuOOH and NaClO₄; c) ¹H NMR spectrum of independently prepared fluorenone cage **1.3**.

While the NMR spectrum of **3.4** is quite complex, the reactive properties were still able to be analyzed. Using a slightly modified procedure from **XE**, complete conversion to a new product was observed upon heating **3.4** with ^tBuOOH (70 % aqueous solution) in CH₃CN at 50 °C for 16 h in the presence of 1 mol.-eq. NaClO₄. The ¹H NMR spectrum of the isolated product was an exact replica of the independently synthesized fluorenone cage **1.3** (Figures 3.3b, 3.3c). Again, the expected ketone oxidation product, in this case a fluorenone M₄L₆ cage, was not observed.

3.5 Summary of Methylene Oxidations

In the case of both **3.1** and **3.4** intermediates in the assembly process were formed instead of the expected ketone product. To make sure this reaction was specific to the cage rather than the ligand scaffold itself, Dr. Holloway synthesized two control ligands by acylating the diamine ligands (**XE** and **F**) (Figure 3.4). Subjecting the control ligands to the same conditions as the cages (^tBuOOH, 50 °C, CD₃CN) yielded no reaction whatsoever. For radical promoted oxidation using ^tBuOOH to occur, uncomplexed Fe salts must be present in solution. The control oxidations were then repeated with added Fe(ClO₄)₂, and the expected ketone products were obtained in quantitative yield. Evidently the oxidation is made possible by small amounts of Fe²⁺ ions being leached from the assembly. Despite this, excellent yields of diastereocontrolled oxidation products can be obtained with no oxidation of the coordinating Fe²⁺ centers. This is further exemplified by catalytic amounts of **3.2** being able to oxidize the control ligand to the ketone as well.

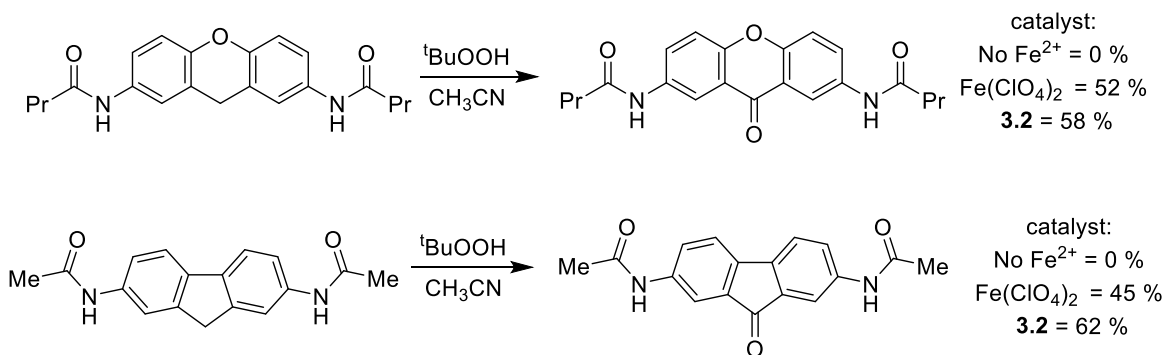


Figure 3.4. Oxidation of acylated control ligands using catalytic Fe²⁺ or **3.2** *meso*-helicite.

More importantly, the structure of the cages governs the reaction outcome. When free ligands are subjected to oxidation the expected ketone product is obtained. However, the ketone product is heavily disfavored for both the **3.1** and **3.4** cages, which favor

intermediates of the oxidation process. The **3.2** *meso*-helicite is paramagnetic and unstable, and diaminoxanthol forms an uncontrolled mixture of M_4L_6 tetrahedra; therefore, oxidation of **3.1** results in the only other possibility, the t-butyl peroxide. In the case of **3.4** product formation is governed by the thermodynamic stability of the product cage: the assembly made using **FO** is disfavored forming a disordered mixture of tetrahedra, self-assembly of **FOH** however crates a highly ordered and stable *mer₃•fac* prism.

3.6 Transimination of a Strained *Meso*-Helicite¹¹

The oxidative reactions on the unfunctionalized methylene units demonstrates one useful method adding new functional groups to an otherwise unfunctional cage. Additionally, it provided useful insights on how the overall assembly process can impact the reactivity of an otherwise predictable reaction. While these types of PAMs can be very powerful, they are limited in their scope due to the necessity for a proper handle. In addition the product outcomes, while unique, did not provide additional function to the cage. An alternative method of introducing function is to perform ligand exchange on a preformed self-assembly via transimination. With this method, the metal centers of the initial cage can be used as a predesigned template, which should limit potential for isomerism and the number of components that need to come together in the assembly process. Transimination of the aldehyde or amine component¹² is a well-known strategy for structural switching of self-assembled cages,^{13,14} and can occur rapidly, allowing facile ligand exchange in complexes that otherwise display very strong metal-ligand coordination. A proposed mechanism for the transimination/cage switching process is shown in Figure 3.5.

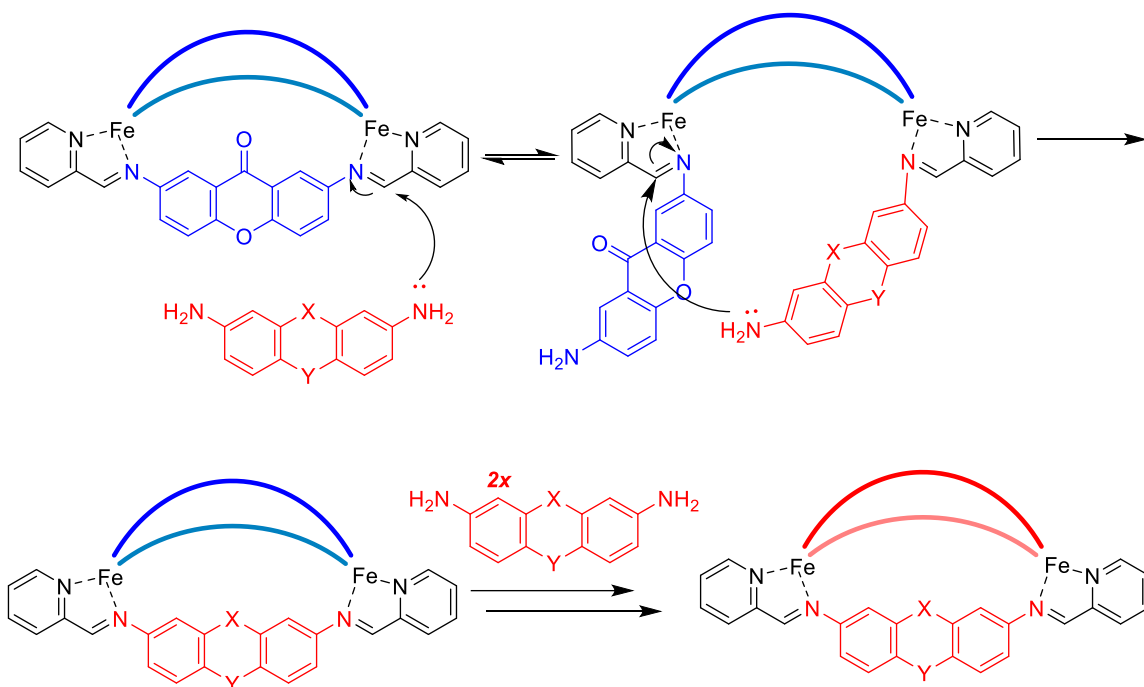


Figure 3.5. Simplified mechanism for transimination of an M_2L_3 meso-helicate.

The key in planning out this sort of PAM is in selecting the proper starting material. For instance, if the starting cage employed were metastable, the assembly could be used as a “springloaded” starting material, and significantly accelerate the transimination process. This accelerated reaction process would enable access to more challenging, less entropically favorable assemblies under equilibrium conditions as well as the potential for ligand exchange to be performed at ambient temperatures and monitored by ^1H NMR spectroscopy. While the use of strained¹⁵ and/or meta-stable^{16,17} complexes is not unprecedented, their use in mechanistic analysis of self-assembly and their conversion to complexes of higher stoichiometry (i.e. M_2L_3 to M_4L_6) is currently underexplored.

The xanthone meso-helicate **3.2** (Figure 3.6a)⁴ is an interesting example of a metastable assembly. Where most Fe_2L_3 helicates known in the literature are diamagnetic and exhibit a deep purple color,^{18,19} **3.2** is slightly paramagnetic at room temperature and

displays a red color indicative of a weaker ligand field. We have previously illustrated the meta-stability of **3.2**, via displacement with diamines such as diamino-suberone under equilibrium conditions (70 °C, > 4 h).⁴ To investigate the cage's ability to act as a “springloaded” precursor for cage assembly, the transimination must be performed under ambient temperatures, allowing the assembly process to be monitored over time. The different aniline displacer ligands used are shown in Figure 3.6. They range from ligands similar to diaminoxanthone **X** (diaminoxanthene **XE**, di(aminophenyl)methane **DPM** and di(aminophenyl)xanthene **DPX**), to ligands that form cages of differing stoichiometries (the diaminofluorenyl ligands **F**, **FOH** and **FO**,^{1,5} and tripodal ligand **APA**²⁰). Each ligand is based on a substituted aniline scaffold and has essentially the same nucleophilicity, which should cause displacement of **X** from **3.2** to occur at generally similar rates.

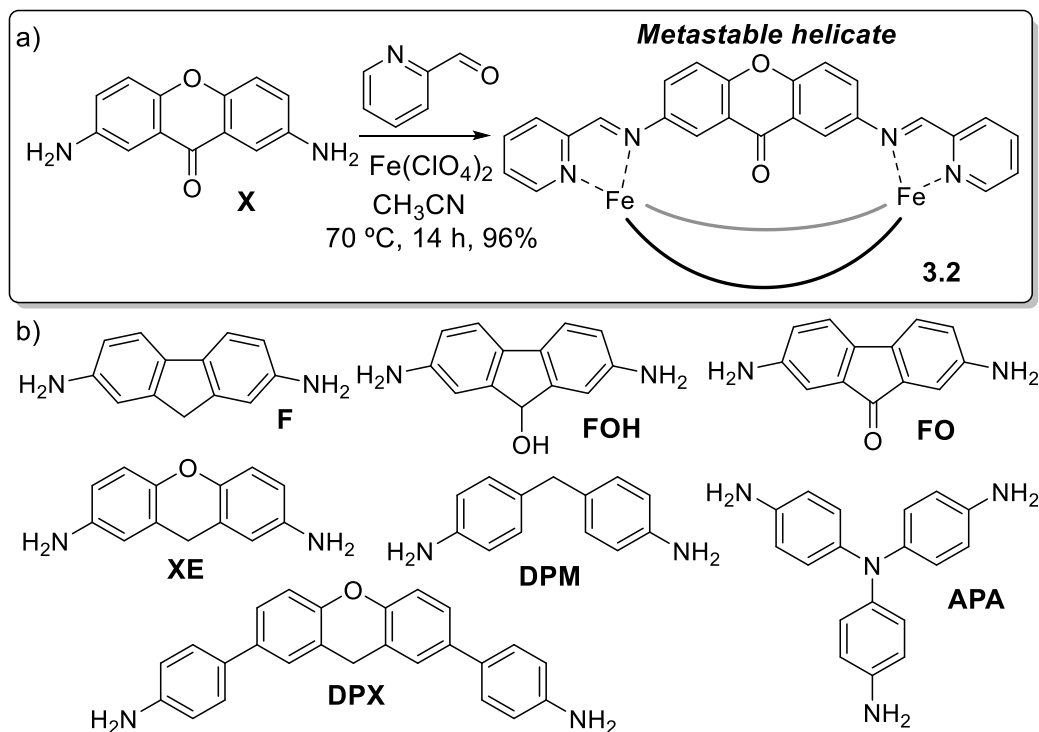


Figure 3.6. a) Multicomponent self-assembly of 2,7-diaminoxanthone **X** into the **3.2** mesocate. b) Structures of the competitive displacer ligands used.

3.7 Displacement of X Using Fluorenyl Ligands

Previous transimination experiments in the Hooley lab were performed as comparative studies between a series of *meso*-helicates, to generate an order of stability rather than investigate potential reaction outcomes. We initially wanted to investigate the ability of the meta-stable mesocate **3.2** to react in an entropically disfavored manner (i.e. increasing stoichiometry from an M_2L_3 mesocate to an M_4L_6 tetrahedron). As such, the initial displacement tests were performed with fluorenyl ligands **F**, **FOH** and **FO**. The three ligands have almost identical coordination angles, rigidities and only small variations in donor ability, however, these minor differences in functionality greatly impact the assembly process (vide supra).

For the displacement experiments, a 7.3 mM CD_3CN solution of **3.2** was prepared, followed by an initial NMR to ensure clean, intact, cage was present in solution. To this solution was added 100 μ L of the chosen dianiline (87 mM, yielding a final dianiline concentration of 17.4 mM and cage **3.2** at a concentration of 5.8 mM). The sample was then shaken by hand for \sim 30 s, and immediately checked by 1H NMR. Initially, the displacement was treated in the same manner we had previously used for equilibrium conditions (70 $^{\circ}C$, 16 h). Under these conditions, addition of either diaminofluorene **FOH** or diaminofluorene **F** resulted in rapid displacement of **X** from **3.2**. Within the time required to re-insert and shim the sample, free **X** was observed accompanied by the formation of several new signals. After heating the sample at 70 $^{\circ}C$ for four hours, complete conversion of mesocate **3.2** to the respective M_4L_6 assembly was observed (Figure 3.7). These displacements were not clean, however, as the initial peaks present at $t = 2$ min did not

resemble either of the expected product cages (**3.4** or **1.3**), and they remained present throughout the entirety of the experiment. While this proves problematic for our initial goal of uphill self-assembly, the phenomenon could hint at the presence of heterocomplexes, or similar intermediates, along the assembly pathway.

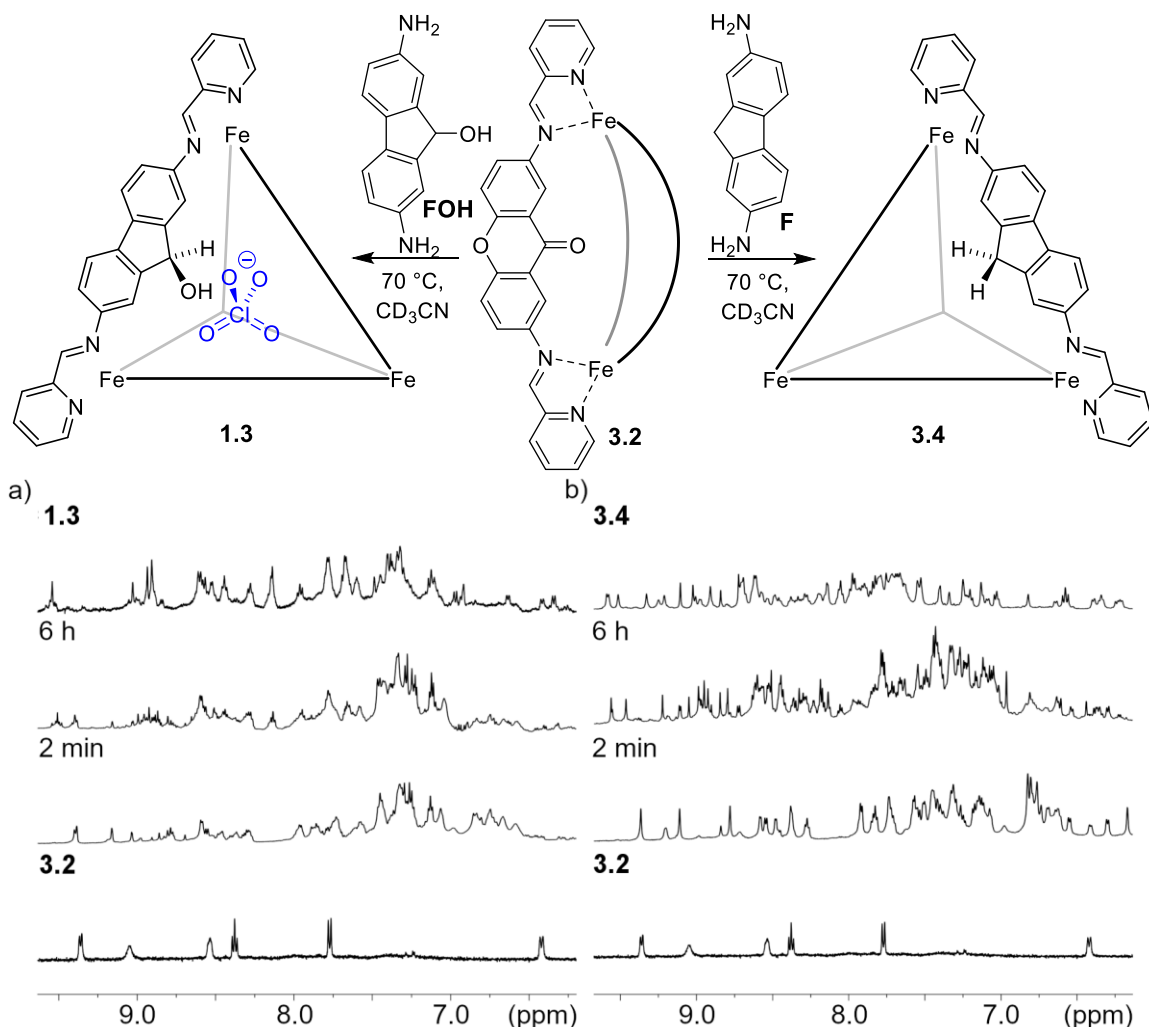


Figure 3.7. Displacement of "springloaded" meso-helicate **3.2** by: a) diaminofluorenol **FOH** and b) diaminofluorene **F** performed at 70 °C in CD₃CN.

The displacement reaction was then performed at ambient temperature in order to slow down the transimination process and enable further observation of the suspected intermediates. Without the ability to equilibrate, the reaction should not be able to proceed

to the larger M_4L_6 tetrahedra. To ensure complete disassembly of cage **3.2**, an excess (4 molar equivalents with respect to **3.2**) of diaminofluorene **F** was added to a 7.3 mM CD_3CN solution of **3.2** at ambient temperature and the process monitored by NMR. As expected, the metastable “springloaded” **3.2** cage reacted rapidly. After only 10 mins, the new products observed in the previous experiment were clearly visible in the 1H NMR spectrum (Figure 3.8a). After 2 h, the reaction was complete, with only two products and free **X** in solution. At all points during the reaction, only **3.2** and the two products were observable. The reaction is surprisingly clean, with no peaks corresponding to cage **3.4** present. Surprisingly, the two products formed were the meridional (*mer*) and facial (*fac*) isomers of the non-cage ML_3 complex $FeF_3 \cdot Py_3$, along with excess ligand **F** and expunged **X**. This assignment is easily confirmed in the ESI spectrum with only peaks for $[FeF_3 \cdot Py_3]^{2+}$ and the **3.2** reactant present in solution (Figure 3.8b). Analysis of the displacement reaction via diffusion NMR offers further confirmation of the existence of the two isomers, as all peaks expected to be part of the $FeF_3 \cdot Py_3$ mixture exhibit the same diffusion constant.

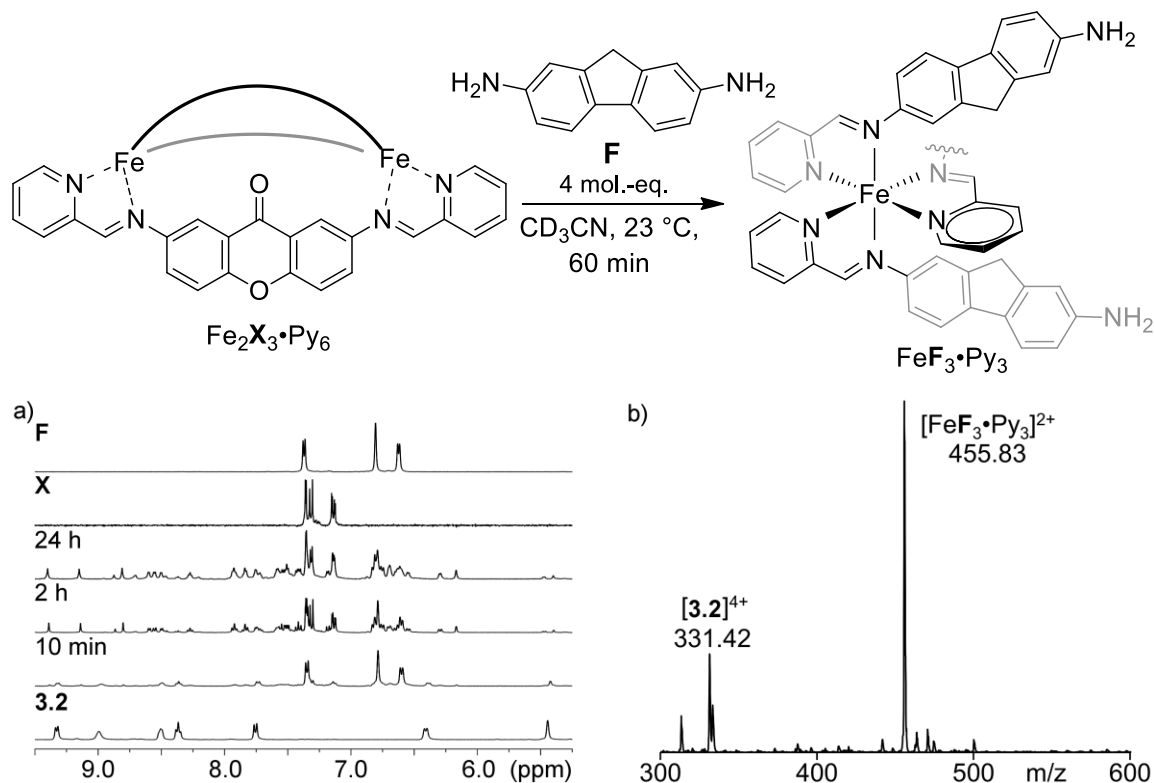


Figure 3.8. Deconstruction of the “springloaded” **3.2** *meso*-helicate. a) Downfield regions of the ^1H NMR spectra of the addition of diamino fluorene **F** (22.9 mM) to **3.2** (5.8 mM) over time (23°C , CD_3CN , 400 MHz). b) Full ESI-MS spectrum of reaction progress at 45 min reaction time in pure CH_3CN .

The complexity of the ^1H NMR stems from the lack of C_3 symmetry in the *mer* isomer. As such each attached ligand experiences its own magnetic environment, resulting in all peaks from the fluorenyl ligand being tripled in the NMR spectrum.²¹ The *fac:mer* ratio was 1:4.6, and this ratio (within integration error) was consistent throughout the reaction, and through multiple iterations of the same experiment. Complete formation of the $\text{FeF}_3\cdot\text{Py}_3$ complex via displacement was enabled by the addition of excess diamino fluorene **F** to meta-stable cage **3.2**, in an attempt to slow the reaction progress and possibly observe heterocomplexes the displacement was carried out at lower concentrations **F** (11.6 mM (2 mol.-eq. with respect to **3.2**), and 5.8 mM (1 mol.-eq. with

respect to **3.2**)) (Figure 3.9). In both these cases, the reaction is still very clean showing a mixture of the *fac* and *mer* $\text{FeF}_3\cdot\text{Py}_3$ complexes, **3.2** and free diaminoxanthone **X** ligand, indicative of a highly selective reaction under these conditions.

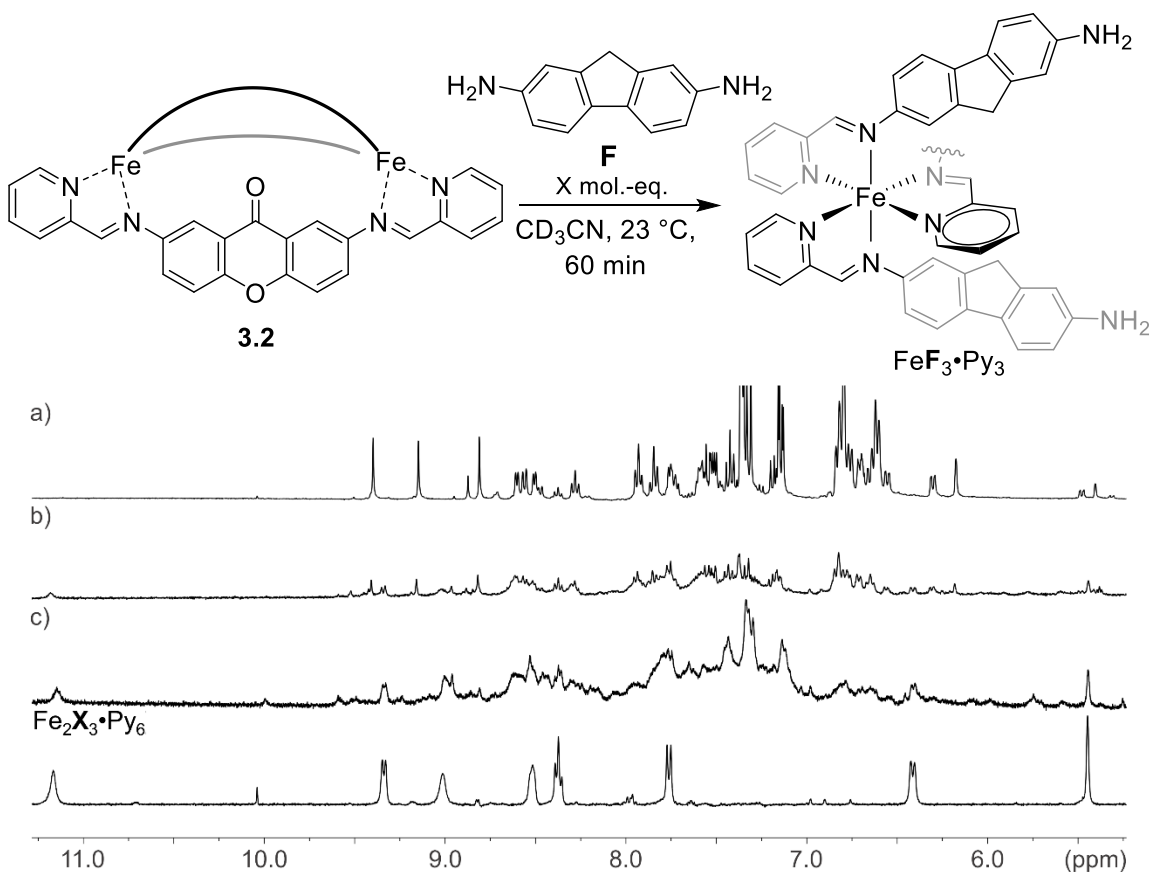


Figure 3.9. Transimination of xanthone cage **3.2** using varying concentrations of diaminoxanthone ligand **F** a) 17.4 mM, b) 11.6 mM, c) 5.8 mM.

To aid in our assignment of the $\text{FeF}_3\cdot\text{Py}_3$ assembly, we synthesized an $\text{FeL}_3\cdot\text{Py}_3$ complex made from p-phenetidine, $\text{Fe}(\text{ClO}_4)_2$ and PyCHO . The resulting complex displayed an NMR spectrum that was consistent with the *fac:mer* mixture seen for $\text{FeF}_3\cdot\text{Py}_3$ (Figure 3.10). Although a higher proportion of the *mer* isomer was present (*fac:mer* ratio = 1:10.7), the phenetidine ML_3 provided a clean and useful analog for differentiating signals in the fluorene spectrum. Using this analog and 2D COSY and

HSQC NMR experiments, from the isolated $\text{FeF}_3 \cdot \text{Py}_3$ complex, complete assignment of the complicated NMR spectrum was achieved (Figure 3.11).

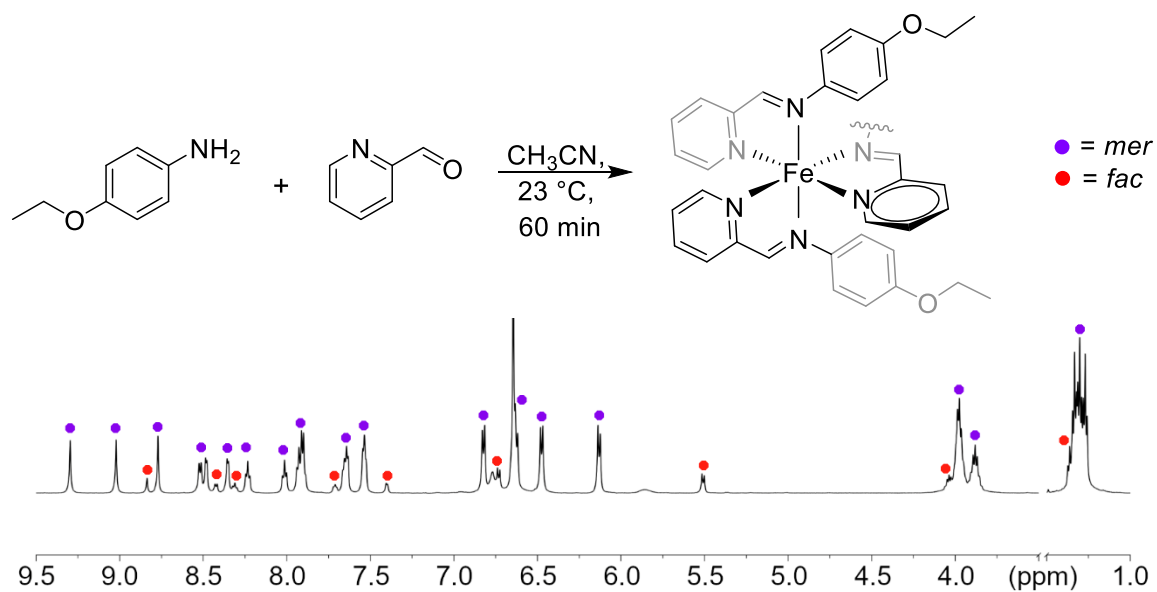


Figure 3.10. Multicomponent self-assembly of *p*-phenetidine ML_3 complex and complete assignment of the ^1H NMR spectrum (298 K, CD_3CN , 400 MHz).

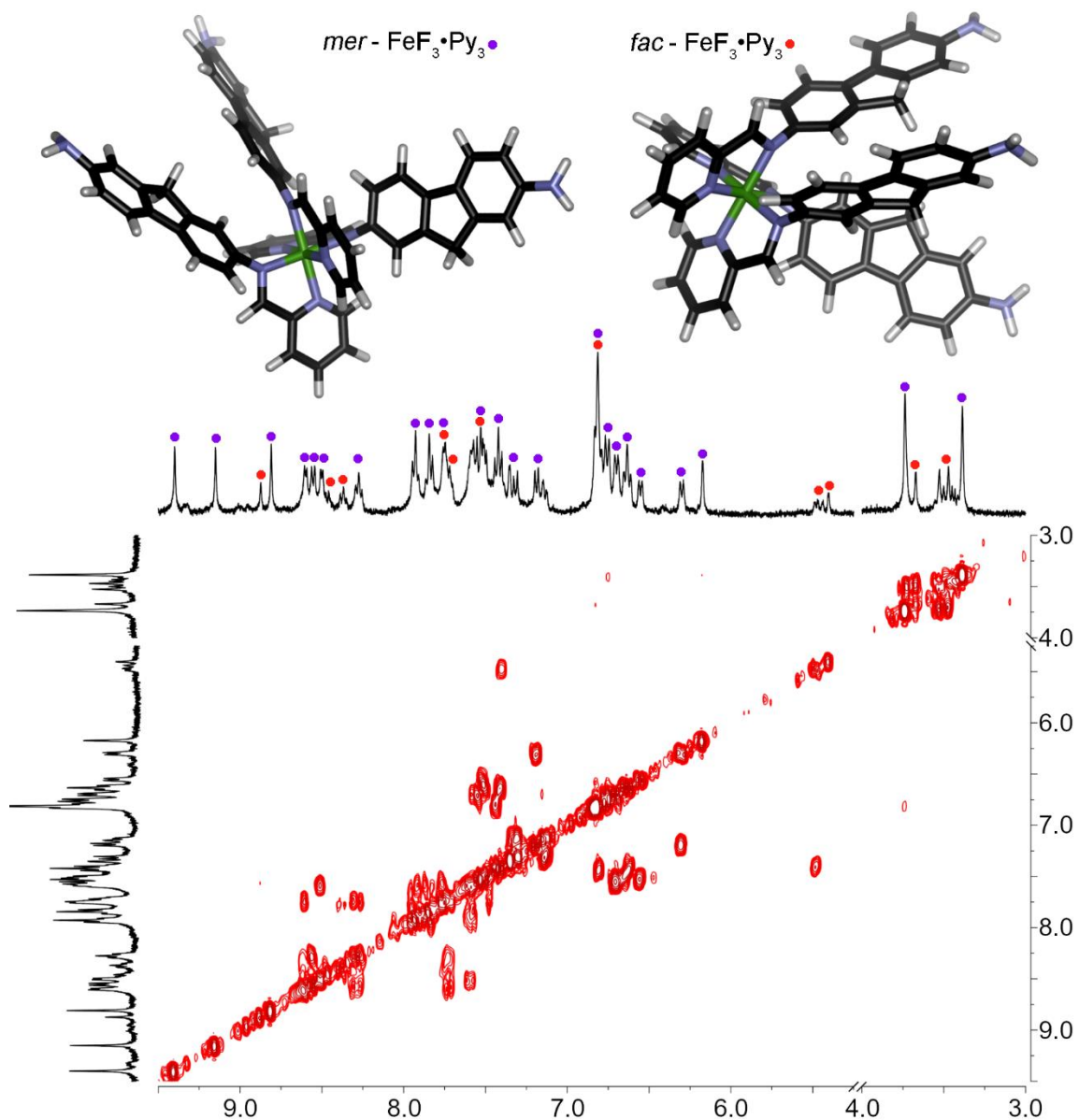


Figure 3.11. COSY NMR of $\text{FeF}_3 \cdot \text{Py}_3$ complex and complete assignment of the downfield regions in the ^1H NMR for $\text{FeF}_3 \cdot \text{Py}_3$ complex (298 K, CD_3CN , 400 MHz).

To determine whether $\text{FeF}_3 \cdot \text{Py}_3$ is an intermediate on the path to **3.4**, two additional experiments were performed. First, we conducted a modified version of the typical thermodynamic displacement conditions. **F** was added to a 7.3 mM solution of **3.2** in CD_3CN and allowed to fully convert to the $\text{FeF}_3 \cdot \text{Py}_3$ complex (~2 h at 23 °C), the sample

was then warmed to 70 °C and monitored over time (Figure 3.12). The ML₃ complex remains unchanged after heating for 16 h, with further reaction time leading to decomposition. Throughout the experiment, no signals corresponding to the larger **3.4** tetrahedron are observed, further demonstrating the thermodynamic stability of the **FeF₃•Py₃** assembly. Second, the multi-component self-assembly of ligand **F** with Fe(ClO₄)₂ and PyCHO was attempted at ambient temperatures. The reactants were combined in an NMR tube in 500 μL CD₃CN and reacted at 23 °C, conditions that are too mild to effect cage formation. In this case, no peaks for the ML₃ fragments were observed, only a non-discrete mixture. However, upon heating, **3.4** was formed as expected.

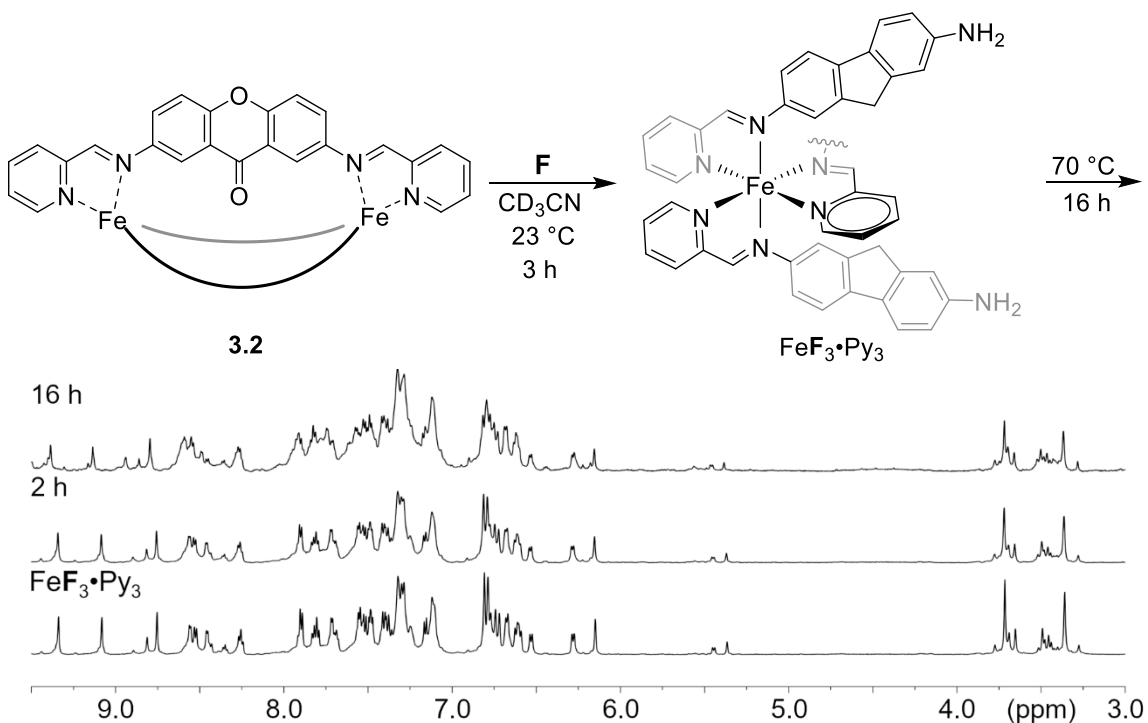


Figure 3.12. Thermodynamic stability of ML₃ complex monitored via heating a displacement experiment post formation of the **FeF₃•Py₃** intermediate at 70 °C for 16 h (CD₃CN, 298 K, 600 MHz).

The formation of the $\text{FeF}_3\cdot\text{Py}_3$ complex is quite surprising: the “hanging” amine groups should remain largely reactive, and the presence of excess PyCHO should enable facile formation of the relatively favorable tetrahedral cage **3.4**. Additionally, free diaminoxanthone **X** is still relatively nucleophilic, and easily forms cage **3.2** under standard self-assembly conditions. Despite these factors, the displacement reaction is very clean, with the ML_3 fragment being completely favored. In addition, no evidence of any incorporation of diaminoxanthone **X** in the reaction pathway or final product was observed, only free **X** ligand and homocomplex $\text{FeF}_3\cdot\text{Py}_3$.

The stability of the $\text{FeF}_3\cdot\text{Py}_3$ complex is rather unique. In our hands,^{7,16,17} all types of Fe_2L_3 or Fe_4L_6 cages react with diamines in one of three ways: complete displacement by the incoming ligand (leading to $\text{Fe}_x\text{L}_2_y + \text{amine L1}$), no reaction (leading to $\text{Fe}_x\text{L}_1_y + \text{amine L2}$), or partial displacement leading to heterocomplexes and/or decomposition. The formation of a self-assembled complex tolerant of free NH_2 groups is very rare, in fact to our knowledge only one other self-assembled system that is tolerant to free NH_2 groups has been reported; that of the assembly of tripodal ligands such as **APA**.¹⁴ Furthermore, the cases where assemblies do exhibit free amines are dubious (e.g. **APA** forms an ML_3 complex while similarly sized *p*-rosaniline does not), and with extensive heating these M_2L_3 cages will equilibrate to their more thermodynamically stable M_4L_4 assemblies. Despite this, the $\text{FeF}_3\cdot\text{Py}_3$ mixture was very stable: no conversion to other products was seen at 23 °C for multiple days or refluxing for 16 h, and the product could be cleanly isolated from the reaction mixture by precipitation and washing.

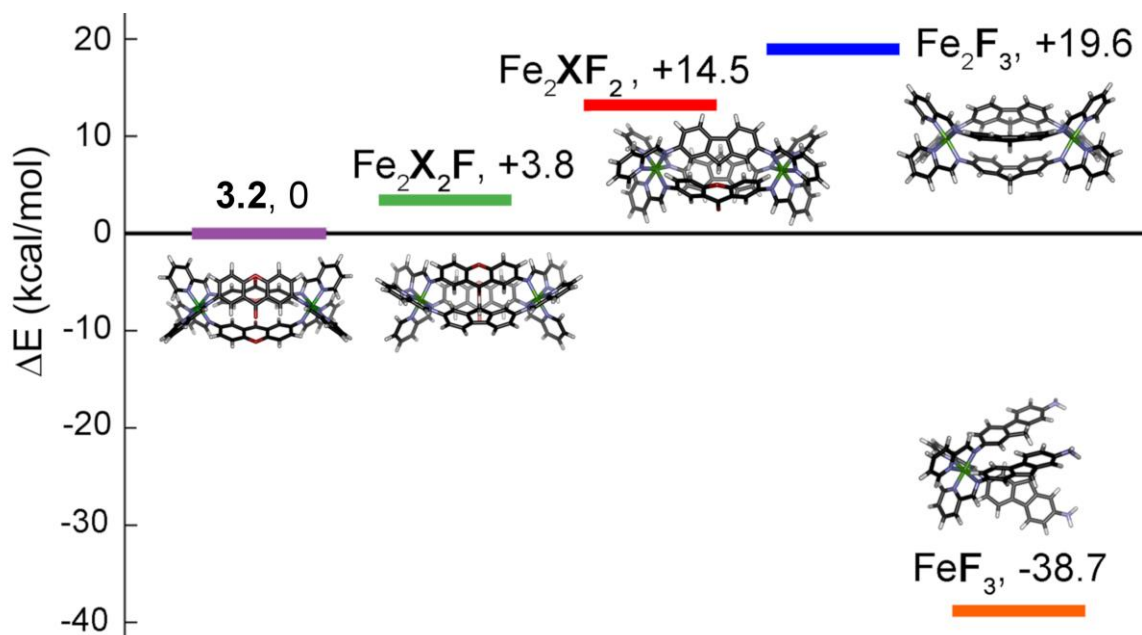


Figure 3.13. Relative single point energies (B3LYP-D3(BJ)/def2-TZVP in implicit acetonitrile) of mixed X/F Fe_2L_3 heterocomplexes, reactant **3.2** and product *fac*- $\text{FeF}_3\cdot\text{Py}_3$ in kcal/mol.

To shed light on this strange phenomenon, we turned to dispersion-corrected density functional theory calculations (Figure 3.13). The geometries of the possible M_2L_3 complexes ($\text{Fe}_2\text{X}_2\text{F}\cdot\text{Py}_6$, $\text{Fe}_2\text{XF}_2\cdot\text{Py}_6$, $\text{Fe}_2\text{F}_3\cdot\text{Py}_6$) were evaluated by Prof. Gregory J. O. Beran and Nicole Onishi, via optimization with B3LYP-D3(BJ) in the 6-31G(d) basis set and implicit acetonitrile polarizable continuum solvent, followed by single point energy refinement in the larger def2-TZVP basis set.^{22,23,24} These energies were then compared to those of **3.2** and two equivalents of *fac*- $\text{FeF}_3\cdot\text{Py}_3$. The reason why M_2L_3 heterocomplexes are not formed in the displacement process becomes immediately obvious when examining the models. Each of the complexes exhibit a significant amount of strain on the ligand components. This visual evaluation was mirrored perfectly in the calculated energies, with each sequential replacement of an X ligand in the M_2L_3 mesocate structure by an F ligand causing an increase in energy. The $\text{Fe}_2\text{F}_3\cdot\text{Py}_6$ complex being the least stable with $\Delta E =$

+19.6 kcal/mol with respect to the starting xanthone cage **3.2**. In contrast, the opened *fac*- $\text{FeF}_3\cdot\text{Py}_3$ product is over 38 kcal/mol more stable than **3.2**. Evidently the metastable xanthone starting material forces the reaction to an outcome unobserved with simple amine/aldehyde assembly processes. The concept of a “goldilocks” scheme²⁵ is present here: neither reactant **3.2** or anticipated product **3.4** are particularly favorable assemblies, therefore the system forms the only other stable product outcome, $\text{FeF}_3\cdot\text{Py}_3$, despite the presence of hanging, reactive NH_2 groups.

The reactivity of cage **3.2** towards displacing ligands is further complicated by the addition of the two other fluorenyl variants **FOH** and **FO** (Figure 3.14). Unlike the very ordered assembly seen when reacting with PyCHO, when **FOH** is added to **3.2** the reaction is completely uncontrolled giving a mixture of complexes, with no peaks that corresponded to either the **1.3** sorting hat or the $\text{FeFOH}_3\cdot\text{Py}_3$ complex. Finally, diaminofluorenone **FO** displayed no reactivity at all. When an excess was added to a solution of **3.2** in CD_3CN , the peaks for **FO** were broad and ill-defined. To ensure **FO** was present in solution, the displacement reaction was carried out in reverse (i.e. addition of cage into a solution of **FO**). However, even after 2 days reaction the meta-stable **3.2** was unchanged. More extensive heating to drive the reaction to product caused decomposition. Despite the similarity in size, angle and nucleophilicity between the fluorenyl ligands **F**, **FOH** and **FO** the reactivity is highly variable. Only **F** was able to form a discrete product when added to **3.2**, the further oxidized ligands displayed uncontrolled reactivity.

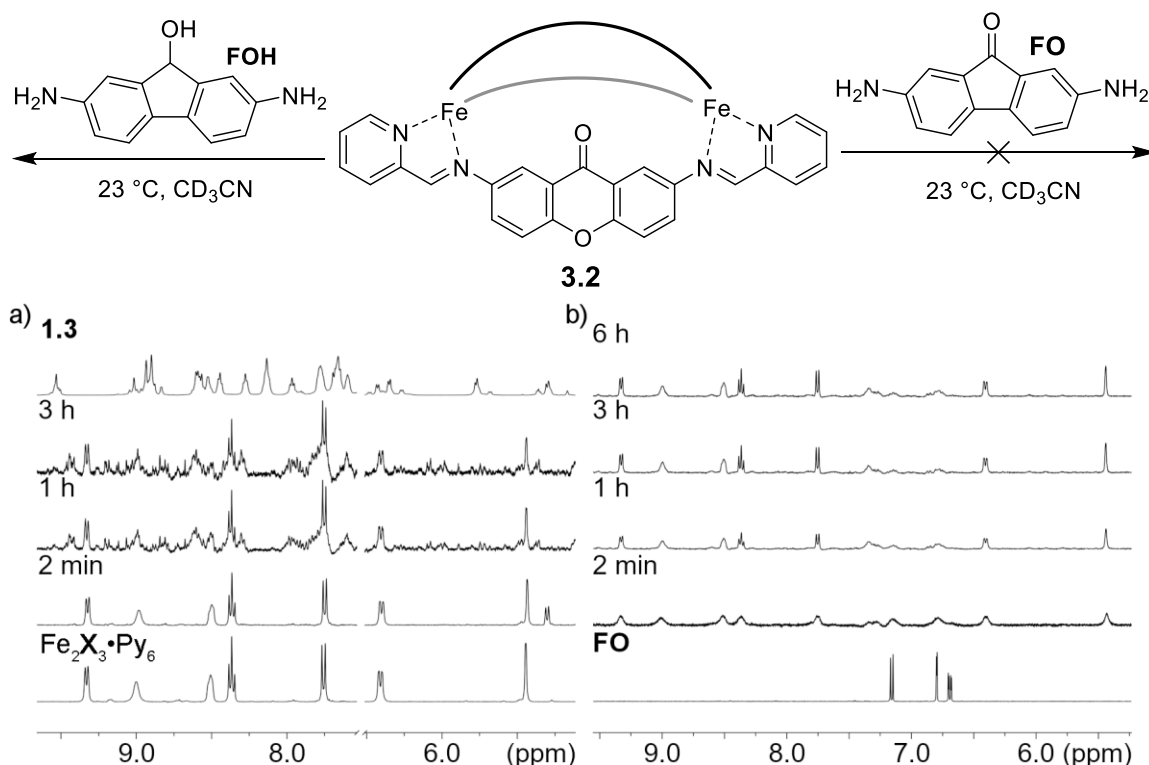


Figure 3.14. Destruction of **3.2** meso-helicate using the oxidized fluorenyl ligands a) **FOH**, b) **FO** (298 K, CD₃CN, 400 MHz).

3.8 Displacement of X Using the Tripodal APA Ligand

To see if these variations in reactivity were a general phenomenon, we analyzed a ligand that is known to tolerate hanging amine groups in its assembly: tripodal ligand **APA**. The **APA** ligand exhibits variable self-assembly pathways when reacted with Fe²⁺ salts and PyCHO forming either: the kinetically trapped M₂L₃ mesocate **3.5** with three unreacted NH₂ groups present, or the fully reacted M₄L₄ tetrahedral cage **3.6**.¹⁴ The product outcome depends on the concentration of PyCHO and temperature: mesocate **3.5** can be converted to cage **3.6** upon heating. By varying the amount of **APA** added to a solution of cage **3.2** the proper ratios to form either the M₄L₄ or M₂L₃ **APA** complexes should be obtainable.

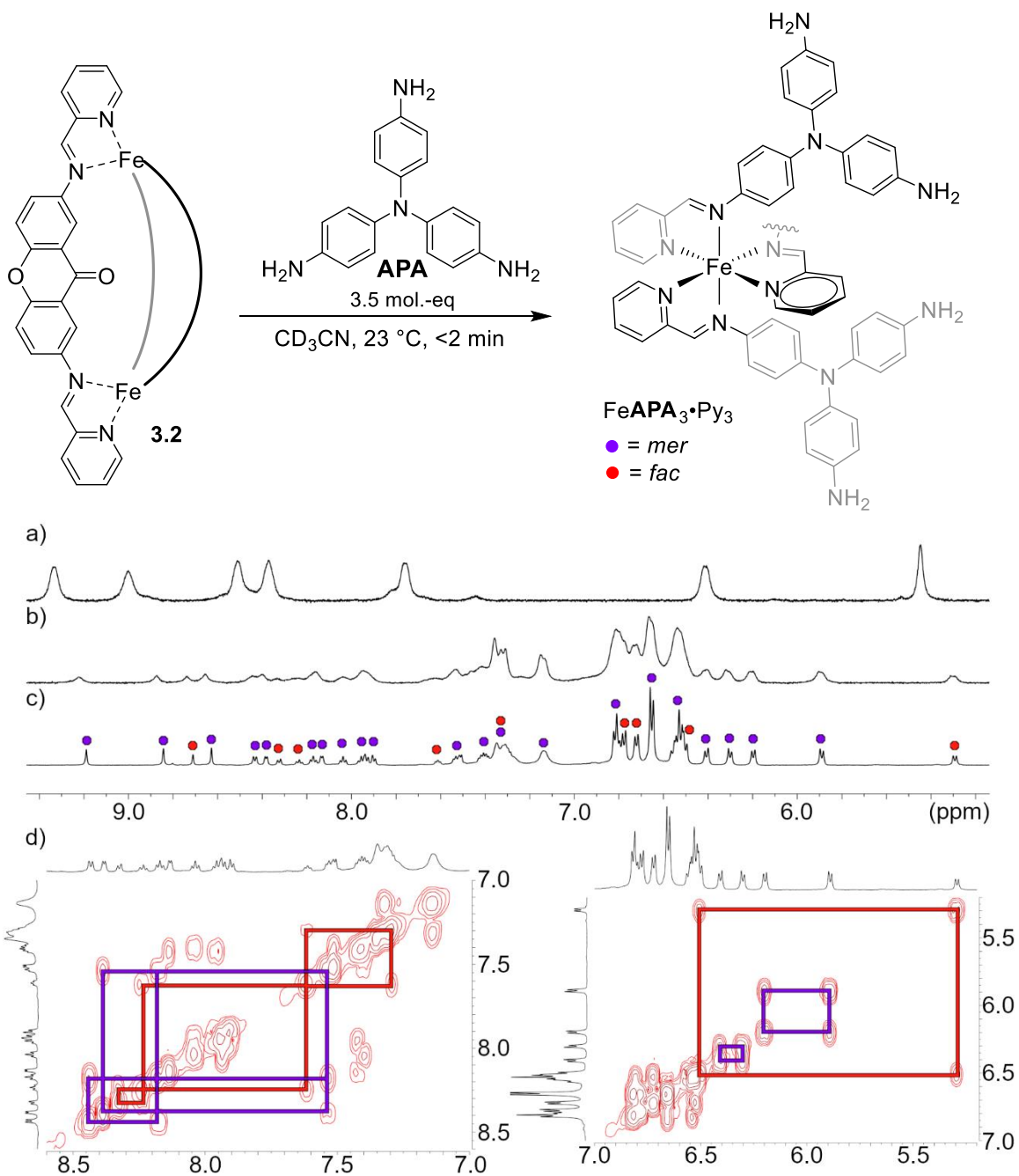


Figure 3.15. Deconstruction of the “springloaded” **3.2** *meso*-helicite using 3.5 eq APA. Downfield region of the ¹H NMR spectra of: a) **3.2** *meso*-helicite, b) displacement of ligand **X** after ~2 min, c) isolated FeAPA₃•Py₃ mixed complex, d) COSY NMR spectra of isolated complex (298 K, CD₃CN, 400 MHz).

Using the same procedure as for **F**, **3.2** was subjected to an excess of APA (up to 4 eq. with respect to **X** in **3.2**) and the reaction monitored by NMR, again the expected

product cage, in this case the **3.5** mesocate, was not observed (Figure 3.15). Instead, rapid formation of the two isomers of the ML_3 fragment $FeAPA_3 \cdot Py_3$ formed within 2 mins of addition. The formed $FeAPA_3 \cdot Py_3$ complex exhibited a *fac:mer* ratio almost identical to that of $FeF_3 \cdot Py_3$ at 1:4.3 respectively. Unlike the fluorene version however, the $FeAPA_3 \cdot Py_3$ mixture was not completely stable. While the product could be isolated in enough purity for NMR analysis (Figure 3.15d), the complex fully decomposed within 24 h of isolation. When the $FeAPA_3 \cdot Py_3$ complex was analyzed by ESI-MS the spectrum is dominated by free ligand and the **3.5** mesocate (Figure 3.16). Evidently the energy required to ionize the complex is sufficient to cause both ligand dissociation and collapsing of the intermediate. Additionally, the $FeAPA_3 \cdot Py_3$ mixture could be completely converted to the M_2L_3 mesocate upon heating the sample at 70 °C for 2 h. Interestingly, we were unable to access the M_4L_4 tetrahedron using this method, another example of biased reactivity: when formed from the aldehyde and amine, **3.5** can easily be converted to **3.6** upon heating.

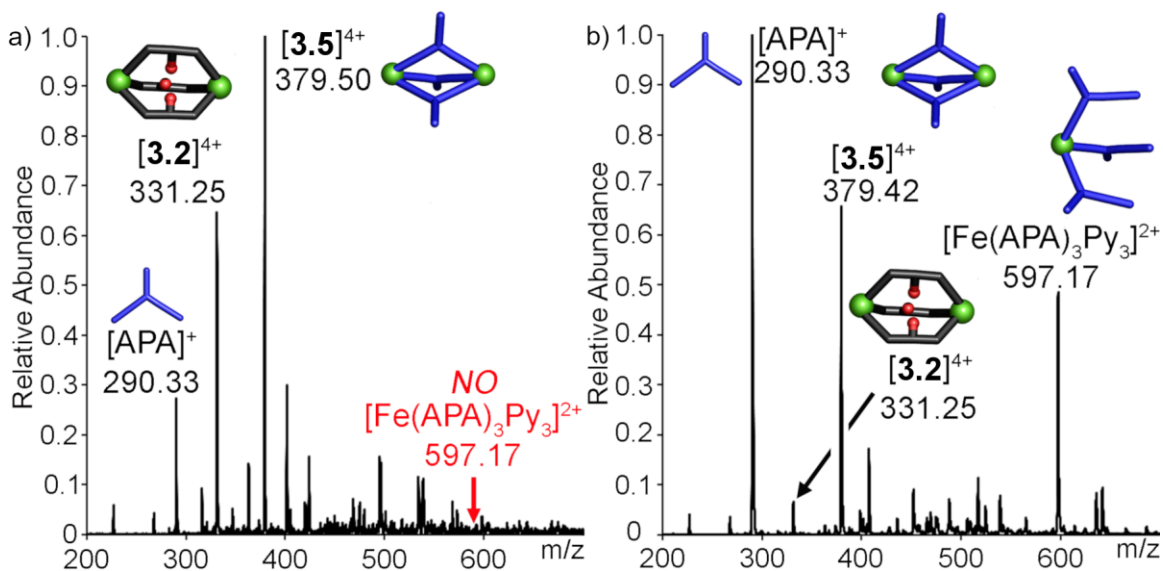


Figure 3.16. ESI-MS spectra of the destruction of mesocate **3.2** upon addition of APA: a) 1.5 mol.-eq. displacer ligand, b) 3.5 mol.-eq. displacer ligand.

In the case of diaminofluorene **F** the concentration of displacing ligand had no effect on the product outcome. As **APA** exhibits multiple coordination modes we wanted to test the effects of concentration on this system as well. Using only a single equivalent of **APA** (with respect to **X** in **3.2**) gives a ratio of ligand:PyCHO that is closer to what is necessary to form the larger **3.6** complex. Under these conditions, the free amines formed the initial displacement reaction will still have a large amount of “springloaded” **3.2** cage present in solution to react with. In contrast to the transimination of **3.2** with **F**, displacement by 1 mol.-eq. **APA** was much slower. Only after 1 h of reacting could a new product be observed, after 2 hours only one product was observed, mesocate **3.5** (Figure 3.17). No further reaction occurs following the formation of the M_2L_3 complex, in addition no M_4L_4 cage or ML_3 fragments were observed at any time.

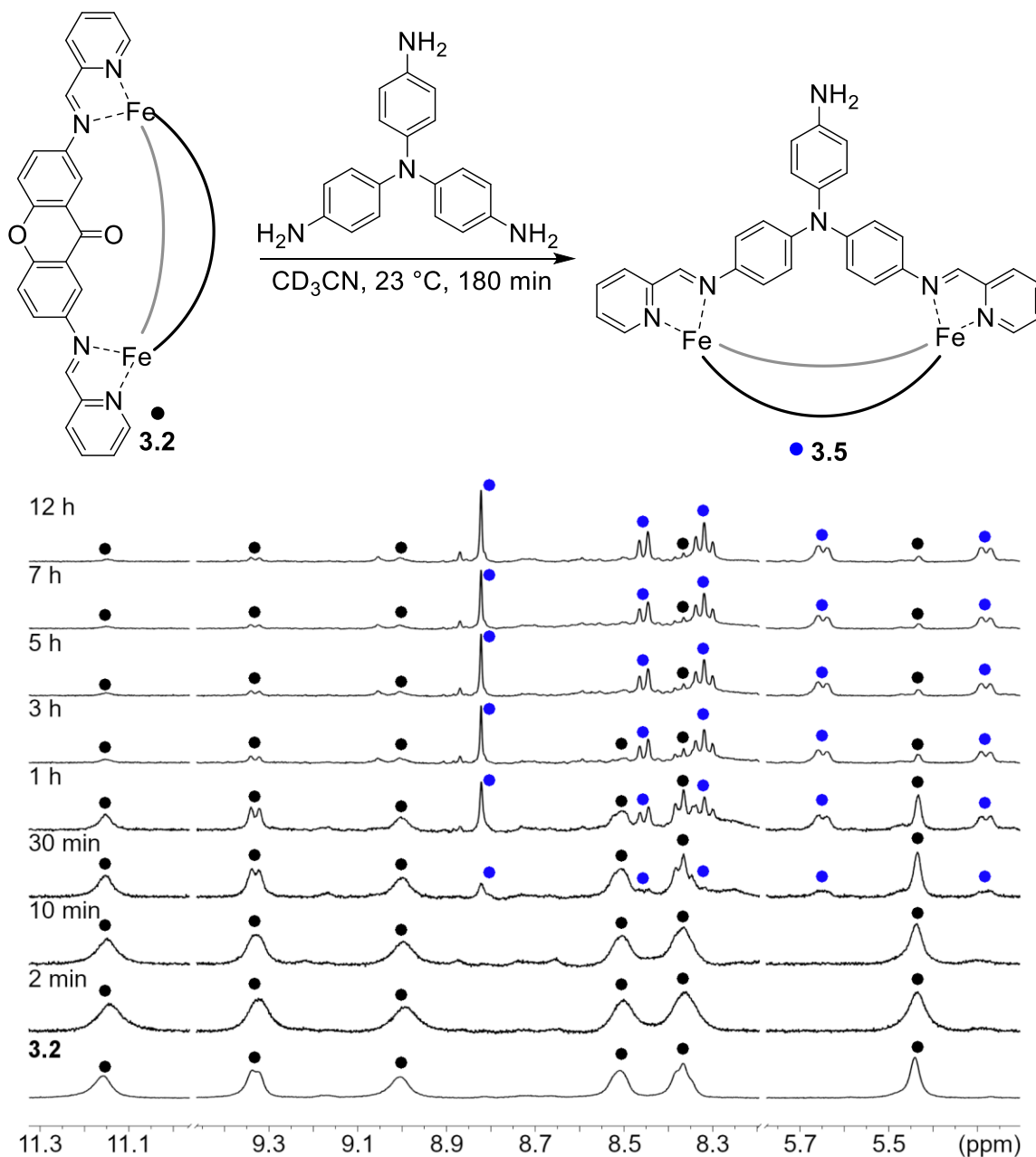


Figure 3.17. Deconstruction of the "springloaded" **3.2** mesocate. Downfield regions of the ^1H NMR spectra of the addition of APA (5.8 mM) to **3.2** (5.8 mM) over time (298 K, CD_3CN , 400 MHz).

3.9 Displacement of X Using Ligands of Similar Size/Electronics

The metastable cage **3.2** exhibits a unique level of control in the transimination reactions with competitive ligands. Evidently, the initial goal of forming entropically

disfavored complexes is prohibited by this system. As such we next investigated ligands exhibiting a very similar structure to **X**, namely diaminoxanthene (**XE**), diaminodiphenyl methane (**DPM**) and di(aminophenyl)xanthene (**DPX**), in an effort to make controlled heterocomplexes, an intermediate as of yet undiscovered in our reaction pathway.

Diaminoxanthene **XE** represents the smallest variation that can be made from the parent ligand **X**, varying only in electron donating ability. In addition, **XE** forms a stable M_2L_3 mesocate upon self-assembly with $Fe(ClO_4)_2$ and PyCHO, with a size similar to that of **3.2** *meso*-helicite.¹ As with the previous examples, a solution of **3.2** in CD_3CN was treated with diaminoxanthene **XE** (4 mol.-eq. with respect to cage) the reaction monitored at 23 °C by NMR (Figure 3.18). Displacement of ligand **X** occurred nearly instantaneously, no peaks for **3.2** remained in the 1H NMR spectrum, after <2 mins reaction time. Only a single new product (plus residual diamines **X** and **XE**) was observed, however the signals for the new product did not match those of the expected **3.1** mesocate, but rather the opened ML_3 complex $FeXE_3 \cdot Py_3$. Unlike the previous ML_3 mixtures observed with *p*-phenetidine, **F**, and **APA** however, only the highly symmetrical *fac* isomer was formed when using **XE**. Additionally, the xanthene equivalent was only observed transiently followed by a sluggish equilibration to the self-assembled **3.1** mesocate. After 24 h, ~50 % conversion is seen, and complete reaction requires 16 h heating at 70 °C.

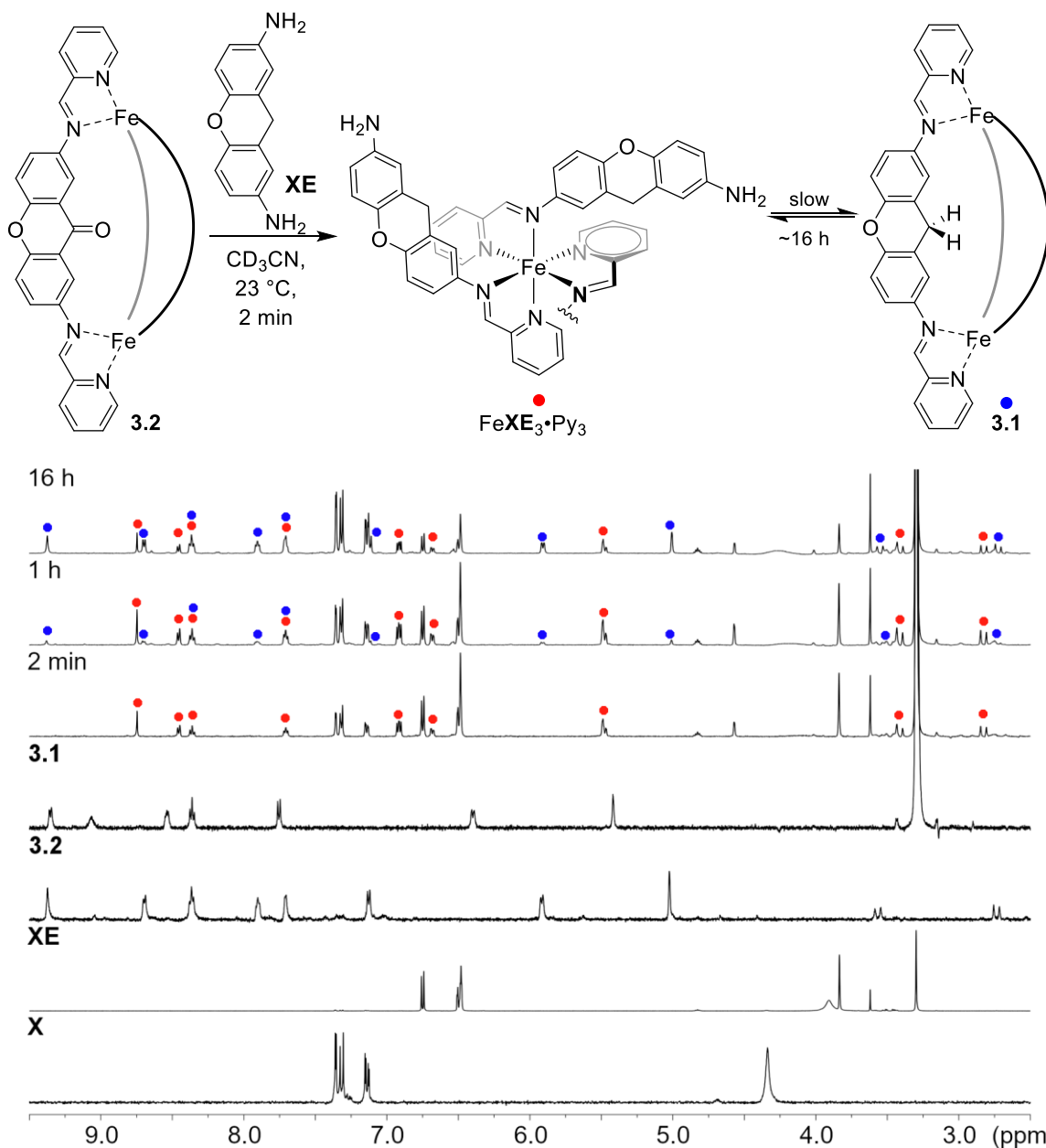


Figure 3.18. ^1H NMR spectrum tracking the destruction of **3.2** (5.8 mM in CD_3CN) upon addition of diaminoxanthene **XE** (17.7 mM) over time. (298 K CD_3CN , 400 MHz).

It was envisioned that a more stable all *fac* ML_3 could be formed by slightly extending the **XE** through the addition of phenyl ring spacers. The di(aminophenyl)xanthene (**DPX**) ligand was synthesized in 3 synthetic steps beginning from 9H-xanthene (Figure 3.19). 9H-Xanthene was selectively brominated at the 2 and 7

positions using Br_2 and acetic acid. The resulting 2,7-dibromoxanthene could then be converted to the extended di(boc-aminophenyl)xanthene, followed by subsequent deprotection with trifluoroacetic acid to give **DPX** in 80 % overall yield. Multicomponent self-assembly of **DPX** with Fe^{2+} salts and PyCHO results in the formation the expected **3.7** complex, but unlike most ligands in our hands, a 2:1 mixture of the mesocate and helicate isomers are formed. The formation of both isomers is presumably due to the greater flexibility in the extended **DPX** ligand.

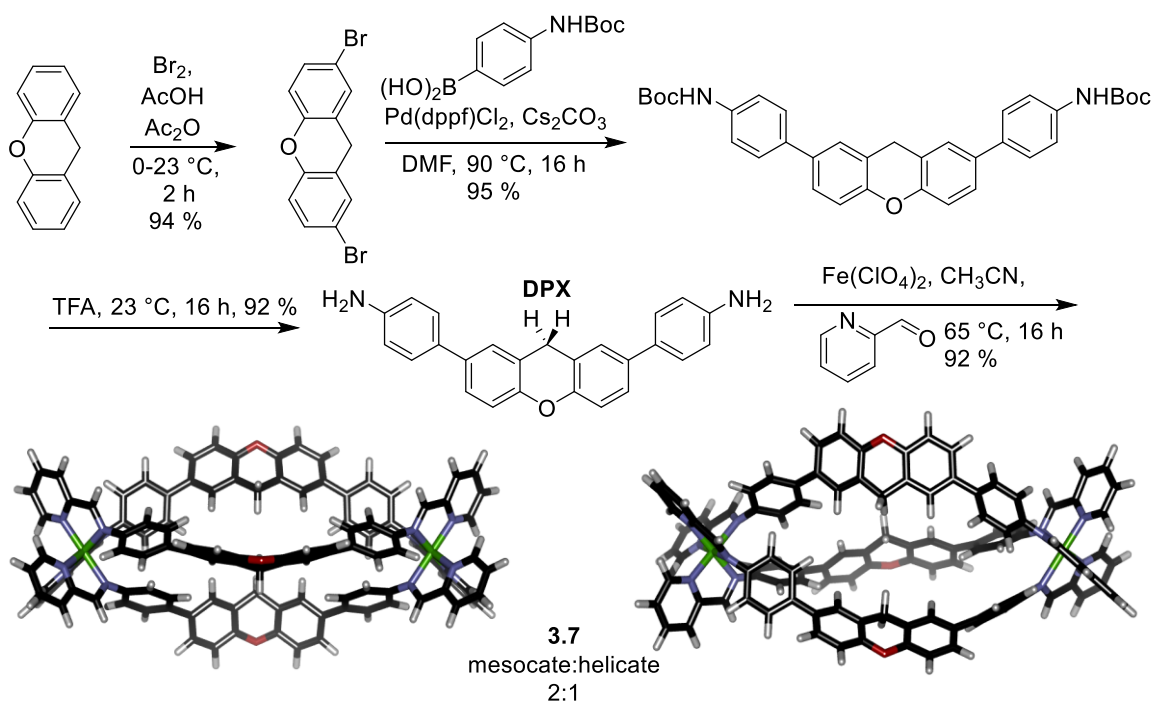


Figure 3.19. Synthesis of di(aminodiphenyl)xanthene ligand (**DPX**) multicomponent self-assembly into Fe_2L_3 mesocate and helicate structures (SPARTAN, semi-empirical).

When **DPX** was added to a solution of the “springloaded” cage **3.2** another new result was observed (Figure 3.20). Much like the previous examples, displacement of diaminoxanthone ligand **X** is complete in < 10 min. However, in this case the reaction is so quick that no fragments or intermediates could be observed. The mesocate and helicate

products are highly favored in this case, and if the M_2L_3 fragment is formed in this case, it is shorter lived than the NMR timescale. Despite **DPX** being a slightly less nucleophilic compound, the complete transimination to the product M_2L_3 was significantly faster than the reaction with **XE**.

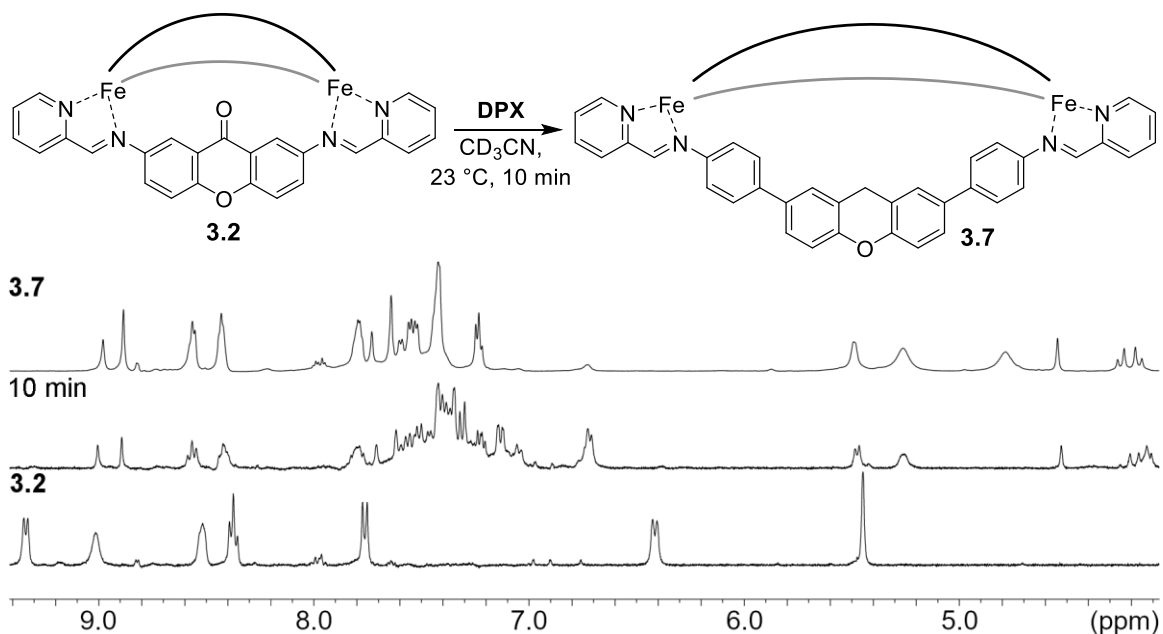


Figure 3.20. Deconstruction of the “springloaded” **3.2** mesocate. Downfield regions of the ^1H NMR spectra of the addition of **DPX** (5.8 mM) to **3.2** (5.8 mM) over time (298 K, CD_3CN , 400 MHz).

The rapid formation of the **3.7** cages is shocking when examining the mechanism of formation (Figure 3.5). It can be assumed that the ligand exchange occurs through sequential additions of **DPX** ligand into the “spring-loaded” $\text{Fe}_2\text{X}_3\cdot\text{Py}_6$ *meso*-helicite. However, after initial insertion, the hanging amine in **DPX** should extend far beyond the adjacent iminopyridine subunit, prohibiting intramolecular substitution. In the case of both **XE** and **DPX**, the initial disruption of the $\text{Fe}_2\text{X}_3\cdot\text{Py}_6$ assembly is rapid, but the conversion of $\text{FeXE}_3\cdot\text{Py}_3$ to $\text{Fe}_2\text{XE}_3\cdot\text{Py}_6$ is slow. Despite the formation of the $\text{FeDPX}_3\cdot\text{Py}_3$ not being observed, the previous data suggests this reaction must also proceed *via* that intermediate.

In contrast to the previous examples, the second step is fast in this case, and steady state kinetics are active, so only **3.7** is observed.

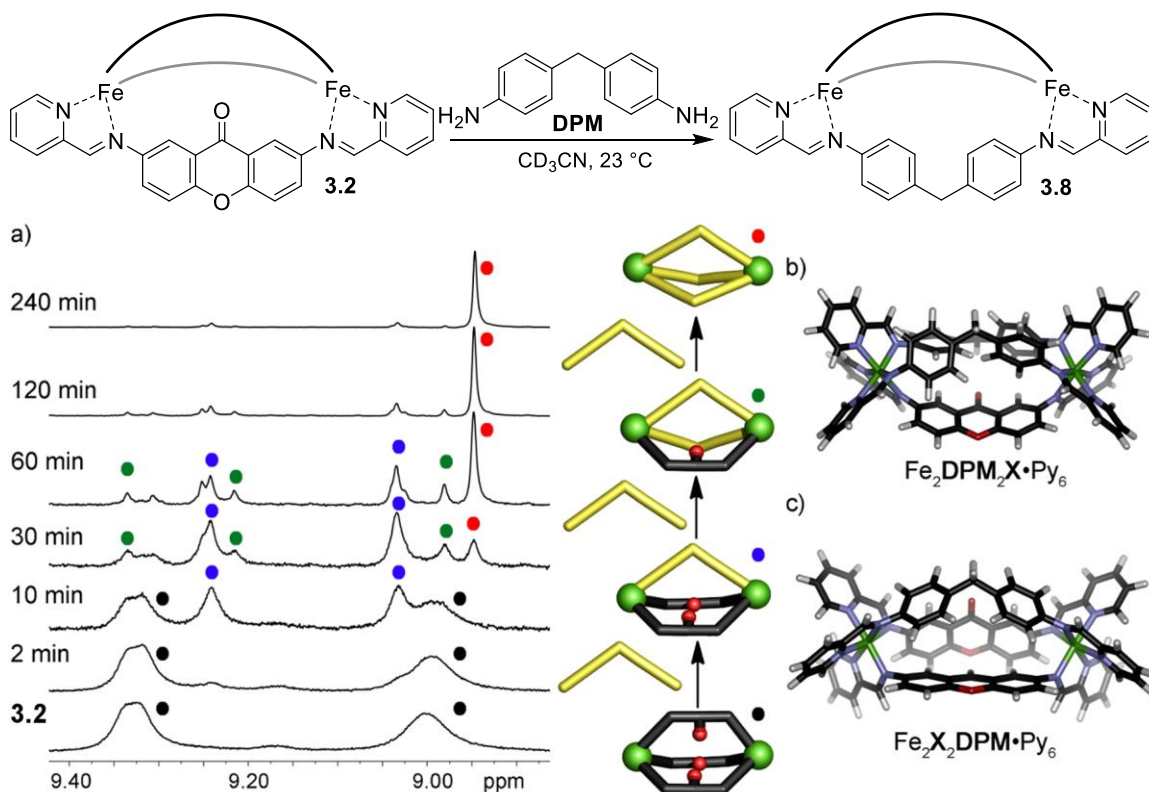


Figure 3.21. Transient Heterocomplex Formation. a) Downfield regions of the ^1H NMR spectra of the addition of diaminodiphenylmethane **DPM** (36.7 mM) to **3.2** (5.8 mM) over time. (298 K, CD_3CN , 400 MHz). Minimized structures of heterocomplexes b) $\text{Fe}_2\text{DPM}_2\text{X}\cdot\text{Py}_6$, c) $\text{Fe}_2\text{X}_2\text{DPM}\cdot\text{Py}_6$ (B3LYP-D3(BJ)/6-31G(d) basis set).

Finally, we tested the simplest diamine displacer ligand, di(aminophenyl)methane **DPM**, which forms a highly stable M_2L_3 mesocate; the Ru equivalent is sufficiently stable *in vivo* to be an effective anti-cancer agent.²⁶ The multicomponent self-assembly, and by association thermodynamic equilibration, of **DPM** with $\text{Fe}(\text{ClO}_4)_2$ and PyCHO , is rapid, effecting complete formation of the mesocate in < 2 h under ambient conditions. In addition to having the simplest structure, **DPM** is the most flexible ligand utilized in this study as its backbone is not locked into a ring. As a result, it is capable of rotating to achieve various

coordination angles upon assembly. When the “springloaded” mesocate **3.2** was treated with **DPM** a fourth behavior was observed. No evidence of ML_3 fragments could be observed at any point during the reaction: instead, **3.2** was converted to **3.8** *via* a series of M_2L_3 heterocomplexes caused by sequential addition of **DPM** ligands (Figure 3.21). The initial displacement occurs rapidly, and after only 10 mins, new signals for the $Fe_2X_2DPM \cdot Py_6$ heterocomplex are seen. This transition can be easily observed by investigating the imine CH region of the spectrum. At 10 min reaction time, the single, symmetric imine 1H signal of the **3.2** splits into the two signals of $Fe_2X_2DPM \cdot Py_6$. After 30 mins, the peaks for the xanthone mesocate have almost completely disappeared and the peaks for $Fe_2X_2DPM \cdot Py_6$ have begun to recede accompanied by new peaks for $Fe_2X \cdot DPM_2 \cdot Py_6$ growing in, followed by those for the **3.8** product. After 120 mins, the reaction is complete, and only the equilibrated **3.8** mesocate is observed. Unlike in the earlier cases, transimination of the “springloaded” *meso*-helcate **3.2** with **DPM** is not controlled by the opening of the cage but rather the stability of the product helicate **3.8**. The **DPM** ligand has the same length as diaminoxanthone **X**, and its additional flexibility allows incorporation into heterocomplex assemblies, which are more stable than the opened ML_3 fragments. The stability of the **3.8** product allows this ligand to behave as expected: only iminopyridine products are seen, with no “hanging” NH_2 groups. As there is a stable cage outlet for the transimination reaction, the process is directed to that product.

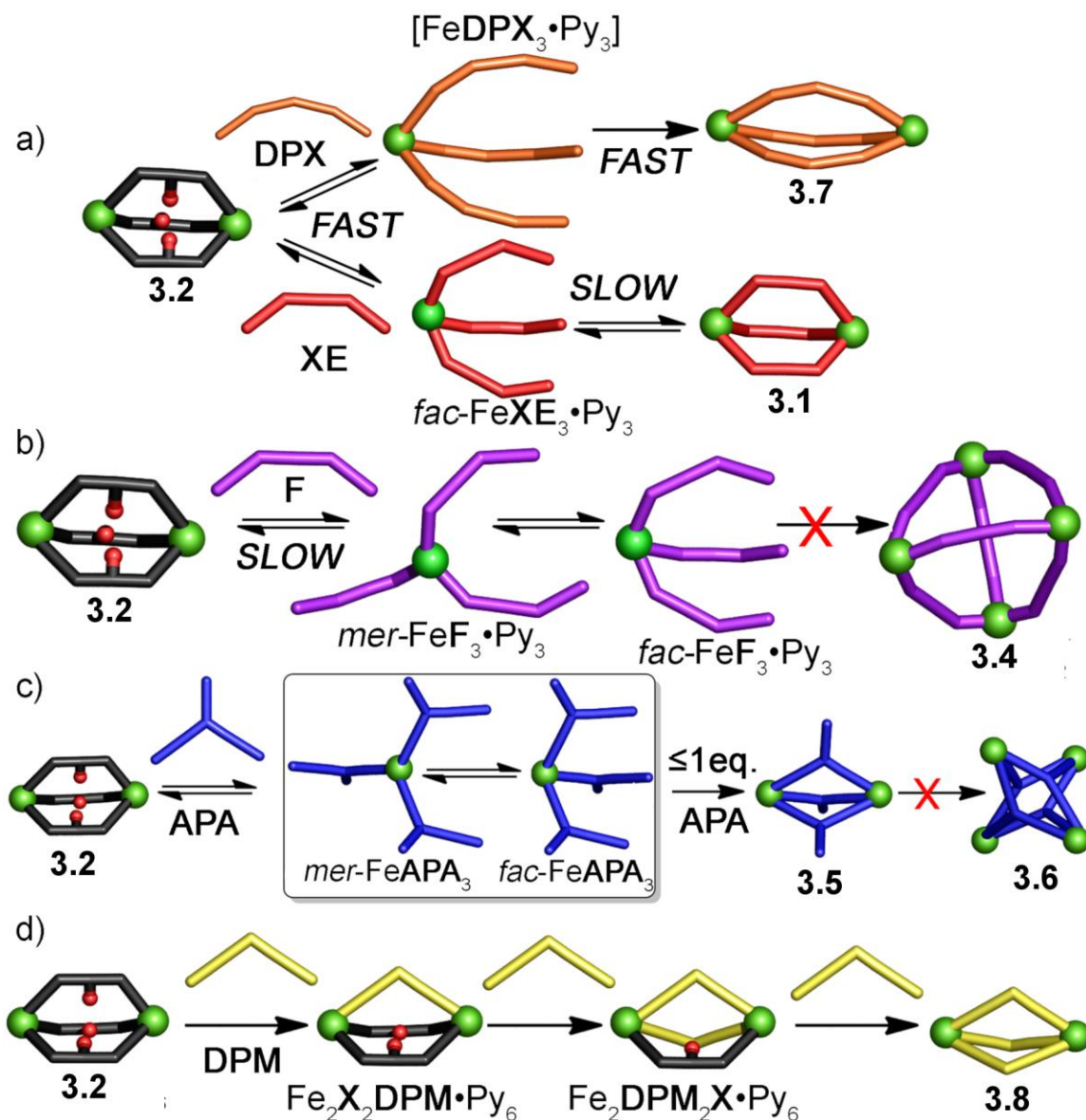


Figure 3.22. Summary of reaction outcomes upon addition of competitive amine ligands to 3.2. a) Xanthenyl ligands XE, DPX; b) Fluorene F; c) tripodal ligand APA; d) flexible ligand DPM.

The 3.2 lies in a goldilocks zone of self-assembled complexes: while it is stable enough to be formed via typical multi-component reaction conditions (PyCHO, X and Fe^{2+} salts), the product is strained and can be easily displaced by aniline-containing molecules under ambient conditions. A schematic summary of the reaction outcomes is shown in Figure 3.22. The reaction outcomes are dependent on the nature of the displacer ligand.

The high variability in products formed is quite unusual given the ostensibly similar size and electronics of the ligands used; however, some conclusions can be made towards the mechanism of the reaction. In almost every case, **FO** excluded, initial substitution of diamine **X** with the incoming amine is rapid, often occurring in the seconds between addition of the ligand and ^1H NMR acquisition. Given the speed of the initial displacement it is far more likely that reaction proceeds through transimination of the preformed complex, rather than by a dissociative mechanism whereby the iminopyridine arm release from the Fe^{2+} center and is replaced by incoming ligand. While the initial addition is the same in all cases, the outcome of the reaction is controlled by the favorability (or lack thereof) of the products. The larger tetrahedral assemblies (**3.4** and **3.6**) possess a larger barrier to equilibration that cannot be reached under ambient conditions, so the reaction ceases at a local energetic minimum, the *fac/mer* mixture of FeL_3 fragments. In the case of **F**, there exists no low barrier assembly pathway, resulting in a surprisingly stable complex despite the hanging NH_2 groups. In contrast, the **3.5** mesocate is significantly more stable than the open ML_3 and can be easily converted over time or with heat. In cases where the energy barrier is low (i.e. a favorable target cage) substrate rate dependent equilibration to the product is observed. Using the xanthyl ligands (**XE** and **DPX**) results in rapid exchange with the **3.2** precursor followed closer of the assembly to the product cage. Finally, when enough flexibility is introduced to the displacing ligand in the case of **DPM**, the strain release is possible upon displacing substitution of **X** for **DPM** from the **3.2** precursor to allow iterative formation of $\text{Fe}_2\text{L}^1_x\text{L}^2_y$ mesocates along the pathway to the $\text{Fe}_2\text{DPM}_3\cdot\text{Py}_6$ product. The mild conditions for transimination enabled using the metastable $\text{Fe}_2\text{X}_3\cdot\text{Py}_6$

allow observation of very rarely seen transient intermediates in multicomponent self-assembly.

3.10 Conclusion

In this chapter, two separate methods were presented for the post-assembly modification of Fe²⁺-iminopyridine base self-assembled cages. The experiments were designed to enable mild conditions which would be tolerant of the sensitive iminopyridine subunits. Through the oxidation of doubly-benzylic methylene ligands, every stage of the oxidation pathway (t-butyl peroxide, alcohol, ketone) could be observed under the proper conditions. By utilizing the metastable **3.2** *meso*-helicite as a springboard for transimination reactions rarely observed transient intermediates along the assembly (ML₃'s and heterocomplexes) were observed. In both cases the reactivity, and observed product, are controlled by the structure and stability of the self-assembled cages. While the t-butylperoxide mesocate **3.3** observed upon oxidation of the xanthene mesocate is controlled by the strain of the cage, almost all other examples presented were governed by the thermodynamic stability of the target cage.

3.11 References

1. Holloway, L. R.; Bogie, P. M.; Lyon, Y.; Julian, R. R.; Hooley, R. J. “Stereoselective Postassembly CH Oxidation of Self-Assembled Metal-Ligand Cage Complexes.” *Inorg. Chem.* **2017**, *56*, 11435–11442.
2. Newhouse, T.; Baran, P. S. “If C–H bonds could talk – selective C–H bond oxidation.” *Angew. Chem. Int. Ed.* **2011**, *50*, 3362–3374.
3. Chen, M. S.; White, M. C. “A predictably selective aliphatic C-H oxidation reaction for complex molecule synthesis.” *Science* **2007**, *318*, 783–787.
4. Burke, M. J.; Nichol, G. S.; Lusby, P. J. “Orthogonal Selection and Fixing of Coordination Self-Assembly Pathways for Robust Metallo-organic Ensemble Construction.” *J. Am. Chem. Soc.* **2016**, *138*, 9308–9315.
5. Symmers, P. R.; Burke, M. J.; August, D. P.; Thomson, P. I. T.; Nichol, G. S.; Warren, M. R.; Campbell, C. J.; Lusby, P. J. *Chem. Sci.* **2015**, *6*, 756–760.
6. Holloway, L. R.; Young, M. C.; Beran, G. J. O.; Hooley, R. J. “High Fidelity Sorting of Remarkably Similar Components via Metal-Mediated Assembly” *Chem. Sci.* **2015**, *6*, 4801–4806.
7. Young, M. C.; Holloway, L. R.; Johnson, A. M.; Hooley, R. J. “A Supramolecular Sorting Hat: Stereocontrol in Metal-Ligand Self-Assembly by Complementary Hydrogen Bonding” *Angew. Chem. Int. Ed.* **2014**, *53*, 9832–9836.
8. Chen, M. S.; White, M. C. “Combined effects on selectivity in Fe-catalyzed methylene oxidation.” *Science* **2010**, *327*, 566–571.
9. Miller, T. F.; Holloway, L. R.; Nye, P. P.; Lyon, Y.; Beran, G. J. O.; Harmen, W. H.; Julian, R. R.; Hooley, R. J. “Small Structural Variations have Large Effects on the Assembly Properties and Spin State of Room Temperature High Spin Fe(II) Iminopyridine Cages.” *Inorg. Chem.* **2018**, *57*, 13386–13396.
10. Meng, W.; Ronson, T. K.; Nitschke, J. R. “Symmetry breaking in self-assembled M₄L₆ cage complexes.” *Proc. Natl. Acad. Sci. U. S. A.* **2013**, *110*, 10531–10535.
11. Bogie, P. M.; Holloway, L. R.; Lyon, Y.; Onishi, N. C.; Beran, G. J. O.; Julian, R. R.; Hooley, R. J. “A Springloaded Metal-Ligand Mesocate Allows Access to Trapped Intermediates of Self-Assembly” *Inorg. Chem.* **2018**, *57*, 4155–4163.

12. Acharyya, K.; Mukherjee, S.; Mukherjee, P. S. "Molecular Marriage through Partner Preferences in Covalent Cage Formation and Cageto-Cage Transformation." *J. Am. Chem. Soc.* **2013**, *135*, 554–557.
13. Mosquera, J.; Ronson, T. K.; Nitschke, J. R. "Subcomponent Flexibility Enables Conversion between D4-Symmetric $\text{Cd}^{\text{II}}_8\text{L}_8$ and TSymmetric $\text{Cd}^{\text{II}}_4\text{L}_4$ Assemblies." *J. Am. Chem. Soc.* **2016**, *138*, 1812–1815.
14. Jimenez, A.; Bilbeisi, R. A.; Ronson, T. A.; Zarra, S.; Woodhead, C.; Nitschke, J. R. "Selective Encapsulation and Sequential Release of Guests Within a Self-Sorting Mixture of Three Tetrahedral Cages." *Angew. Chem., Int. Ed.* **2014**, *53*, 4556–4560.
15. Holloway, L. R.; McGarraugh, H. H.; Young, M. C.; Sontising, W.; Beran, G. J. O.; Hooley, R. J. "Structural Switching in Self-Assembled Metal-Ligand Helicate Complexes via Ligand Centered Reactions." *Chem. Sci.* **2016**, *7*, 4423–4427.
16. Ronson, T. K.; Pilgrim, B. S.; Nitschke, J. R. "Pathway Dependent Post-assembly Modification of an Anthracene-Edged $\text{M}^{\text{II}}_4\text{L}_6$ Tetrahedron." *J. Am. Chem. Soc.* **2016**, *138*, 10417–10420.
17. Roberts, D. A.; Castilla, A. M.; Ronson, T. K.; Nitschke, J. R. "Postassembly Modification of Kinetically Metastable $\text{Fe}^{\text{II}}_2\text{L}_3$ Triple Helicates." *J. Am. Chem. Soc.* **2014**, *136*, 8201–8204.
18. Mal, P.; Nitschke, J. R. "Sequential self-assembly of iron structures in water." *Chem. Commun.* **2010**, *46*, 2417–2419.
19. Burke, M. J.; Nichol, G. S.; Lusby, P. J. "Orthogonal Selection and Fixing of Coordination Self-Assembly Pathways for Robust Metallo-organic Ensemble Construction." *J. Am. Chem. Soc.* **2016**, *138*, 9308–93153.
20. Bilbeisi, R. A.; Clegg, J. K.; Elgrishi, N.; de Hatten, X.; Devillard, M.; Breiner, B.; Mal, P.; Nitschke, J. R. "Subcomponent Self-Assembly and Guest-Binding Properties of Face-Capped $\text{Fe}_4\text{L}_4^{8+}$ Capsules." *J. Am. Chem. Soc.* **2012**, *134*, 5110–5119.
21. Kieffer, M.; Pilgrim, B. S.; Ronson, T. K.; Roberts, D. A.; Aleksanyan, M. J.; Nitschke, J. R. "Perfluorinated ligands induce meridional metal stereochemistry to generate M_8L_{12} , $\text{M}_{10}\text{L}_{15}$ and $\text{M}_{12}\text{L}_{18}$ prisms." *J. Am. Chem. Soc.* **2016**, *138*, 6813–6821.
22. Becke, A. D. "Density-functional thermochemistry. III. The role of exact exchange." *J. Chem. Phys.* **1993**, *98*, 5648–5652.

23. Rassolov, V. A.; Ratner, M. A.; Pople, J. A.; Redfern, P. C.; Curtiss, L. A. "6-31G* basis set for third-row atoms." *J. Comput. Chem.* **2001**, *22*, 976–984.
24. Weigend, F.; Ahlrichs, R. "Balanced basis sets of split valence, triple zeta valence and quadruple zeta valence quality for H to Rn: Design and assessment of accuracy." *Phys. Chem. Chem. Phys.* **2005**, *7*, 3297–3305.
25. Bloch, W. M.; Abe, Y.; Holstein, J. J.; Wandtke, C. M.; Dittrich, B.; Clever, G. H. "Geometric Complementarity in Assembly and Guest Recognition of a Bent Heteroleptic cis-[Pd₂L^A₂L^B₂] Coordination Cage." *J. Am. Chem. Soc.* **2016**, *138*, 13750–13755.
26. Hannon, M. J.; Painting, C. L.; Jackson, A.; Hamblin, J.; Errington, W. "An inexpensive approach to supramolecular architecture." *Chem. Commun.* **1997**, 1807–1808.

Chapter 4 – Design and Applications of an Acid-Containing Biomimetic Nano Reactor

4.1 Introduction

While the results obtained with **DPX** (section 3.9) demonstrate the usefulness of elongating the ligand scaffold, an M_2L_3 complex is still formed and the cavity is essentially non-existent. To create a supramolecular cage with a more useful cavity, capable of molecular recognition and catalysis, complexes of larger stoichiometry need to be synthesized.¹ The fluorenyl scaffold almost exclusively forms M_4L_6 tetrahedra upon self-assembly with 2-pyridine carboxaldehyde. Further, many possible modifications of the fluorenyl scaffold exist that can be used to provide internal functionality, making it an ideal candidate as the core ligand for the formation of a catalytic cage. Molecular modeling of the extended fluorene ligand **4.A** reveals that an M_4L_6 tetrahedron is likely to be formed with a large cavity suitable for both molecular recognition, and incorporation of functional groups to produce reactivity (Figure 4.1).

4.2 Synthesis of Extended Fluorenyl Ligands and Multicomponent Self-Assembly

The elongated fluorene ligand could be easily obtained in two steps via Suzuki-Miyaura coupling of commercially available 2,7-dibromo-9H-fluorene with 4-Boc-aminophenylboronic acid, followed by deprotection of the aniline using neat trifluoroacetic acid. With the ligand in hand, multicomponent self-assembly was attempted using 2-pyridine carboxaldehyde (PyCHO) and $Fe(ClO_4)_2$ in CH_3CN . Surprisingly, the resulting complex was only sparingly soluble in CH_3CN and analysis via NMR proved challenging. When freshly synthesized $Fe(NTf_2)_2$ was employed in place of $Fe(ClO_4)_2$, the reaction gave the deep purple color expected of Fe^{2+} -iminopyridine complexes and a much more

soluble complex was obtained. The resulting complex was analyzed by ^1H NMR (Figure 4.1c).

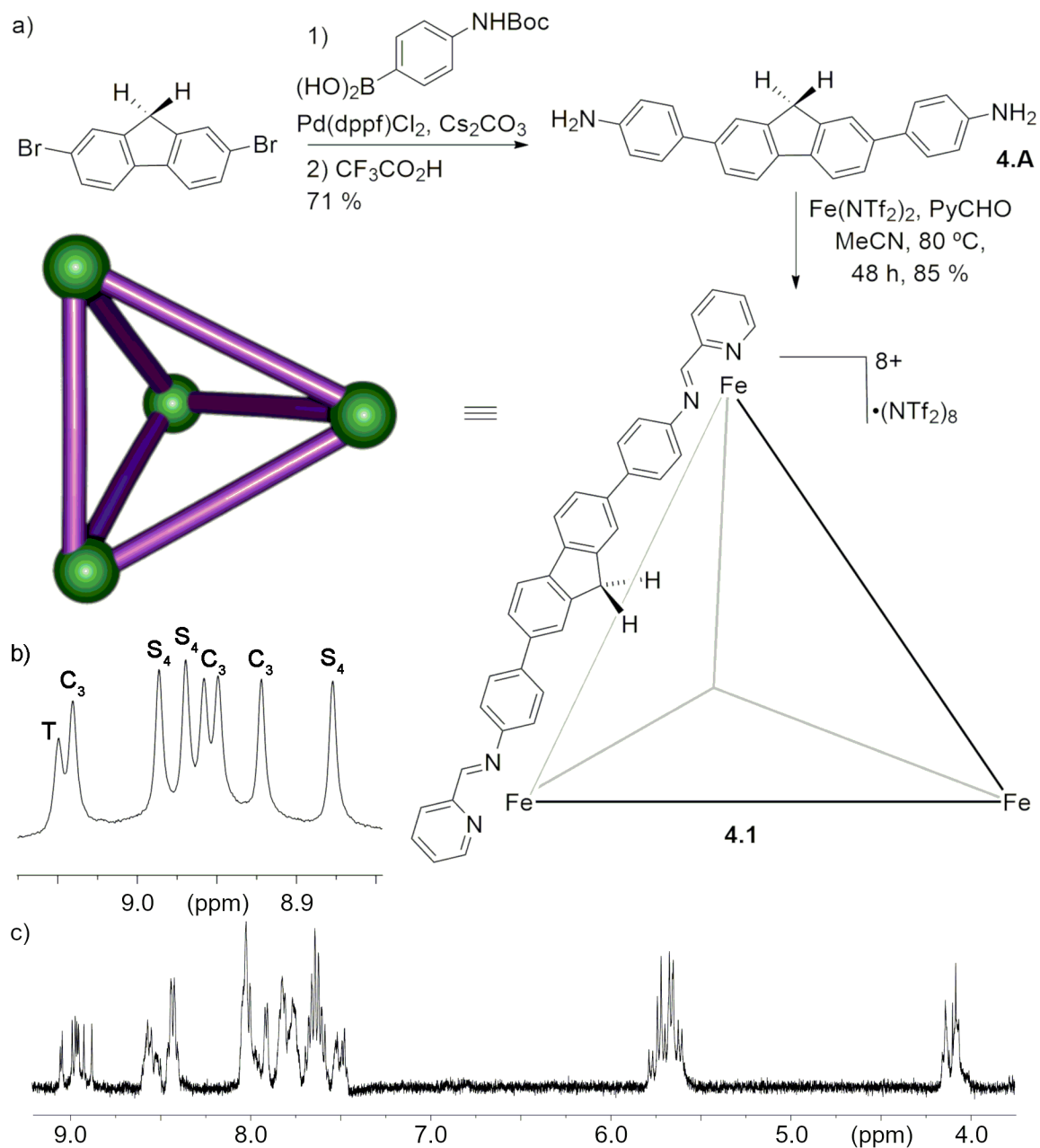


Figure 4.1. a) Synthesis of extended fluorene ligand **4.A** and multicomponent self-assembly in to M_4L_6 tetrahedron **4.1**; b) ^1H NMR spectrum of cage **4.1** (CD_3CN , 298 K, 600 MHz).

Although the ^1H NMR spectrum of cage **4.1** is complex, it is significantly less so than the observed spectrum of the shorter 2,7-diaminofluorene cage $\text{Fe}_4\text{F}_6\cdot\text{Py}_{12}$ (see Chapter 3).² A closer look at the imine region of the assembly reveals that cage **4.1** exists as a mixture of 3 all-*fac* isomers commonly found in M_4L_6 tetrahedra.³ The isomeric ratio was calculated via integration of the imine peaks, with the ratio for cage **4.1** being: 48 % **4.1-C**₃, 11 % **4.1-T**, 41 % **4.1-S**₄. The purity of the sample was confirmed using 2D-DOSY NMR (which indicated that all peaks belonged to complexes of the same diffusion constant), and elemental analysis. With the help of COSY, TOCSY and NOESY NMR techniques, each signal in the NMR spectra was assigned to the respective proton in the cage. Finally, Dr. Yana Lyon helped confirm the stoichiometry of the complex via ESI-MS using an Orbitrap Velos Pro mass spectrometer with the standard HESI source at a flow rate of 3 $\mu\text{L}/\text{min}$. The mass spectrum of the complex was dominated by the 8+ ion of the M_4L_6 cage, as well as many different fragments. The full mass spectrum of cage **4.1** is shown in Figure 4.2, along with an assignment of all signals present in the mass spectrum.

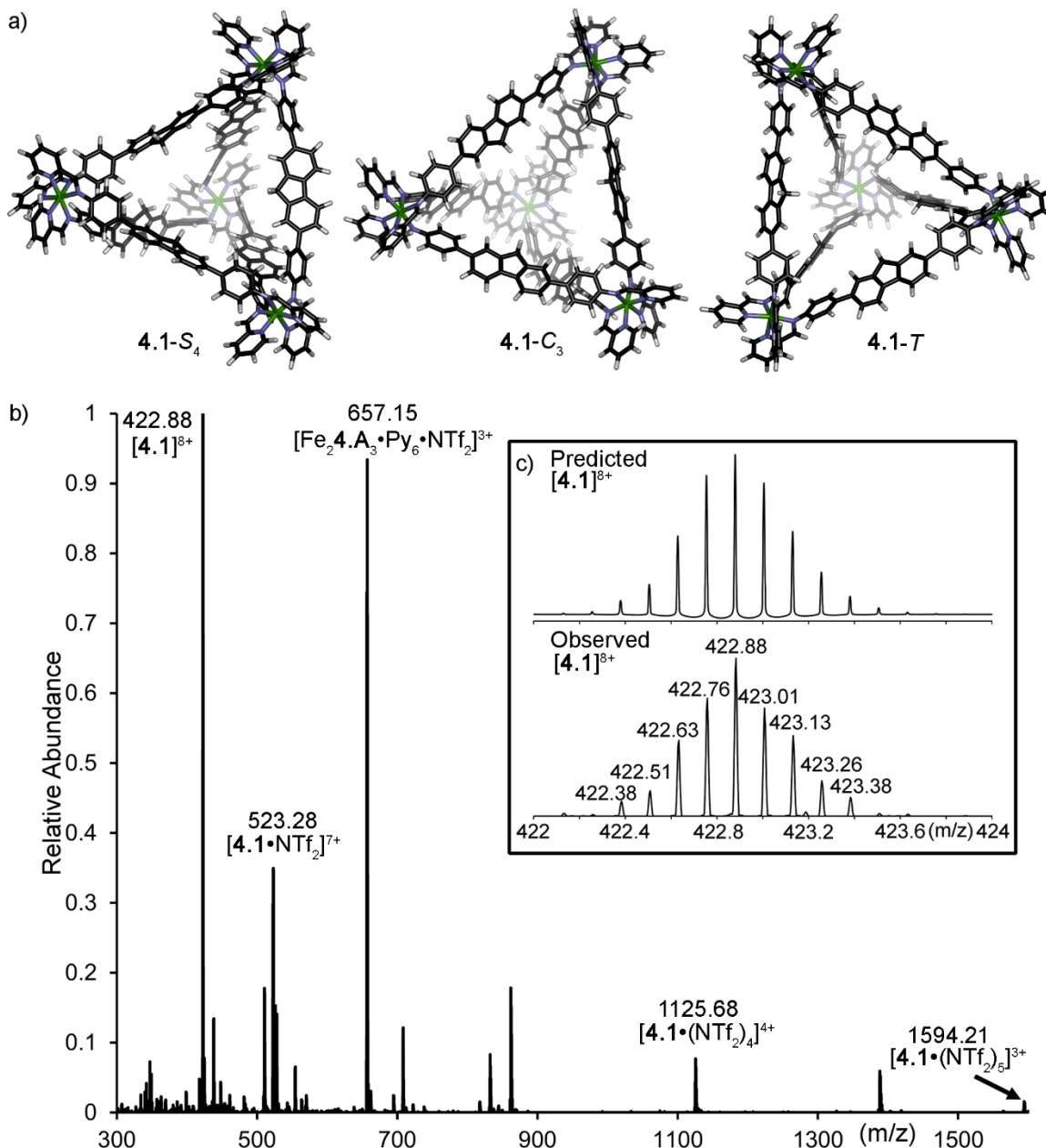


Figure 4.2. a) Molecular modeling of the three isomers of cage **4.1** (SPARTAN, semi-empirical); b) full positive mode ESI-mass spectrum of cage **4.1** obtained in pure CH₃CN; c) comparison of predicted ion [4.1]⁸⁺ versus experimentally observed peaks (m/z = 422.88).

The facile synthesis of cage **4.1** is promising, with molecular models indicating that the very large cavity and windows can accommodate a range of different sized guest molecules. However, cage **4.1** is unfunctionalized and does not possess molecular

reactivity on its own. To synthesize a cage capable of directing catalysis, the ligand must be appended with functional groups. While The proposed ligand **4.D** exhibits a structural scaffold like that of **4.A**, the inclusion of functional groups presents additional synthetic challenges, such as varying protonation states, including zwitterionic species. To avoid potential issues with water solubility, we investigated several synthetic routes. Initially the synthesis of **4.D** approached with 4-nitrophenylboronic acid (4-NPBA) used in place of the Boc-group (Figure 4.3). The boronic acid was prepared in a single step, from 4-nitroaniline. The aniline moiety is converted into a diazonium salt in situ, followed by substitution for the boronic acid. The product could then be easily purified by extraction into a 1 M sorbitol and NaCO₃ solution in water, followed by acidification of the aqueous layer and secondary extraction of the released product into ethyl acetate.

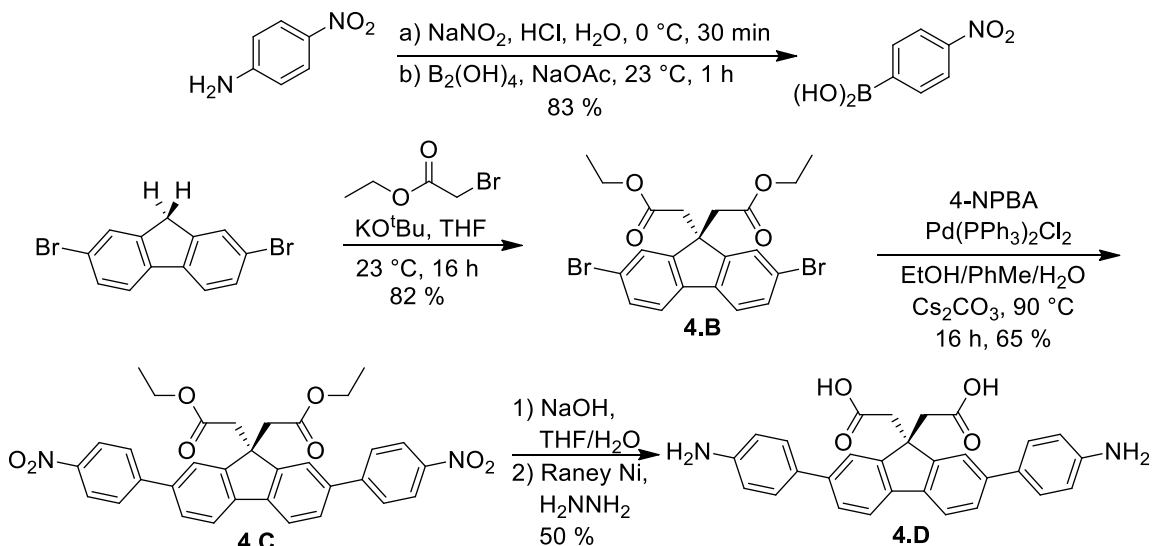


Figure 4.3. Synthesis of ligand **4.D** using 4-nitrophenylboronic acid.

Starting again from 2,7-dibromo-9H-fluorene, the scaffold could be functionalized via S_N2 reaction with ethylbromoacetate and potassium tert-butoxide to give diester **4.B**. The diester is purified through column chromatography using an EtOAc/hexanes gradient.

Following purification, **4.B** was elongated via Suzuki-Miyaura coupling with 4-nitrophenylboronic acid. The Suzuki-Miyaura coupling resulted in a mixture of the mono-reacted and bis-reacted products, the desired bis-nitrodiester **4.C** was isolated via column chromatography in pure CH_2Cl_2 . The ester groups in **4.C** were hydrolyzed using NaOH in $\text{THF}/\text{H}_2\text{O}$, and finally the nitro-groups were reduced using Raney $\text{Ni}^{\text{®}}$ and hydrazine to give ligand **4.D** in 27 % overall yield. With ligand **4.D** in hand, multi component self-assembly was attempted with $\text{Fe}(\text{NTf}_2)_2$ and PyCHO was attempted (Figure 4.4a).

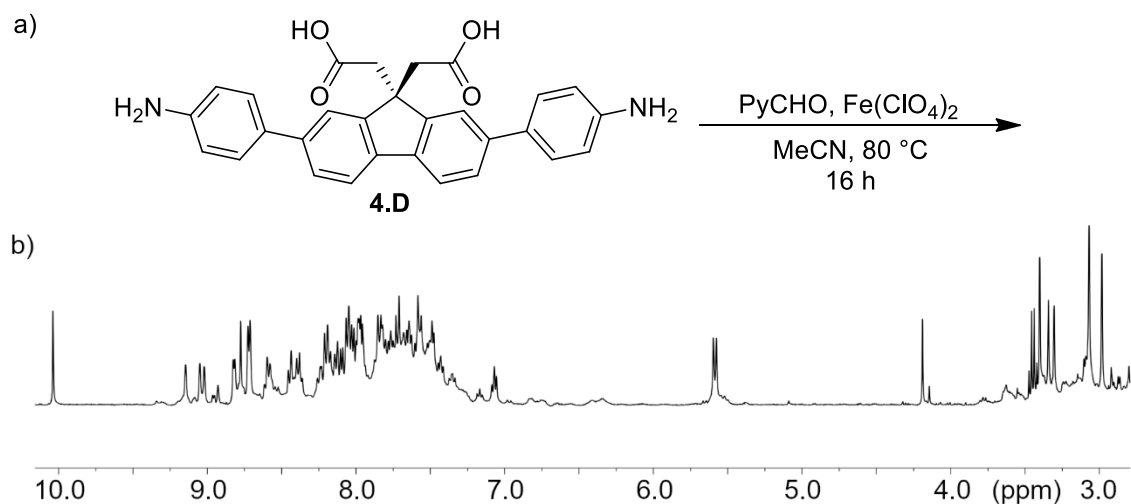


Figure 4.4. a) Multi-component self-assembly of **4.D** (Figure 4.3) with $\text{Fe}(\text{NTf}_2)_2$ and PyCHO . b) ^1H -NMR spectrum of the assembly process (CD_3CN , 298 K, 400 MHz).

Despite the additional bulk present in ligand **4.D** compared to the unfunctionalized ligand **4.A**, the ^1H NMR spectrum of the assembly product was suspiciously far less complicated than cage **4.1** (Figure 4.4b). Further examination of the ^1H NMR spectrum revealed two large concerns with the complex formed under these conditions: 1) the imine region of the spectrum exhibits 4 total signals, 3 with the same intensity and 1 at about half the height; 2) in almost all imino-pyridine cages several doublet peaks should exist around 5 ppm as a result of shielding from the metal center.^{1,2,4} In the NMR spectrum for the

assembly of **4.D** only a single peak is present. In the mass spectrum, no signals corresponding to the expected M_4L_6 tetrahedron of ligand **4.D** were observed, however, there were several peaks present that exhibited the characteristic splitting pattern of an Fe-containing complex. It is reasonable to assume that the ML_3 complex of ligand **4.2** is formed in this case, but is not particularly stable and decomposes upon ionization.

While the result of the self-assembly above was discouraging, the acid-containing cage **4.2** is still highly desirable in supramolecular catalysis so alternative synthetic methods were investigated. It was hypothesized that the use of metal and hydrazine in the reduction step lead to trace impurities, which were the cause of the unforeseen difficulties in the previous synthetic pathway. In contrast, the synthesis of ligand **4.A** and cage **4.1** were largely uncomplicated. Despite the risk of using water, synthesis of ligand **4.D** was attempted using a slightly modified procedure from **4.A** (Figure 4.5). Facile formation of the Boc-extended fluorenyl diester **4.E** was achieved via Suzuki coupling with 4-Boc-aminophenylboronic acid. The Boc-protecting groups were first removed by treating **4.E** with neat trifluoroacetic acid at room temperature for 16 h. The TFA was removed *in vacuo* and the resulting aniline-TFA salt was immediately subjected to hydrolysis conditions in a mixture of $H_2O/MeOH$. As expected, ligand **4.D** was highly soluble in basic H_2O , but could be precipitated by neutralization. Unfortunately, this procedure resulted in at most 30 % yield of ligand **4.2** and often precipitation failed altogether. To maximize the yield of pure ligand **4.2**, the filtrate of the reaction could be recycled. The water of the filtrate was removed *in vacuo* and redissolved in MeOH followed by vacuum filtration to remove any salts. The MeOH was then removed *in vacuo* and the solid redissolved in minimal H_2O .

Addition of $\sim 3 \mu\text{L}$ 5 M HCl results in rapid precipitation of pure ligand **4.D**; this procedure could be repeated increasing the yield from 30 % up to 80-85 %.

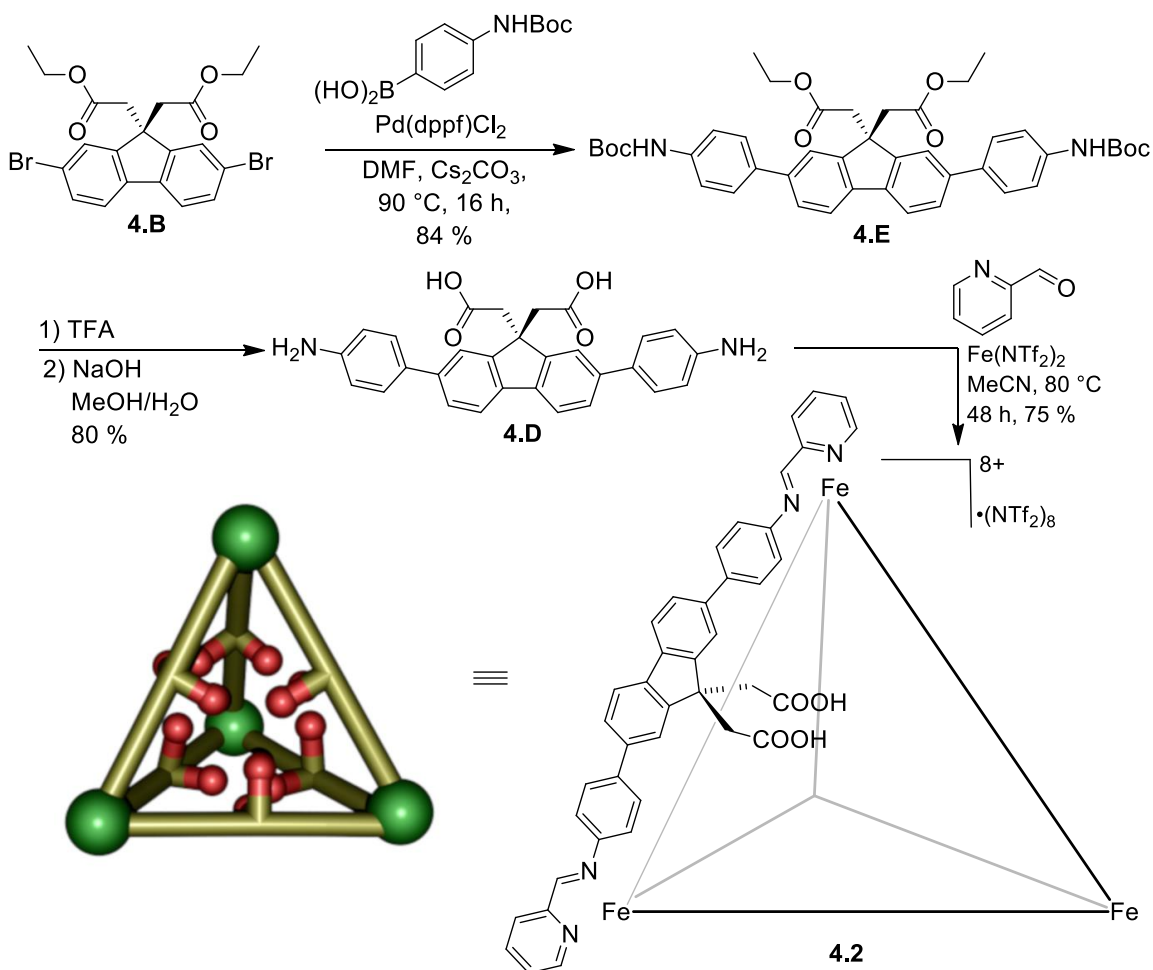


Figure 4.5. Synthesis of ligand **4.D** using 4-Bocaminophenylboronic acid, and multi-component self-assembly into M_4L_6 tetrahedron **4.2**.

The method presented in Figure 4.5 proved to be successful in many areas where the previous method (Figure 4.3) had failed: first the Suzuki-Miyaura coupling was significantly cleaner using the 4-Boc-aminophenylboronic acid, likely due to increased solubility from the Boc groups. Also, the resulting ligand **4.D** was isolated in a highly pure form and was able to self-assemble into the expected **4.2** tetrahedron. The ^1H NMR spectrum of cage **4.2** was similar to that of cage **4.1**, although the T-symmetric isomer was

not present (Figure 4.6 and 4.7a). Synthesis of the acid cage **4.2** does present some unique challenges in the self-assembly process. The primary issue arises from varied protonation states within the ligand (most commonly deprotonation of the acid). As this does not cause a change in the integration of the majority of the peaks, these differences can often be overlooked, but causes coordination of Fe^{2+} to the internal groups in the self-assembly process, causing a broad, paramagnetic spectrum (Figure 4.7d). Further, the concentration of the reaction is very important: if the reaction is too dilute the assembly process can remain incomplete and difficult to purify. Whereas, if the reaction is run too concentrated, intermediate complexes will precipitate before the equilibrated product can be reached.

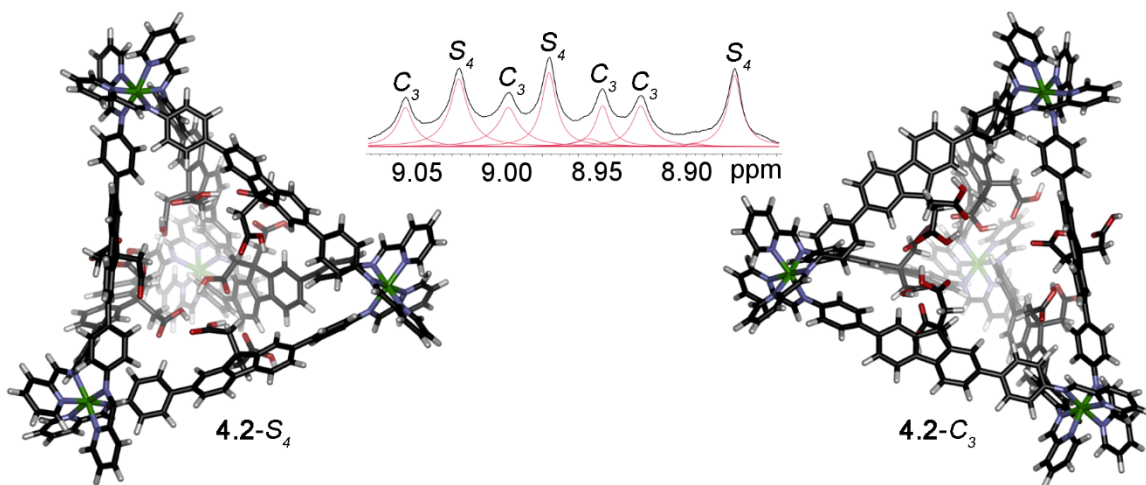


Figure 4.6. a) Molecular modeling of C_3 -**4.2** and S_4 -**4.2**; b) ^1H NMR spectrum of **4.2** tetrahedron (CD_3CN , 273K, 600 MHz).

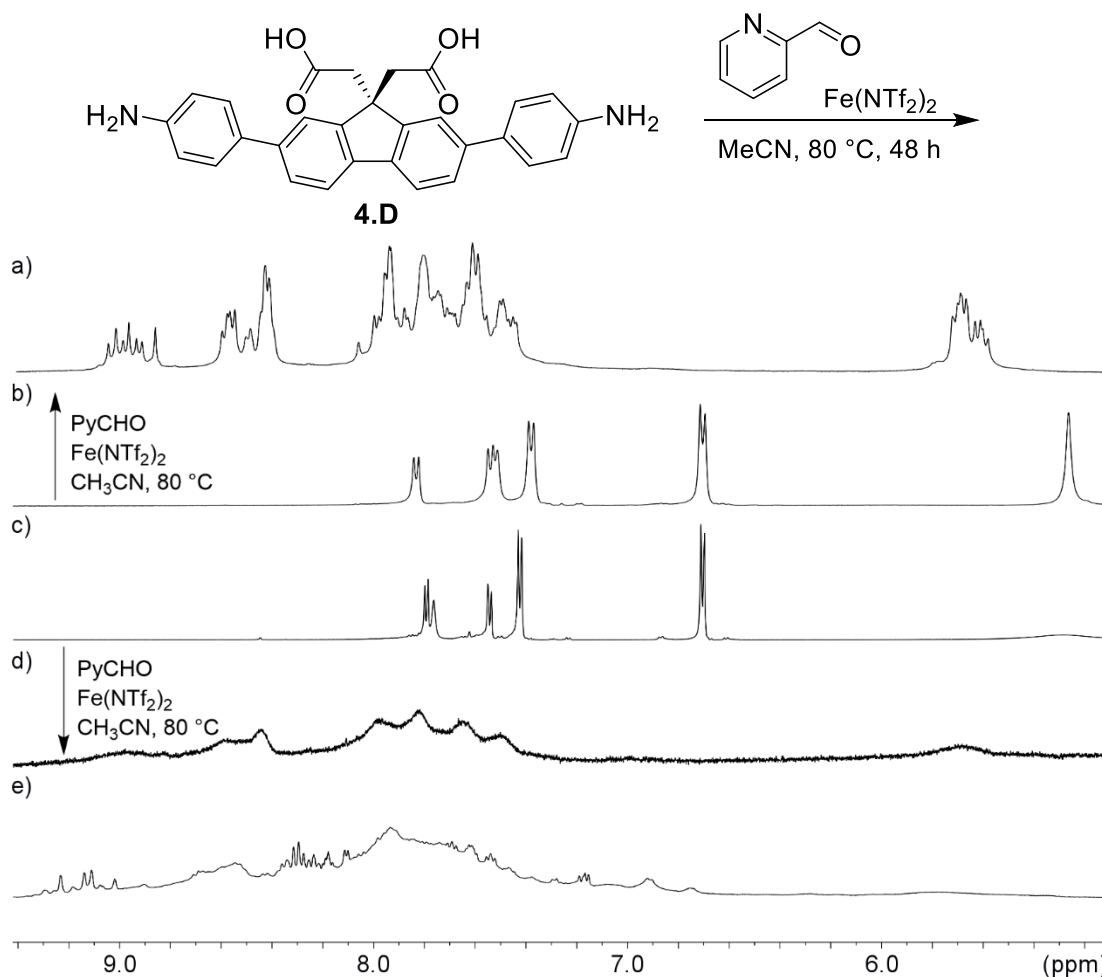


Figure 4.7. ^1H NMR spectra of the multicomponent self-assembly for acid-cage: a) cage **4.2**; b) neutral ligand **4.D**; c) anionic ligand **4.Dⁿ⁻**; d) self-assembly product using **4.Dⁿ⁻**; product of an overly concentrated reaction (CD_3CN , 298 K, 600 MHz).

The acidic cage **4.2** exists in 45:55 % ratio of the C_3 and S_4 isomers (Figure 4.6). While suitable crystals for X-ray diffraction could not be obtained, molecular modeling (semi-empirical, AM1 forcefield) of the two isomers shows nearly all the carboxylic acid functional groups are pointed towards the interior of the cage. Further, rotating the fluorenyl scaffold to orient the acid groups exohedrally resulted in a large increase in strain, and energy, of the complex. Again, the assignment of the NMR spectrum was corroborated using 2D NMR techniques, and elemental analysis. NOESY NMR (Supporting

Information) shows intra-ligand NOE correlations that are likely due to free rotation of the phenyl spacers. This does not rule out rotation of the fluorenyl moiety, but if any rotation does occur, the barrier is low, and the acids can easily be oriented to the cavity interior at 23 °C.

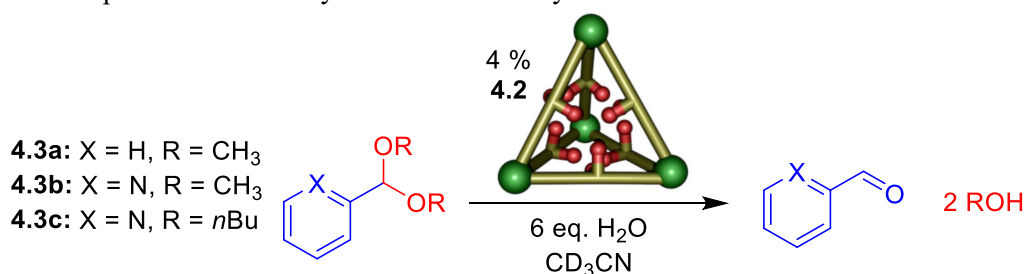
4.3 Acid Catalyzed Solvolysis of Aromatic Acetals.

The use of Fe-iminopyridine cages as catalysts can be quite challenging as they are often fragile. Disassembly of the cage often occurs in the presence of strongly coordinating anions (e.g. Cl⁻) and other exogenous nucleophiles.^{5,6} To evaluate the competency of cage **4.2** as a supramolecular catalyst, Dr. Holloway initially investigated a mild acetal hydrolysis.⁷ The final product of this reaction is an aldehyde, one of the building blocks of the **4.2** cage and should be easily tolerated, further the reaction occurs using a very mild nucleophile, H₂O. Aromatic acetals **4.3a-c** were chosen to examine how minor differences such as addition of heteroatoms and chain length can impact the reactivity. The acetals were treated with 4 mol% cage and 6 equivalents of water in CD₃CN, and the reaction was monitored over time using ¹H NMR. The results of the initial study are summarized in Table 4.1.

Treatment of **4.3a** with catalytic cage **4.2** resulted in rapid solvolysis of the acetal groups, with 99 % conversion after only 5 h under ambient conditions. A significantly slower reaction was observed when the reaction was performed on the pyridyl equivalent **4.3b**. In contrast with **4.3a**, **4.3b** required heating to 77 °C for solvolysis to occur as well as a longer reaction time (14 h) to effect complete conversion. Finally, the larger dibutylpyridyl acetal **4.3c** exhibited similar reactivity to the smaller **4.3b** (96 %, 14 h):

evidently the extended length of the alkyl chain was not enough to enable size discrimination within the large cavity of **4.2**. In all cases **4.3a-c**, no decomposition of the **4.2** catalyst was observed, as evidenced by the unchanging imine C-H region of the ^1H NMR. The initial rates of each of the reactions were calculated as the slope of concentration of starting material over time of the first three non-zero linear datapoints. Solvolysis of acetals **4.3a** and **4.3b** catalyzed by **4.2** had initial rates of $V = 2410$ and 440×10^{-4} mM/min respectively.

Table 4.1: Supramolecular catalysis of acetal solvolysis.

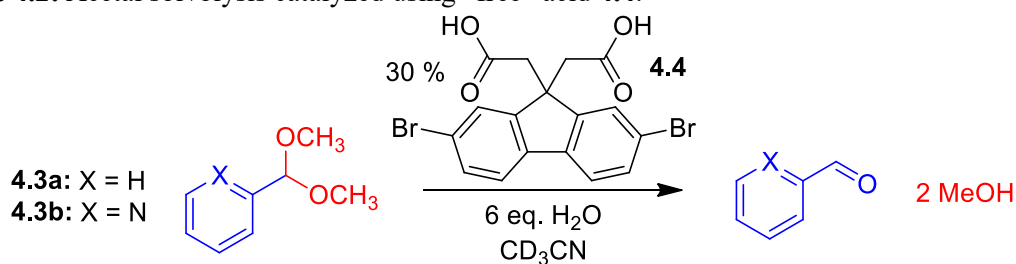


Substrate	t (h)	T (°C)	Catalyst	Initial Rate V (x10 ⁻⁴ mM/min)	Conversion (%)
4.3a	1	23	4.2	2410	79
4.3a	5	23	4.2		99
4.3b	4	77	4.2	440	60
4.3b	14	77	4.2		99
4.3c	14	77	4.2	418	96

More importantly, significant enhancement in initial rate was observed in the reactions catalyzed by **4.2** over control processes. To create a control molecule that should illustrate the reactivity of the acid groups in free solution (as opposed to encapsulated in a cage), a free acid catalyst **4.4** was prepared via hydrolysis of ester **4.B** (Table 4.2).

Treatment of **4.3a** with 30 mol % control acid **4.4** (i.e. an equivalent number of COOH groups as used with **4.2**) gave only 1 % conversion to benzaldehyde after 24 h under ambient conditions ($V = 2.26 \times 10^{-4}$ mM/min). Even at elevated temperature (50 °C, 24 h) the reaction was slower, with only 20 % conversion observed. Solvolysis of **4.3b** was similarly slow, exhibiting only 6 % conversion after 24 h at 77 °C ($V = 4.03 \times 10^{-4}$ mM/min). The internalization of the carboxylic acid groups towards the cavity of the cage is crucial for the rate enhancement, with a 1070-fold increase in reactivity for **4.3a**, and a 100-fold increase for **4.3b**. This is further illustrated when analyzing the treatment of **4.3a** with the combination of unfunctionalized cage **4.1** and control acid **4.4**. The observed initial rate in this case is nearly identical to the reaction with only control acid **4.4** ($V = 2.87 \times 10^{-4}$ mM/min), indicating that not only is the internal cavity necessary, but also the internalization of the acidic groups.

Table 4.2: Acetal solvolysis catalyzed using “free” acid **4.4**.



Substrate	t (h)	T (°C)	Catalyst	Initial Rate V ($\times 10^{-4}$ mM/min)	Conversion (%)
4.3a	24	23	4.4	2.26	1
4.3a	24	23	4.4 + 4.1	2.87	1
4.3b	24	77	4.4	4.03	6

The large rate accelerations suggest that the reaction likely occurs on the interior of the cage. While cage **4.2** does exhibit a large cavity and internal carboxylic acid groups that are conducive to encapsulation it is a relatively unusual host. In most cases, guest egress from host cavities is restricted by large flat panels (like those in Raymond's Gallatecholates tetrahedron⁸ or Fujita's tripyridyltriazine octahedron⁹), which are not present in **4.2**. Long-lived Michaelis complexes could not be observed in the NMR due to fast in-out exchange with cage **4.2**, however strong affinities of the acetals **4.3a-c** were still observed. The binding of the acetals was observed by UV-Vis titrations of guests into a 3 μM solution of cage **4.2** in CH_3CN (Figure 4.8). The binding affinities of the acetals for cage **4.2** were calculated via Stern-Volmer analysis of the absorbance spectra, illustrating the strong (μM) host:guest affinity of the acetals for the cage, with $K_a(\mathbf{4.2}\cdot\mathbf{4.3a}) = 13,158 \text{ M}^{-1}$ and $K_a(\mathbf{4.2}\cdot\mathbf{4.3b}) = 22,727 \text{ M}^{-1}$. No change in the absorbance spectrum was observed when **4.4** was treated with any of the acetals showing the interaction is cavity specific. In contrast, strong affinity is observed with unfunctionalized cage **4.1** further demonstrating the necessity for both the cavity and internalized acids as **4.1** is an ineffective catalyst.

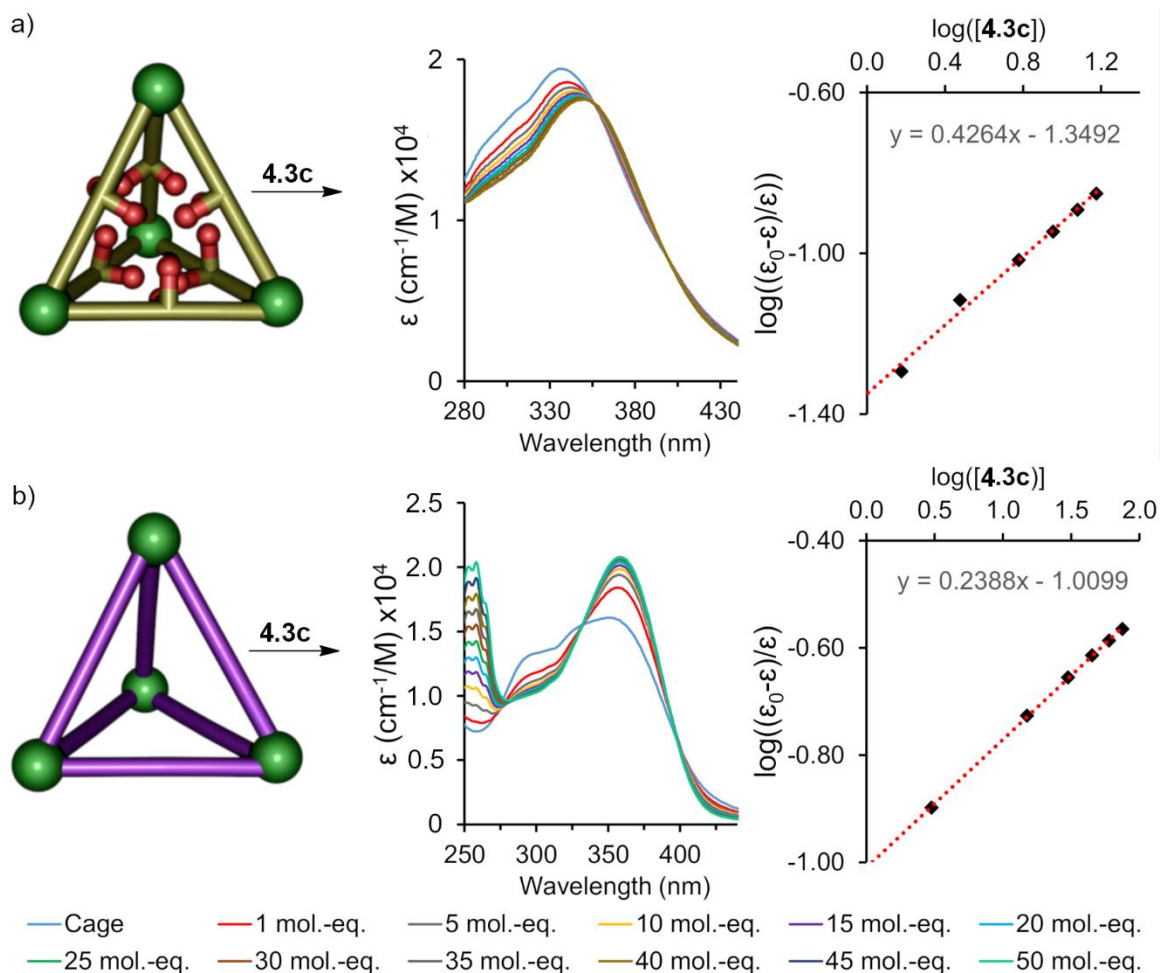


Figure 4.8. UV-Vis absorption spectra and Stern-Volmer analysis of the titration of pyridyl acetal **4.3c** into solutions of: a) acid cage **4.2** (3 μ M in CH₃CN); b) unfunctionalized cage **4.1** (3 μ M in CH₃CN).

4.4 Tandem Reactivity Effecting Cage-to-Cage Transformation

In addition to increasing the effective concentration, sequestration of the reactive groups to the interior of the cage has an additional advantage over small molecule catalysis. By compartmentalizing the reactive functions, tandem reactivity becomes possible.¹⁰ Figure 4.9 shows an example of this type of catalysis. We have previously shown that the use of self-assembled M₂L₃ helicates formed with electron poor aldehydes, as is the case in **1.1**•Br, can perform cage-to-cage transformations by introducing 2-pyridine

carboxaldehyde and water to the system (Figure 1.5).¹¹ Performing this reaction in tandem with an acetal hydrolysis however is challenging, as the M-L contacts in iminopyridine helicates are sensitive to acid and strongly coordinating anions such as Cl⁻ or RCOO⁻. For this reaction to successfully occur, the choice of acid is crucial: if the acid is too strong, such as CF₃COOH, the cage will simply decompose, whereas if the acid is too weak the helicate will survive but the acetals will remain unreacted. As such, performing this reaction with a “free” acid catalyst presents a significant challenge.

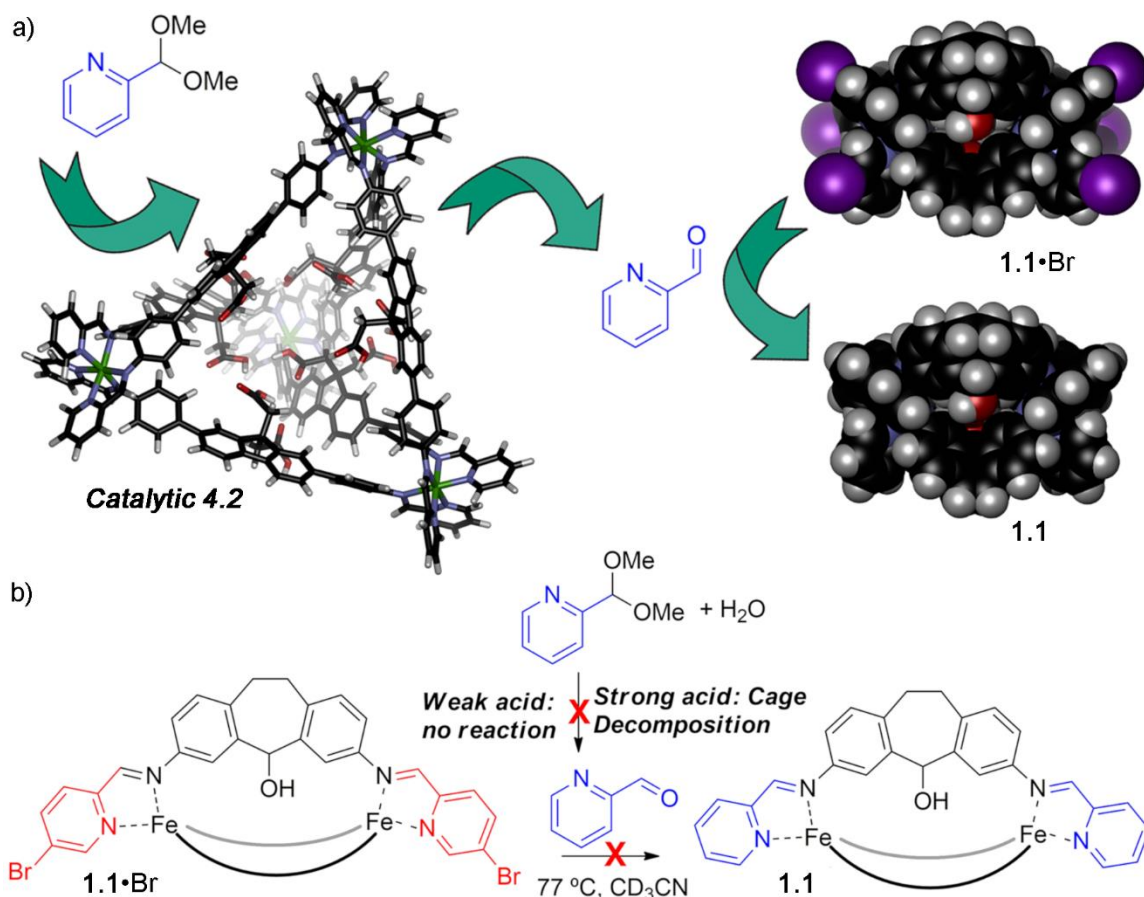


Figure 4.9. Tandem acetal solvolysis and cage-to-cage transformation catalyzed with a) cage **4.2**; b) “free” acid.

In contrast, the acid cage **4.2**, with its sequestered functional groups, is perfectly suited for this type of tandem process. Dr. Holloway tested the proposed tandem process, by preparing a solution of 4 % cage **4.2** in a mixture of water and CD₃CN and treating it with acetal **4.3b**, and the brominated helicate **1.1•Br** at refluxing temperatures (Figure 4.9). Rapid solvolysis of **4.3b** was observed accompanied by incorporation of the resultant PyCHO into **1.1•Br**. After only 30 mins, signals for the free BrPyCHO are seen as well as a receding signal for helicate **1.1•Br**. Evidently the solvolysis is the rate limiting step in the tandem process as the signals for PyCHO are not observed until after 3 hours. After 8 h the reaction ceases at a conversion of 92%. Clean transformation of the **1.1•Br** to **1.1** with no decomposition of the helicates occurs. Further, despite the relatively low concentration of **4.2** in solution, no incorporation of Br-PyCHO is observed.

While cage **4.2** is an effective catalyst for this tandem solvolysis/exchange reaction, other “free” acids are not (Figure 4.9b). Control acid **4.4** is incapable of solvolysis of acetal **4.3b**, as a result no reaction is observed after 8 h. Extended heating of the solution (120 h) led to decomposition of **1.1•Br**. When the control acid is replaced by one more suitable for the solvolysis (CF₃CO₂H), rapid decomposition of the parent cage **1.1•Br** is observed after only 10 mins at 77 °C. The helicate complexes are not tolerant of strong acids even at ambient temperature, therefore despite acetal solvolysis, the reaction cannot proceed. Finally, the unfunctionalized cage **4.1** was used for the reaction; however, again no acetal solvolysis was observed and the helicate **1.1•Br** remained even after extended reaction times. The combination of enhanced reactivity and compartmentalization of the acid

groups in cage **4.2** allows it to be an effective tandem catalyst: reactive enough to be functional, but mild enough to work with sensitive tandem partners.

4.5 Cage Catalyzed Thioetherification *via* Acid Promoted Dissociation

The strong rate accelerations for acetal hydrolysis (>1000 fold) demonstrate the effectiveness of acid cage **4.2** as a supramolecular catalyst. This reactivity is aided by a significantly increased effective concentration of acids on the interior of the cage as well as a strong molecular recognition element (e.g **4.3a**, with $K_a = 1.3 \times 10^4 \text{ M}^{-1}$). Both these elements suggest that cage **4.2** should be amenable to further use as a supramolecular catalyst for other acid-mediated reactions. One limitation in supramolecular catalysis is in the performance of polar reactions, especially encapsulated nucleophilic substitutions, because the M-L complexes are often sensitive to even weak nucleophiles. While there are some examples of polar reactions being performed in supramolecular assemblies,^{12, 13} including one with inverted stereochemistry in an S_N2 reaction,¹⁴ their use in supramolecular cages is still quite limited. Herein a substitution reaction catalyzed by the acidic **4.2** cage is shown. The cage can effect high rate acceleration and vary the molecularity of the reaction.

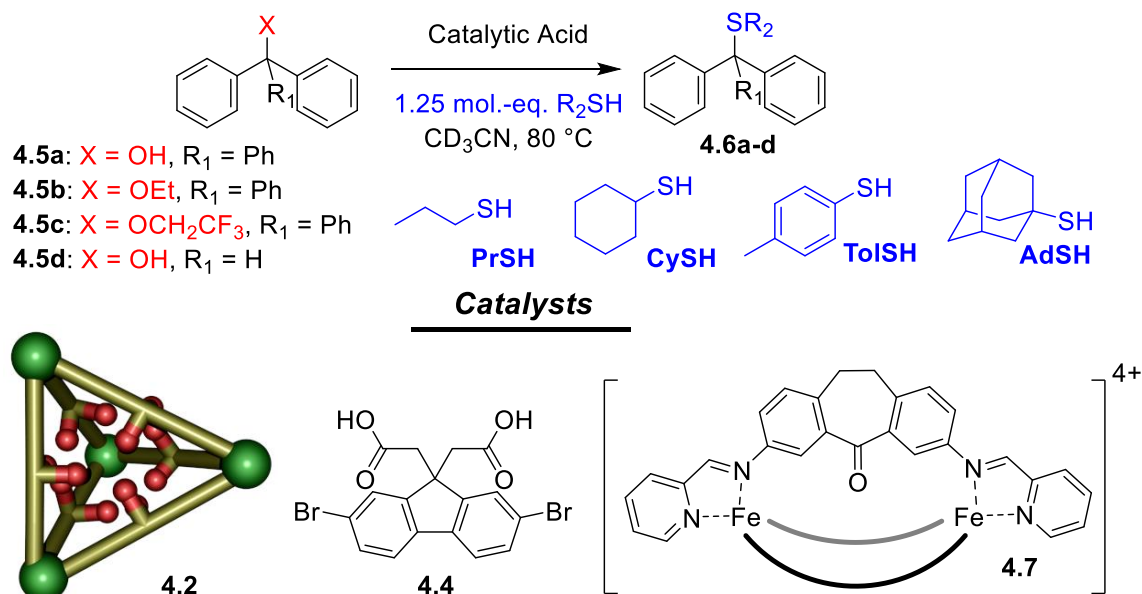


Figure 4.10. Summary of the acid catalyzed substitution processes tested.

To limit decomposition of the cage, a mild acid-catalyzed substitution reaction was chosen (Figure 4.10). Trityl- and diphenylmethyl electrophiles are well-known S_N1 substrates due to their highly stabilized cationic intermediates.¹⁵ Four different activated electrophiles were tested that vary in reactivity, triphenylmethanol **4.5a**, its ethyl (**4.5b**) and trifluoroethyl (**4.5c**) ethers, and benzhydrol **4.5d**. In addition to being highly reactive, the leaving groups are either water or alcohols, which should prevent cage decomposition. To further ensure the integrity of the cage, the substitution reactions were performed with mild, neutral nucleophiles. The synthesis of thioethers using trityl- or diphenylmethyl electrophiles in conjunction with thiols occurs via an acid-catalyzed dissociative substitution mechanism and is well-precedented in highly acidic media.^{16,17}

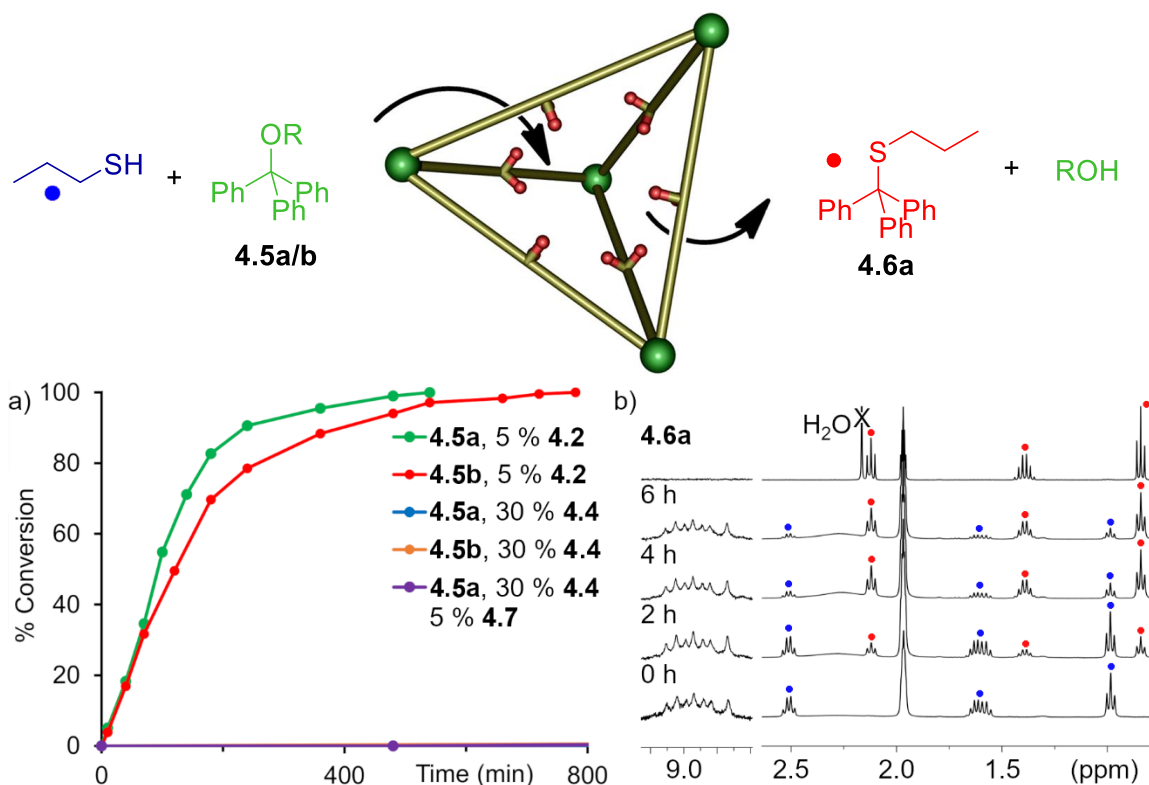


Figure 4.11. Accelerated Substitution Catalyzed by Cage 4.2. a) Reaction progress over time for the transformation of electrophiles **4.5a** and **4.5b** with either 5% cage **4.2** or 30% control acid **4.4** catalyst (CD₃CN, 353 K). b) ¹H NMR spectra of the reaction of **4.5a** with PrSH catalyzed by **4.2** at various intervals (CD₃CN, 400 MHz, 298 K). Blue = PrSH; Red = thioether product; downfield region shows the imine CH region of the C₃/S₄ isomers of **4.2**, and that cage **4.2** remains intact throughout the reaction.

Initially, the reactivity of *n*-propanethiol (PrSH) was investigated, paired with the four electrophiles, and two previously mentioned catalysts (acid cage **4.2** and control acid **4.4**) in CD₃CN. The reaction progress and relative rates were monitored via ¹H NMR. The acid cage **4.2** was highly effective at catalyzing the dissociative process (Figure 4.11). In the case of both **4.5a** and **4.5b**, the reaction was complete within 8 h with 100 % conversion observed using only 5 % cage **4.2** as catalyst. The reaction is clean, with no evidence of product inhibition, and only the cage, reactants and propyl trityl sulfide product **4.6a** can be observed in the NMR spectrum. It is important to note that cage **4.2** is undamaged

throughout the reaction process. The characteristic imine CH signals of the C_3 and S_4 isomers of cage **4.2** at δ 8.9-9.1 remain unchanged, indicating that despite refluxing conditions, the cage is completely tolerant to thiol nucleophiles. To illustrate the effectiveness of the acidic cage, the substitution of **4.5a** and **4.5b** was repeated using 30 mol% control acid **4.4** (i.e. an equivalent concentration of acid in solution). The “free” acid catalyzed reaction was sluggish, and no conversion to sulfide product **4.6a** was observed after 10 h at 80 °C for either electrophile (Figure 4.12a). After 24 h the product can be observed, however only at 1 % conversion. As the reaction is acid-catalyzed, it is conceivable for the reaction to be promoted by small amounts of leached Fe^{2+} ions. To eliminate this possibility, the reaction was repeated with *meso*-helicite **4.7** as catalyst (Figure 4.12b). The *meso*-helicite does not contain a defined cavity nor acidic functionality, as such would only be able to catalyze the reaction in a Lewis acidic manner. Under these conditions, no reaction is observed even after 48 h heating.

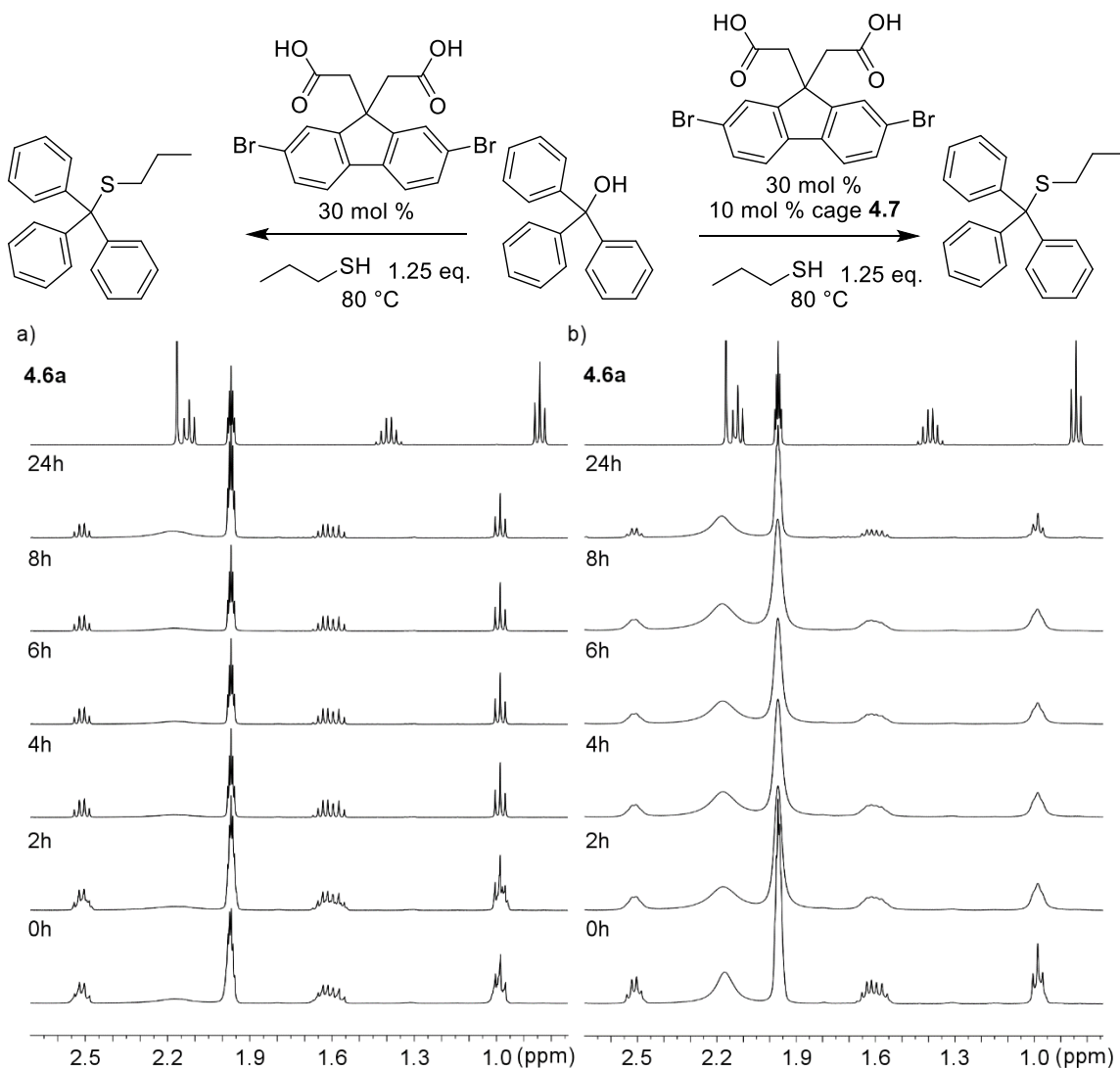


Figure 4.12. Thioetherification of PrSH with 4.5a mediated by control processes: a) 30 mol % control acid 4.4 b) 30 mol % control acid 4.4 and 10 mol % suberone *meso*-helicate 4.7 (400 MHz, 298 K, CD₃CN). 10 mol % of the M₂L₃ 4.7 was used to maintain the number of Fe^{II}-iminopyridine units in solution while the smaller structure is unable to bind substrates within a cavity. Both reactions were performed at 80 °C and monitored over time (400 MHz, 298 K, CD₃CN).

Table 4.3 shows a summary of the average initial rates and relative rate accelerations of the thioetherification process. Rate accelerations of up to 1023-fold over the “free” acid catalyst (4.4) were observed using the acid cage 4.2, despite essentially identical acidity of the reactive group. The reactivity appears to show little dependence on the basicity of the electrophile employed. Trityl electrophiles 4.5a and 4.5b exhibit

significant differences in basicity (conjugate acid pKa of \sim -3.5 vs -2), however, the relative rates of substitution and \sim 1000-fold accelerations are nearly identical. Only with extreme changes in basicity, as is the case with the trifluoroethyl ether **4.5c**, is reactivity impacted, with no observed product formation even after extended reaction times. As expected, the removal of a phenyl ring in benzhydrol **4.5d** resulted in a much slower reaction than with **4.5a**. After 72 h reaction only 58 % conversion was observed. Significant rate acceleration is still present in this case however as reaction with 30 % control acid **4.4** gave no conversion at all.

Table 4.3. Supramolecular Substitution Catalysis.^a

5 % **4.2**, or 30 % **4.4**
1.25 mol.-eq. R₂SH
CD₃CN, 80 °C

Substrate	Nucleophile	Initial Rate V(4.2), x10 ⁻⁴ mM/min	Initial Rate V(4.4), x10 ⁻⁴ mM/min	V(4.1) V(4.4)
4.5a	PrSH	778	0.76	1023
4.5a	CySH	541	1.4	386
4.5a	TolSH	211	0.81	260
4.5a	AdSH	n.r.	n.r.	n.d.
4.5a	EtOH	77	n.r.	n.d.
4.5b	PrSH	723	0.65	1112
4.5b	TolSH	156	1.1	107
4.5b	CySH	156	2.9	47
4.5c	PrSH	n.r.	n.r.	n.d.
4.5d	PrSH	39	n.r.	n.d.

^a353 K, CD₃CN, [**4.5**] = 15.8 mM, [Nu] = 19.8 mM, [**4.2**] = 0.8 mM; [**4.4**] = 4.74 mM, concentrations confirmed using dioxane as standard (7.9 mM). n.r. = no reaction; n.d. = not determined.

Other thiol nucleophiles were likewise tolerated for the cage-catalyzed substitution reaction. When the reaction was performed with the more hindered cyclohexane thiol (**CySH**), the initial rate was slightly slower than the rate observed with **PrSH**. Despite the decrease in reactivity, smooth conversion to sulfide product **4.6b** was observed for both

electrophiles, **4.5a** and **4.5b** in the presence of 5 % cage **4.2**. The use of similarly sized *p*-tolylthiol (**ToISH**) gave similar rate accelerations to that of **CySH**, however the reaction was complicated by competitive formation of the *p*-tolyl disulfide oxidation product (Figure 4.13). Formation of disulfides catalyzed by Fe²⁺ and oxygen is known,¹⁷ and so to limit formation of the side product the reaction was repeated under inert (N₂) atmosphere in a J-Young tube. While formation of the disulfide decreased, it was still observed as the major product in the reaction. Despite all other reactions being open to air, only the more easily oxidized **ToISH** was susceptible to disulfide formation. Further, this oxidation is catalyzed by the cage itself, in the control reaction with **4.4**, minimal disulfide product is observed, and then only after 72 h reflux.

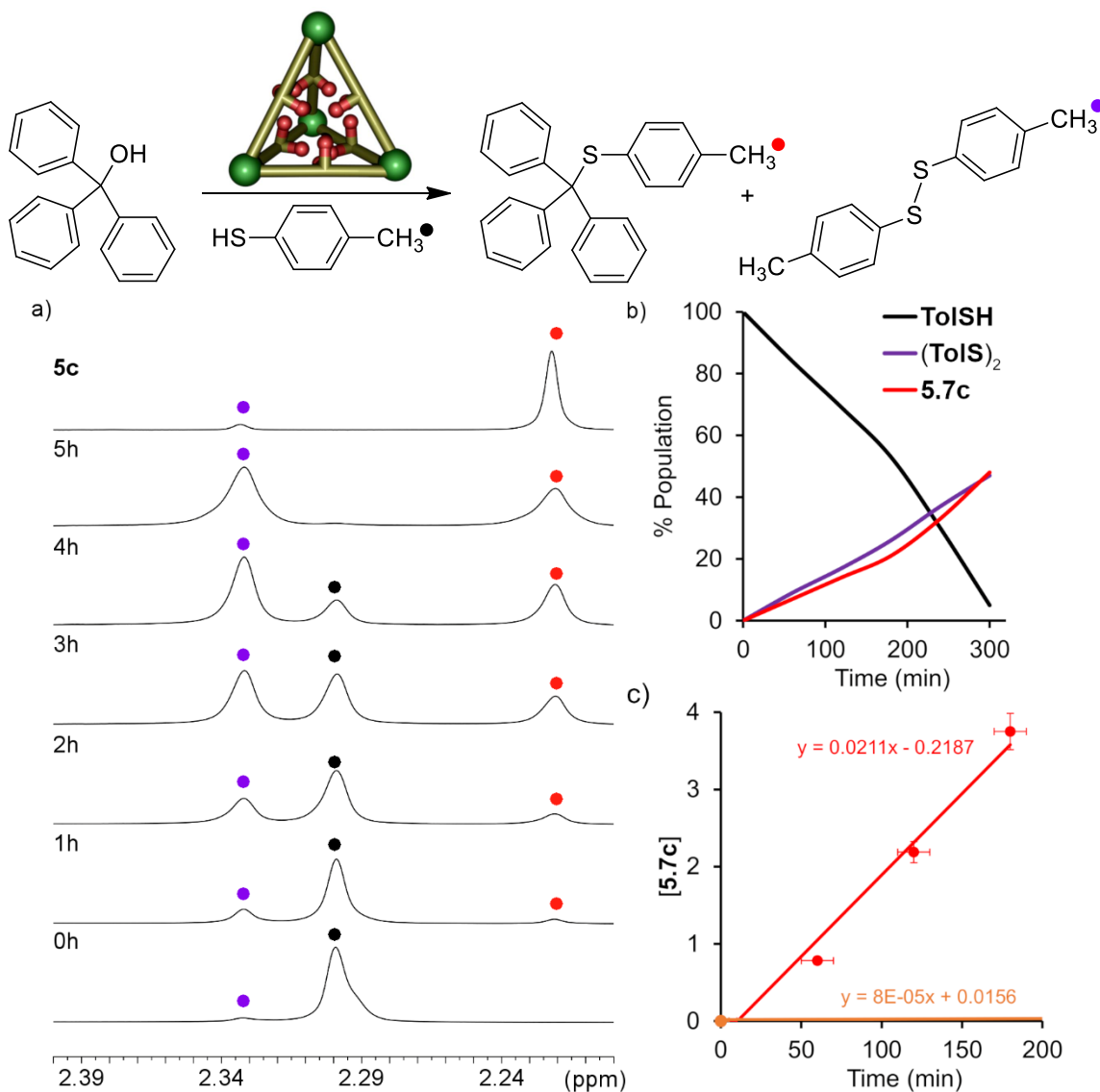


Figure 4.13. Thioetherification and oxidative dimerization of *p*-tolylthiol promoted by acid cage **4.2**. a) methyl region of the ^1H NMR spectrum monitored over time (CD_3CN , 298 K, 400 MHz). b) change in % sulfur containing compounds present over time. c) Initial rate calculations for thioetherification using 5 % cage **4.2** (red) and 30 % control acid **4.4** (orange).

Substitution with weak nucleophiles like EtOH was also possible, albeit at a much slower rate. While the use of **CySH** and **TolSH** only showed modest reductions in initial rate, no reaction was observed using the much bulkier 1-adamantanethiol (**AdSH**) after 24 h, with longer reaction times leading to decomposition of cage **4.2**. While the mild thiol

and alcohol nucleophiles were well tolerated by the system, more reactive carbon-based nucleophiles proved problematic. Some conversion was observed when using dimedone or indole, however decomposition of the cage was rapid. With complete destruction in <2 h in the case of indole (Figure 4.14).

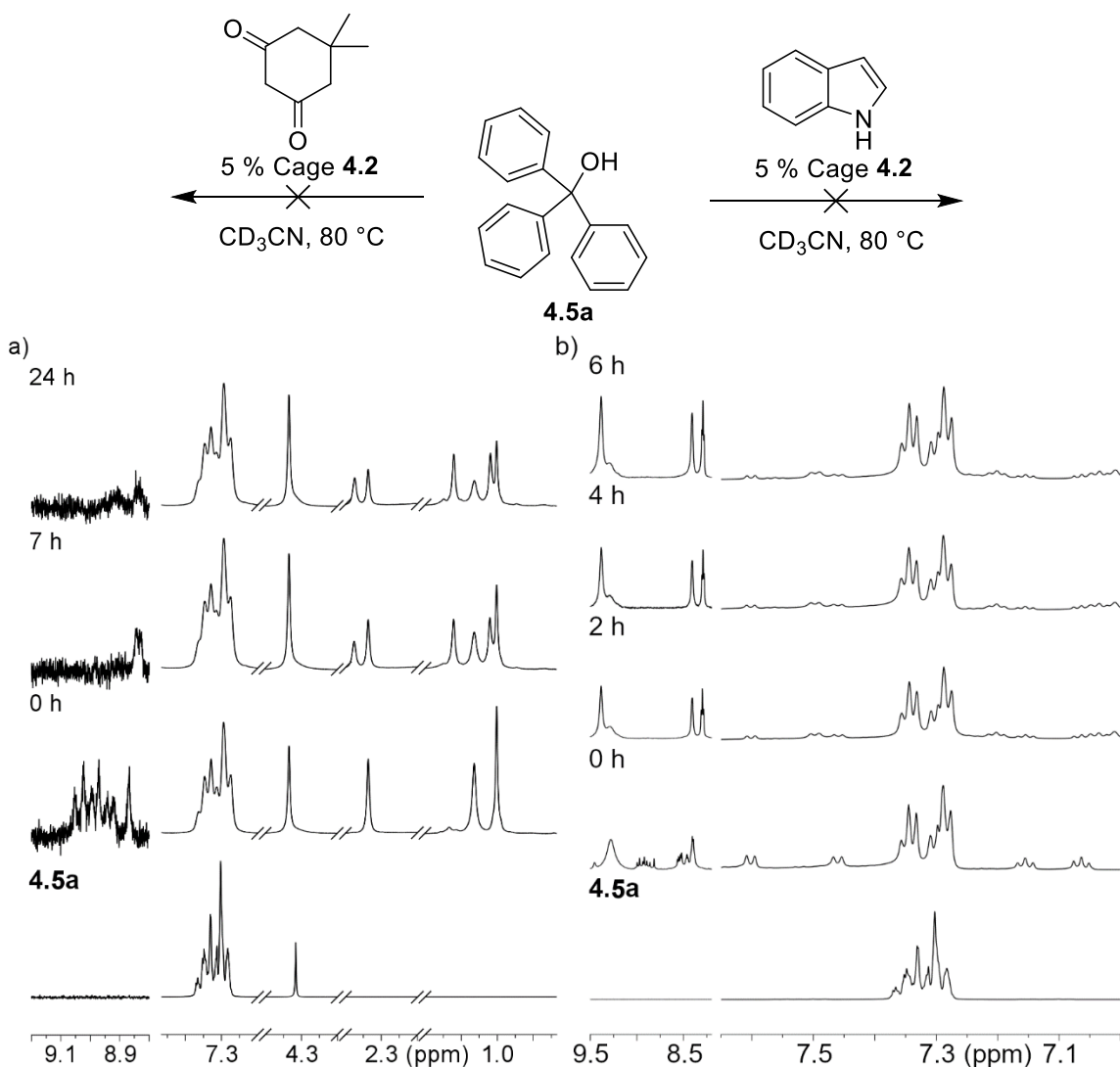


Figure 4.14. ^1H NMR spectra of the acid promoted substitution reaction between **4.5a** and a) dimedone or b) diethylmalonate in the presence of 5 mol % cage **4.2**. The reaction was performed at 80 °C and monitored over time (400 MHz, 298K, CD_3CN).

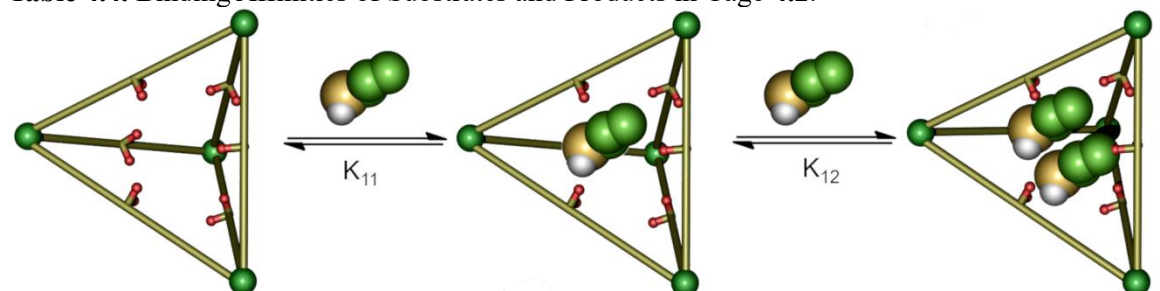
The variable reactivity for the different thiols provides insight toward the “biomimetic” nature of the catalysis. The classic acid-catalyzed S_N1 mechanism, which would be expected under these conditions,¹⁸ has a rate determined by the slow dissociation to form the trityl cation with the initial potentiation and final nucleophilic addition being rapid. The rate is not dependent on the nucleophile, and only the concentration of electrophile and acid appear in the rate equation. Under this classic S_N1 mechanism, essentially the same initial rate should be observed regardless of the nucleophile, as is the case for reactions catalyzed by control acid **4.4**. However, when the reaction is catalyzed by cage **4.2**, large variations in the reaction rate are observed between the nucleophiles employed. As much as a 10-fold difference in reaction rate is observed between nucleophiles when comparing the fastest and slowest rates (**PrSH** and **EtOH** respectively). For the cage to be able to bias the reactivity of the added components, a high level of molecular recognition must be present. We therefore investigated the binding affinity of the various reaction components in “host” cage **4.2**.

4.6 Molecular Recognition and Mechanistic Analysis

As expected, all guests tested exhibited rapid in/out kinetics preventing the formation of long-lived Michaelis complexes that could be observed via NMR. To quantify the binding affinities of the various components of the reaction, we turned to UV-Vis titrations. While the previously used Stern-Volmer analysis is useful in fitting a 1:1 binding model, little information about the adequacy of the fit can be obtained from this method. Given the complexity of the overall system, we decided to use a more rigorous method of calculation. The binding affinities were calculated in Bindfit¹⁹ via linear regression analysis

(Nelder-Mead method) and fit to both a 1:1 and 1:2 binding model.²⁰ To ensure the best possible fit, the spectrum was analyzed by monitoring the change in absorbance at two points (300/330 nm and 370 nm; Table 4.4). The large electrophiles **4.5a-d** predictably fit best in the 1:1 binding model. The binding of thiols however was much more ambiguous; the smallest thiols **PrSH** and **CySH** had a significantly improved fit upon switching to a 1:2 model as shown in Figure 4.13. In contrast, little to no improvement in fit was observed for the bulky **AdSH** suggesting a 1:1 binding model. Finally, when analyzing the affinity of **TolSH**, high levels of error were present in the calculation preventing the data from being analyzed in a 1:2 model.

Table 4.4. Binding Affinities of Substrates and Products in Cage **4.2**.^[a]



Guest	K_{11} (4.2), $\times 10^3 \text{ M}^{-1}$	Guest	K_{11} (4.2), $\times 10^3 \text{ M}^{-1}$	K_{12} (4.2) $\times 10^3 \text{ M}^{-1}$
4.5a	15.8 ± 0.3	PrSH	114 ± 15	0.75 ± 0.008
4.5b	20.1 ± 1.2	TolSH	80.6 ± 9.7	N/A
4.5c	3.2 ± 1.3	CySH	116 ± 10	4.0 ± 0.4
4.5d	6.9 ± 0.4	AdSH	199 ± 17	N/A
4.6a	6.5 ± 1.3			

^[a] in CH_3CN , $[\mathbf{1}] = 3 \mu\text{M}$, absorbance changes measured at 300/330 nm and 370 nm.^{19,20}

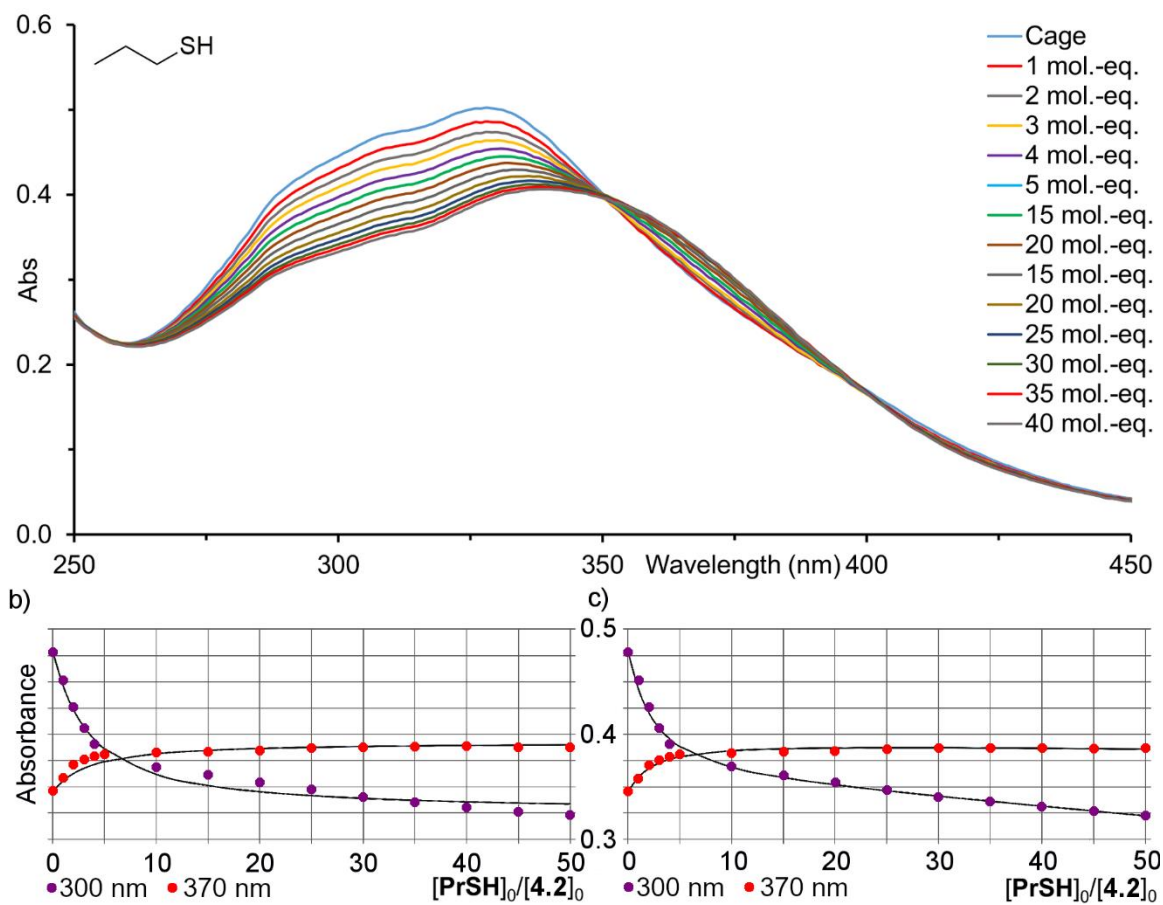


Figure 4.15. UV-Vis absorption spectrum of the titration of **PrSH** into a 3 μM solution of cage **4.2** in CH_3CN . **PrSH** was added in 1-5 μL aliquots from a 9 mM stock solution in CD_3CN . b) 1:1 binding fit model for guest **PrSH** ($K_a = 113.9 \pm 15.0 \times 10^3 \text{ M}^{-1}$). c) 1:2 binding fit model ($K_{11} = 182.4 \pm 19.9 \times 10^3 \text{ M}^{-1}$, $K_{12} = 0.75 \pm 0.08 \times 10^3 \text{ M}^{-1}$). Fits were calculated via linear regression analysis using the Nelder-Mead method from the change in absorbance at two points (300 nm and 370 nm) using supramolecular.org.^{19,20}

Surprisingly high affinities were again observed for the reactants with cage **4.2** ranging from 3200 M^{-1} (trifluoroethyl ether **4.5c**) to $199,000 \text{ M}^{-1}$ (**AdSH**). The properties that govern binding in the cage are not entirely obvious, the thiol guests bind strongest in the cage ranging from $80,000 \text{ M}^{-1}$ up to $199,000 \text{ M}^{-1}$, so the presence of both H-bond donor and acceptor groups likely play a large role. This is further supported by no affinity observed when hydrocarbons such as adamantane are added. However, shape-based cavity occupancy does not appear to play a large role, as the electrophiles were still strongly bound

but at lower affinities up to $20,100 \text{ M}^{-1}$ (ethyl ether **4.5b**). Most importantly, a significantly lower binding affinity was observed for the thioether product **4.6a** (6500 M^{-1}). The most likely scenario is that, a mix of polar interactions with the acid groups and CH- π or π - π interactions with the aromatic cage walls are the key determinants in obtaining high affinities.

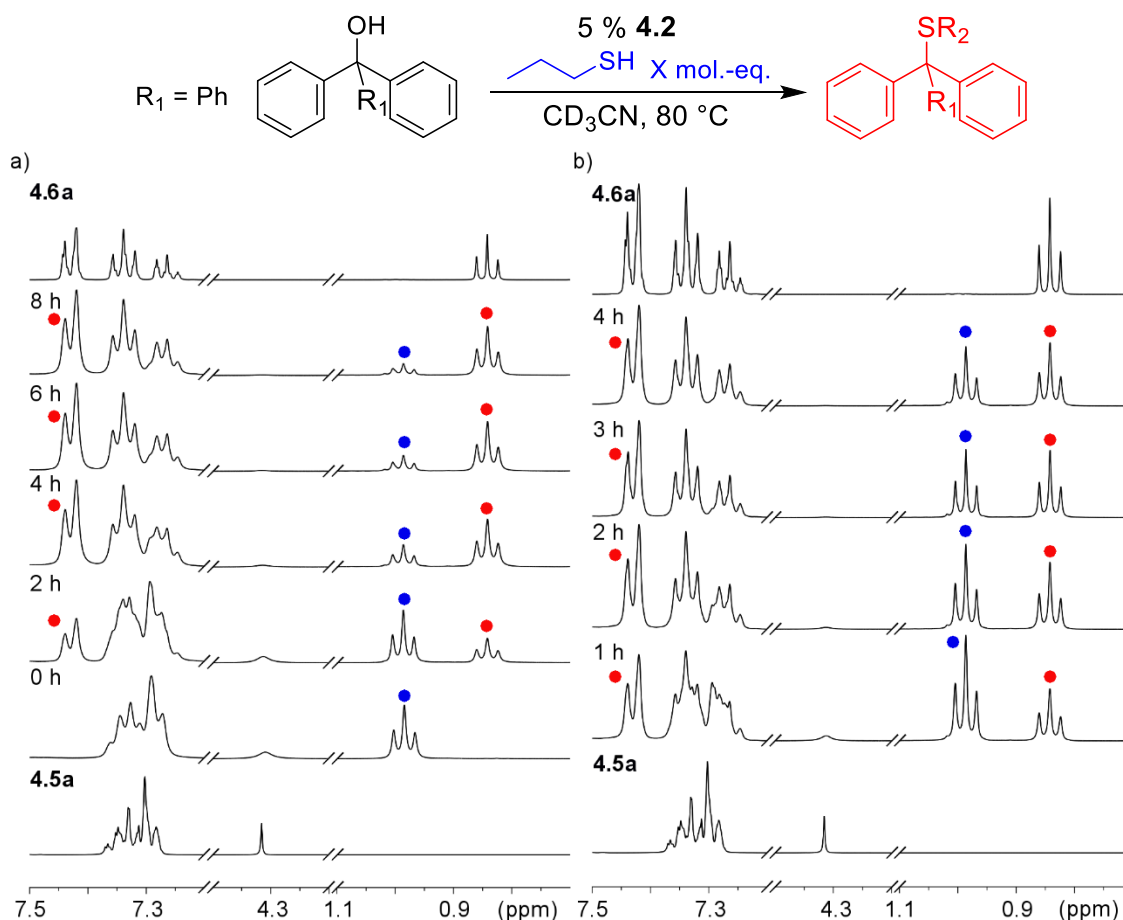


Figure 4.16. Acid promoted substitution reaction between **4.5a** and *n*-propyl thiol in the presence of 5 mol % cage **4.2**, at varying concentrations of **PrSH** a) 19.75 mM b) 39.5 mM performed at 80°C and monitored over time (400 MHz, 298K, CD_3CN).

The reaction observed from the cage-catalyzed substitution shows variable molecularity depending on the individual components, meaning it is not the simple $\text{S}_{\text{N}}1$ process expected for acid catalyzed substitutions. The strong affinities for various guests

enable the cage to direct the outcome of the reaction. To further illustrate this point, the cage-catalyzed substitution reaction of **4.5a** and **4.5b** with **PrSH** was repeated with varying concentrations of nucleophile. Surprisingly, the small change in leaving group from OH to OEt had a large effect on the dependence on nucleophile. When triphenyl methanol **4.5a** is treated with **PrSH** and 5 % acid cage **4.2**, a strong dependence on the nucleophile concentration is observed (Figure 4.16/4.17a). Increasing the concentration of **PrSH** results in an increased initial rate for the reaction, the order in this case was measured to ~ 1.2 with respect to $[\text{PrSH}]$. In contrast, the reaction of the larger, more basic, ether **4.5b**, shows *zero* dependence on $[\text{PrSH}]$ (Figure 4.17b), with initial rate characteristics like that of a unimolecular rate-determining step. Despite nearly identical binding affinities and initial rates ($[\text{PrSH}] = 19.8 \text{ mM}$), the molecularity of the reaction processes is completely different.

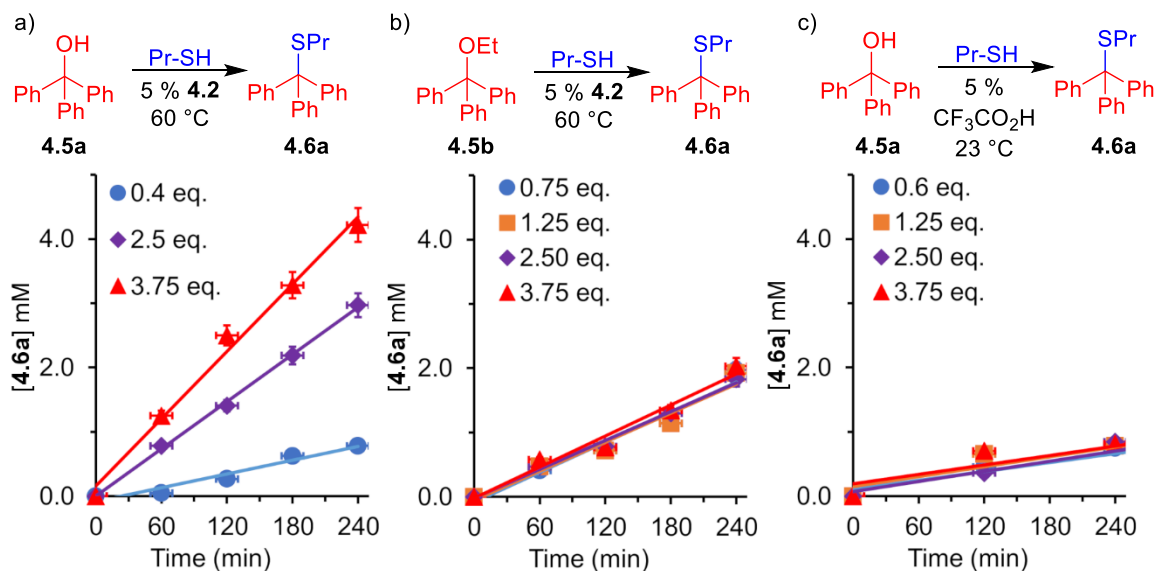


Figure 4.17. Initial rates of thioetherification with varying $[\text{PrSH}]$ of a) **4.5a** with 5 % **1**, 333 K; b) **4.5b** with 5 % **4.2**, 333 K; c) **4.5a** with 5 % $\text{CF}_3\text{CO}_2\text{H}$, 273 K. $[\text{4.5}] = 15.8 \text{ mM}$, $[\text{4.2}]$, $[\text{TFA}] = 0.8 \text{ mM}$ in CD_3CN ; concentrations confirmed using dioxane as standard (7.9 mM), rates monitored by ^1H NMR.

To prove the acid-catalyzed mechanism is truly a classic S_N1 process, control reactions were performed to determine the dependence on nucleophile with “free” acid. The reaction with control acid **4.4** was far too slow (requiring over 4 days), so the process was analyzed using 5 % CF₃CO₂H in CD₃CN as the catalyst. The reactions, performed by Courtney Ngai, were run at ambient temperature and monitored over the course of several hours. As expected for the simple S_N1 process, under these conditions the initial rates are completely independent of nucleophile (Figure 4.17c). The importance of molecular recognition in cage **4.2** goes beyond varying the molecularity of the reaction. The rate of catalysis can be significantly impaired through the addition of a large excess of **PrSH** (Figure 4.18). **PrSH** has a significantly higher binding affinity for cage **4.2** than either **4.5a** or **4.5b** and can bind in a 1:2 fashion. At high concentrations **PrSH** can saturate the cavity of **4.2**, preventing binding and activation of the electrophile, resulting in *substrate inhibition*.

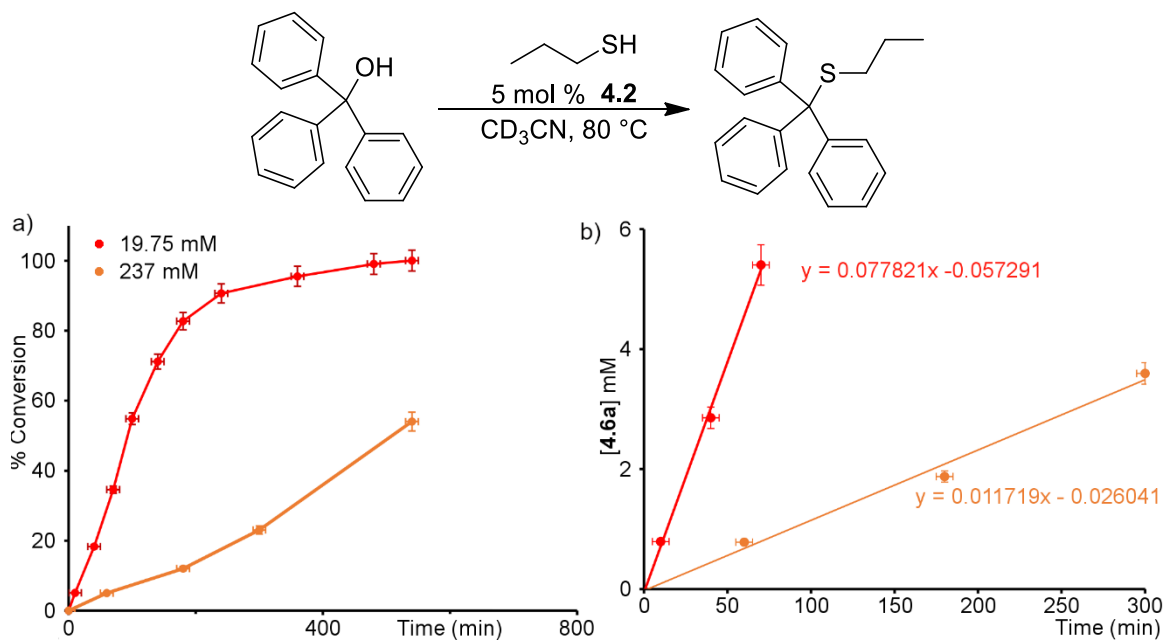


Figure 4.18. Substrate inhibition of the acid-catalyzed substitution of **4.5a** with **PrSH** in the presence of 5 % cage **4.2** in CD_3CN . a) Averaged percent conversion over time (min); b) initial rates, using 19.75 mM **PrSH** (red) and 237 mM **PrSH** (orange).

The catalysis with acid cage exhibits very efficient turnover: with no product inhibition seen at only 5 % **4.2** used. This level of turnover is rare in bimolecular reactions mediated by a host molecule. In general, entropy favors the host-guest binding of the single large product rather than the two smaller reactants, leading the reaction to be stoichiometric rather than catalytic.^{21,22} To overcome these challenges, most receptors used as supramolecular catalysts for bimolecular reactions proceed by varying the binding affinity of the product, typically through solubility effects in water.^{23,24} In the case of **4.2** this is not a problem as both reactants **4.5a/b** and **PrSH** exhibit significantly higher affinities ($K_a = 15,800/20,100$ and $114,000$ respectively) over the resultant product **4.6a** ($K_a = 6500 M^{-1}$).

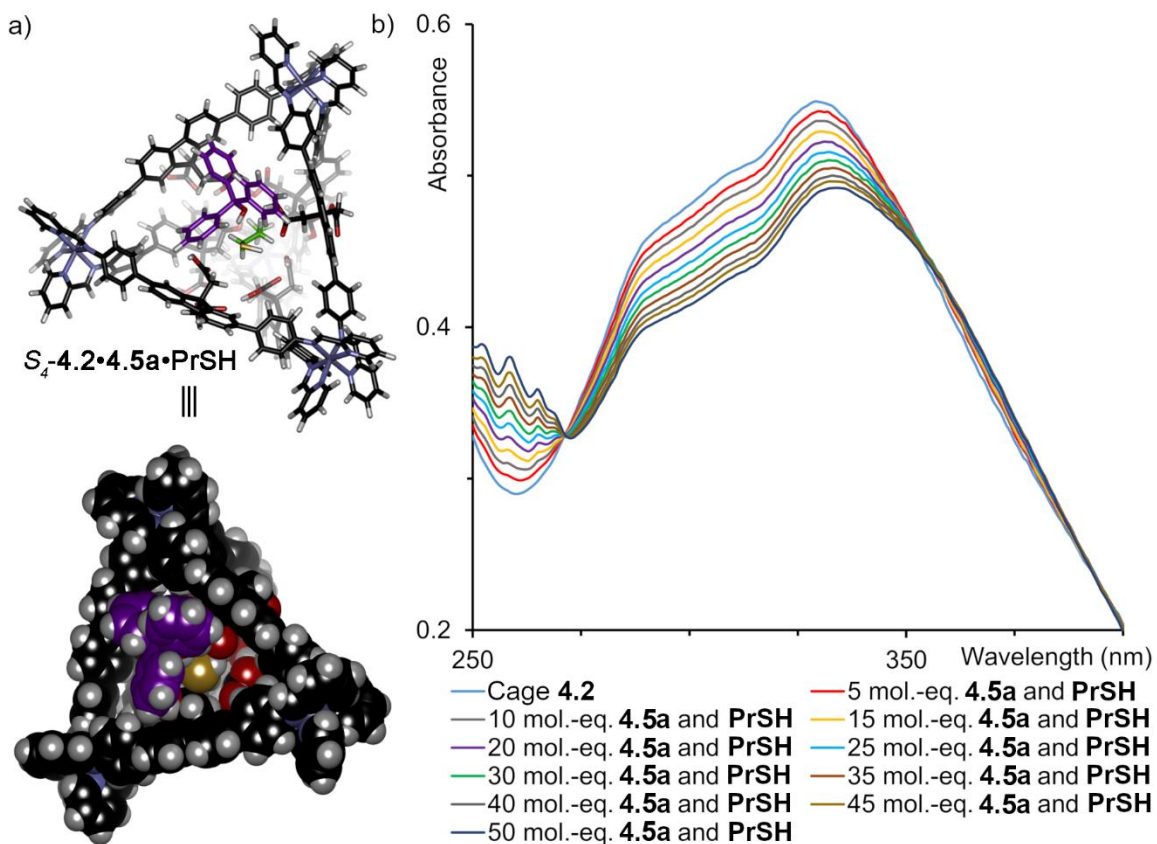


Figure 4.19. a) Minimized structure of the S_4 isomer of cage **4.2** co-encapsulating **PrSH** and triphenylmethanol **4.5a**, with spacefilling model (Hartree-Fock, SPARTAN). b) UV-Vis absorption spectrum of the titration of a 1:1 solution of **4.5a** and **PrSH** into a 3 μ M solution of cage 1 in CH_3CN , the guests were added until saturation was achieved. **4.5a** and **PrSH** were added in 10 μ L aliquots from a 4.5 mM stock solution in CH_3CN .

While this analysis explains the turnover, the question of why putatively similar reactants have such variable rate profiles remains. All components in the reaction exhibit strong binding affinities for **4.2** and exhibit variable binding modes including the formation of *ternary complexes* (Table 4.4). The variable binding affinities present several pre-equilibrium states that can exist in the reaction. Cage **4.2** exhibits a particularly large cavity, and is not limited to the formation of homo-ternary complexes, but hetero-ternary complexes as well. The ease with which both reactants (**4.5a** and **PrSH**) can fit into the

cavity of **4.2** is demonstrated in a minimized (SPARTAN, Hartree-Fock) structure of the ternary complex **4.2•4.5a•PrSH** (Figure 4.19a). To demonstrate formation of the ternary complex, a preformed host:guest complex of cage **4.2** and **4.5a** was formed followed by titration of **PrSH**. With each addition of **PrSH** further changes in the absorbance spectra were observed with continuing isosbestic points. Similarly, clean transition is observed upon addition of a 1:1 mixture of **PrSH:4.5a** to a solution of **4.2** in CH₃CN (Figure 4.19b). The further changes in the spectrum illustrate that despite the cavity of **4.2** already containing **4.5a**, **PrSH** can still be bound. Unfortunately, it is difficult to determine whether these changes result from formation of the **4.2•4.5a•PrSH**, or simply displacement of **4.5a** as little difference in the change of cage absorbance is seen for different guests (lowering of absorbance at 330 nm and increasing absorbance at 370 nm, with a slight red-shifting of absorbance frequency). While this prevents unambiguous determination of the individual K_{11} and K_{12} heterocomplex formation constants, these spectra, as well as the reaction rate data and modeling, support the possibility of a **4.2•4.5a•PrSH** host:guest complex in solution.

A schematic of the possible equilibria present in the reaction mechanism is shown in Figure 4.20. Both the electrophile and nucleophile exhibit strong affinity for cage **4.2** and are likely to compete for binding in the cavity. With this in mind, four possible pre-equilibria are present: empty **4.2** (expected to be minimal at these concentrations), **4.2•(PrSH)**, **4.2•4.5a**, and the heterocomplex **4.2•4.5a•PrSH**. Within the equilibria presented, there exists two possible rate determining steps. The first is a unimolecular process reminiscent of the classic S_N1 reaction: the electrophile is bound and activated by

4.2, the trityl cation is released and rapidly reacts with **PrSH** externally. The reaction in this case is entirely dependent on encapsulation of the electrophile, so the nucleophile would not factor into the rate equation. In contrast, the reaction may also occur via a bimolecular process in which activation of the electrophile occurs after formation of the **4.2•4.5a•PrSH** ternary complex, resulting in a rate equation dependent on [Nu].²⁵ A switch between these two mechanisms is possible by simply changing the leaving group from water to an alcohol. The unimolecular mechanism is dominant for **4.5b** where the reaction rate remains unchanged despite increasing [**PrSH**]. However, in the case of **4.5a**, a dependence on [**PrSH**] is observed (~1.2) suggesting that the mechanism partially proceeds through the **4.2•4.5a•PrSH** complex. It is not entirely clear why the molecularity of the reaction is so different between **4.5a** and **4.5b**. While differences in basicity exists, the initial rates using 1.25 mol.-eq. **PrSH** are identical. Further, the binding affinities of **4.5a** and **4.5b** are generally similar, ruling our rate determination caused by competitive binding. The observed substrate inhibition can be explained by the high affinity of **PrSH** however, as high [**PrSH**] would saturate the cage preventing encapsulation, and activation, of the electrophile.

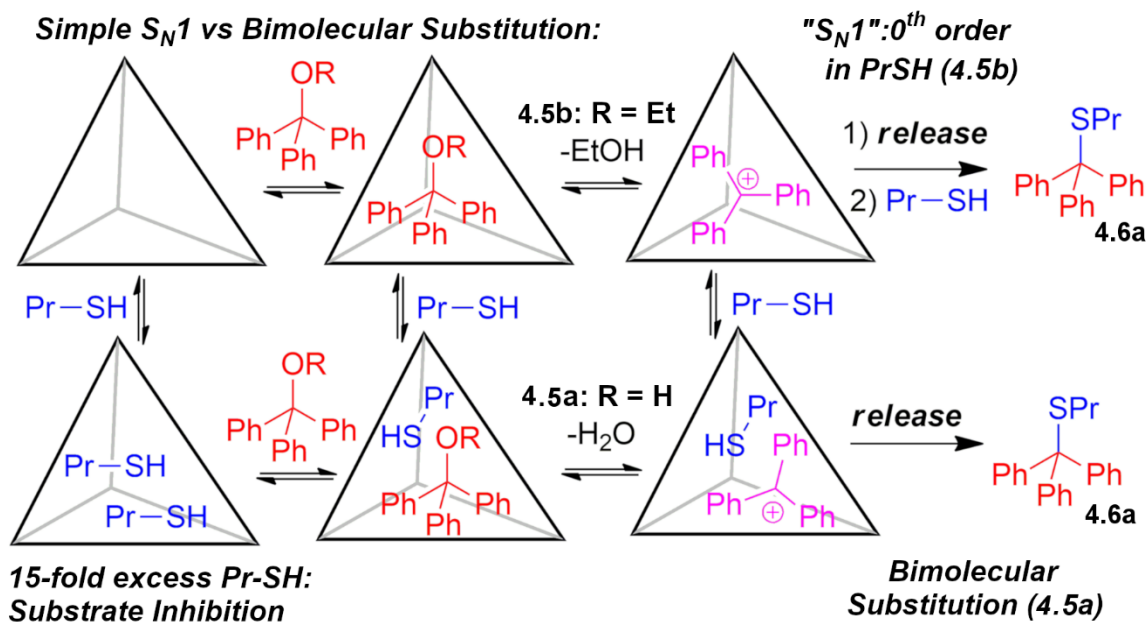


Figure 4.20. Substrate-dependent thioetherification mechanisms in cage 4.2.

The most practical explanation for why variable molecularity exists in the substitution reactions exists in the size of the molecules. The ether **4.5b** is larger than the alcohol which limits the formation of ternary complex inside the cage. As such the activation and expulsion of the cation is more favourable than the binding of multiple guests. The formation of a ternary complex is specific to the combination of **PrSH** and **4.5a**, likely due to proper size matching and beneficial interactions through hydrogen bonding. This theory is also applicable to the varying reaction rates of the different nucleophiles (**PrSH**, **CySH**, **TolSH**, **AdSH**). The changing affinities of each thiol for the cage can bias the equilibrium populations of **4.2•4.5a**, and in some cases **4.2•4.5a•RSH** which will modify the observed rate. Based on the proximity of the reactive species seen in Figure 4.19a, it is conceivable that the substitution reaction between **PrSH** and **4.5a** can occur via a concerted process, however there is no evidence of this occurring. It is more likely that the loss of water occurs within the ternary complex, followed by rapid collapse

to product. The key to the bimolecularity of reaction is the selective substrate molecular recognition inside the active site of **4.2**. These results, as well as the different reactivities shown by different nucleophiles, illustrate the importance of the cage in the reaction mechanism.

4.7 Catalytic Self-Destruction: Design of a Negative Feedback Loop

So far, the effectiveness of acid internalization has been demonstrated through large increases in initial rate versus control processes. In this study electrophiles containing alcoholic leaving groups were chosen for their mild reactivity, however the cage catalyzed substitution process is not limited to these compounds. Tritylanilines are much more basic than their alcoholic counterparts which should allow for more rapid solvolysis. This sort of reaction presents a unique opportunity to probe the catalytic efficiency of cage **4.2**: the resultant amine leaving group is capable of reacting with the cage *via* subcomponent exchange^{3,26} causing destruction of the catalyst as the reaction progresses which should in turn negatively impact the rate. The substitution of *N*-trityl-4-bromo-phenylaniline **4.5e** with **PrSH** and 5 % cage **4.2** is extremely rapid, with trityl sulfide product **4.6a** appearing in minutes at room temperature (Figure 4.21). The substitution reaction is evidently the faster mechanism as ~25 % conversion to product **4.6a**, before the byproduct 4-bromoaniline can react with cage **4.2**. The expunged diacid ligand **4.D** is still capable of activating the trityl starting material **4.5e**, however the reaction proceeds at a much slower rate. The result is a bifurcated reaction plot: initial reaction with **4.2** is rapid until subcomponent exchange and host decomposition occurs, the reaction then proceeds slowly with the weaker free diacid ligand until ceasing at ~50 % conversion. When the substitution

was repeated using control acid **4.4** as catalyst, the reaction proceeds at a speed mirroring that of the post-destruction rate. The importance of internalization of the acid groups in cage **4.2** is well portrayed in this experiment: large acceleration of the reaction is seen initially while the cage is intact but becomes markedly slower once liberated despite identical catalytic groups. Use of this substrate creates a “negative feedback loop”, where the catalyst is inhibited by a secondary coupled reaction that effects its self-destruction.

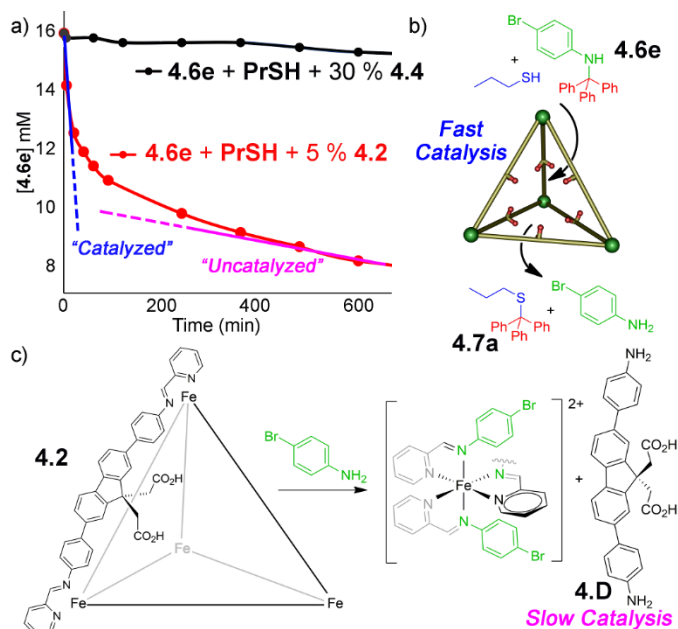


Figure 4.21. Self-destruct sequence. Detritylation of aniline **4.5e** causes a negative feedback loop, whereby the product turns off the catalyst via transimination. $[4.5e] = 15.8$ mM, $[PrSH] = 19.75$ mM, $[4.2] = 0.8$ mM in CD_3CN ; concentrations confirmed using dioxane as standard (7.9 mM), rates monitored by 1H NMR.

4.8 Conclusion

Here, we have shown the synthesis a new M_4L_6 tetrahedron formed *via* Fe-iminopyridine coordination. The cage exhibits 12-internalized carboxylic acid functional groups that are capable of general acid catalysis. Using this cage, rate accelerations of >1000-fold are possible for both the solvolysis of aromatic acetals and the

thioetherification of trityl alcohols and ethers, relative to the rate catalyzed by “free”, small molecule acid analogs. The cage is an impressive host with binding affinities ranging from $K_a = 3,200 - 199,000 \text{ M}^{-1}$ enabling unique reactivity that is not possible using small molecule catalysis. The internalization of the acid sub-units enables a cascade reaction involving the solvolysis of a pyridyl acetal followed by cage-to-cage transformation *via* subcomponent exchange. The analogous TFA-catalyzed process results in immediate decomposition of the initial cage. Further, both catalytic processes are not troubled by product inhibition (except for reactions where the product obliterates the cage), unlike many processes promoted by self-assembled cages. Most importantly for the substitution process, cage 4.2 alters the molecularity of the acid-promoted substitution reactions. While the TFA-catalyzed process follows a normal, unimolecular S_N1 -type mechanism, the host-mediated reaction with electrophile 4.5a is dependent on the concentration of nucleophile. This variable molecularity is substrate dependent, completely different molecularity is observed even with changes as small as transitioning from triphenylmethanol and *O*-tritylethyl ether. The catalyst is also capable of a self-destruct sequence in the presence of tritylated amines, where fast initial reaction is rapidly turned off by destruction of the catalyst by product, essentially a negative feedback loop. All of these properties require strong molecular recognition of multiple reactants in a catalytic pathway, indicating the potential of functionalized cage hosts as enzyme-mimicking nanoreactors.

4.9 References

1. Bogie, P. M.; Miller, T. F.; Hooley, R. J. "Synthesis and Applications of Endohedrally Functionalized Metal-Ligand Cage Complexes." *Isr. J. Chem.* **2019**, *59*, 130–139.
2. Holloway, L. R.; Bogie, P. M.; Lyon, Y.; Julian, R. R.; Hooley, R. J. "Stereoselective Postassembly CH Oxidation of Self-Assembled Metal-Ligand Cage Complexes." *Inorg. Chem.* **2017**, *56*, 11435–11442.
3. Ronson, T. K.; Meng, W.; Nitschke, J. R. "Design Principles for the Optimization of Guest Binding in Aromatic-Paneled Fe^{II}₄L₆ Cages" *J. Am. Chem. Soc.* **2017**, *139*, 9698–9707.
4. Bogie, P. M.; Holloway, L. R.; Lyon, Y.; Onishi, N. C.; Beran, G. J. O.; Julian, R. R.; Hooley, R. J. "A Springloaded Metal-Ligand Mesocate Allows Access to Trapped Intermediates of Self-Assembly." *Inorg. Chem.* **2018**, *57*, 4155–4163.
5. Holloway, L. R.; McGarraugh, H. H.; Young, M. C.; Sontising, W.; Beran, G. J. O.; Hooley, R. J. "Structural Switching in Self-Assembled Metal-Ligand Helicate Complexes via Ligand-Centered Reactions." *Chem. Sci.* **2016**, *7*, 4423–4427.
6. Ma, S.; Smulders, M. M. J.; Hristova, Y.; Clegg, J. K.; Ronson, T. K.; Zarra, S.; Nitschke, J. R. "Chain-Reaction Anion Exchange between Metal–Organic Cages." *J. Am. Chem. Soc.* **2013**, *135*, 5678–5684.
7. Holloway, L. R.; Bogie, P. M.; Lyon, Y.; Ngai, C.; Miller, T. F.; Hooley, R. J. "Tandem Reactivity of a Self-Assembled Cage Catalyst with Endohedral Acid Groups." *J. Am. Chem. Soc.* **2018**, *140*, 8078–8081.
8. Hong, C. M.; Bergman, R. G.; Raymond, K. N.; Toste, F. D. "Self-Assembled Tetrahedral Hosts as Supramolecular Catalysts." *Acc. Chem. Res.* **2018**, *51*, 2447–2455.
9. Fujita, M.; Umemoto, K.; Yoshizawa, M.; Fujita, N.; Kusukawa, T.; Biradha, K. "Molecular paneling *via* coordination." *Chem. Commun.* **2001**, 509–518.
10. Ueda, Y.; Ito, H.; Fujita, D.; Fujita, M. "Permeable Self-Assembled Molecular Containers for Catalyst Isolation Enabling Two-Step Cascade Reactions." *J. Am. Chem. Soc.* **2017**, *139*, 6090–6093.
11. Wiley, C. A.; Holloway, L. R.; Miller, T. F.; Lyon, Y.; Julian, R. R.; Hooley, R. J. "Electronic Effects on Narcissistic Self-Sorting in Multicomponent Self-Assembly of Fe-Iminopyridine meso-Helicates." **2016**, *55*, 9805–9815.

12. W. Cullen, M. C. Misuraca, C. A. Hunter, N. H. Williams, M. D. Ward “Highly efficient catalysis of the Kemp elimination in the cavity of a cubic coordination cage.” *Nat. Chem.* **2016**, *8*, 231–236.
13. T. Murase, Y. Nishijima, M. Fujita, “Cage-Catalyzed Knoevenagel Condensation under Neutral Conditions in Water.” *J. Am. Chem. Soc.* **2012**, *134*, 162–164.
14. C. Zhao, F. D. Toste, R. G. Bergman, K. N. Raymond “Nucleophilic Substitution Catalyzed by a Supramolecular Cavity Proceeds with Retention of Absolute Stereochemistry.” *J. Am. Chem. Soc.* **2014**, *136*, 14409–14412.
15. Manabe, K.; Imura, S.; Sun, X.-M.; Kobayashi, S. “Dehydration Reactions in Water. Brønsted Acid-Surfactant-Combined Catalyst for Ester, Ether, Thioether, and Dithioacetal Formation in Water.” *J. Am. Chem. Soc.*, **2002**, *124*, 11971–11978.
16. Sharma, R. K.; Tam, J. P. “Tandem Thiol Switch Synthesis of Peptide Thioesters via N–S Acyl Shift on Thiazolidine.” *Org. Lett.* **2011**, *13*, 5176–5179.
17. Vishwanatha, T. M., Bergamaschi, E., Dömling, A. “Sulfur-Switch Ugi Reaction for Macrocyclic Disulfide-Bridged Peptidomimetics.” *Org. Lett.* **2017**, *19*, 3195–3198.
18. Manabe, K.; Imura, S.; Sun, X.-M.; Kobayashi, S. “Dehydration Reactions in Water. Brønsted Acid–Surfactant-Combined Catalyst for Ester, Ether, Thioether, and Dithioacetal Formation in Water.” *J. Am. Chem. Soc.* **2002**, *124*, 11971–11978.
19. Association constants calculated using software found at <http://supramolecular.org>.
20. Hibbert, D. B.; Thordarson, P. “The death of the Job plot, transparency, open science and online tools, uncertainty estimation methods and other developments in supramolecular chemistry data analysis.” *Chem. Commun.*, **2016**, *52*, 12792–12805.
21. Nishioka, Y.; Yamaguchi, T.; Yoshizawa, M.; Fujita, M. “Unusual [2+4] and [2+2] Cycloadditions of Arenes in the Confined Cavity of Self-Assembled Cages.” *J. Am. Chem. Soc.* **2007**, *129*, 7000–7001.
22. Kang, J. M.; Rebek, J., Jr. “Entropically driven binding in a self-assembling molecular capsule.” *Nature* **1996**, *382*, 239–241.
23. Leung, D. H.; Fiedler, D.; Bergman, R. G.; Raymond, K. N. “Selective C–H Bond Activation by a Supramolecular Host–Guest Assembly.” *Angew. Chem. Int. Ed.* **2004**, *43*, 963–966.

24. Hooley, R. J.; Biros, S. M.; Rebek, J., Jr. "A Deep, Water-Soluble Cavitand Acts as a Phase-Transfer Catalyst for Hydrophobic Species." *Angew. Chem. Int. Ed* **2006**, *45*, 3517–3519.
25. Anslyn, E. V.; Dougherty, D. *in Modern Physical Organic Chemistry*, University Science Books, **2004**.
26. Roberts, D. A.; Pilgrim, B. S.; Sirvinskaite, G.; Ronson, T. K.; Nitschke, J. R. "Covalent Post-assembly Modification Triggers Multiple Structural Transformations of a Tetrazine-Edged Fe₄L₆ Tetrahedron." **2018**, *140*, 9616–9623.

Chapter 5 – Biomimetic Catalysis via a Cofactor Type Mechanism

5.1 Introduction

An alternate method to mimicking the natural reactivity of nature is to target the cofactor mediated process of apoenzymes. Apoenzymes are inactive on their own, however after binding species such as flavins¹ or pyridoxal phosphate,² become a reactive holoenzyme complex that is capable of binding additional substrates and mediating their reactivity. While the mechanism of cofactor catalysis has inspired many famous synthetic transformations over the years,³ mimics in supramolecular chemistry are far less common.⁴ This is primarily because of the inherent challenge in binding, activating, and turning over multiple different species within a synthetic host.⁵ The examples that do exist are typically very large ($>1800 \text{ \AA}^3$)⁶ Pd₁₂L₂₄ and Pd₂₄L₄₈ nanospheres,⁷ or self-assembled resorcinarene hexamers.⁸ These internal “nanophases” can be used to bind multiple small molecules and catalyze reactions promoted either with Brønsted acid^{9,10} or gold catalyzed cyclization reactions.^{11,12} In these cases the receptors are more akin to zeolites than enzymes due to their size, as a result, the binding affinities are relatively low. In contrast, the two tetrahedral Fe₄L₆ cages **4.1** and **4.2** presented in the previous chapter (Figure 5.1), show high affinity ($K_a \sim 10^5 \text{ M}^{-1}$ in CH₃CN) of neutral small molecules.¹³ Further, the substitution process with cage **4.2** requires the formation of mixed ternary host:guest complexes, hinting at the possibility for cofactor-mediated catalysis in our synthetic receptors.¹⁴ As the thioetherification described in chapter 4 is well-suited for mechanistic analysis, we initially tested whether unfunctionalized cage **4.1** could promote the reaction in the presence of a suitably sized acidic cofactor.

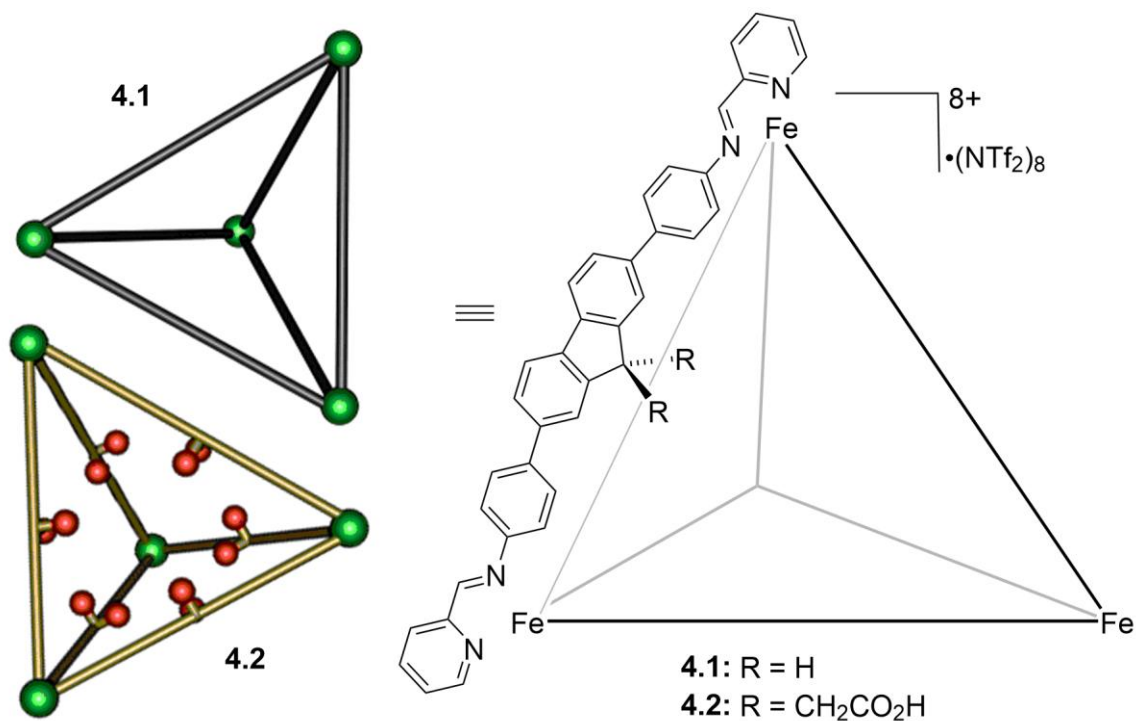


Figure 5.1. Structural and cartoon representations of unfunctionalized cage **4.1** and acid-decorated cage **4.2**.

5.2 Acid Catalyzed Thioetherification Mediated by a Non-Reactive Host

Initially we focused on the reaction between triphenyl methanol **4.5a** and *n*-propane thiol **PrSH**. When these reagents were treated with cage **4.2**, a significant enhancement in rate was observed over the control process. To test the cooperative **4.1•4.4** process, the same fluorenyl-based diacid **4.4** was utilized this time in the presence of unfunctionalized cage **4.1**. Triphenylmethanol **4.5a** was heated with 1.25 mol.-eq. **PrSH** in the presence of 5% cage **4.1** and 30 % cofactor **4.4** in CD₃CN, and the initial rate of the reaction forming thioether **4.6a** was monitored by ¹H NMR. Figure 5.2 shows the relative rate of reaction compared with the rate of closely related catalysts. Surprisingly, unlike the case with the acetals,¹³ the host-guest complex **4.1•4.4** is an effective catalyst for the substitution reaction, showing a 20-fold increase in rate when compared to the free acid catalyzed

process (30 % **4.4** in the absence of **4.1**). No reaction is observed when the substitution is performed with cage **4.1** alone, and a very slow reaction is seen with “free” **4.4**. While the reaction is far slower ($V = 16 \times 10^{-4}$ mM/min) than the acid-functionalized cage **4.2** ($V = 778 \times 10^{-4}$ mM/min), the initial experiment illustrates the effectiveness of combining cage **4.1** with an acidic co-factor.

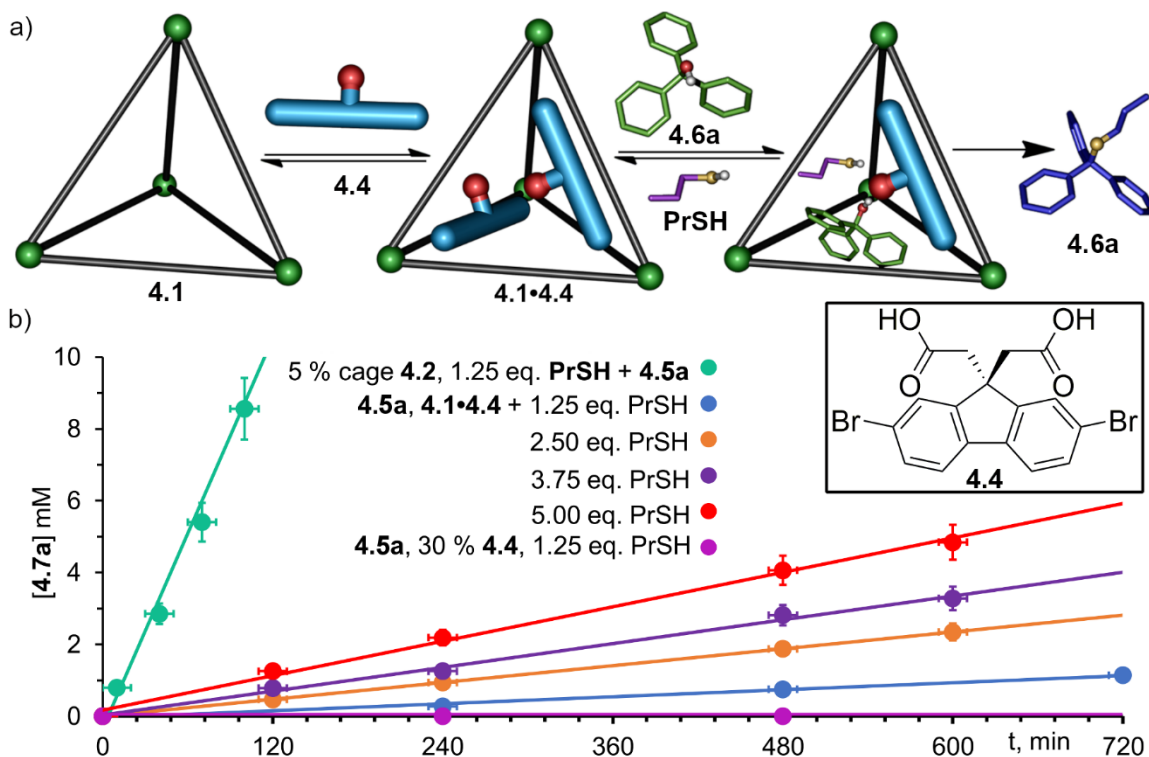


Figure 5.2. a) summary of the acid catalyzed substitution processes tested ($4.1 \cdot 4.4 = 1:6$ ratio of cage); b) reaction progress over time for the thioetherification of triphenyl methanol **4.5a** with **PrSH** and either 5 % cage **4.2** or 5 % cage **4.1/30 % 4.4** as catalyst. $[4.5a] = 15.8$ mM, reactions were performed at 80 °C in CD_3CN .

One of the hallmarks of the enzymatic catalysis of the reaction with 5 % acid cage **4.2** was the ability to alter the molecularity of the reaction. To see if this was generally true for this sort of catalysis, the substitution of **4.5a** was repeated at varying $[PrSH]$. Surprisingly, as was the case for **4.2**, the reaction rate for the substitution catalyzed by the $4.1 \cdot 4.4$ complex increases with increasing $[PrSH]$. The catalysis of this reaction with small

molecules shows no dependence on nucleophile:¹¹ only when cage catalysts capable of molecular recognition (such as **4.2**) are used is this dependence observed. This data strongly indicates that the **4.1•4.4** complex is acting as a “holoenzyme” catalyst, with the cage as the “apoenzyme” and the acid **4.4** as the cofactor. To further test the similarities between the two catalysts we then investigated the effects of changing the electrophile. In the reaction with cage **4.2**, the substitution of trityl ethyl ether **4.5b** progressed at essentially the same rate as the alcohol **4.5a**. The only difference in this case being the lack of nucleophile dependence in the reaction. The reaction with the **4.1•4.4** complex mirrored these results.

5.3 Kinetic Analysis of Nucleophile Variations

Following this initial success, we systematically varied the components of the reaction to further implicate the reactivity of the host:cofactor system. Initially we focused on a variety of different nucleophiles varying in length (*n*-octylthiol, **OctSH**), substitution (cyclohexylthiol, **CySH**) and nucleophilicity (4-methylbenzene thiol, **TolSH** and ethanol, **EtOH**). The nucleophiles were subjected to the same conditions as **PrSH** (5 mol % **4.1**, 30 mol % **4.4**, 400 μ L CD₃CN, 80 °C). The reaction with cyclohexyl thiol and ethanol both behaved as expected, with both **CySH** and **EtOH** showing significantly decreased reactivity ($V = 0.2 \times 10^{-4}$ mM/min) compared to that of **PrSH**. Additionally, the reaction with **TolSH** was dominated by the formation of the tolyldisulfide (**TolS**)₂, with no formation of product, further indicating that this reaction is enhanced by encapsulation in the presence of catalytic acid. Only the reaction of *n*-octane thiol **OctSH** exhibited similar reactivity to that of **PrSH**.

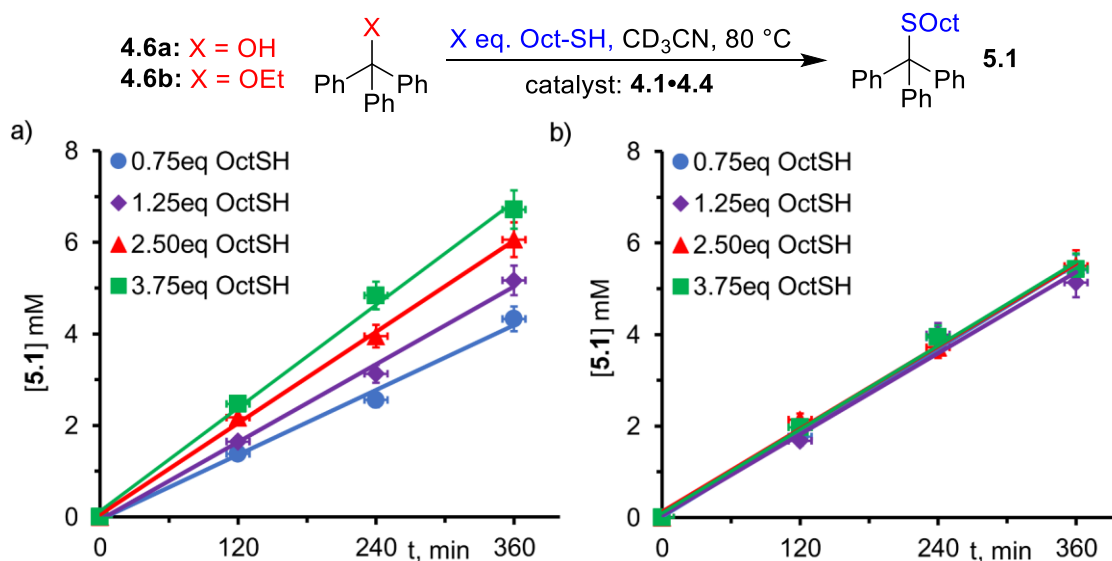


Figure 5.3. Reaction progress over time for the thioetherification of a) triphenyl methanol **4.6a**, or b) O-trityl ethyl ether **4.5b**, with **OctSH** and 5 % cage **4.1**/30% **4.4** as catalyst. $[\mathbf{4.5a}] = 15.8$ mM, reactions were performed at 80 °C in CD_3CN .

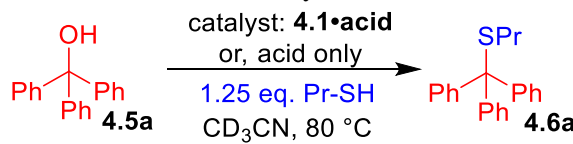
PrSH and **OctSH** exhibit essentially the same nucleophilicity, and as such would be expected react in the same manner. While this is true for the rate of the reaction with 30 % acid **4.4** alone ($V \approx 0$), when a co-worker in the Hooley lab, Courtney Ngai, performed the reaction with the cooperative complex **4.1**•**4.4**, the reaction outcomes were slightly different from that of **PrSH**. The longer **OctSH** is evidently more easily oxidized than the other alkyl thiols tested, as a significant amount of disulfide is observed in addition to the thioether product. Fortunately, the formation of the disulfide appears in a different location than the signals of the product thioether so an initial rate of thioetherification could still be calculated. The substitution reaction with **OctSH** is also surprisingly much faster ($V = 141.5 \times 10^{-4}$ mM/min) than that of **PrSH**, this observation further exemplified by an increased rate of catalysis for not only alcohol **4.5a**, but the ether **4.5b** as well (Figure 5.3). Given the enhanced reactivity of **OctSH**, Courtney then tested the reaction at differing concentrations of nucleophile. As expected, the co-factor mediated substitution of **4.5a**

with **OctSH** was indeed still dependent on nucleophile concentration. Further, variation of the nucleophile showed no change in reactivity with the similarly reactive trityl ether **4.5b**.

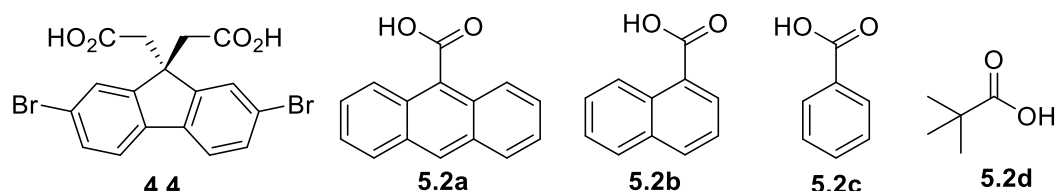
5.4 Kinetic Analysis of Co-Factor Variations

Following the insights gathered from changing the nucleophile and electrophile, we analyzed the effect of varying the acidic cofactor on the substitution process of **4.5a** with **PrSH**. For this study, four additional acid cofactors were tested (**5.2a-d**) which vary both in size and acidity. The fluorenyl diacid **4.4** is the largest substrate with an estimated pKa of ~3.7 (based on comparison with 3,3-dimethylglutarate). The other cofactors **5.2a-d** have only slight discrepancies in pKa (**5.2a** = 3.65, **5.2b** = 3.69, **5.2c** = 4.20, **5.2d** = 5.03),^{15,16} but have substantial differences in volume. Despite these small differences, the various cofactors show appreciable variation in catalytic activity, even in the absence of cage **4.1**. A summary of the reactivity is shown in Figure 5.4 and Table 5.1. Some variation in the “free” cofactor catalyzed rates can be seen, but not in the expected trend of pKa; the best catalyst is naphthoic acid **5.2b**, while the worst is diacid **4.4**, despite roughly identical pKa. The relative order of effectiveness is **5.2b**>**5.2c**>**5.2a**>>**5.2d**>**4.4**. None of the free catalysts **4.4/5.2a-d** are particularly effective, however, with all of the reactions only reaching <30 % conversion after 6 h reflux.

Table 5.1. Supramolecular Cofactor-Mediated Catalysis.^a



Acid Cofactors:



Acid cofactor	V(4.1•acid), x10 ⁻⁴ mM/min	V(acid only), x10 ⁻⁴ mM/min	V(4.1•acid)/V(acid only)
4.4	16	0.8	20
5.2a	230	17	13.5
5.2b	121	59	2.0
5.2c	101	28	3.6
5.2d	86	6	14.3

^a [4.5a] = 15.8 mM, [PrSH] = 19.8 mM, reactions were performed at 80 °C in CD₃CN. Initial rates were determined using the first set of linear timepoints under 50 % conversion by comparing Δ[4.6a]/T(min). Concentrations were confirmed using dioxane as a standard (7.9 mM). Reactions were performed at 293 K.

Upon addition of 5 % cage **4.1**, noticeable differences in both the reactivity trend of the cofactors, and their rate accelerations were observed. The overall reaction rate order for the cooperative complexes is **4.1•5.2a**>**4.1•5.2b**~**4.1•5.2c**>**4.1•5.2d**>**4.1•4.4**. Diacid **4.4**, anthroic acid **5.2a** and pivalic acid **5.2d** are the substrates that are most heavily impacted by the addition of cage **4.1**, with 15-20 fold enhancements in initial rate. Alternatively, significantly lower accelerations in initial rate (~2-fold) are observed for the reactions catalyzed by naphthoic acid **5.2b** and benzoic acid **5.2c**. The large variations in initial rate and rate acceleration across cofactors of putatively similar acidities suggests that molecular recognition within cage **4.1** plays an extensive role in the catalytic process.

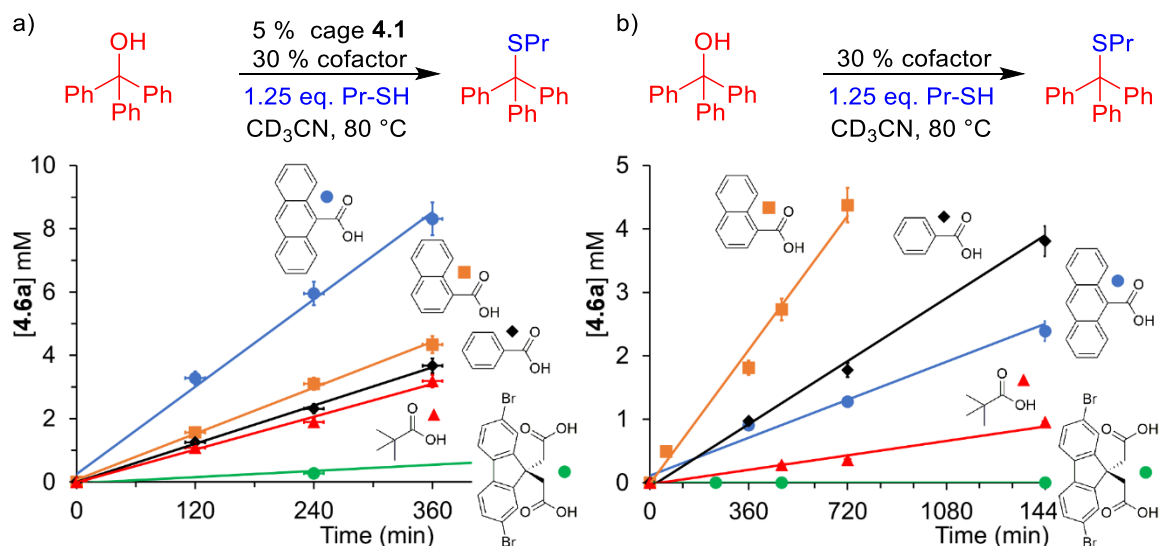


Figure 5.4. Reaction progress over time for the thioetherification of electrophile **4.5a** with **PrSH** a) 5 % cage **4.1**/30 % cofactor **5.2a-d** catalyst, and b) 30 % **5.2a-d** alone. $[\mathbf{4.6a}] = 15.8 \text{ mM}$, reactions were performed at 80°C in CD_3CN .

After determining the reaction could in fact be utilized to perform the cofactor mediated catalysis, the next step was to determine their overall effect on the mechanism. As discussed earlier, the reaction of **4.5a** and **PrSH** with the **4.1•4.4** complex displayed a dependence on the nucleophile indicating controlled changing in the molecularity of the reaction. As diacid **4.4** is the least suited to catalyze the substitution reaction, we wanted to investigate how the use of the new mono-acids affected this observation. Anthroic acid **5.2a** had the highest initial rate, and rate acceleration of the other acids tested, so we decided to focus on that reaction for our analysis. First, the substitution of **4.5a** with **PrSH** and a mixture of 5 % cage **4.1** and 30 % cofactor **5.2a** was performed, with varying concentrations of **PrSH** (Figures 5.5 and 5.6a). In contrast to the bimolecular reactivity of **4.1•4.4**, the substitution reaction with **4.1•5.2a** proceeded at essentially the same initial rate regardless of $[\text{PrSH}]$, consistent with the classical $\text{S}_{\text{N}}1$ mechanism. It is not entirely clear why nucleophile dependence is observed when using diacid **4.4**, and not with cofactor

5.2a, but it does show some unique recognition in the host:cofactor mechanism. The unique pairing of **4.4**, **4.5a**, and **RSH** gives rise to a mechanism dependent on **[RSH]** while all others do not.

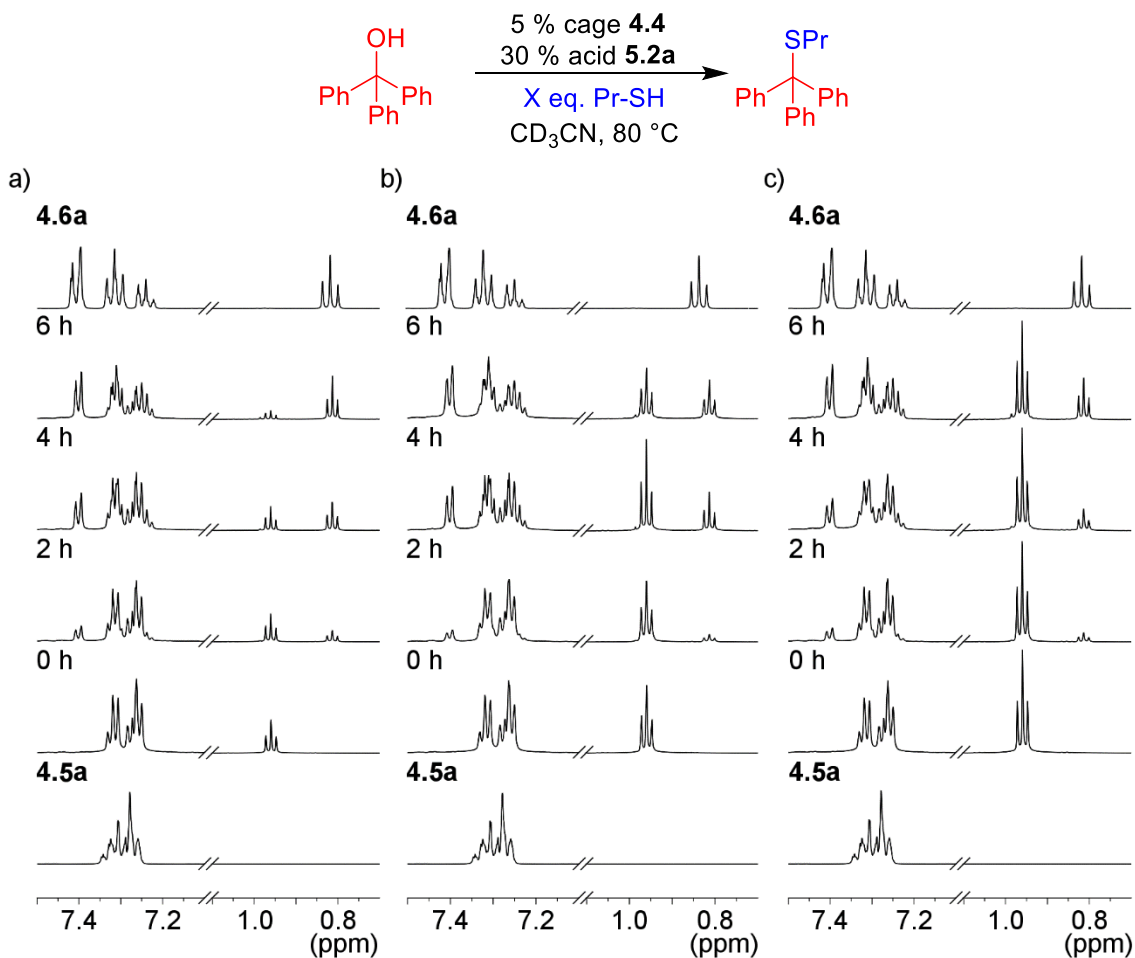


Figure 5.5. Acid promoted substitution reaction between **4.5a** and **PrSH** in the presence of 5 mol % cage **4.1** and 30 mol % **5.2a**, at varying concentrations of **PrSH** a) 9.5 mM b) 22.1 mM and c) 33.2 mM, performed at 80 °C and monitored over time (600 MHz, 298K, CD₃CN).

In conjunction with my investigation of nucleophile dependence, Courtney investigated the effect concentration of the acidic cofactor had in the system. The purpose being to establish the best concentration to run the reaction at; anthroic acid **5.1a** has one of the highest association constants (vide infra) and could cause product inhibition if it

heavily occupies the cavity. The tests for cofactor dependence were performed at 5 %, 10 %, 20 % and 30 % cofactor loading for the substitution of **4.5a** with **PrSH**. Unsurprisingly, the reaction rate increases with increasing [**5.2a**] indicating, the reaction is indeed mediated by the cofactor. Further, there appears to be an upper limit to the effect on increasing [**5.2a**] as a graph of the rate versus concentration begins to plateau around 30 %.

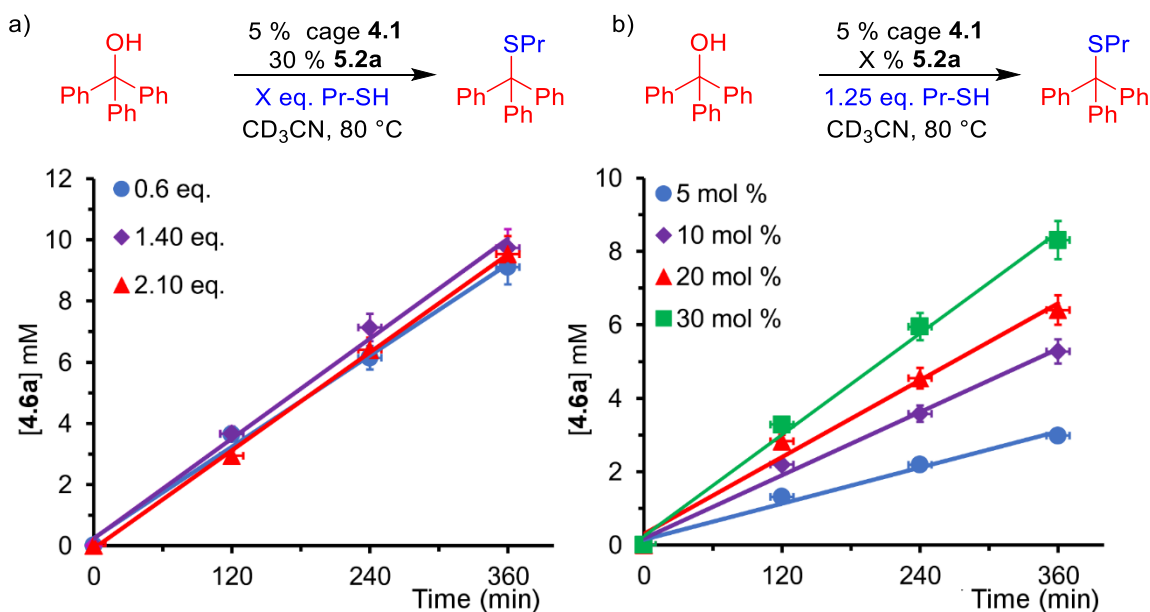


Figure 5.6. a) substitution reaction of **4.5a** with varying concentrations of **PrSH** catalyzed by 5 % cage **4.1** and 30 % cofactor **5.2a**; b) substitution reaction of **4.5a** with 1.25 eq. **PrSH** catalyzed by 5 % cage **4.1** and varying concentration of cofactor **5.2a**. [**4.5a**] = 15.8 mM, reactions were performed at 80 °C in CD_3CN .

The systematic changes in reaction components for this system illustrates the large impact that small changes can have in the cofactor catalyzed process. The size of the molecule can cause significant changes in the molecularity and rate of the **4.1**•(**4.4/5.2**) reaction, this is true for each of the components (nucleophile, electrophile, and cofactor). Further, the modified reactivity is atypical for what one would expect of an acid catalyzed S_N1 reaction: the rate of reaction inside **4.1** is indiscriminate of the pKa, of the cofactor, and can be modified based on the properties of the incoming nucleophile. These

observations strongly suggest molecular recognition events are occurring in the cage-catalyzed reaction. In the previous chapter we observed that strong binding affinities exist between small molecules and the extended fluorenyl scaffold in acetonitrile. In both cases, however, the rate of ingress and egress was too fast for the NMR timescale, necessitating analysis by UV/Vis absorbance titrations.

5.5 Determination of Binding Affinities

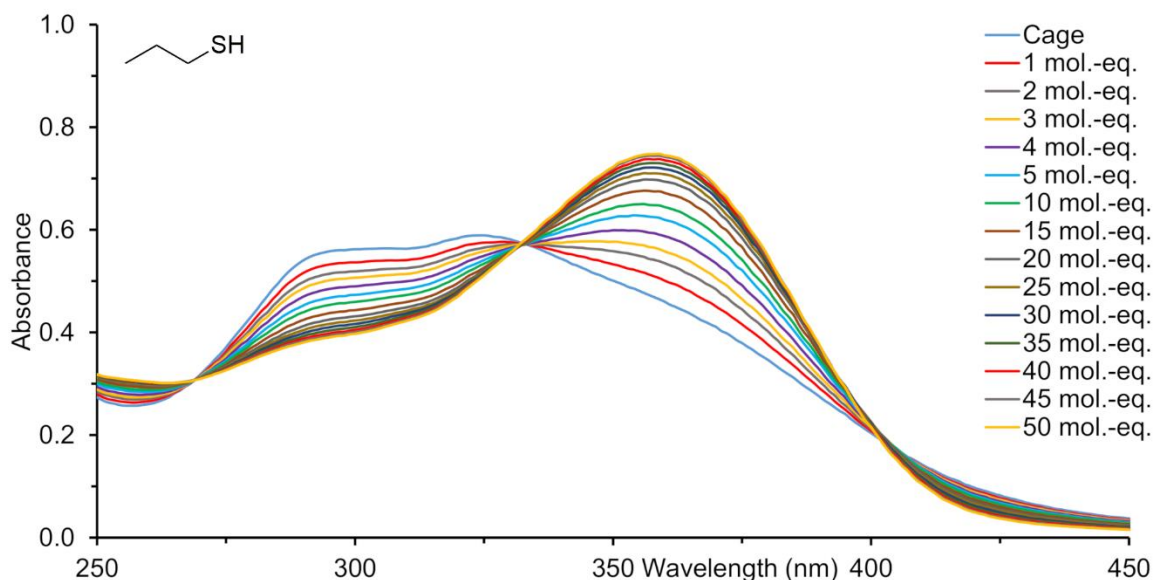
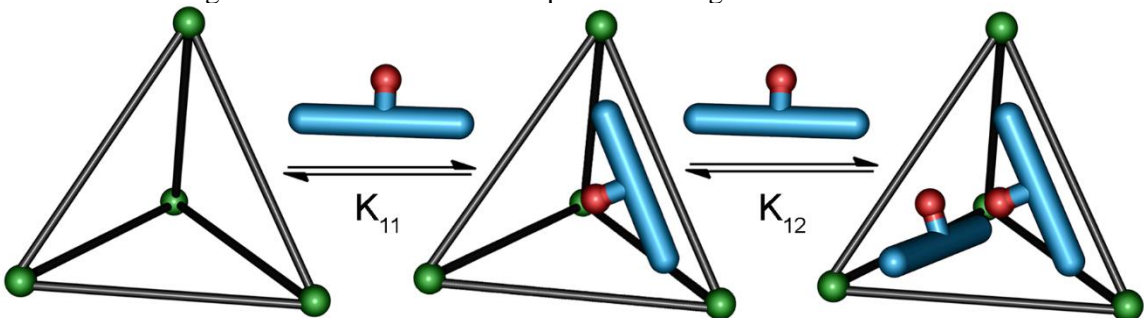


Figure 5.7. UV/Vis absorption titration of **PrSH** into a solution of **4.1** in CH₃CN. **PrSH** was added in 1 – 5 μ L increments from a 9mM solution in CH₃CN, [**4.2**] = 3 μ M.

Aside from a similar scaffold, there are several differences between cages **4.1** and **4.2** to consider when investigating the binding. First, the unfunctionalized **4.1** exhibits a substantially larger internal cavity than the acid cage. Further, the carboxylic acid functional groups in **4.2** allowed that cage to exploit polar interactions between the host and guest. Therefore, a detailed investigation into the affinities and more importantly the stoichiometry of the binding of the various components with cage **4.1** was conducted. A 1.5 μ M solution of cage **4.1** was prepared in CH₃CN (4.5 μ mol in 3 mL) and an initial

measurement was taken. To this solution was then added 1 μL aliquots from a 4.5 mM solution of the corresponding guest molecule, equating to one molar equivalent guest to cage. Following five additions of 1 μL aliquots. These additions were continued until there was no observable change in the absorption spectrum. The affinities were initially fit to 1:1 and 1:2 binding models through Bindfit[®],^{17,18} the affinities were then recalculated by Dr. Len Mueller using the same equations to determine the best fit for each compound. The affinities, and certainties of fit are shown in Table 5.2.

Table 5.2. Binding Affinities of Reaction Components in Cage 4.1.^a



1:2 guests	K_{11} ($\times 10^3 \text{ M}^{-1}$)	K_{12} ($\times 10^3 \text{ M}^{-1}$)	α ($4K_2/K_1$)	1:1 guests	K_{11} ($\times 10^3 \text{ M}^{-1}$)	1:1 guests	K_{11} ($\times 10^3 \text{ M}^{-1}$)
OctSH	174 ± 43	0.78 ± 0.53	0.018	PrSH	58.5 ± 4.7	4.5a	14.5 ± 0.8
4.5b	47.1 ± 8.5	2.11 ± 0.38	0.18	5.2a	95.4 ± 5.5	4.6a	24.8 ± 1.5
4.4	19 ± 11	244 ± 89	51	5.2b	102.1 ± 5.2	5.1	91.7 ± 7.8
				5.2c	25.5 ± 1.0	(OctS)₂	76.1 ± 3.8
				5.2d	2.4 ± 0.15		

^ain CH_3CN , **[4.1]** = 1.5 μM , absorbance changes measured at 300/330nm and 370 nm.^{14,15}

Affinity for the cage is observed with all components tested, including the small species such as **PrSH**. The internal cavity of cage **4.1** quite large and in theory, can form ternary (or higher stoichiometry) complexes with all the components. The molecular model of the ternary complex of trityl ethyl ether **4.1•4.5b₂** (Figure 5.8a), demonstrates the ease with which ternary complexes can be formed, even with the larger substrates used. The

binding affinities for the cage are strong, with the weakest affinity being pivalic acid **5.2d** ($K_a = 2.4 \times 10^3$), and the strongest being naphthoic acid **5.2b** ($K_a = 102 \times 10^3$). To determine the preference of each molecule for either the 1:1 or 1:2 binding model, the titration data was subjected to the same equations used for Chapter 4 and confirmed through statistics by Dr. Len Mueller. From this analysis, we can see that several of the largest guests fit excellently ($<10^{-4}$ % error in confidence) to the 1:2 binding model. The 1:2 binding mode can be unambiguously assigned to the fluorenyl diacid **4.4**, *n*-octanethiol **OctSH** and trityl ethyl ether **4.5b**. Slightly smaller guests such as anthroic acid **5.2a** and triphenyl methanol **4.5a** are slightly more ambiguous, and could bind in a 1:2 fashion, however the 1:1 complex is statistically more likely. Finally, analysis of the smallest guests (naphthoic acid **5.1b**, benzoic acid **5.2c**, pivalic acid **5.2d**, and *n*-propane thiol **PrSH**) shows little improvement between the 1:1 and 1:2 binding models, as such they should be considered as binary 1:1 complexes.

The analysis of the binding affinities sheds some light on several observations of the cofactor catalysis. First, the question of why disulfide is observed in the catalysis of *n*-octanethiol and not *n*-propane thiol. The titration of **OctSH** fits best to a 1:2 binding model, as such the two thiol groups would be placed in close proximity to each other, which could facilitate the reaction. The much more ambiguous binding of **PrSH** is less conducive to the dimerization reaction, resulting in only the substitution product and unreacted starting material.

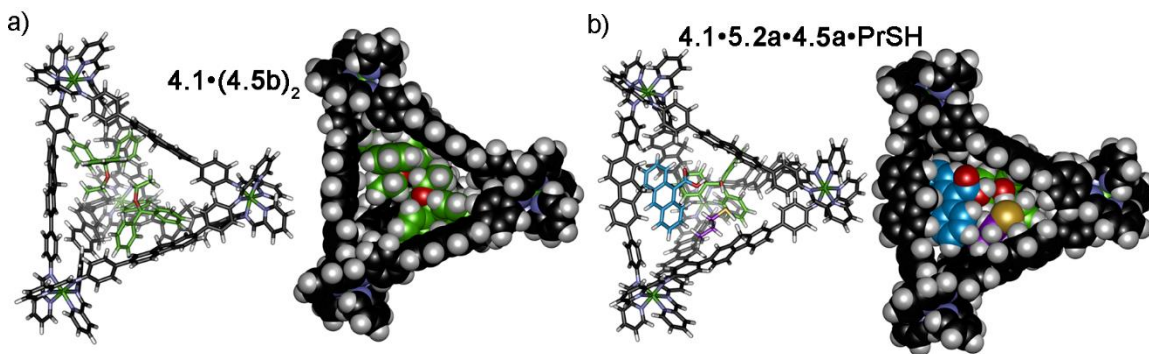


Figure 5.8. Minimized structures (Hartree-Fock) of two views (stick and space-filling) a) S_4 -**4.1•4.5b₂** and b) S_4 -**4.1•5.2a•4.5a•PrSH**.

The question of why differences in the molecularity of the reactions exist with such small changes in reagents is still confusing. While it is conceivable that a quaternary complex (**4.1•4.4•4.5a•RSH**) can be formed, this requires a high entropic penalty. Despite this, the space filling model of the proposed complex is shown in Figure 5.8b and illustrates the ease with which the quaternary complex can be formed. Determination of this structure however, is much more challenging. As mentioned previously, the in-out rate of guest encapsulation is rapid, prohibiting analysis by NMR. When triphenyl methanol **4.5a** and *n*-propane thiol **PrSH** were titrated consecutively into a solution of **4.1** in CD₃CN, broadening of the cage peaks was observed but no noticeable shift in the signals. Additionally, the changes in absorbance are dependent only on the concentration of guest added, with little variance in host-guest spectrum between substrates. The simplest explanation for the varying dependence on nucleophile could be the need for two carboxylic acid groups in the mechanism. While the diacid **4.4** has this built into its scaffold, the reaction with anthroic acid **5.2a** would require an additional molecule to be bound which is likely not possible in the cavity (Figure 5.8b). A potential mechanism

detailing the two reaction outcomes, including possible pre-equilibrium states, is shown in Figure 5.9.

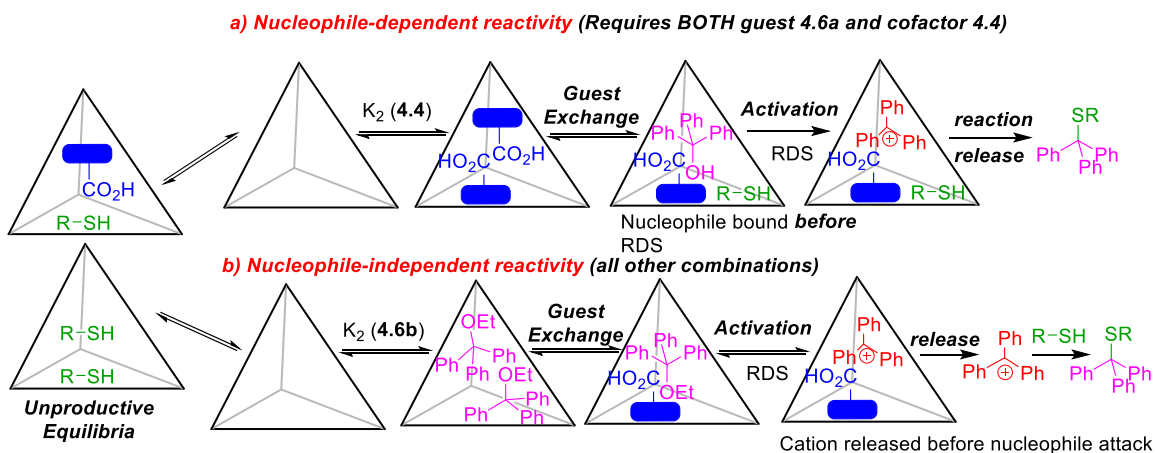


Figure 5.9. Proposed mechanism and pre-equilibrium for the “holoenzyme” mediated substitution process.

5.6 Summary of Cofactor Mediated Substitution of Trityl Compounds

Here we demonstrated the ability of an unfunctionalized receptor to bind a reactive cofactor to catalyze the thioetherification of triphenyl methanol and O-trityl ethyl ether. The cage is capable of modest accelerations in reaction rate of a variety of acidic cofactors. More importantly, the reactivity of these acids is directed by the cage, whereby cofactors exhibiting a higher binding affinity for cage **4.1** exhibit greater reaction rates, and rate accelerations, over more weakly bound substrates. Further, the cage can modify the molecularity of a simple S_N1 reaction, to a mechanism that depends on the concentration of the nucleophile. This phenomenon is specific to the combination of fluorenyl diacid **4.4** used in tandem with triphenylmethanol. All the properties reported are dependent on a high level of molecular recognition, demonstrating the ability of cage **4.1** to act as an apoenzyme analog upon encapsulation of a reactive cofactor.

5.7 Investigation of Additional Cofactors for New Forms of Reactivity

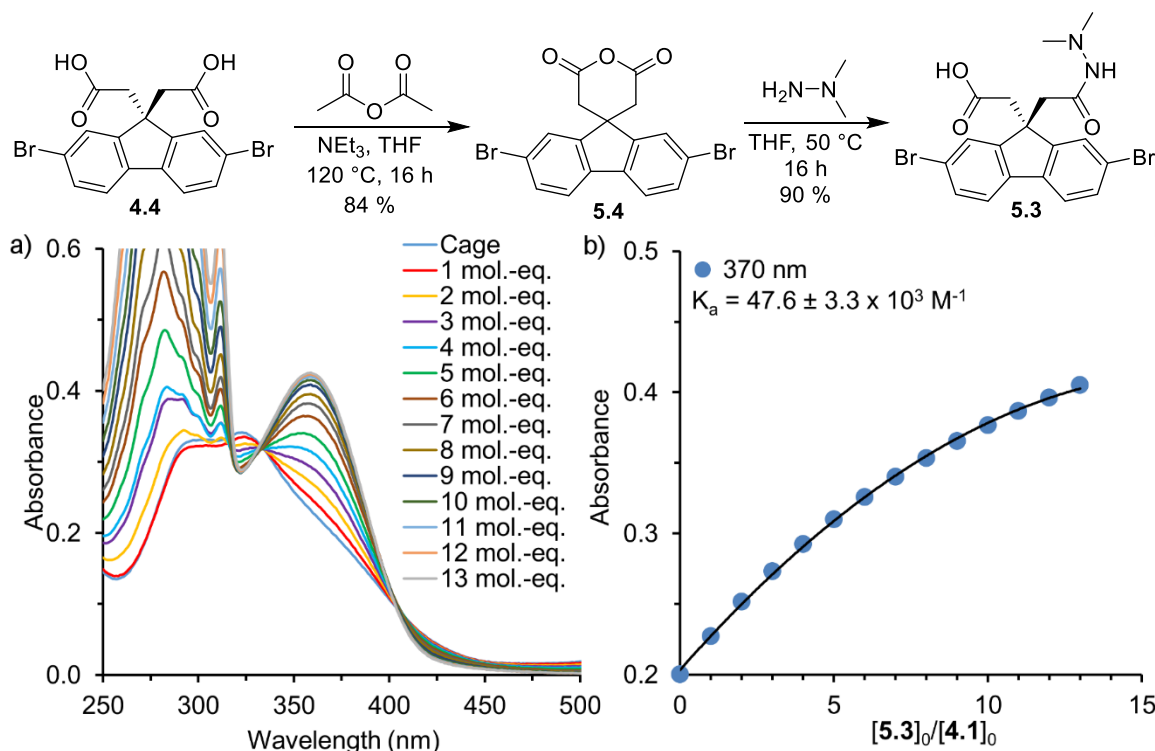


Figure 5.10. a) Synthesis of amphiphilic cofactor **5.3**; b) titration of cofactor **5.3** into a $1.5\ \mu\text{M}$ solution of cage **4.1** in CH_3CN ; c) 1:1 binding model of the **4.1**•**5.3** complex calculated from the change in absorbance at 370 nm (Nelder Mead).

The elongated fluorene cage **4.1** is an exceptional host for a wide range of molecules of varying properties. As such, barring destruction of the cage, it should be amenable to many different transformations given the appropriate cofactor. While the acid catalysis shown above exemplified the ability of the cofactor system to act as a “holoenzyme”, a large drawback exists in that the cage contains Lewis acidic Fe^{2+} , which has been previously shown to leach from the cages.¹⁹ As such we wanted to investigate reactions that moved away from simple general acid catalysis to more challenging examples. The shortest leap is to design a cofactor that exhibits both an acidic and basic functional group within the same molecule. This would allow two different types of

activation to occur within the cage, and could enable the catalysis of several reactions that have eluded the acid cage, such as Michael additions and the Henry reaction.

The proposed molecule **5.3** can be easily accessed from the fluorenyl diacid **4.4** (Figure 5.10). Treatment of diacid **4.4** with Ac_2O gives anhydride **5.4** in 84 % yield. The anhydride can then be treated with the desired nucleophile to create a library of amphiphilic cofactors. To install the desired basic functional group, N,N-dimethyl hydrazine was added to a solution of **5.4** in dry THF. Following opening of the ring, the acid-base cofactor **5.3** precipitates cleanly out of solution. The affinity of **5.3** for cage **4.1** was tested in acetonitrile, unsurprisingly a strong affinity ($K_a = 47.6 \pm 3.3 \times 10^3 \text{ M}^{-1}$) was observed (Figure 5.10b). The ability of the cooperative **4.1**•**5.3** complex is currently in progress.

Finally, we wanted to investigate the use of organometallic compounds. Co-Salen complexes are well studied organometallic complexes known for carbonylation with CO and benzylic alcohols,²⁰ as well as polymerization²¹ and oxidation reactions.²² The encapsulation of these complexes in cage **4.1** could enable enhanced reactivity and selectivity in these compounds. The bromine functionalized Co-Salen **5.5** was initially chosen for analysis as it is a similar size to that of the strongly bound fluorenyl cofactors (**4.4** and **5.3**). Dana Chambers, from the Martin lab at UCR, synthesized the desired complex. A 4.5 mM solution of **5.5** in CH_3CN was prepared followed by titration into a 3 μM solution of **4.1** in CH_3CN . As anticipated, the **5.5** complex exhibited a high affinity for the cage and fit well to the 1:1 binding model ($40 \pm 2.5 \times 10^3 \text{ M}^{-1}$, Figure 5.11). The Salen ligands can be easily modified, which would allow further investigation into the factors that impact binding within the cavity of **4.1**. The encapsulation of these compounds enables

us to investigate reactions that can either Lewis acid catalyzed or specific to the Co-Salen scaffold. Finally, the strong affinity of the **5.5**, complex could provide added stability to the complex and provide access to reactions that would otherwise decompose the catalyst.

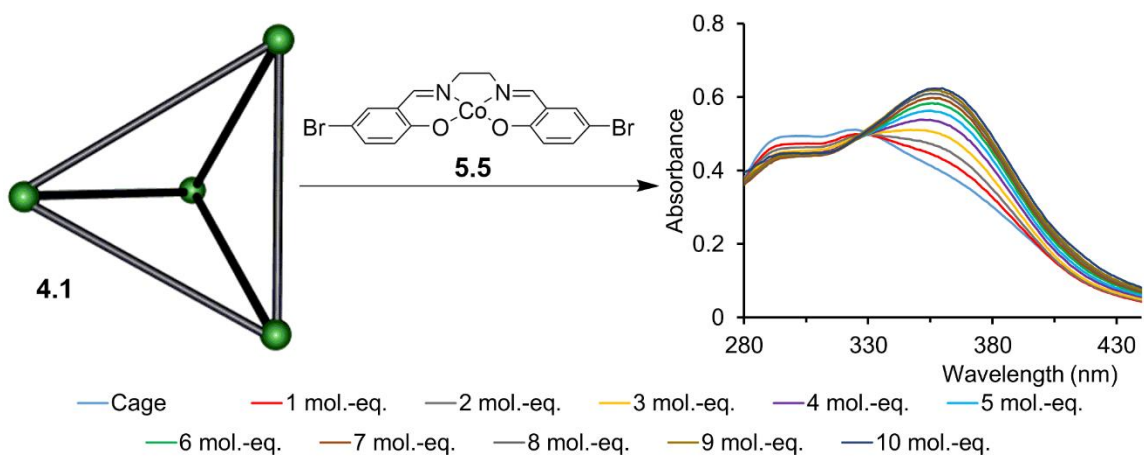


Figure 5.11. UV/Vis titration of Co-salen complex **5.5** into a 3 μM solution of **4.1** in CH_3CN .

5.8 References

1. Drewe, W. F., Jr.; Dunn, M. F. "Detection and identification of intermediates in the reaction of L-serine with Escherichia coli tryptophan synthase via rapid-scanning ultraviolet-visible spectroscopy." *Biochemistry* **1985**, *24*, 3977–3987.
2. Fagan, R.L.; Palfey, B.A. "Flavin-Dependent Enzymes." *Comprehensive Natural Products II - Chemistry and Biology*, **2010**, *7*, 37–113.
3. Eliot, A. C.; Kirsch, J. F. "Pyridoxal phosphate enzymes: mechanistic, structural, and evolutionary considerations." *Annu. Rev. Biochem.* **2004**, *73*, 383–415.
4. Dong, Z.; Luo, Q.; Liu, J. "Artificial enzymes based on supramolecular scaffolds." *Chem. Soc. Rev.* **2012**, *41*, 7890–7908.
5. Brown, C. J.; Toste, F. D.; Bergman, R. G.; Raymond, K. N. "Supramolecular Catalysis in Metal-Ligand Cluster Hosts" *Chem. Rev.* **2015**, *115*, 3012–3035.
6. MacGillivray, L. R.; Atwood, J. L. "A chiral spherical molecular assembly held together by 60 hydrogen bonds." *Nature* **1997**, *389*, 469–472.
7. Harris, K.; Fujita, D.; Fujita, M. "Giant hollow M_nL_{2n} spherical complexes: structure, functionalisation and applications." *Chem. Commun.* **2013**, *49*, 6703–6712.
8. Zhang, Q.; Catti, L.; Tiefenbacher, K. "Catalysis inside the Hexameric Resorcinarene Capsule." *Acc. Chem. Res.* **2018**, *51*, 2107–2114.
9. Zhang, Q.; Tiefenbacher, K. "Terpene cyclization catalyzed inside a self-assembled cavity." *Nat. Chem.* **2015**, *7*, 197–202.
10. Catti, L.; Tiefenbacher, K. "Brønsted Acid-Catalyzed Carbonyl-Olefin Metathesis inside a Self-Assembled Supramolecular Host." *Angew. Chem. Int. Ed.* **2018**, *57*, 14589–14592.
11. Gramage-Doria, R.; Hessels, J.; Leenders, S. H. A. M.; Tröppner, O.; Dürr, M.; Ivanović-Burmazović, I.; Reek, J. N. H. "Gold(I) Catalysis at Extreme Concentrations Inside Self-Assembled Nanospheres." *Angew. Chem. Int. Ed.* **2014**, *53*, 13380–13384.
12. Wang, Q.-Q.; Gonell, S.; Leenders, S. H. A. M.; Dürr, M.; Ivanović-Burmazović, I.; Reek, J. N. H. "Self-assembled nanospheres with multiple endohedral binding sites pre-organize catalysts and substrates for highly efficient reactions." *Nat. Chem.* **2016**, *8*, 225–230.

13. Holloway, L. R.; Bogie P. M.; Lyon, Y.; Ngai, C.; Miller, T. F.; Hooley, R. J. "Tandem Reactivity of a Self-Assembled Cage Catalyst with Endohedral Acid Groups." *J. Am. Chem. Soc.* **2018**, *140*, 8078–8081.
14. Bogie, P. M.; Holloway, L. R.; Ngai, C.; Miller, T. F.; Grewal, D. K.; Hooley, R. J. "A Self-Assembled Cage with Endohedral Acid Groups both Catalyzes Substitution Reactions and Controls their Molecularity." *Chem. Eur. J.* **2019**, ASAP, DOI: 10.1002/chem.201902049
15. Brown, H.C. et al., in Braude, E.A. and F.C. Nachod *Determination of Organic Structures by Physical Methods*, Academic Press, New York, **1955**.
16. Dippy, J. F. J.; Hughes, S. R. C.; Rozanski, A. "Dissociation constants of some symmetrically disubstituted succinic acids." *J. Chem. Soc.* **1959**, 2492.
17. Hibbert, D. B.; Thordarson, P. "The death of the Job plot, transparency, open science and online tools, uncertainty estimation methods and other developments in supramolecular chemistry data analysis." *Chem. Commun.*, **2016**, *52*, 12792–12805.
18. Association constants were calculated through Bindfit[®] using supramolecular.org.
19. Holloway, L. R.; Bogie, P. M.; Lyon, Y.; Julian, R. R.; Hooley, R. J. "Stereoselective Postassembly CH Oxidation of Self-Assembled Metal-Ligand Cage Complexes." *Inorg. Chem.* **2017**, *56*, 11435–11442.
20. Chambers, D. R.; Sullivan, R. E.; Martin, D. B. C. "Synthesis and Characterization of Alkoxy carbonyl Cobalt Complexes via Direct Carbonylation Methods." *Organometallics* **2017**, *36*, 1630–1639.
21. Hiranoi, Y.; Nakano, K. "Copolymerization of epoxides with cyclic anhydrides catalyzed by dinuclear cobalt complexes." *Beilstein J. Org. Chem.* **2018**, *14*, 2779–2788.
22. Liu, T.-T.; Liang, J.; Huang, Y.-B.; Cao, R. "Salen-Co(III) insertion in multivariate cationic metal–organic frameworks for the enhanced cycloaddition reaction of carbon dioxide." *Chem. Commun.* **2019**, *55*, 4063–4066.

Chapter 6: New Ligand Scaffolds for Endohedral Functionalization

6.1 Introduction

While there are several examples of placing relatively inert functions within self-assembled cages,¹ the inclusion of cages with more reactive functionalities is far more limited.² Further, almost all cases of exceptionally reactive cages are of the large M_xL_y nanospheres,³ which are formed via robust coordination between pyridyl linkages and either Pd or Pt. The main drawback of these complexes is that they are so large, the uptake and egress of guest molecules is rapid, lowering their potential contacts with the reactive functional groups inside the cage, thereby lowering reaction turnover. In order to meet the challenges of designing new functional cages we aimed to solve 3 challenges: 1) creating new chelating motifs capable of strong coordination that are tolerant to reaction conditions such as acids or bases, nucleophilic displacement, etc. 2) incorporating new reactive functionalities into the attached ligand, 3) designing a complex containing a moderately sized internal cavity to enable space for reactive functional groups and guests, while slowing the egress of potential reactants.

6.2 Phenanthroline

The 1,10-phenanthroline motif is a well-studied metal coordinator, one which holds several advantages over typically used chelators in supramolecular cages.⁴ The inclusion of the third ring in 1,10-phenanthroline makes a more rigid structure which locks the coordinating nitrogens in place. This rigidity makes metal coordination with phenanthroline entropically favored over more commonly used systems such as bipyridine and iminopyridine.⁵ Further, metal-phenanthroline complexes can be formed more quickly

and strongly as a result. The robust coordination, and lack of sensitive structural components such as the imine bond present in iminopyridine complexes, makes phenanthroline-based coordination complexes desirable targets in the pursuit of reactive self-assembled cages.

Addition of phenanthroline chelator to aromatic aldehydes via the cyclization of the aldehyde and 1,10-phenanthroline-5,6-dione in the presence of NH_4OAc is extensively used.⁶ By coupling the phenanthroline chelator with a terphenyl ligand, the complex could be easily functionalized via common substitution techniques.¹ In order to test the efficacy of this strategy, initially the cyclization was performed using benzaldehyde (Figure 6.1). 1,10-Phenanthroline-5,6-dione was easily accessed via oxidation of 1,10-phenanthroline with HNO_3 and H_2SO_4 . Treatment of phenanthroline dione with benzaldehyde and NH_4OAc in AcOH gave the mono-dentate ligand **6.1** in good yield.

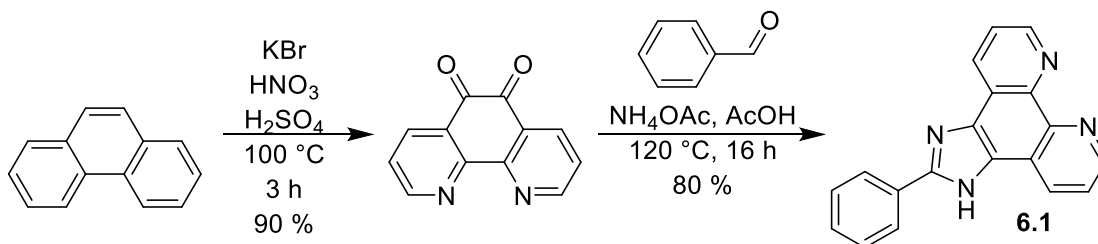


Figure 6.1. Synthesis of mono-chelating phenanthroline imidazole ligand **6.1**.

After the initial success of the small ligand, we turned our sites to the creation of the larger bidentate ligand capable of supramolecular self-assembly. It was envisioned that the prerequisite terphenyl dialdehyde compound could be accessed via Suzuki-Miyaura coupling of 4-formalphenylboronic acid with 1,3-dibromobenzene, followed by cyclization with phenanthroline dione would give the desired ligand in only 2 synthetic steps (Figure 6.2). Initial attempts to form the ligand proved challenging, however after optimization of

the Suzuki coupling, the dialdehyde was obtained in 85 % yield. Dialdehyde **6.A** was then treated with a large excess of NH_4OAc in AcOH to give ligand **6.2**.

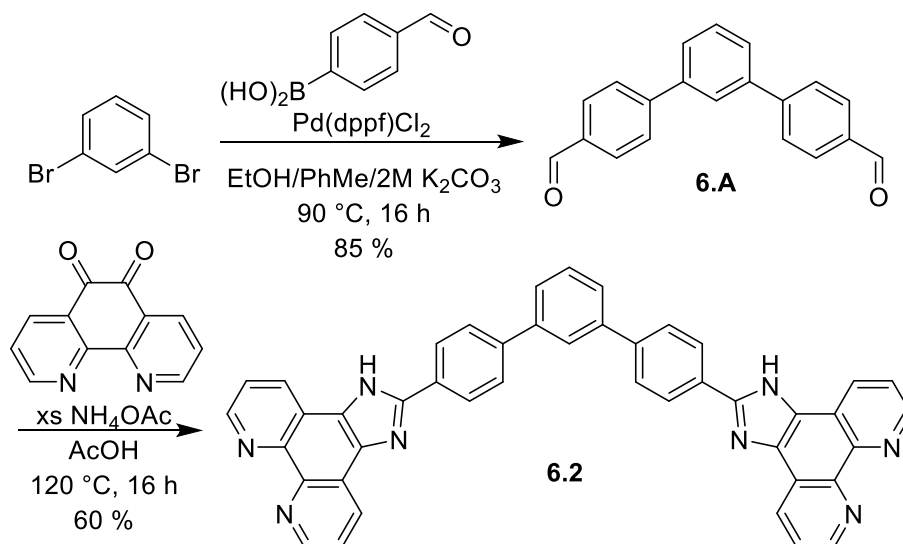


Figure 6.2. Synthesis of bis-chelating phenanthroline imidazole ligand **6.2**.

While synthesis of the ligand was largely straightforward, formation of the self-assembled complex was anything but. The phenanthroline ligand exhibited two major challenges preventing facile self-assembly. The first is that the ligand is very limited in its solubility. Ligand **6.2** is only sparingly soluble in solvents commonly used in cage formations such as acetonitrile and in water. In fact, the only solvents capable of fully dissolving the ligand were highly polar solvents such as DMSO or DMF, which can often cause problems in self-assembly by interacting with the metals themselves. Second, the metal coordinating abilities of the ligand were exceedingly strong. Attempts to column impure iterations of the ligand proved unsuccessful as the ligand could pull trace amounts of metal, such as iron, out of the silica gel. Further, prolonged exposure of metal instruments, such as a spatula, to a solution of ligand resulted in a change in color in the solution, and discoloration of the utensil. Such strong coordination can prove problematic

when attempting to form a cage, as the self-assembly relies on reversible bonds between the metal salt and the ligand to equilibrate to a thermodynamic minimum rather than forming disordered aggregates and polymers.⁷ Despite these challenges, the self-assembly of the unfunctionalized phenanthroline ligand **6.2** was attempted with several metal salts (Figure 6.3).

The complexes formed by ligand **6.2** are all broad and ill-defined, indicating there are likely multiple isomers present in solution, or incomplete equilibrium to the desired product. The assembly is further complicated when analyzing the complexes made by Fe²⁺ and Co²⁺ salts as the resulting complexes are paramagnetic, stretching as far as 38 ppm in the case of Co. Further, the complex exhibits even greater solubility issues than the initial ligand. While the ligand was sparingly soluble in some organic solvents, the resulting complexes are only capable of dissolving in DMSO and DMF. The presence of distinct paramagnetic signals, as opposed to the large mounds observed from aggregates and coordination polymers, suggests the formation of a discrete supramolecular assembly.⁸ Further characterization of the complexes using ESI-MS was ineffective as the poor solubility of the complex gave no observable signals. MALDI-TOF mass spectrometry was also attempted, but proved unsuccessful. The poor solubility of the complexes also prohibited the formation of crystals suitable for single crystal X-Ray diffraction as only amorphous powders could be obtained.

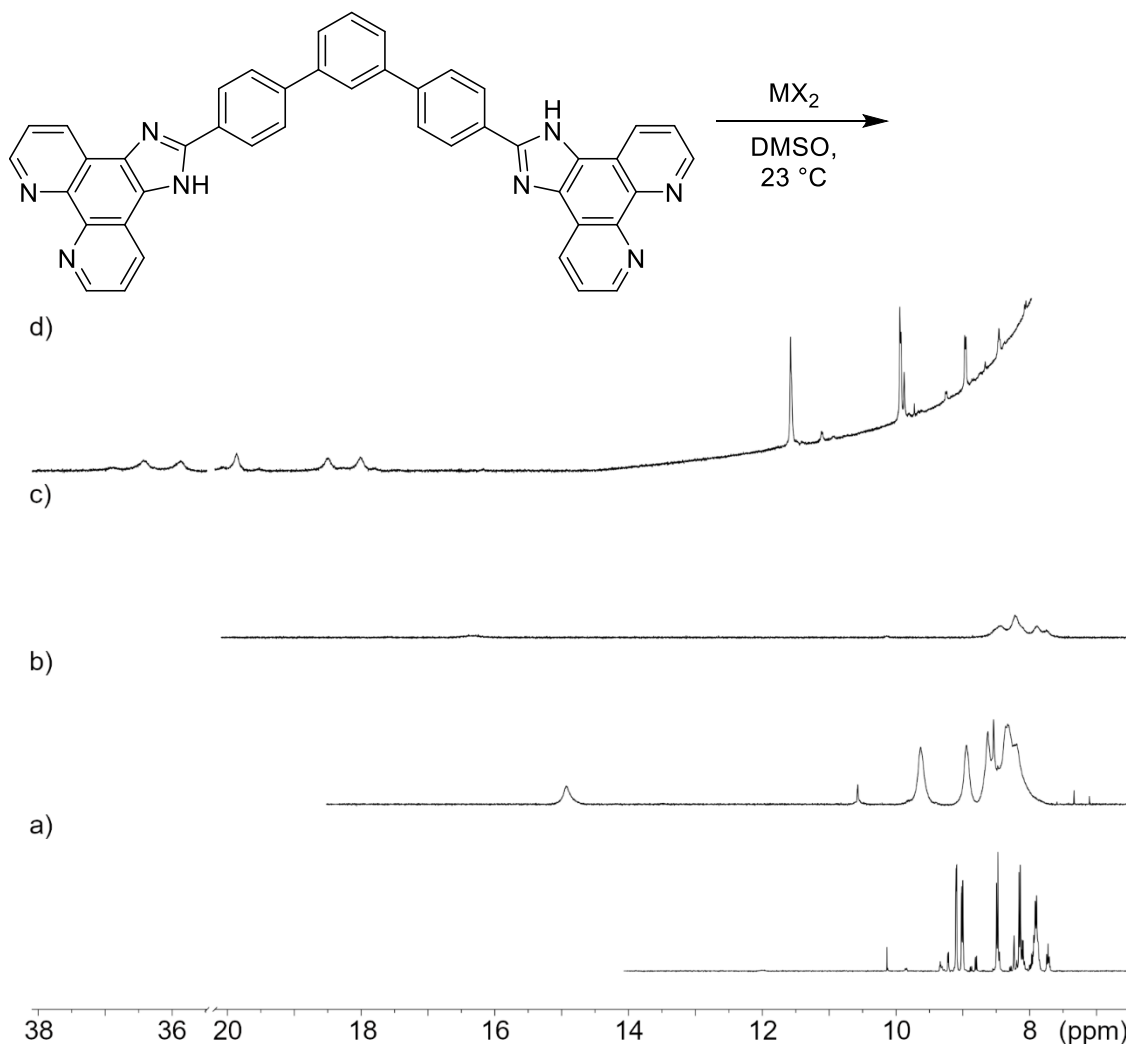


Figure 6.3. a) ^1H NMR spectra of ligand **6.2** and self-assembly with various metals: a) ligand **6.2**, b) $\text{Fe}(\text{ClO}_4)_2$; c) $\text{Zn}(\text{OTf})_2$; d) $\text{Co}(\text{ClO}_4)_2$ ($\text{DMSO-}d_6$, 298 K, 500 MHz).

Traditionally the method for improving the solubility of self-assembled cages comes from the metal linkages themselves, as increased charge gives increased solubility in polar solvents in cases where the complex itself is particularly insoluble. Another common strategy in supramolecular chemistry is the addition of solubilizing groups such as long alkane or PEG chains to allow dissolution in polar and non-polar solvents respectively.⁹ One of the hallmarks of the terphenyl ligand scaffold is the ease with which the central ring can be functionalized. While changing the functionalization of the interior

can be used to augment the usefulness of the internal cavity, the exterior may also be modified to aid in solubility. To that end, a few structural modifications of the phenanthroline ligands were synthesized in an effort to make more useful and soluble supramolecular assemblies.

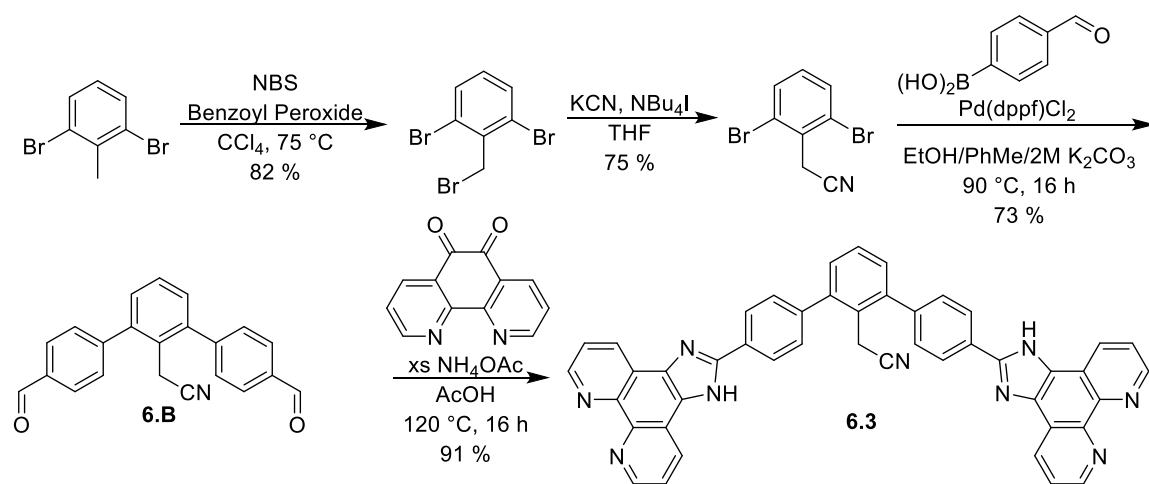


Figure 6.4. Synthesis of nitrile-containing phenanthroline ligand **6.3**.

3,5-Dibromo-4-methyl benzoate was one of the most promising starting points for these modifications. The interior could be easily functionalized via radical bromination, followed by S_N2 reaction. This method enabled facile addition of both azide and nitrile groups to the interior of the ligand. The nitrile functional group is relatively unreactive and could be carried out through the entirety of the ligand synthesis. In contrast, the azide group is significantly more sensitive, but can be converted to various other, more useful, functional groups such as amines, ureas, and triazoles after installation. Finally, the exterior of the ligand can be easily modified through Fischer esterification of the ester group with alkyl alcohols such as 1-octanol.

Unfortunately, the functionalized complexes suffered from the same solubility issues as the unfunctionalized versions and were not pursued further. Evidently the

presence of a significant number of aromatic rings, and the bulk coordination around the metal centers was too big of a challenge to overcome by simple functionalization. The use of a more solubilizing counter-ion such as NTf_2 could prove useful in forming more versatile self-assemblies, if this ligand scaffold were further investigated in the future.

6.3 Extending the Iminopyridine Scaffold

The iminopyridine chelating motif has been extensively studied for its use in self-assembled cages. From these studies, several advancements have been made in molecular recognition,^{10,11} and post-assembly modification,¹² but their use in catalysis has been limited^{13,14} due to relatively small internal cavities. In the previous chapters I have shown that the extension of the ligand scaffold can enable new properties that were not accessible using the smaller dianiline ligands. Most of the previous examples of extension were performed using 4-Boc-aminophenyl boronic acid, however the use of 4-nitrophenyl boronic acid (4-NPBA) can also provide access to the extended ligands and in some cases is the superior method.

A library of dibromo ligands based on previously published cores was synthesized to allow a thorough investigation into the effects of ligand extension. The diaminosuberone ligand creates one of the most stable M_2L_3 mesocates we have studied to date,¹⁵ and represents an ideal starting point. Bromination of the suberone scaffold proved more challenging than anticipated. The methylene units on the backbone are reactive towards radical mechanisms, meaning the choice of reagent was crucial. Accessing dibromo suberone **6.C** was made possible through treatment with Cu(II)Br_2 and ${}^t\text{BuNO}_2$ (Figure 6.5). Finally, the fluorenyl core was one of the more easily derivatized ligands and therefore

has been heavily studied. Facile formation of the ketone and alcohol compounds has been previously shown by members of the Hooley lab. In addition, the central methylene unit can be easily derivatized through the substitutions of dibromofluorene with using KO^tBu and the desired electrophile.

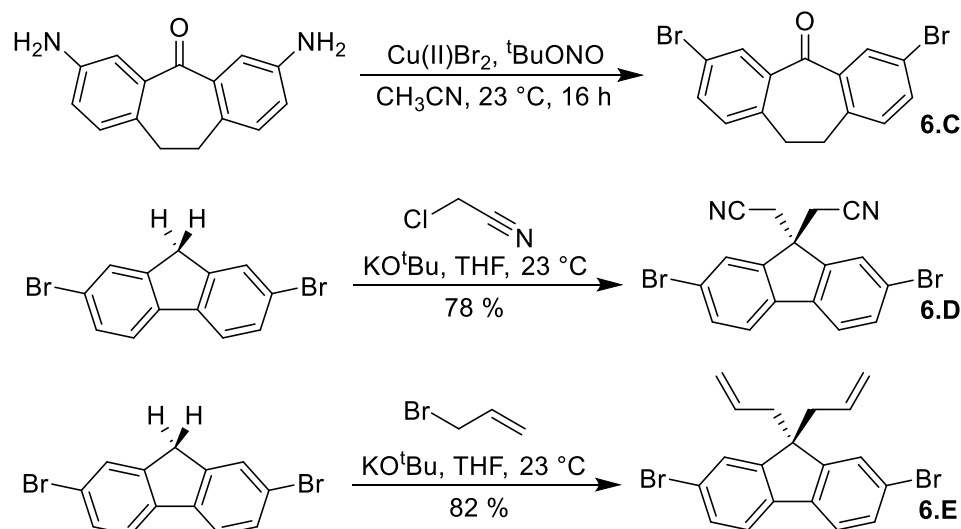


Figure 6.5. Synthesis of dibromo ligand cores.

Following formation of several dihalide cores, the conditions of the Suzuki coupling were investigated. Treatment of **4.B** and 4-NPBA with Pd(dppf)Cl₂ (conditions from Figure 6.2) resulted in little conversion to the dinitro product. Switching the ligand to triphenylphosphine improved the conversion, however still gave relatively low yields. The formation of product was further increased using the more donating tricyclohexyl phosphine ligand. Finally, the highest yield of ~80 % was obtained by changing the base to the larger base Cs₂CO₃ in conjunction with PCy₃ and Pd(OAc)₂.

With coupling conditions optimized, the synthesis of a variety of extended dinitro-ligands was attempted. The dibromosuberone species was surprisingly resistant to elongation, and conditions that worked well for the other scaffolds tested were low yielding

(< 30 %). In addition, the reduction to the dianiline gave a complicated NMR spectrum, likely due to unwanted side reactions of the ketone with either produced aniline or the reducing agent. Regardless, it is unlikely the extended suberone scaffold would produce anything larger than an M_2L_3 *meso*-helicite so the synthesis was later abandoned.

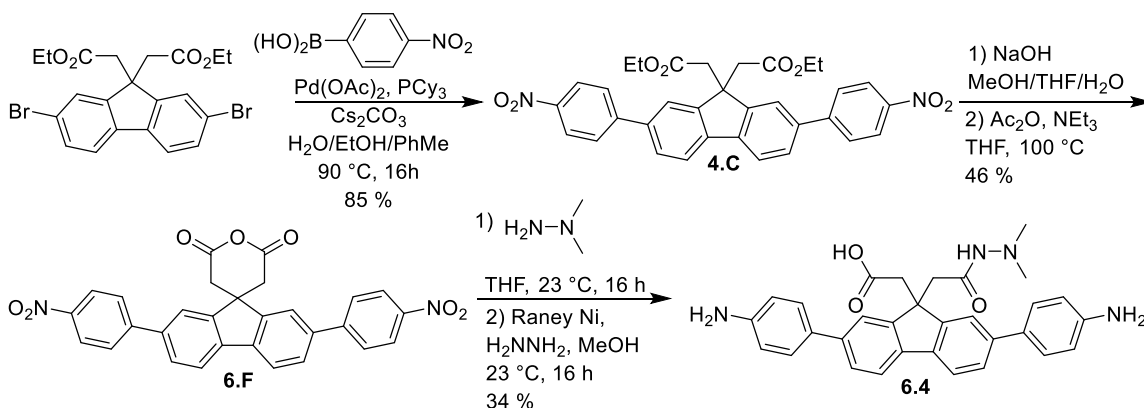


Figure 6.6. Synthesis of amphiphilic ligand **6.4**.

In contrast, the variations of the fluorenyl scaffold were significantly more interesting. The formation of the elongated amphiphilic ligand **6.4** is a promising target for future use in catalysis. The synthesis of the smaller dibromo species, was presented in the previous chapter (Section 5.6). While the use of this small molecule is interesting use as a catalytic cofactor, the reaction rate of the acid cage **4.2** is far more efficient than the analogous cofactor **4.4**. It is reasonable to assume the same will be true in the case of amphiphilic catalysis. Many of the steps necessary to form this ligand have detrimental interactions with the Boc-protecting groups. As such the synthesis of the ligand was approached using 4-NPBA (Figure 6.6). Suzuki coupling of the anhydride proved problematic, so the transformations were conducted from the elongated nitro-ester **4.C**. The ester could be converted to the anhydride **6.F**, by hydrolyzing the ester groups in a solution of MeOH and concentrated NaOH in H_2O , followed by treatment with acetic

anhydride in THF at refluxing temperatures. The anhydride could then be opened to the amphiphilic core by introduction of N,N-dimethyl hydrazine. Subsequent reduction of the nitro-groups with Raney Nickel[®] and hydrazine gave ligand **6.1** in 34 % yield. The multicomponent self-assembly of the amphiphilic ligand was then attempted with Fe(NTf₂)₂ and PyCHO. The product was analyzed by ¹H NMR (Figure 6.7). The spectrum was complicated, with some sharp signals appearing on top of larger mounds, likely the result of an incomplete assembly. Early synthetic attempts of acid cage **4.2** met similar results, and more troubleshooting of the reaction will be necessary to form a discrete cage.

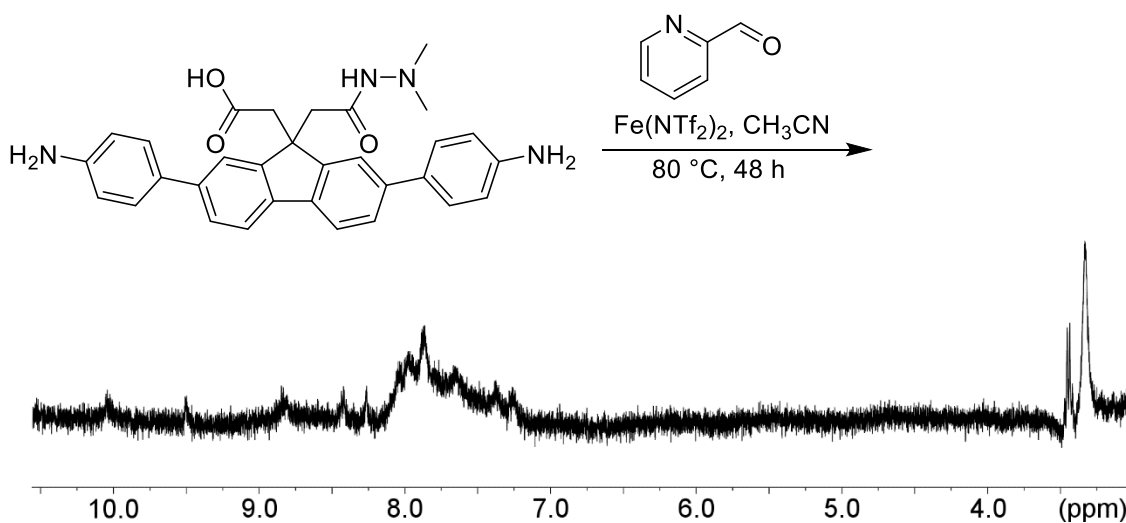


Figure 6.7. ¹H NMR spectrum of the multicomponent self-assembly of amphiphilic ligand **6.4** with Fe(NTf₂)₂ and PyCHO (CD₃CN, 298 K, 600 MHz).

6.4 Reverse Iminopyridine

Formation of iminopyridine self-assemblies is not limited to the condensation of di- and tripodal aniline species with pyridine carboxaldehyde. More recently, several examples of the reverse system (i.e. multipodal pyridyl aldehyde species with mono-anilines such as toluidine) have been shown. The formation of such compounds presents several advantages over the traditional scaffold: 1) The assembly is more robust, as the

aniline can be modified to create stronger metal coordination, 2) the use of chiral alkyl amines, such as amino acids, can confer stereocontrol to the assembly process,¹⁶ 3) introduction of the pyridyl aldehyde functionality extends the scaffold beyond that of the typical dianilines.

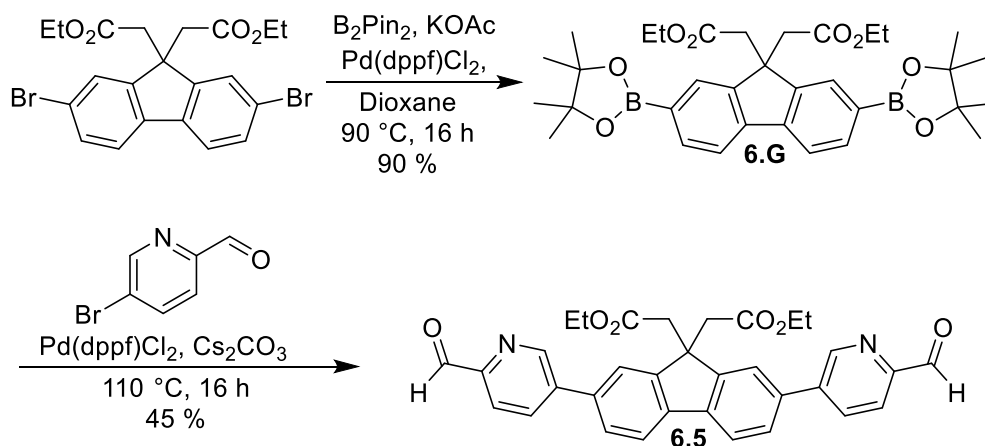


Figure 6.8. Synthesis of diester reverse iminopyridine ligand **6.5**.

We sought to synthesize the reverse iminopyridine version of the acid ligand via similar routes to those mentioned previously, Suzuki-Miyaura coupling followed by hydrolysis of the esters (Figure 6.8). We envisioned two methods of performing the Suzuki-Miyaura coupling. Either by using the dibromofluorenyl ester **4.B** with 5-pinacolboronate ester of pyridine carboxaldehyde or by first converting **4.B** to a bis-pinacol boronate ester, followed by coupling with 5-bromo-2-formylpyridine. As discussed previously, borylation of pyridine carboxaldehyde was problematic, preventing synthesis via the first route. The second method was possible and could be achieved through palladium catalyzed borylation with $Pd(dppf)Cl_2$ and *bis*-pinacolatodiboron, and purified through column chromatography in 10 % EtOAc/Hexanes. Following formation of the bis-boronate species **6.G**, coupling with 5-bromo-2-formylpyridine and $Pd(dppf)Cl_2$ was performed giving a 45 % yield of the

desired dialdehyde **6.5**. Multicomponent self-assembly of the ligand was conducted using *p*-toluidine and $\text{Fe}(\text{ClO}_4)_2$. The resulting ^1H NMR spectrum (Figure 6.9) was ill-defined and broad however, signals at 9.0 and 5.5 strongly indicate the formation of an M_4L_6 tetrahedron with excess Fe^{2+} in solution. The complexity of the synthesis, and final product led us to abandon this project in lieu of more promising alternatives such as those presented in chapters 4 and 5.

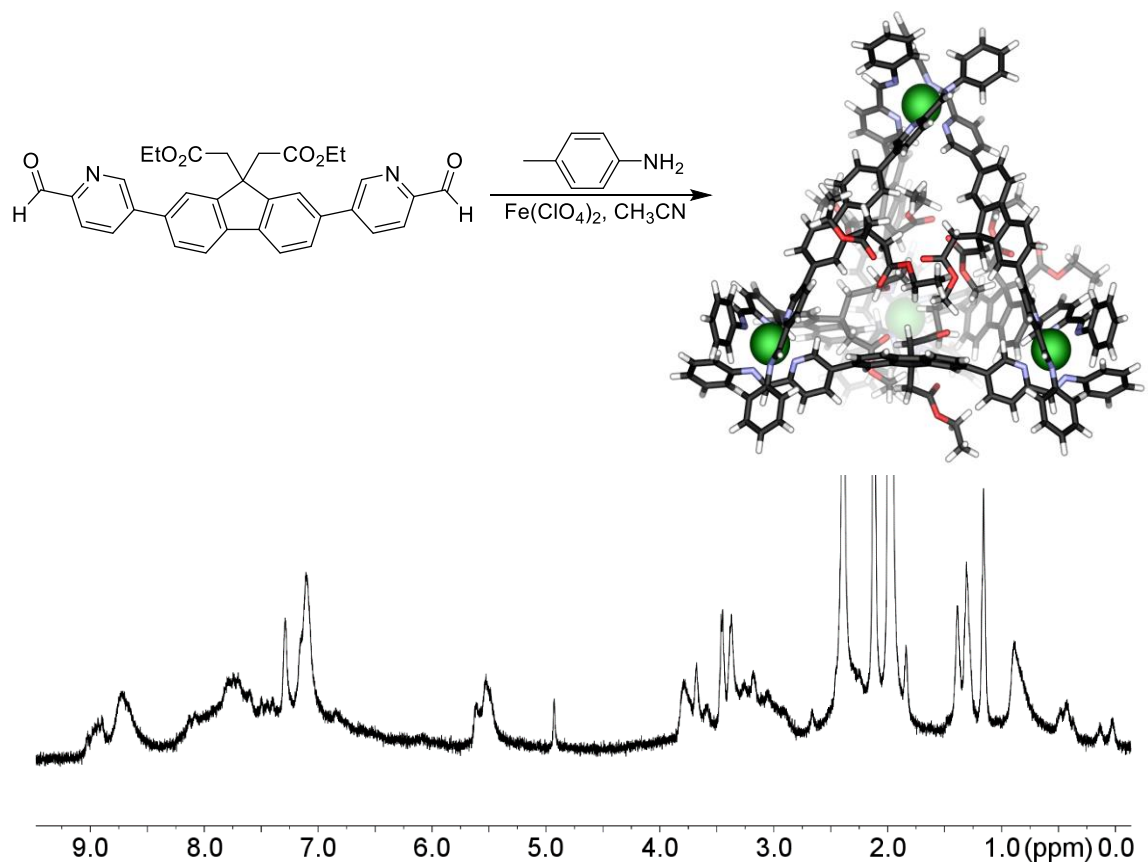


Figure 6.9. ^1H NMR spectrum of the multicomponent self-assembly of ligand **6.5** with $\text{Fe}(\text{ClO}_4)_2$ and *p*-toluidine (CD_3CN , 298 K, 500 MHz).

6.6 References

1. Harris, K.; Fujita, D.; Fujita, M. "Giant hollow M_nL_{2n} spherical complexes: structure, functionalization and applications." *Chem. Commun.* **2013**, *49*, 6703–6712.
2. Bogie, P. M.; Miller, T. F.; Hooley, R. J. "Synthesis and Applications of Endohedrally Functionalized Metal-Ligand Cage Complexes." *Isr. J. Chem.* **2019**, 130–139.
3. Ueda, Y.; Ito, H.; Fujita, D.; Fujita, M. "Permeable Self-Assembled Molecular Containers for Catalyst Isolation Enabling Two-Step Cascade Reactions." *J. Am. Chem. Soc.* **2017**, *139*, 6090–6093.
4. Sammes, P. G.; Yahiolu, G. "1,10-Phenanthroline: A Versatile Ligand." *Chem. Soc. Rev.* **1994**, *23*, 327–334.
5. Accorsi, G.; Listorti, A.; Yoosaf, K.; Armaroli, N. "1,10-Phenanthrolines: versatile building blocks for luminescent molecules, materials, and metal complexes." *Chem. Soc. Rev.* **2009**, *38*, 1690–1700.
6. Herrero, C.; Hughes, J. L.; Quaranta, A.; Cox, N.; Rutherford, A. W.; Leibl, W.; Aukauloo, A. "Intramolecular light induced activation of a Salen–Mn^{III} complex by a ruthenium photosensitizer." *Chem. Commun.* **2010**, *46*, 7605–7607.
7. Holloway, L. R.; McGarraugh, H. H.; Young, M. C.; Sontising, W.; Beran, G. J. O.; Hooley, R. J. "Structural Switching in Self-Assembled Metal-Ligand Helicate Complexes via Ligand-Centered Reactions." *Chem. Sci.* **2016**, *7*, 4423–4427.
8. Miller, T. F.; Holloway, L. R.; Nye, P. P.; Lyon, Y.; Beran, G. J. O.; Harman, W. H.; Julian, R. R.; Hooley, R. J. "Small Structural Variations have Large Effects on the Assembly Properties and Spin State of Room Temperature High Spin Fe(II) Iminopyridine Cages." *Inorg. Chem.* **2018**, *57*, 13386–13396.
9. Oshovosky, G. V.; Reinhoudt, D. N.; Verboom, W. "Supramolecular Chemistry in Water." *Angew. Chem. Int. Ed.* **2007**, *46*, 2366–2393.
10. Young, M. C.; Holloway, L. R.; Johnson, A. M.; Hooley, R. J. "A Supramolecular Sorting Hat: Stereocontrol in Metal-Ligand Self-Assembly by Complementary Hydrogen Bonding." *Angew. Chem. Int. Ed.* **2014**, *53*, 9832–9836.
11. Mal, P.; Briener, B.; Rissanen, K.; Nitschke, J. R. "White Phosphorus is Air-Stable Within a Self-Assembled Tetrahedral Capsule." *Science*, **2009**, *324*, 1697–1699.
12. Roberts, D. A.; Pilgrim, B. S.; Nitschke, J. R. "Covalent post-assembly modification in metallosupramolecular chemistry." *Chem. Soc. Rev.* **2018**, *47*, 626–644.

13. Bogie, P. M.; Holloway, L. R.; Ngai, C.; Miller, T. F.; Grewal, D. K.; Hooley, R. J. “A Self-Assembled Cage with Endohedral Acid Groups both Catalyzes Substitution Reactions and Controls their Molecularity.” *Chem. Eur. J.* **2019** ASAP DOI: 10.1002/chem.201902049
14. Bolliger, J. L.; Belenguer, A. M.; Nitschke, J. R. “Enantiopure Water-Soluble [Fe₄L₆] Cages: Host–Guest Chemistry and Catalytic Activity.” *Angew. Chem. Int. Ed.* **2013**, *52*, 7958–7962.
15. Holloway, L. R.; Young, M. C.; Beran, G. J. O.; Hooley, R. J. “High Fidelity Sorting of Remarkably Similar Components via Metal-Mediated Assembly.” *Chem. Sci.* **2015**, *6*, 4801–4806.
16. Castilla, A. M.; Miller, M. A.; Nitschke, J. R.; Smulders, M. M. J. “Quantification of Stereochemical Communication in Metal–Organic Assemblies.” *Angew. Chem. Int. Ed.* **2016**, *55*, 10616–10620.

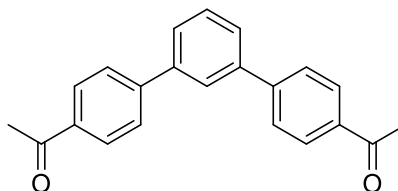
Chapter 7 - Experimental

7.1 General Information

^1H and ^{13}C NMR spectra were recorded on either a Varian Inova 400 MHz or 500 MHz NMR spectrometer, an Avance NEO 400 MHz spectrometer or a Bruker 600 MHz spectrometer and processed using MestReNova by Mestrelab Research S. L. gCOSY, NOESY, ROESY, TOCSY, and DOSY NMR were recorded on a Bruker 600 MHz spectrometer or a Varian Inova 400 MHz spectrometer equipped with TopSpin. HMBC and HSQC spectra were recorded on an Avance NEO 400 MHz spectrometer. Proton (^1H) chemical shifts are reported in parts per million (ppm) with respect to tetramethylsilane (TMS, $\delta = 0$). ^1H and ^{13}C spectra are referenced internally with respect to the solvent residual peak. Deuterated NMR solvents were obtained from Cambridge Isotope Laboratories, Inc., Andover, MA, and used without further purification. Mass spectra were recorded on an Agilent 6210 LC TOF mass spectrometer using electrospray ionization with fragmentation voltage set at 115 V and processed with an Agilent MassHunter Operating System for data collected in chapters 2-4. Mass spectrometric analysis for Chapter 5 was performed using a Thermo LTQ linear ion trap with a standard electrospray ionization source (Thermo Fisher Scientific, San Jose, CA, USA). Samples were directly infused at 3 $\mu\text{L}/\text{min}$ in 100 % MeCN, with the source voltage set to 3 kV, tube lens at 75 kV and the capillary temperature at 270 $^\circ\text{C}$. CID spectra were collected in ZoomScan mode where the isolation window = 5 m/z, normalized collision energy (nCE) = 30 and activation time = 30 ms. MS data was analyzed using Thermo XCalibur. Mass spectroscopic samples for Chapter 6 were infused into an Orbitrap Velos Pro mass spectrometer with the standard

HESI source at a flow rate of 3 $\mu\text{L}/\text{min}$. The spray voltage was 3 kV, capillary temperature was set to 170 $^{\circ}\text{C}$ and an S-lens RF level of 45% was applied. Full FTMS were acquired with a resolution of $r = 30,000$, and ambient ions were used as internal lock mass calibrants. CID spectra were collected in ZoomScan mode where the isolation window = 5 m/z , normalized collision energy (nCE) = 30 and activation time = 30 ms. MS data was analyzed using Thermo XCalibur. Predicted isotope patterns were prepared using ChemCalc.¹ All other materials were obtained from Aldrich Chemical Company, St. Louis, MO and were used as received. Solvents were dried through a commercial solvent purification system (Pure Process Technologies, Inc.). Molecular modeling (semi-empirical calculations) was performed using the AM1 force field using SPARTAN.²

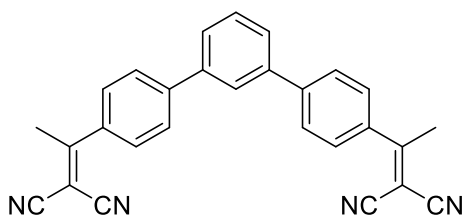
7.2 Experimental for Chapter 2



Synthesis of 1-(4''-Acetyl-[1,1';3',1'']terphenyl-4-yl)-ethanone (2.A):

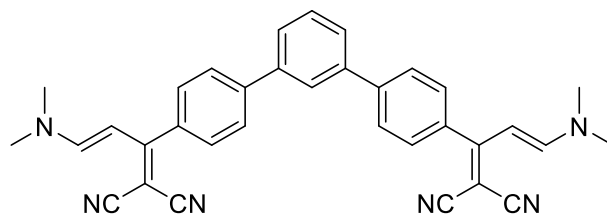
A 50 mL round bottom flask was charged with 1,3-Dibromobenzene (513 μL , 4.24 mmol), 4-acetylphenylboronic acid (1.8 g, 11.02 mmol) and bis(triphenylphosphine) palladium(II) dichloride (297 mg, 0.42 mmol). A 1:1:1 mixture of 2M K_2CO_3 in water:ethanol:toluene (24 mL) was added to the flask. The flask was purged with N_2 , and refluxed for 16 h. Methanol was added to the reaction mixture and the precipitate filtered via vacuum filtration to afford a tan solid. The solid was dissolved in dichloromethane and filtered through a silica/celite plug and the filtrate concentrated in vacuo (1.274 g, 4.05 mmol, 96

%). ^1H NMR: (500 MHz, CDCl_3) δ 8.07 (dt, $J = 8\text{ Hz}, 1.8\text{ Hz}, 4\text{ H}$), 7.83 (t, $J = 1.7\text{ Hz}, 1\text{ H}$), 7.74 (dt, $J = 8\text{ Hz}, 1.8\text{ Hz}, 4\text{ H}$), 7.66 (d, $J = 6.9\text{ Hz}, 2\text{ H}$), 7.58 (dd, $J = 8.5, 6.8\text{ Hz}, 1\text{ H}$), 2.66 (s, 6H). ^{13}C NMR: (125 MHz, CDCl_3) δ 197.6, 145.4, 140.7, 136.1, 129.6, 128.9, 127.3, 127.1, 126.2, 26.7. HRMS (ESI+) calc. $\text{C}_{22}\text{H}_{18}\text{O}_2$ 314.1307; found, 315.1475 ($\text{M}+\text{H}$) $^+$. IR 1667 cm^{-1} , 1600 cm^{-1} , 1355 cm^{-1} , 1286 cm^{-1} , 1187 cm^{-1} , 957 cm^{-1} , 832 cm^{-1} , 793 cm^{-1} , 693 cm^{-1} , 590 cm^{-1} .



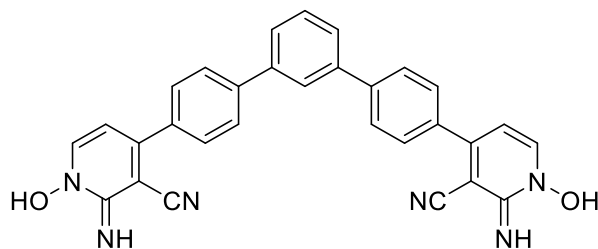
Synthesis of 2-Cyano-3-[4'-(2,2-dicyano-1-methyl-vinyl) [1,1';3',1'']terphenyl-4-yl]-but-2-enitrile (2.B):³

A 50 mL round bottomed flask was charged with **2.A** (410 mg, 1.30 mmol), malononitrile (430 mg, 6.52 mmol) and 4 mL THF. Pyridine (210 μL , 1.74 mmol) was then added to the flask followed by $\text{Ti}(\text{O}^i\text{Pr})_4$ (1.15 mL, 3.90 mmol). The reaction was allowed to stir at 25 $^\circ\text{C}$ for 16 h. The product was precipitated with water, and isolated via vacuum filtration. The resulting solid was then dissolved in acetone, filtered and concentrated in vacuo to afford a yellow solid (477 mg, 1.16 mmol, 89 %). ^1H NMR: (500 MHz, CDCl_3) δ 7.83 (s, 1H), 7.78 (d, $J = 8.4\text{ Hz}, 4\text{ H}$), 7.67 (d, $J = 8.4\text{ Hz}, 4\text{ H}$), 7.64 (dd, $J = 7.0, 1.7\text{ Hz}, 2\text{ H}$), 7.58 (t, $J = 7.0\text{ Hz}, 1\text{ H}$), 2.71 (s, 6H). ^{13}C NMR: (125 MHz, CDCl_3) δ 174.5, 144.7, 140.2, 134.9, 129.8, 128.1, 127.7, 127.2, 126.1, 112.9, 112.7, 84.5, 24.1. HRMS (ESI-) calc. $\text{C}_{28}\text{H}_{18}\text{N}_4$, 410.1531; found, 409.1464 ($\text{M}-\text{H}$) $^-$. IR 2223 cm^{-1} , 1601 cm^{-1} , 1571 cm^{-1} , 1476 cm^{-1} , 1390 cm^{-1} , 1302 cm^{-1} , 1007 cm^{-1} , 907 cm^{-1} , 836 cm^{-1} , 791 cm^{-1} , 731 cm^{-1} , 696 cm^{-1} .



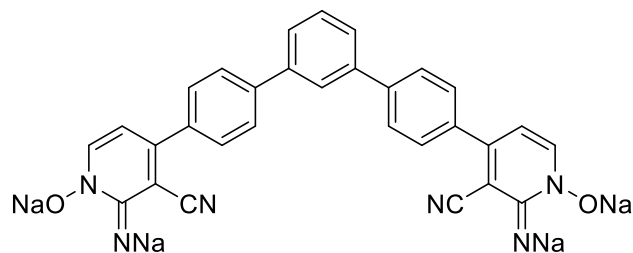
Synthesis of 2-(1-{4''-[2,2-Dicyano-1-(2-dimethylamino-vinyl)-vinyl]-[1,1';3',1'']terphenyl-4-yl}-3-dimethylamino-allylidene)-malononitrile (2.C):⁴

Compound **2.B** (0.1 M, 350 mg, 0.85 mmol) and Ac₂O (0.4 M, 32 μL, 0.34 mmol) were dissolved in 1 mL anhydrous DCM. The solution was stirred vigorously while DMF-DMA (270 μL, 2.04 mmol) was added to the reaction mixture. The reaction was allowed to stir at room temperature for 24 h. The solvent was removed under vacuum to give a red residue which was triturated with water and filtered to yield the final product (354 mg, 0.68 mmol, 80 %). ¹H NMR: (500 MHz, CDCl₃) δ 7.84 (s, 1H), 7.73 (d, *J* = 8.1 Hz, 4H), 7.64 (dd, *J* = 6.9 Hz, 1.5 Hz, 2H), 7.56 (dd, *J* = 8.4 Hz, 6.9 Hz, 1H), 7.38 (d, *J* = 8.1 Hz, 4H), 6.73 (d, *J* = 12.4 Hz, 2H), 5.87 (d, *J* = 12.4 Hz, 2H), 3.08 (s, 6H), 3.05 (s, 6H). ¹³C NMR: (125 MHz, CDCl₃) δ 171.3, 155.9, 142.6, 140.7, 133.9, 129.5, 129.4, 127.4, 126.6, 126.2, 116.7, 116.1, 98.1, 64.9, 45.8, 37.7. HRMS calc. C₃₄H₂₈N₆, 520.2375; found, 565.2356 (M+HCOO)⁻. IR 2200 cm⁻¹, 1613 cm⁻¹, 1503 cm⁻¹, 1463 cm⁻¹, 1408 cm⁻¹, 1378 cm⁻¹, 1333 cm⁻¹, 1261 cm⁻¹, 1109 cm⁻¹, 792 cm⁻¹, 551 cm⁻¹.



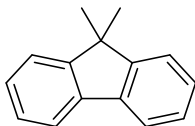
Synthesis of Phenyl-1,3-di-(1-Hydroxy-2-imino-4-phenyl-1,2-dihydro-pyridine-3-carbonitrile) (2.1):⁵

Compound **2.C** (604 mg, 1.16 mmol) was dissolved in anhydrous DCM (3.5 mL). Hydroxylamine hydrochloride (484 mg, 6.96 mmol) and triethylamine (970 μ L, 6.96 mmol) were added to the reaction mixture which was allowed to stir for 24 h, then the solvent removed under vacuum. The residue was then triturated in water and isolated via vacuum filtration to afford a yellow-orange solid (551 mg, 1.11 mmol, 95 %). ¹H NMR: (500 MHz, DMSO-*d*₆) δ 8.49 (d, *J* = 6.8 Hz, 2H), 8.11 (s, 1H), 8.04 (s, 4H), 8.01 (d, *J* = 8.2 Hz, 4H), 7.81 (d, *J* = 7.7 Hz, 2H), 7.76 (d, *J* = 8.1 Hz, 4H), 7.64 (t, *J* = 7.7 Hz, 1H), 6.92 (d, *J* = 6.7 Hz, 2H). ¹³C NMR: (125 MHz, DMSO-*d*₆) δ 153.2, 142.2, 141.4, 140.4, 140.4, 135.4, 130.3, 129.3, 127.8, 126.9, 125.8, 115.5, 112.8, 90.1. ITMS + p ESI calc. C₃₀H₂₀N₆O₂, 496.1648; found 497.2526 (M+H)⁺. IR 3105 cm⁻¹, 1618 cm⁻¹, 1454 cm⁻¹, 1215 cm⁻¹, 791 cm⁻¹. Sample was purified via treatment with conc. HCl and analyzed as the salt. Elemental Analysis: Theoretical (C₃₀H₂₁ClN₆O₂•H₂O): C: 65.39, H: 4.21, Cl: 6.53, N: 15.05, O: 8.81. Found: C: 66.71, H: 4.21, N: 14.69, O: 8.45.



Synthesis of Anionic Ligand 2.1 (Na•2.1):

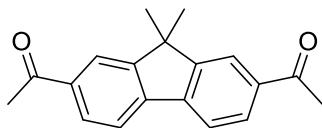
Ligand **2.1** (50 mg, 0.10 mmol) was dissolved in anhydrous DCM (30 mL) and stirred vigorously. NaH (16 mg, 0.40 mmol) was added to the reaction mixture which was allowed to stir overnight. The stirring was stopped and the solution allowed to settle for 1 h before being filtered to afford an orange powder (35 mg, 0.06 mmol, 60 %). ^1H NMR: (500 MHz, $\text{DMSO-}d_6$) δ 8.06 (s, 1H), 7.89 (d, $J = 8.1$ Hz, 4H), 7.76 (m, 5H), 7.64 (d, $J = 8.1$ Hz, 4H), 5.54 (d, $J = 6.0$ Hz, 2H). ^{13}C NMR: (125 MHz, $\text{DMSO-}d_6$) δ 158.8, 143.2, 140.8, 140.0, 138.4, 136.7, 130.1, 128.7, 127.2, 126.4, 125.4, 124.5, 121.1, 98.4, 85.2.



Synthesis of 9,9-dimethyl-9H-fluorene:⁶

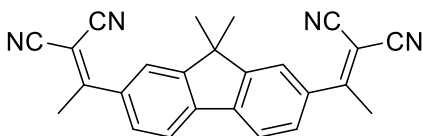
Fluorene, (1 g, 6.01 mmol) was placed in a Schlenk flask along with 3 eq potassium tert-butoxide (2.02 g, 18.05 mmol). The flask was purged with N_2 followed by the addition of 30 mL THF. The orange solution was stirred for 10 minutes. Iodomethane (1.12 mL, 18.05 mmol) was added slowly to the flask over a period of 10 minutes. The reaction was heated at 65 °C for 16 h then cooled, diluted with 100 mL ice water and extracted with DCM. The organic layer was washed with brine and saturated sodium bicarbonate (30 mL each), dried with magnesium sulfate, and the solvent removed in vacuo to afford yellow waxy solid

(1.074 g, 5.53 mmol, 92 %). ^1H NMR spectra were in agreement with previously reported results.



Synthesis of **1**, 1-(7-Acetyl-9,9-dimethyl-9H-fluoren-2-yl)-ethanone:⁷

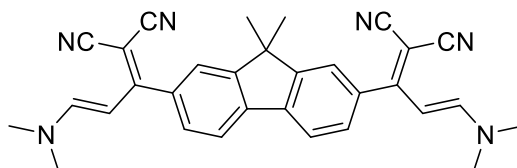
Acetyl chloride (1.83 mL, 25.74 mmol) was dissolved in 50 mL dichloromethane in a round bottomed flask. Aluminum chloride (3.43 g, 25.74 mmol) was added and the flask placed in an ice bath with stirring. Dimethyl fluorene (1 g, 5.15 mmol) was dissolved in 5 mL DCM and added dropwise to the cooled flask over 5 minutes. The flask was removed from the ice bath and heated to reflux for 2.5 hours or until complete via TLC analysis. Once complete, the reaction mixture was poured over 150 g of ice and extracted with DCM. The organic layer was washed with brine (2 x 50 mL) and saturated sodium bicarbonate (2 x 50 mL), dried over magnesium sulfate, and the solvent removed in vacuo to give a tan crystalline solid (1.120 g, 4.02 mmol, 78 %). ^1H NMR spectra were in agreement with previously reported results.



Synthesis of **2-Cyano-3-[7-(2,2-dicyano-1-methyl-vinyl)-9,9-dimethyl-9H-fluoren-2-yl]-but-2-enitrile (7.1)**:

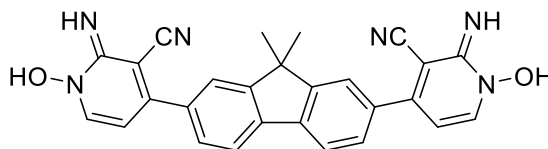
Synthesized from 1,1'-diacetyl-9,9-dimethyl-9H-fluorene using the same procedure reported for **2.B**. Isolated as an orange powder (984 mg, 2.63 mmol, 80 %). ^1H NMR: (500

MHz, CDCl₃) δ 7.87 (*d*, *J* = 7.9 Hz, 2H), 7.70 (*s*, 2H), 7.59 (*d*, *J* = 7.2 Hz, 2H), 2.71 (*s*, 6H), 1.56 (*s*, 6H). ¹³C NMR: (125 MHz, CDCl₃) δ 175.0, 154.9, 141.7, 135.8, 127.1, 122.3, 121.4, 113.1, 112.8, 84.4, 47.7, 26.5, 24.2. HRMS (ESI-) calc. C₂₅H₁₈N₄, 374.1531; found, 373.1459 (M-H)⁻.



Synthesis of 2-Cyano-3-{7-[2,2-dicyano-1-(2-dimethylamino-vinyl)-vinyl]-9,9-dimethyl-9H-fluoren-2-yl}-5-dimethylamino-allylidene-malononitrile (7.2):

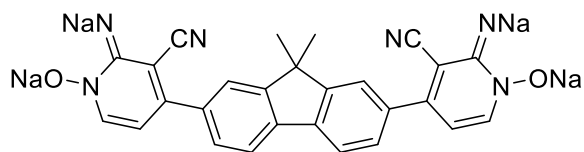
synthesized from **7** using the same procedure reported for **2.C**, isolated as an orange waxy solid (1.033 g, 2.13 mmol, 83 %). ¹H NMR: (500 MHz, CDCl₃) δ 7.81 (*d*, *J* = 7.8 Hz, 2H), 7.39 (*s*, 2H), 7.27 (*t*, *J* = 8.8 Hz, 2H), 6.73 (*d*, *J* = 12.4 Hz, 2H), 5.87 (*d*, *J* = 12.4 Hz, 2H), 3.06 (*s*, 6H), 3.05 (*s*, 6H), 1.55 (*s*, 6H). ¹³C NMR: (125 MHz, DMSO-*d*₆) δ 172.0, 156.1, 154.2, 140.1, 134.3, 128.1, 123.6, 120.5, 116.7, 116.3, 98.0, 47.3, 45.8, 37.7, 26.7. HRMS (ESI-) calc. C₃₁H₂₈N₆, 484.2375; found, 529.2357 (M+HCOO)⁻.



Synthesis of 9,9-dimethyl-9H-fluorene-1,1'-di-(1-Hydroxy-2-imino-4-phenyl-1,2-dihydro-pyridine-3-carbonitrile) (2.2):

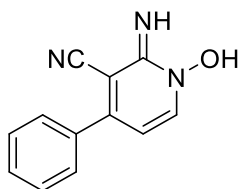
synthesized from **7.2** using the same procedure reported for Compound **2.1**. Isolated as a tan powder (1.080 g, 2.33 mmol, 92 %). ¹H NMR: (500 MHz, DMSO-*d*₆) δ 8.44 (*d*, *J* = 6.7 Hz, 2H), 8.07 (*d*, *J* = 7.9 Hz, 2H), 7.89 (*s*, 2H), 7.82 (*s*, 4H), 7.65 (*d*, *J* = 8.1 Hz, 2H), 6.91

(d, $J = 6.7$ Hz, 2H), 1.54 (s, 6H). ^{13}C NMR: (125 MHz, $\text{DMSO-}d_6$) δ 154.6, 153.2, 143.0, 140.4, 139.4, 135.6, 128.1, 123.6, 121.5, 115.6, 112.9, 90.2, 47.5, 26.8. HRMS (ESI-) calc. $\text{C}_{27}\text{H}_{20}\text{N}_6\text{O}_2$, 460.1648; found, 459.1575 (M-H) $^-$. Purified and isolated as the HCl salt. Elemental Analysis: Theoretical ($\text{C}_{27}\text{H}_{20}\text{ClN}_6\text{O}_2$): C: 65.52, H: 4.45, Cl: 7.12, N: 16.88, O: 6.03. Found: C: 66.86, H: 4.69, N: 17.03, O: 6.30.



Synthesis of Anionic Ligand 2 (Na•2.2):

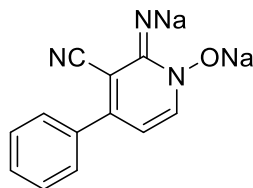
Na•2.2 was synthesized using the procedure reported for Na•2.1. Isolated as a dark brown powder (33 mg, 0.06 mmol, yield = 56 %). ^1H NMR: (500 MHz, $\text{DMSO-}d_6$) δ 7.93 (d, $J = 7.8$ Hz, 2 H), 7.75 (d, $J = 6.2$ Hz, 4H), 7.72 (s, 2H), 7.53 (d, $J = 7.8$ Hz, 2H), 5.59 (d, $J = 6.3$ Hz, 2H), 1.53 (s, 6H). ^{13}C NMR: (125 MHz, $\text{DMSO-}d_6$) δ 156.5, 154.3, 143.5, 138.9, 138.3, 137.2, 127.7, 123.2, 120.9, 118.9, 104.7, 87.42, 55.4, 47.3, 27.0.



Synthesis of 1-Hydroxy-2-imino-4-phenyl-1,2-dihydro-pyridine-3-carbonitrile (2.3):

(3-(dimethylamino)-1-phenyl-2-propenylidene) malononitrile (332 mg, 1.44 mmol) was dissolved in anhydrous DCM (3 mL). To the solution was added hydroxylamine hydrochloride (484 mg, 4.33 mmol) and trimethylamine (970 μL , 4.33 mmol). The mixture was allowed to stir for 24 h, then reduced under vacuum. The solid was then sonicated in

water and isolated via vacuum filtration to afford a yellow powder (128 mg, 0.60 mmol, 42 %). ^1H NMR: (500 MHz, $\text{DMSO-}d_6$) δ 8.41 (d, $J = 6.7$ Hz, 1H), 7.80 (s, 2H), 7.60 (d, $J = 7.3$ Hz, 2H), 7.52 (p, $J = 6.2$ Hz, 3H), 6.78 (d, $J = 6.7$ Hz, 1H). ^{13}C NMR: (125 MHz, $\text{DMSO-}d_6$) δ 153.1, 142.8, 140.4, 140.3, 136.2, 129.9, 129.2, 128.7, 115.4, 112.8, 112.8, 90.3. HRMS (ESI-) calc. $\text{C}_{12}\text{H}_9\text{N}_3\text{O}$, 211.0746; found, 210.0673 (M-H) $^-$. Elemental Analysis: Theoretical ($\text{C}_{12}\text{H}_9\text{N}_3\text{O}$): C: 68.24, H: 4.29, N: 19.89, O: 7.57. Found: C: 68.31, H: 4.33, N: 20.08, O: 7.28.



Synthesis of Anionic Ligand 3 (Na•2.3):

Synthesized from **2.3** using the procedure reported for Na•**2.1** (yield = 26 mg, 0.101 mmol, 43 %). ^1H NMR: (500 MHz, $\text{DMSO-}d_6$) δ 7.72 (d, $J = 6.3$ Hz, 1H), 7.50 (d, $J = 7.4$ Hz, 2H), 7.45 (t, $J = 7.5$ Hz, 2H), 7.40 (t, $J = 6.9$ Hz, 1H), 6.61 (s, 1H), 5.45 (d, $J = 6.3$ Hz, 1H). ^{13}C NMR: δ (125 MHz, $\text{DMSO-}d_6$) 158.7, 143.7, 139.2, 136.6, 136.5, 128.6, 128.2, 121.1, 98.3, 98.3.

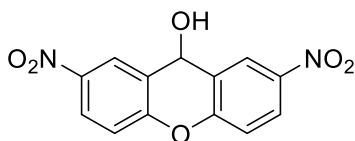
Experimental Procedures

Complex Formation: The deprotonated ligand (Na•**2.1**, Na•**2.2**, or Na•**2.3**) was dissolved in DMSO. The appropriate amount of metal salt for the ligand (0.66 eq, 0.66 eq, and 0.33 eq respectively) were added to the solution which was placed in an ultrasonication bath for 5 min. This resulted in complex formation indicated by a color change in the solution and

in the emissive properties. Complex formation was then confirmed by NMR, UV/Vis and mass spectrometry.

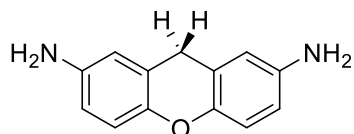
7.3 Experimental for Chapter 3

Cages **3.2**,⁸ **1.3**,⁹ **3.5**,¹⁰ **3.6**¹⁰ and **3.8**¹¹ were synthesized according to literature procedures.



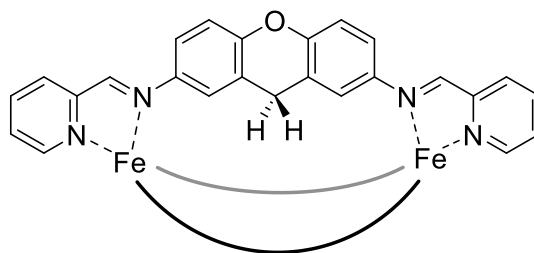
Synthesis of 2,7-Dinitroanthrol:

2,7-Dinitroanthrone (1.00 g, 3.49 mmol) was placed in a 250 mL round bottomed flask and dissolved in 100 mL of dry tetrahydrofuran and 25 mL of methanol. Sodium borohydride (150 mg, 3.97 mmol) was slowly added to the flask and the reaction was allowed to stir at room temperature. After 12 h, a second portion of sodium borohydride (30 mg) was added to the flask and the reaction stirred for one hour. The reaction mixture was then poured into a beaker containing 500 mL of ice water. The mixture was rapidly stirred and brought to a pH of 3 using 1M hydrochloric acid. The product was then filtered and collected as a tan solid (942 mg, 85 %). ¹H NMR (400 MHz, DMSO-*d*₆): δ 8.46 (d, *J* = 2.7 Hz, 2H), 8.23 (dd, *J* = 9.0, 2.7 Hz, 2H), 7.46 (d, *J* = 9.1 Hz, 2H), 6.84 (d, *J* = 6.8 Hz, 1H), 5.90 (d, *J* = 6.5 Hz, 1H). ¹³C NMR (100 MHz, DMSO-*d*₆): δ 154.2, 144.2, 126.1, 125.4, 124.7, 118.5, 60.7. HRMS (ESI) *m/z* calcd. for C₁₃H₉N₂O₆ ([M•H]⁺) 289.0234, found 289.0259.



Synthesis of 2,7-Diaminoxanthene (XE):

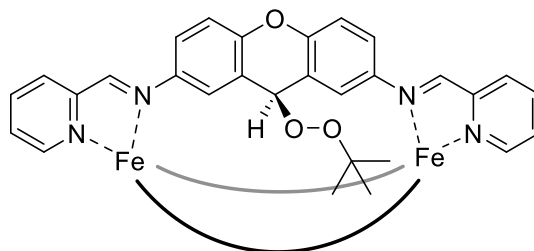
2,7-Dinitroxanthol (300 mg, 1.1 mmol) was placed in a long-necked Schlenk flask with a septum and stir bar and the flask was purged with nitrogen. Methanol (15 mL) and a large excess of Raney nickel slurry in water (5 mL) were injected into the flask and the system was quickly purged with nitrogen a second time. Hydrazine monohydrate (1 mL) was slowly injected into the flask and the reaction allowed to stir overnight at room temperature. The mixture was diluted with additional methanol (25 mL) and the solid catalyst was carefully removed via filtration through a Celite plug. The filtrate solvent was removed *in vacuo* to afford clean product as a pale yellow solid (291 mg, 76 %). ^1H NMR (400 MHz, DMSO- d_6): δ 6.65 (d, $J = 8.1$ Hz, 2H), 6.37 (m, 4H), 4.67 (s, 4H), 3.71 (s, 2H). ^{13}C NMR (100 MHz, DMSO- d_6): δ 144.4, 143.8, 121.0, 116.7, 114.2, 113.9, 28.4. HRMS (ESI) m/z calcd. for $\text{C}_{13}\text{H}_{13}\text{N}_2\text{O}$ ([dianiline **XE**•H] $^+$) 213.0493, found 213.1062.



Synthesis of Xanthene cage 3.1:

Dianiline **XE** (100 mg, 0.47 mmol), 2-pyridine carboxaldehyde (90 μL , 0.94 mmol) and $\text{Fe}(\text{ClO}_4)_2 \cdot 4\text{H}_2\text{O}$ (103 mg, 0.31 mmol) were combined in anhydrous acetonitrile (10 mL) in a 25 mL round-bottomed flask under a blanket of nitrogen gas. The solution was heated

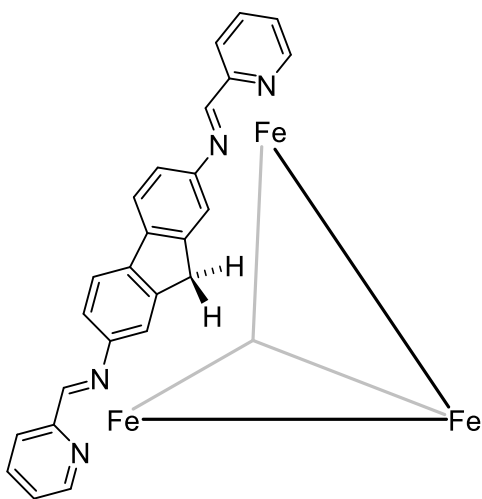
at 45 °C for 10 h with stirring. The reaction was diluted with diethyl ether (25 mL), and the resulting precipitate was filtered. After drying, the product was isolated as a purple solid (201 mg, 80 %). ¹H NMR (400 MHz; CD₃CN) δ 9.38 (s, 2H), 8.69 (d, *J* = 7.5 Hz, 2H), 8.35 (t, *J* = 7.3 Hz, 2H), 7.9 (t, *J* = 5.4 Hz, 2H), 7.71 (d, *J* = 5.1 Hz, 2H), 7.12 (d, *J* = 8.1 Hz, 2H), 5.9 (d, *J* = 6.9 Hz, 2H), 5.01 (s, 2H), 3.55 (d, *J* = 19.9 Hz, 1H) 2.72 (d, *J* = 19.9 Hz, 1H). ¹³C NMR (125 MHz, CD₃CN): δ 173.6, 157.1, 156.1, 151.4, 148.2, 139.6, 132.2, 131.4, 124.1, 121.7, 121.0, 27.5. HRMS (ESI) *m/z* calcd. for C₇₅H₅₄Cl₃Fe₂N₁₂O₁₅ ([**3.1**•(ClO₄)₃]⁺) 1581.3561, found 1581.3427. Elemental Analysis: Calc. for C₇₅H₅₄Cl₄Fe₂N₁₂O₁₉ C: 53.59; H: 3.24; N: 10.01; Found: C: 53.46; H: 3.35; N: 9.97.



Oxidation of *meso*-helicate **3.1** to xanthyl peroxide cage **3.3**:

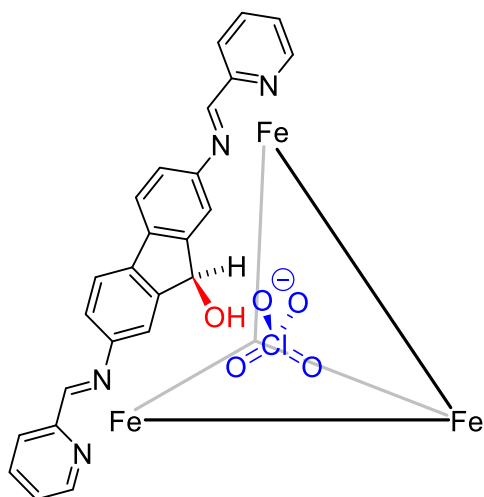
One equivalent of xanthene *meso*-helicate **3.1** (30 mg, 0.018 mmol) was dissolved in 2 mL of acetonitrile in a 10 mL round bottomed flask. 3.3 mol.-eq. of *tert*-butyl hydroperoxide 70 % solution in water (7.6 μL 0.059 mmol) was then added, and the reaction mixture was allowed to stir at room temperature for 8 h. Diethyl ether (10 mL) was then added to the solution, and xanthyl peroxide cage **3.3** precipitated as a purple solid that was filtered and dried (29 mg, 88 %). ¹H NMR (400 MHz; CD₃CN) δ 8.99 (s, 2H), 8.65 (d, *J* = 7.4 Hz, 2H), 8.41 (t, *J* = 7.5 Hz, 2H), 7.82 (t, *J* = 7.4 Hz, 2H), 7.41 (d, *J* = 5.3 Hz, 2H), 7.36 (d, *J* = 8.7 Hz, 2H), 6.22 (dd, *J* = 8.6, 2.6 Hz, 2H), 5.19 (s, 2H), 4.11 (s, 1H), 1.14 (s, 9H). ¹³C NMR

(125 MHz, CD₃CN) δ 175.4, 157.5, 156.1, 151.7, 147.4, 139.7, 132.1, 130.5, 124.7, 124.5, 119.1, 117.8, 80.7, 72.9, 25.6. HRMS (ESI) m/z calcd. for C₈₇H₇₈Fe₂N₁₂O₉ (**3.3**⁴⁺) 386.5788, found 386.6403. Elemental Analysis: Calc. for C₈₇H₇₈Cl₄Fe₂N₁₂O₂₅ C: 53.72; H: 4.04; N: 8.64; Found: C: 53.67; H: 4.10; N: 8.58.



Synthesis of Fluorene Cage **3.4**:

2,7-Diaminofluorene **F** (100 mg, 0.51 mmol), 2-pyridine carboxaldehyde (96.9 μ L, 1.02 mmol) and Fe(ClO₄)₂•4H₂O (111 mg, 0.34 mmol) were combined in anhydrous acetonitrile (10 mL) in a 50 mL Schlenk flask under a nitrogen atmosphere, followed by heating to 60 °C for 10 h. The solution was cooled to room temperature, diluted with diethyl ether (30 mL), and the resulting precipitate was filtered. Product was collected as a purple solid (187 mg, 94 %). ¹H NMR and ¹³C NMR: Complex mixture of isomers. HRMS (ESI) m/z calcd for C₁₅₀H₁₀₈Cl₈Fe₄N₂₄O₃₂ ([**3.4**•(ClO₄)₂]⁶⁺) 444.5932, found 444.8816. Elemental Analysis: Calc. for C₁₅₀H₁₀₈Cl₈Fe₄N₂₄O₃₂ C: 55.17; H: 3.33; N: 10.29; Found: C: 55.25; H: 3.37; N: 10.39.

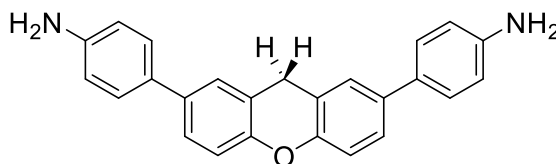


Oxidation of fluorene cage **3.4** to fluorenol cage **1.3**:

One equivalent of fluorene cage **3.4** (30 mg, 0.009 mmol) was dissolved in acetonitrile (2 mL) in a 10 mL round bottomed flask. *Tert*-butyl hydroperoxide 70 % solution in water (7.6 μ L, 0.055 mmol) and sodium perchlorate (1 mg) were added, and the reaction was allowed to stir at 50°C for 24 h. Diethyl ether (10 mL) was added to the solution, and fluorenol cage **5** precipitated as a purple solid that was filtered and dried (28 mg, 87 %). ^1H NMR and ^{13}C NMR consistent with published spectra.⁹ HRMS (ESI) m/z calcd for $\text{C}_{150}\text{H}_{108}\text{Cl}_2\text{Fe}_4\text{N}_{24}\text{O}_{14}$ ($[\mathbf{1.3}\cdot(\text{ClO}_4)_2]^{6+}$) 460.5881, found 460.8312.

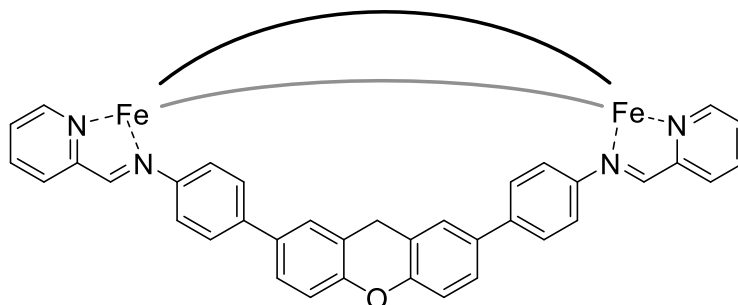
General Procedure for Control Ligand Oxidations: Xanthene control ligand (25 mg, 0.072 mmol) was placed in in a 10 mL round bottomed flask and dissolved in acetonitrile (5 mL). *Tert*-butyl hydroperoxide 70 % solution in water (10.1 μ L 0.078 mmol) and catalytic $\text{Fe}(\text{ClO}_4)_2\cdot 4\text{H}_2\text{O}$ (0.2 mg, 0.007 mmol) were added. The reaction was allowed to stir at room temperature (or at 50 °C) for 8 h. Chloroform (5 mL) was added to the flask and the reaction products were extracted with brine (2 x 5 mL). The organic layer was dried with MgSO_4 and the solvent was removed *in vacuo*. All products were obtained in 89 – 95

% yields. The spectra of the oxidation products was compared to those of independently synthesized ketone and alcohol products.



Synthesis of 4,4'-(9H-xanthene-2,7-diyl)dianiline (DPX):

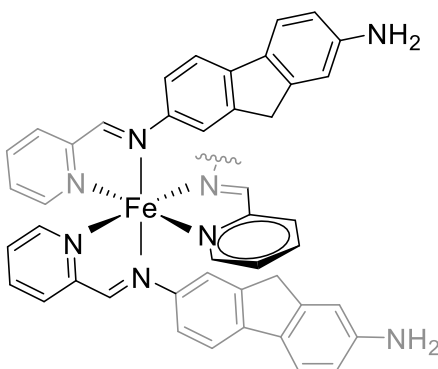
Di-tert-butyl ((9H-xanthene-2,7-diyl)bis(4,1-phenylene))dicarbamate (see Supporting Information for synthesis) (150 mg, 0.27 mmol) was placed in a 10 mL round bottomed flask with a stir bar. Trifluoroacetic acid (neat, 2 mL) was slowly added to the flask. The reaction mixture was allowed to stir at room temperature for 12 hours. The reaction mixture was then slowly added dropwise to a beaker containing 10 g crushed ice and 30 mL saturated sodium bicarbonate solution. When all the reaction mixture had been added, the pH of the solution was tested, and more bicarbonate solution was added as necessary to reach a pH of 8. The solid product was then filtered, washed with hexane and dried to give DPX as a tan solid (92 mg, 0.252 mmol, 92 %). ^1H NMR (400 MHz, DMSO- d_6) δ 7.43 (d, $J = 2.2$ Hz, 2H), 7.39 (dd, $J = 8.5, 2.3$ Hz, 2H), 7.36 – 7.32 (m, 4H), 7.07 (d, $J = 8.4$ Hz, 2H), 6.66 – 6.62 (m, 4H), 5.18 (s, 4H), 4.13 (s, 2H). ^{13}C NMR (151 MHz, DMSO) δ 150.10 (s), 148.45 (s), 136.26 (s), 127.35 (s), 127.26 (s), 126.30 (s), 125.09 (s), 120.97 (s), 116.70 (s), 114.65 (s), 27.66 (s). (HRMS (ESI $^+$) m/z calcd for $\text{C}_{25}\text{H}_{20}\text{N}_2\text{O}$ 464.21, found 465.1422 (M+H) $^+$).



Synthesis of cage 3.7:

DPX (50 mg, 0.137 mmol) was added to a 25 mL round bottom and dissolved in acetonitrile (5 mL). 2-pyridinecarboxaldehyde (26.1 μ L, 0.274 mmol) was added to the solution followed by $\text{Fe}(\text{OTf})_2$ (38.93 mg, 0.091 mmol), the reaction was heated to 65 $^{\circ}\text{C}$ for 16 h. The reaction was cooled to room temperature and diluted with Et_2O . The solution was filtered, and the resulting precipitate was washed with EtOAc to give $\text{Fe}_2\text{DPX}_3\cdot\text{Py}_6$ as a purple powder (95 mg, 0.041 mmol, 90 %). ^1H NMR and ^{13}C NMR: Complex mixture of two isomers (helicate and mesocate are both present). ^1H NMR (400 MHz, CD_3CN) δ 9.02 (s, 1H), 8.90 (s, 2H), 8.62 – 8.53 (m, 4H), 8.43 (t, $J = 7.3$ Hz, 4H), 7.84 – 7.76 (m, 4H), 7.73 (s, 1H), 7.64 (s, 2H), 7.60 (d, $J = 8.7$ Hz, 3H), 7.54 (t, $J = 8.2$ Hz, 6H), 7.47 (d, $J = 5.8$ Hz, 2H), 7.43 (d, $J = 6.8$ Hz, 7H), 7.27 – 7.20 (m, 4H), 5.49 (d, $J = 7.6$ Hz, 2H), 5.26 (s, 3H), 4.56 (s, 1H), 4.22 (dd, $J = 37.3, 18.5$ Hz, 2H). ^{13}C NMR (101 MHz, CD_3CN) δ 174.81, 174.56, 158.57, 158.38, 156.20, 153.53, 152.61, 150.02, 149.46, 140.59, 140.00, 135.05, 134.52, 131.63, 131.37, 130.42, 130.10, 128.77, 128.07, 127.74, 127.46, 126.31, 126.01, 125.01, 123.78, 122.65, 122.31, 122.10, 121.89, 118.10, 117.23, 28.83, 28.45. HRMS (ESI) m/z calcd for $\text{C}_{112}\text{H}_{78}\text{F}_3\text{Fe}_2\text{N}_{12}\text{O}_6\text{S}$ ($[\text{Fe}_2(\text{DPX})_3\cdot\text{Py}_6(\text{OTf})]^{3+}$) 629.4852, found 629.48.

General Displacement Conditions. To an NMR tube was added 400 μL of a 7.3 mM solution of mesocate $\text{Fe}_2\text{X}_3\cdot\text{Py}_6$ in CD_3CN . This solution was checked via ^1H NMR prior to the reaction to confirm the integrity of the sample. To this solution was added 100 μL of the chosen dianiline (87 mM, yielding a final dianiline concentration of 17.4 mM and $\text{Fe}_2\text{X}_3\cdot\text{Py}_6$ at a concentration of 5.8 mM). The sample was then shaken by hand for ~ 30 s. A ^1H NMR spectrum was immediately taken following mixing. Periodic monitoring of the sample was then conducted via ^1H NMR to determine the degree and products of the displacement reactions.



Characterization of $\text{FeF}_3\cdot\text{Py}_3$:

Mesocate **3.2** (20 mg, 0.012 mmol) was added to a 5 mL round bottom flask and dissolved in acetonitrile (1.6 mL). Dianiline **F** (7 mg, 0.036 mmol) was dissolved in 200 μL acetonitrile then added to the cage solution. The solution was shaken for 5 s to facilitate mixing and allowed to sit. After 3 h diethyl ether was added to the solution and the reaction was filtered as a brown powder (7 mg, 0.006 mmol, 54 %). **Fac**: ^1H NMR (400 MHz, CD_3CN) δ 8.87 (s, 1H), 8.47 (d, $J = 7.6$ Hz, 1H), 8.37 (t, $J = 7.5$ Hz, 1H), 7.76 (s, 1H), 7.64 (d, $J = 7.0$ Hz, 1H), 7.24 (d, $J = 8.6$ Hz, 2H), 5.47 (d, $J = 8.0$ Hz, 1H), 5.40 (s, 1H), 3.52 (s, 2H), 3.47 (s, 2H). **Mer**: ^1H NMR (400 MHz, CD_3CN) δ 9.40 (s, 1H), 9.16 (s, 1H), 8.81

(s, 1H), 8.60 (d, $J = 5.3$ Hz, 2H), 8.56 (d, $J = 8.0$ Hz, 2H), 8.50 (d, $J = 5.4$ Hz, 1H), 8.27 (t, $J = 7.6$ Hz, 1H), 7.95 – 7.91 (m, 2H), 7.84 (d, $J = 8.8$ Hz, 2H), 7.76 (d, $J = 4.8$ Hz, 2H), 7.74 – 7.71 (m, 2H), 7.55 (d, $J = 4.4$ Hz, 1H), 7.53 (d, $J = 6.2$ Hz, 2H), 7.51 (d, $J = 7.7$ Hz, 2H), 7.44 (s, 1H), 7.42 (d, $J = 5.7$ Hz, 1H), 7.40 (s, 1H), 7.32 (d, $J = 8.9$ Hz, 2H), 7.19 (d, $J = 8.1$ Hz, 1H), 6.81 (t, $J = 12.7$ Hz, 6H), 6.76 (d, $J = 13.1$ Hz, 3H), 6.70 (dd, $J = 8.1, 1.9$ Hz, 2H), 6.64 (ddd, $J = 13.8, 8.2, 1.9$ Hz, 3H), 6.55 (d, $J = 8.1$ Hz, 1H), 6.30 (d, $J = 8.1$ Hz, 1H), 6.17 (s, 1H), 3.74 (s, 2H), 3.39 (s, 2H) ^{13}C NMR (101 MHz, CD_3CN) δ 195.21, 177.09, 173.85, 171.69, 170.12, 159.60, 159.02, 158.80, 157.38, 156.92, 156.23, 149.75, 149.40, 149.24, 148.33, 146.37, 144.76, 144.51, 139.34, 139.11, 138.93, 131.74, 131.14, 130.55, 129.93, 129.44, 128.75, 124.57, 123.78, 122.25, 121.97, 121.80, 121.28, 121.11, 119.80, 119.55, 119.22, 118.81, 117.91, 114.09, 111.23, 111.15, 110.53, 107.65, 36.99, 36.44. HRMS (ESI) m/z calcd for $\text{C}_{57}\text{H}_{45}\text{FeN}_9$ ($[\text{Fe}(\mathbf{F})_3\cdot\text{Py}_3]^{2+}$) 455.6568, found 455.65. Elemental Analysis: Theoretical ($\text{C}_{57}\text{H}_{46}\text{Cl}_3\text{FeN}_9\text{O}_{12}$): C: 56.52, H: 3.83, Cl: 8.78, Fe: 4.61, N: 10.41, O: 15.85. Found: C: 56.25, H: 3.84, N: 9.89.

Computational Methods

To compare the stabilities of the various species involved, we constructed a series of reaction equilibria with total stoichiometry of 2 Fe, 3 **X**, and 6 **F** for each group of species:

$$\text{Fe}_2\mathbf{X}_3 + 6 \mathbf{F} \rightleftharpoons \text{Fe}_2\mathbf{X}_2\mathbf{F} + 5 \mathbf{F} + 1 \mathbf{X} \rightleftharpoons \text{Fe}_2\mathbf{XF}_2 + 4 \mathbf{F} + 2 \mathbf{X} \rightleftharpoons \text{Fe}_2\mathbf{F}_3 + 3 \mathbf{F} + 3 \mathbf{X} \rightleftharpoons 2 \text{Fe}\mathbf{F}_3 + 3 \mathbf{X}$$

In these reactions, each iron atom is always coordinated to 3 ligands, and there are 12 unused coordination sites on the ligands (e.g. zero on the double coordinated ligands, one on the singly coordinated ligands in $\text{Fe}\mathbf{F}_3$, and two on each free **F** or **X** ligand). The reported

energetics were then computed for each set of species relative to the energy of $\text{Fe}_2\text{X}_3 + 6$

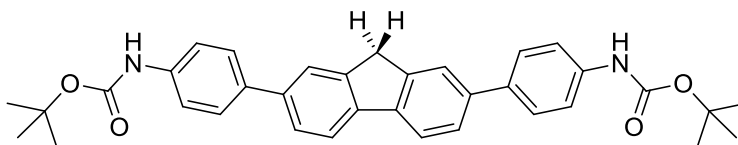
B3LYP-D3(BJ)/def2-TZVP in implicit Acetonitrile polarizable continuum

Using geometries optimized under identical conditions except in the smaller 6-31G(d) basis set:

Raw Energy (hartree)		Convert to Relative Energies with a common stoichiometry		
			Total Energy (hartree)	Relative Energies (kcal/mol)
X	-761.7440161		-	
F	-612.4315279	$\text{Fe}_2\text{X}_3 + 6 \text{ F}$	10198.942000	0.0
Fe_2X_3	-6524.352832	$\text{Fe}_2\text{X}_2\text{F} + 5 \text{ F} + 1 \text{ X}$	10198.935939	3.8
$\text{Fe}_2\text{X}_2\text{F}_1$	-6375.034284	$\text{Fe}_2\text{XF}_2 + 4 \text{ F} + 2 \text{ X}$	10198.918851	14.5
$\text{Fe}_2\text{X}_1\text{F}_2$	-6225.704707	$\text{Fe}_2\text{F}_3 + 3 \text{ F} + 3 \text{ X}$	10198.910832	19.6
Fe_2F_3	-6076.3842000	$2 \text{ FeF}_3 + 3 \text{ X}$	10199.003622	-38.7
FeF_3	-3956.885787			

Each calculation has a total stoichiometry of 2 Fe, 3 X, and 6 F, relative energies are expressed relative to $\text{Fe}_2\text{X}_3 + 6 \text{ F}$.

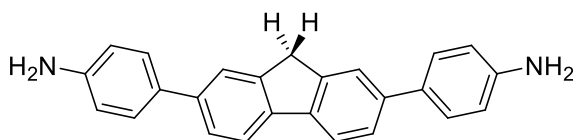
7.4 Experimental for Chapter 4



Synthesis of di-tert-butyl ((9H-fluorene-2,7-diyl)bis(4,1-phenylene))dicarbamate (7.3):

To a Schlenk flask was added 2,7-dibromo-9H-fluorene (259 mg, 0.8 mmol), 4-Boc-aminophenylboronic acid (474 mg, 2 mmol), cesium carbonate (1.56 g, 4.8 mmol), and

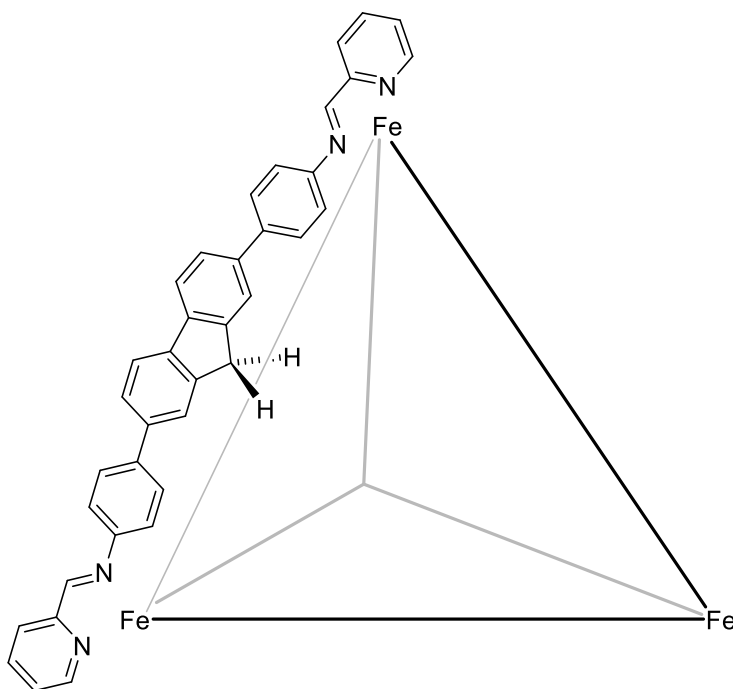
Pd(dppf)Cl₂ (59 mg, 0.08 mmol). The flask was then purged with N₂, 2 mL of DMF was added and the flask quickly purged a second time. The mixture was stirred at 90 °C for 16 h, then the reaction was cooled to room temperature and diluted with 100 mL of water. The product was extracted with diethyl ether (4 x 60 mL) and the organic layer washed with a solution of 1 M NaCO₃ and 1 M sorbitol in water (30 mL) followed by washings with saturated sodium bicarbonate and brine (2 x 20 mL each). The cloudy organic layer was dried with magnesium sulfate, filtered through a celite plug and the solvent removed in vacuo to give the product as a tan solid (420 mg, 85 %). ¹H NMR (400 MHz, CDCl₃) δ 7.85 (d, *J* = 7.9 Hz, 2H), 7.78 (s, 2H), 7.65 – 7.60 (m, 6H), 7.48 (d, *J* = 8.3 Hz, 4H), 6.55 (s, 2H), 4.03 (s, 2H), 1.57 (s, 18H). ¹³C NMR (101 MHz, DMSO-*d*₆) δ 153.24, 144.53, 140.10, 139.39, 138.87, 134.45, 127.31, 125.52, 123.32, 120.84, 118.93, 79.59, 37.08, 28.61. HRMS (ESI) *m/z* calcd for C₃₅H₃₅N₂O₄ 547.27, found 547.3401 (M-H)⁻



Synthesis of 4,4'-(9H-fluorene-2,7-diyl)dianiline (4.A):

7.3 (250 mg, 0.456 mmol) was placed in a round-bottomed flask with a stir bar. Trifluoroacetic acid (5 mL, neat) was added to the flask and the mixture was stirred overnight at room temperature. The mixture was slowly added to a beaker containing 100 mL of ice water. The solution was brought to pH 9 using 1 M NaOH, and the precipitate filtered and washed with hexane to yield product as a tan powder (154 mg, 94 %). ¹H NMR (400 MHz, DMSO-*d*₆) δ 7.84 (d, *J* = 8.0 Hz, 2H), 7.74 (s, 2H), 7.56 (dd, *J* = 8.0, 1.4 Hz,

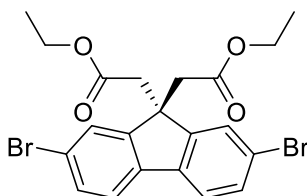
2H), 7.43 (d, $J = 8.5$ Hz, 4H), 6.67 (d, $J = 8.5$ Hz, 4H), 5.23 (s, 4H), 3.97 (s, 2H). ^{13}C NMR (101 MHz, $\text{DMSO-}d_6$) δ 148.71, 144.26, 139.58, 139.25, 128.22, 127.64, 124.65, 122.46, 120.45, 114.75, 37.04. HRMS (ESI) m/z calcd for $\text{C}_{25}\text{H}_{21}\text{N}_2$: 349.1626, found 349.1488 ($\text{M}+\text{H}$) $^+$.



Synthesis of Extended Fluorene Cage 4.1:

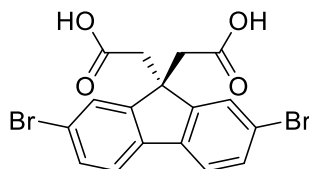
Ligand **4.A** (35 mg, 0.08 mmol) was placed in a round bottomed flask with a stir bar and acetonitrile (9 mL) was added to the flask followed by 2-formylpyridine (14.4 μL , 0.16 mmol). Iron (II) triflimide (33 mg, 0.05 mmol) was added, and the solution stirred at reflux for 24 hours. The solution was allowed to cool and was filtered to remove any undissolved solids. The acetonitrile was removed in vacuo and the solid residue sonicated for 30 minutes with 20 mL of a 1:3 mixture of MeOH/Et₂O followed by filtration and collection of the dark purple solid, which was washed with an additional 15 mL of Et₂O (57 mg, 82

%). See figures S9–S28 for full characterization. Elemental Analysis: Calc. for $C_{238}H_{156}F_{48}Fe_4N_{32}O_{32}S_{16}$ C: 50.82; H: 2.80; N: 7.97; Found: C: 50.60; H: 3.03; N: 7.86.



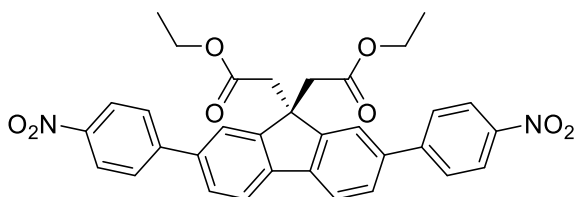
Synthesis of Diethyl 2,2'-(2,7-dibromo-9H-fluorene-9,9-diyl)diacetate (4.B):

2,7-Dibromo-9H-fluorene (500 mg, 1.54 mmol) and KO^tBu (865 mg, 7.71 mmol) were added to a two-neck round bottom flask equipped with a stir bar and a septum. The flask was purged with N_2 , and anhydrous THF (15 mL) was then added via syringe. To the flask was then added α -bromoethylacetate (510 μ L, 4.62 mmol) dropwise over 5 min. The solution was then stirred for 16 h at 23 $^{\circ}C$. The reaction was diluted with 20 mL Et_2O and filtered. The resulting solution was then extracted with saturated $NaHCO_3$ (3 x 20 mL) and brine (2 x 20 mL) and dried over Na_2SO_4 . The reaction mixture was filtered, transferred to a round bottom flask and concentrated in vacuo to afford an orange crystalline solid. The compound was then further purified using an $EtOAc/Hexanes$ gradient column (614 mg, 85 %). 1H NMR: (500 MHz, $CDCl_3$) δ 7.68 (d, J = 1.4 Hz, 2H), 7.55 (d, J = 8.1 Hz, 2H), 7.51 (dd, J = 8.1, 1.6 Hz, 2H), 3.97 (q, J = 7.1 Hz, 4H), 3.03 (s, 4H), 1.06 (t, J = 7.1 Hz, 6H). ^{13}C NMR (101 MHz, $CDCl_3$) δ 169.99, 150.38, 138.17, 131.26, 127.34, 121.55, 121.38, 60.47, 50.01, 41.73, 13.95. HRMS (ESI) m/z calcd for $C_{21}H_{20}Br_2O_4$: 493.9728, found 494.0067 (M) $^+$.



Synthesis of 2,2'-(2,7-Dibromo-9H-fluorene-9,9-diyl)diacetic acid (4.4):

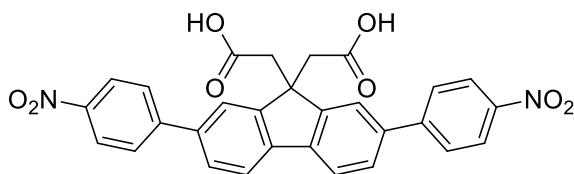
Compound **4.B** (100 mg, 0.2 mmol), was placed in a 10 mL round bottomed flask. Methanol (3 mL) was added along with excess aqueous 2 M NaOH solution (1.5 mL). The reaction was refluxed for 7 hours. The mixture was allowed to cool, and the pH brought to 4 using 1 M HCl. The product was extracted using Et₂O (10 mL) and washed with brine (2 x 15 mL). The organic layer was dried with magnesium sulfate, and the solvent removed *in vacuo* to give product as a pale yellow solid (84 mg, 95 %). ¹H NMR: (400 MHz, CD₃CN) δ 8.88 (s, 2H), 7.78 (d, J = 1.7 Hz, 2H), 7.71 (d, J = 8.1 Hz, 2H), 7.57 (dd, J = 8.1, 1.8 Hz, 2H), 3.09 (s, 4H). ¹³C NMR (101 MHz, CD₃CN) δ 170.28, 150.90, 138.92, 130.92, 126.98, 121.77, 120.81, 49.77, 41.06. HRMS (ESI) m/z calcd for C₁₇H₁₁Br₂O₄: 438.9009, found 438.9246 (M-H)⁻.



Synthesis of diethyl 2,2'-(2,7-bis(4-nitrophenyl)-9H-fluorene-9,9-diyl)diacetate (4.C):

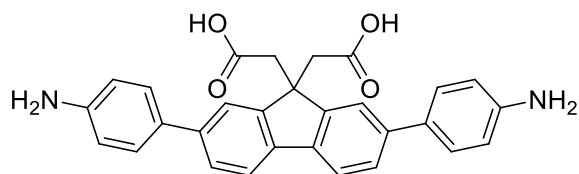
To a round bottom flask was added **4.B** (500 mg, 1.0 mmol), (4-nitrophenyl)boronic acid (420 mg, 2.5 mmol), tricyclohexylphosphine (56 mg, 0.2 mmol), and palladium(II) acetate (22 mg, 0.1 mmol). The flask was then charged with 9 mL of a 1:1:1 mixture of 2M K₂CO₃

in H₂O:toluene:ethanol, followed by purging. The mixture was allowed to stir at 90 °C for 16 h. The reaction was cooled to 23 °C and filtered through a celite plug. This was then diluted with CH₂Cl₂ and washed with NaHCO₃, and concentrated *in vacuo* to give a brown solid. The solid was columned in CH₂Cl₂ and concentrated *in vacuo* to give the product as a yellow powder (453 mg, 78 %). ¹H NMR (500 MHz, CDCl₃) δ 8.34 (d, *J* = 8.1 Hz, 4H), 7.91 (s, 2H), 7.89 (d, *J* = 8.0 Hz, 2H), 7.82 (d, *J* = 7.7 Hz, 4H), 7.71 (d, *J* = 8.0 Hz, 2H), 3.96 (q, *J* = 13.8, 6.7 Hz, 4H), 3.20 (s, 4H), 1.00 (t, *J* = 7.0 Hz, 6H). ¹³C NMR (126 MHz, CDCl₃) δ 170.29, 150.08, 147.50, 147.06, 140.12, 138.35, 127.76, 127.63, 124.19, 123.15, 120.99, 60.42, 50.14, 42.13, 13.91.



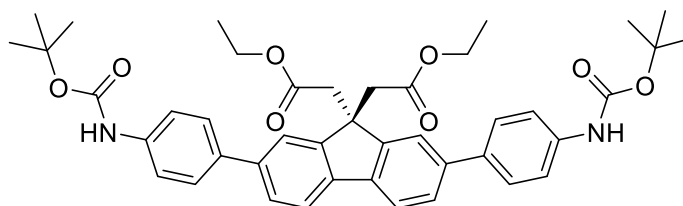
Synthesis of 2,2'-(2,7-bis(4-nitrophenyl)-9H-fluorene-9,9-diyl)diacetic acid (7.4):

4.C (300 mg, 0.5 mmol) was added to a 100 mL flask with 30 mL of MeOH and the mixture heated to 50 °C to dissolve the solid. To this solution was added 10 mL concentrated NaOH in water. The reaction was stirred overnight at 65 °C and then allowed to cool. The reaction was then filtered through a celite plug to remove any solid impurities and the pH brought to 7 using 1 M HCl. The product was then extracted from the aqueous mixture using DCM (3 x 50 mL), the organic portion was dried using magnesium sulfate, and the solvent removed *in vacuo* to give a yellow powder (340 mg, 65 %). ¹H NMR (500 MHz, DMSO-*d*₆) δ 11.91 (s, 2H), 8.35 (d, *J* = 7.9 Hz, 4H), 8.11 (d, *J* = 7.2 Hz, 2H), 8.04 (s, 2H), 8.02 (d, *J* = 7.3 Hz, 4H), 7.84 (d, *J* = 7.4 Hz, 2H), 3.18 (s, 4H).



Synthesis of 2,2'-(2,7-bis(4-aminophenyl)-9H-fluorene-9,9-diyl)diacetic acid (4.D):

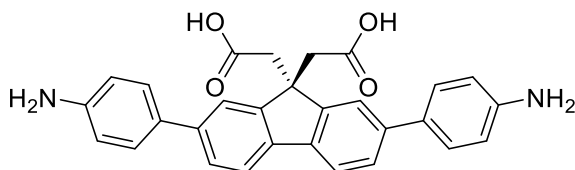
7.4 (279 mg, 0.53 mmol) was added to a 5 mL round bottom flask and dissolved in MeOH (5 mL). To this solution was added hydrazine monohydrate (1.45 mL, 15.9 mmol) and Raney Ni (747 μ L), and stirred overnight at room temperature. The reaction was then filtered through a celite plug to remove all Raney Ni, followed by concentration *in vacuo* to give a tan powder (189 mg, 77 %). HRMS (ESI) m/z calcd for $C_{33}H_{28}N_2O_4$ 464.18, found 463.2344 (M-H) $^-$.



Synthesis of Diethyl 2,2'-(2,7-bis(4-nitrophenyl)-9H-fluorene-9,9-diyl)diacetate (4.E):

To a Schlenk flask was added **4.B** (397 mg, 0.8 mmol), 4-Boc-aminophenylboronic acid (474 mg, 2 mmol), cesium carbonate (1.56 g, 4.8 mmol), and Pd(dppf)Cl₂ (59 mg, 0.08 mmol). The flask was then purged with N₂, 2 mL of DMF was added and the flask quickly purged a second time. The mixture was stirred at 90 °C for 16 h, then the reaction was cooled to room temperature and diluted with 100 mL of water. The product was extracted with diethyl ether (2 x 60 mL) and the organic layer washed with a solution of 1 M NaCO₃ and 1 M sorbitol in water (30 mL) followed by washings with saturated sodium bicarbonate and brine. The organic layer was dried with magnesium sulfate, filtered through a celite

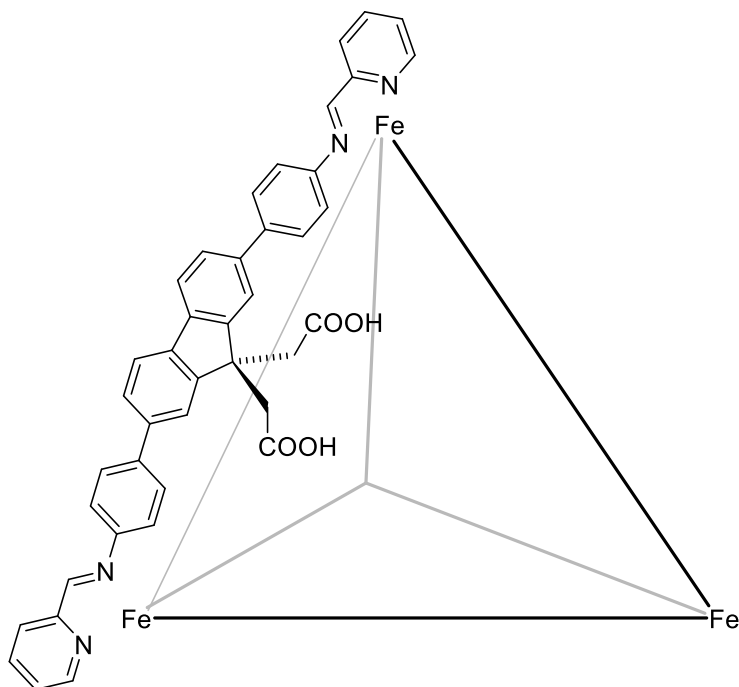
plug and the solvent removed in vacuo to give the product as an orange solid (403 mg, 70 %). ^1H NMR (500 MHz, CDCl_3) δ 7.78 – 7.75 (m, 4H), 7.61 – 7.57 (m, 6H), 7.46 (d, J = 8.0 Hz, 4H), 6.58 (s, 2H), 3.96 (q, J = 7.1 Hz, 4H), 3.16 (s, 4H), 1.56 (s, 18H), 1.00 (t, J = 7.1 Hz, 6H). ^{13}C NMR (101 MHz, CDCl_3) δ 170.74, 152.77, 149.61, 139.79, 138.64, 137.68, 136.02, 127.60, 126.70, 122.26, 120.25, 118.83, 80.65, 60.26, 49.92, 42.17, 28.39, 13.92. HRMS (ESI) m/z calcd for $\text{C}_{43}\text{H}_{48}\text{N}_2\text{O}_8$: 721.3406, found 721.2795 ($\text{M}+\text{H}$) $^+$.



Synthesis of 2,2'-(2,7-Bis(4-aminophenyl)-9H-fluorene-9,9-diyl)diacetic acid (4.D):

4.E (300 mg, 0.4 mmol) was added to a 5 mL round bottom flask and dissolved in 5 mL neat trifluoroacetic acid and stirred at room temperature overnight. The TFA was then removed in vacuo to give the deprotected amine as the TFA salt. 30 mL of MeOH was added to the flask and the mixture heated to 50 °C to dissolve the solid. To this solution was added 5 mL concentrated NaOH in water. The reaction was stirred overnight at 65 °C and then allowed to cool. The reaction was then filtered through a celite plug to remove any solid impurities and the pH brought to 7 using 1 M HCl. The product was then extracted from the aqueous mixture using DCM (3 x 50 mL), the organic portion was dried using magnesium sulfate, and the solvent removed in vacuo to give a tan powder (137 mg, 71 %). ^1H NMR (400 MHz, $\text{DMSO}-d_6$) δ 11.90 (s, 2H), 7.78 – 7.72 (m, 4H), 7.51 (d, J = 8.0 Hz, 2H), 7.39 (d, J = 8.3 Hz, 4H), 6.67 (d, J = 8.3 Hz, 4H), 5.24 (s, 4H), 3.33 (s, 4H). ^{13}C NMR (101 MHz, $\text{DMSO}-d_6$) δ 172.37, 150.59, 148.73, 139.82, 137.78, 128.37, 127.68,

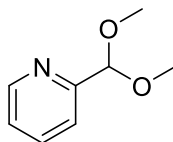
125.17, 121.20, 120.44, 114.69, 49.79, 42.63. HRMS (ESI) m/z calcd for $C_{29}H_{23}N_2O_4$: 463.1701, found 463.2344 (M-H)⁻.



Synthesis of fluorenyl acid cage 4.2:

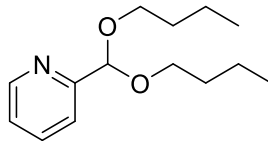
Ligand 4.D (35 mg, 0.08 mmol) was placed in a Schlenk flask with a stir bar and the flask purged with N_2 gas. Anhydrous acetonitrile (9 mL) was added to the flask along with 2-formylpyridine (14.4 μ L, 0.16 mmol). Iron (II) triflimide (33 mg, 0.05 mmol) was dissolved in a vial with 1 mL of anhydrous acetonitrile, and the solution added to the flask via cannula transfer. The reaction mixture immediately turned a burgundy color and was allowed to stir at reflux for 24 hours. The solution was allowed to cool and was filtered to remove any undissolved solids. The acetonitrile was removed in vacuo and the solid residue sonicated for 30 minutes with 20 mL of a 1:3 mixture of MeOH/Et₂O followed by filtration and collection of the dark purple solid, which was washed with an additional 15

mL of Et₂O. (57 mg, 82 %). See figures S37–S56 for full characterization. Elemental Analysis: Calc. for C₂₆₂H₁₈₀F₄₈Fe₄N₃₂O₅₆S₁₆ C: 49.79; H: 2.87; N: 7.09; Found: C: 49.71; H: 2.97; N: 7.33.



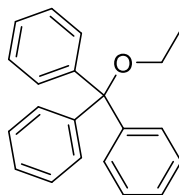
Synthesis of 2-(Dimethoxymethyl)pyridine (Acetal 4.3b):

2-Formylpyridine (1 mL, 0.011 mol) was placed in a 100 mL round bottomed flask along with 10 mL of methanol. *p*-Toluenesulfonic acid monohydrate (30 mol %, 0.003 mol, 627 mg) was added to the flask. The reaction mixture was refluxed overnight under N₂, then allowed to cool. The reaction mixture was slowly poured into a beaker containing 50 mL of saturated sodium bicarbonate solution. The pH was tested, and more sodium bicarbonate solution was added as needed to bring the pH to between 7 and 8. The product was extracted using 15 mL of hexane and washed extensively with brine (5 x 20 mL) to remove any remaining starting material. The organic layer was dried with magnesium sulfate and the solvent removed *in vacuo* to give product as a red-brown oil (1.08 g, 64 %). ¹H NMR (400 MHz, CD₃CN) δ 8.58 (d, J = 4.7 Hz, 1H), 7.81 (td, J = 7.7, 1.7 Hz, 1H), 7.53 (d, J = 7.9 Hz, 1H), 7.34 (ddd, J = 7.5, 4.8, 1.0 Hz, 1H), 5.30 (s, 1H), 3.37 (s, 6H). ¹³C NMR (101 MHz, CDCl₃) δ 157.13, 149.12, 136.66, 123.49, 121.24, 103.94, 53.64. HRMS (ESI) *m/z* calcd for C₈H₁₂NO₂: 154.0717, found 154.0786 (M+H)⁺.



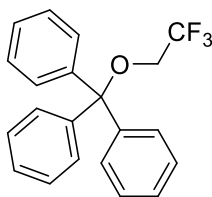
Synthesis of 2-(Dibutoxymethyl)pyridine (Acetal 4.3c)

2-Formylpyridine (1 mL, 0.011 mol) was placed in a 100 mL round bottomed flask along with 10 mL of n-butanol. *p*-Toluenesulfonic acid monohydrate (30 mol %, 0.003 mol, 627 mg) was added to the flask. The reaction mixture was heated to 80 °C overnight under N₂, then the reaction mixture was allowed to cool. The solution was slowly poured into a beaker containing 50 mL of saturated sodium bicarbonate solution. The pH was tested, and more sodium bicarbonate solution was added as needed to bring the pH to between 7 and 8. The product was extracted using 15 mL of hexane and washed extensively with brine (5 x 20 mL) to remove any remaining starting material. The organic layer was dried with magnesium sulfate and the solvent removed *in vacuo* to give product as a red-brown oil (1.28 g, 49 %). ¹H NMR (400 MHz, CD₃CN) δ 8.56 (dd, J = 4.1, 0.7 Hz, 1H), 7.80 (ddd, J = 9.5, 6.6, 2.7 Hz, 1H), 7.56 (dd, J = 9.6, 4.6 Hz, 1H), 7.33 – 7.27 (ddd, 9.5, 6.6, 4.1 1H), 5.40 (s, 1H), 3.67 – 3.48 (m, 4H), 1.61 – 1.32 (m, 8H), 0.92 (t, J = 5.5 Hz, 6H). ¹³C NMR (101 MHz, CDCl₃) δ 158.35, 148.89, 136.58, 123.28, 121.07, 102.86, 66.40, 31.80, 19.35, 13.86. HRMS (ESI) m/z calcd for C₁₄H₂₄NO₂: 238.1721, found 238.1667 (M+H)⁺.



Trityl Ethyl Ether (4.5b):

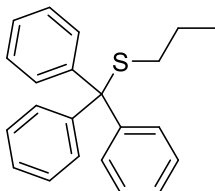
Trityl chloride (100 mg, 0.36 mmol) was placed in a Schlenk flask with excess sodium carbonate (250 mg) and a stir bar and the flask purged with N₂. Neat anhydrous ethanol (3 mL) was added to the flask, and the reaction was stirred at 50 °C overnight. The reaction mixture was cooled and filtered. The solvent was removed, and the solid product was sonicated in DI water and dried *in vacuo* to yield pure product as a white crystalline solid in quantitative yield (97 %). ¹H NMR (400 MHz, CD₃CN) δ 7.47 (dd, J = 5.3, 3.4 Hz, 6H), 7.41 – 7.34 (m, 6H), 7.32 – 7.24 (m, 3H), 3.08 (q, J = 7.0 Hz, 2H), 1.22 (t, J = 7.0 Hz, 3H). ¹³C NMR (101 MHz, CD₃CN) δ 144.64 (s), 128.47 (s), 127.82 (s), 126.99 (s), 86.40 (s), 59.20 (s), 14.57 (s).



2,2,2-Trifluoroethyl-O-Trityl Ether (4.5c):

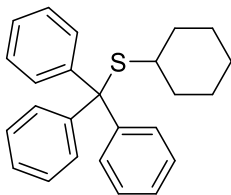
Trityl chloride (200 mg, 0.72 mmol) was placed in a Schlenk flask with a stir bar and purged with N₂. Neat 2,2,2-trifluoro ethanol (5 mL) was added to the flask, along with NaHCO₃ (200mg). The reaction was stirred at 23 °C overnight. The resulting solution was filtered to remove excess NaHCO₃. The solvent was removed and the product dried *in vacuo* to yield pure product as a white crystalline solid in quantitative yield (98 %). ¹H

NMR (400 MHz, CD₃CN) δ 7.49 – 7.45 (m, 6H), 7.40 (dd, J = 9.9, 4.8 Hz, 6H), 7.37 – 7.32 (m, 3H), 3.59 (q, J = 8.7 Hz, 2H). ¹³C NMR (101 MHz, CD₃CN) δ 142.74 (s), 128.35 (s), 128.19 (s), 127.67 (s), 120.51 (s), 87.48 (s), 62.24 – 60.86 (q).



Propyl Trityl Sulfide (4.6a):

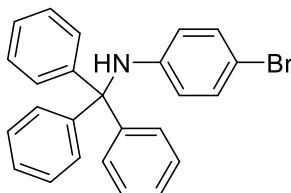
Trityl chloride (100 mg, 0.36 mmol) was placed in a Schlenk flask with a stir bar and purged with N₂. Neat *n*-propyl thiol (3 mL) was added to the flask, and the reaction was stirred at 50 °C overnight. The solvent was removed and the product dried *in vacuo* to yield pure product as a white crystalline solid in quantitative yield (98 %). ¹H NMR (400 MHz, CD₃CN) δ 7.43 (dd, J = 5.6, 3.7 Hz, 6H), 7.40 – 7.31 (m, 6H), 7.29 – 7.23 (m, 3H), 2.12 (t, J = 7.4 Hz, 2H), 1.46 – 1.32 (m, 2H), 0.84 (t, J = 7.4 Hz, 3H). ¹³C NMR (101 MHz, CD₃CN) δ 145.15 (s), 129.44 (s), 127.88 (s), 126.65 (s), 66.12 (s), 33.58 (s), 21.76 (s), 12.99 (s).



Cyclohexyl Trityl Sulfide (4.6b):

Trityl chloride (100 mg, 0.36 mmol) was placed in a Schlenk flask with a stir bar and purged with N₂. The trityl chloride was dissolved in anhydrous THF (1 mL), followed by cyclohexane thiol (40 μ L, 0.33 mmol). The reaction was stirred at 50 °C overnight. The solution was cooled to room temperature and diluted with Et₂O (10 mL), and washed with

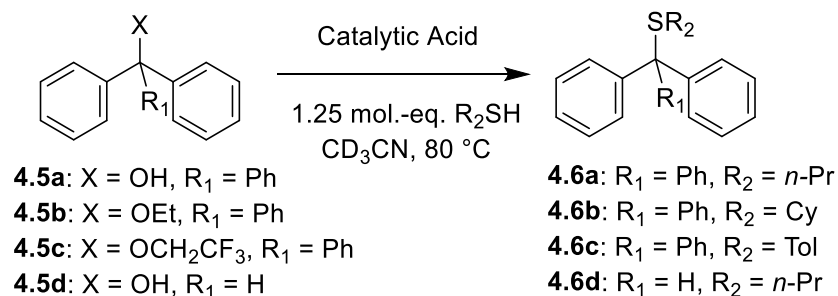
saturated NaHCO₃ (3 x 10 mL). The solvent was removed and the product dried *in vacuo* to afford a white powdery solid (74 %). ¹H NMR (400 MHz, CDCl₃) δ 7.56 (d, J = 7.4 Hz, 6H), 7.32 (t, J = 7.4 Hz, 6H), 7.23 (t, J = 7.3 Hz, 3H), 2.20 (ddd, J = 13.7, 7.1, 3.6 Hz, 1H), 1.65 – 1.56 (m, 2H), 1.47 (td, J = 13.1, 4.1 Hz, 3H), 1.31 – 0.99 (m, 5H). ¹³C NMR (101 MHz, CDCl₃) δ 145.50, 129.72, 127.75, 126.44, 67.40, 44.23, 34.53, 26.37, 25.66.



4-Bromo-N-Trityl Aniline (4.5e):

Trityl chloride (306 mg, 1.1 mmol) and 4-bromoaniline (172 mg, 1 mmol) were combined in a round bottom with triethylamine (167 μL, 1.2 mmol) and dichloromethane (5 mL) at 0 °C. The reaction was slowly brought to 23 °C and stirred overnight. The solution was washed with 10 mL of DI water and brine (3 x 10 mL). The solvent was removed and dried *in vacuo*. The solid was purified via column chromatography (10 % EtOAc/Hexanes) to afford a white crystalline solid (98 %). ¹H NMR (400 MHz, CD₃CN) δ 7.39 (d, 6H), 7.30 (t, J = 7.6, 6H), 7.23 (t, 3H), 6.97 (d, J = 8.7 Hz, 2H), 6.37 (d, J = 8.7 Hz, 2H), 5.82 (s, 1H). ¹³C NMR (151 MHz, CD₃CN) δ 145.68, 144.73, 130.17, 128.66, 127.52, 126.47, 117.73, 108.11, 70.83.

General Method for Acid-Promoted Substitution Reactions:



Trityl Substrate (6.3 μmol , 1 mol. -eq.) was placed in an NMR tube followed by 5 mol % acid cage **4.2** (0.31 μmol , 2 mg) or 30 mol % control acid **4.4** (1.86 mmol, 0.95 mg). The nucleophile (1.25 mol. -eq., 7.9 μmol , 3.9 μL of 2 M solution in CD₃CN) was then added followed by 1,4-Dioxane as the internal standard (0.5 mol. -eq. 3.2 μmol , 1.6 μL of 2 M solution in CD₃CN). 400 μL of CD₃CN was added, and the tube was capped and quickly shaken to dissolve all solids. Control trials use 30 mol % of diacid **4.4** to maintain the same concentration of COOH groups present in 5 mol % of the M₄L₆ cage **4.2**. An initial ¹H NMR spectrum of the reaction mixture was obtained to verify the correct amounts of reagents. The sample was then heated at the specified temperature and the reaction progress monitored over time. Rate calculation trials were performed in triplicate. The percent conversion values were obtained via integration of the product and substrate peaks against the internal standard and the calculated values of duplicate trials were averaged.

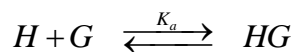
Binding Calculations for Trityl Substitution Experiments

Binding constants for 1:1 and 1:2 host-guest complex models were determined by UV/Vis titration experiments and binding constants extracted following the general approach outlined by Thordarson,¹² modified as described below. In brief, UV/Vis absorptions at 300 and 370 nm were monitored as a function of added guest and simultaneously fit using a

non-linear least-squares (maximum likelihood) approach written within the Mathematica programming environment.¹³ For the 1:1 equilibrium model, the binding constant (K_a) and molar absorptivities (at both wavelengths) for the pure host (H) and host-guest (HG) complex were determined. For the 1:2 equilibrium model, both the first (K_1) and second (K_2) binding constants were determined, along with molar absorptivities for the host, host-guest (HG), and host-dual-guest (HG₂) complexes. The precise equilibria and corresponding equations are detailed below. Error bars for each of the fit parameters were determined by a numerical calculation of the covariance matrix and are reported above as \pm standard error.¹⁴ The error analysis assumes normally distributed, random error that is independent of data point; in such a case, the sum of the squared-residuals follows the chi-squared distribution for $N-k$ degrees of freedom, where N is the number of measured data points and k the number of fit parameters (5 and 8 for the 1:1 and 1:2 models, respectively). The significance of the 1:2 model was judged based on the inverse ratio of the squared residuals compared to the 1:1 model. Again, if the errors are normally distributed, this ratio follows the F-distribution for $N-5$ (numerator) and $N-8$ (denominator) degrees of freedom.¹⁵ To be considered statistically “better,” the 1:2 model must improve the residuals beyond what normal statistical fluctuations would be expected to sample with the observed noise and finite number of measured points. This is quantified via the p-value, which gives the probability that the observed improvement in residuals for the 1:2 complex model can be explained as statistical “luck.” A small value indicates that the model truly is better – that is, that more of the underlying data trends are reproduced so that the residuals are actually smaller. To be considered significant in this context, we take p-values below 0.001.

Equilibrium Models:¹

The 1:1 host-guest binding



has an association constant

$$K_a = \frac{[HG]}{[H][G]}$$

from which the concentration of the host, guest, and complex can be related back to initial (or total added) concentrations, H_0 and G_0 , of each

$$[H] = \frac{1}{2} \left(H_0 - G_0 - \frac{1}{K_a} \right) + \frac{1}{2} \sqrt{\left(G_0 - H_0 - \frac{1}{K_a} \right)^2 + 4 \frac{G_0}{K_a}}$$

$$[G] = \frac{1}{2} \left(G_0 - H_0 - \frac{1}{K_a} \right) + \frac{1}{2} \sqrt{\left(G_0 - H_0 - \frac{1}{K_a} \right)^2 + 4 \frac{G_0}{K_a}}$$

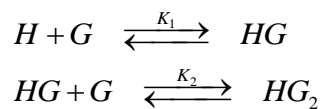
$$[HG] = \frac{1}{2} \left(G_0 + H_0 + \frac{1}{K_a} \right) - \frac{1}{2} \sqrt{\left(G_0 - H_0 - \frac{1}{K_a} \right)^2 + 4 \frac{G_0}{K_a}}$$

The absorbance at a given wavelength λ can then be written as

$$\begin{aligned} A^\lambda &= \varepsilon_H^\lambda [H] + \varepsilon_{HG}^\lambda [HG] \\ &= \varepsilon_H^\lambda \left\{ \frac{1}{2} \left(H_0 - G_0 - \frac{1}{K_a} \right) + \frac{1}{2} \sqrt{\left(G_0 - H_0 - \frac{1}{K_a} \right)^2 + 4 \frac{G_0}{K_a}} \right\} + \\ &\quad \varepsilon_{HG}^\lambda \left\{ \frac{1}{2} \left(G_0 + H_0 + \frac{1}{K_a} \right) - \frac{1}{2} \sqrt{\left(G_0 - H_0 - \frac{1}{K_a} \right)^2 + 4 \frac{G_0}{K_a}} \right\} \end{aligned}$$

where it assumed that the guest on its own does not absorb. This is the expression that is used to simultaneously fit the experimental absorption data at 300 and 370 nm, A^{300} and A^{270} , as a function of added guest, G_0 , to determine K_a and ε_H^{300} , ε_{HG}^{300} , ε_H^{370} , and ε_{HG}^{370} .

The 1:2 host-guest binding is assumed to be a non-cooperative, sequential two-step process



which is characterized by two binding constants

$$\begin{aligned}
K_1 &= \frac{[HG]}{[H][G]} \\
K_2 &= \frac{[HG_2]}{[HG][G]}
\end{aligned}$$

We analyze this for the case in which the approximation $[G] \approx G_0$ is valid, which corresponds to the limit in which $K_1[H] \ll 1$ or when G_0 is in large excess. This condition can be relaxed, but appears valid in our situation. With these caveats,

$$\begin{aligned}
[H] &= \frac{H_0}{1 + K_1G_0 + K_1K_2G_0^2} \\
[G] &\approx G_0 \\
[HG] &= \frac{K_1H_0G_0}{1 + K_1G_0 + K_1K_2G_0^2} \\
[HG_2] &= \frac{K_1K_2H_0G_0^2}{1 + K_1G_0 + K_1K_2G_0^2}
\end{aligned}$$

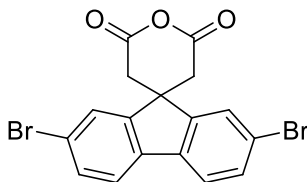
and the absorbance can be written

$$\begin{aligned}
A^\lambda &= \varepsilon_H^\lambda [H] + \varepsilon_{HG}^\lambda [HG] + \varepsilon_{HG_2}^\lambda [HG_2] \\
&= \varepsilon_H^\lambda \frac{H_0}{1 + K_1G_0 + K_1K_2G_0^2} + \varepsilon_{HG}^\lambda \frac{K_1H_0G_0}{1 + K_1G_0 + K_1K_2G_0^2} + \varepsilon_{HG_2}^\lambda \frac{K_1K_2H_0G_0^2}{1 + K_1G_0 + K_1K_2G_0^2} .
\end{aligned}$$

This expression is used to simultaneously fit the experimental absorption data at 300 and

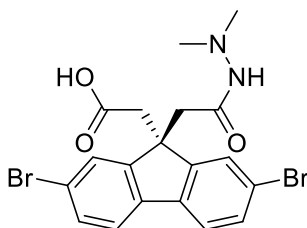
370 nm, A^{300} and A^{270} , as a function of added guest, G_0 , to determine K_1 , K_2 , ε_H^{300} , ε_{HG}^{300} , $\varepsilon_{HG_2}^{300}$, ε_H^{370} , ε_{HG}^{370} , and $\varepsilon_{HG_2}^{370}$.

7.5 Experimental for Chapter 5



Synthesis of 2,7-dibromospiro[fluorene-9,4'-pyran]-2',6'(3'H,5'H)-dione (5.4):

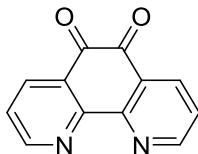
To a 15 mL two neck flask was added **4.4** (100 mg, 0.23 mmol). The flask was placed on a Schlenk line and placed under inert atmosphere. 1 mL anhydrous THF was added to the flask, followed by NEt_3 (31 μL , 0.23 mmol) and Ac_2O (150 μL , 1.59 mmol), and the solution was refluxed for 16 h. The reaction was cooled to 23 °C and concentrated *in vacuo* to give a white solid (81 mg, 84 %). ^1H NMR (500 MHz, CD_3CN) δ 7.63 – 7.58 (m, 4H), 7.51 (s, 2H), 3.02 (s, 4H).



Synthesis of 2-(2,7-dibromo-9-(2-(2,2-dimethylhydrazinyl)-2-oxoethyl)-9H-fluoren-9-yl)acetic acid (5.3):

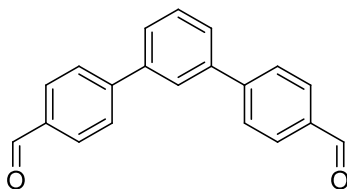
To a 10 mL round bottom flask was added **5.4** (50 mg, 0.24 mmol), *N,N*-dimethylhydrazine (9 μL , 0.24 mmol) and THF (5 mL). The resulting solution was allowed to for 16 h at 23 °C. A white precipitate formed throughout the reaction, and was isolated through vacuum filtration (41 mg, 72 %).

7.6 Experimental for Chapter 6



1,10-Phenanthroline-5,6-Dione:¹⁶

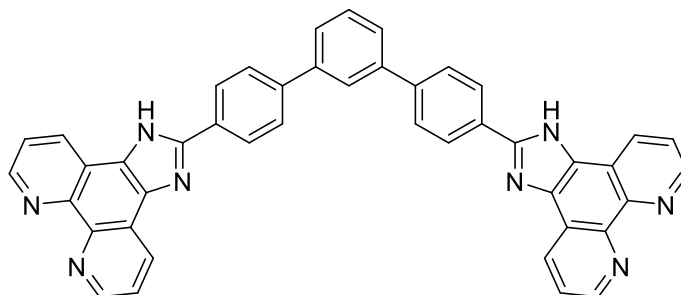
1,10-phenanthroline (5.5 mmol, 1 g) and KBr (8.4 mmol, 1 g) were added to a 100 mL round flask. The flask was cooled to 0 °C followed by addition of 10 mL H₂SO₄ and 5 mL HNO₃. The mixture was for 3 h then poured over 500 mL of ice and neutralized with NaOH. The resulting solution was extracted with CHCl₃ (3 x 30 mL), and the organic layer was concentrated *in vacuo* to give a yellow powder (1.05 g, 91 %). Spectra were in agreement with previously reported results.



Synthesis of [1,1':3',1''-terphenyl]-4,4''-dicarbaldehyde (6.A):

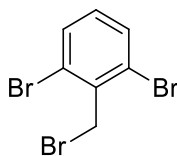
A 50 mL round bottom flask was charged with 1,3-Dibromobenzene (256 μ L, 2.0 mmol), 4-formylphenylboronic acid (715 mg, 4.80 mmol) and bis(triphenylphosphine) palladium(II) dichloride (163 mg, 0.20 mmol). A 1:1:1 mixture of 2M K₂CO₃ in water:ethanol:toluene (9 mL) was added to the flask. The flask was purged with N₂, and refluxed for 16 h. Methanol was added to the reaction mixture and the precipitate filtered via vacuum filtration to afford a tan solid. The solid was dissolved in dichloromethane and filtered through a silica/celite plug and the filtrate concentrated *in vacuo* (243 mg, 85 %).

^1H NMR (400 MHz, CDCl_3) δ 10.06 (s, 2H), 7.97 (d, $J = 8.1$ Hz, 4H), 7.85 (s, 1H), 7.79 (d, $J = 8.1$ Hz, 4H), 7.67 (d, $J = 7.0$ Hz, 2H), 7.58 (t, 1H).



Synthesis of phenanthroline ligand **6.2**:

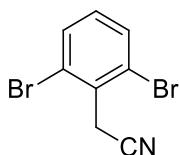
To a 25 mL round bottom flask was added dialdehyde **6.A** (100 mg, 0.36 mmol), 1,10-phenanthroline-5,6-dione (200 mg, 1 mmol), and NH_4OAc (453 mg, 5.8 mmol). The reagents were dissolved in AcOH (9 mL), under a N_2 atmosphere, and refluxed for 16 h. The reaction was then cooled to room temperature and quenched with aqueous NH_4OH resulting in a tan precipitate. The solid was collected via vacuum filtration to give **6.2** (144 mg, 60 %). ^1H NMR (400 MHz, $\text{DMSO}-d_6$) δ 13.83 (s, 2H), 9.04 – 9.01 (m, 4H), 8.95 (d, $J = 8.0$ Hz, 4H), 8.42 (d, $J = 8.5$ Hz, 4H), 8.17 (s, 1H), 8.08 (d, $J = 8.5$ Hz, 4H), 7.84 (ddd, $J = 18.8, 8.1, 4.3$ Hz, 6H), 7.66 (t, $J = 7.7$ Hz, 1H).



Synthesis of 1,3-dibromo-2-(bromomethyl)benzene:

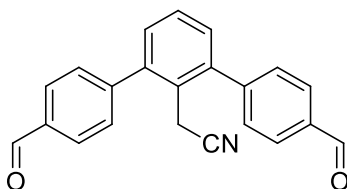
To a 10 mL round bottom flask was added 2,6-dibromotoluene (282 μL , 2.05 mmol), N-bromosuccinamide (365 mg, 2.05 mmol), and benzoyl peroxide (50 mg, 0.21 mmol). The reagents were dissolved in CCl_4 (5 mL), under a N_2 atmosphere, and refluxed for 16 h. The

reaction was then cooled to room temperature and the solid impurities were removed by vacuum filtration. Following filtration, the solution was concentrated *in vacuo* to give a white powder (554 mg, 82 %). $^1\text{H NMR}$ (400 MHz, CDCl_3) δ 7.53 (d, $J = 8.0$ Hz, 2H), 7.00 (t, $J = 8.0$ Hz, 1H), 4.81 (s, 2H).



Synthesis of 2-(2,6-dibromophenyl)acetonitrile:

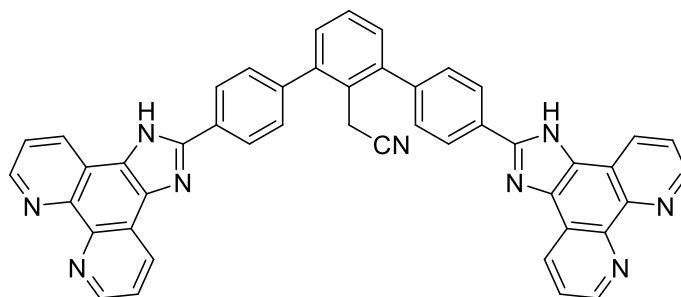
To a 10 mL round bottom flask was added 2,6-dibromobenzyl bromide (100 mg, 0.31 mmol), KCN (30 mg, 0.46 mmol), and NBu_4I (20 mg, 0.06 mmol). The reagents were dissolved in THF (1.5 mL), and stirred at 23 °C. After 3 days, diethyl ether was added to the reaction resulting in a tan precipitate. The solid was isolated by vacuum filtration, and purified through recrystallization in ethanol to give a white crystalline solid (74 mg, 89 %). $^1\text{H NMR}$ (400 MHz, CDCl_3) δ 7.58 (d, $J = 8.1$ Hz, 2H), 7.08 (t, $J = 8.1$ Hz, 1H), 4.10 (s, 2H).



Synthesis of 2-(4,4'-diformyl-[1,1':3',1''-terphenyl]-2'-yl)acetonitrile (6.B):

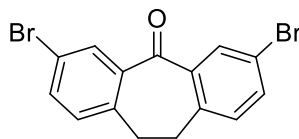
A 50 mL round bottom flask was charged with 1,3-Dibromobenzene (256 μL , 2.0 mmol), 4-formylphenylboronic acid (715 mg, 4.80 mmol) and bis(triphenylphosphine) palladium(II) dichloride (163 mg, 0.20 mmol). A 1:1:1 mixture of 2M K_2CO_3 in

water:ethanol:toluene (9 mL) was added to the flask. The flask was purged with N₂, and refluxed for 16 h. Methanol was added to the reaction mixture and the precipitate filtered via vacuum filtration to afford a tan solid. The solid was dissolved in dichloromethane and filtered through a silica/celite plug and the filtrate concentrated in vacuo (243 mg, 85 %). ¹H NMR (400 MHz, CDCl₃) δ 10.09 (s, 2H), 8.01 (d, *J* = 8.2 Hz, 4H), 7.61 (d, *J* = 8.1 Hz, 4H), 7.50 (t, *J* = 8.1, 1H), 7.35 (d, *J* = 7.7 Hz, 2H), 3.36 (s, 2H).



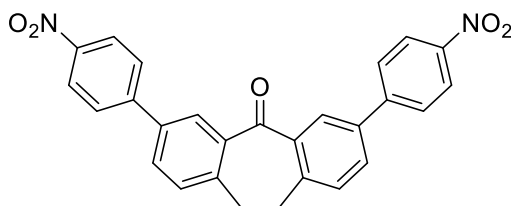
Synthesis of nitrile phenanthroline ligand **6.3**:

To a 25 mL round bottom flask was added dialdehyde **6.B** (100 mg, 0.31 mmol), 1,10-phenanthroline-5,6-dione (168 mg, 0.8 mmol), and NH₄OAc (393 mg, 16.61 mmol). The reagents were dissolved in AcOH (8 mL), under a N₂ atmosphere, and refluxed for 16 h. The reaction was then cooled to room temperature and quenched with aqueous NH₄OH resulting in a tan precipitate. The solid was collected via vacuum filtration to give **6.3** (198 mg, 91 %). ¹H NMR (400 MHz, DMSO-*d*₆) δ 9.01 – 8.98 (m, 4H), 8.89 (d, *J* = 8.0 Hz, 4H), 8.40 (d, *J* = 7.6 Hz, 4H), 7.82 – 7.77 (m, 4H), 7.67 (d, *J* = 7.9 Hz, 4H), 7.59 (t, *J* = 7.2 Hz, 1H), 7.46 (d, *J* = 7.7 Hz, 2H), 3.80 (s, 2H).



Synthesis of Dibromo Suberone (6.C):

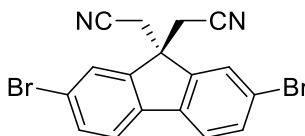
To a 100 mL round bottom flask was added CuBr_2 (2.275 g, 9.75 mmol), $t\text{BuONO}$ (1.24 mL, 10.45 mmol) and 13 mL MeCN. A solution of diaminosuberone (925 mg, 3.89 mmol) in 17 mL MeCN was slowly added to the reaction mixture, and the reaction was allowed to stir for 16 h at 23 °C. Following overnight reaction, the solution was refluxed for 2.5 h. 20 % HCl (40 mL) was then added to the reaction and the product was extracted with Et_2O (3 x 30 mL). The organic layer was concentrated *in vacuo* to give a dark brown powder (1.2g, 82 %). $^1\text{H NMR}$ (500 MHz, CDCl_3) δ 8.13 (d, $J = 1.5$ Hz, 2H), 7.56 (dd, $J = 8.1, 1.5$ Hz, 2H), 7.12 (d, $J = 8.1$ Hz, 2H), 3.15 (s, 4H).



Synthesis of 3,7-(4,4'-Dinitrophenyl)-Suberone (7.5):

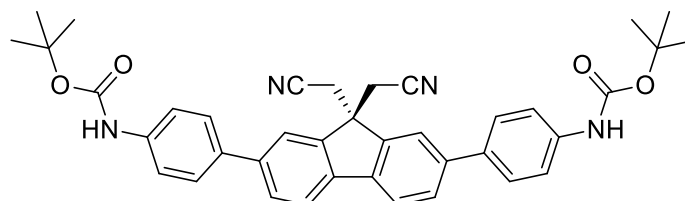
To a round bottom flask was added 3,7-dibromosuberone (174 mg, 0.48 mmol), (4-nitrophenyl)boronic acid (200 mg, 1.19 mmol) and $\text{Pd}(\text{PPh}_3)_2\text{Cl}_2$ (33 mg, 0.05 mmol). The flask was then charged with 3 mL of a 1:1:1 mixture of 2M K_2CO_3 in H_2O :toluene:ethanol, followed by purging. The mixture was allowed to stir at 90 °C for 16 h. The reaction was cooled to 23 °C and filtered through a celite plug. This was then diluted with CH_2Cl_2 and washed with NaHCO_3 , and concentrated *in vacuo* to give a brown solid. The solid was

columned in CH_2Cl_2 and concentrated *in vacuo* to give the product as a yellow powder (96 mg, 44 %). ^1H NMR (500 MHz, CDCl_3) δ 8.34 (d, $J = 2.0$ Hz, 2H), 8.33 (d, $J = 4.6$ Hz, 4H), 7.81 (d, $J = 8.7$ Hz, 4H), 7.75 (dd, $J = 7.9, 2.0$ Hz, 2H), 7.43 (d, $J = 7.9$ Hz, 2H), 3.34 (s, 4H).



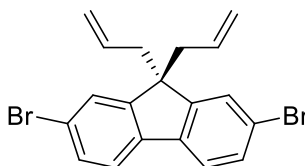
Synthesis of 2,2'-(2,7-dibromo-9H-fluorene-9,9-diyl)diacetonitrile (6.D):

2,7-Dibromo-9H-fluorene (324 mg, 1.0 mmol) and KO^tBu (336 mg, 3.0 mmol) were added to a two-neck round bottom flask equipped with a stir bar and a septum. The flask was purged with N_2 , and anhydrous THF (7 mL) was then added via syringe. To the flask was then added chloroacetonitrile (189 μL , 3.0 mmol) dropwise over 5 min. The solution was then stirred for 16 h at 23 $^\circ\text{C}$. The reaction was diluted with 20 mL Et_2O and filtered. The resulting solution was then extracted with saturated NaHCO_3 (3 x 20 mL) and brine (2 x 20 mL) and dried over Na_2SO_4 . The reaction mixture was filtered, transferred to a round bottom flask and concentrated *in vacuo* to afford a tan powder (311 mg, 77 %). ^1H NMR (500 MHz, CDCl_3) δ 7.85 (s, 2H), 7.67 – 7.63 (m, 4H), 3.01 (s, 4H).



Synthesis of di-tert-butyl ((9,9-bis(cyanomethyl)-9H-fluorene-2,7-diyl)bis(4,1-phenylene))dicarbamate (7.6):

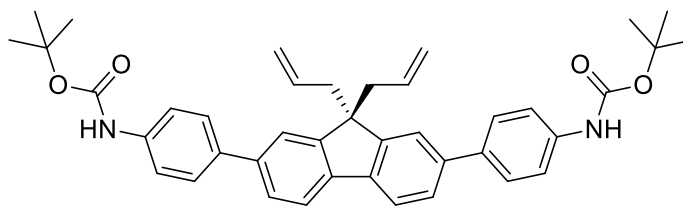
To a Schlenk flask was added **6.D** (311 mg, 0.8 mmol), 4-Boc-aminophenylboronic acid (474 mg, 2 mmol), cesium carbonate (1.56 g, 4.8 mmol), and Pd(dppf)Cl₂ (59 mg, 0.08 mmol). The flask was then purged with N₂, 2 mL of DMF was added and the flask quickly purged a second time. The mixture was stirred at 90 °C for 16 h, then the reaction was cooled to room temperature and diluted with 100 mL of water. The product was extracted with diethyl ether (2 x 60 mL) and the organic layer washed with a solution of 1 M NaCO₃ and 1 M sorbitol in water (30 mL) followed by washings with saturated sodium bicarbonate and brine. The organic layer was dried with magnesium sulfate, filtered through a celite plug and the solvent removed in vacuo to give the product as tan solid (300 mg, 62 %). ¹H NMR (500 MHz, CDCl₃) δ 7.93 (s, 2H), 7.84 (d, *J* = 7.7 Hz, 2H), 7.72 (d, *J* = 7.7 Hz, 2H), 7.61 (d, *J* = 8.4 Hz, 4H), 7.49 (d, *J* = 8.4 Hz, 4H), 6.62 (s, 2H), 3.10 (s, 4H), 1.56 (s, 18H).



Synthesis of 9,9-diallyl-2,7-dibromo-9H-fluorene (6.E):

2,7-Dibromo-9H-fluorene (324 mg, 1.0 mmol) and KO^tBu (336 mg, 3.0 mmol) were added to a two-neck round bottom flask equipped with a stir bar and a septum. The flask was

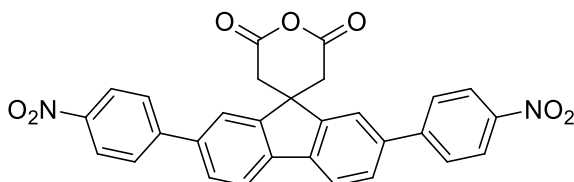
purged with N₂, and anhydrous THF (7 mL) was then added via syringe. To the flask was then added allyl bromide (259 μ L, 3.0 mmol) dropwise over 5 min. The solution was then stirred for 16 h at 23 °C. The reaction was diluted with 20 mL Et₂O and filtered. The resulting solution was then extracted with saturated NaHCO₃ (3 x 20 mL) and brine (2 x 20 mL) and dried over Na₂SO₄. The reaction mixture was filtered, transferred to a round bottom flask and concentrated in vacuo to afford a tan powder (295 mg, 73 %). ¹H NMR (500 MHz, CDCl₃) δ 7.53 (d, *J* = 4.5 Hz, 4H), 7.47 (d, *J* = 8.1 Hz, 2H), 5.22 (td, *J* = 16.4, 8.0 Hz, 2H), 4.87 (d, *J* = 16.4 Hz, 2H), 4.81 (d, *J* = 8.0 Hz, 2H).



Synthesis of di-tert-butyl ((9,9-diallyl-9H-fluorene-2,7-diyl)bis(4,1-phenylene))dicarbamate (7.7):

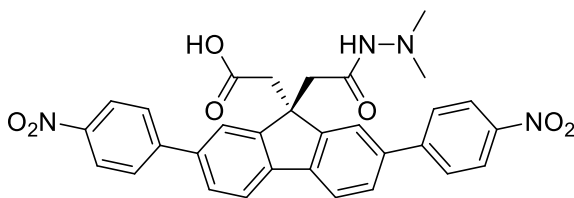
To a Schlenk flask was added **6.E** (332 mg, 0.8 mmol), 4-Boc-aminophenylboronic acid (474 mg, 2 mmol), cesium carbonate (1.56 g, 4.8 mmol), and Pd(dppf)Cl₂ (59 mg, 0.08 mmol). The flask was then purged with N₂, 2 mL of DMF was added and the flask quickly purged a second time. The mixture was stirred at 90 °C for 16 h, then the reaction was cooled to room temperature and diluted with 100 mL of water. The product was extracted with diethyl ether (2 x 60 mL) and the organic layer washed with a solution of 1 M NaCO₃ and 1 M sorbitol in water (30 mL) followed by washings with saturated sodium bicarbonate and brine. The organic layer was dried with magnesium sulfate, filtered through a celite plug and the solvent removed in vacuo to give the product as tan solid (307 mg, 61 %). ¹H

NMR (500 MHz, CD₃CN) δ 7.74 (d, J = 7.7 Hz, 1H), 7.69 (s, 2H), 7.60 (d, J = 8.1 Hz, 4H), 7.55 (d, J = 7.6 Hz, 4H), 7.47 (d, J = 7.7 Hz, 4H), 5.18 (td, J = 17.0, 8.6 Hz, 2H), 4.79 (d, J = 17.0 Hz, 2H), 4.64 (d, J = 8.6 Hz, 2H), 1.47 (s, 18H).



Synthesis of 2,7-bis(4-nitrophenyl)spiro[fluorene-9,4'-pyran]-2',6'(3'H,5'H)-dione (6.F):

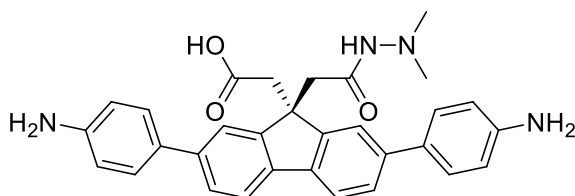
To a 15 mL two neck flask was added **4.D** (100 mg, 0.19 mmol). The flask was placed on a Schlenk line and placed under inert atmosphere. 1 mL anhydrous THF was added to the flask, followed by Ac₂O (125 μ L, 1.33 mmol), and the solution was refluxed for 16 h. The reaction was cooled to 23 °C and concentrated *in vacuo* to give a white solid (46 mg, 48 %). ¹H NMR (600 MHz, CDCl₃) δ 8.35 (d, J = 8.6 Hz, 4H), 7.96 (d, J = 8.1 Hz, 2H), 7.77 (d, J = 8.6 Hz, 2H), 7.75 (d, J = 8.6 Hz, 4H), 7.64 (s, 2H), 3.17 (s, 4H).



Synthesis of 2-(9-(2-(2,2-dimethylhydrazinyl)-2-oxoethyl)-2,7-bis(4-nitrophenyl)-9H-fluoren-9-yl)acetic acid (7.8):

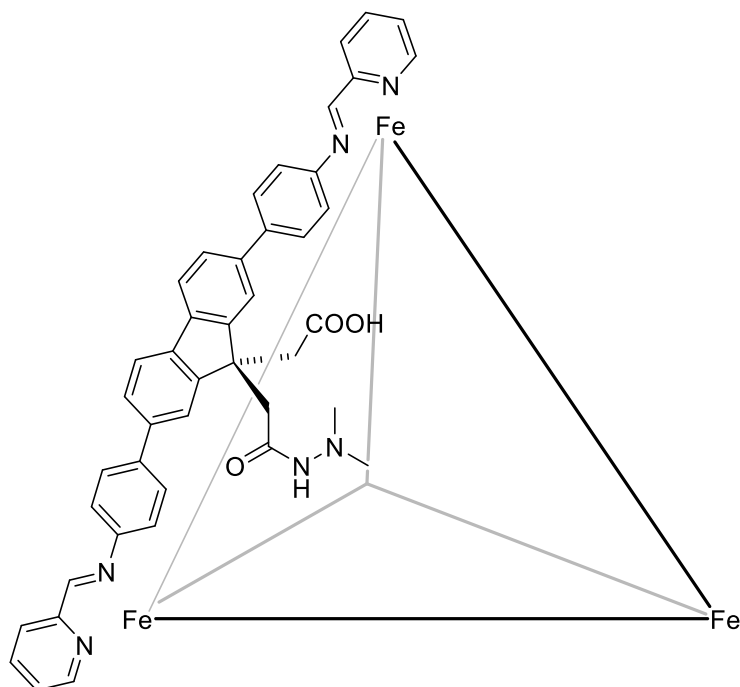
To a 10 mL round bottom flask was added **6.F** (50 mg, 0.10 mmol), N,N-dimethyl hydrazine (9 μ L, 0.12 mmol) and THF (5 mL). The resulting solution was allowed to for 16 h at 23 °C. A white precipitate formed throughout the reaction, and was isolated through

vacuum filtration (40 mg, 71 %). $^1\text{H NMR}$ (500 MHz, $\text{DMSO-}d_6$) δ 11.84 (s, 1H), 8.56 (s, 1H), 8.36 (dd, $J = 10.4, 5.6$ Hz, 4H), 8.08 – 7.99 (m, 8H), 7.84 (d, $J = 6.5$ Hz, 2H), 3.34 (s, 6H).



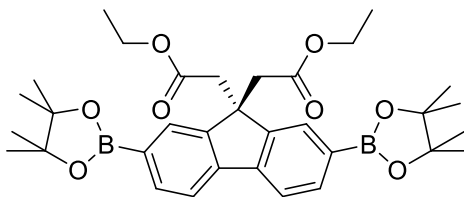
Synthesis of 2-(2,7-bis(4-aminophenyl)-9-(2-(2,2-dimethylhydrazinyl)-2-oxoethyl)-9H-fluoren-9-yl)acetic acid (6.4):

To a round bottom flask was added **7.8** (50 mg, 0.08 mmol) and EtOH (750 μL). The flask was warmed to facilitate dissolution of **7.8**. A solution of $\text{Na}_2\text{S}\cdot 9\text{H}_2\text{O}$ (92 mg, 0.38 mmol) and NaOH (34 mg, 0.8 mmol) in H_2O (1.5 mL) was prepared and added to the flask. The mixture was refluxed for 6 h, then cooled to room temperature and allowed to stir overnight. The reaction was then acidified using 6 M HCl to $\sim\text{pH}$ 3 and mixed for min. Using 2 M NaOH, the solution was then basified to $\sim\text{pH}$ 8 and the solid was filtered off to give a white solid (21 mg, 48 %).



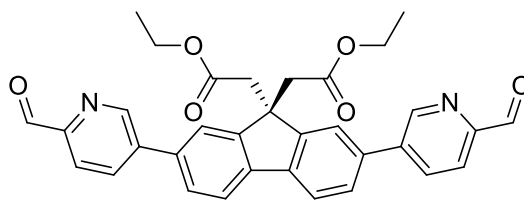
Multicomponent Self-Assembly of Ligand 6.4:

Ligand 6.4 (10 mg, 0.02 mmol) was placed in a Schlenk flask with a stir bar and the flask purged with N₂ gas. Anhydrous acetonitrile (5 mL) was added to the flask along with 2-formylpyridine (3.8 μL, 0.04 mmol). Iron (II) triflimide (8.8 mg, 0.01 mmol) was dissolved in a vial with 1 mL of anhydrous acetonitrile, and the solution added to the flask via cannula transfer. The reaction mixture immediately turned a burgundy color and was allowed to stir at reflux for 24 hours. The solution was allowed to cool and was filtered to remove any undissolved solids. The acetonitrile was removed in vacuo and the solid residue sonicated for 30 minutes with 20 mL of a 1:3 mixture of MeOH/Et₂O followed by filtration and collection of the dark purple solid.



Synthesis of diethyl 2,2'-(2,7-bis(4,4,5,5-tetramethyl-1,3,2-dioxaborolan-2-yl)-9H-fluorene-9,9-diyl)diacetate (6.G):

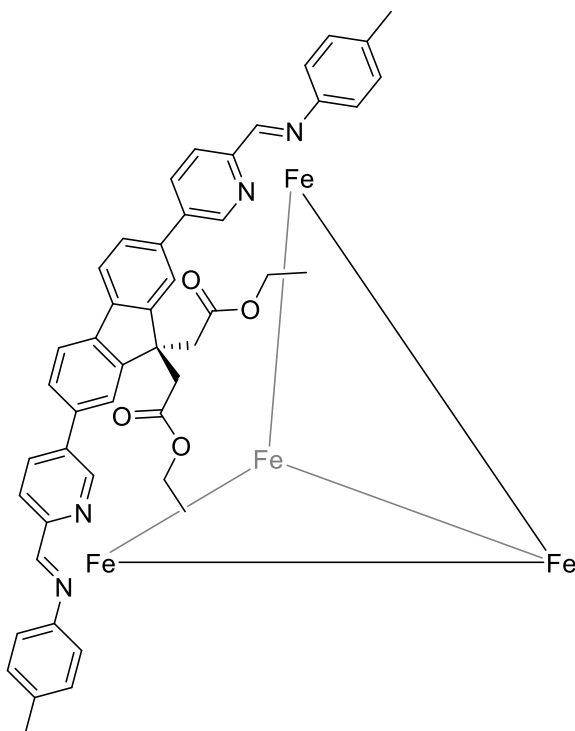
Two a 25 mL two neck flask was added **4.B** (300 mg, 0.6 mmol), bispinacolatodiboron (613 mg, 2.4 mmol), KOAc (296 mg, 3.0 mmol) and Pd(dppf)Cl₂ (44 mg, 0.06 mmol). The flask was purged 5 times to remove excess air and was placed under an N₂ atmosphere. 5 mL 1,4-dioxane was then added to the flask, and the solution was refluxed for 16 h. The reaction was cooled to room temperature, filtered through a celite plug and concentrated *in vacuo* to give a brown solid. The product was further purified via column chromatography (10 % EtOAc/Hexanes) to give a white powdery solid (125 mg, 35 %). ¹H NMR (500 MHz, CDCl₃) δ 7.91 (s, 1H), 7.84 (d, *J* = 7.5 Hz, 2H), 7.75 (d, *J* = 7.5 Hz, 2H), 3.89 (q, *J* = 7.1 Hz, 4H), 3.08 (s, 4H), 1.37 (s, 24H), 0.97 (t, *J* = 7.1 Hz, 6H).



Synthesis of diethyl 2,2'-(2,7-bis(6-formylpyridin-3-yl)-9H-fluorene-9,9-diyl)diacetate (6.5):

A 50 mL round bottom flask was charged with **6.G** (200 mg, 0.34 mmol), 5-bromo-2-formylpyridine (157 mg, 0.85 mmol), Cs₂CO₃ (331 mg, 1.01 mmol) and Pd(dppf)Cl₂ (25 mg, 0.03 mmol). DMF (6 mL) was added to the flask, the solution was purged with N₂,

and refluxed for 16 h. Methanol was added to the reaction mixture and the precipitate filtered via vacuum filtration to afford a tan solid. The product was further purified via column chromatography in 5 % EtOAc/Hexanes (84 mg, 45 %). $^1\text{H NMR}$ (500 MHz, CDCl_3) δ 10.15 (s, 2H), 9.08 (s, 2H), 8.13 (d, $J = 8.0$ Hz, 2H), 8.08 (d, $J = 8.1$ Hz, 2H), 7.92 (d, $J = 7.9$ Hz, 4H), 7.73 (d, $J = 7.8$ Hz, 2H), 3.96 (q, $J = 7.8$ Hz, 4H), 3.20 (s, 4H), 1.00 (t, $J = 7.1$ Hz, 6H).



Multicomponent Self-Assembly of Ligand 6.5:

Ligand 6.5 (32 mg, 0.06 mmol) was placed in a Schlenk flask with a stir bar and the flask purged with N_2 gas. Anhydrous acetonitrile (8 mL) was added to the flask along with *p*-toluidine (13 mg, 0.12 mmol). $\text{Fe}(\text{ClO}_4)_2 \cdot 6\text{H}_2\text{O}$ (13 mg, 0.04 mmol) was dissolved in a vial with 1 mL of anhydrous acetonitrile, and the solution added to the flask via cannula transfer. The reaction mixture immediately turned a burgundy color and was allowed to

stir at reflux for 24 hours. The solution was allowed to cool and was filtered to remove any undissolved solids. The acetonitrile was removed in vacuo and the solid residue sonicated for 30 minutes with 20 mL of a 1:3 mixture of MeOH/Et₂O followed by filtration and collection of the dark purple solid.

7.7 Selected Spectra for Chapter 2

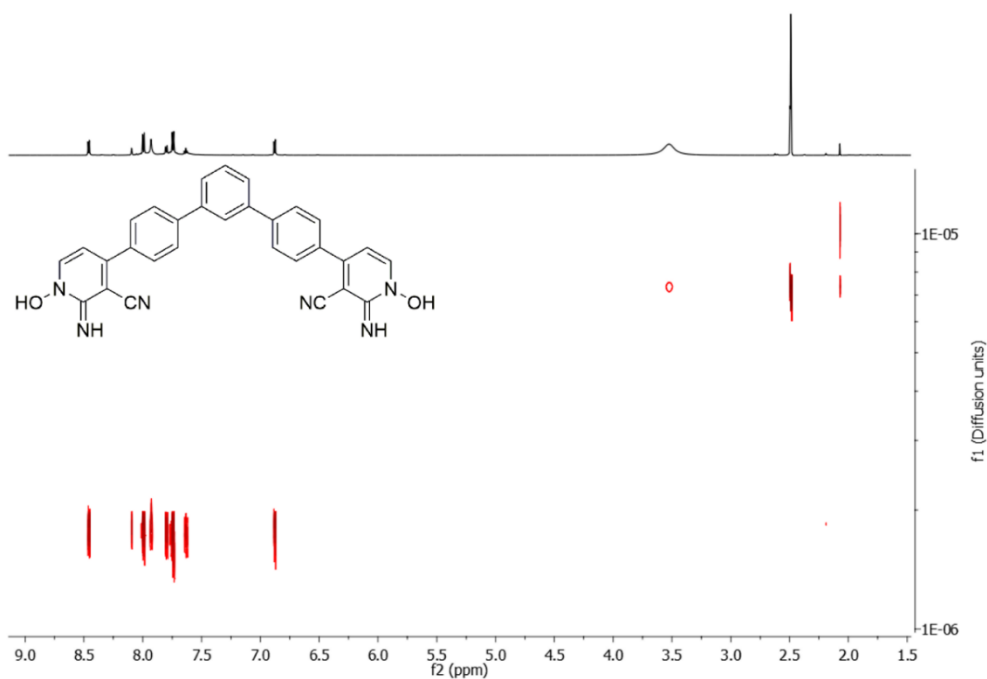


Figure 7.1. DOSY NMR spectrum of ligand **2.1**. Diffusion Coefficient = $2.72 \times 10^{-9} \text{ m}^2/\text{s}$ vs. $9.86 \times 10^{-9} \text{ m}^2/\text{s}$ for solvent (DMSO-*d*₆, 600 MHz, 298 K, $\Delta = 100 \text{ ms}$, $\delta = 1.8 \mu\text{s}$).

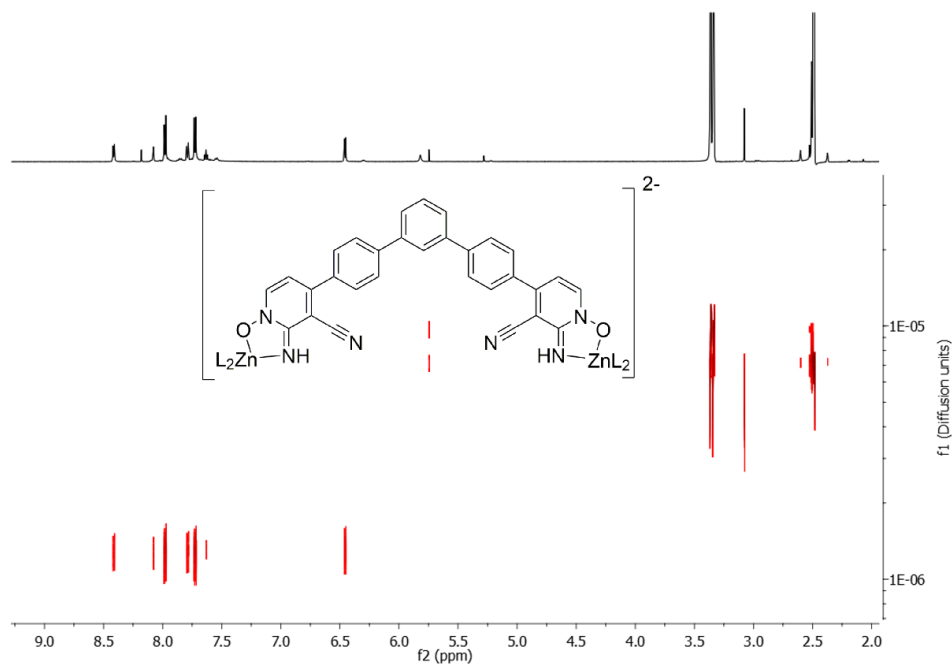


Figure 7.2. DOSY NMR spectrum of Zn₂·2.1₃ cage. Diffusion Coefficient = $1.29 \times 10^{-9} \text{ m}^2/\text{s}$ vs. $9.55 \times 10^{-9} \text{ m}^2/\text{s}$ for solvent (DMSO-*d*₆, 600 MHz, 298 K, $\Delta = 100 \text{ ms}$, $\delta = 1.8 \mu\text{s}$).

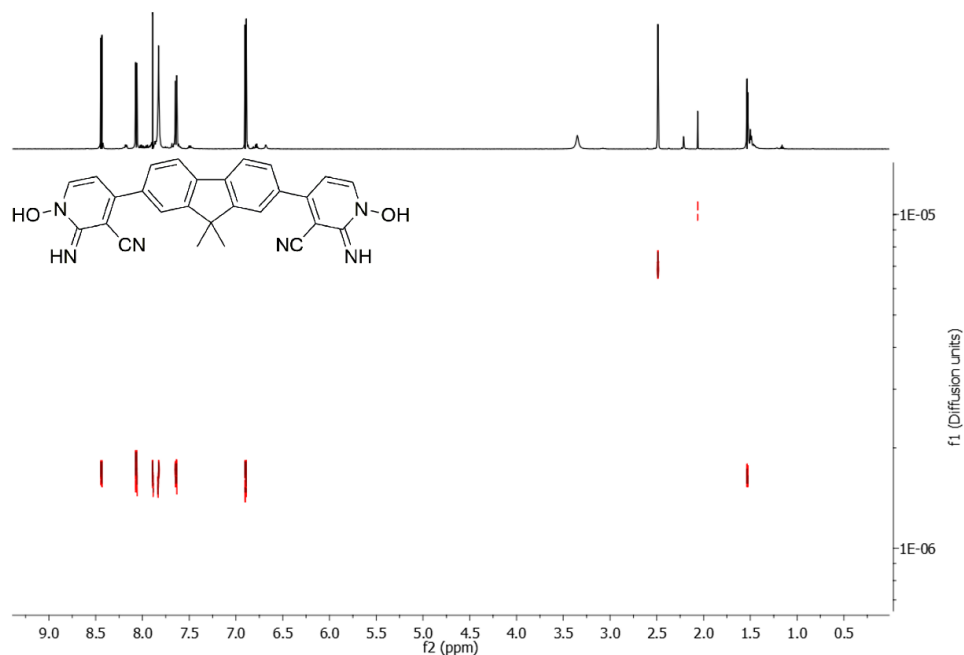


Figure 7.3. DOSY NMR spectrum of ligand 2.2. Diffusion Coefficient = $2.85 \times 10^{-9} \text{ m}^2/\text{s}$ vs. $9.62 \times 10^{-9} \text{ m}^2/\text{s}$ for solvent (DMSO-*d*₆, 600 MHz, 298 K, $\Delta = 100 \text{ ms}$, $\delta = 1.8 \mu\text{s}$).

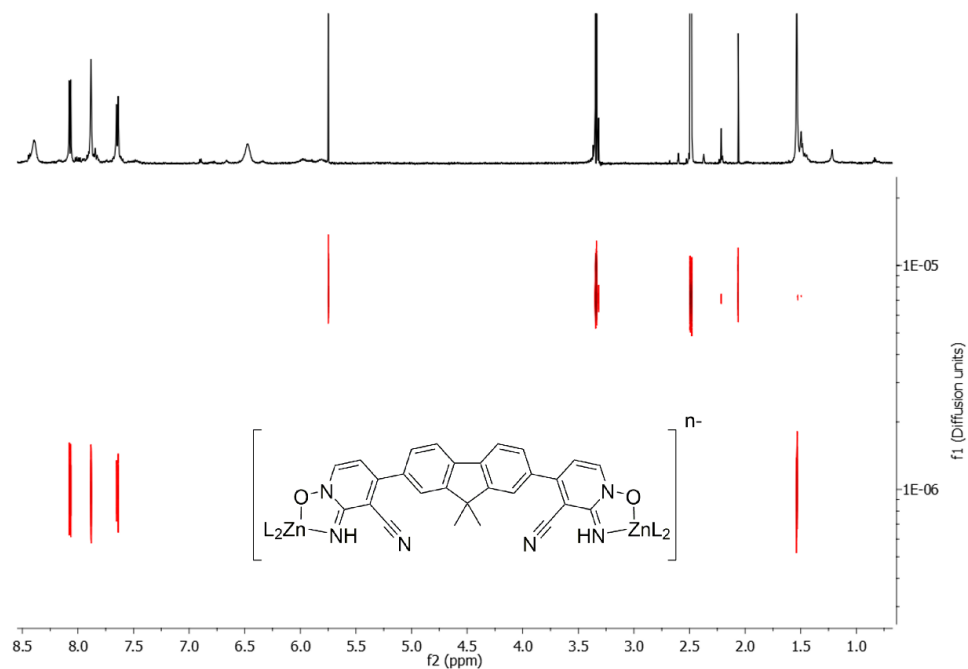


Figure 7.4. DOSY NMR spectrum of Na•2.2-Zn(OTf)₂ complex. Diffusion Coefficient = 1.54×10^{-9} m²/sec vs. 9.79×10^{-9} m²/s for solvent (DMSO-*d*₆, 600 MHz, 298 K, Δ = 100 ms, δ = 1.8 μ s).

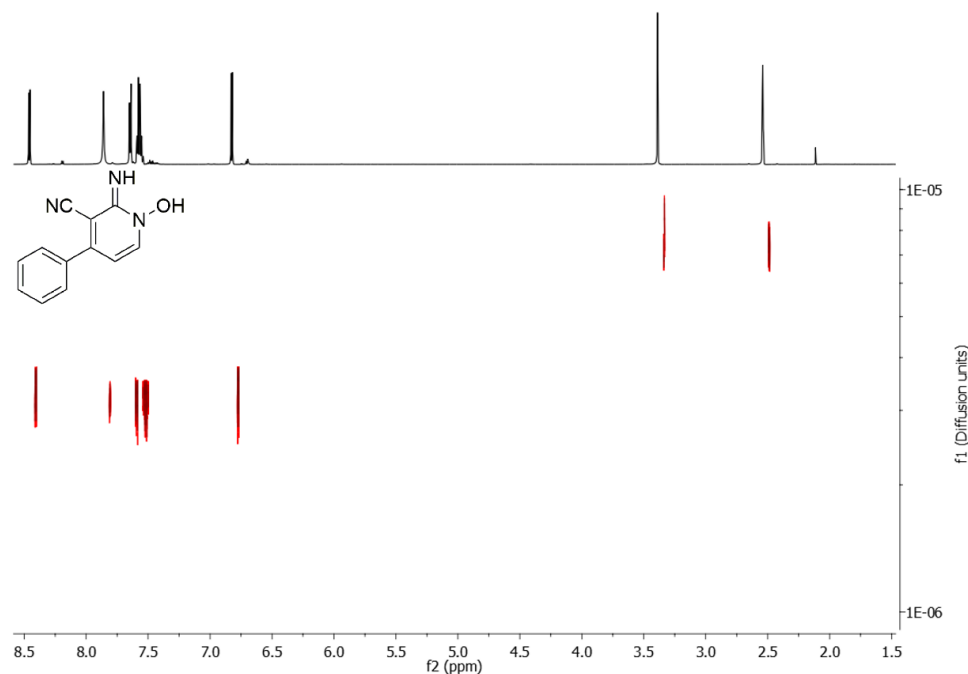


Figure 7.5. DOSY NMR spectrum of ligand 2.3. Diffusion Coefficient = 3.38×10^{-9} m²/sec vs. 9.23×10^{-9} m²/s for solvent (DMSO-*d*₆, 600 MHz, 298 K, Δ = 100 ms, δ = 1.8 μ s).

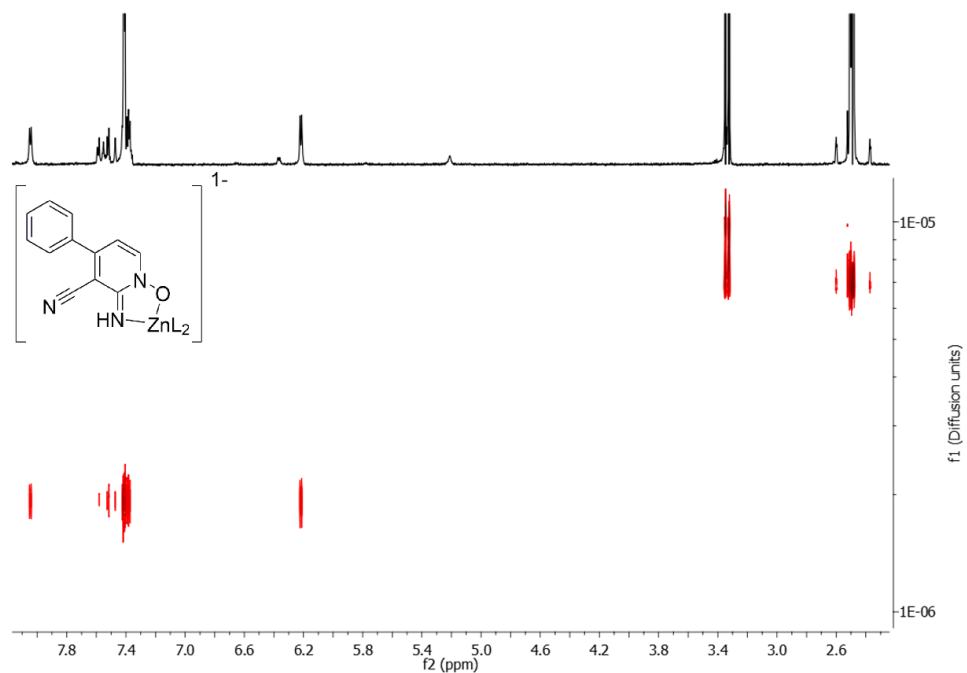


Figure 7.6. DOSY NMR spectrum of Zn 2.3 complex. Diffusion Coefficient = $2.25 \times 10^{-9} \text{ m}^2/\text{sec}$ vs. $9.33 \times 10^{-9} \text{ m}^2/\text{s}$ for solvent (DMSO- d_6 , 600 MHz, 298 K, $\Delta = 100 \text{ ms}$, $\delta = 1.8 \mu\text{s}$).

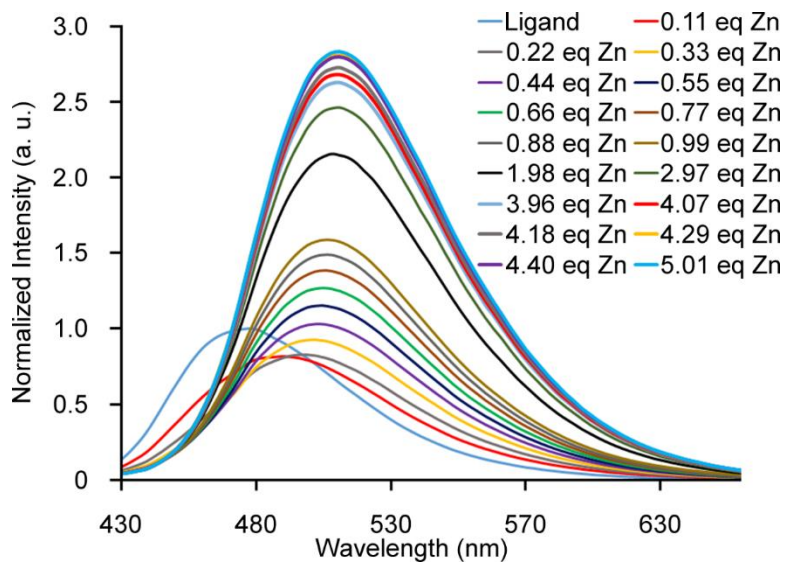


Figure 7.7. Emission spectra of a solution of Na• 2.1 in spectral grade DMSO ($30 \mu\text{M}$) upon addition of aliquots of 10 mM Zn(OTf) $_2$ solution in DMSO. Carried out to $4.51 \text{ mol eq. Zn}^{2+}$ (397 nm excitation wavelength).

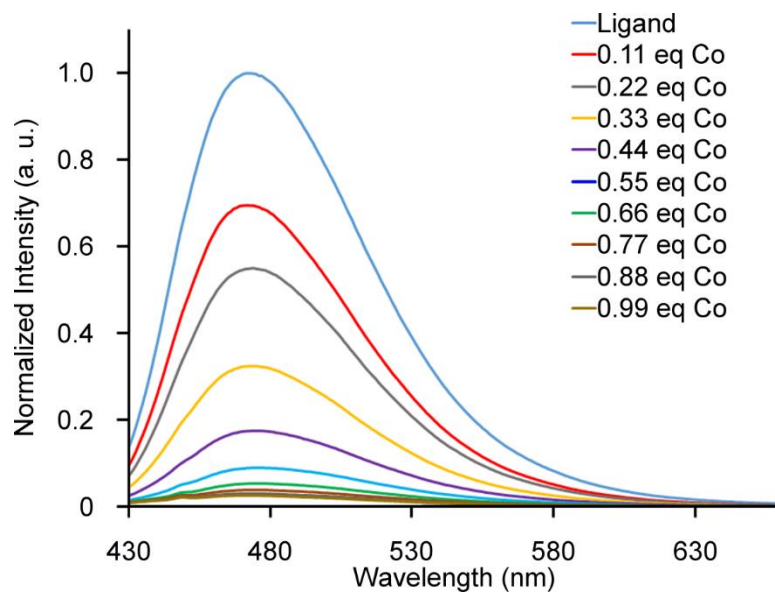


Figure 7.8. Emission spectra of a solution of Na•2.1 in spectral grade DMSO (30 μ M) upon addition of aliquots of 10 mM $\text{Co}(\text{ClO}_4)_2$ solution in DMSO. (397 nm excitation wavelength).

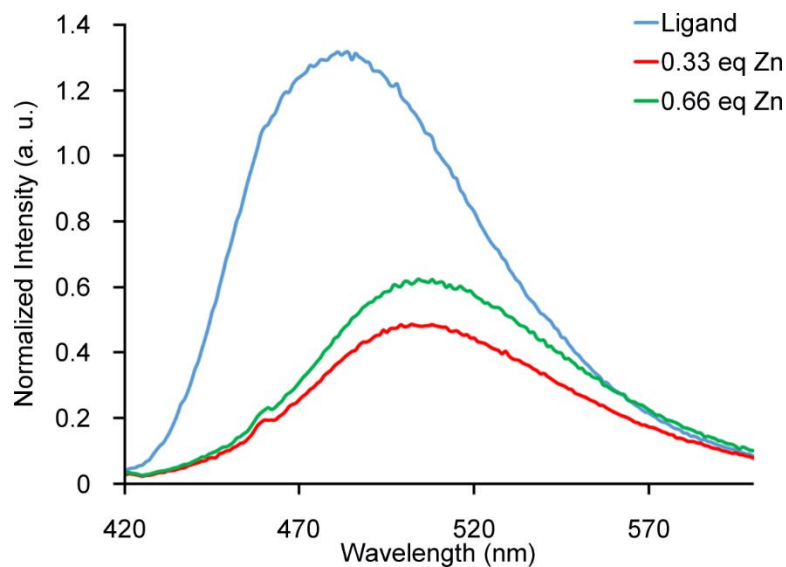


Figure 7.9. Emission spectra of a solution of Na•2.2 in spectral grade DMSO (30 μ M) upon addition of aliquots of 10 mM $\text{Zn}(\text{OTf})_2$ solution in DMSO. (404 nm excitation wavelength).

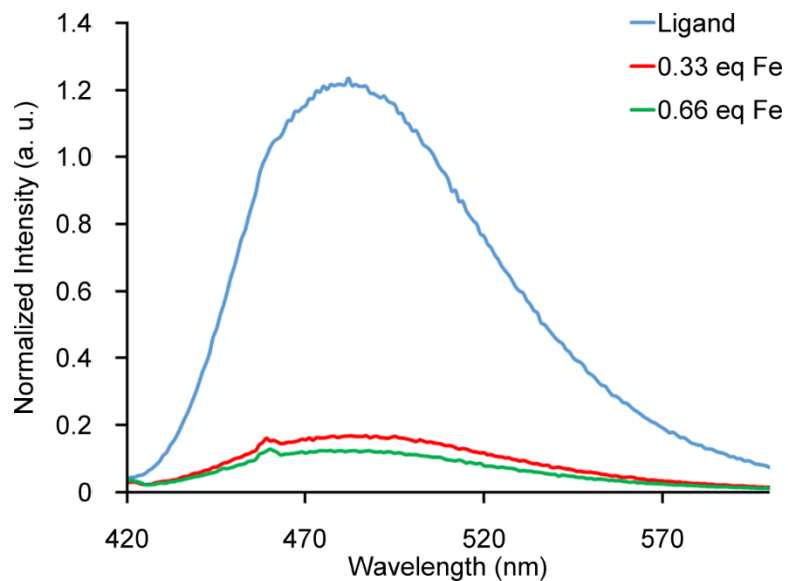


Figure 7.10. Emission spectra of a solution of Na•2.2 in spectral grade DMSO (30 μ M) upon addition of aliquots of 10 mM Zn(OTf)₂ solution in DMSO. (404 nm excitation wavelength).

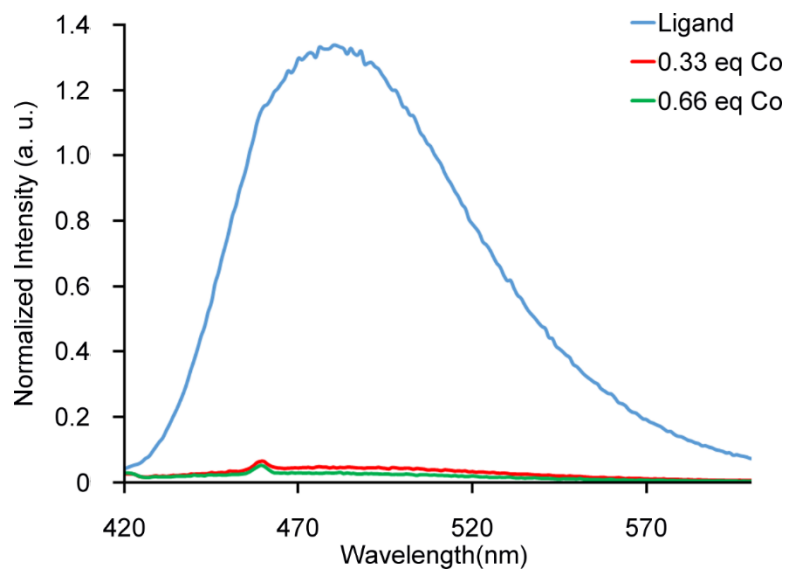


Figure 7.11. Emission spectra of a solution of Na•2.2 in spectral grade DMSO (30 μ M) upon addition of aliquots of 10 mM Zn(OTf)₂ solution in DMSO. (404 nm excitation wavelength).

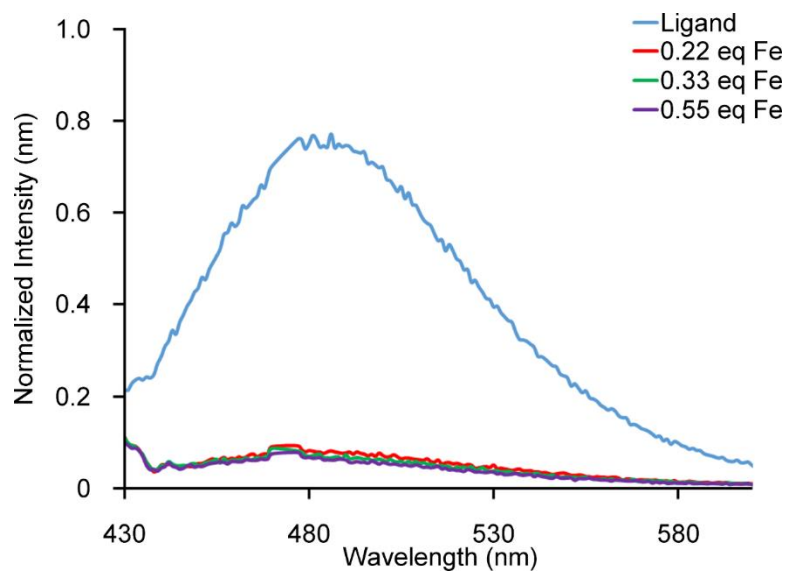


Figure 7.12. Emission spectra of a solution of Na•2.3 in spectral grade DMSO (60 μ M) upon addition of aliquots of 10 mM Fe(ClO₄)₂ solution in DMSO. (420 nm excitation wavelength).

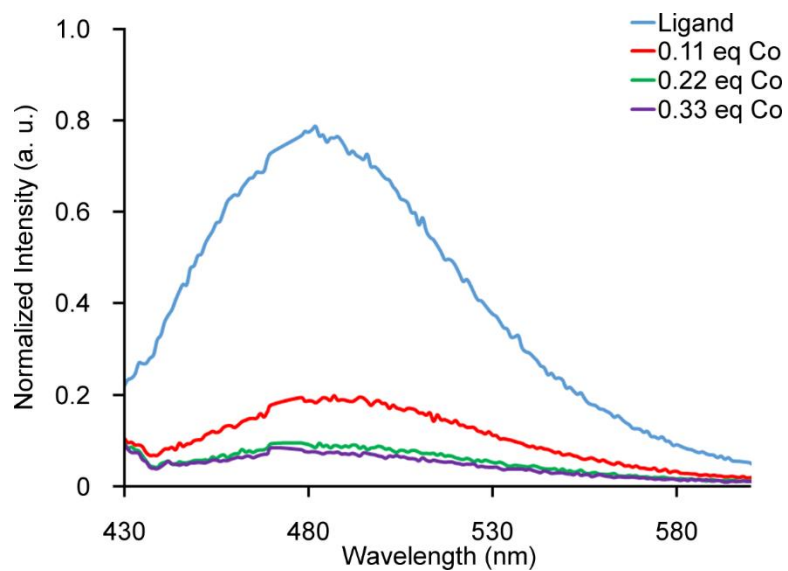


Figure 7.13. Emission spectra of a solution of Na•2.3 in spectral grade DMSO (60 μ M) upon addition of aliquots of 10 mM Co(ClO₄)₂ solution in DMSO. (420 nm excitation wavelength).

Method for Quantum Yield Calculation:

Quantum yields were calculated using quinine hemisulfate in 1M H₂SO₄ as a standard. All ligand and cage spectra were obtained using spectral grade DMSO as the solvent. For each experiment samples were prepared at concentrations of 0 μM, 15 μM, 20 μM, 25 μM and 30 μM. Emission spectra were taken immediately following the acquisition of a sample's absorption spectrum. For emission spectra, all samples were excited at 366 nm using front facing 3mL quartz cuvettes. The quantum yields were calculated using the following equation, where (*Grad*) is the slope of the graph of the integral of the emission spectra against the absorbance at the excitation wavelength, and (*n*) is the refractive index of the solvent.

$$\Phi_x = \Phi_{ST} \left(\frac{Grad_x}{Grad_{ST}} \right) \left(\frac{n_x^2}{n_{ST}^2} \right)$$

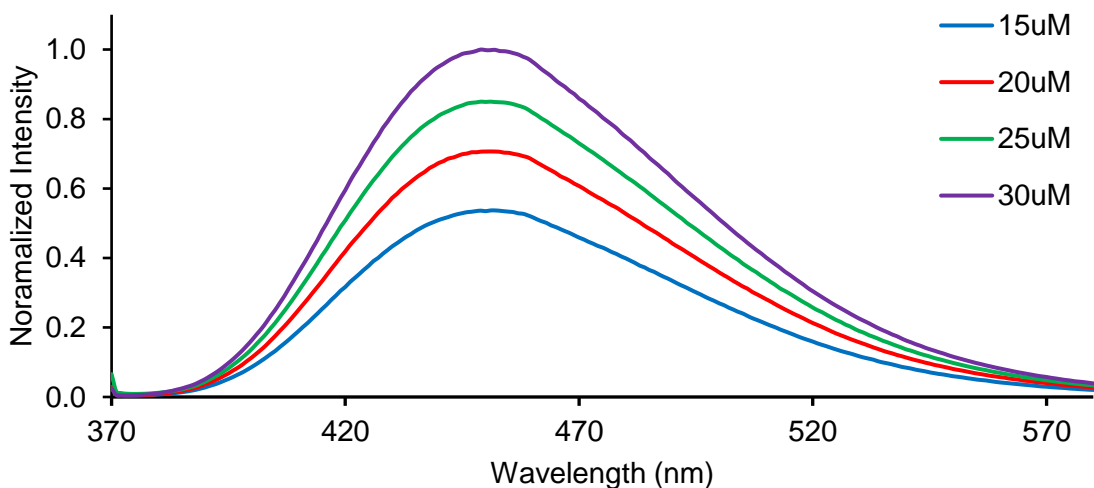


Figure 7.14. Emission spectra of Quinine hemisulfate standard in 1 M H₂SO₄ at varying concentrations (366 nm excitation wavelength).

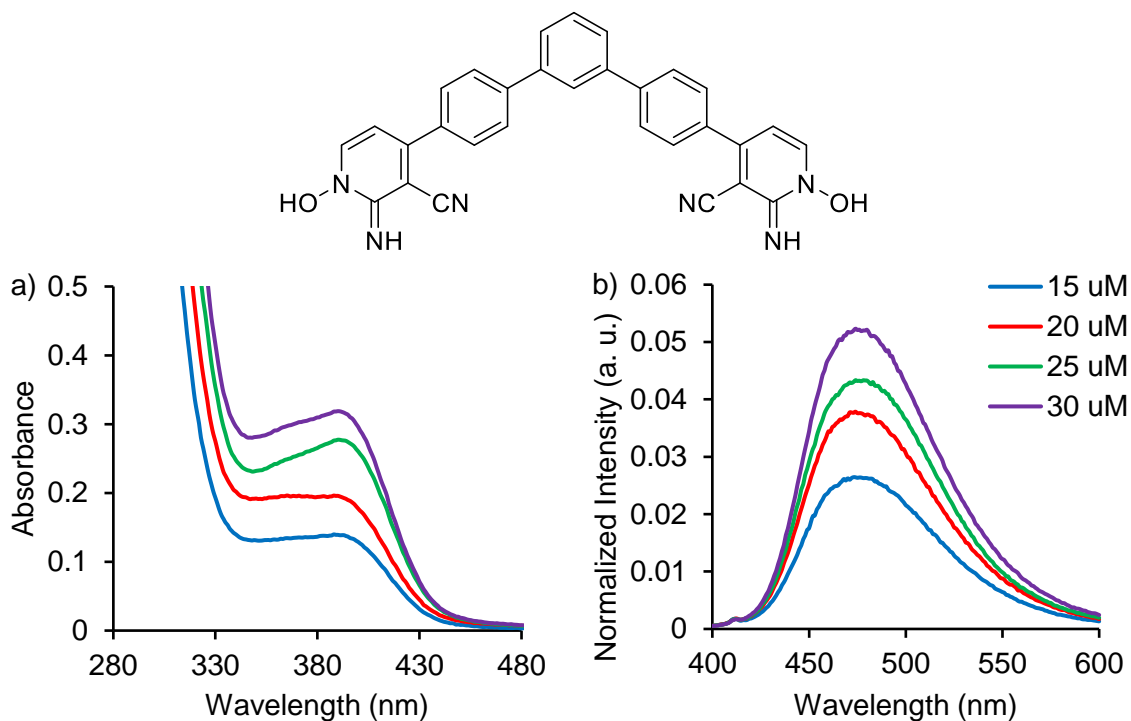


Figure 7.15. UV/Vis absorption and normalized emission spectra of **2.1** ligand in DMSO at varying concentrations (excitation wavelength 366 nm).

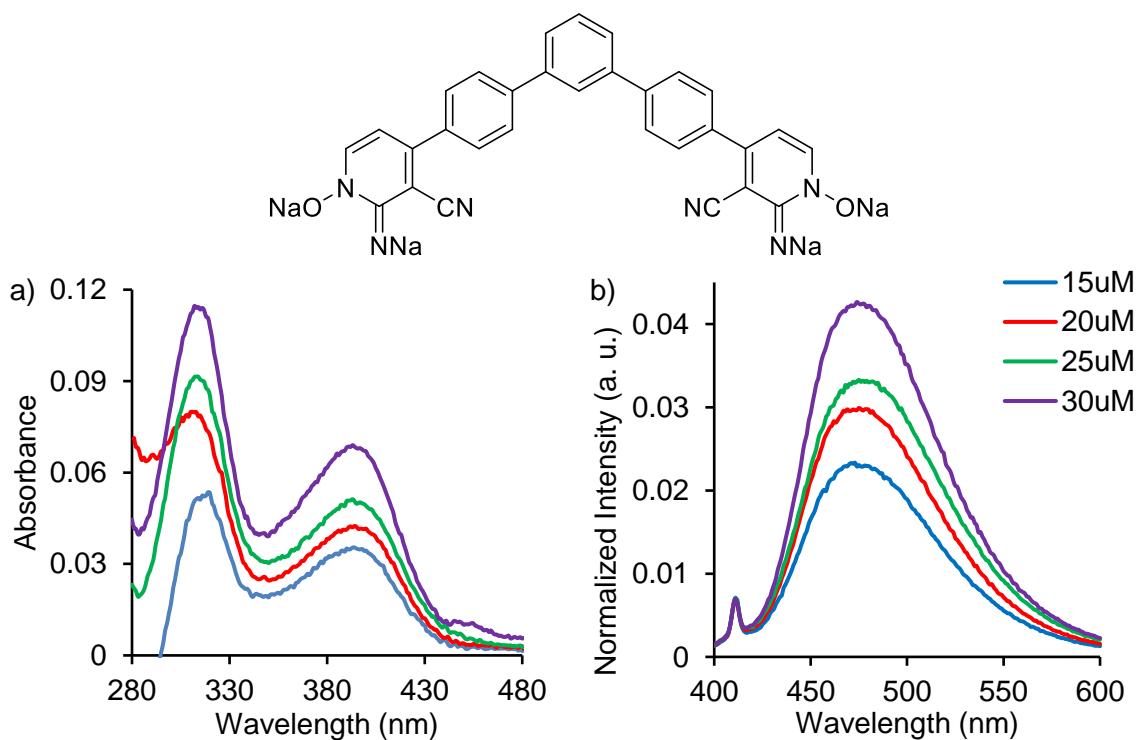


Figure 7.16. UV/Vis absorption and normalized emission spectra of Na•**2.1** ligand in DMSO at varying concentrations (excitation wavelength 366 nm).

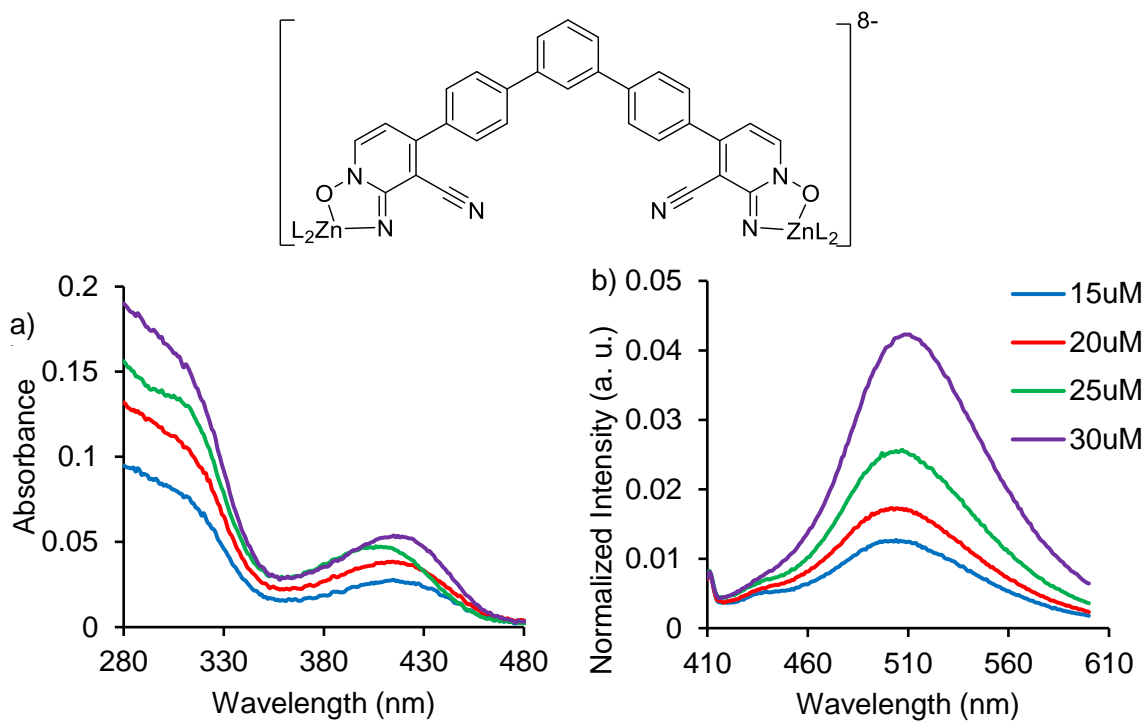


Figure 7.17. UV/Vis absorption and normalized emission spectra of $Zn_2\mathbf{2.13}$ in DMSO at varying concentrations (excitation wavelength 366 nm).

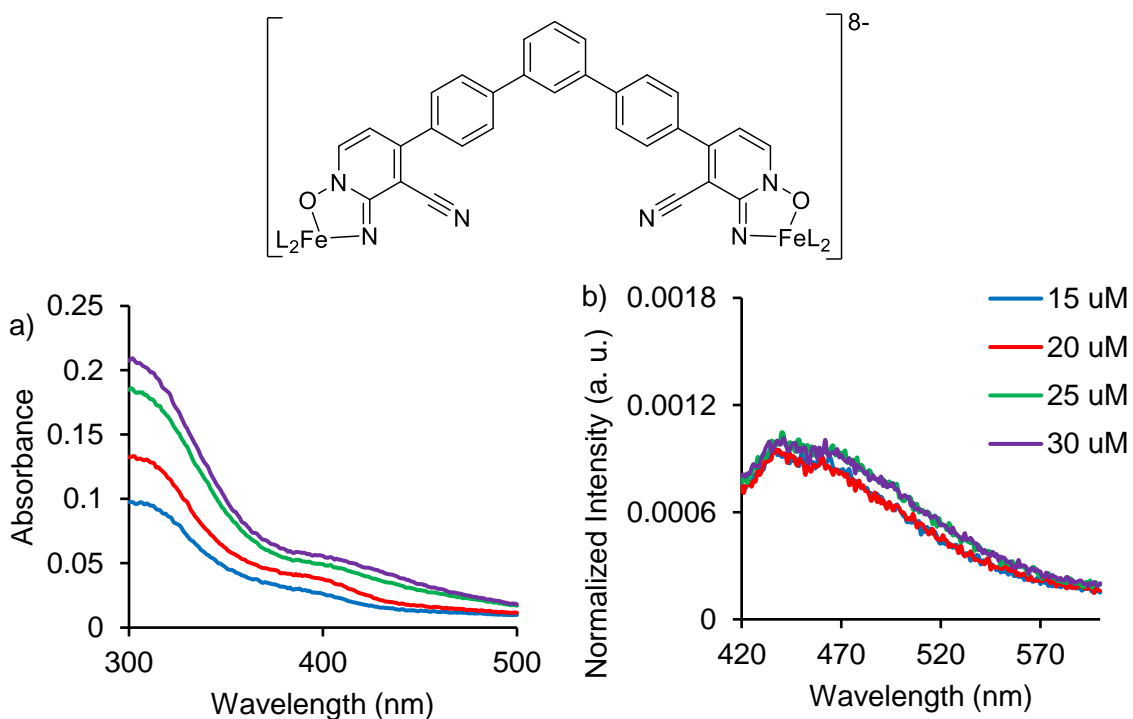


Figure 7.18. UV/Vis absorption and normalized emission spectra of $Fe_2\mathbf{2.13}$ in DMSO at varying concentrations (excitation wavelength 366 nm).

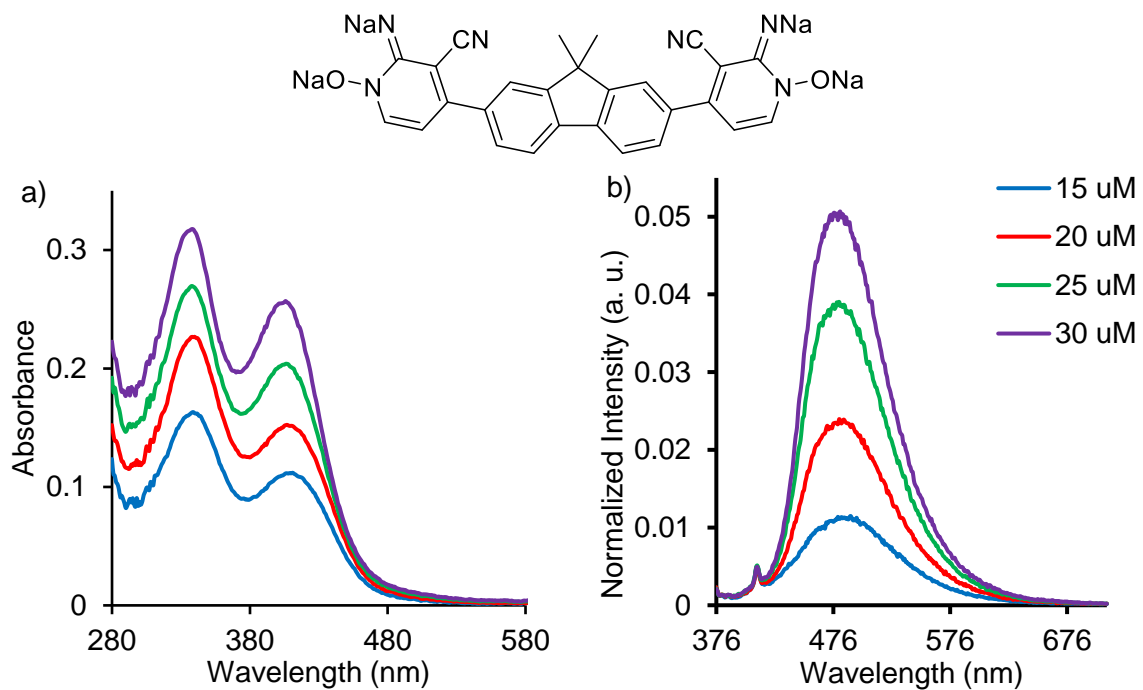


Figure 7.19. a) UV/Vis absorption and b) normalized emission spectra of Na•2.2 ligand in DMSO at varying concentrations (excitation wavelength 366 nm).

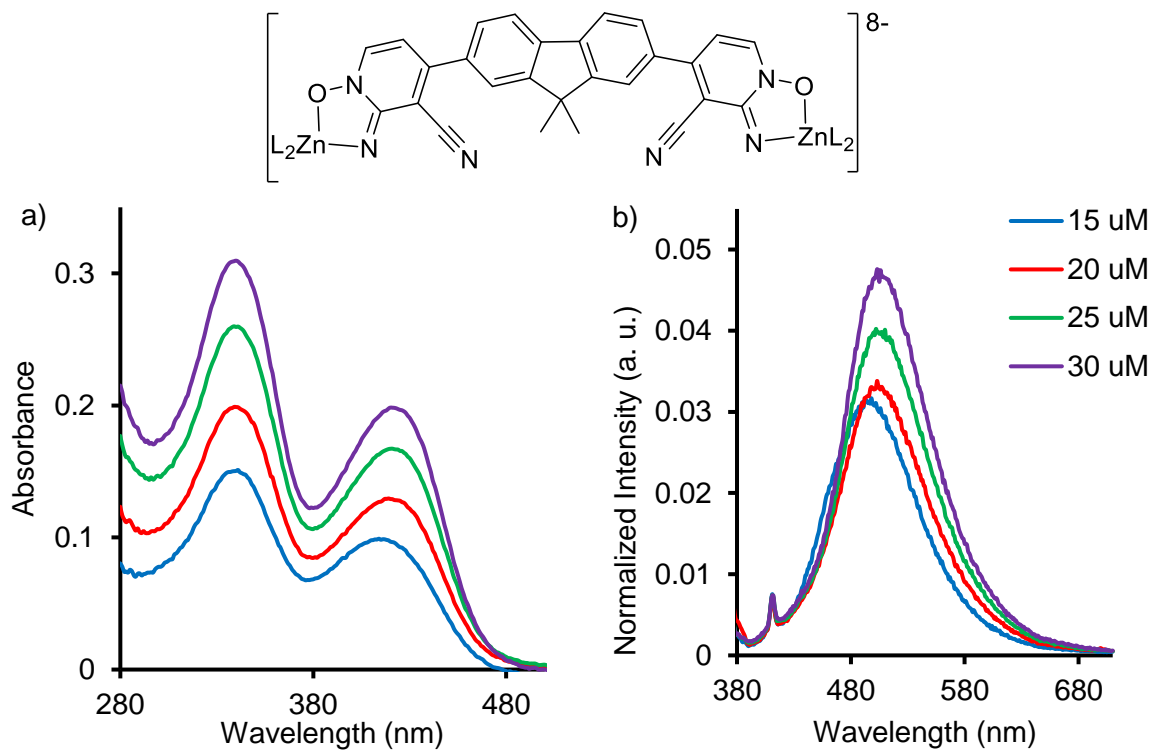


Figure 7.20. a) UV/Vis absorption and b) normalized emission spectra of Zn_x•2.2_y in DMSO at varying concentrations (excitation wavelength 366 nm).

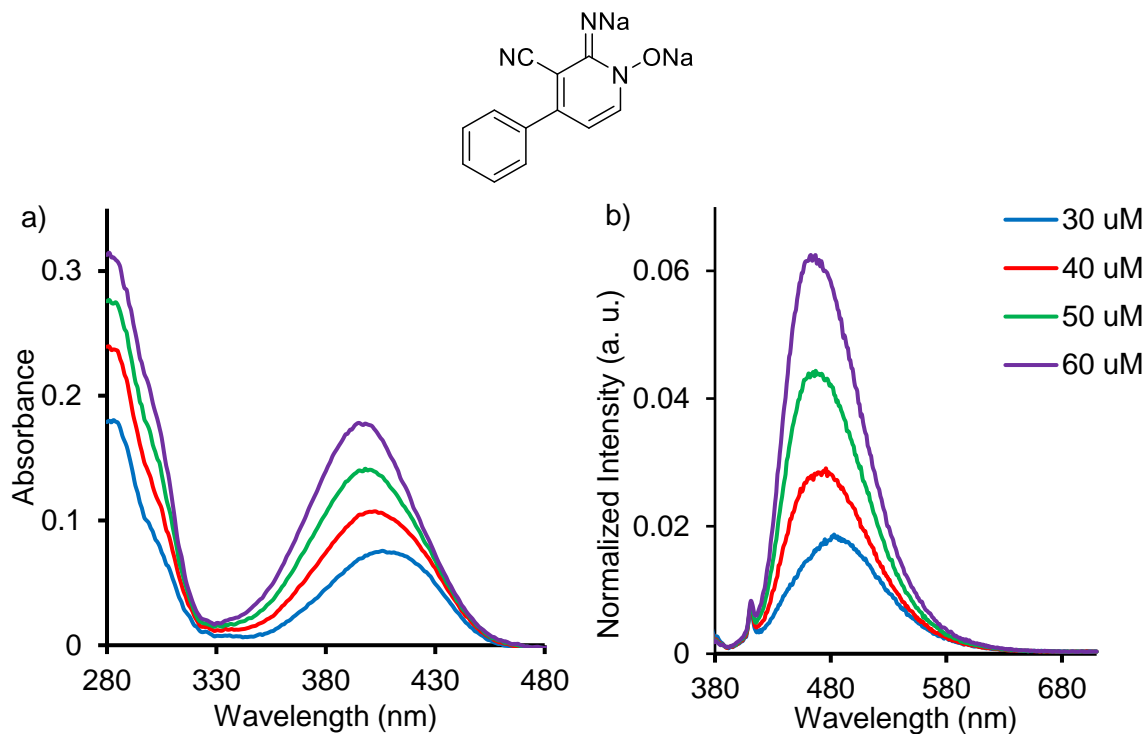


Figure 7.21. UV/Vis absorption and normalized emission spectra of Na•2.3 ligand in DMSO at varying concentrations (excitation wavelength 366 nm).

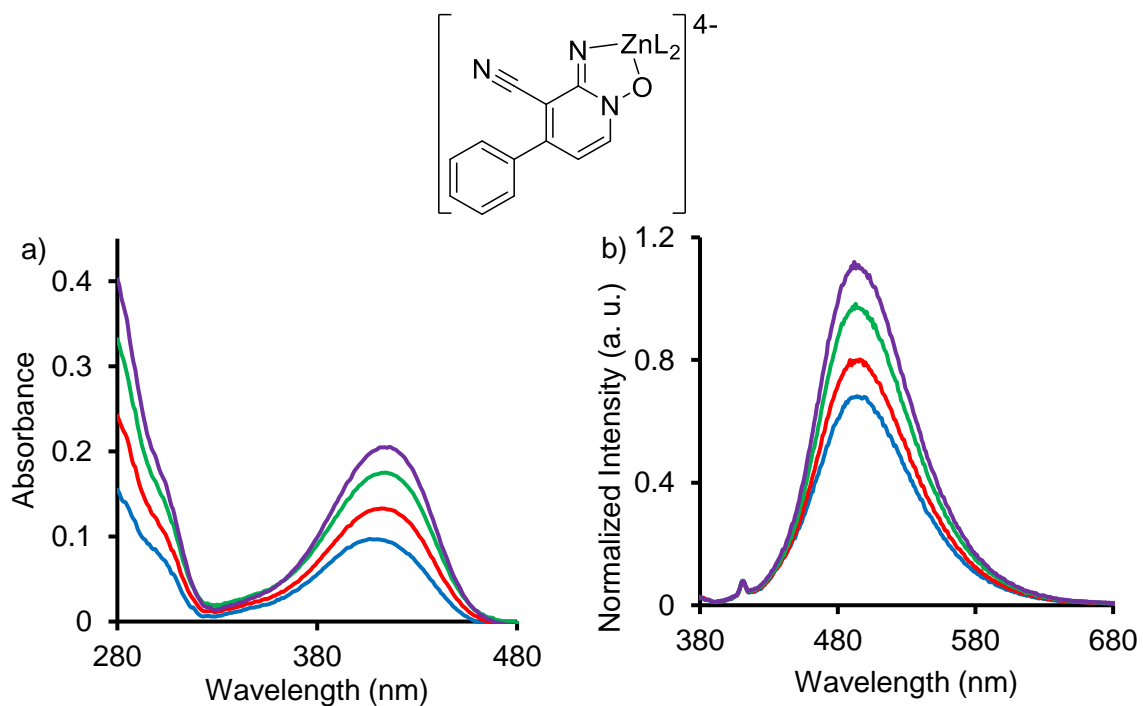


Figure 7.22. UV/Vis absorption and normalized emission spectra of Zn2.33 in DMSO at varying concentrations (excitation wavelength 366 nm).

Table 7.1. Summary of fluorescence data for Na•2.1, Na•2.2 and Na•2.3 and their respective complexes.

Ligand	max.	ϕ	Zn max	Zn ϕ	Fe max	Fe ϕ	Co max
Na41	477 nm	5.20 %	508 nm	6.40 %	478 nm	0.12 %	481 nm
Na42	478 nm	1.50 %	504 nm	2.00 %	480 nm	-	483 nm
Na23	477 nm	4.19 %	495 nm	10.53 %	490 nm	-	487 nm

7.8 Selected Spectra for Chapter 3

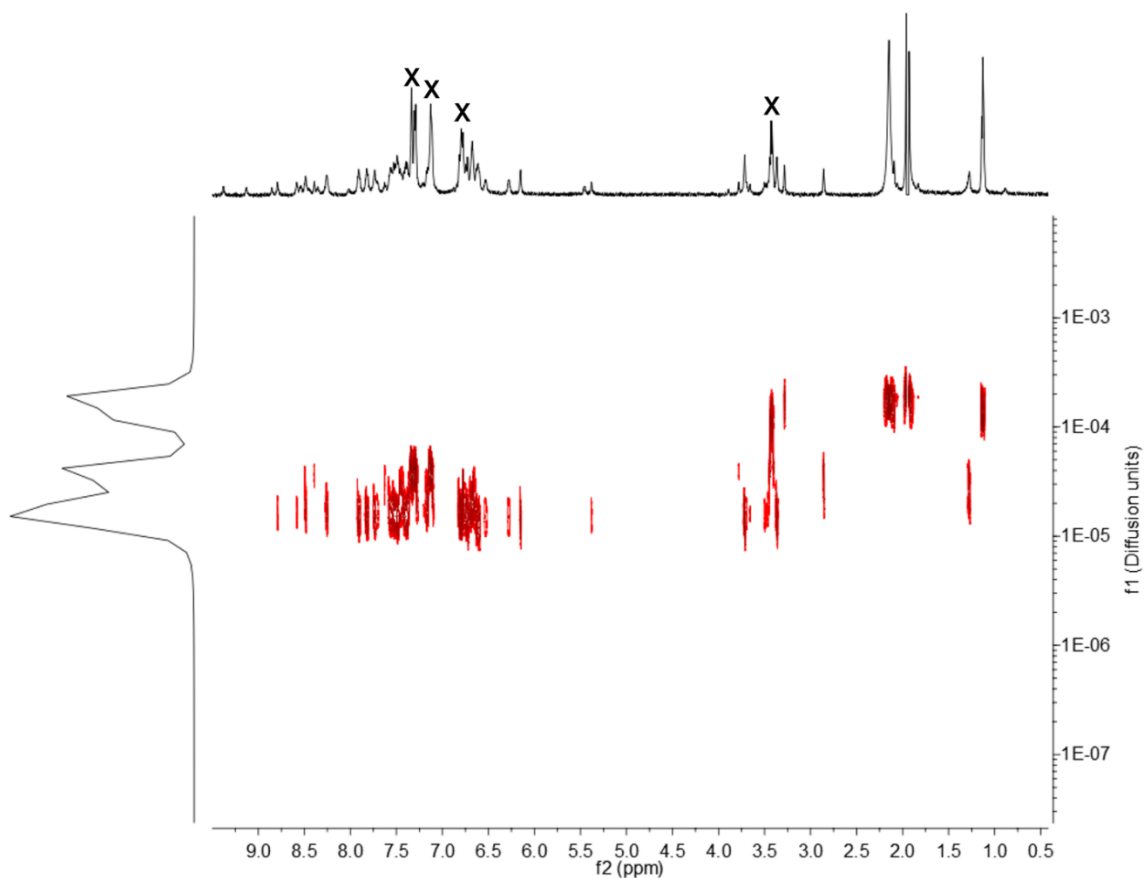


Figure 7.23: 2D-DOSY NMR spectrum of the displacement reaction of **3.2** (5.8 mM) using **F** (17.5 mM). (CD₃CN, 600 MHz, 298 K). **X** = displaced diaminoxanthone **X**.

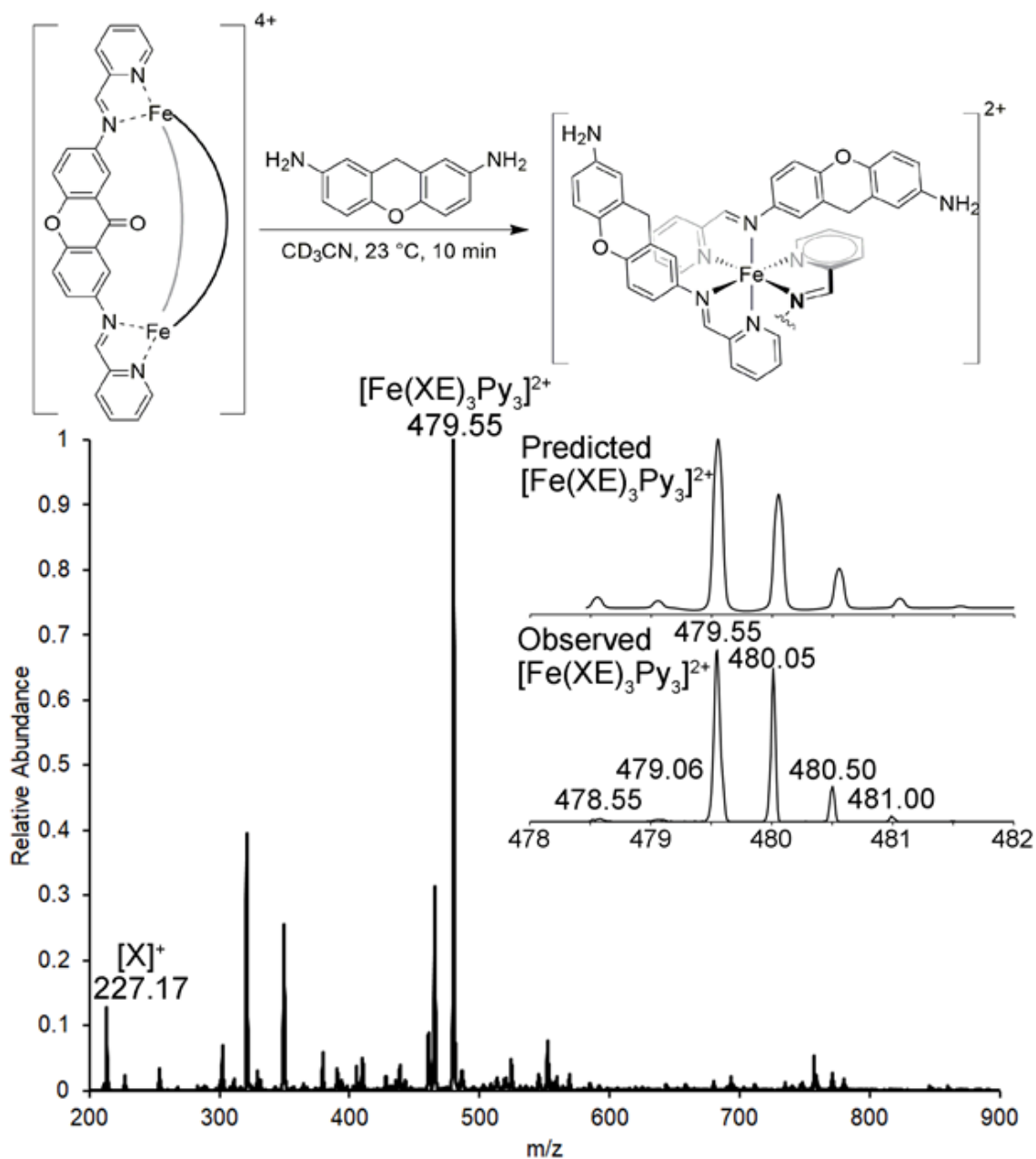


Figure 7.24: Full MS of the ligand displacement reaction of **3.2** and dianiline **XE** (3 mol.-eq) in CH_3CN at $t = 6$ h. With stacked comparison of the predicted $[\text{Fe}(\text{XE})_3\text{Py}_3]^{2+}$ ion versus the experimentally observed peak.

7.9 Selected Spectra for Chapter 4

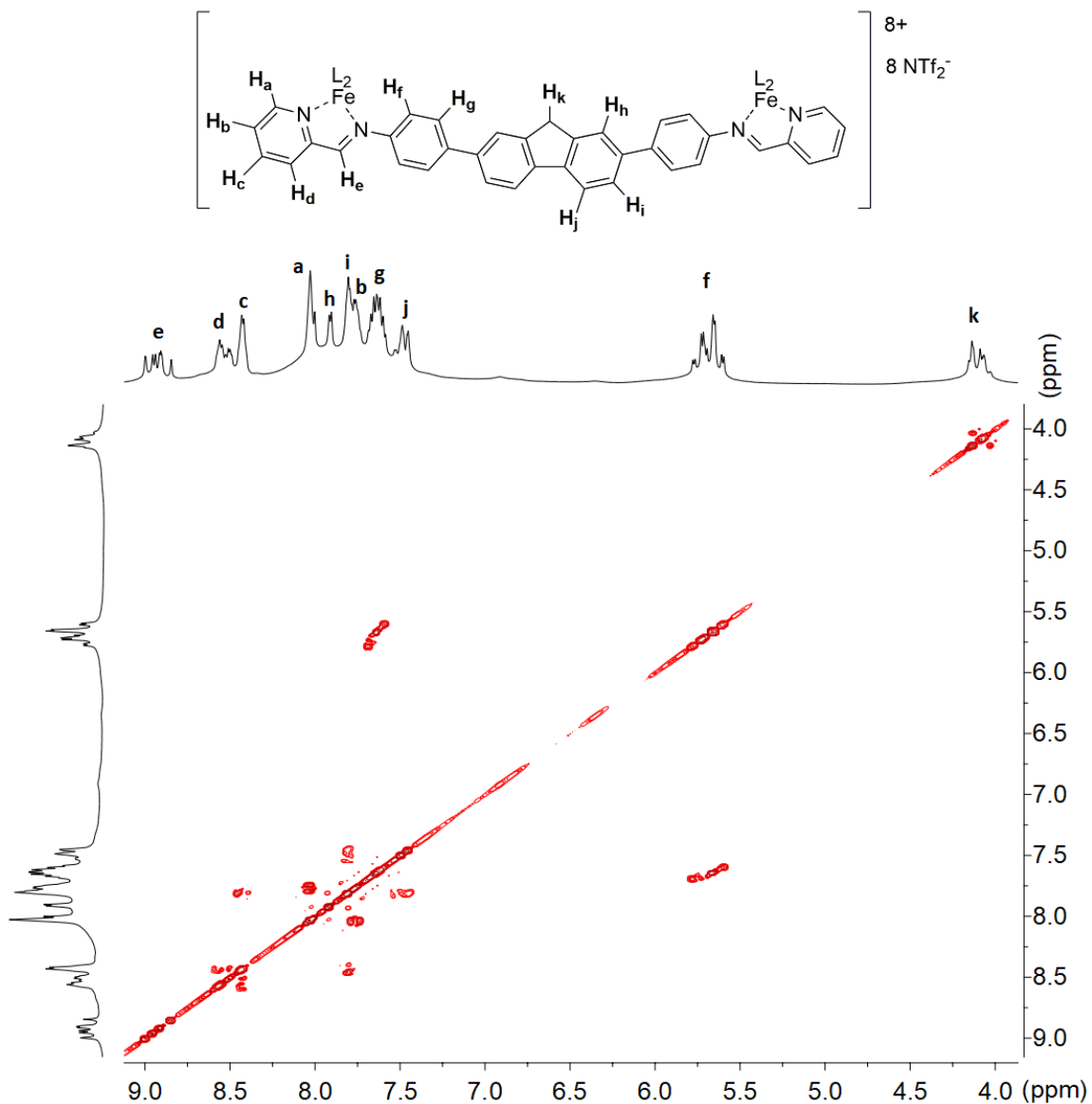


Figure 7.25. gCOSY NMR spectrum of fluorene cage **4.1** (CD_3CN , 600 MHz, 298 K).

Note - the assignments here (and throughout Section 7.9) refer to the contributing ligand protons in the cage. There is obviously clustering of these peaks for each of the T, S3 and C4 isomers: each label corresponds to all protons a-k in the cages. For isomer assignment (for protons where the peaks are sufficiently separated), see Figures 4.1, 4.4, 7.35 and 7.44).

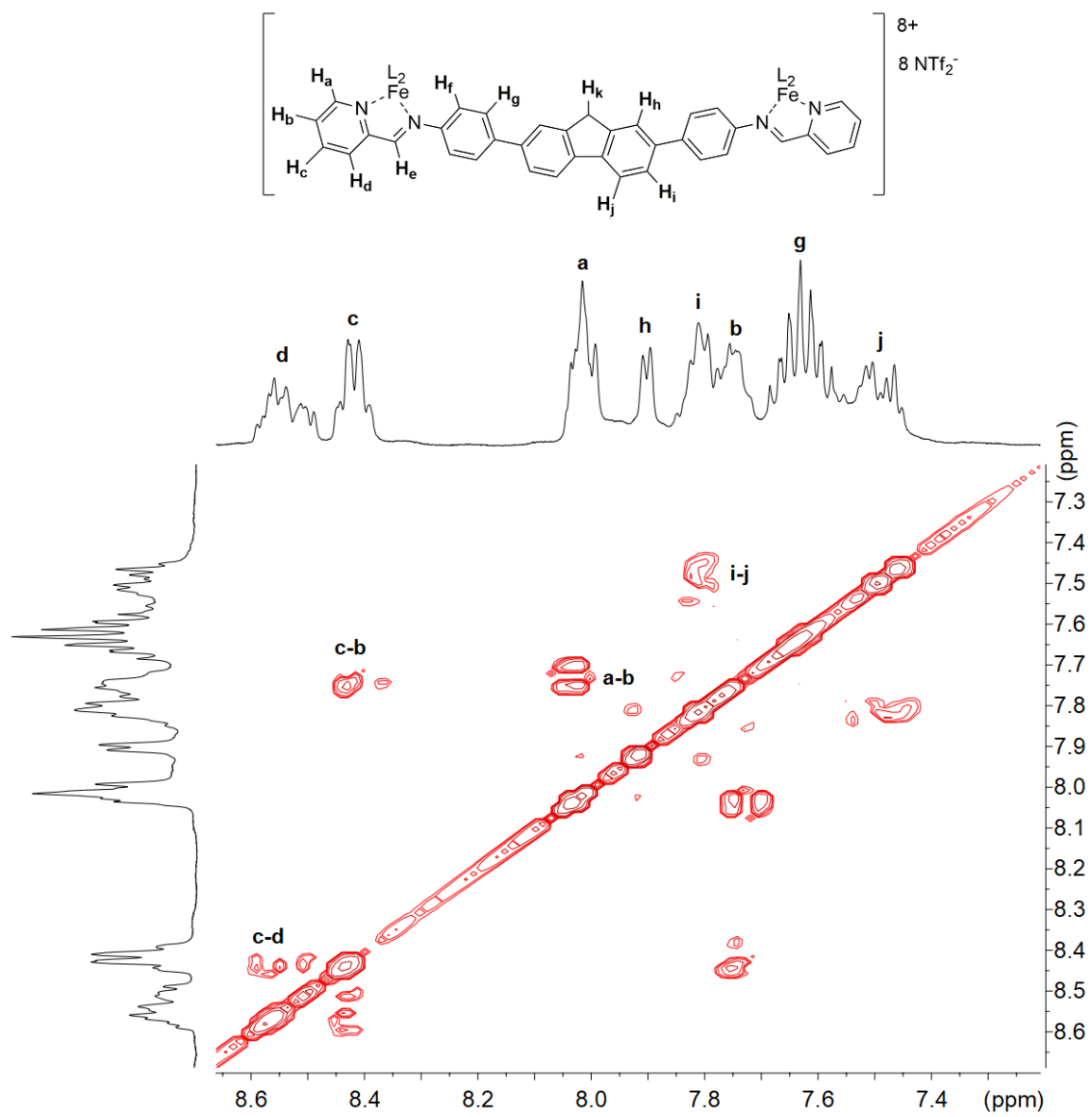


Figure 7.26. gCOSY NMR spectrum of fluorene cage **4.1**. Expansion of the 7.2-8.6 ppm region (CD₃CN, 600 MHz, 298 K).

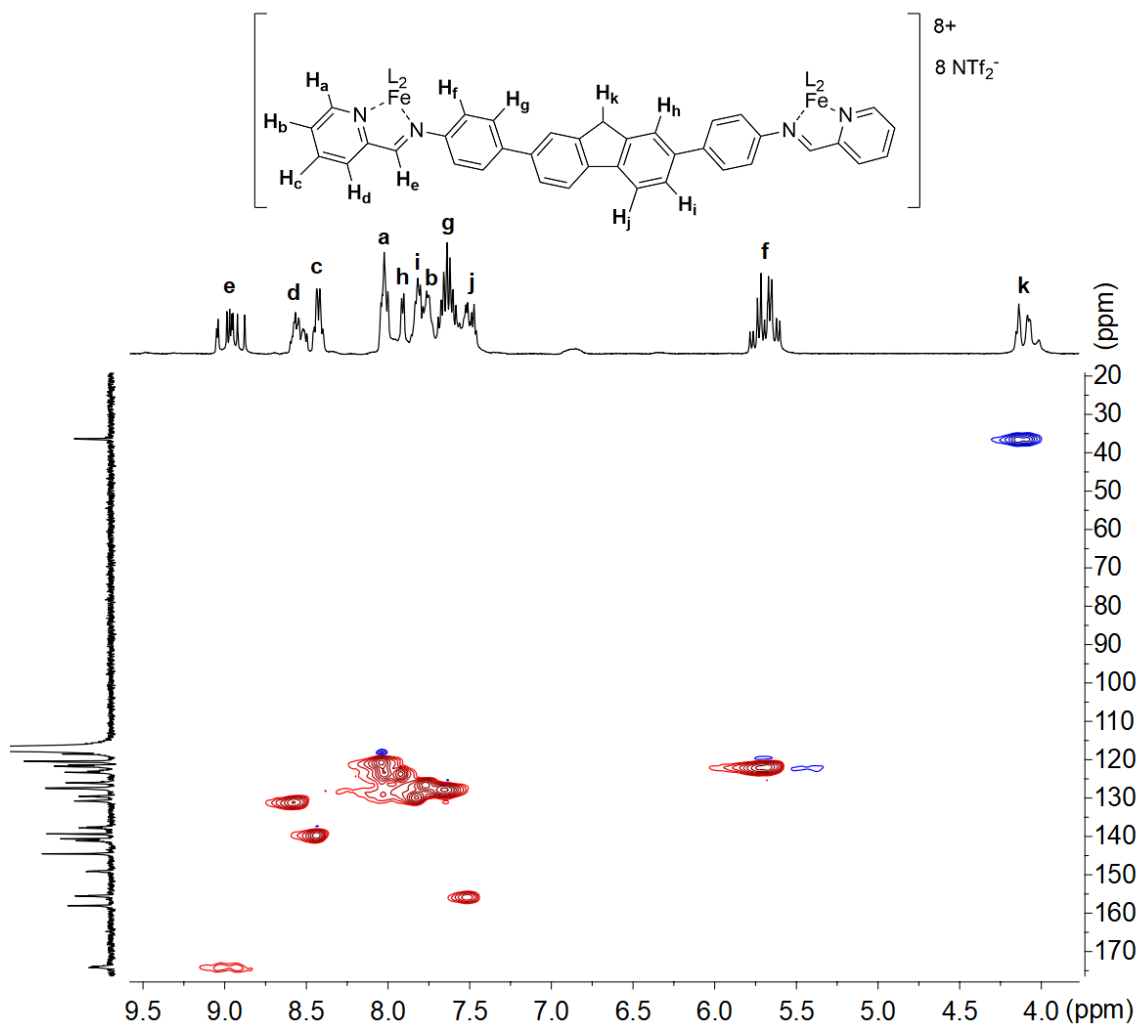


Figure 7.27. DEPT-HSQC NMR spectrum of fluorene cage **4.1** (CD_3CN , 400 MHz, 298 K).

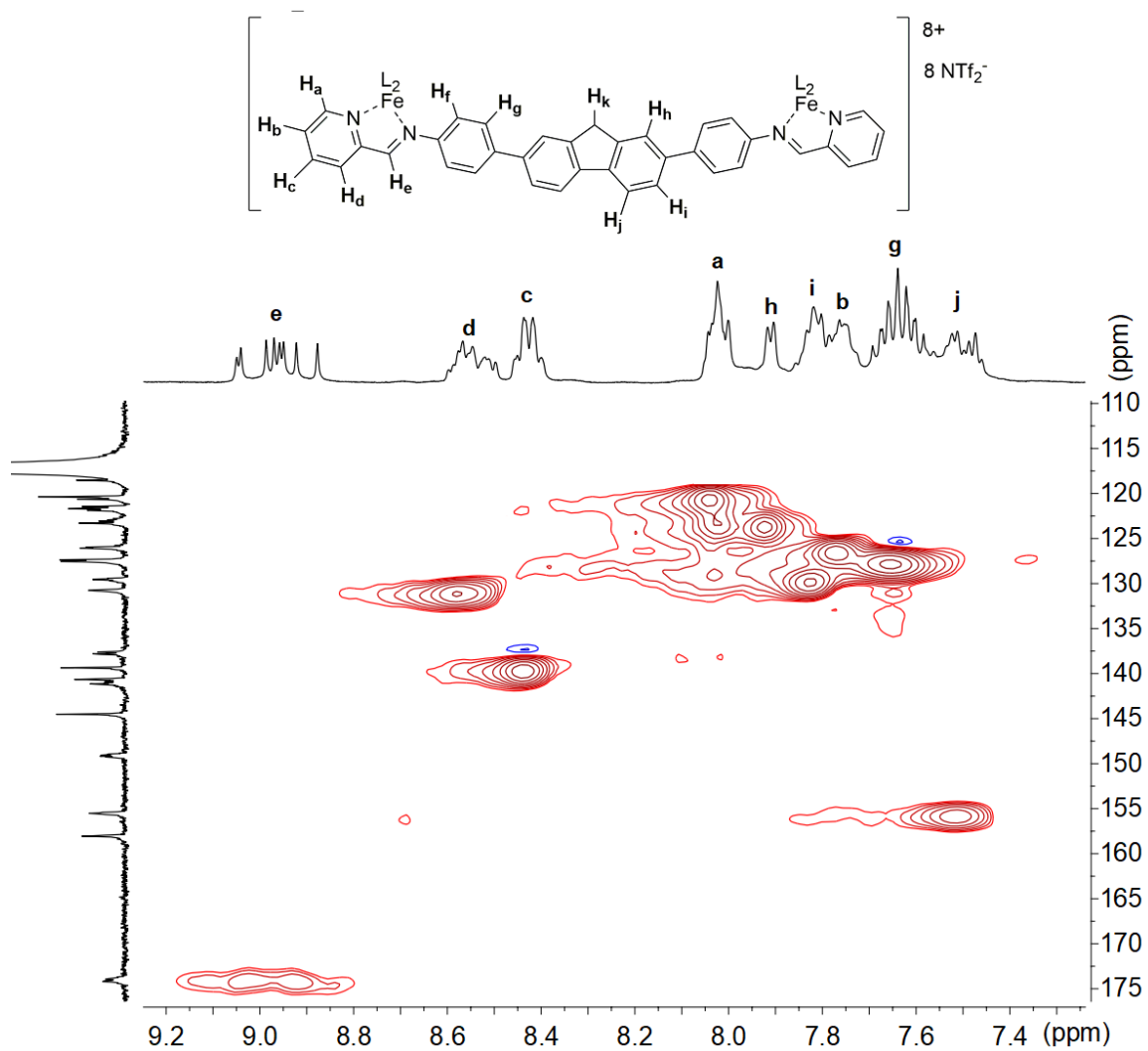


Figure 7.28. Expanded DEPT-HSQC NMR spectrum of fluorene cage **4.1** (CD_3CN , 400 MHz, 298 K).

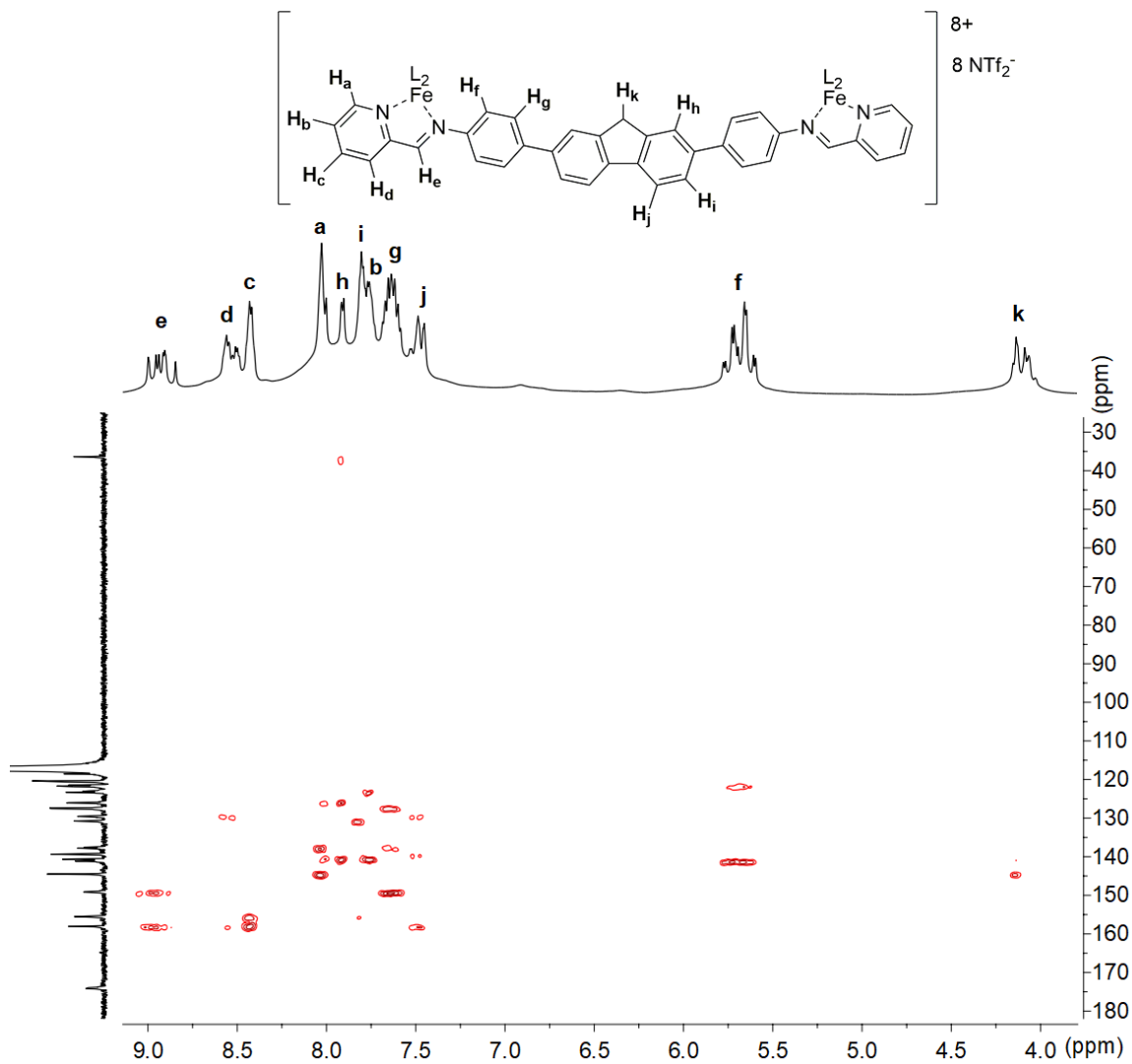


Figure 7.29. HMBC NMR spectrum of fluorene cage **4.1** (CD_3CN , 400 MHz, 298 K).

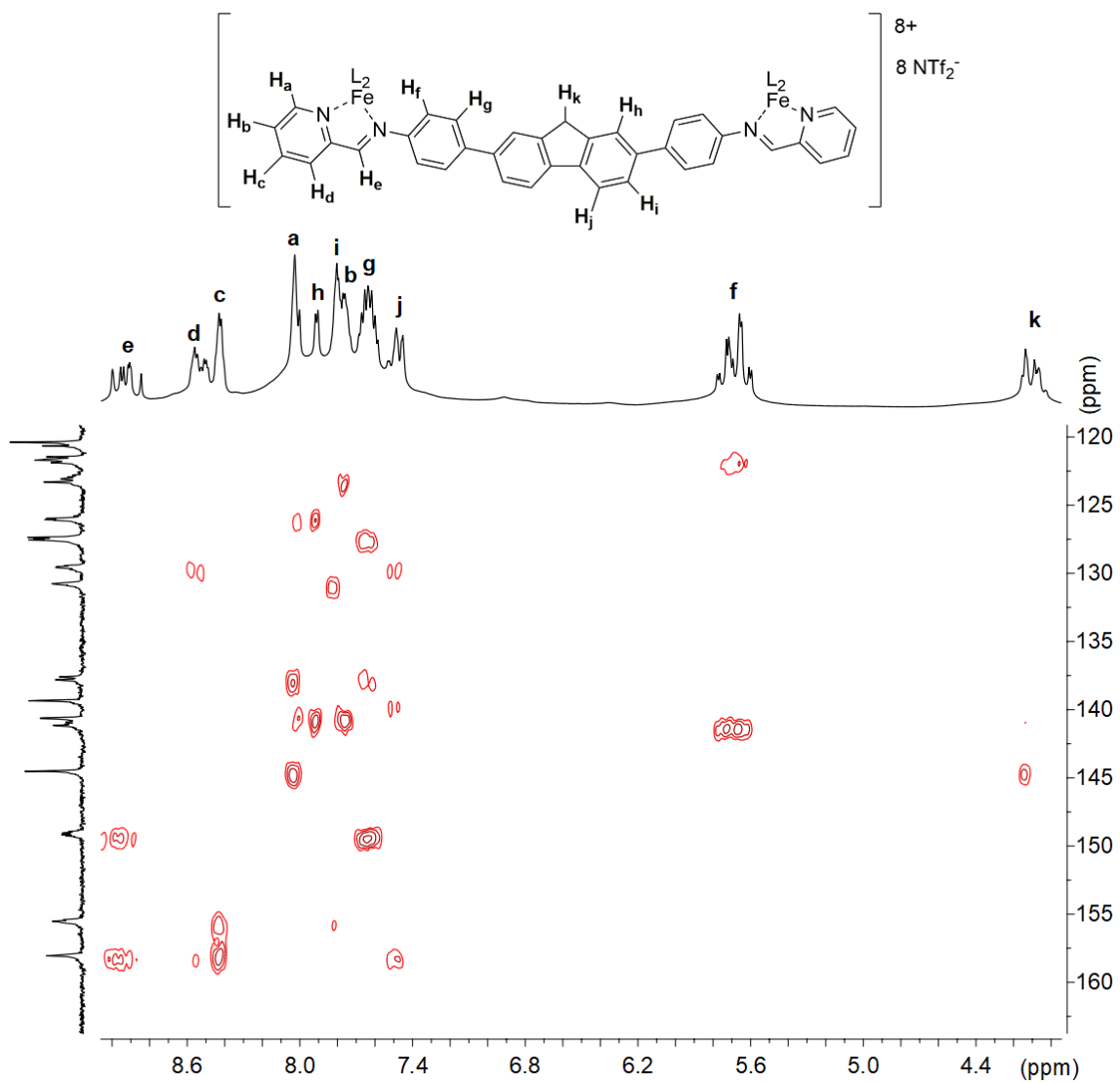


Figure 7.30. Expanded HMBC NMR spectrum of fluorene cage **4.1** (CD_3CN , 400 MHz, 298 K).

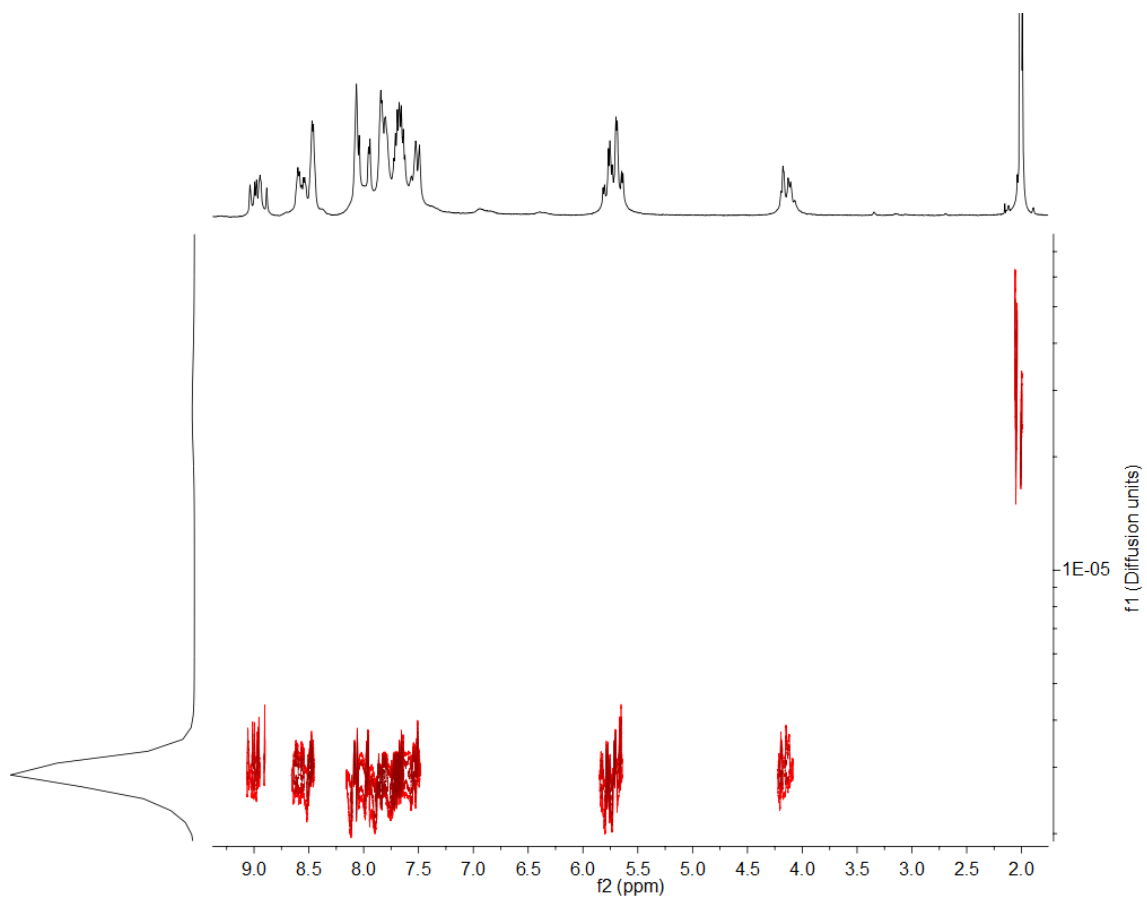


Figure 7.31. ¹H-DOSY NMR spectrum of fluorene cage **4.1** (CD₃CN, 600 MHz, 298 K, Δ = 100 ms, δ = 1.8 μs, Diffusion constant = 3.020 × 10⁻¹⁰ m²/s for cage **1** vs. 3.890 × 10⁻⁹ m²/s for the solvent).

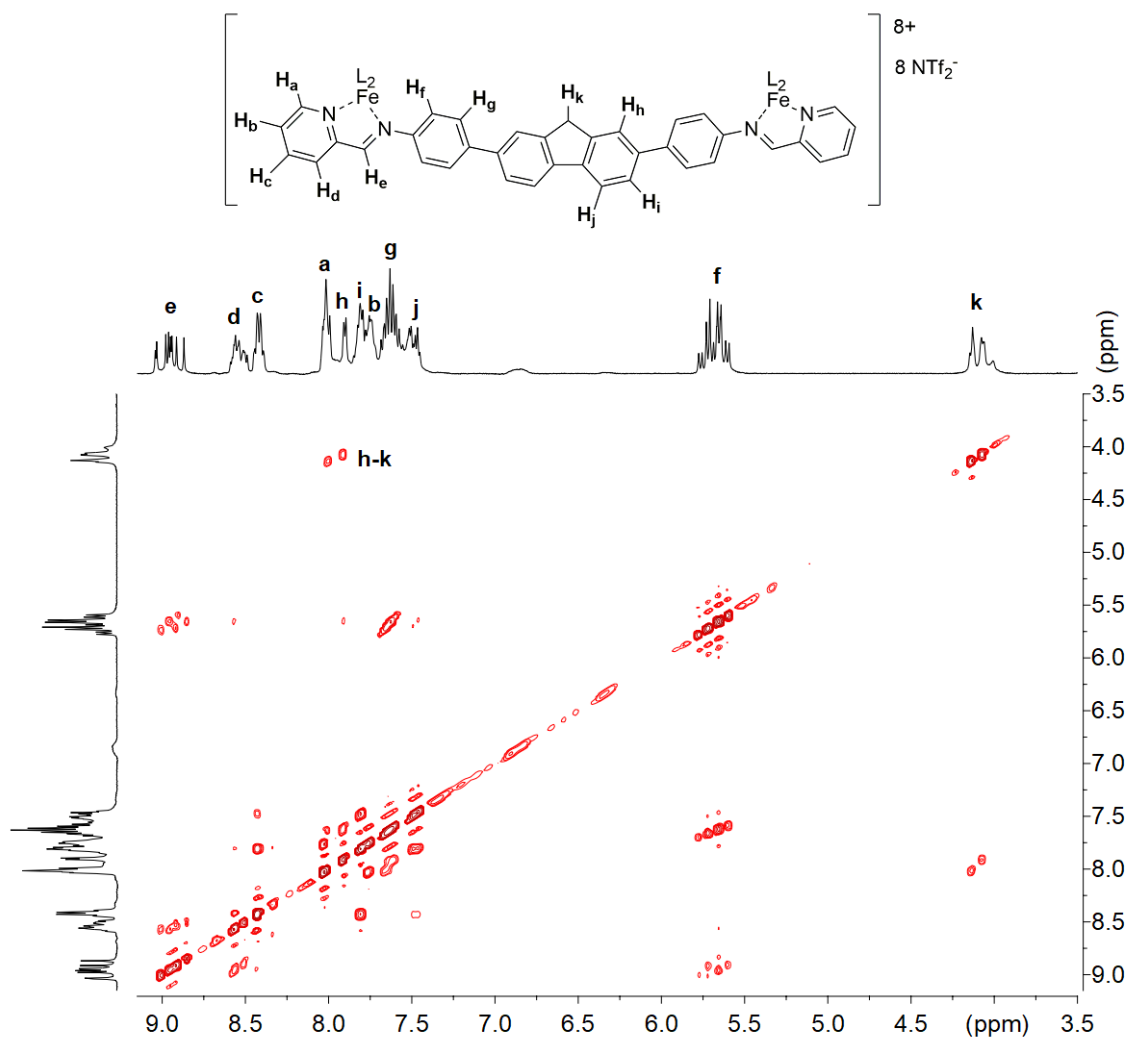


Figure 7.32. gNOESY NMR spectrum of fluorene cage **4.1** (CD_3CN , 600 MHz, 298 K, mixing time = 300 ms).

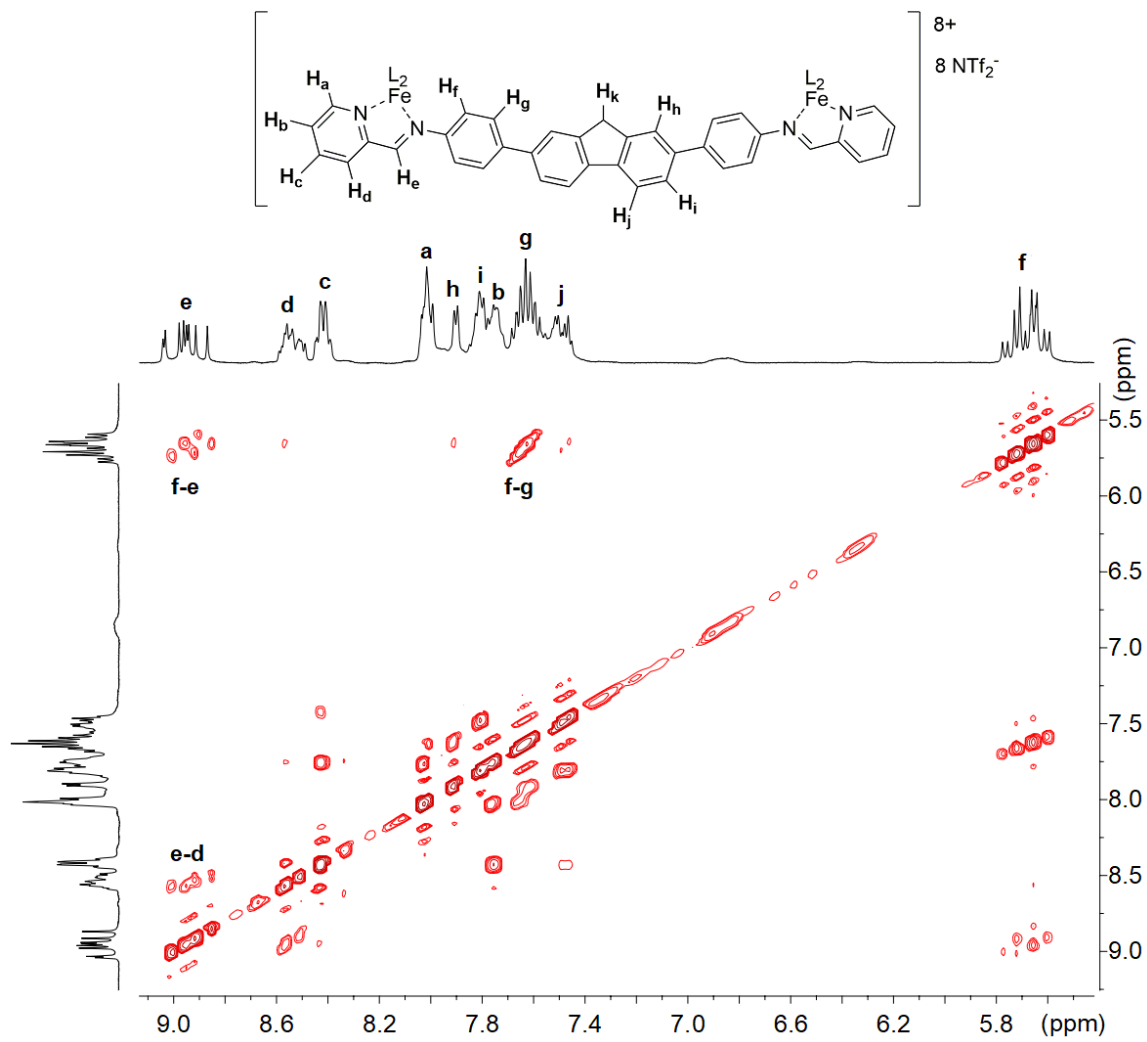


Figure 7.33. Expanded gNOESY NMR spectrum of fluorene cage **4.1** (CD_3CN , 600 MHz, 298 K, mixing time = 300 ms).

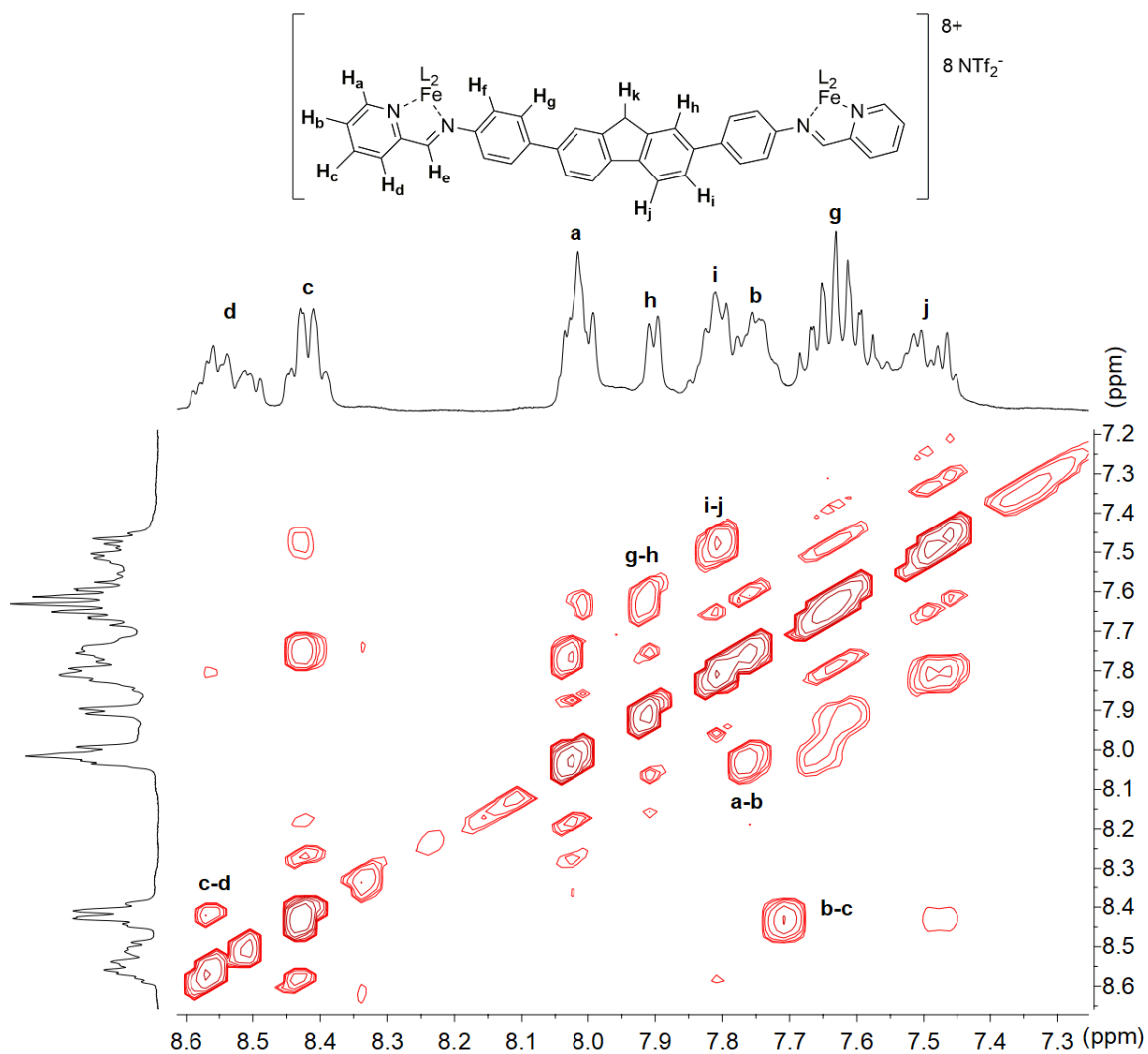


Figure 7.34. Expanded aromatic region of the gNOESY NMR spectrum of fluorene cage **4.1** (CD_3CN , 600 MHz, 298 K, mixing time = 300 ms).

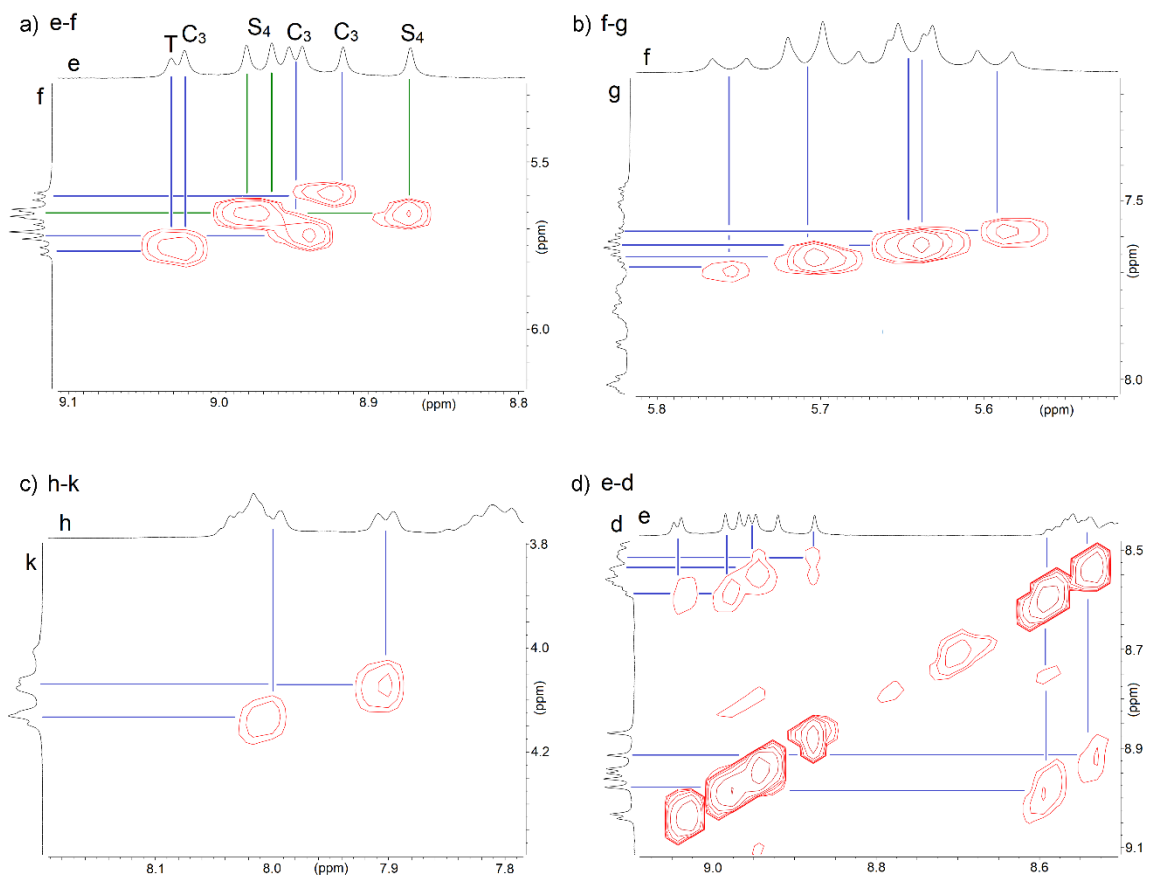


Figure 7.35. Expanded aromatic regions of the gNOESY NMR spectrum of fluorene cage **4.1** illustrating the presence of three different isomers through correlations of protons a) e and f, b) f and g, c) h and k, and d) e and d. (CD₃CN, 600 MHz, 298 K, mixing time = 300 ms).

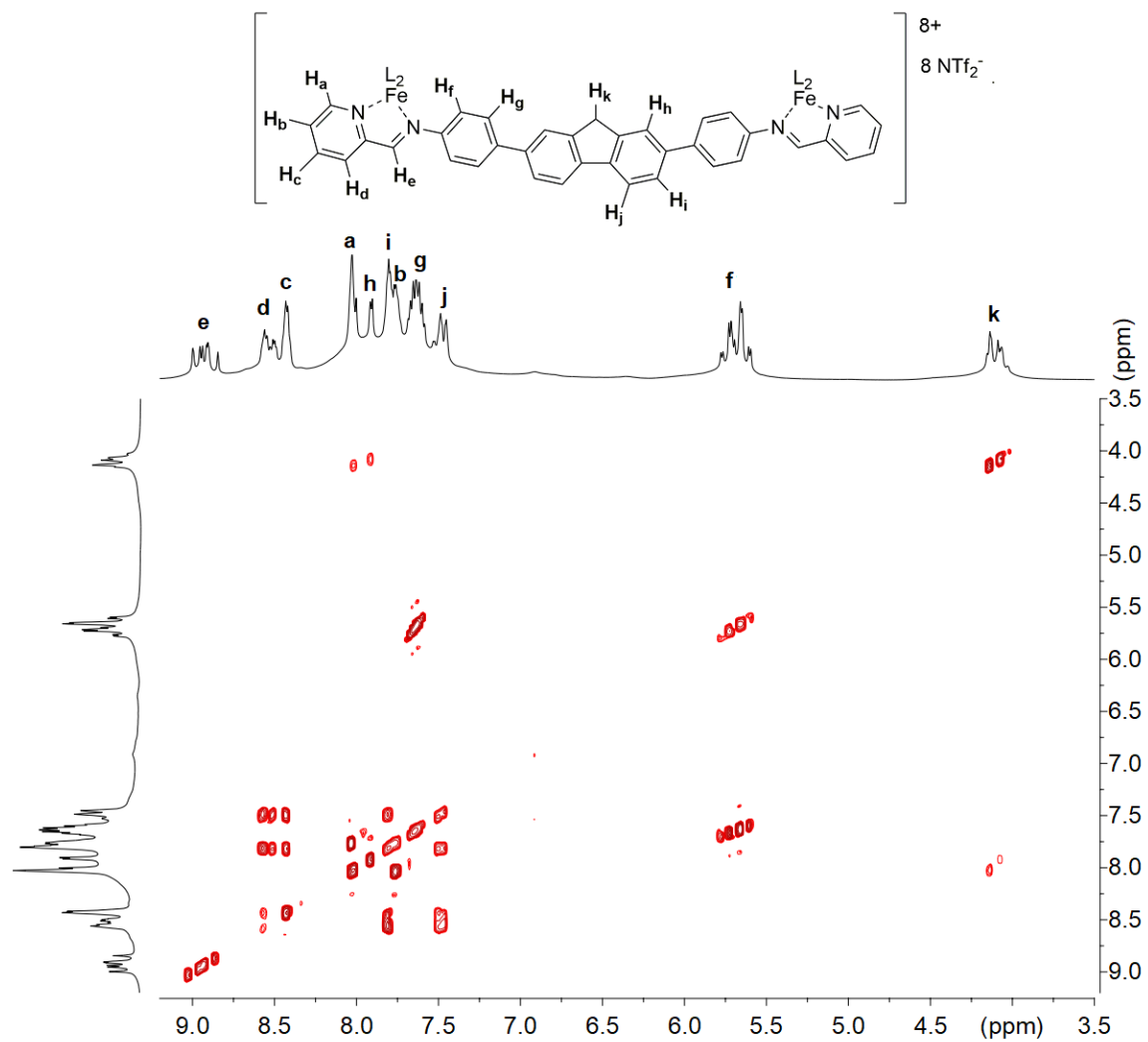


Figure 7.36. TOCSY NMR spectrum of fluorene cage **4.1** (CD₃CN, 600 MHz, 298 K, mixing time = 80 ms).

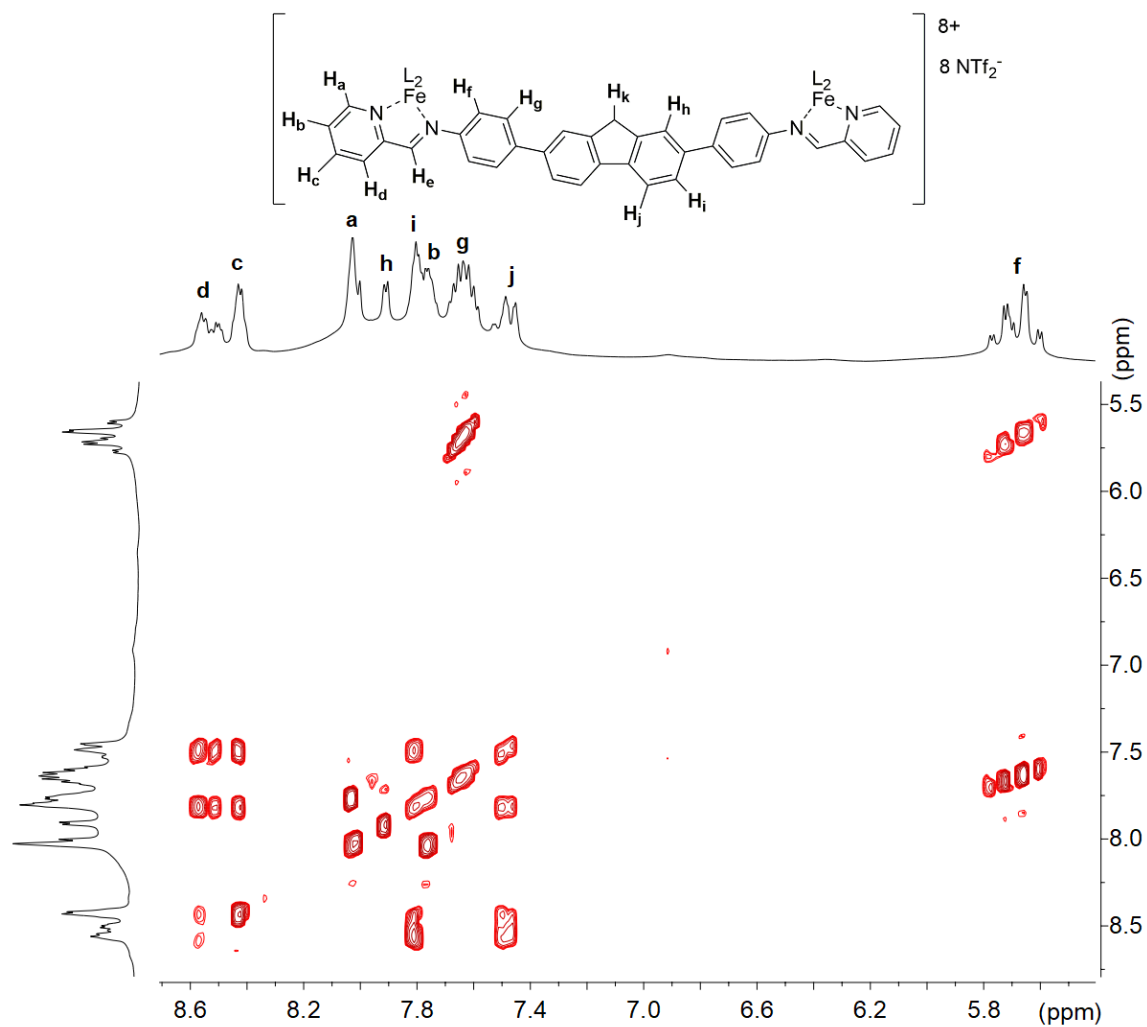


Figure 7.37. Expanded TOCSY NMR spectrum of fluorene cage **4.1**. (CD_3CN , 600 MHz, 298 K, mixing time = 80 ms).

Table 7.2. Assigned ions for experimentally observed peaks (**7.5** = full iminopyridine ligand of **4.A**).

Ion	Charge	Observed (m/z)	Predicted (m/z)
[4.1]	8+	422.88	422.89
[4.A •Py+1H]	1+	438.21	438.20
[Fe ₃ 7.5 ₄ •NTf ₂]	5+	510.73	510.72
[4.1 •NTf ₂]	7+	523.29	523.28
[Fe ₂ 7.5 ₃ •NTf ₂]	3+	657.15	657.16
[Fe ₃ 7.5 ₄ •2NTf ₂]	4+	708.39	708.39
[Fe ₂ 7.5 ₄ •NTf ₂]	3+	823.57	832.55
[Fe ₂ 7.5 ₂ •2NTf ₂]	2+	862.09	862.07
[4.1 •4NTf ₂]	4+	1125.68	1125.68
[Fe ₂ 7.5 ₃ •2NTf ₂]	2+	1125.68	1125.68
[Fe 7.5 ₂ •NTf ₂]	1+	1388.30	1388.28
[4.1 •5NTf ₂]	3+	1594.25	1594.21

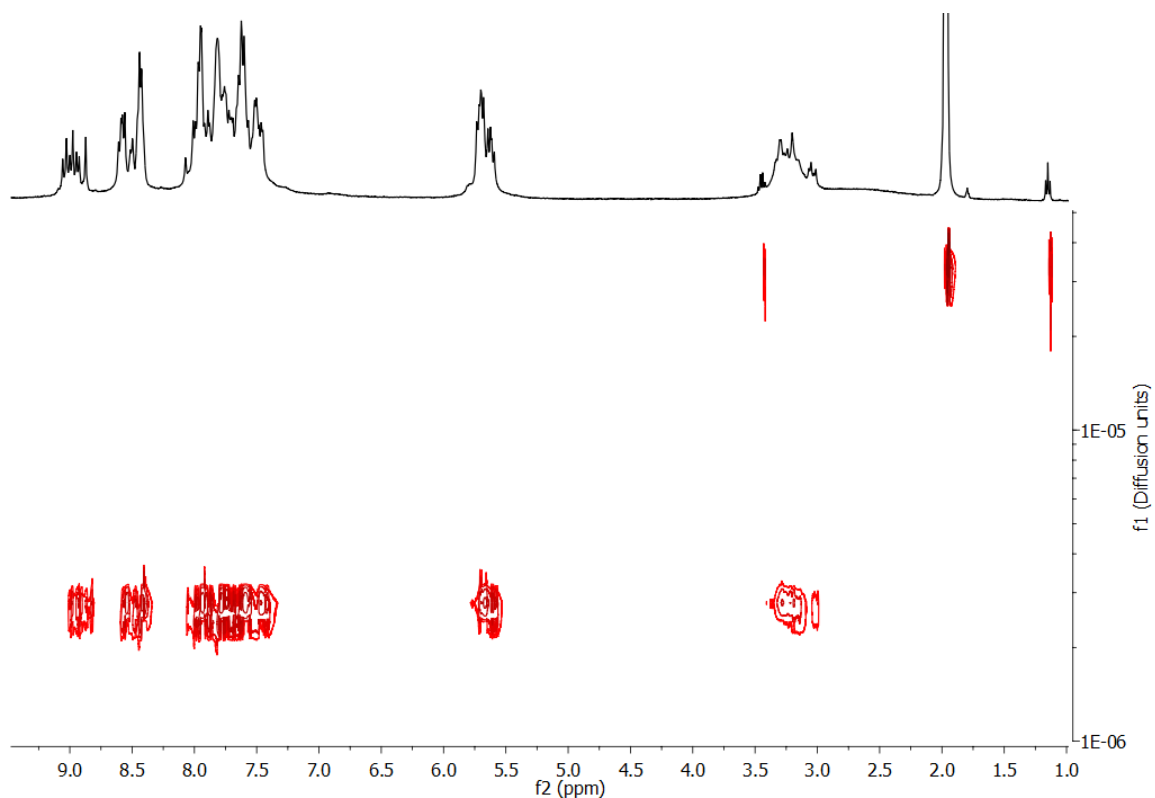


Figure 7.38. ¹H-DOSY NMR spectrum of acid cage **4.2** (CD₃CN, 600 MHz, 298 K, Δ = 100 ms, δ = 1.8 μs, Diffusion constant = 3.090 × 10⁻¹⁰ m²/s for cage **4.2** vs. 3.467 × 10⁻⁹ m²/s for the solvent).

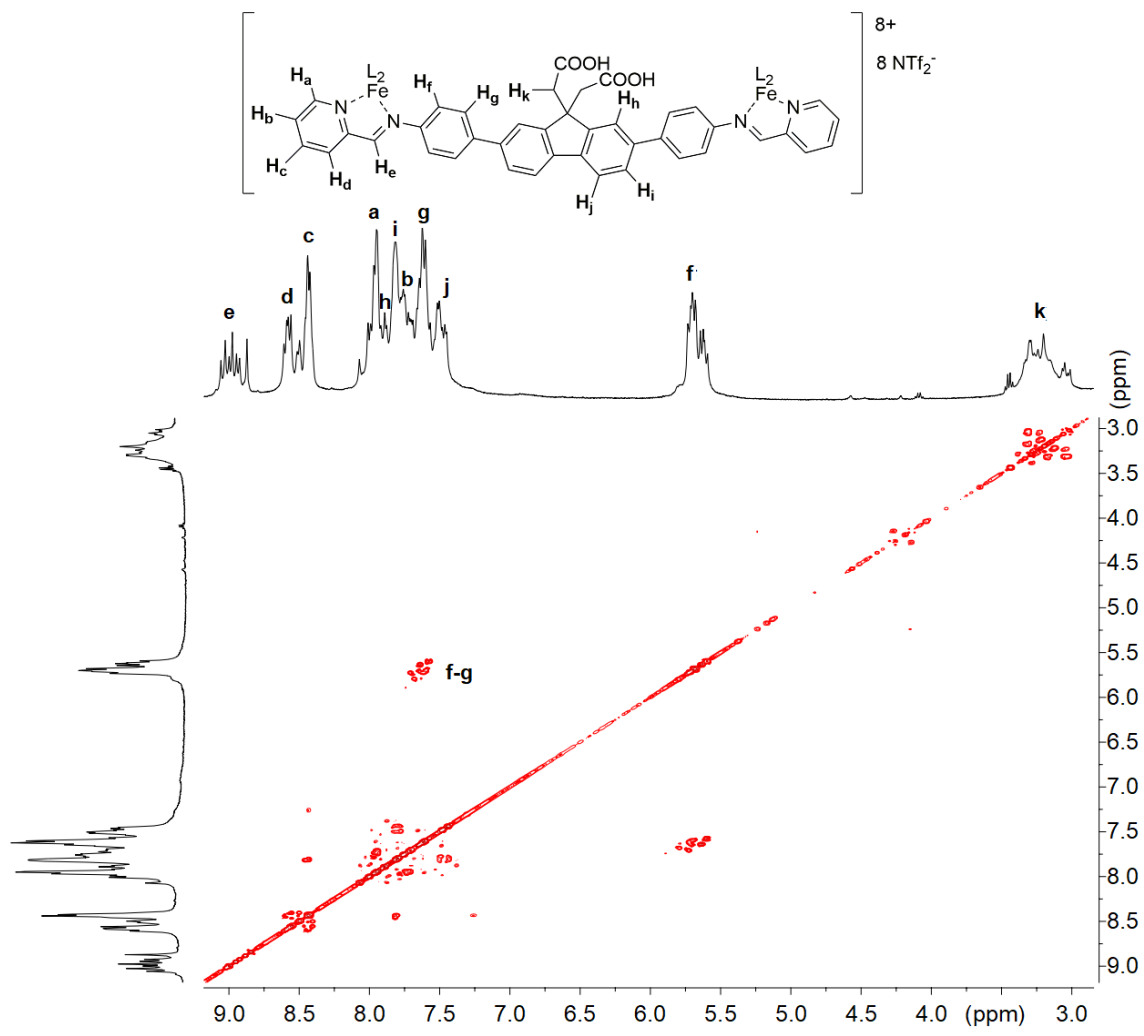


Figure 7.39. gCOSY NMR spectrum of acid cage **4.2** (CD₃CN, 600 MHz, 298 K).

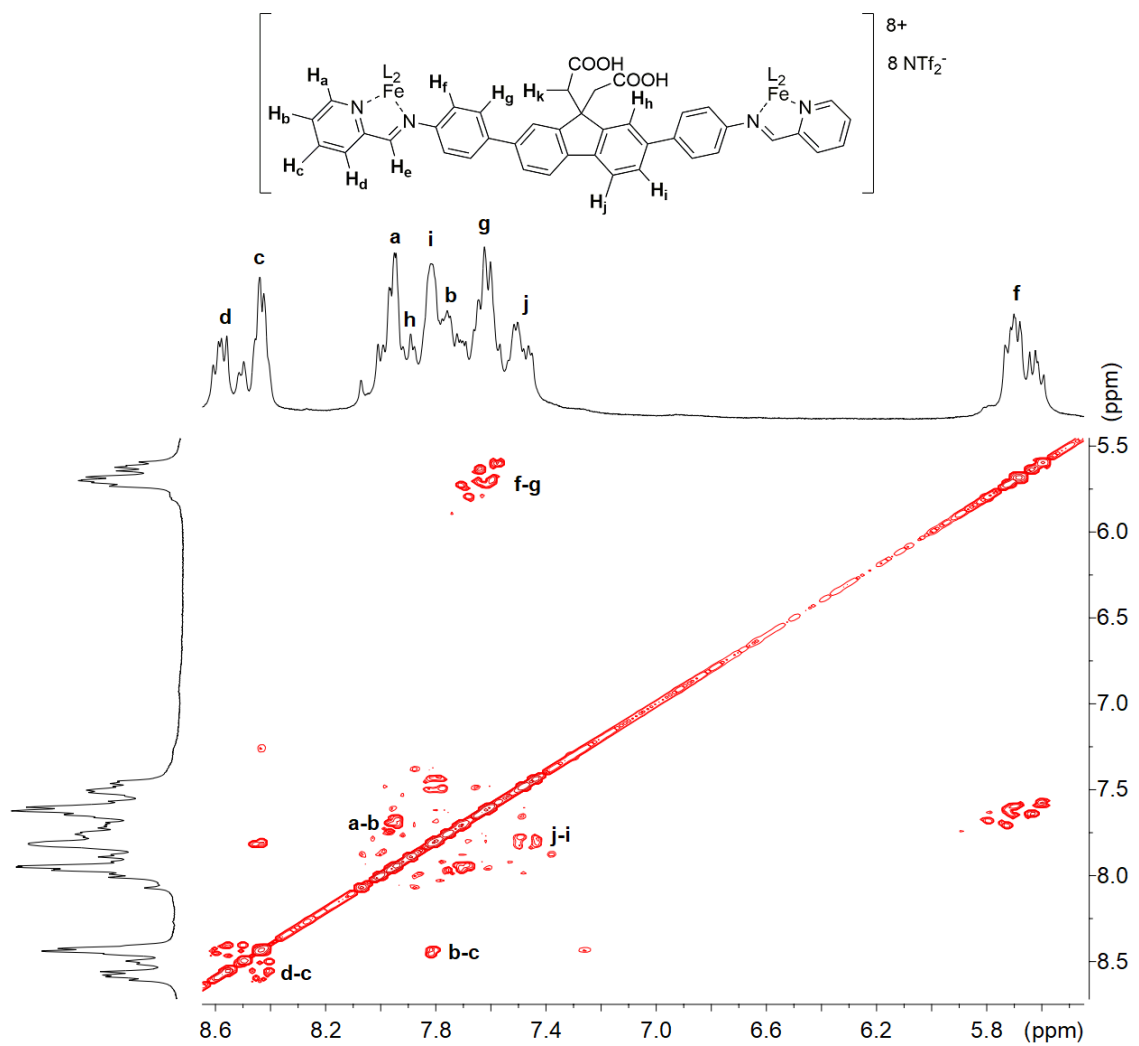
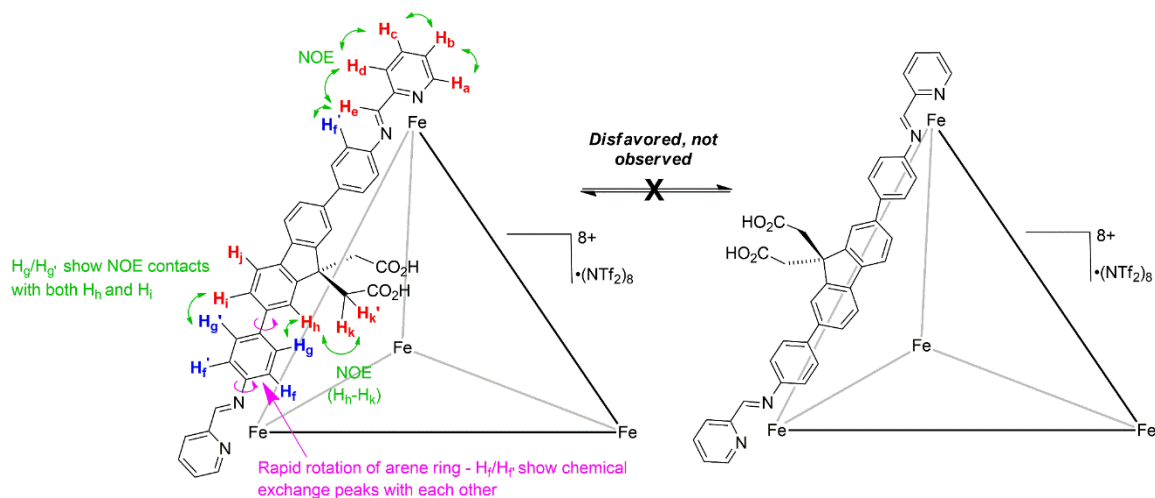


Figure 7.40. gCOSY NMR spectrum of acid cage **4.2**. Expansion of the 5.6-8.6 ppm region (CD₃CN, 600 MHz, 298 K).

Discussion of NMR Structural Data of **2**.

The 2D NMR data allows some analysis of the structure of **4.2**, notably in regards to the positioning of the acid groups (either internally or externally). Molecular modeling shows that the structure with the fluorenyl core rotated such that the $\text{CH}_2\text{CO}_2\text{H}$ groups are positioned externally is extremely unfavorable: any minimizations force the $\text{CH}_2\text{CO}_2\text{H}$ groups to the interior, and not even local minima are observed. The 2D COSY spectra, comparison with the spectra of **4.1**, and the TOCSY/HSQC/HMBC were used to assign the structure of **4.2**, most importantly the fluorenyl protons $\text{H}_h/\text{H}_i/\text{H}_j$ and the arene protons H_f/f' and H_g/g' . The NOESY spectra do not show any obvious interligand correlations, as expected - the central groups are too far apart to show NOE contacts. Correlations in the individual isomers can be (in some cases) determined, as shown in Figure **7.42**. In terms of the internal/external positioning of the acid groups, there are two important correlations - H_g/g' to H_h , and H_g/g' to H_i , plus chemical exchange correlations between H_f and H_f' . These show that rotation of the p-arene rings is possible, and rapid on the NMR timescale. There is no evidence for rotation of the central fluorenyl core.



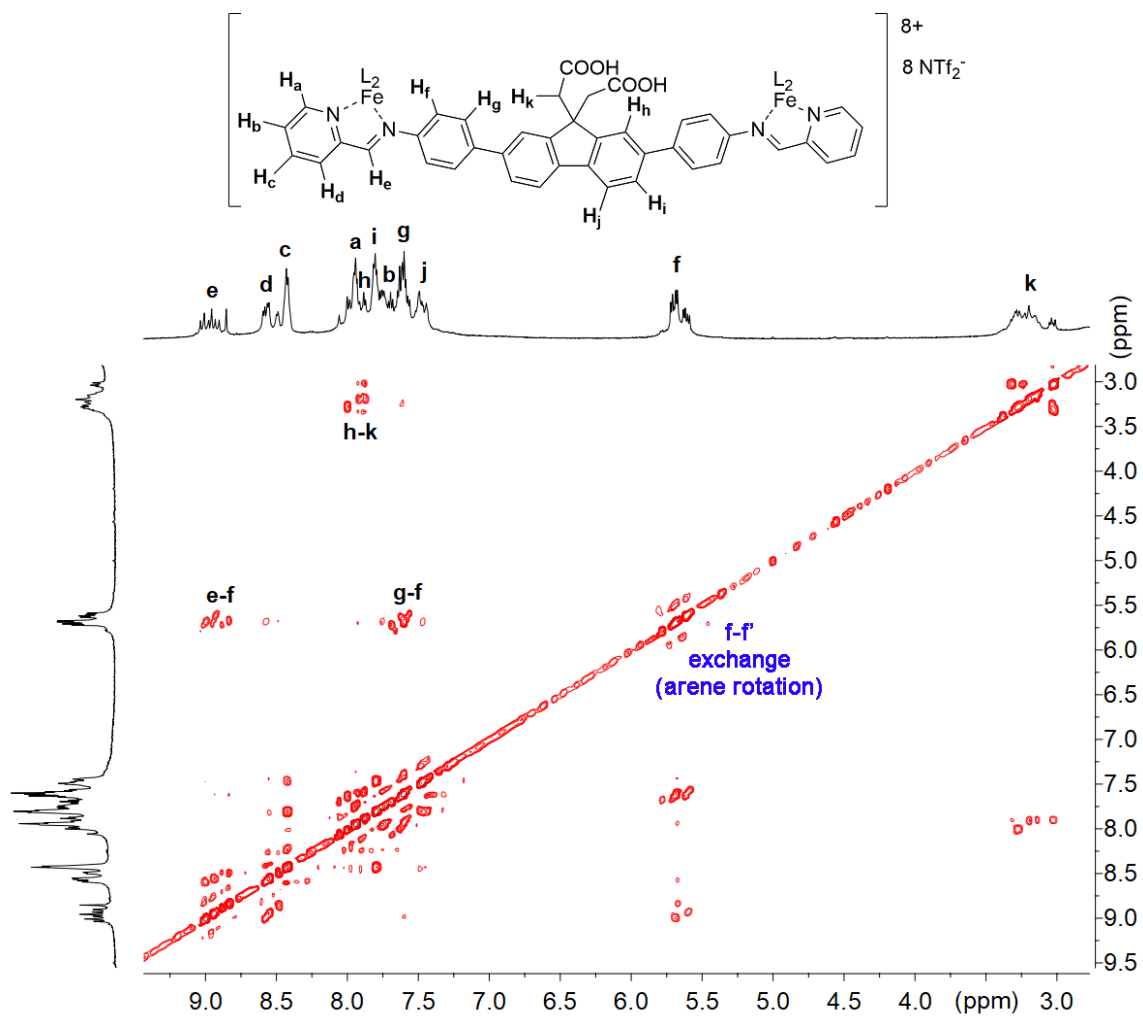


Figure 7.41. NOESY NMR spectrum of acid cage **4.2** (CD₃CN, 600 MHz, 298 K, mixing time = 300 ms).

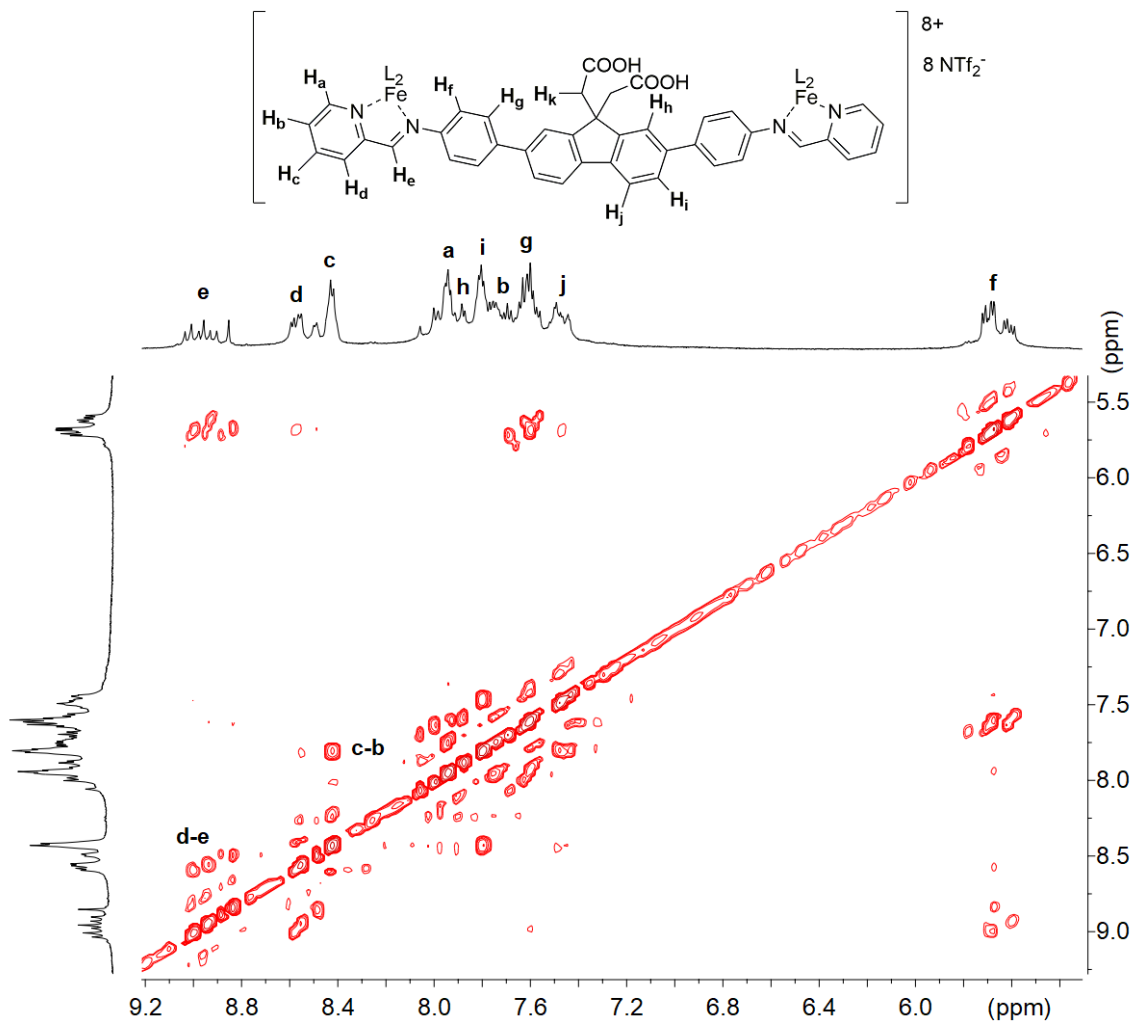


Figure 7.42. Expanded NOESY NMR spectrum of acid cage **4.2** (CD_3CN , 600 MHz, 298 K, mixing time = 300 ms).

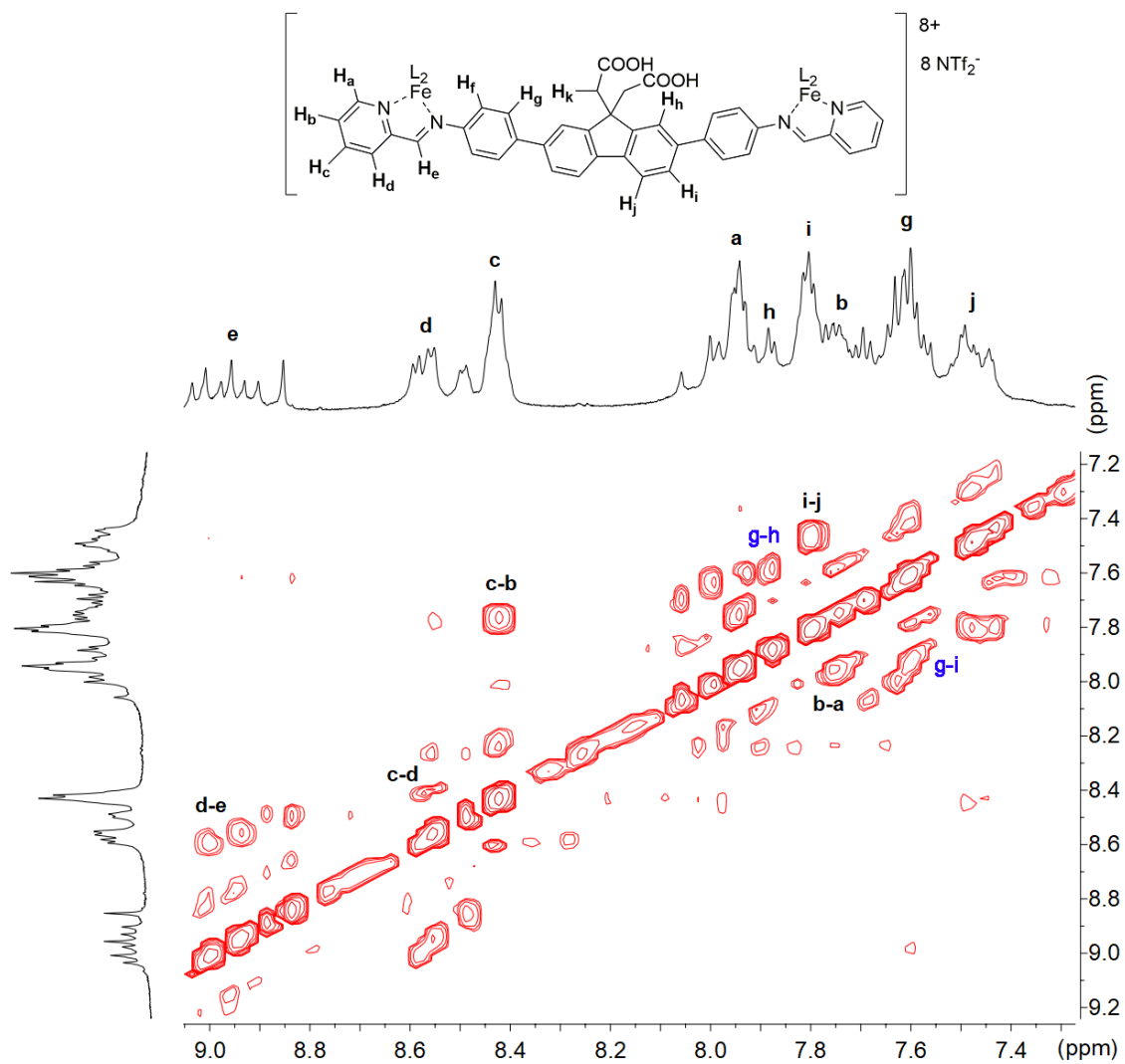


Figure 7.43. Expanded downfield region of the NOESY NMR spectrum of acid cage **4.2** (CD_3CN , 600 MHz, 298 K, mixing time = 300 ms).

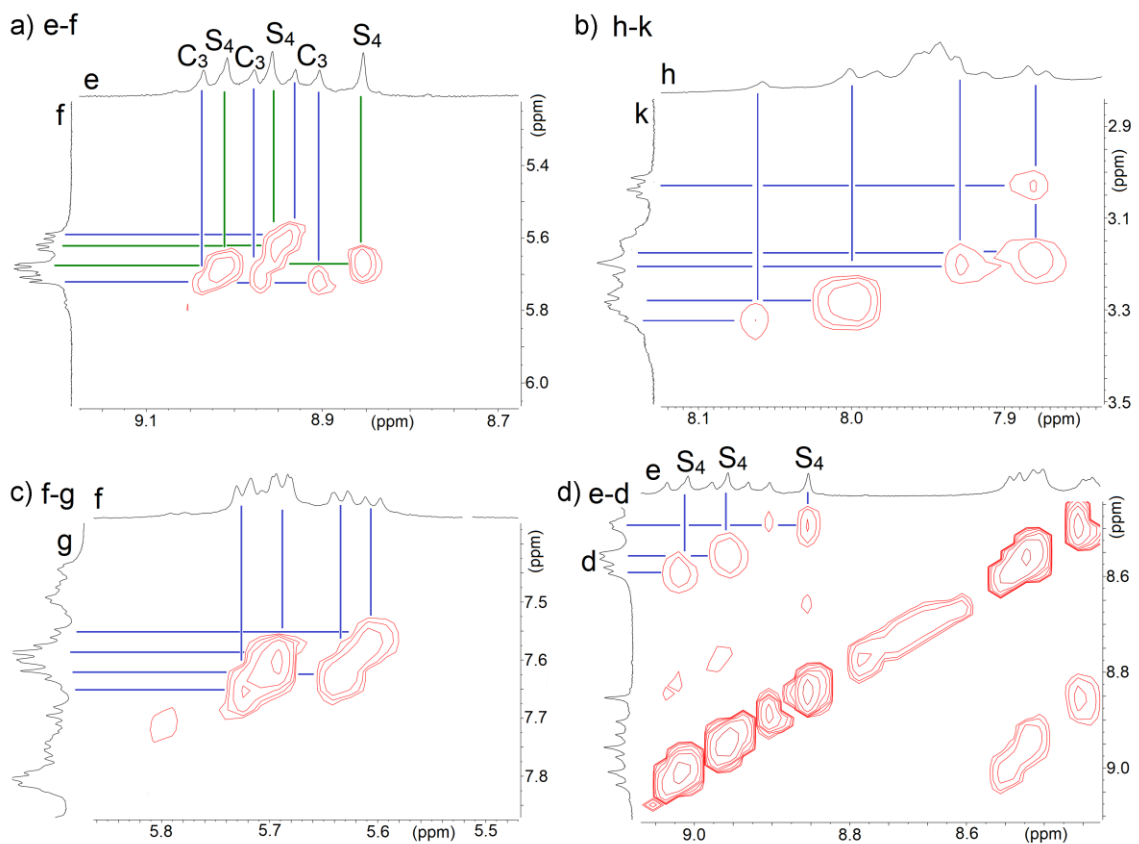


Figure 7.44. Expanded aromatic regions of the gNOESY NMR spectrum of acid cage **4.2** illustrating the presence of three different isomers through correlations of protons a) e and f, b) h and k, c) f and g, and d) e and d. (CD₃CN, 600 MHz, 298 K, mixing time = 300 ms).

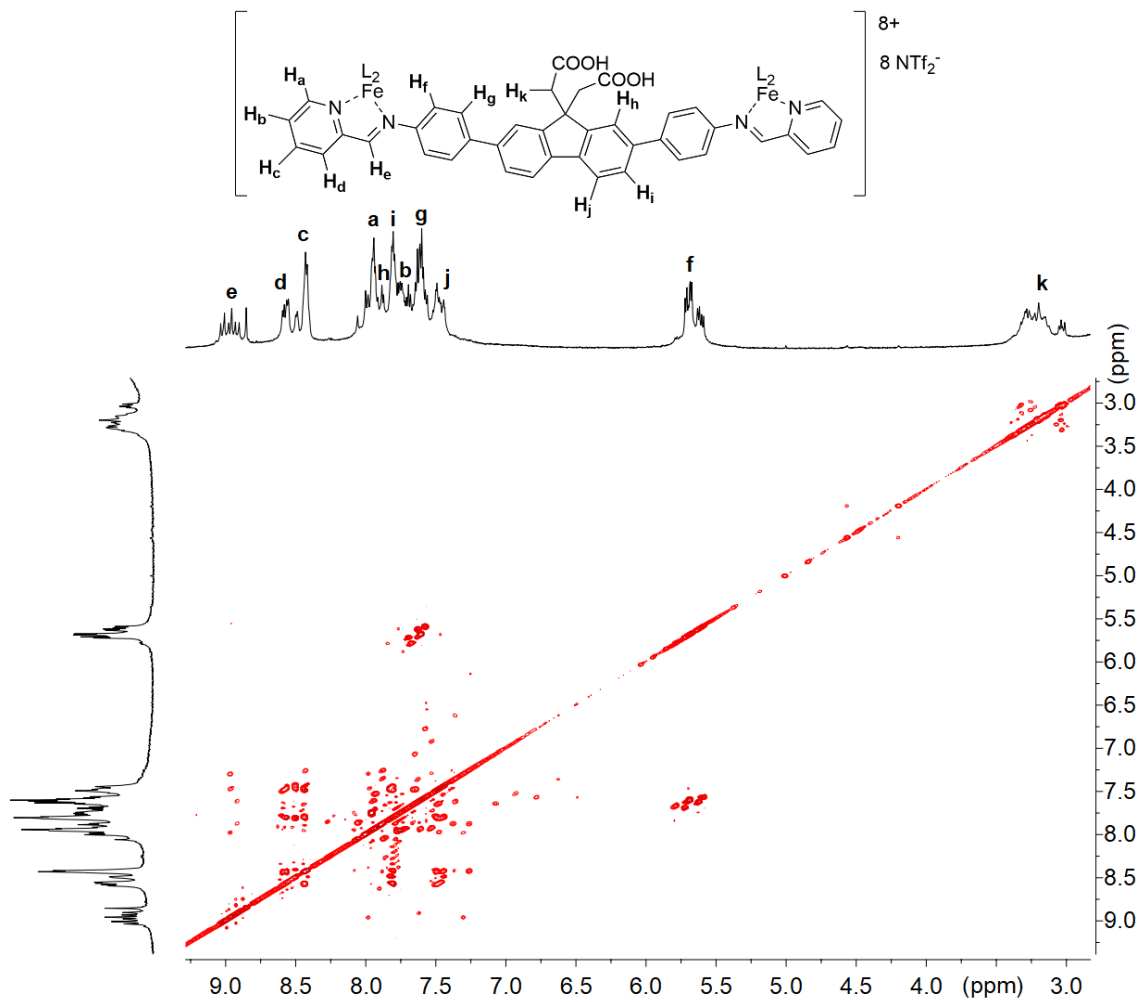


Figure 7.45. TOCSY NMR spectrum of acid cage **4.2** (CD₃CN, 600 MHz, 298 K, mixing time = 60 ms).

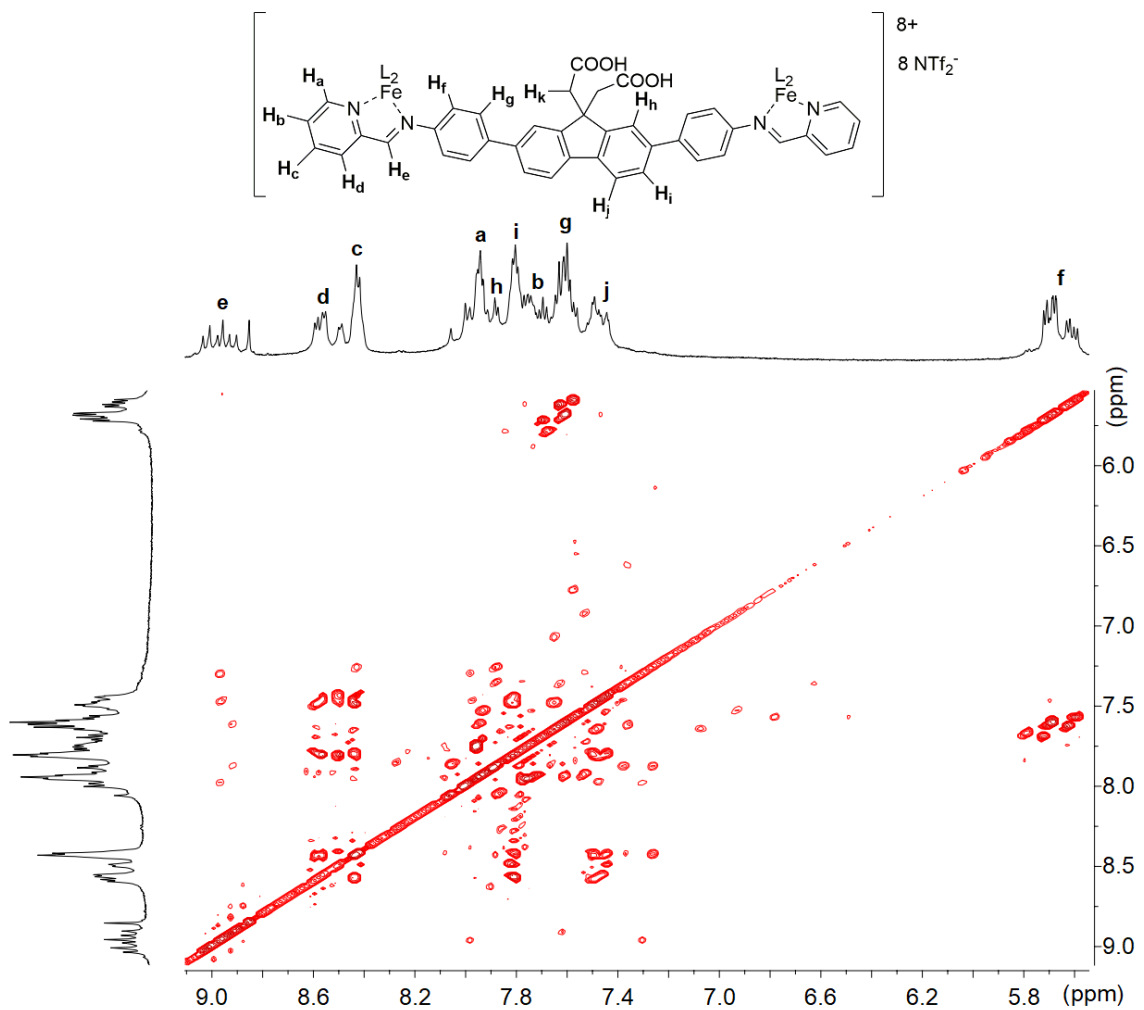


Figure 7.46. Expanded TOCSY NMR spectrum of acid cage **4.2** (CD_3CN , 600 MHz, 298 K, mixing time = 60 ms).

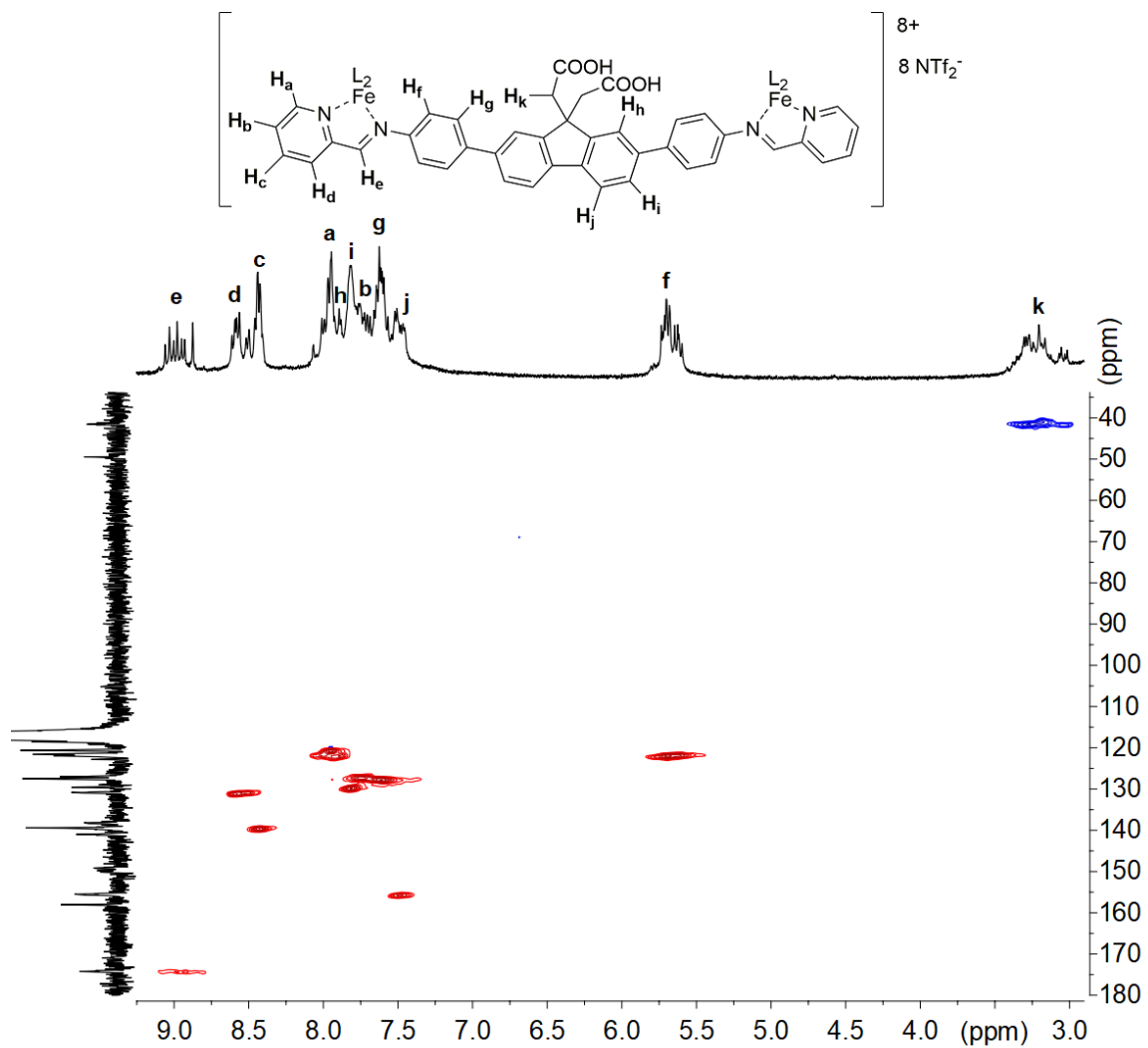


Figure 7.47. DEPT-HSQC NMR spectrum of acid cage **4.2** (CD₃CN, 400 MHz, 298 K).

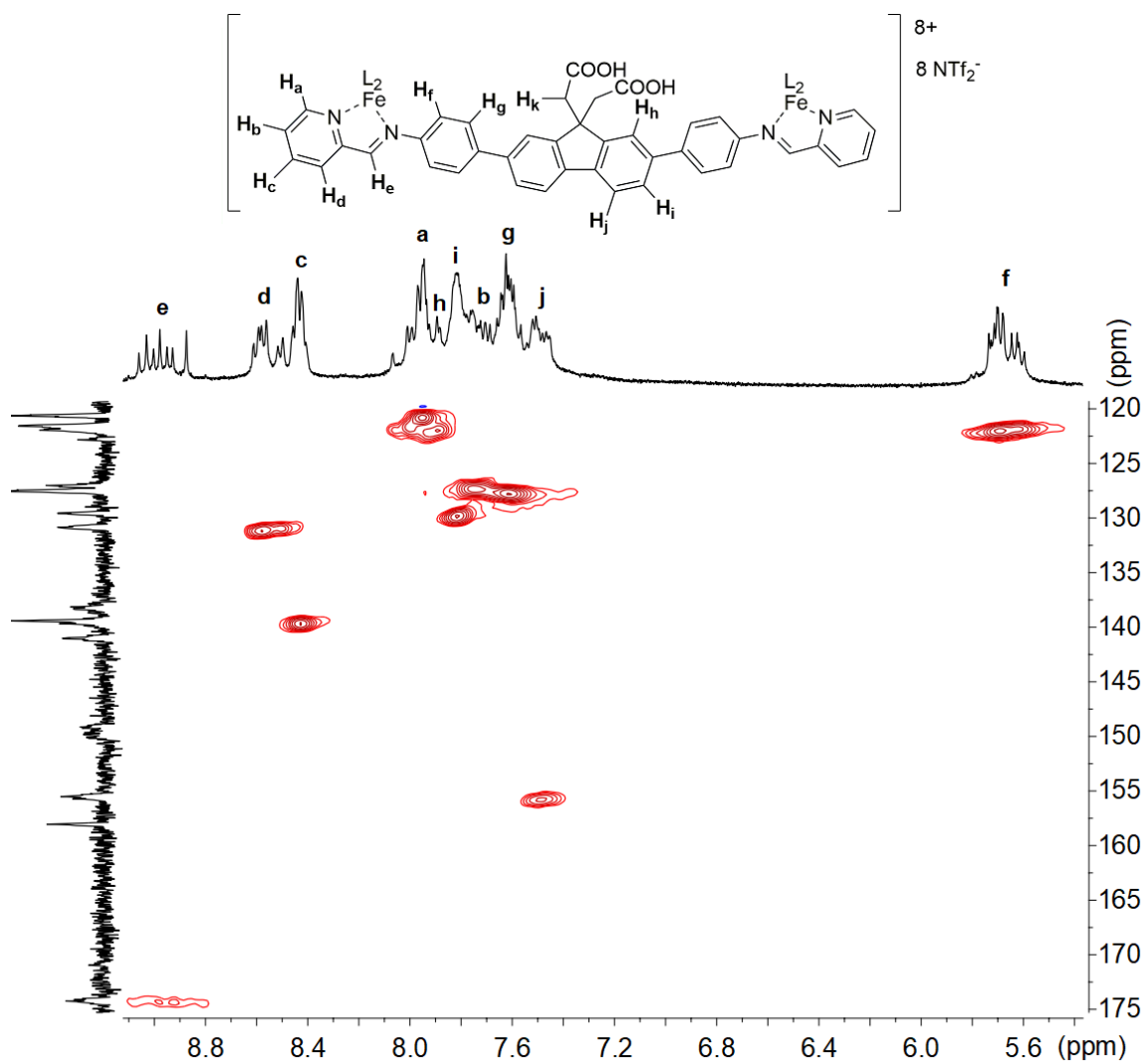


Figure 7.48. Expanded DEPT-HSQC NMR spectrum of acid cage **4.2** (CD₃CN, 400 MHz, 298 K).

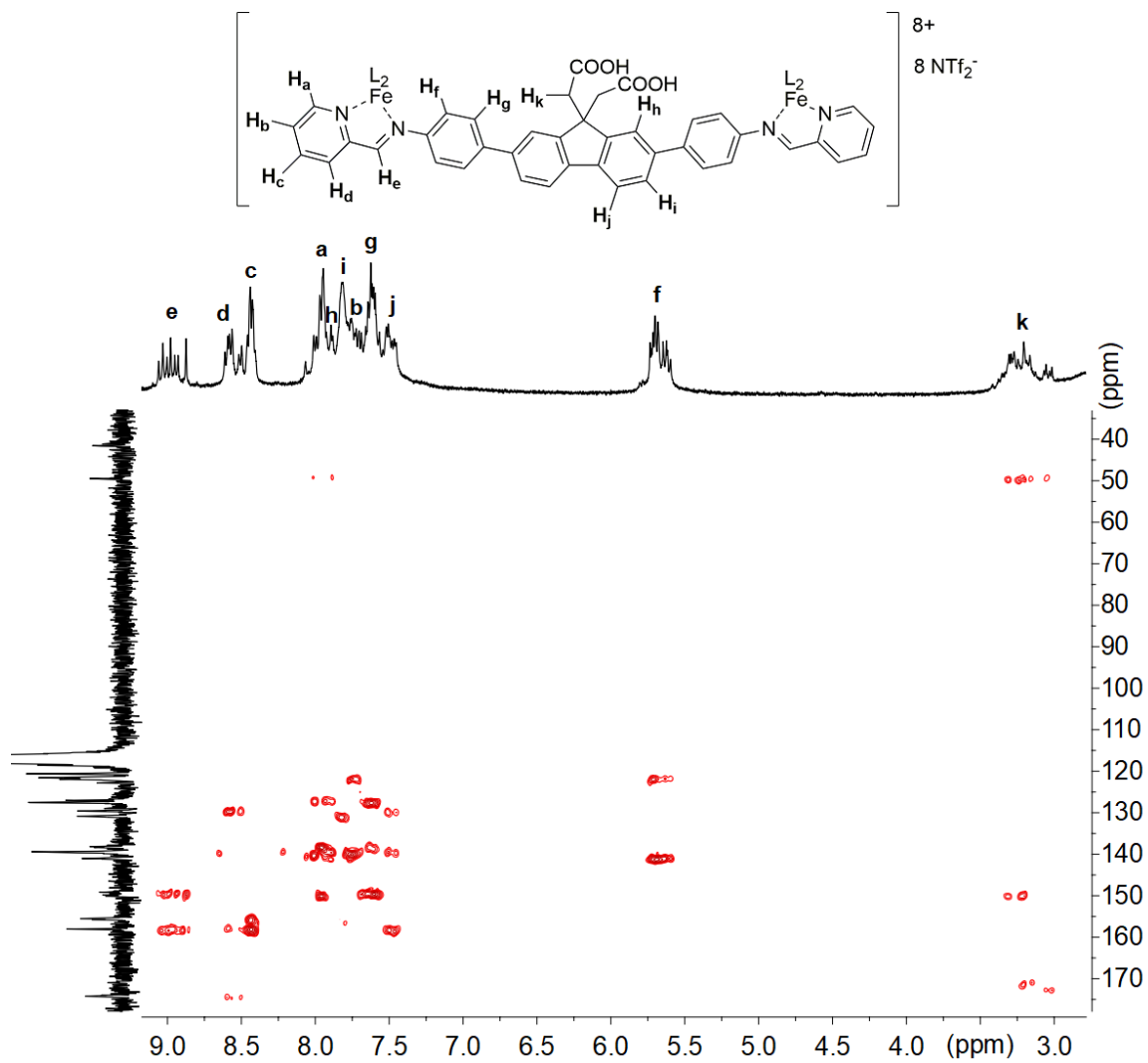


Figure 7.49. HMBC NMR spectrum of acid cage **4.2** (CD₃CN, 400 MHz, 298 K).

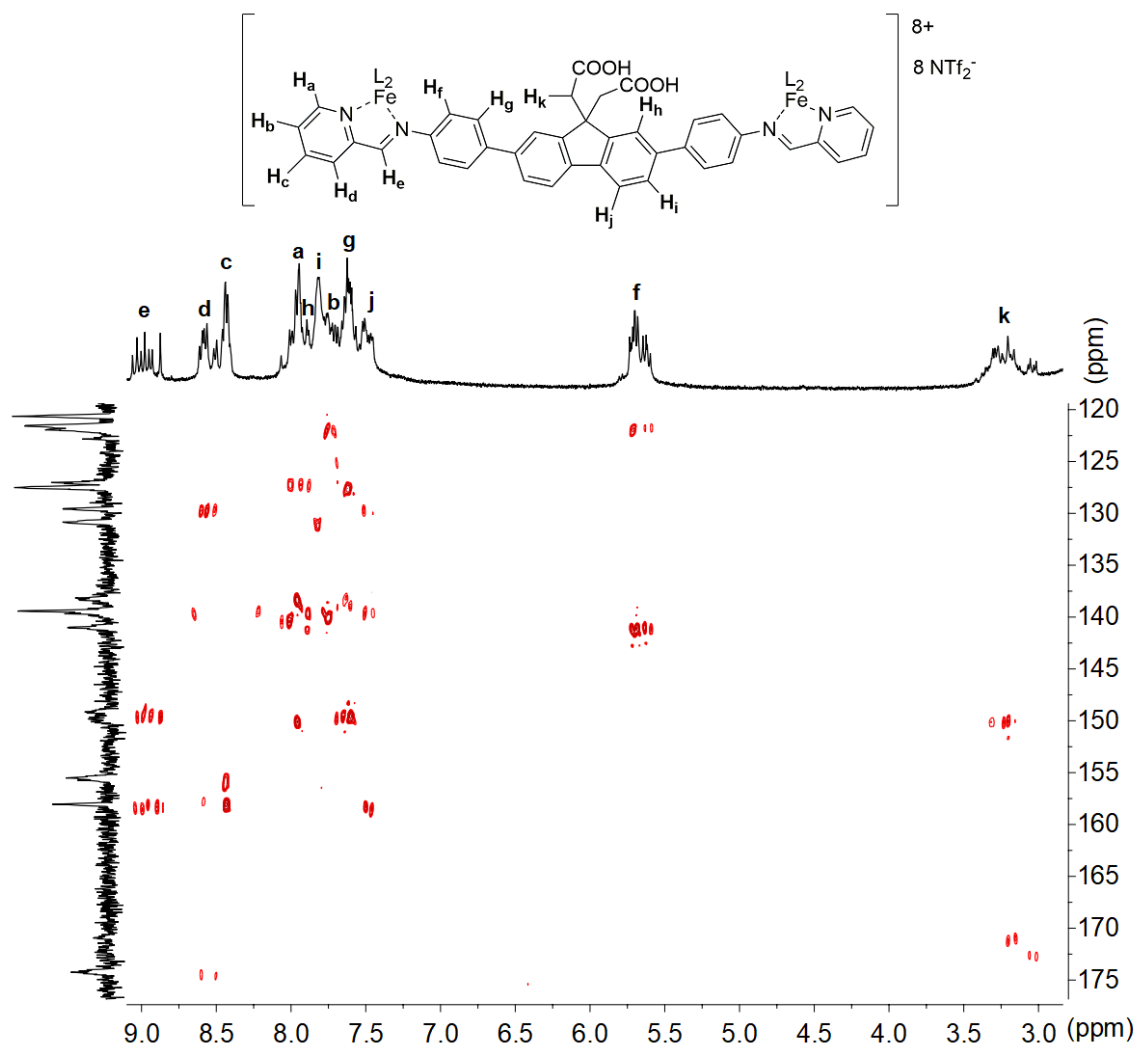


Figure 7.50. Expanded HMBC NMR spectrum of acid cage **4.2** (CD₃CN, 400 MHz, 298 K).

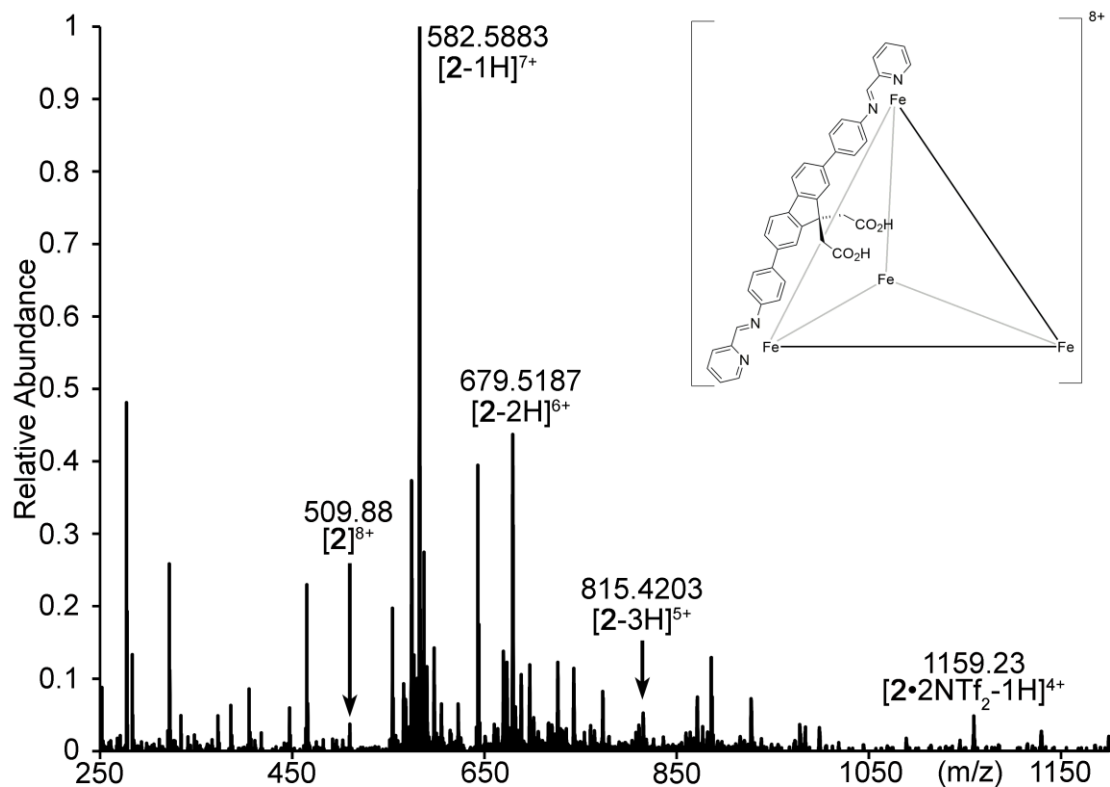


Figure 7.51. Full positive mode ESI-mass spectrum of acid cage **4.2** in 100 % CH₃CN.

Table 7.3. Assigned ions for experimentally observed peaks. (**7.6** = full iminopyridine ligand of **4.A**).

Ion	Charge	Observed (m/z)	Predicted (m/z)
[7.6 •Py+2H]	2+	277.61	277.61
[7.6 •2Py+2H]	2+	322.12	322.12
[7.6 +1H]	1+	465.18	465.18
[4.2]	8+	509.89	509.89
[7.6 •Py+1H]	1+	554.21	554.21
[4.2 -1H-CO ₂ H]	7+	574.30	574.30
[4.2 -1H]	7+	582.59	582.59
[4.2 •NTf ₂]	7+	622.72	622.71
[7.6 •2Py+1H]	1+	643.24	643.23
[4.2 -2H]	6+	679.52	679.51
[4.2 •NTf ₂ -1H]	6+	726.34	726.34
[4.2 •2NTf ₂]	6+	773.16	773.16
[4.2 -3H]	5+	815.22	815.22
[4.2 •2NTf ₂ -1H]	5+	927.59	927.59
[4.2 -4H]	4+	1018.77	1018.77
[4.2 •NTf ₂ -3H]	4+	1089.01	1089.01
[4.2 •2NTf ₂ -2H]	4+	1159.23	1159.23
[4.2 •3NTf ₂ -1H]	4+	1229.47	1229.46
[4.2 •4NTf ₂]	4+	1299.70	1299.69

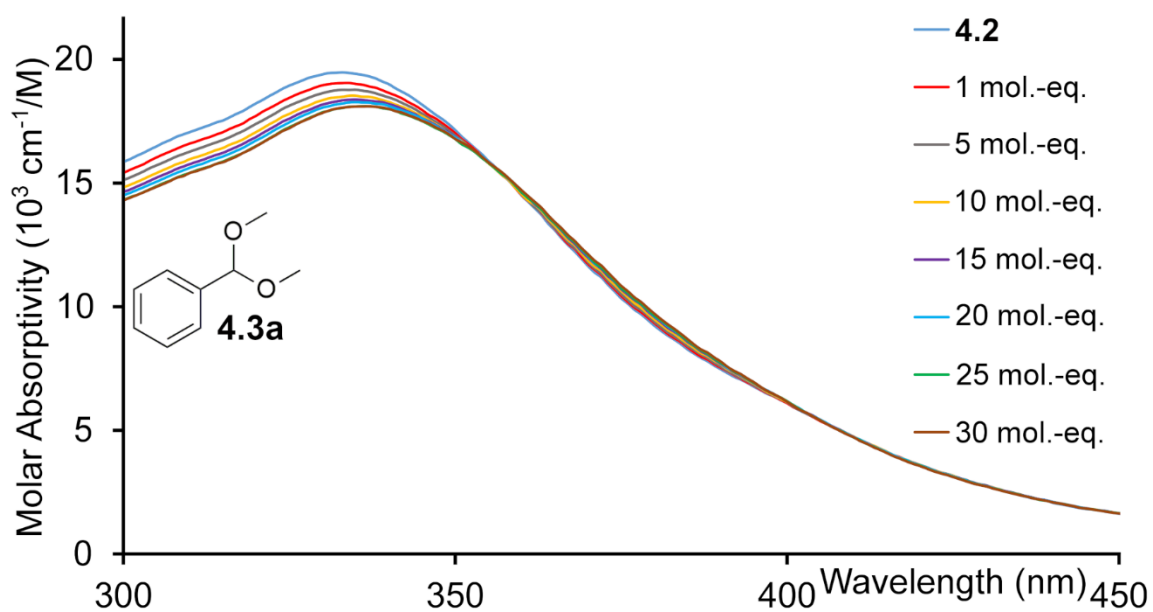


Figure 7.52. UV-Vis absorption spectrum of the titration of a 9 mM solution of acetal **4.3a** CH_3CN into a 3 μM solution of cage **4.2** in CH_3CN . **4.3a** was added in 1-5 μL aliquots.

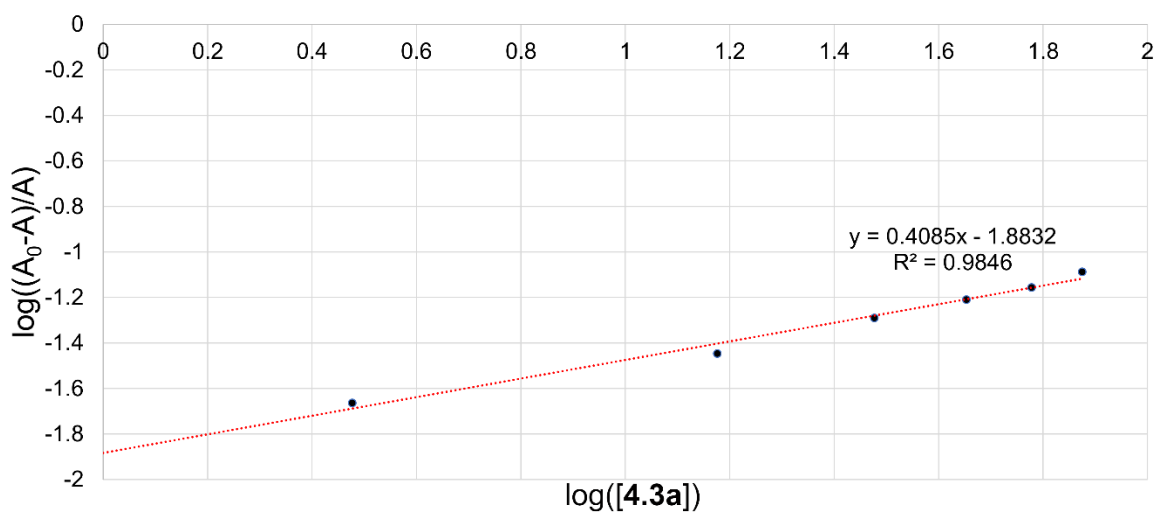


Figure 7.53. Stern-Volmer plot analysis of cage **4.2** binding to acetal **4.3a** measured by the absorbance change at 335 nm. ($K_d = 76.4 \mu\text{M}$).

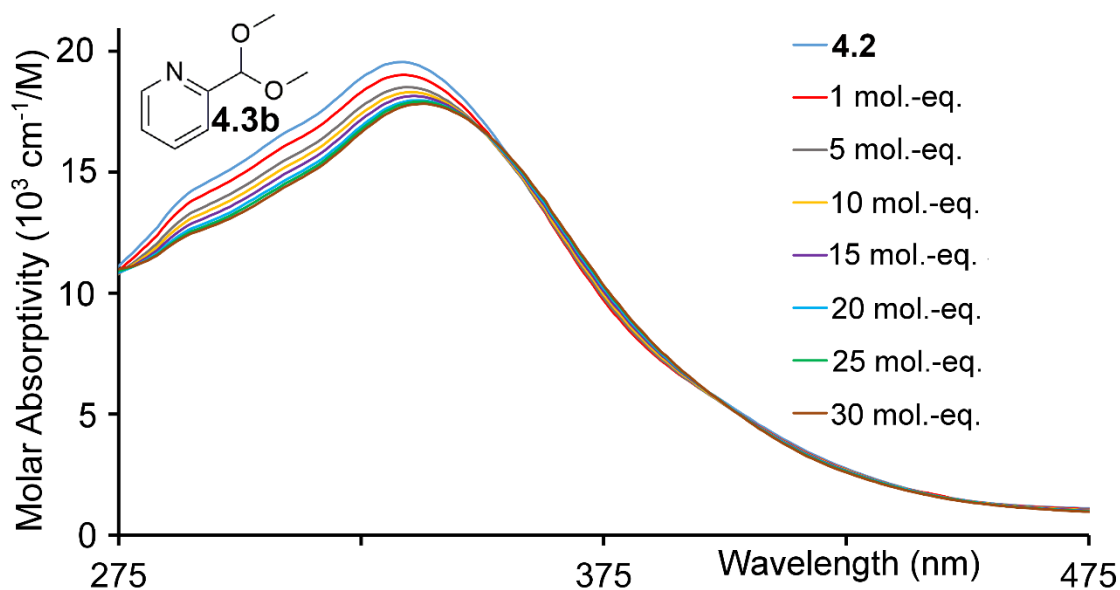


Figure 7.54. UV-Vis absorption spectrum of the titration of a 9 mM solution of acetal **4.3b** CH₃CN into a 3 μM solution of cage **4.2** in CH₃CN. **4.3b** was added in 1-5 μL aliquots.

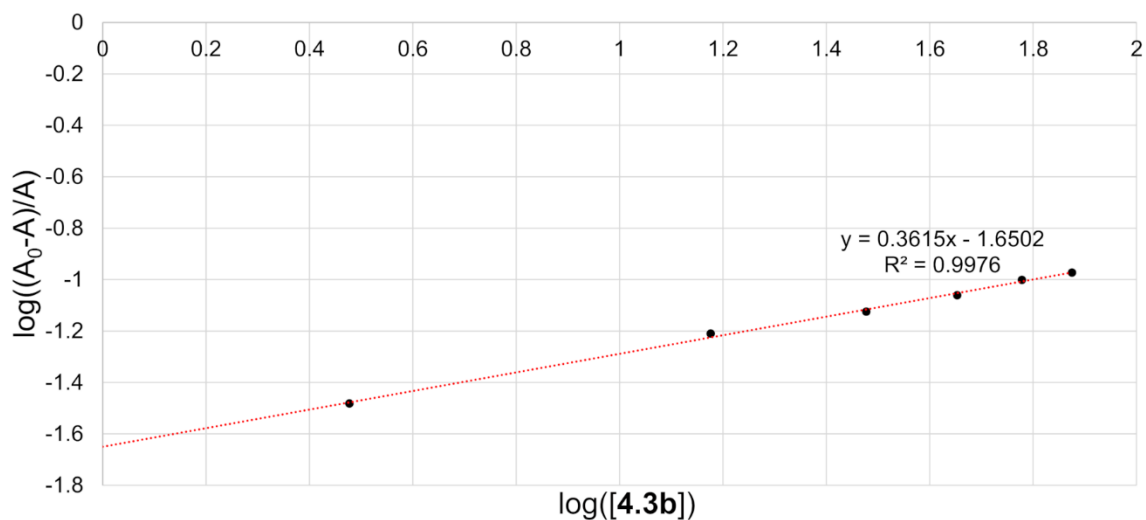


Figure 7.55. Stern-Volmer plot analysis of cage **4.2** binding to acetal **4.3b** measured by the absorbance change at 335 nm. ($K_d = 44.7 \mu\text{M}$).

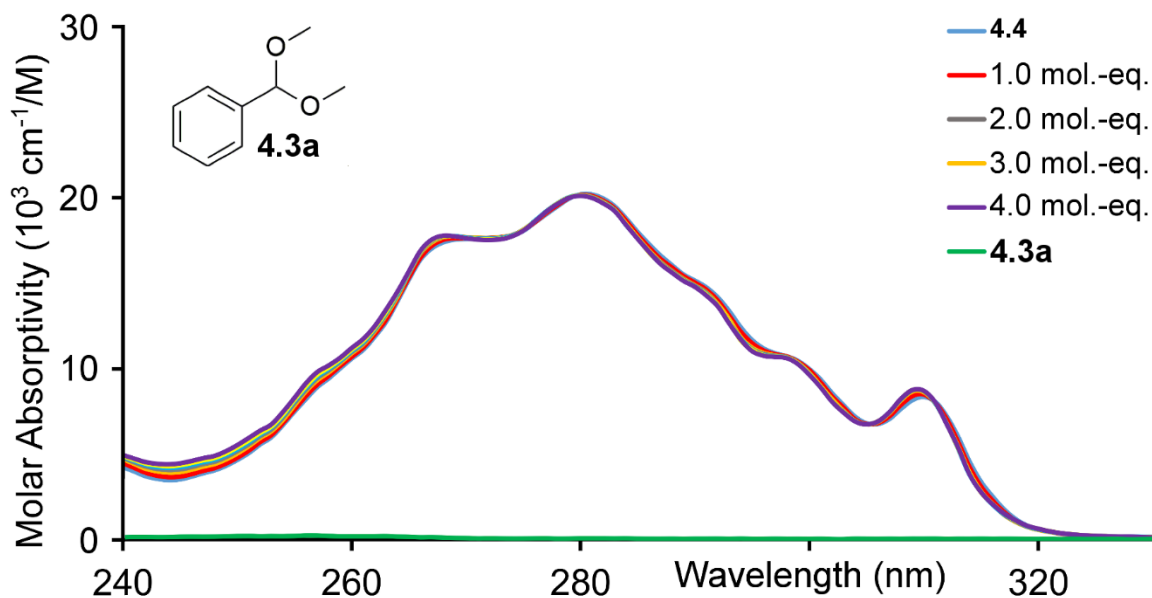


Figure 7.56. UV-Vis absorption spectrum of titration of acetal **4.3a** into an 18 μM solution of control acid **4.4** in CH_3CN , and absorption spectrum of acetal **4.3a** (15 μM in CH_3CN).

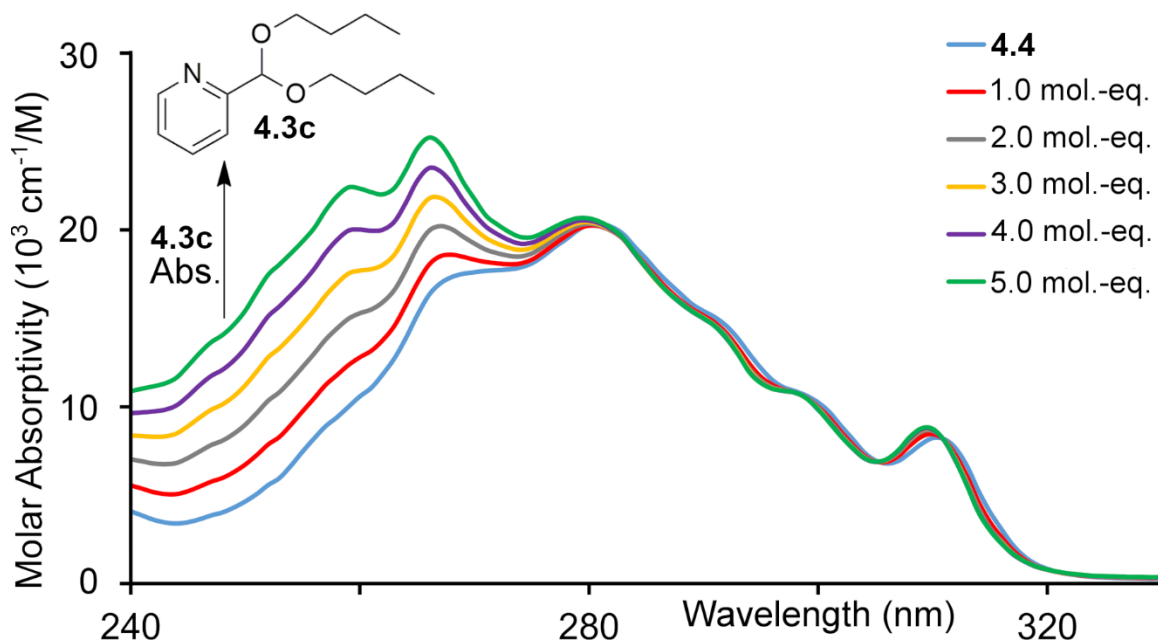


Figure 7.57. UV-Vis absorption spectrum of titration of acetal **4.3c** into an 18 μM solution of control acid **4.4** in CH_3CN , and absorption spectrum of acetal **4.3c** (15 μM in CH_3CN).

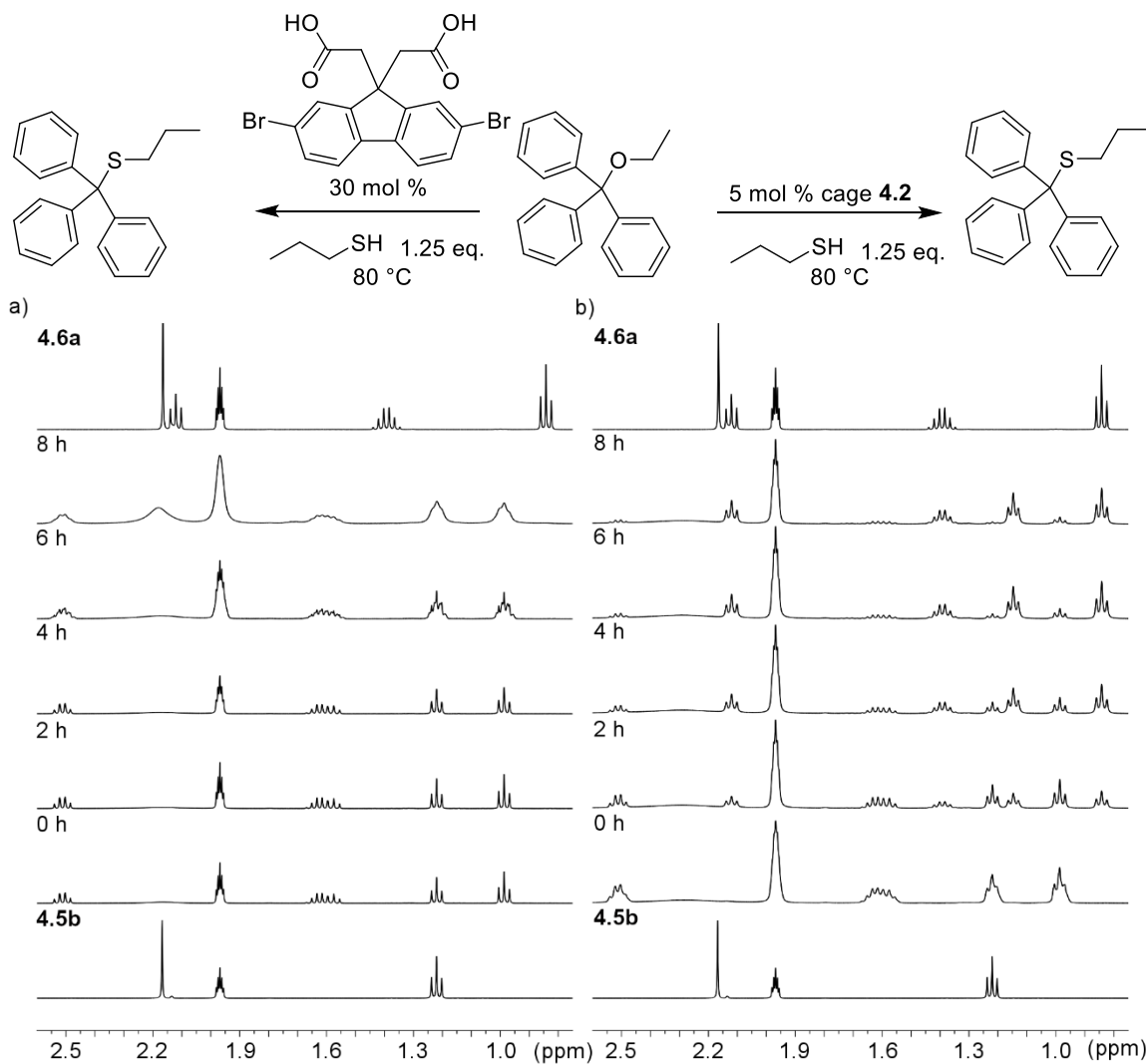


Figure 7.58. 1H NMR spectra (2.60-0.75 ppm) of the acid promoted S_N1 reaction between **4.5b** and *n*-propyl thiol in the presence of: a) 30 mol % control acid **4.4** or b) 5 mol % cage **4.2** in 400 μ L CD_3CN . The reaction was performed at 80 °C and monitored over time (400 MHz, 298K, CD_3CN).

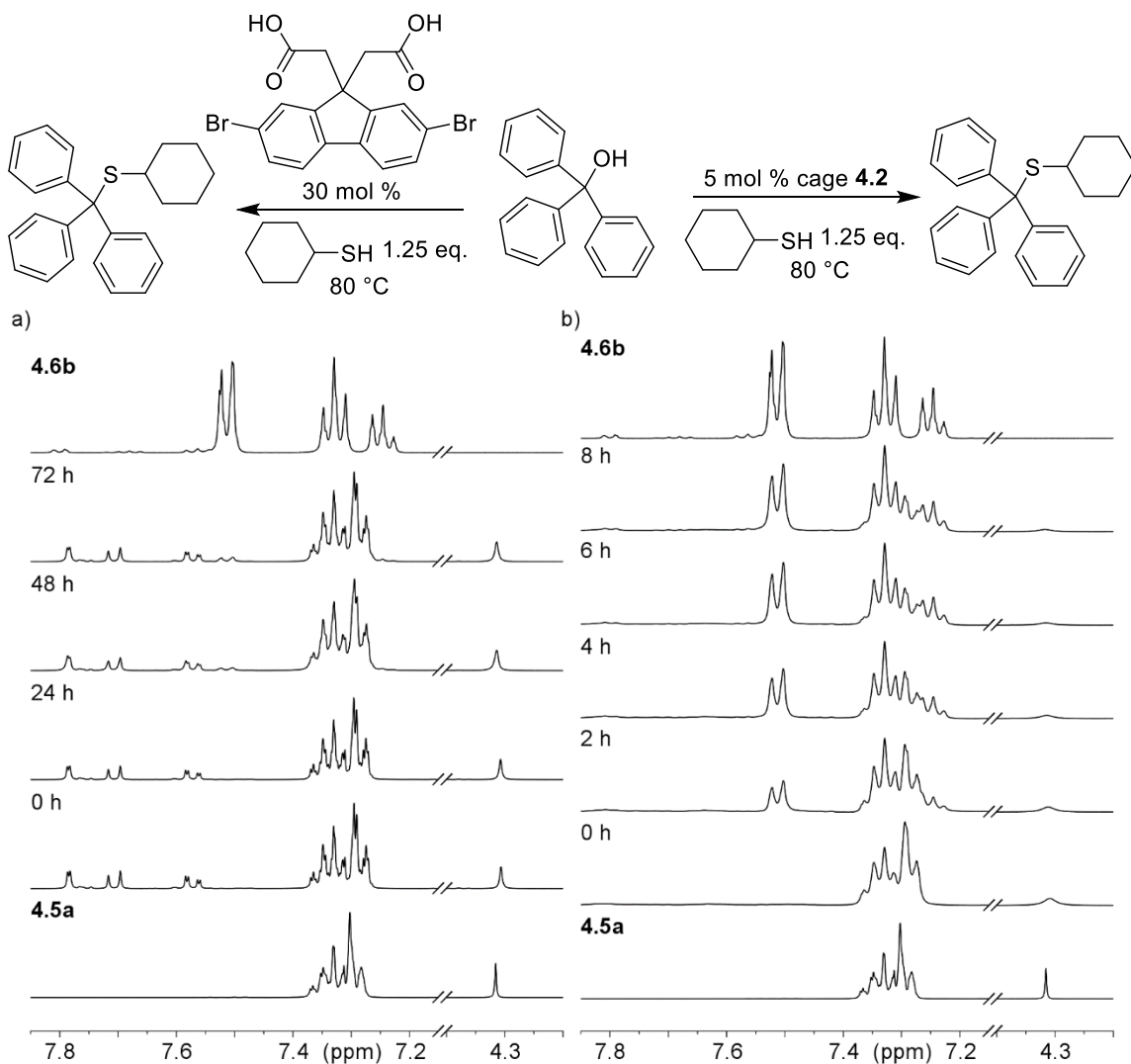


Figure 7.59. ^1H NMR spectra (7.80-7.20 ppm, 4.40-4.20 ppm) of the acid promoted substitution reaction between **4.5a** and cyclohexyl thiol in 400 μL CD_3CN in the presence of: a) 30 mol % control acid **4.4** b) 5 mol % cage **4.2**. Both reactions were performed at 80 $^\circ\text{C}$ and monitored over time (400 MHz, 298 K, CD_3CN).

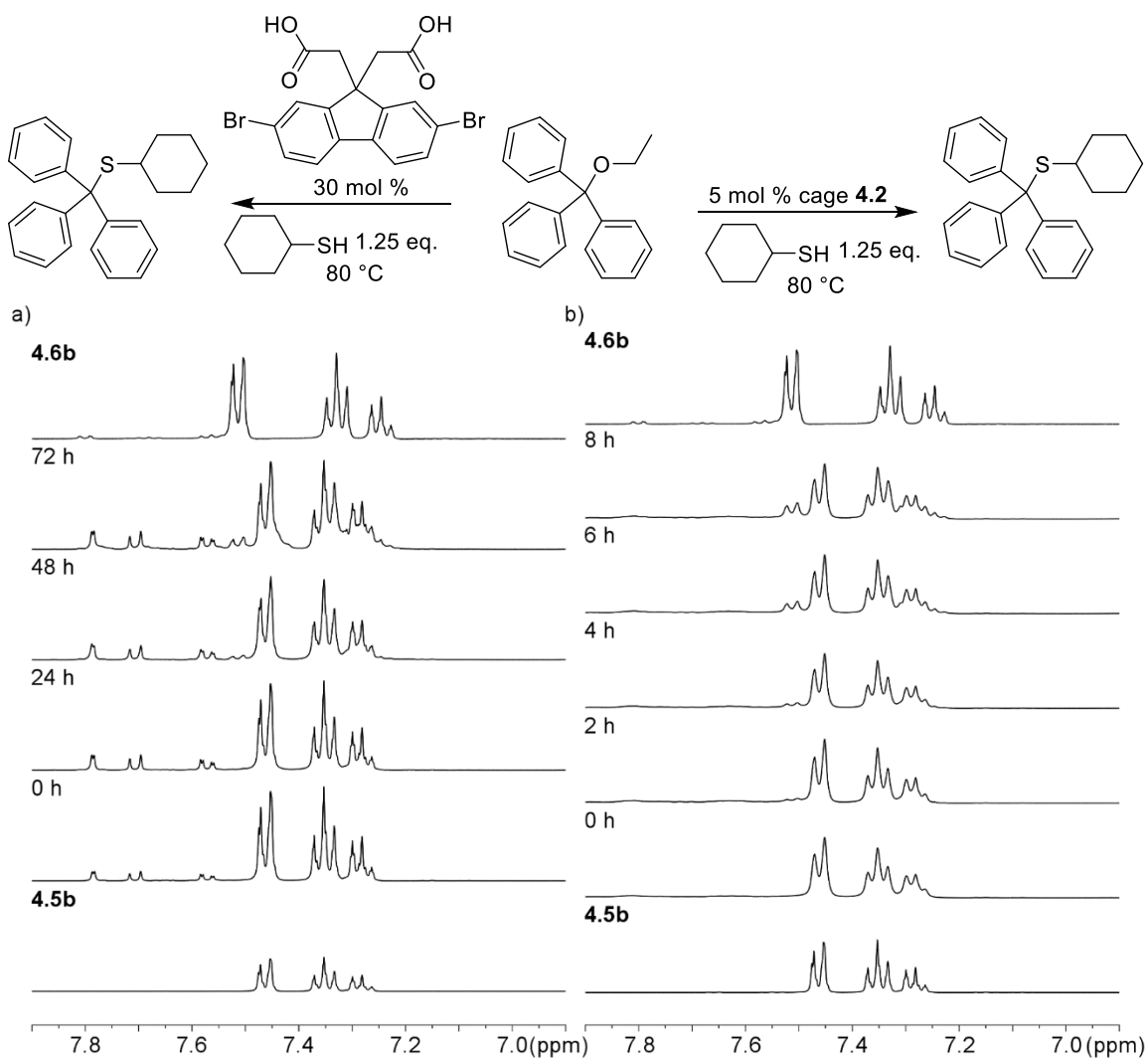


Figure 7.60. 1H NMR spectra (7.90-6.90 ppm) of the acid promoted S_N1 reaction between **4.5b** and cyclohexyl thiol in the presence of: a) 30 mol % control acid **4.4** or b) 5 mol % cage **4.2**. The reaction was performed at $80\text{ }^\circ\text{C}$ and monitored over time (400 MHz, 298K, CD_3CN).

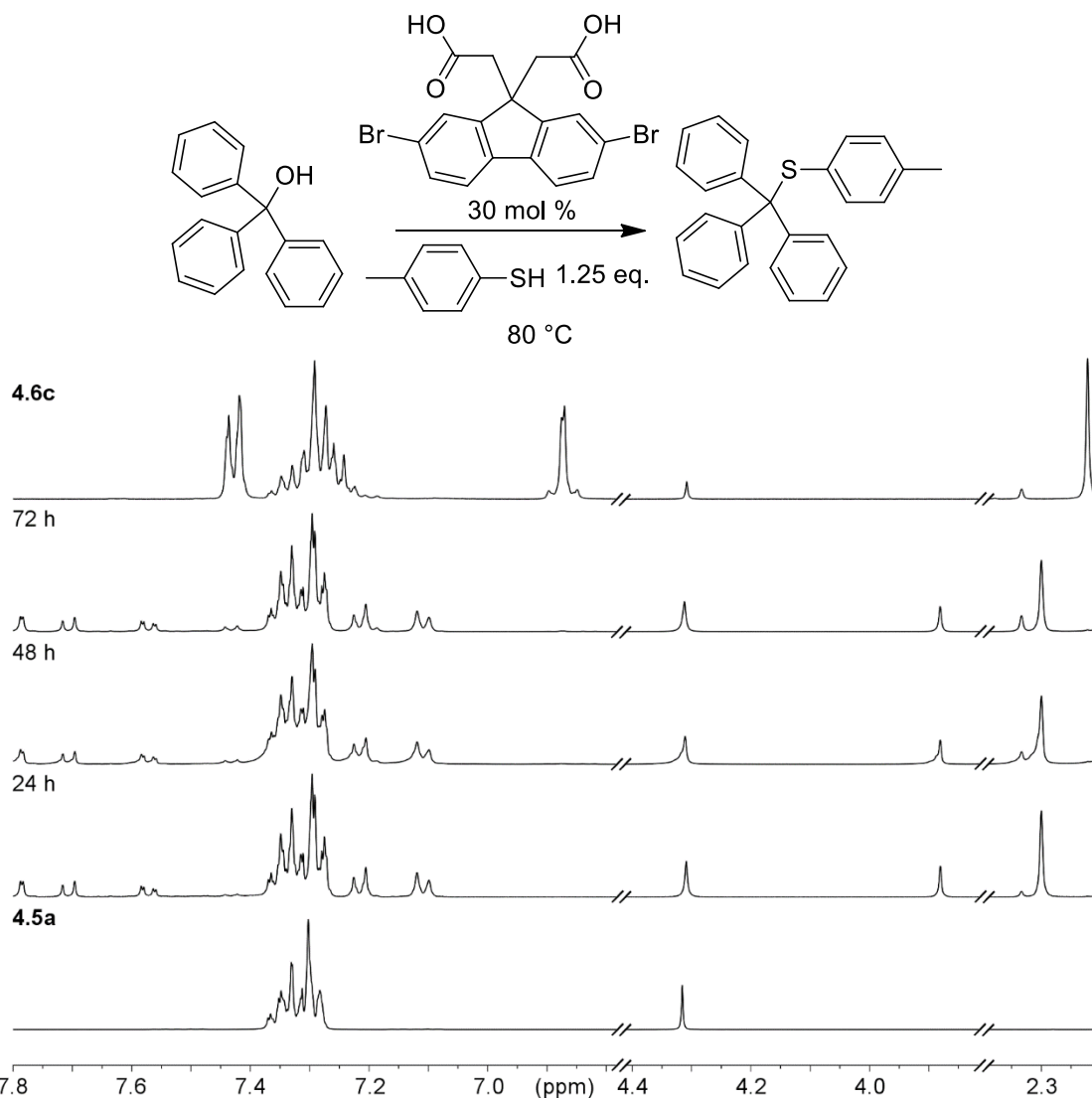


Figure 7.61. ^1H NMR spectra (7.80-7.10 ppm, 4.40-3.80 ppm, 2.40-2.20 ppm) of the acid promoted substitution reaction between **4.5a** and 4-methylbenzene thiol in the presence of 30 mol % control acid **4.4**. The reaction was performed at 80 °C and monitored over time by ^1H NMR (400 MHz, 298 K, CD_3CN).

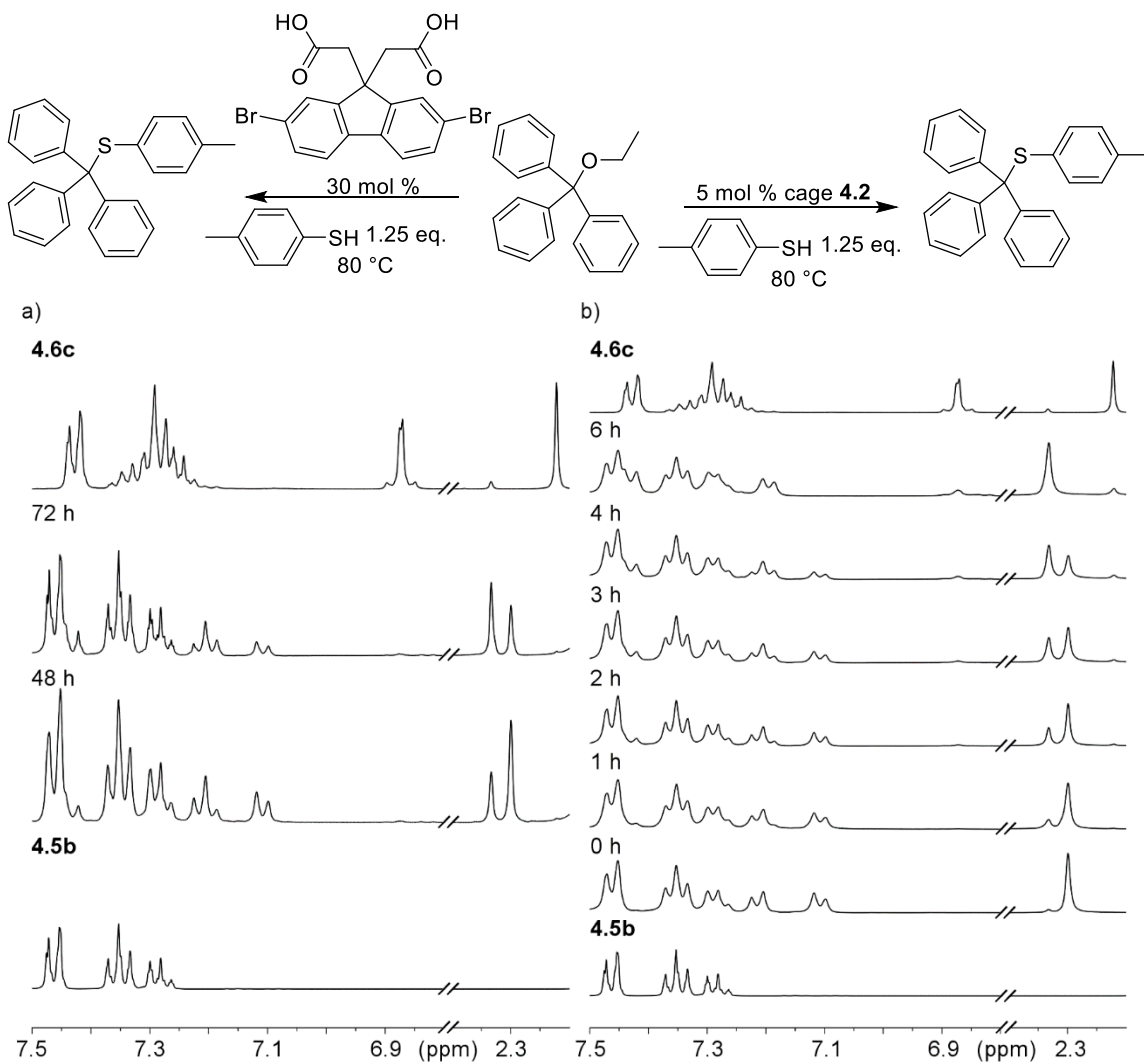


Figure 7.62. ^1H NMR spectra (7.50-6.80 ppm, 2.40-2.20 ppm) of the acid promoted S_N1 reaction between **4.5b** and 4-methylbenzenethiol in the presence of: a) 30 mol % control acid **4.4** or b) 5 mol % cage **4.2**. The reaction was performed at 80 °C and monitored over time (400 MHz, 298K, CD_3CN).

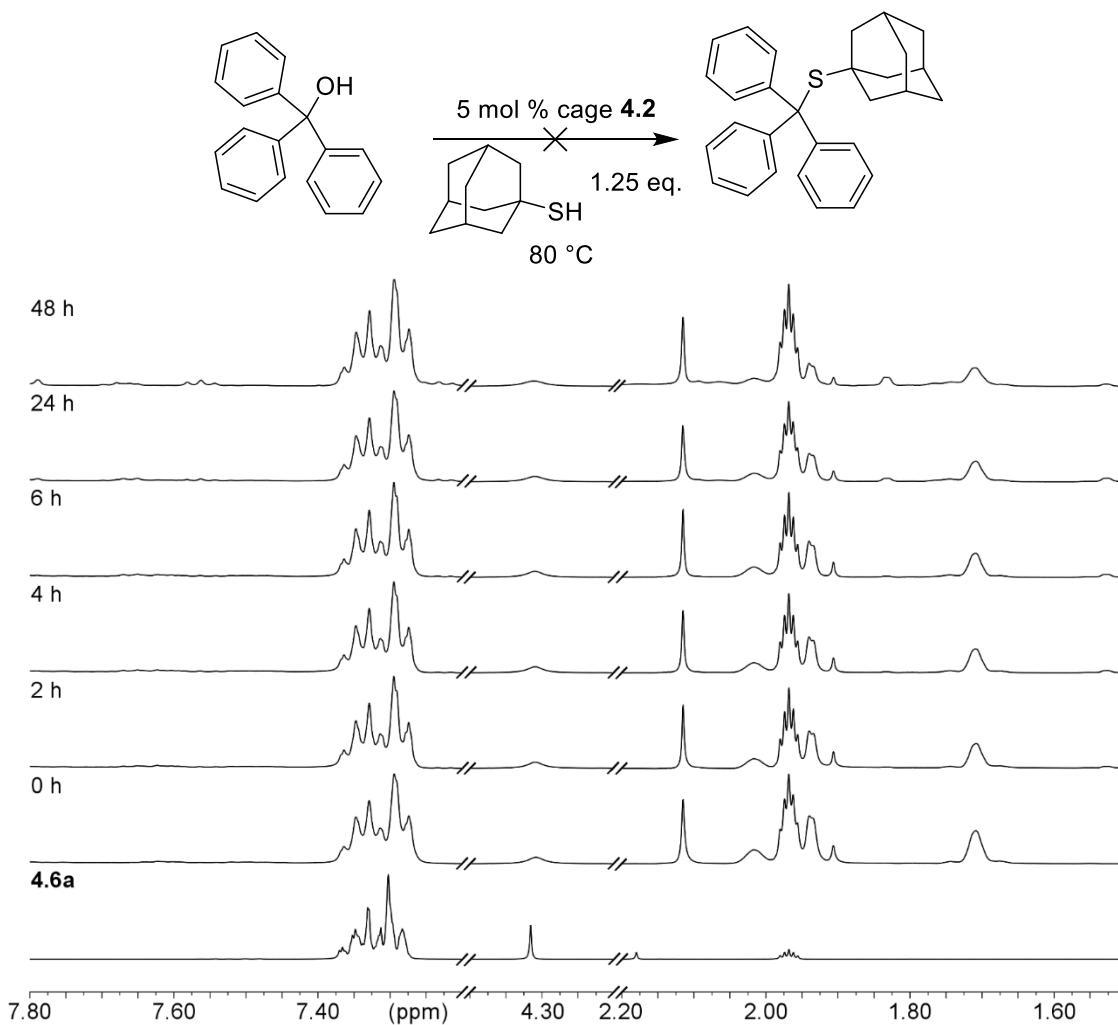


Figure 7.63. ¹H NMR spectra (7.80-7.20 ppm, 4.40-4.20 ppm, 2.20-1.50 ppm) of the acid promoted substitution reaction between **4.5a** and adamantane thiol in the presence of 5 mol % cage **4.2**. The reaction was performed at 80 °C and monitored over time (400 MHz, 298K, CD₃CN).

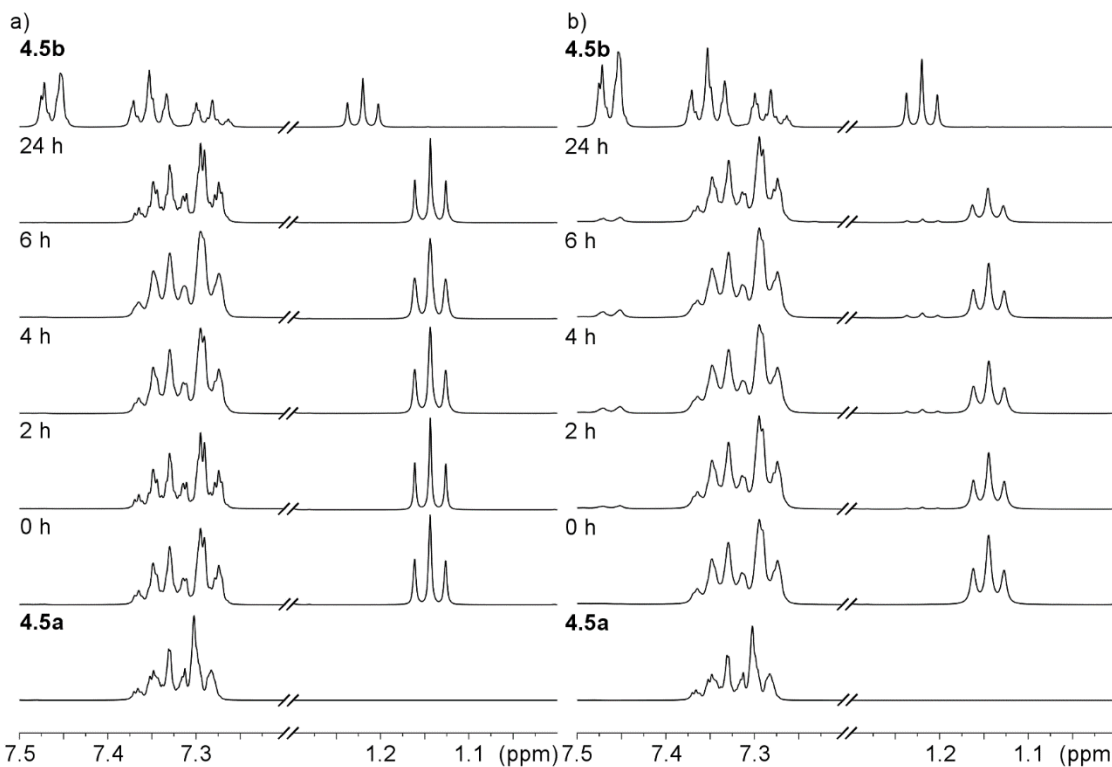
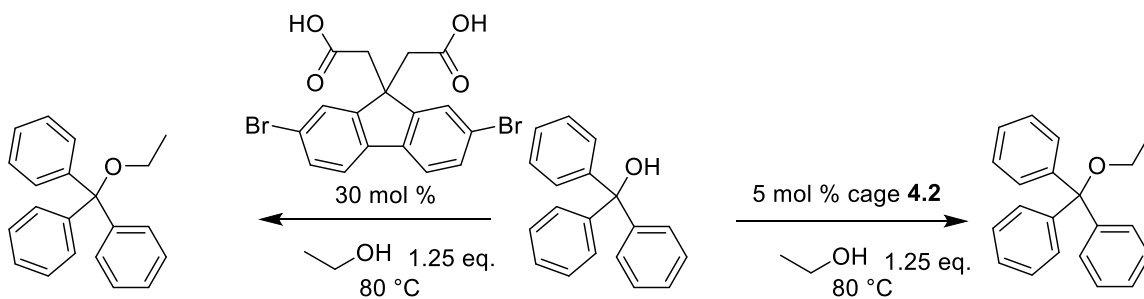


Figure 7.64. ^1H NMR spectra (7.50-7.20 ppm, 1.30-1.00 ppm) of the acid promoted substitution reaction between **4.5a** and ethanol in the presence of 5 mol % cage **4.2**. The reaction was performed at 80 °C and monitored over time (400 MHz, 298K, CD_3CN).

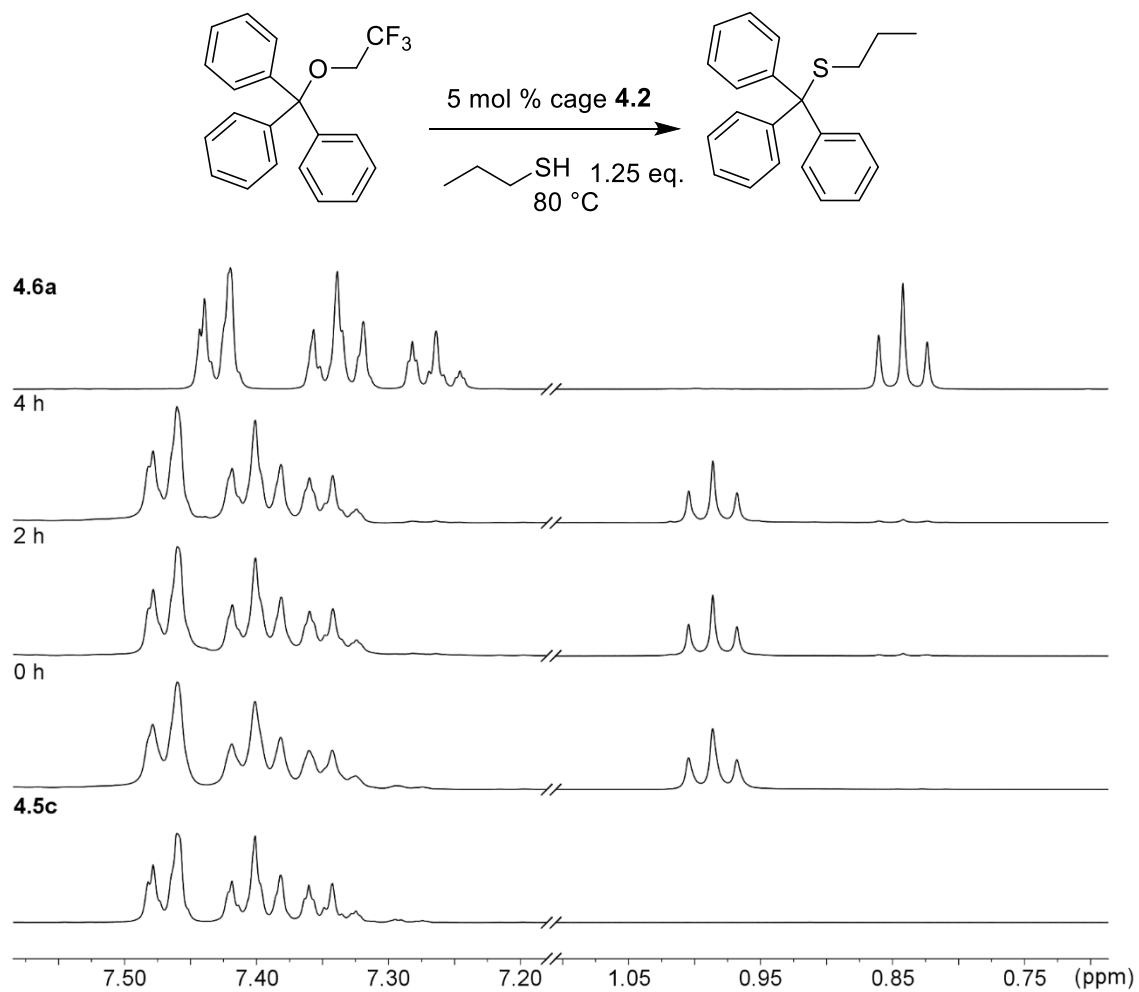


Figure 7.65. ¹H NMR spectra (7.60-7.20 ppm, 1.10-0.70 ppm) of the acid promoted S_N1 reaction between **4.5c** and *n*-propyl thiol in the presence of 5 mol % cage **4.2**. The reaction was performed at 80 °C and monitored over time (400 MHz, 298K, CD₃CN).

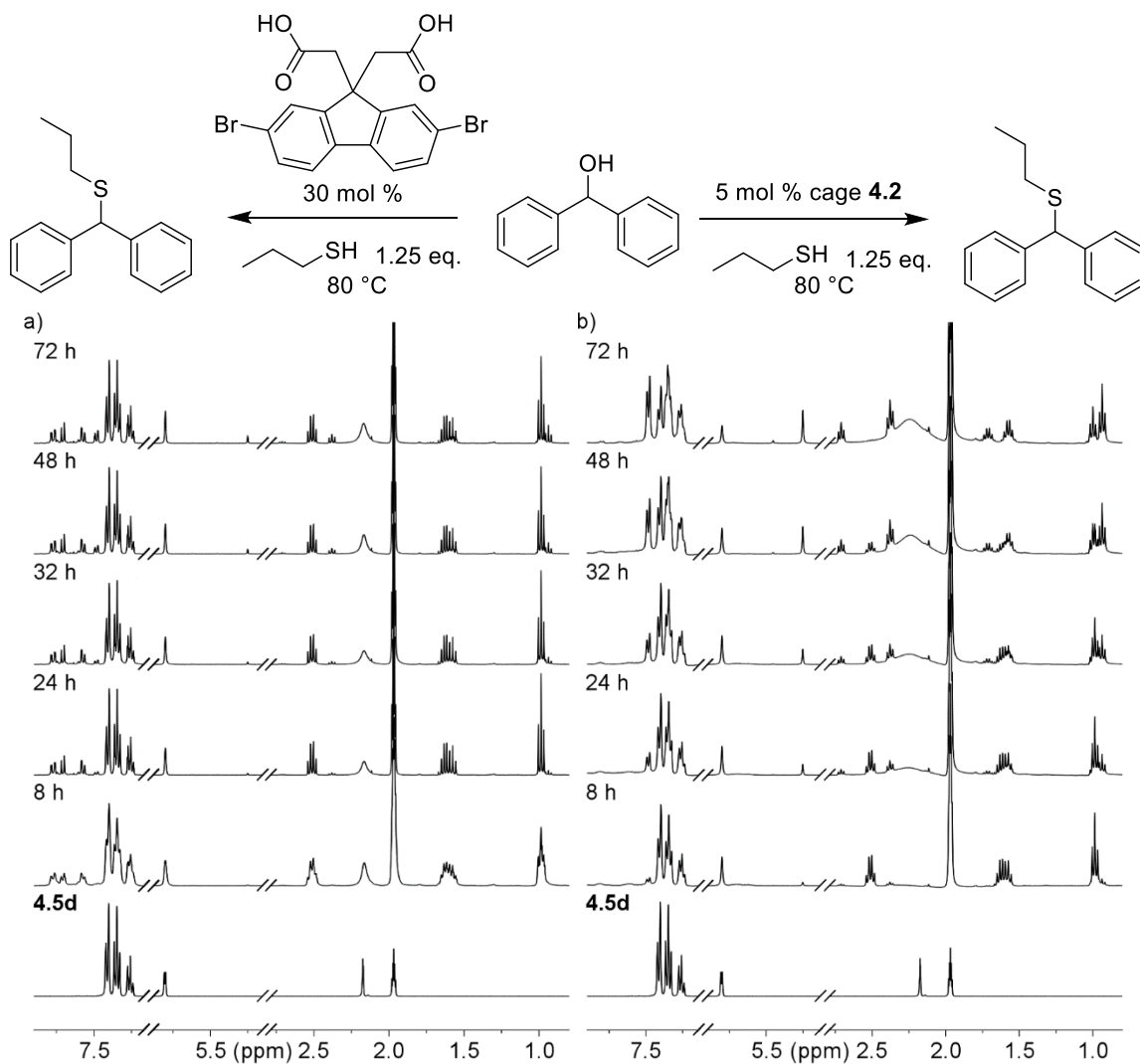


Figure 7.66. 1H NMR spectra (7.90-7.45 ppm, 5.6-5.4 ppm, 2.55-0.80 ppm) of the acid promoted S_N1 reaction between **4.5d** and *n*-propyl thiol in $400\ \mu L$ CD_3CN in the presence of: a) 30 mol % control acid **4.4** or b) 5 mol % cage **4.2**. The reaction was performed at $80^\circ C$ and monitored over time (400 MHz, 298K, CD_3CN).

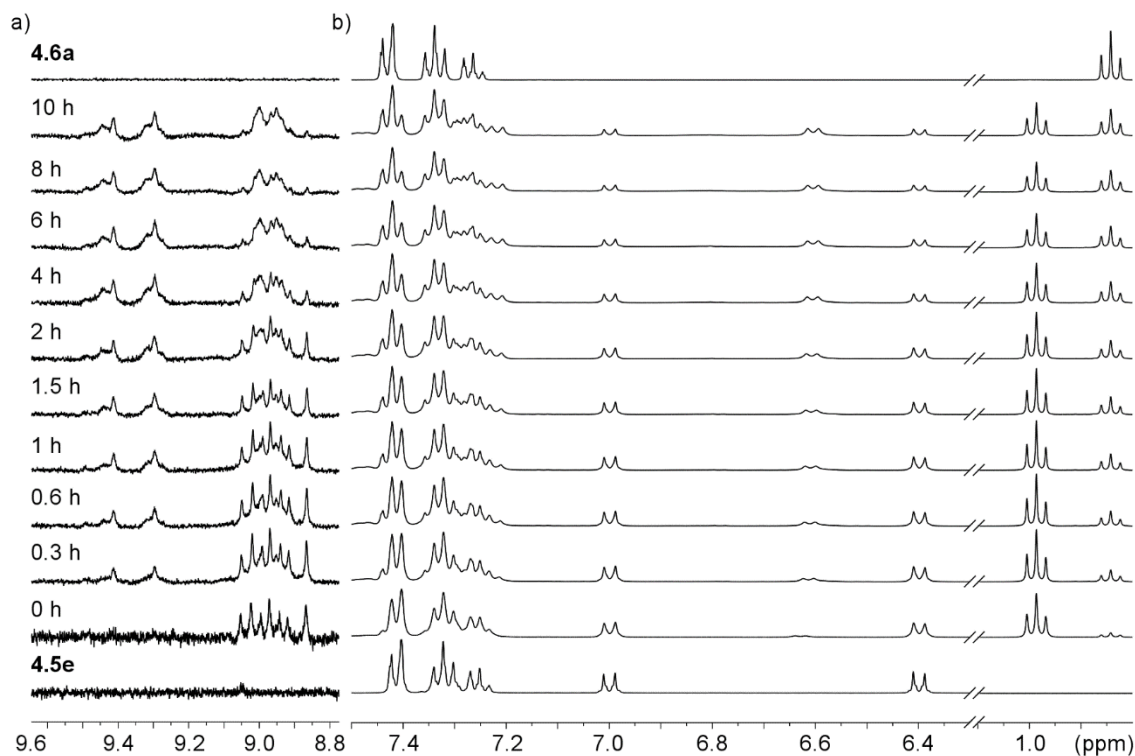
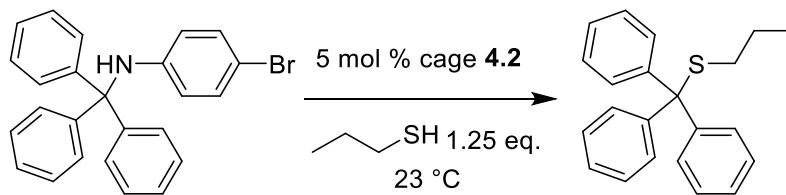


Figure 7.67. ^1H NMR spectra (9.60-8.80 ppm, 7.50-5.80 ppm, 1.10-0.80 ppm) of the acid promoted substitution reaction between 4-bromo-N-trityl aniline **4.5e** and *n*-propyl thiol in the presence of 5 mol % cage **4.2**. The reaction was performed at 23 °C and monitored over time (400 MHz, 298K, CD_3CN).

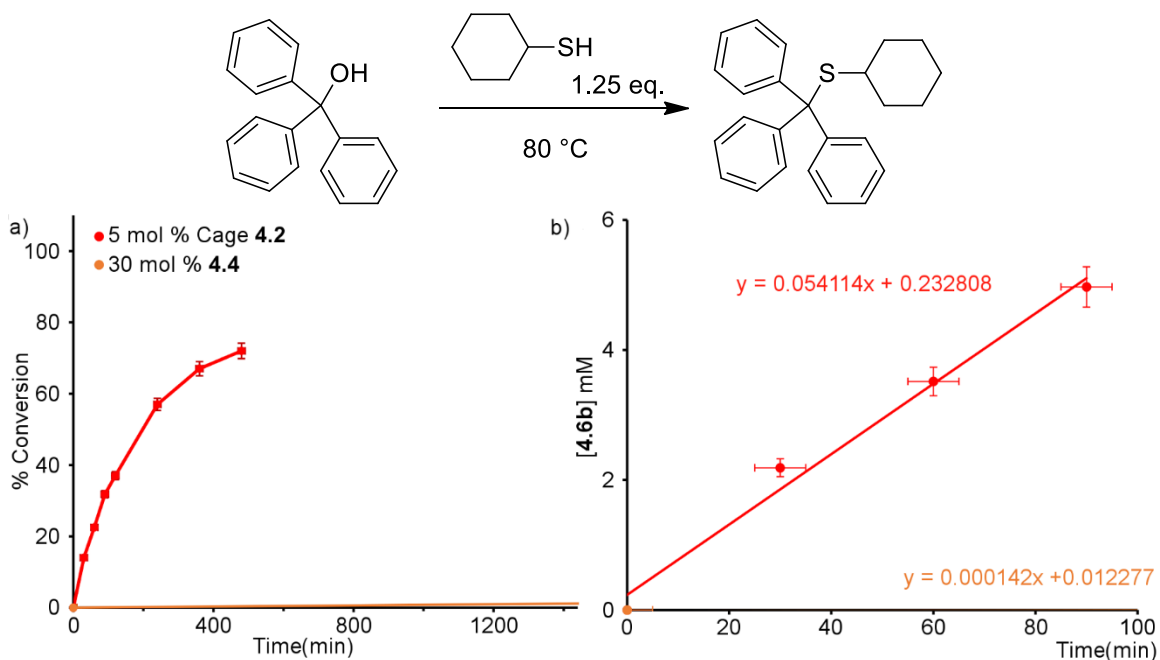


Figure 7.68. Graphed results of the acid promoted substitution reaction between **4.5a** and cyclohexyl thiol in the presence of: 5 mol % cage **4.2** (red), 30 mol % control acid **4.4** (orange). a) Averaged percent conversion values are plotted against time in minutes. b) Calculation of initial rate based on change in concentration of product **[4.6b]** over time in minutes.

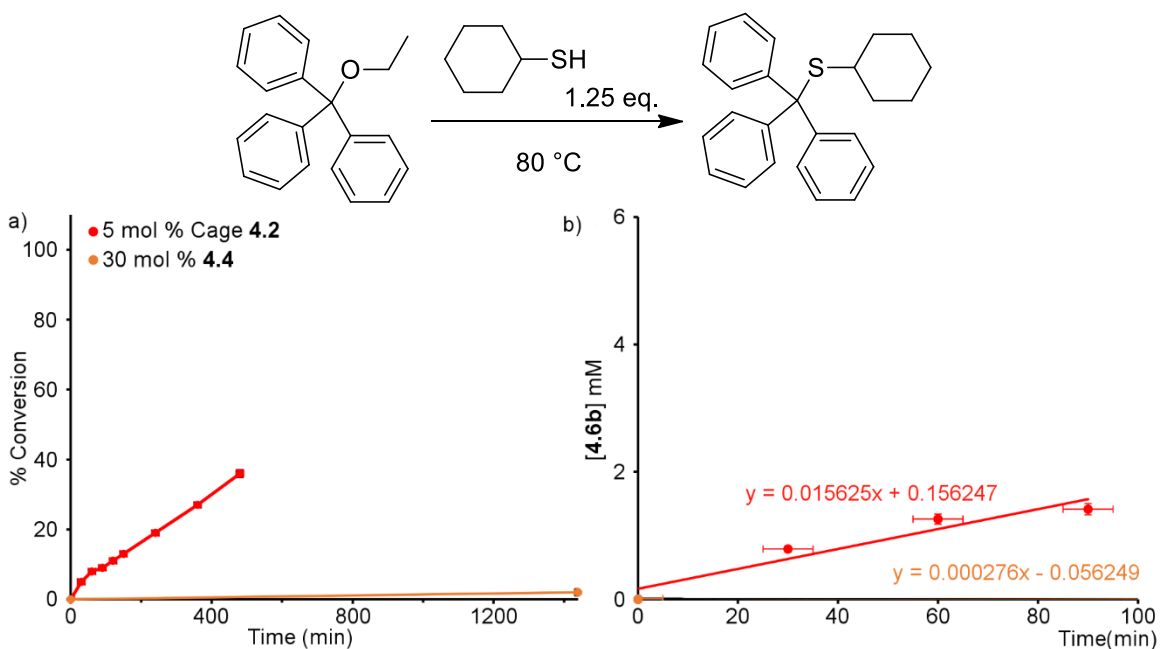


Figure 7.69. Graphed results of the acid promoted substitution reaction between **4.5b** and cyclohexyl thiol in the presence of: 5 mol % cage **4.2** (red), 30 mol % control acid **4.4** (orange). a) Averaged percent conversion values are plotted against time in minutes. b) Calculation of initial rate based on change in concentration of product **[4.6b]** over time in minutes.

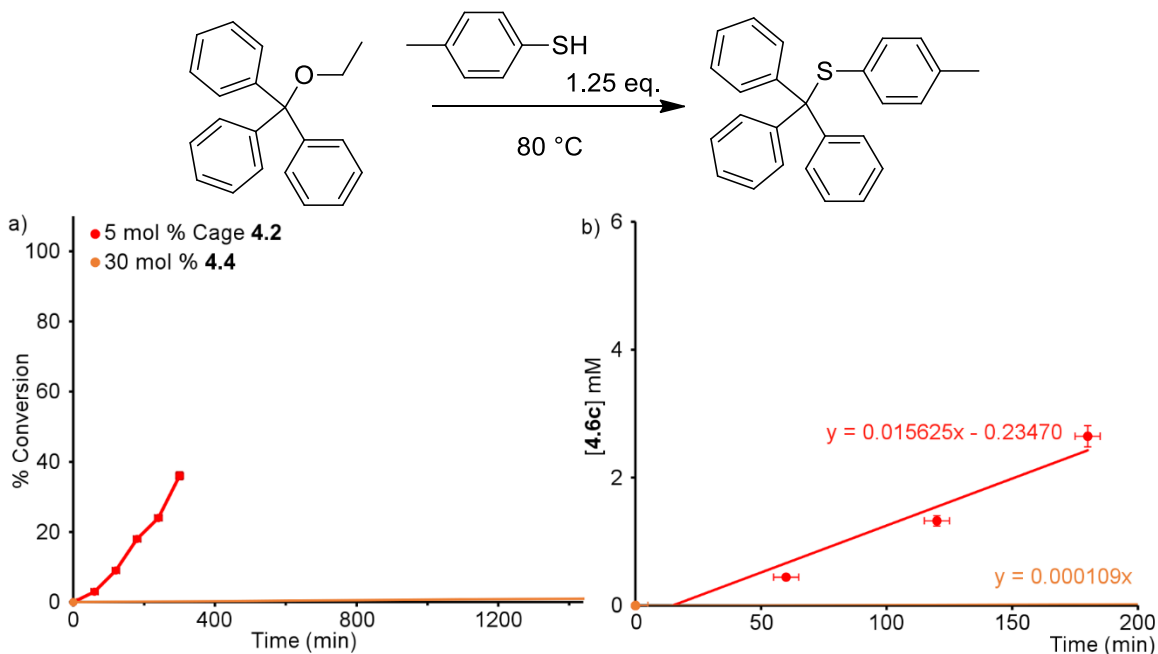


Figure 7.70. Graphed results of the acid promoted S_N1 reaction between **4.5b** and 4-methylbenzene thiol in the presence of: 5 mol % cage **4.2** (red), 30 mol % control acid **4.4** (orange). a) Averaged percent conversion values are plotted against time in minutes. b) Calculation of initial rate based on change in concentration of product [**4.6c**] over time in minutes.

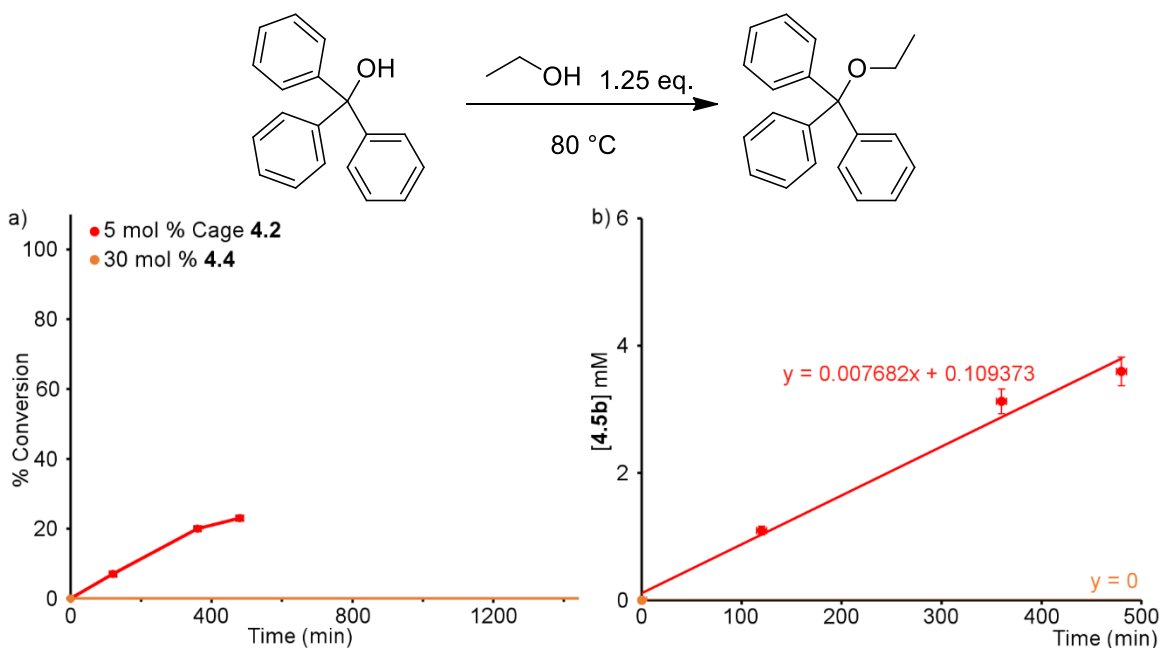


Figure 7.71. Graphed results of the acid promoted substitution reaction between **4.5a** and ethanol in the presence of: 5 mol % cage **4.2** (red), 30 mol % control acid **4.4** (orange). a) Averaged percent conversion values are plotted against time in minutes. b) Calculation of initial rate based on change in concentration of product [**4.6b**] over time in minutes.

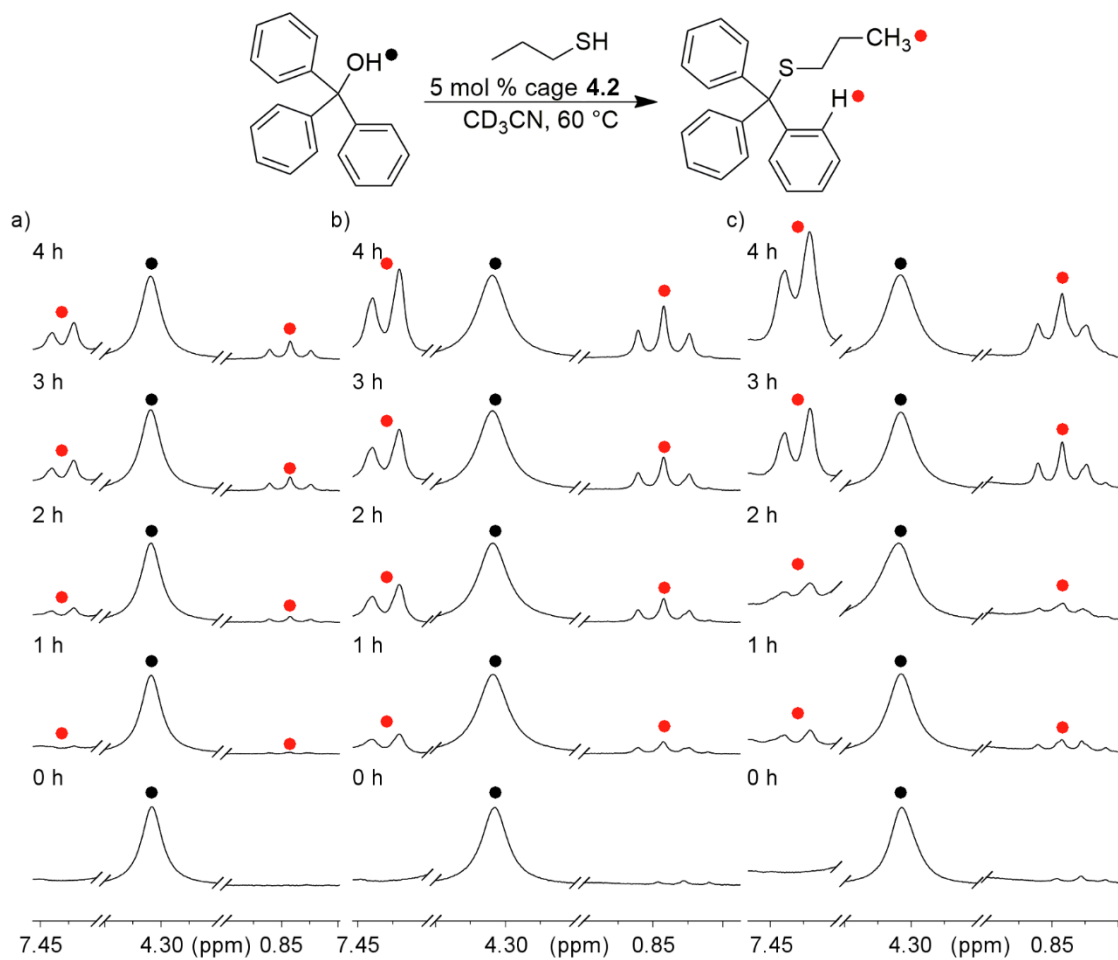


Figure 7.72. ¹H NMR spectra of the acid promoted substitution reaction between **4a** and *n*-propyl thiol in the presence of 5 mol % cage **4.1**, at varying concentrations of **PrSH** a) 8 mM b) 39.5 mM and c) 59.25 mM, performed at 60 °C and monitored over time (400 MHz, 298K, CD₃CN).

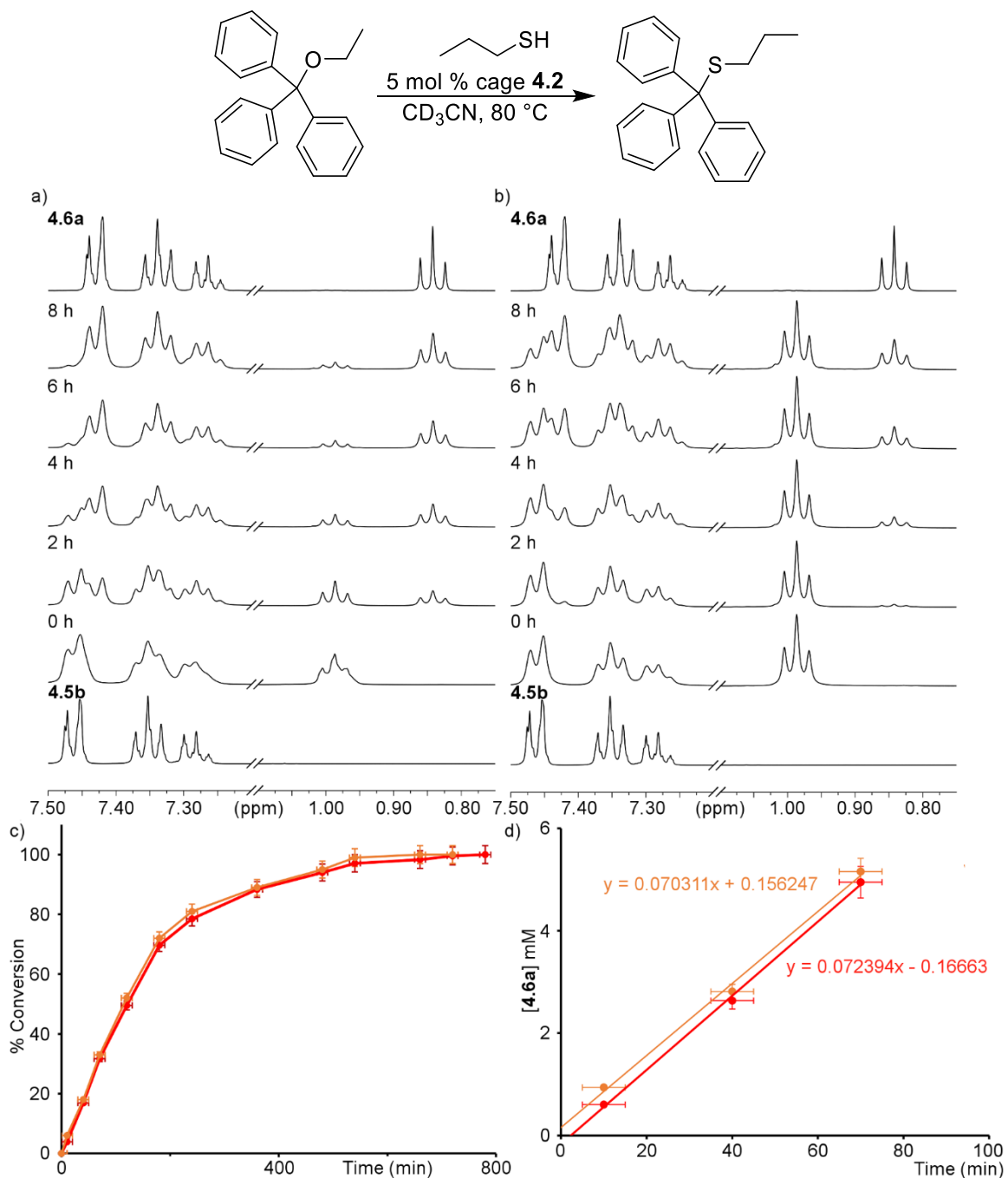


Figure 7.73. ¹H NMR spectra of the acid promoted substitution reaction between **4.5b** and *n*-propyl thiol in the presence of 5 mol % cage **4.2**, at varying concentrations of PrSH a) 20 mM and b) 60 mM, performed at 80 °C and monitored over time (400 MHz, 298K, CD₃CN). c) Averaged percent conversion over time (min) using 20 mM PrSH (orange) and 60 mM PrSH (red).

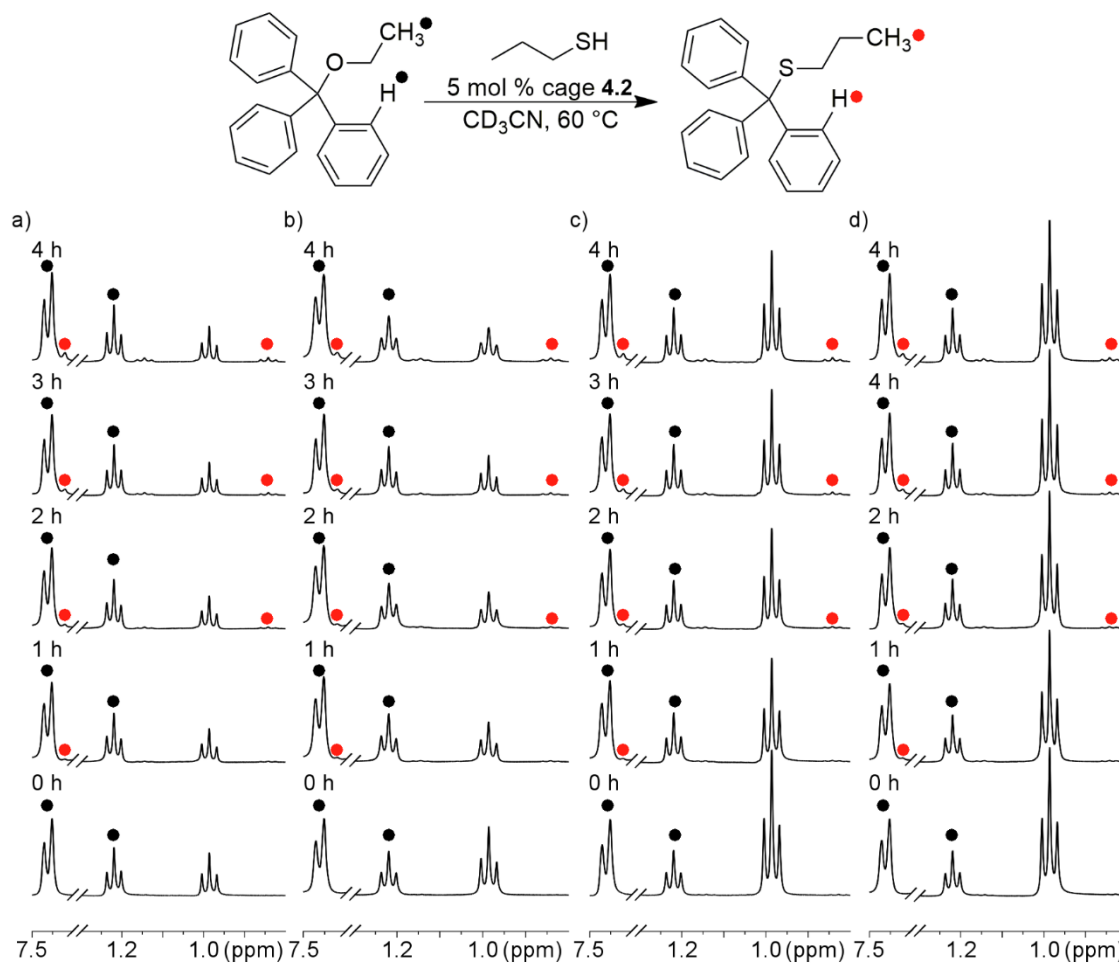


Figure 7.74. ^1H NMR spectra of the acid promoted substitution reaction between **4.5b** and **PrSH** in the presence of 5 mol % cage **4.2**, at varying concentrations of **PrSH** a) 9.88 mM, b) 19.75, c) 39.5 mM, and d) 59.25 mM, performed at 60°C and monitored over time (400 MHz, 298K, CD_3CN).

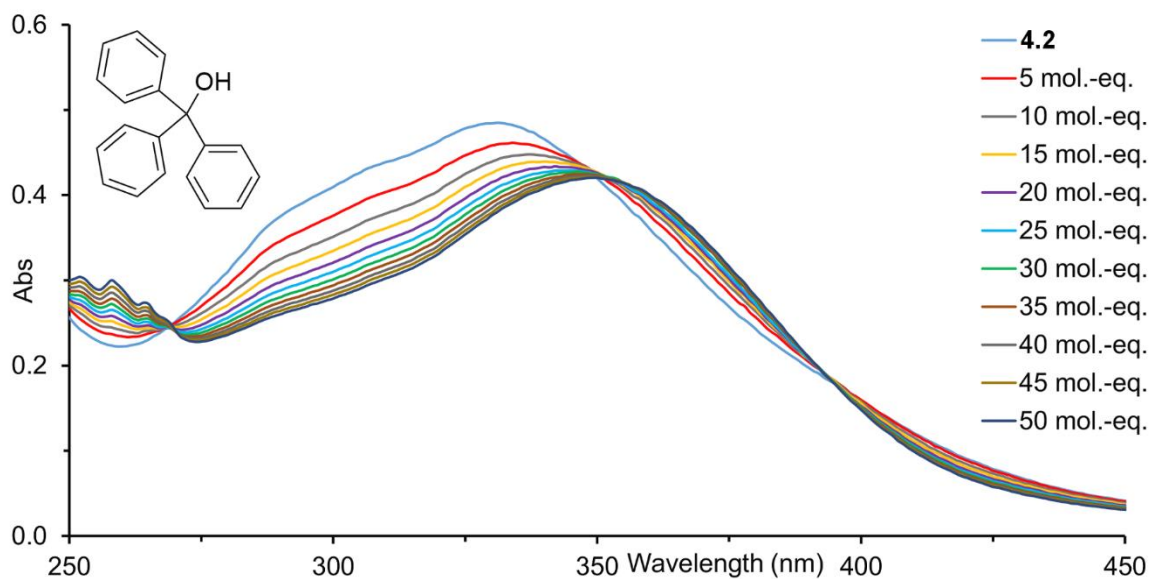


Figure 7.75. UV-Vis absorption spectrum of the titration of **4.5a** into a 3 μM solution of cage **4.2** in CH_3CN . **4.5a** was added in 5 μL aliquots from a 9 mM stock solution in CD_3CN .

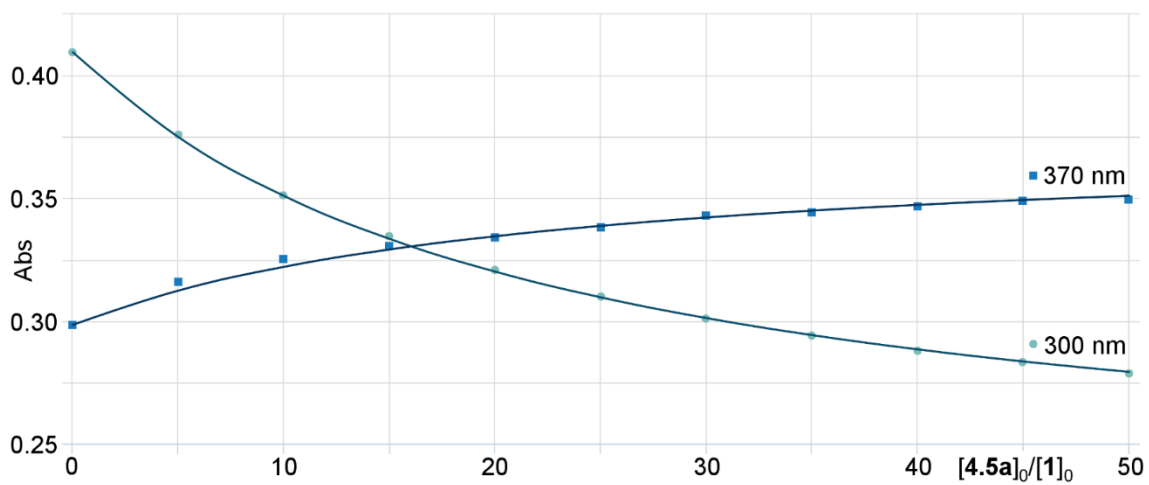


Figure 7.76. 1:1 binding fit model for guest **4.5a** calculated via linear regression analysis using the Nelder-Mead method from the change in absorbance at two points (300 nm and 370 nm) using supramolecular.org^{1,2} ($K_a = 15.8 \pm 0.3 \times 10^3 \text{ M}^{-1}$).

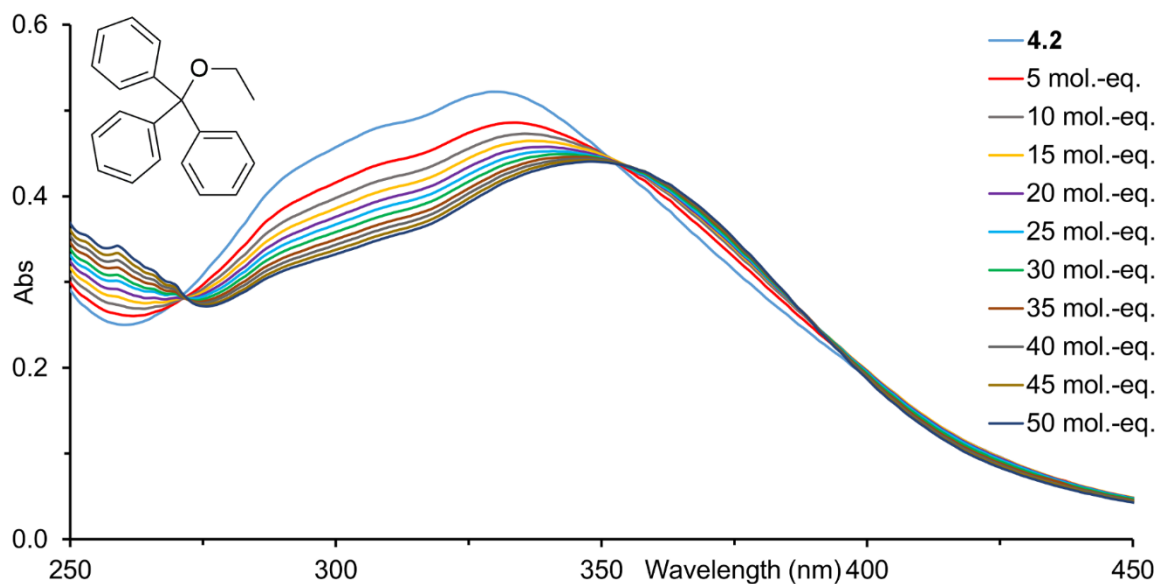


Figure 7.77. UV-Vis absorption spectrum of the titration of **4.5b** into a 3 μM solution of cage **4.2** in CH_3CN . **4.5b** was added in 5 μL aliquots from a 9 mM stock solution in CD_3CN .

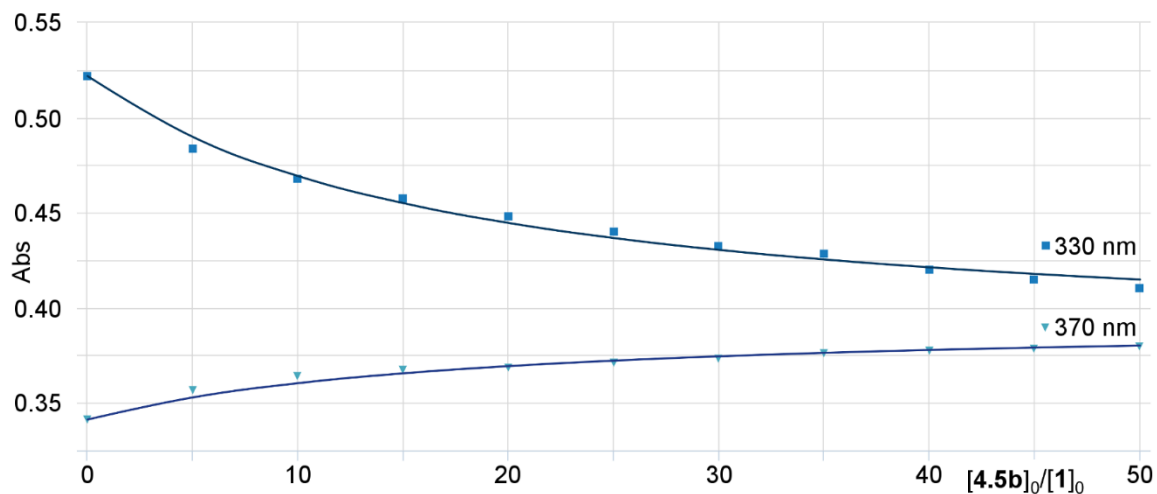


Figure 7.78. 1:1 binding fit model for guest **4.5b** calculated via linear regression analysis using the Nelder-Mead method from the change in absorbance at two points (330 nm and 370 nm) using supramolecular.org^{1,2} ($K_a = 20.1 \pm 1.2 \times 10^3 \text{ M}^{-1}$).

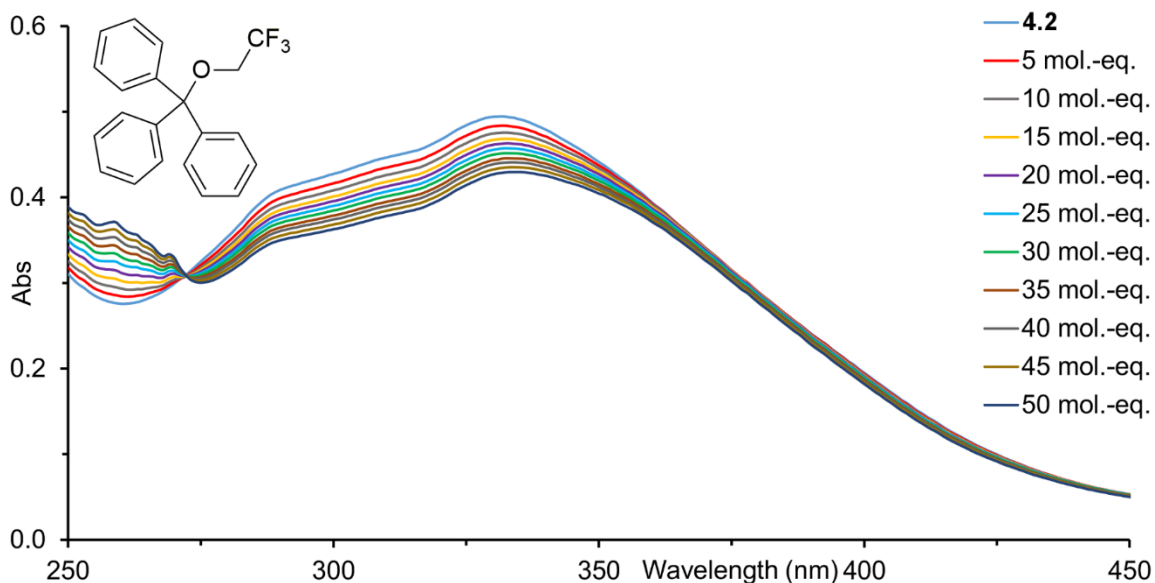


Figure 7.79. UV-Vis absorption spectrum of the titration of **4.5c** into a 3 μM solution of cage **4.2** in CH_3CN . **4.5c** was added in 5 μL aliquots from a 9 mM stock solution in CD_3CN .

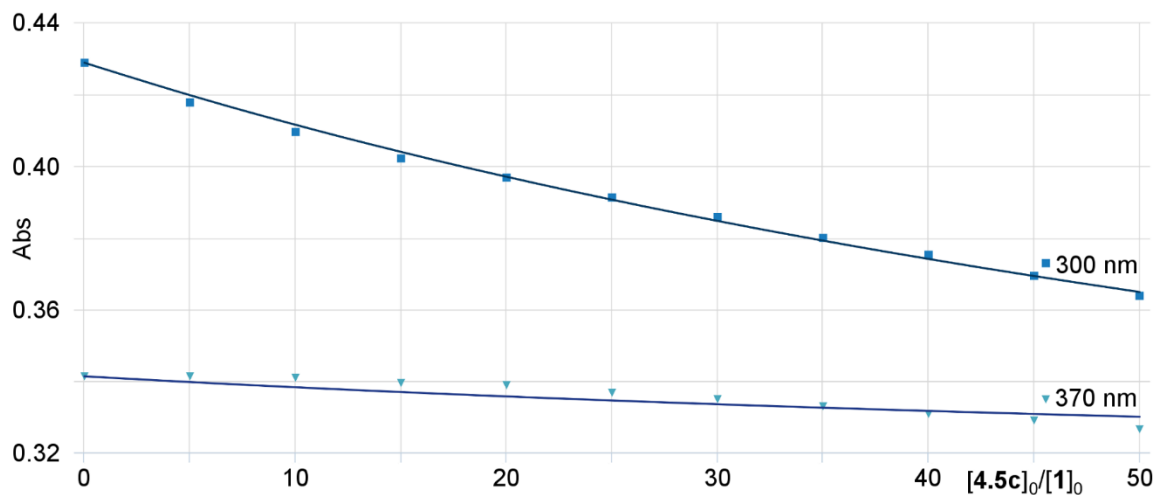


Figure 7.80. 1:1 binding fit model for guest **4.5c** calculated via linear regression analysis using the Nelder-Mead method from the change in absorbance at two points (300 nm and 370 nm) using supramolecular.org^{1,2} ($K_a = 3.2 \pm 1.3 \times 10^3 \text{ M}^{-1}$).

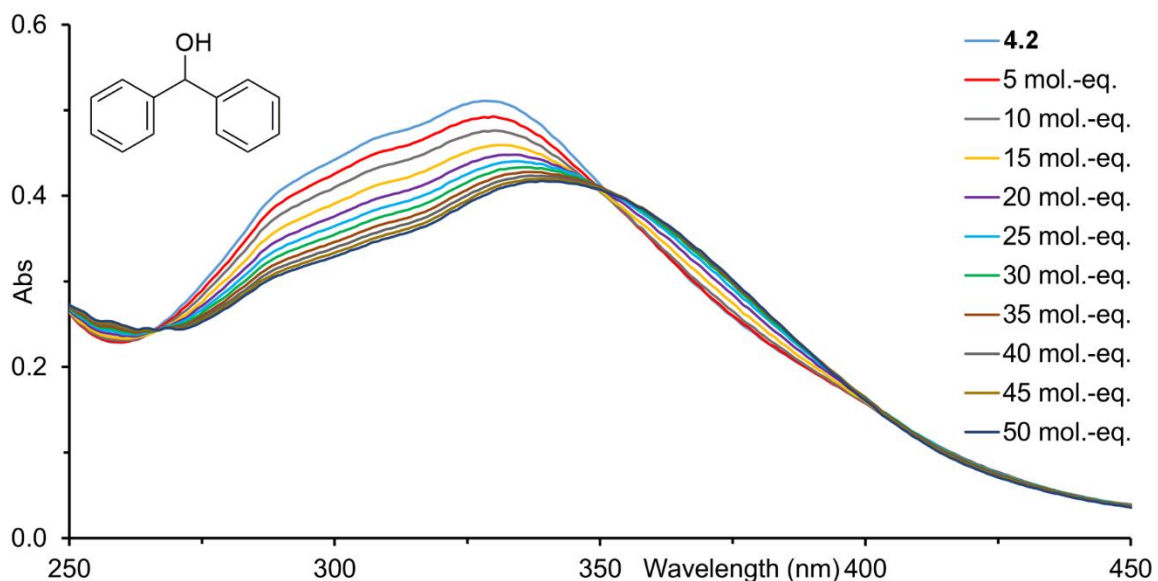


Figure 7.81. UV-Vis absorption spectrum of the titration of **4.5d** into a 3 μ M solution of cage **4.2** in CH_3CN . **4.5d** was added in 5 μ L aliquots from a 9 mM stock solution in CD_3CN .

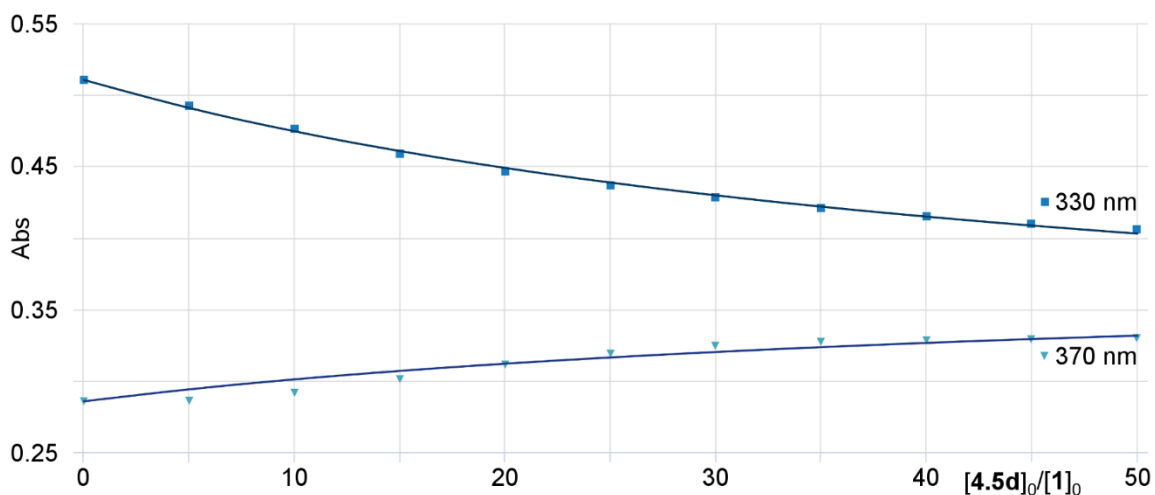


Figure 7.82. 1:1 binding fit model for guest **4.5d** calculated via linear regression analysis using the Nelder-Mead method from the change in absorbance at two points (330 nm and 370 nm) using supramolecular.org^{1,2} ($K_a = 6.9 \pm 0.4 \times 10^3 \text{ M}^{-1}$).

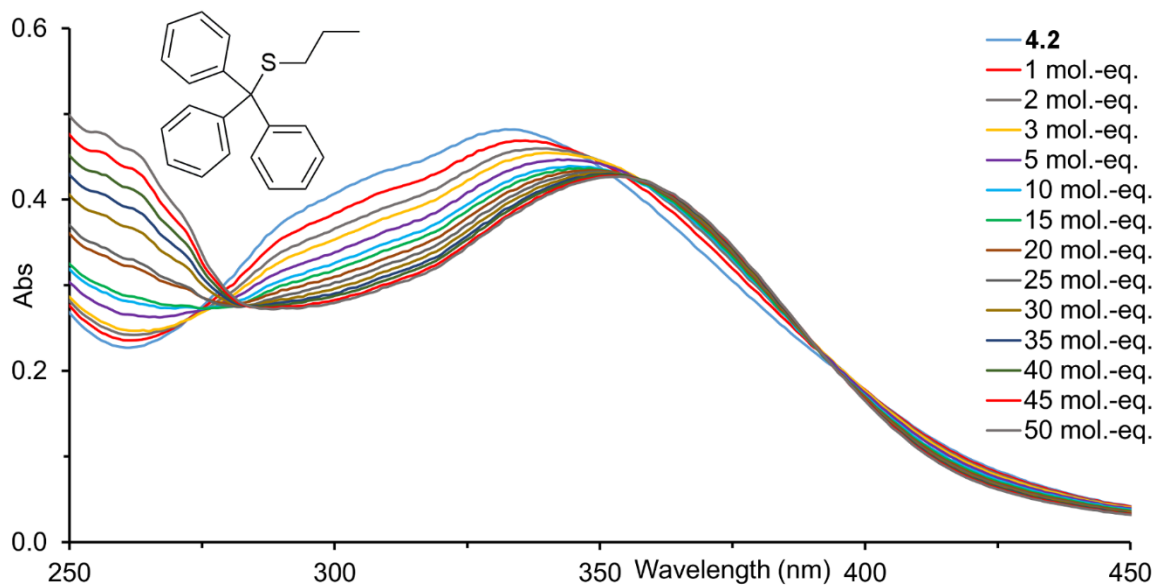


Figure 7.83. UV-Vis absorption spectrum of the titration of **4.6a** into a 3 μM solution of cage **4.2** in CH_3CN . **4.6a** was added in 1-5 μL aliquots from a 9 mM stock solution in CH_3CN .

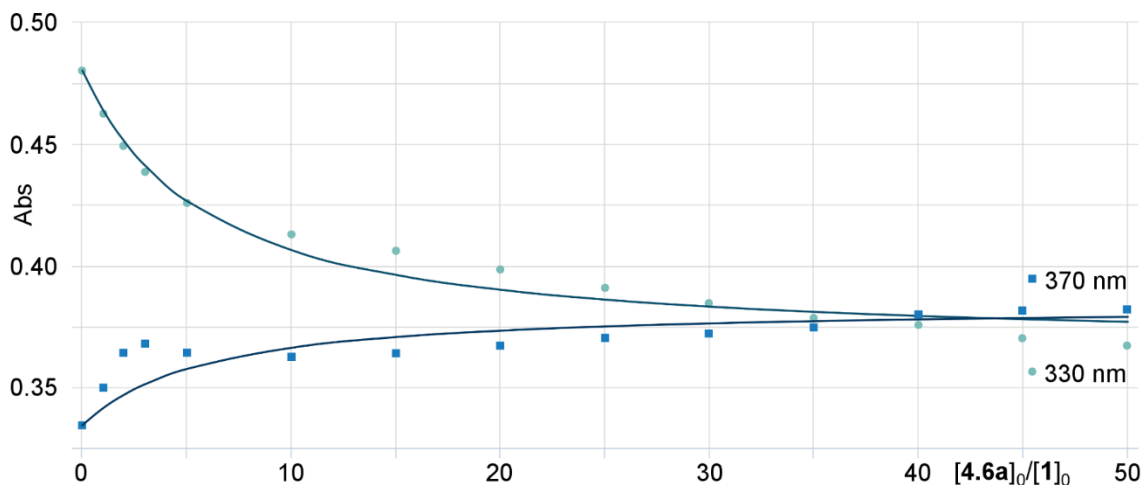


Figure 7.84. 1:1 binding fit model for guest **4.6a** calculated via linear regression analysis using the Nelder-Mead method from the change in absorbance at two points (330 nm and 370 nm) using supramolecular.org^{1,2} ($K_a = 6.5 \pm 1.3 \times 10^3 \text{ M}^{-1}$).

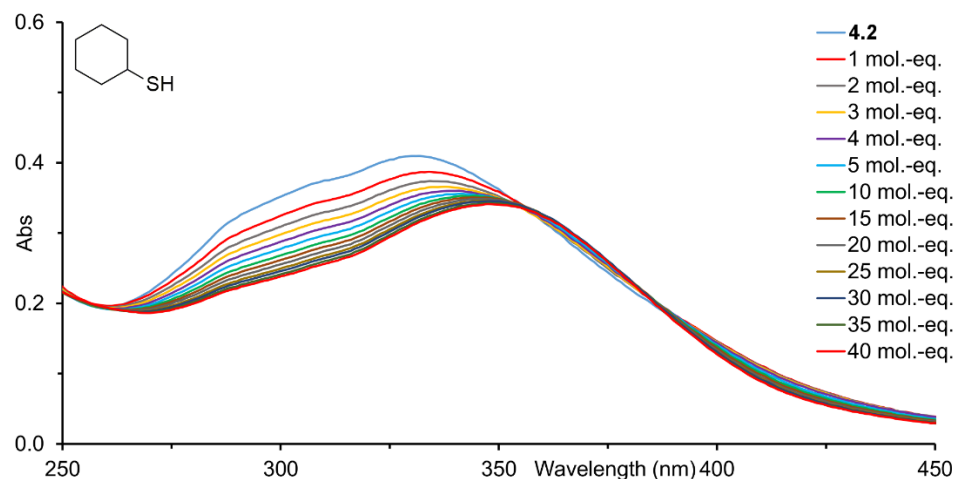


Figure 7.85. UV-Vis absorption spectrum of the titration of **CySH** into a 3 μM solution of cage **4.2** in CH_3CN . **CySH** was added in 1-5 μL aliquots from a 9 mM stock solution in CD_3CN .

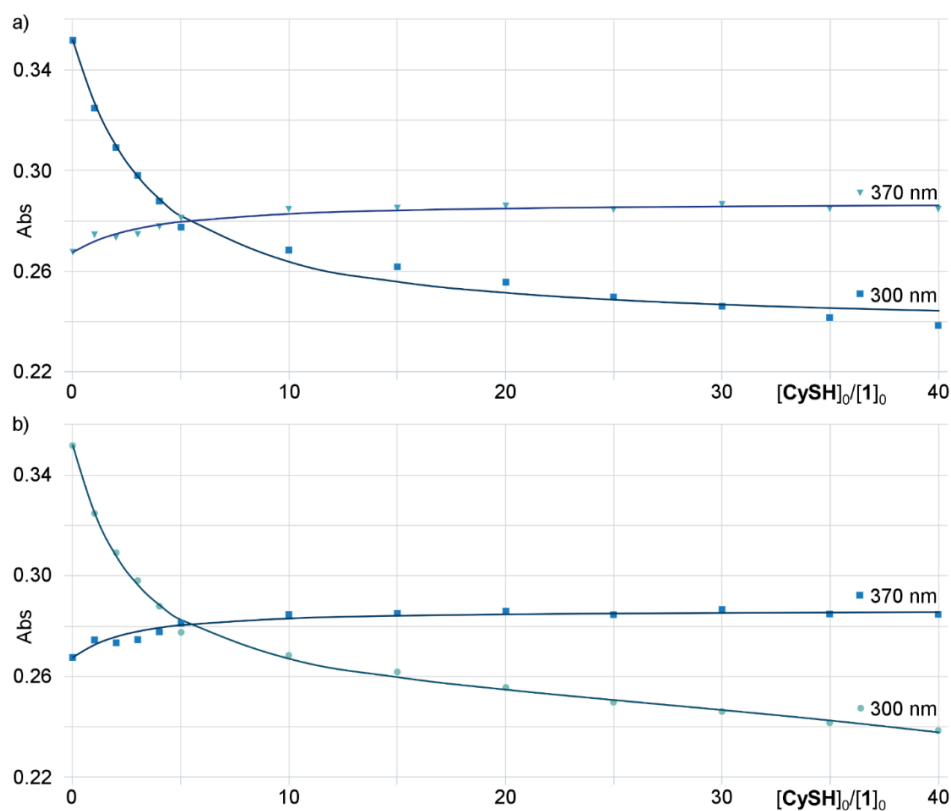


Figure 7.86. a) 1:1 binding fit model for guest **CySH** calculated via linear regression analysis using the Nelder-Mead method from the change in absorbance at two points (300 nm and 370 nm) using supramolecular.org^{1,2} ($K_a = 113.9 \pm 15.0 \times 10^3 \text{ M}^{-1}$). b) 1:2 binding fit model calculated via linear regression analysis using the Nelder-Mead method from the change in absorbance at two points (300 nm and 370 nm) using supramolecular.org^{1,2} ($K_{11} = 156.1 \pm 11.2 \times 10^3 \text{ M}^{-1}$, $K_{12} = 4.0 \pm 0.4 \times 10^3 \text{ M}^{-1}$).

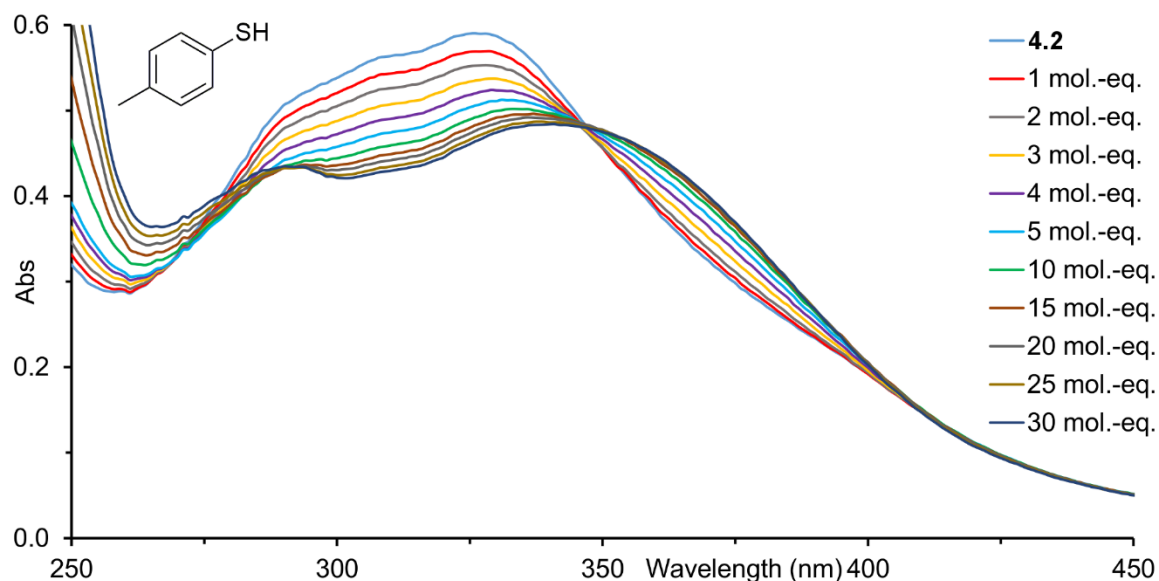


Figure 7.87. UV-Vis absorption spectrum of the titration of **TolSH** into a 3 μM solution of cage **4.2** in CH_3CN . **TolSH** was added in 1-5 μL aliquots from a 9 mM stock solution in CD_3CN .

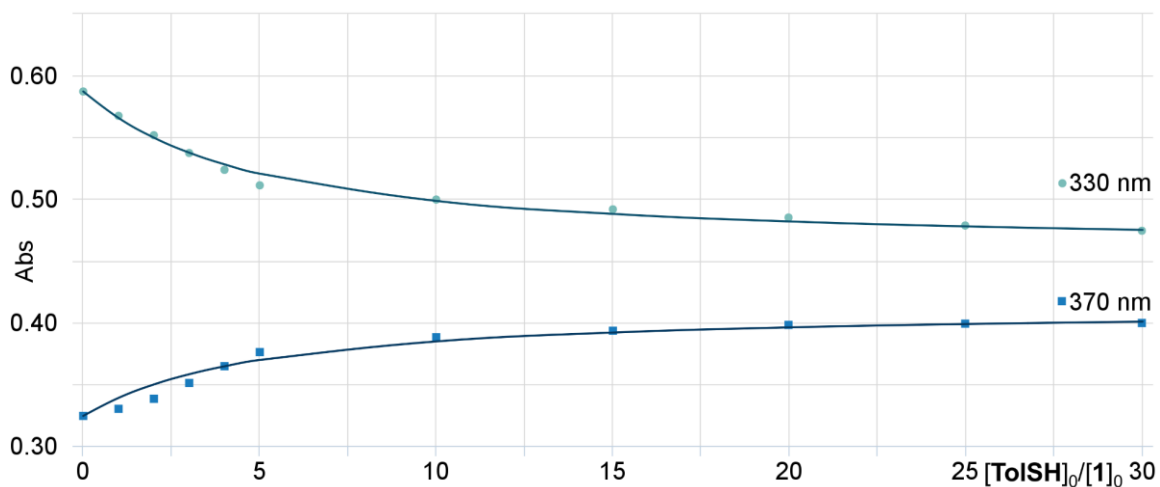


Figure 7.88. 1:1 binding fit model for guest **TolSH** calculated via linear regression analysis using the Nelder-Mead method from the change in absorbance at two points (330 nm and 370 nm) using supramolecular.org^{1,2} ($K_a = 80.6 \pm 9.7 \times 10^3 \text{ M}^{-1}$).

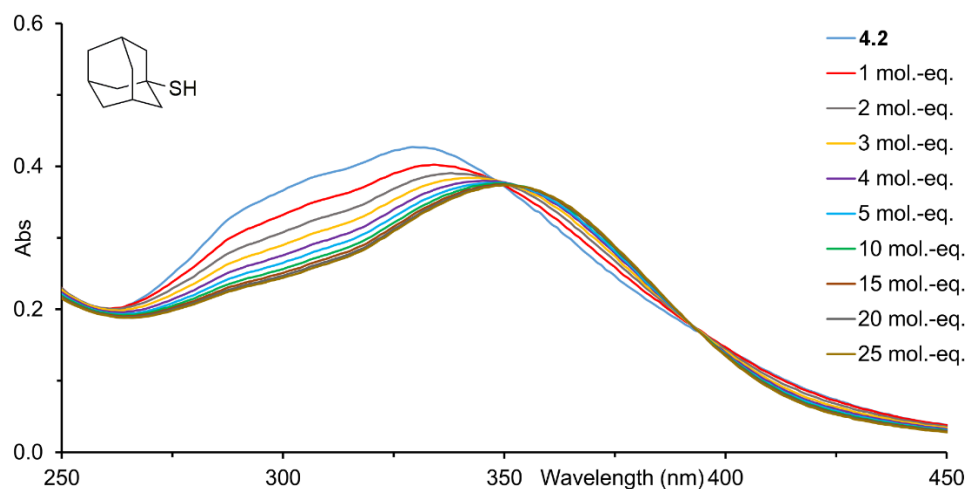


Figure 7.89. UV-Vis absorption spectrum of the titration of AdSH into a 3 μM solution of cage **4.2** in CH_3CN . AdSH was added in 1-5 μL aliquots from a 9 mM stock solution in CD_3CN .

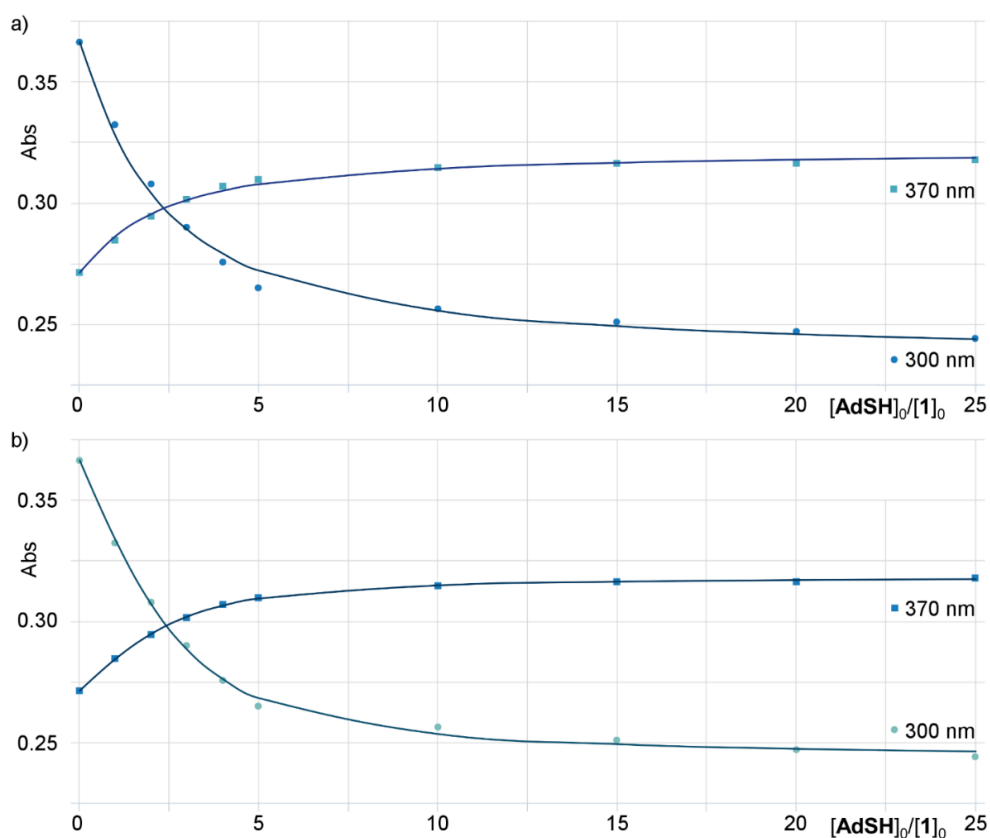


Figure 7.90. a) 1:1 binding fit model for guest AdSH calculated via linear regression analysis using the Nelder-Mead method from the change in absorbance at two points (300 nm and 370 nm) using supramolecular.org^{1,2} ($K_a = 199.4 \pm 17.0 \times 10^3 \text{ M}^{-1}$). b) 1:2 binding fit model calculated for guest AdSH via linear regression analysis using the Nelder-Mead method from the change in absorbance at two points (300 nm and 370 nm) using supramolecular.org^{1,2} ($K_{11} = 362.7 \pm 100.1 \times 10^3 \text{ M}^{-1}$, $K_{12} = 220.8 \pm 45.3 \times 10^3 \text{ M}^{-1}$).

7.10 Selected Spectra for Chapter 5

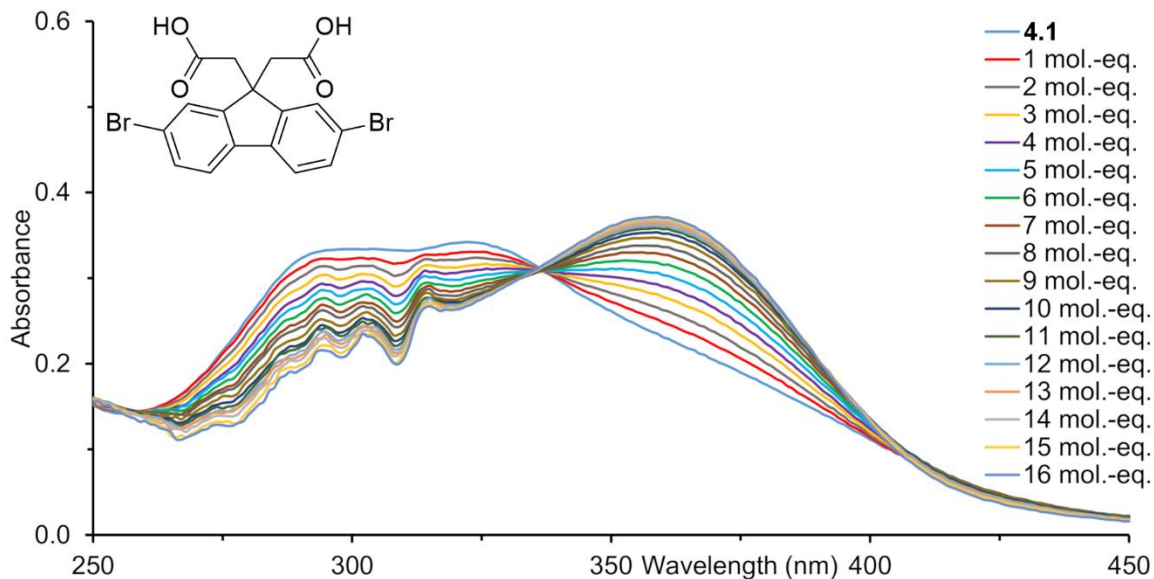


Figure 7.91. UV-Vis absorption spectrum of the titration of **4.4** into a 1.5 μM solution of cage **4.1** in CH_3CN . **4.4** was added in 1 μL aliquots from a 4.5 mM stock solution in CD_3CN .

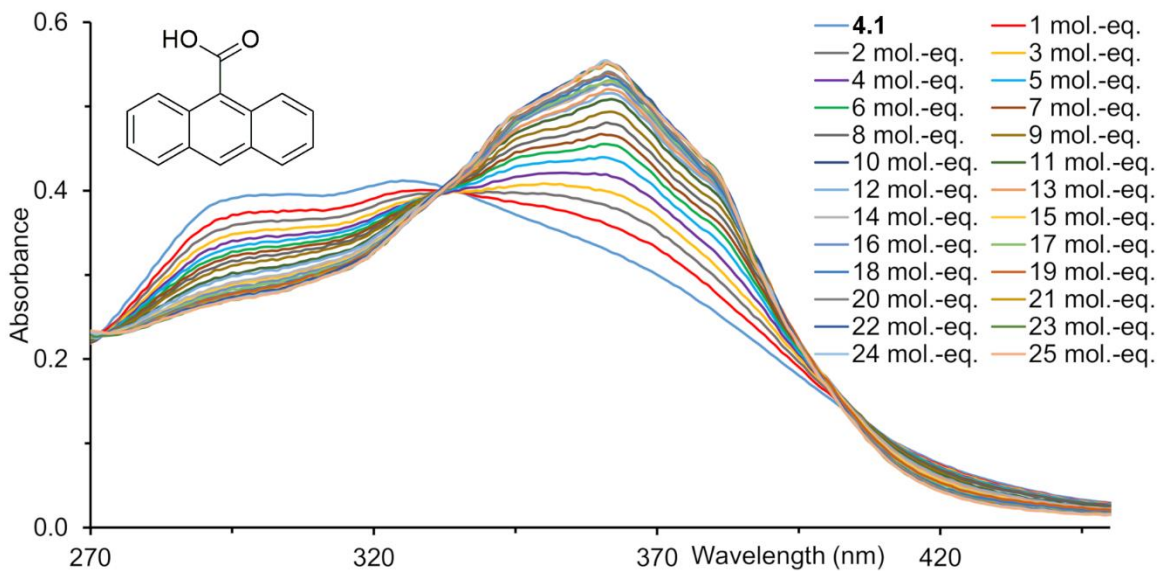


Figure 7.92. UV-Vis absorption spectrum of the titration of **5.2a** into a 1.5 μM solution of cage **4.1** in CH_3CN . **5.2a** was added in 1 μL aliquots from a 4.5 mM stock solution in CD_3CN .

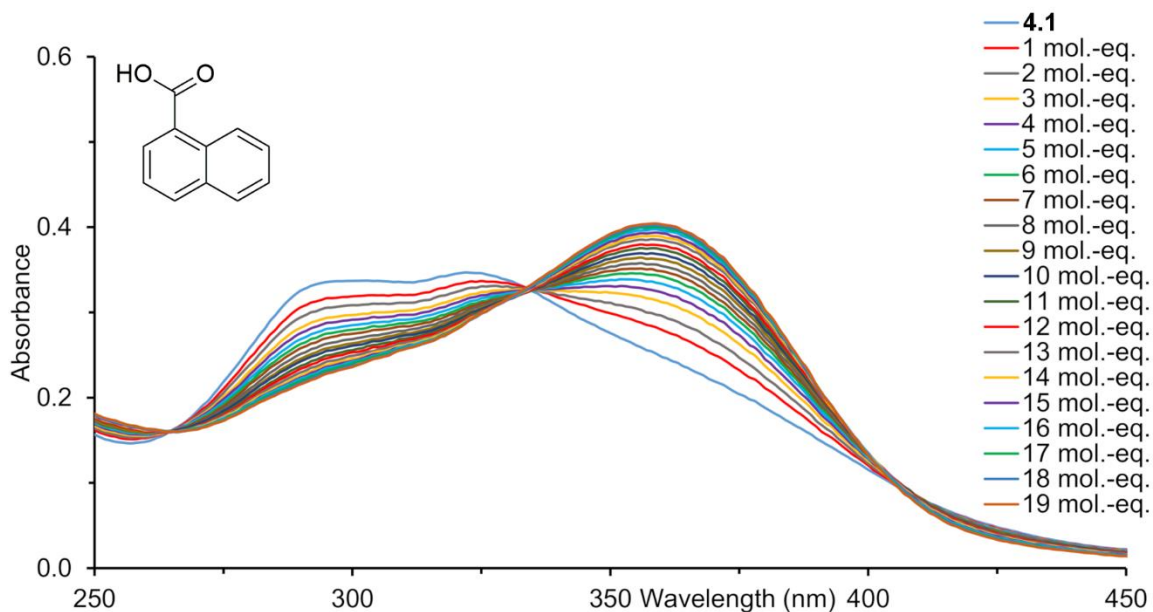


Figure 7.93. UV-Vis absorption spectrum of the titration of **5.2b** into a 1.5 μM solution of cage **4.1** in CH_3CN . **5.2b** was added in 1 μL aliquots from a 4.5 mM stock solution in CD_3CN .

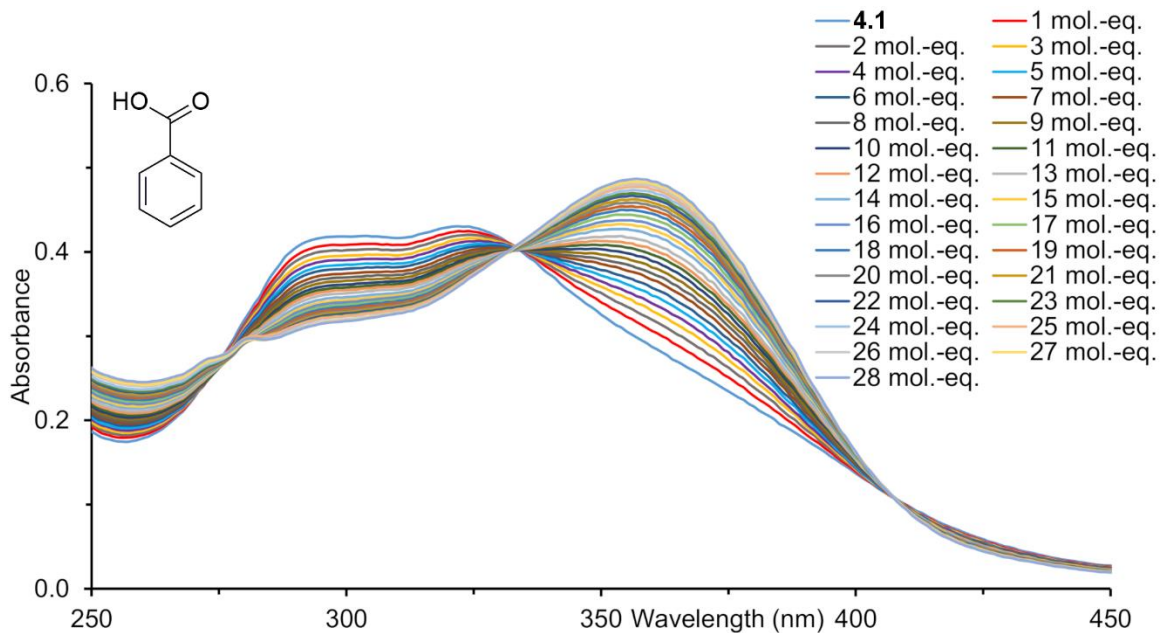


Figure 7.94. UV-Vis absorption spectrum of the titration of **5.2c** into a 1.5 μM solution of cage **4.1** in CH_3CN . **5.2c** was added in 1 μL aliquots from a 4.5 mM stock solution in CD_3CN .

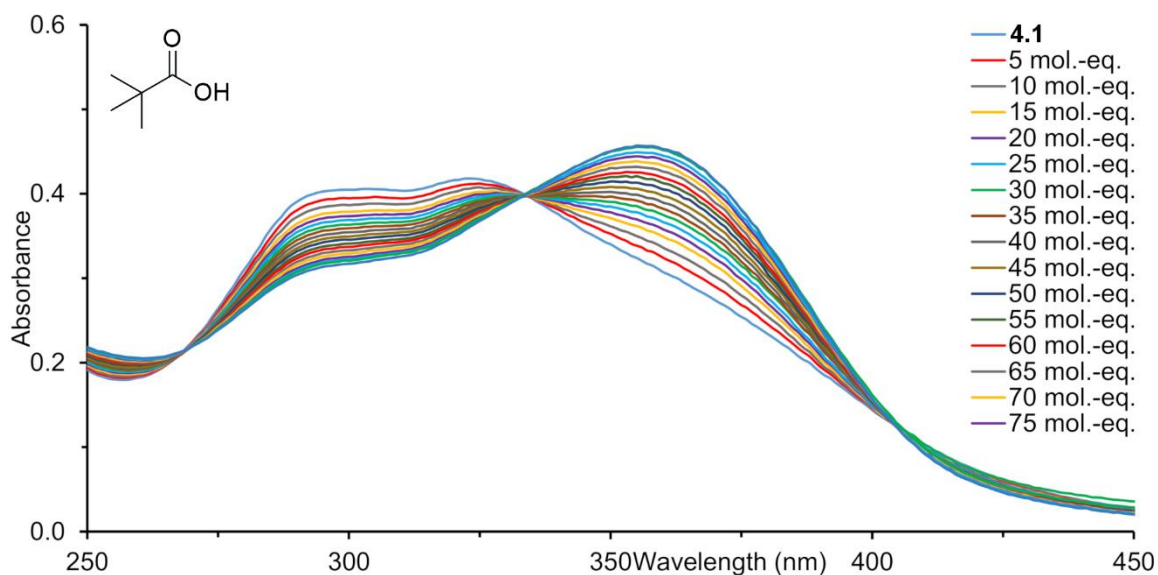


Figure 7.95: UV-Vis absorption spectrum of the titration of **5.2d** into a 3 μM solution of cage **4.1** in CH_3CN . **5.2d** was added in 5 μL aliquots from a 9 mM stock solution in CD_3CN .

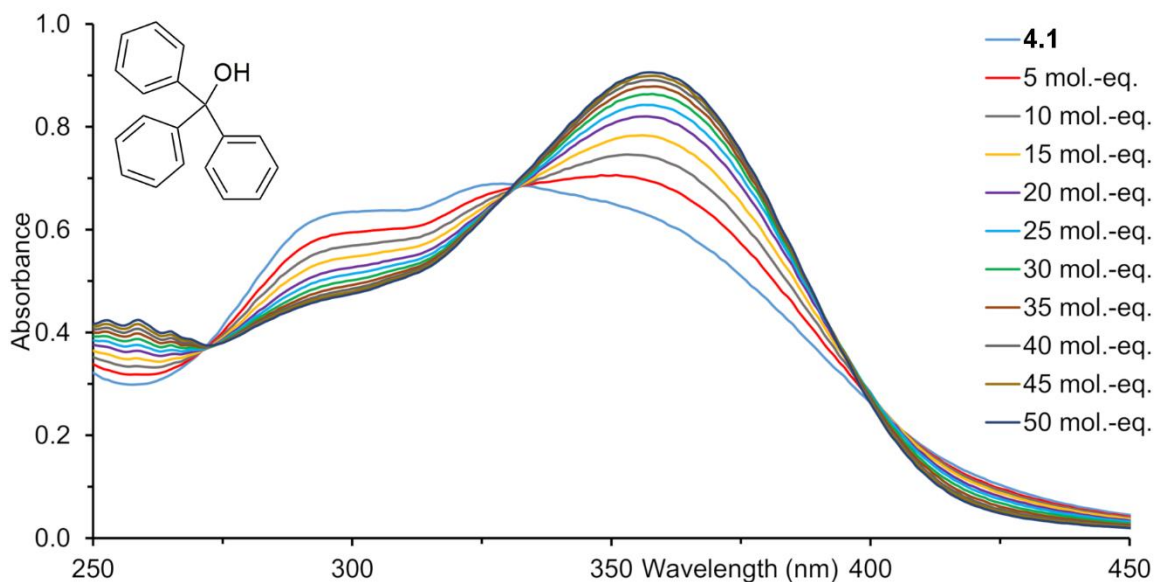


Figure 7.96: UV-Vis absorption spectrum of the titration of **4.5a** into a 3 μM solution of cage **4.1** in CH_3CN . **4.5a** was added in 5 μL aliquots from a 9 mM stock solution in CD_3CN .

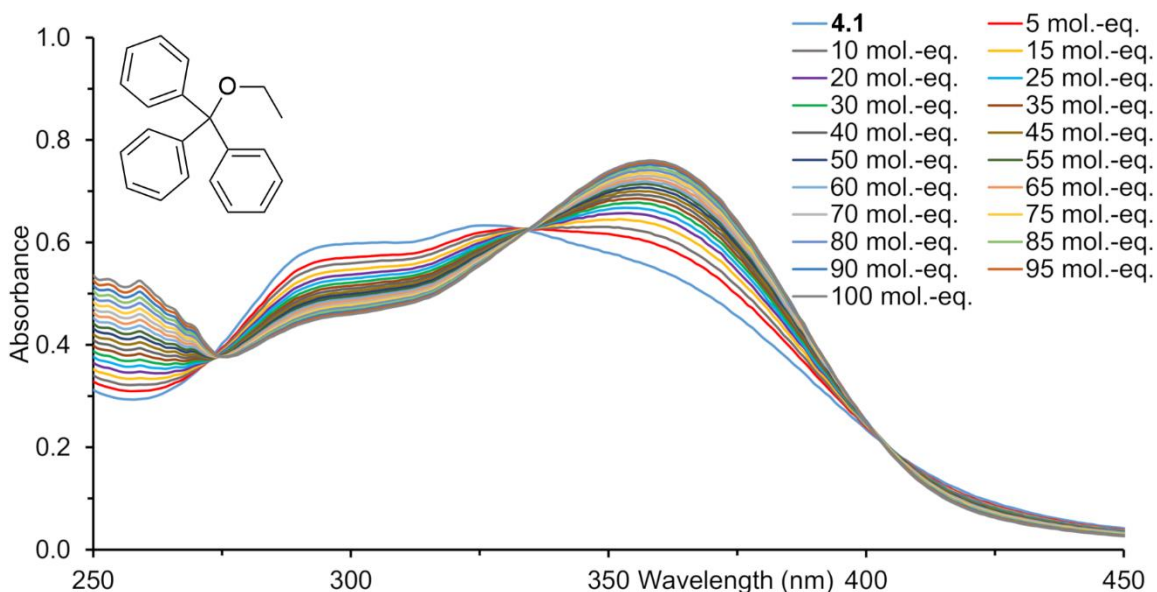


Figure 7.97. UV-Vis absorption spectrum of the titration of **4.5b** into a 3 μM solution of cage **4.1** in CH_3CN . **4.5b** was added in 5 μL aliquots from a 9 mM stock solution in CD_3CN .

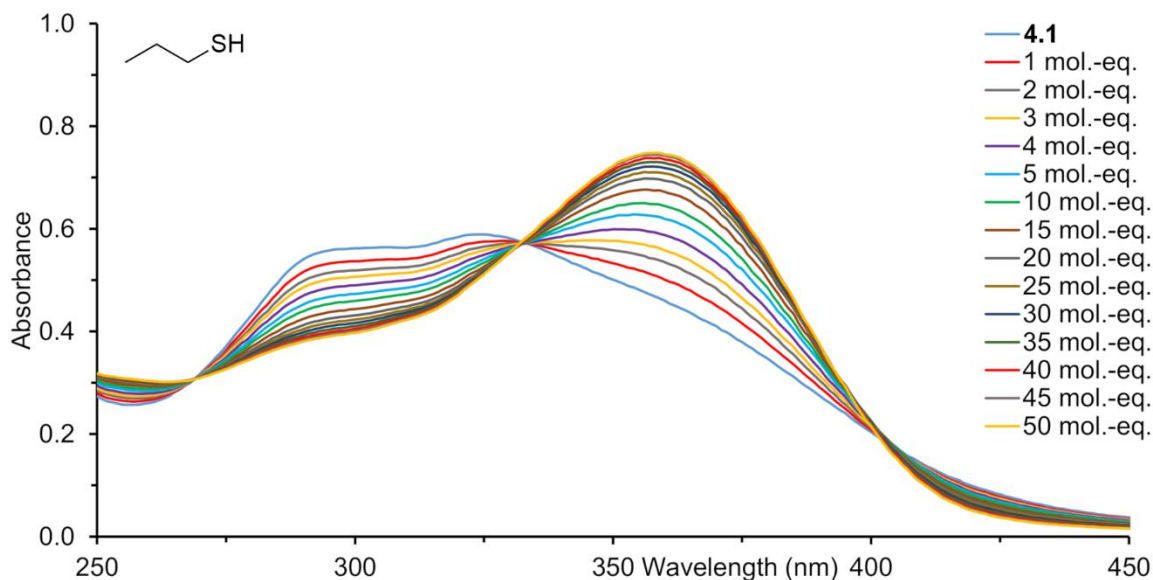


Figure 7.98. UV-Vis absorption spectrum of the titration of **4.6a** into a 1.5 μM solution of cage **4.1** in CH_3CN . **4.6a** was added in 1 μL aliquots from a 4.5 mM stock solution in CD_3CN .

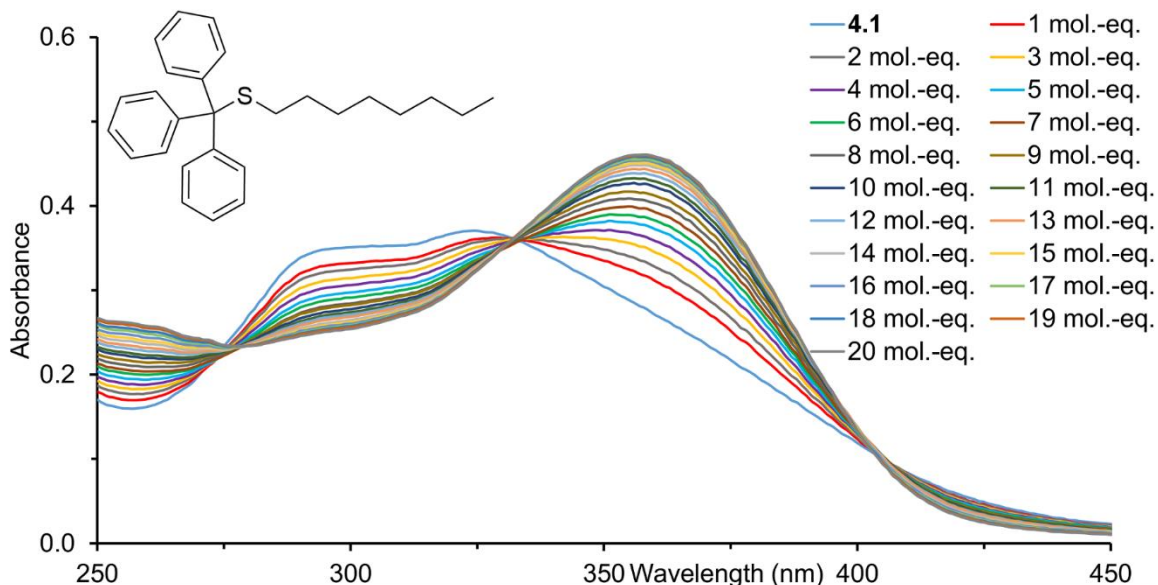


Figure 7.99: UV-Vis absorption spectrum of the titration of **5.1** into a 1.5 μM solution of cage **4.1** in CH_3CN . **5.1** was added in 1 μL aliquots from a 4.5 mM stock solution in CD_3CN .

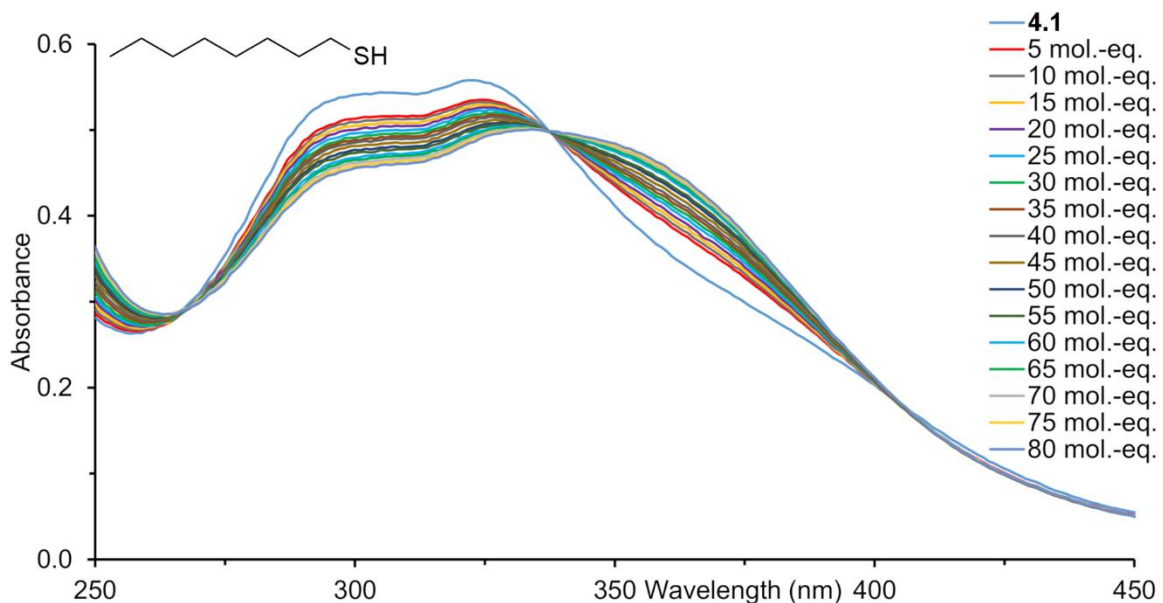


Figure 7.100: UV-Vis absorption spectrum of the titration of **OctSH** into a 3 μM solution of cage **4.1** in CH_3CN . **OctSH** was added in 1-5 μL aliquots from a 9 mM stock solution in CD_3CN .

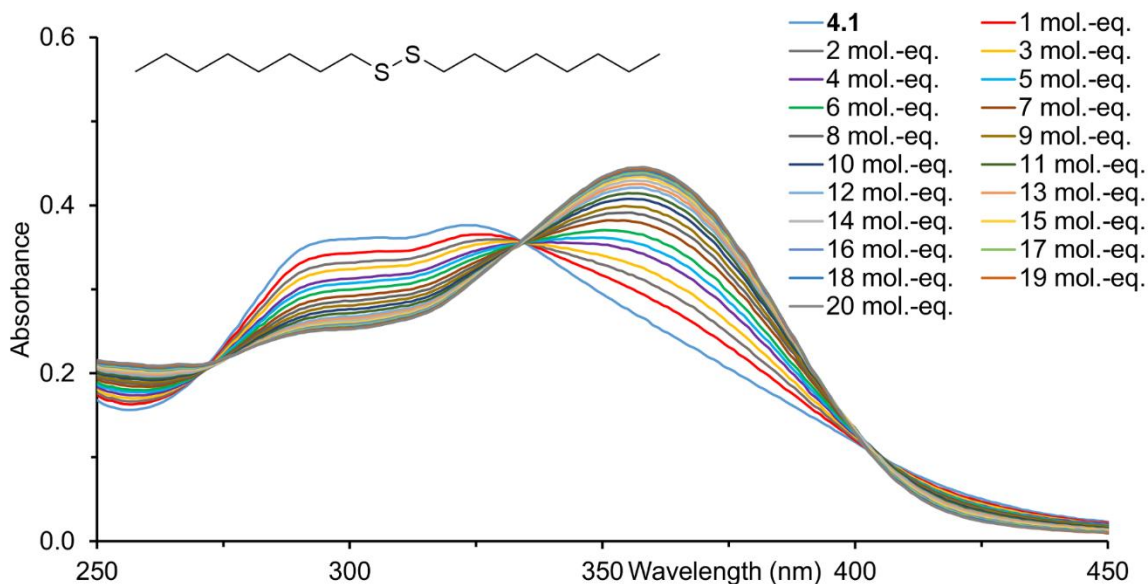


Figure 7.101. UV-Vis absorption spectrum of the titration of $(\text{OctS})_2$ into a 1.5 μM solution of cage **4.1** in CH_3CN . $(\text{OctS})_2$ was added in 1-5 μL aliquots from a 4.5 mM stock solution in CD_3CN .

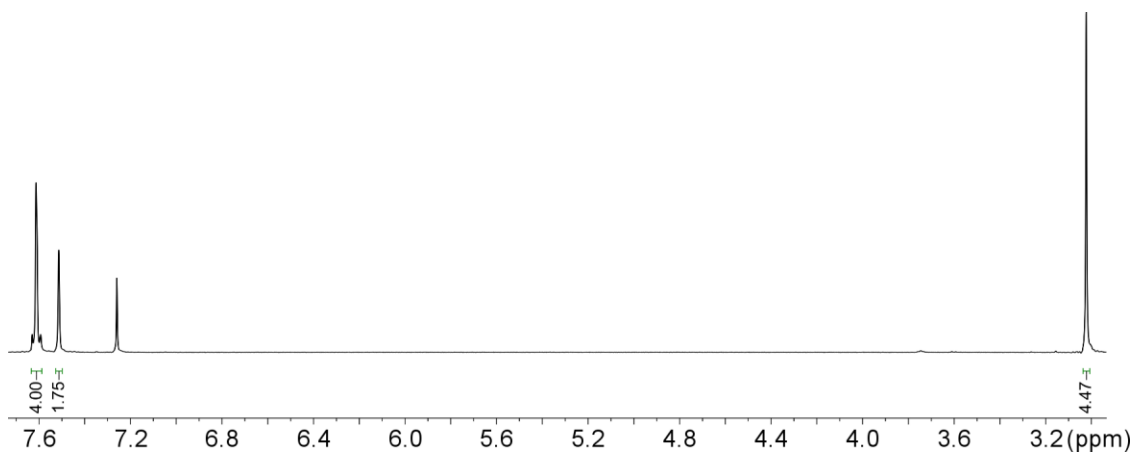


Figure 7.102. ^1H NMR spectrum of **5.4** (500 MHz, 298 K, CDCl_3).

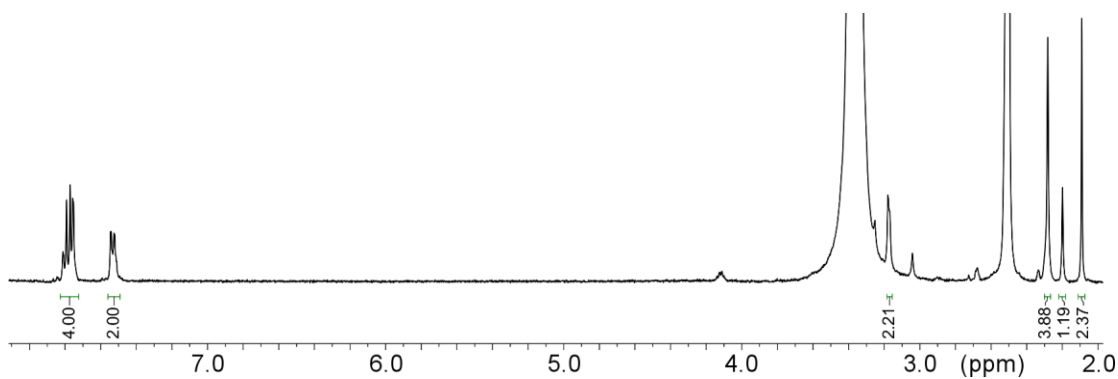


Figure 7.103. ^1H NMR spectrum of **5.3** (400 MHz, 298 K, $\text{DMSO}-d_6$).

7.11 Selected Spectra for Chapter 6

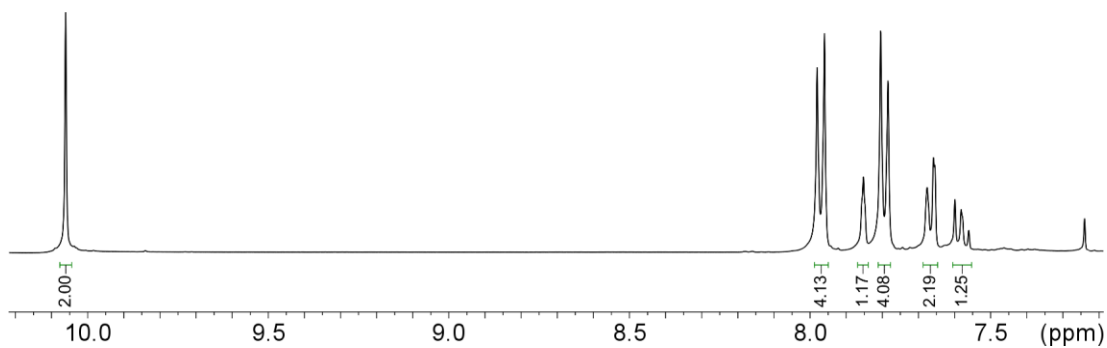


Figure 7.104. ¹H NMR spectrum of dialdehyde **6.A** (400 MHz, 298 K, CDCl₃).

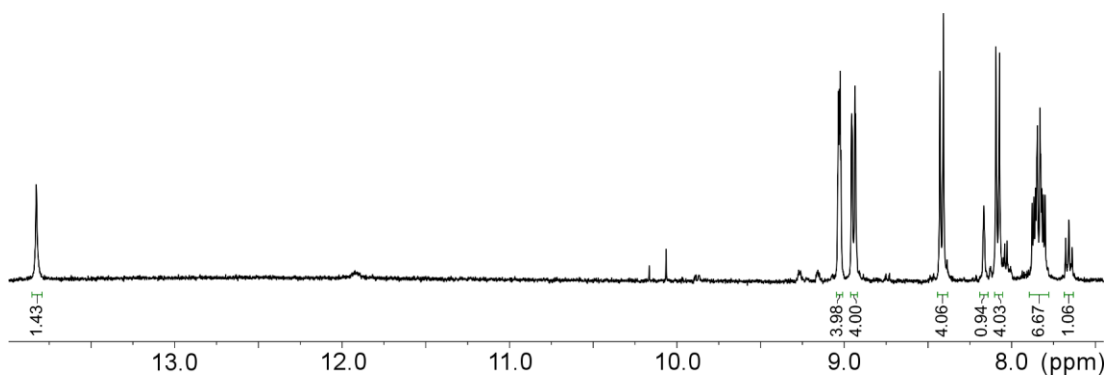


Figure 7.105. ¹H NMR spectrum of phenanthroline ligand **6.2** (400 MHz, 298 K, DMSO-*d*₆).

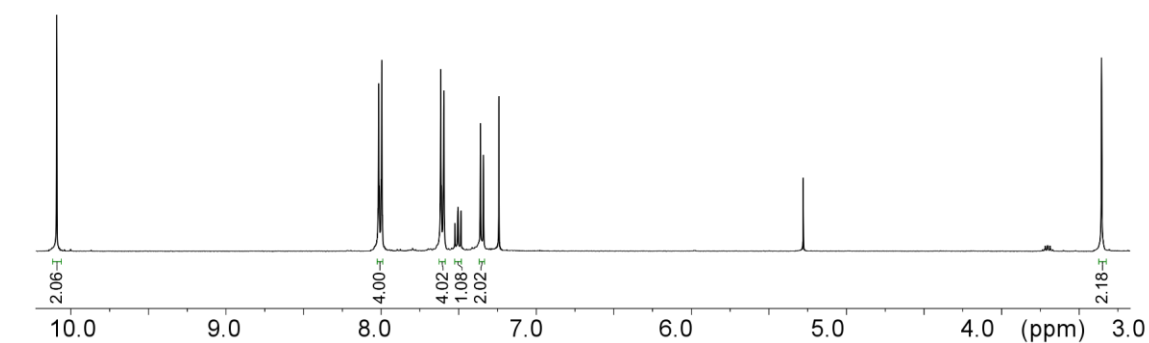


Figure 7.106. ¹H NMR spectrum of **6.B** (400 MHz, 298 K, CDCl₃).

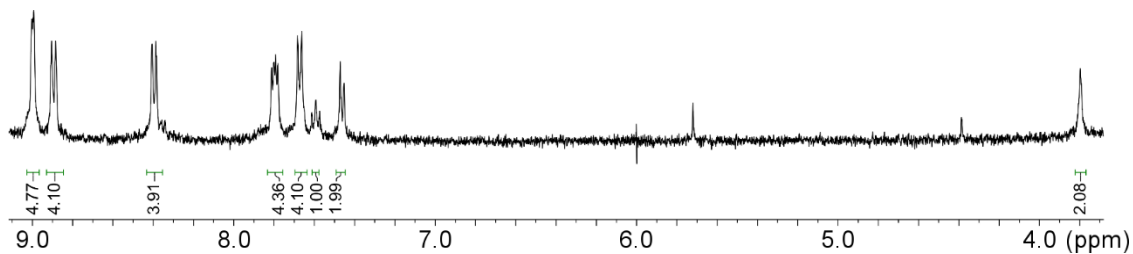


Figure 7.107. ¹H NMR spectrum of phenanthroline ligand **6.3** (400 MHz, 298 K, DMSO-*d*₆).

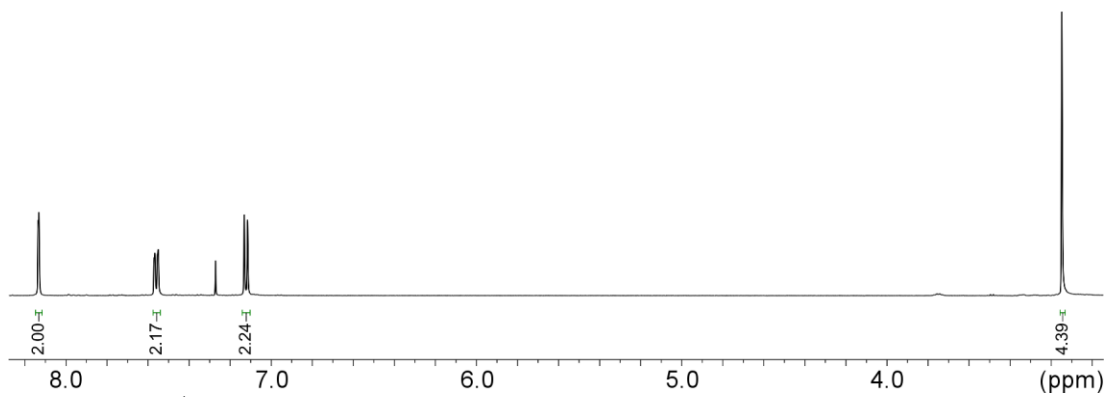


Figure 7.108. ¹H NMR spectrum of 3,7-dibromosuberone (500 MHz, 298 K, CDCl₃).

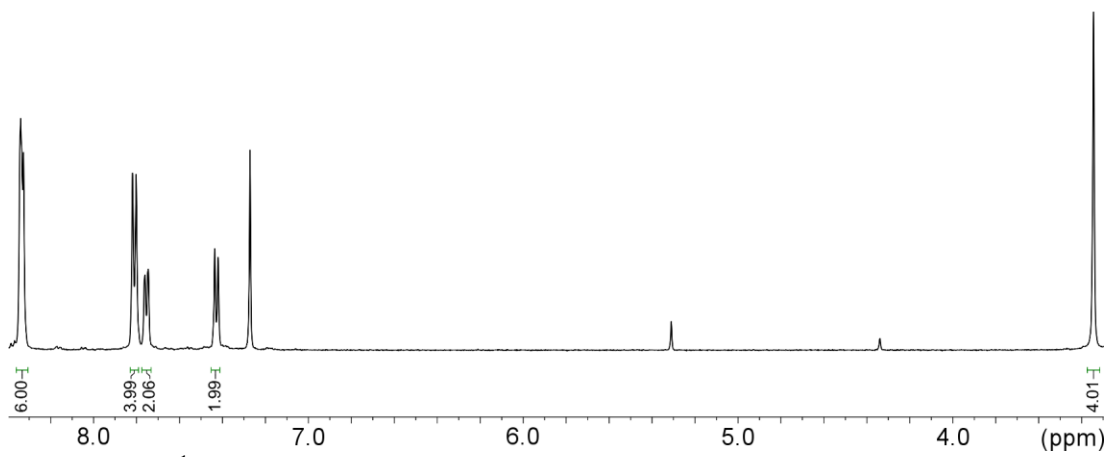


Figure 7.109. ¹H NMR spectrum of 7.5 (500 MHz, 298 K, CDCl₃).

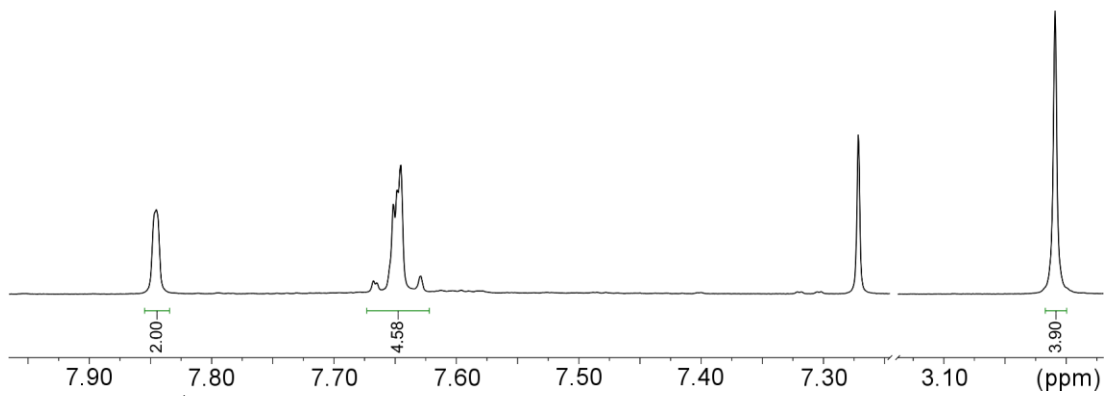


Figure 7.110. ¹H NMR spectrum of 6.D (500 MHz, 298 K, CDCl₃).

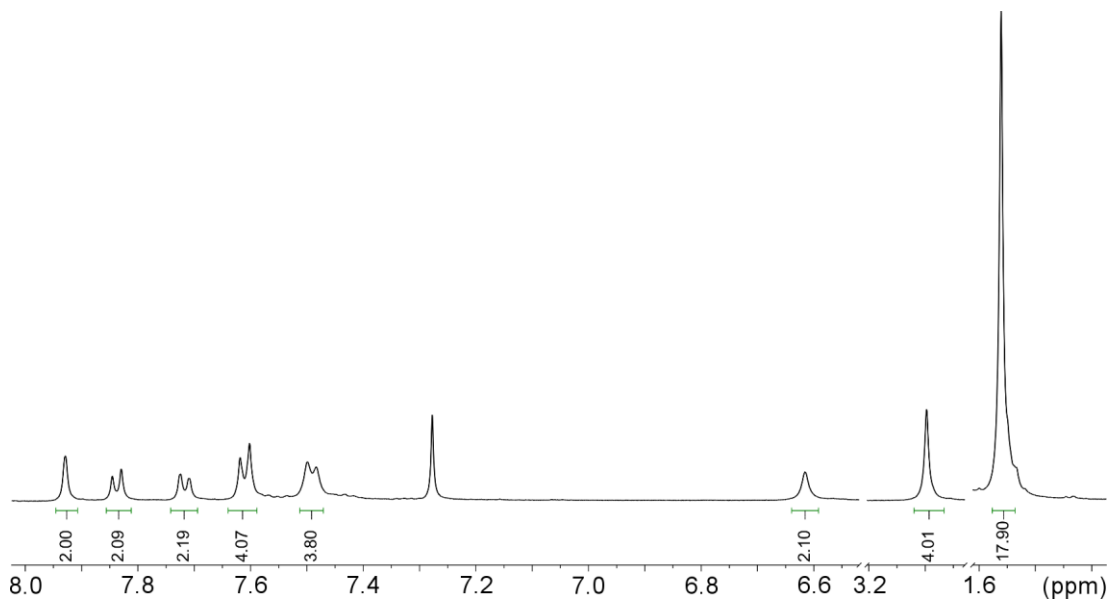


Figure 7.111. ^1H NMR spectrum of **7.6** (500 MHz, 298 K, CDCl_3).

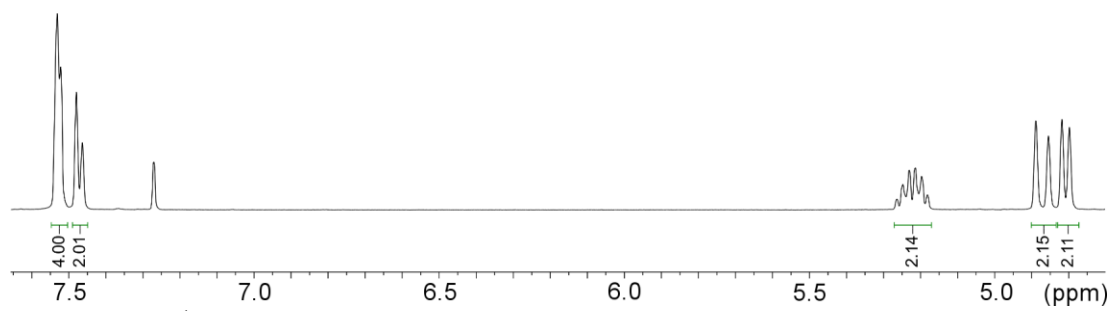


Figure 7.112. ^1H NMR spectrum of **6.E** (500 MHz, 298 K, CDCl_3).

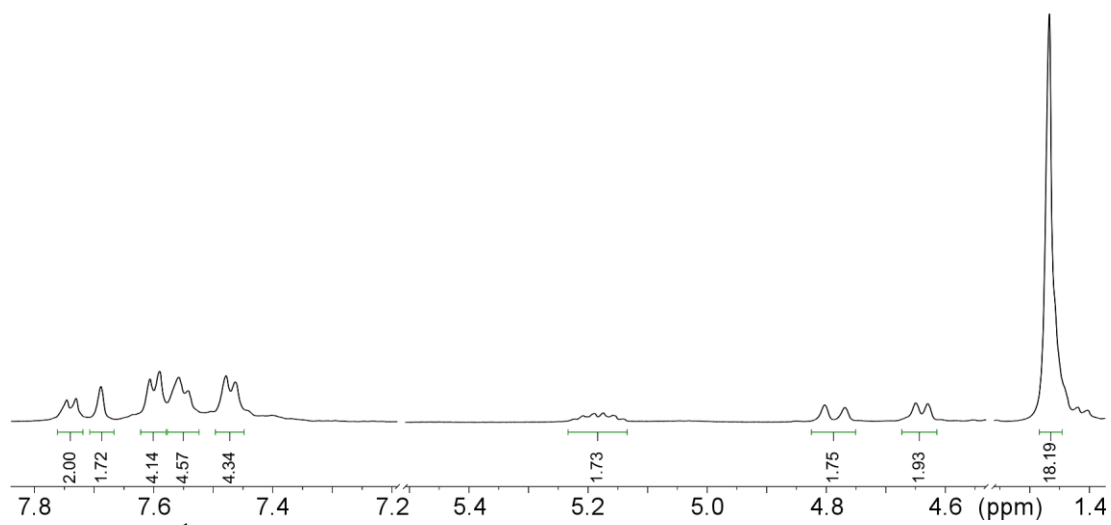


Figure 7.113. ^1H NMR spectrum of **7.7** (500 MHz, 298 K, CD_3CN).

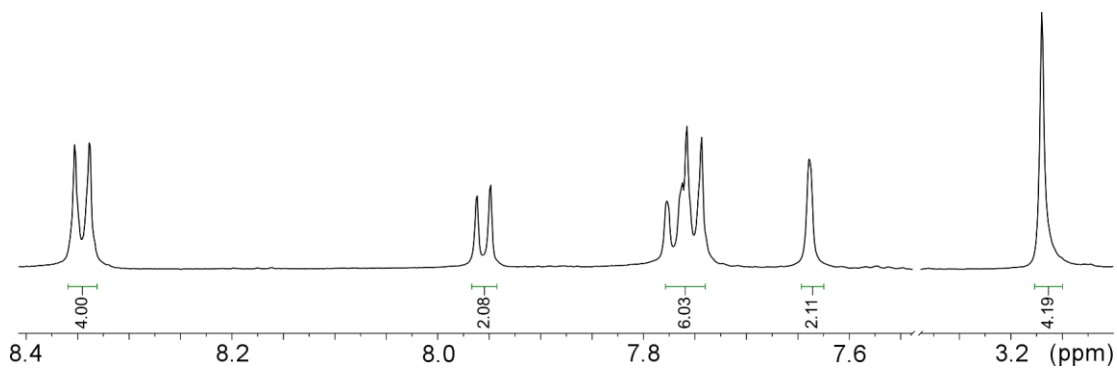


Figure 7.114. ^1H NMR spectrum of **6.F** (600 MHz, 298 K, CDCl_3).

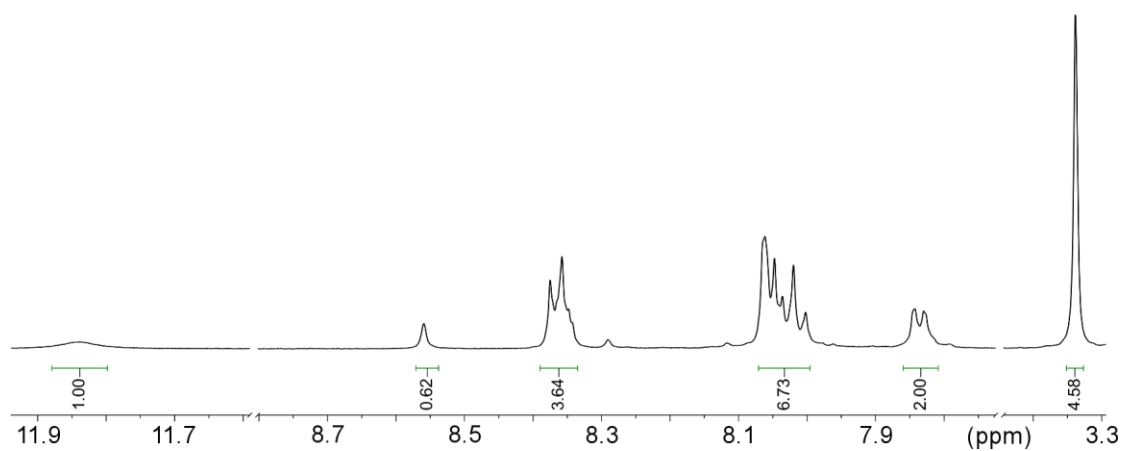


Figure 7.115. ^1H NMR spectrum of **7.8** (500 MHz, 298 K, $\text{DMSO}-d_6$).

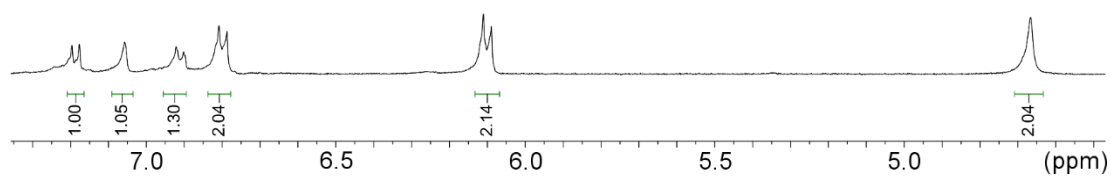


Figure 7.116. ^1H NMR spectrum of **6.4** (400 MHz, 298 K, CD_3CN).

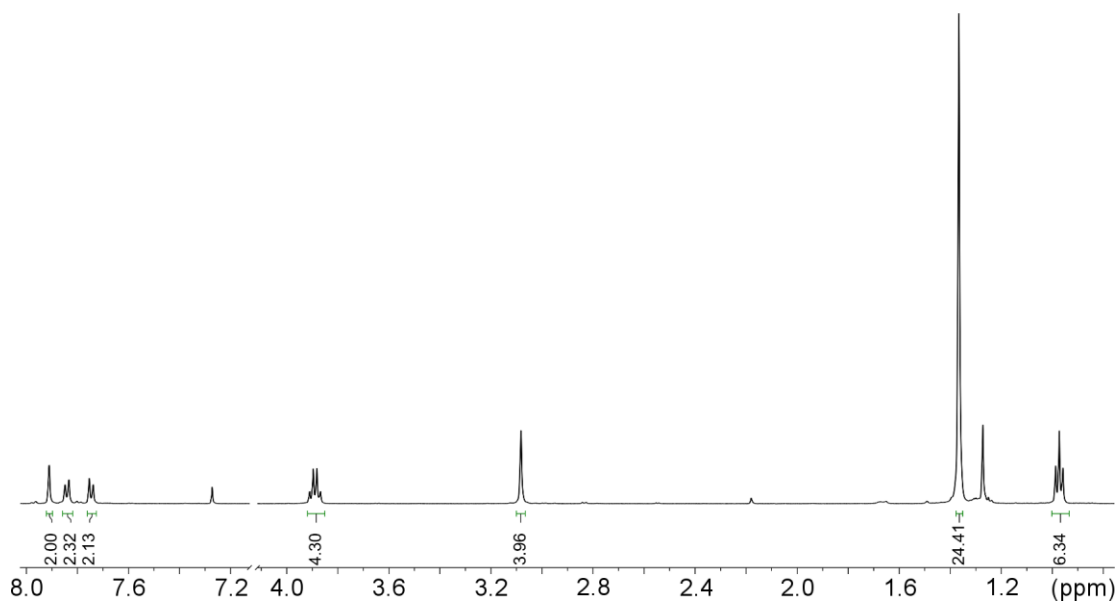


Figure 7.117. ^1H NMR spectrum of **7.G** (500 MHz, 298 K, CDCl_3).

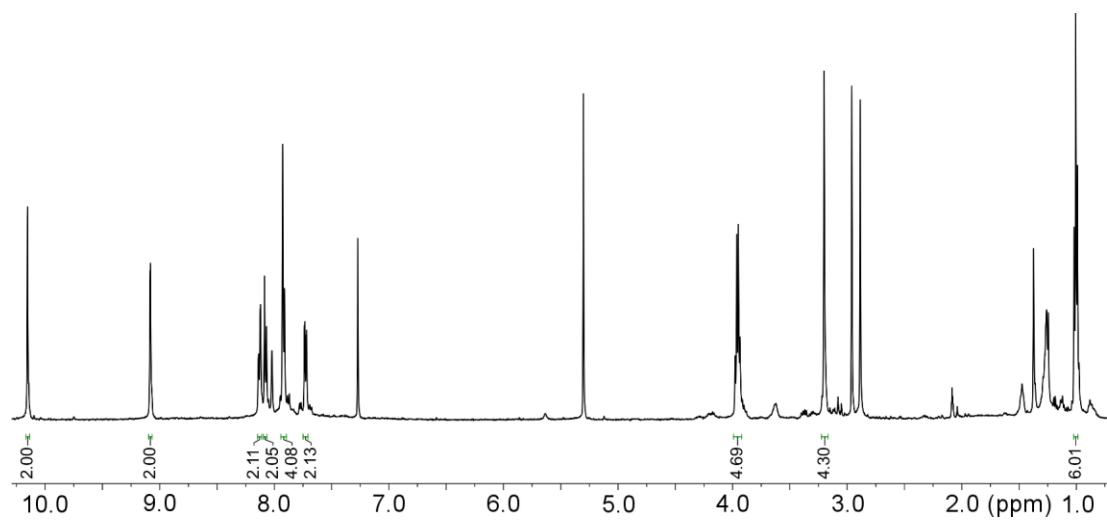


Figure 7.118. ^1H NMR spectrum of **6.5** (500 MHz, 298 K, CDCl_3).

7.12 References

1. Patiny, L.; Borel, A. "ChemCalc: A Building Block for Tomorrow's Chemical Infrastructure." *J. Chem. Inf. Model.*, **2013**, *53*, 1223–1228.
2. Dewar, M. J. S.; Zoebisch, E. G.; Healy, E. F.; Stewart, J. J. P. "Development and Use of Quantum Mechanical Molecular Models. 76. AM1: A New General-Purpose Quantum Mechanical Molecular Model." *J. Am. Chem. Soc.*, **1985**, *107*, 3902–3909; calculations performed on SPARTAN 06, Wavefunction Inc.
3. Robichaud, B.A.; Liu, K. G. "Titanium Isopropoxide/Pyridine Mediated Knoevenagel Reactions." *Tetrahedron Lett.* **2011**, *52*, 6935–6938.
4. Longstreet, A. R.; Campbell, B. S.; Gupton, B. F.; McQuade, D. T. "Improved Synthesis of Mono- and Disubstituted 2-Halonicotinonitriles from Alkylidene Malononitriles." *Org. Lett.* **2013**, *15*, 5298–5301.
5. Longstreet, A. R.; Jo, M.; Chandler, R. R.; Hanson, K.; Zhan, N.; Hrudka, J. J.; Mattoussi, H.; Shatruk, M.; McQuade, D. T. "Ylidenemalononitrile Enamines as Fluorescent "Turn-On" Indicators for Primary Amines." *J. Am. Chem. Soc.* **2014**, *136*, 15493–15496.
6. Ball, L. T.; Lloyd-Jones, G. C.; Russell, C. A. "Gold-Catalyzed Oxidative Coupling of Arylsilanes and Arenes: Origin of Selectivity and Improved Precatalyst." *J. Am. Chem. Soc.* **2014**, *136*, 254–264.
7. Cerrada, E.; Laguna, M.; Lardies, N. "Bis(1,2,3-thiadiazole)s as Precursors in the Synthesis of Bis(alkynethiolate)gold(I) Derivatives." *Eur. J. Inorg. Chem.* **2009**, *1*, 137–146.
8. Holloway, L. R.; Young, M. C.; Beran, G. J. O.; Hooley, R. J. "High fidelity sorting of remarkably similar components via metal-mediated assembly." *Chem. Sci.* **2015**, *6*, 4801–4806.
9. Young, M. C.; Holloway, L. R.; Johnson, A. M.; Hooley, R. J. "A supramolecular sorting hat: stereocontrol in metal–ligand self-assembly by complementary hydrogen bonding." *Angew. Chem. Int. Ed.* **2014**, *53*, 9832–9836.
10. Bilbeisi, R. A.; Clegg, J. K.; Elgrishi, N.; de Hatten, X.; Devillard, M.; Breiner, B.; Mal, P.; Nitschke, J. R. "Subcomponent Self-Assembly and Guest-Binding Properties of Face-Capped Fe₄L₄⁸⁺ Capsules." *J. Am. Chem. Soc.* **2012**, *134*, 5110–5119.
11. Hannon, M. J.; Painting, C. L.; Jackson, A.; Hamblin, J.; Errington, W. "An inexpensive approach to supramolecular architecture." *Chem. Commun.* **1997**, 1807–1808.

12. Thordarson, P. “Determining association constants from titration experiments in supramolecular chemistry.” *Chem. Soc. Rev.* **2011**, *40*, 1305–1323.
13. Wolfram_Research_Inc, Mathematica. 11.2, Wolfram Research, Inc., Champaign, Illinois 2017.
14. Press, W.H.; Teukolsky, S.A.; Vetterling, W.T.; Flannery, B.P. Numerical Recipes in C, 2nd edition, Cambridge University Press, Cambridge, 1992.
15. Garland, C. W.; Nibler, J. W.; Shoemaker, D. P. Experiments in Physical Chemistry, 8th ed.; McGraw-Hill Higher Education: Boston, MA, 2009.
16. Herrero, C.; Hughes, J. L.; Quaranta, A.; Cox, N.; Rutherford, A. W.; Leibl, W.; Aukauloo, A. “Intramolecular light induced activation of a Salen–Mn^{III} complex by a ruthenium photosensitizer.” *Chem. Commun.* **2010**, *46*, 7605–7607.